NEW INSIGHTS INTO PALEOPROTEROZOIC GRANULAR IRON FORMATION DEPOSITION AND PALEO-ENVIRONMENT FROM THE CA. 1.88 GA SOKOMAN IRON FORMATION, LABRADOR TROUGH

by © Gabriel P. Sindol, B.Sc. (Hons.)

A thesis submitted to the School of Graduate Studies

in partial fulfillment of the requirements for the degree of

Master of Science

Department of Earth Sciences

Memorial University of Newfoundland

August 2021

St. John's, Newfoundland and Labrador

ABSTRACT

The ca. 1.88 Ga Sokoman continental margin-type iron formation (IF) was studied by detailed mineral-chemical analyses of drill core to better understand tectonically stable, shallow-shelf marine environments of the late Paleoproterozoic. Suboxic (Fe-oxide-rich, including paragenetically early hematite) and anoxic (Fe-silicate/carbonate-rich) mineral paragenetic pathways operated during IF deposition; post-depositional alteration beyond late diagenesis/metamorphism was negligible. Chemostratigraphic variations in detrital element, rare earth element and yttrium (REE+Y), and redox-sensitive and nutrient-type trace element parameters, evaluated within a sequence-stratigraphic framework, were controlled by a combination of base-level fluctuations, terrigenous input, basin redox stratification, and microbial activity. The REE+Y in the Sokoman IF, like contemporaneous IF localities, exhibit several features reminiscent of modern seawater (LREE-depletion, small negative Ce anomalies, small positive La, Gd, and Y anomalies), but also strong positive Ce anomalies. This study reveals that the redoxcline was very shallow and likely spatially dynamic, producing separate Mn- and Fe-oxide shuttles controlled by different microbes. During Sokoman IF deposition, continental weathering of predominantly felsic Archean rocks under an oxygen-poor atmosphere and locally arid conditions limited the terrestrial supply of redox-sensitive and nutrient-type elements into the ocean, thus restricting the spatial extent of primary productivity to the photic zone of shallow-marine environments.

GENERAL SUMMARY

Iron-rich chemical precipitates (iron formation) accumulated in many shallow-marine environments roughly 1.88 billion years ago. Iron deposits of this age in the Labrador Trough, Canada, record valuable clues for understanding past oceanic and atmospheric conditions. Mineralogical and geochemical variations from these deposits, as reported here, reveal new insights into specific formation pathways of the iron minerals and better define overall controls on the genesis of iron formations due to changes in relative sea-level rise, continental sediment supply, oxygen levels in the shallow ocean and atmosphere, and microbial activity. Geochemical proxies reveal new details about the separation of upper, oxygen-bearing waters from deeper, oxygen-deficient waters in marine environments at the time, and the role that different microbes played in developing these conditions. Lower atmospheric oxygen levels relative to those of the present aided oceanic Fe accumulation but also limited supply of elements from the continents to the oceans that were essential for marine microbial activity.

ACKNOWLEDGEMENTS

The presented research would not have been possible without the assistance and guidance of many individuals. To the many people who I have encountered over the course of my Master's degree studies, you have my thanks for making it a truly enjoyable and fruitful endeavour. To my supervisor, Dr. Michael Babechuk, your dedication, enthusiasm, and passion for learning have instilled in me a yearning for challenging the unknown. Through your supervision, I have learned the value of hard work, perseverance, and the joys of eating döner kebabs. To my supervisory committee members, Dr. James Conliffe (Geological Survey of Newfoundland and Labrador) and Dr. John Slack (MUN; United States Geological Survey), your insights and many years of research experience have vastly improved the robustness of my interpretations. Furthermore, Dr. Conliffe provided the critical logistical support and arranged access to field outcrops and drill core samples. Both New Millennium Iron Corp. and Labec Century Iron Ore Inc. are thanked for permitting access and sampling of their drill cores.

To the members of the MUN-SEG Student Chapter, Babechuk Research Group, Piercey Research Group, and the Beranek Research Group, thank you for the camaraderie, endless banter, and many meaningful discussions.

To Dr. Ronny Schoenberg, Dr. Carolina Rosca, Dr. Stephan König, Dr. Frantz Ossa Ossa, Dr. Gülüm Albut, Dr. Heinrich Taubald, Dr. Ilka Kleinhanns, Bernd Steinhilber, Elmar Reitter, and other members of the Isotopengeochemie Group at the University of Tübingen, you have my sincere gratitude for accommodating me and allowing me the opportunity to conduct my work using your lab facilities and resources. These people have welcomed me with open arms and made my visits to Germany truly enjoyable.

Thanks are extended to the staff of the Department of Earth Sciences at Memorial University of Newfoundland and the CREAIT network for providing invaluable administrative and technical support, including Michelle Miskell, Keir Hiscock, Diane Guzzwell, Danyelle Drodge, Jane O'Neill, Matthew Crocker, Sherri Strong, Dr. Wanda Aylward, Dr. Geert Van Biesen, Dr. Inês Nobre Silva, Dylan Goudie, and Dr. David Grant.

To my closest friends and roommates, Adam, Aragorne, Calum, Jack, Jessica, Joud, Laura, Nick, and Stacey, thanks for the many fun shenanigans and for making the daily grind much more bearable. To my partner, Maya, your unwavering support has allowed me to overcome the many challenges that have come my way. You have been, and continue to be, a great source of inspiration in my life. To my parents, Roberta and Gerardo, thank you for always supporting all of my endeavours and for constantly showering me with your love and encouragement. Words cannot express how thankful I am for having been given such great parents.

Funding for this research was primarily provided by a Natural Sciences and Engineering Research Council of Canada (NSERC) Discovery Grant to Dr. Michael Babechuk. Supplementary funding was provided by a NSERC CGS-M Scholarship, a Society of Economic Geologists (SEG) Graduate Student Fellowship, and a MUN School of Graduate Studies F.A. Aldrich Fellowship to Gabriel Sindol. Additional funding for SEM-MLA work was provided by the Geological Survey of Newfoundland and Labrador.

TABLE OF CONTENTS

LIST OF FIGURES

Chapter 1

Chapter 2

LIST OF TABLES

Chapter 2

LIST OF ABBREVIATIONS

°C	degrees Celsius
μm	micrometer(s)
Ank	ankerite
Ap	apatite
BC	Black chert
BIF	banded iron formation
Cal	calcite
Ccp	chalcopyrite
ChmMg	chamosite + magnesium
DE	detrital element
DOL	Purdy dolomite
Dol	dolomite
EC	evolving upper continental crust
EF	enrichment factor
FWWB	fairweather wave base
FSST	falling-stage systems tract
Ga	giga annum; also billion years ago
GC	Green chert
GIF	granular iron formation
GOE	Great Oxidation Event
Gre	greenalite
GRGN	granitic gneiss

GXMAP	grain-based X-ray mapping
h	hour(s)
Hemag	hematite or magnetite
HFSE	high field strength elements
HL	Hayot Lake
HREE	heavy rare earth element
HST	highstand systems tract
ICP-MS	inductively coupled plasma mass spectrometry
IF	iron formation
JUIF	Jasper upper iron formation
JSP	Jaspilite
km	kilometer(s)
kV	kilovolt(s)
kW	kilowatt(s)
LC	Lean chert
LIF	Lower iron formation
LILE	large-ion lithophile element
Ln	lanthanide(s)
LOI	loss on ignition
LR	Lac Ritchie
LRC	Lower red chert
LRGC	Lower red green chert
LREE	light rare earth element

LST	lowstand systems tract
mfs	maximum flooding surface
min	minute(s)
MLA	mineral liberation analysis
Mns	minnesotaite
MREE	middle rare earth element
ms	millisecond(s)
MS	Menihek Formation
MuQ	Mud from Queensland
NQO	New Québec Orogen
OM	organic matter
Or	orthoclase
PGC	Pink grey chert
ppb	parts per billion (equivalent to ng/g)
ppm	parts per million (equivalent to µg/g)
Py	pyrite
Qz	quartz
Rbk	riebeckite
REY / REE+Y	rare earth elements and yttrium
RTH	Ruth Slate Member
sb	sequence boundary
Sch	scheelite
Sd	siderite

SdMn	manganoan siderite
SEM	scanning electron microscopy
SL	Sheps Lake
Stp	stilpnomelane
SWB	storm wave base
TE	trace element
THO	Trans-Hudson Orogen
Tlc	talc
ts	transgressive surface
TST	transgressive systems tract
URC	Upper red chert
VMS	volcanogenic massive sulfide
WQ	Wishart Formation
wt. %	weight percent
XRF	X-ray fluorescence

LIST OF APPENDICES

Appendix 8: Drill core Photographs and Thin Section Scans

CHAPTER 1: INTRODUCTION

1.1 Iron formations: An overview

Iron formations (IFs) are chemogenic sedimentary rocks composed of chert, Fe-silicates, Fe-oxides, and/or Fe-carbonates that are common in many Archean to Paleoproterozoic marine sequences (Bekker et al., 2010, 2014; Bekker and Kovalick, 2020; Konhauser et al., 2017; Pufahl and Hiatt, 2012). On the basis of depositional environments, IFs can be broadly divided into three categories, namely Algoma-, Superior-, and Rapitan-type. Algoma-type IFs are hosted in submarine-emplaced volcanic rocks typically located in greenstone belts, whereas Superior-type IFs occur in shallow-marine sequences deposited on continental margins (**Fig. 1.1**; Gourcerol et al., 2016; Gross, 1980, 1983). Superior-type IFs tend to be laterally extensive owing to their deposition in tectonically stable environments, and are typically interbedded with sandstone, black shale, and dolomite that unconformably overlie older basement rocks (Gole and Klein, 1981; Pufahl, 2010). However, due to genetic and textural complexities (e.g., IFs occurring in settings between those of Algoma- and Superior-type endmembers) involved with classifying Archean and Paleoproterozoic IFs, several workers favour a classification scheme that highlights depositional context rather than type localities (Bekker and Kovalick, 2020; Pufahl, 2010; Pufahl and Hiatt, 2012; Pufahl et al., 2014; Trendall, 2012). Instead of using the traditional Algoma- and Superior-type nomenclature, Pufahl (2010) proposed the use of exhalative- and continental margin-types, whereas Bekker and Kovalick (2020) advocated source-proximal (also exhalite-type) and source-distal (also plume-generated) criteria, respectively. In contrast, Rapitan-type IFs are associated with major Neoproterozoic glacial episodes and are inferred to have been deposited in partially restricted to completely isolated basins (Baldwin et al., 2012, 2016; Cox et al., 2013).

On a textural basis, IFs can be divided into banded iron formations (BIFs) and granular iron formations (GIFs) (Bekker et al., 2010, 2014; Konhauser et al., 2017). Banded iron formations are most common in Eoarchean to early Paleoproterozoic successions and are characterized by microbanding and thin laminations that indicate deposition below fairweather wave base (FWWB). Granular iron formations, which are prevalent in the late Paleoproterozoic, are distinguished by predominance of granules and pore-filling cements that suggest deposition in nearshore shelf environments (Bekker et al., 2010, 2014; Konhauser et al., 2017). As a consequence of these sedimentological differences, it has been proposed that BIFs likely originated as laminated chemical muds, whereas GIFs formed as well-sorted chemical sands (Simonson, 2003).

The widespread occurrence of IFs during the Precambrian reflects the predominance of anoxic and ferruginous conditions in Earth's early oceans (Planavsky et al., 2011; Poulton and Canfield, 2011). Owing to the wide spatio-temporal range of IFs, the relative timing of their appearance and disappearance in the rock record (**Fig. 1.2A**) has been used to infer concomitant changes in magmatic activity, nutrient fluxes, ocean chemistry, and by extension, atmospheric oxygenation (**Figs. 1.2B–G**; Bekker et al., 2010, 2014; Konhauser et al., 2017; Rasmussen et al., 2012), especially during the ca. 2.45–2.32 Ga Great Oxidation Event (GOE) (Holland, 2002, 2006; Lyons et al., 2014). Although the exact timing and duration of the GOE still remain points of contention (Gumsley et al., 2017; Lyons et al., 2014; Poulton et al., 2021), the application of geochemical proxies, primarily trace elements and stable metal isotopes, to IFs through time has provided new insights into Earth's interconnected systems in the Precambrian. For example, secular changes in Ni/Fe ratios of IFs have been linked to the timing and causation of the GOE (Konhauser et al., 2009, 2015). A marked decline in Ni/Fe ratios at ca. 2.7 Ga has been

interpreted to reflect a decrease in the oceanic Ni flux caused by a progressively cooling Archean mantle that limited the eruption of Ni-rich komatiitic volcanic rocks (Konhauser et al., 2009, 2015). Thus, the lower availability of Ni in Archean seawater drastically restricted the production of methane (CH_4) by methanogens, which ultimately permitted oxygenic photosynthesis to flourish (Konhauser et al., 2009, 2015). Moreover, many studies of IFs have utilized enrichments and related isotopic fractionations in other redox-sensitive trace elements including Cr (Frei et al., 2009; Konhauser et al., 2011), Mo (Planavsky et al., 2014), and U (Partin et al., 2013a) to deduce the timing and magnitude of other atmospheric oxygenation events. Secular changes across other biogeochemical systems have been constrained by studying the element abundances of bioessential trace elements in IFs including P (Bjerrum and Canfield, 2002; Konhauser et al., 2007; Planavsky et al., 2010a), Zn (Robbins et al., 2013), and Co (Swanner et al., 2014). Rare earth element (REE) patterns in IFs have long been used to infer redox conditions and solute sources in the early oceans (e.g., Bau and Dulski, 1996; Derry and Jacobsen, 1990; Graf, 1978; Kato et al., 2006; Planavsky et al., 2010b). Hence, IFs are extensively studied due to their ability to capture and generally preserve geochemical signatures across a wide spatio-temporal range, and their chemogenic nature and intrinsic association with surface oxygenation that enable these rocks to offer insights into the behaviour of elements in the ancient oceans and links with biological evolution (Bekker et al., 2010, 2014; Robbins et al., 2016; Konhauser et al., 2017).

1.2 Resurgence of iron formations at ca. 1.88 Ga

The temporary resurgence of voluminous IF deposition at ca. 1.88 Ga (**Fig. 1.2**; Bekker et al., 2010; Isley and Abbott, 1999; Konhauser et al., 2017) is primarily expressed in deposits

around the margins of the Superior Craton in North America, which includes the Animikie Basin and the Labrador Trough, as well as in the Earaheedy Basin in Western Australia (Bekker et al., 2010; Klein, 2005; Konhauser et al., 2017; Rasmussen et al., 2012; Simonson, 2003). This resurgence was subsequently followed by the cessation of IF deposition at ca. 1.85 Ga (excluding Neoproterozoic IFs associated with glacial episodes), implying a possible cause related to a distinct change in the redox state of the deep ocean (Slack and Cannon, 2009). The ca. 1.88 Ga GIFs are characterized by the precipitation of dissolved Fe(II) in shallow-water environments along continental margins, suggesting the need for a mechanism that accounts for a likely long-distance submarine transport of Fe(II) from the original source. One of the hypotheses on IF resurgence at ca. 1.88 Ga invokes pumping extensive amounts of hydrothermal Fe into the oceans during intense mantle plume activity (Bekker et al., 2010; Condie et al., 2000; Isley and Abbott, 1999; Reddy and Evans, 2009) and associated contributions from volcanogenic massive sulfide (VMS) hydrothermal systems (Isley, 1995), as suggested by coincident peaks in VMS deposits and IFs at ca. 1.88 Ga (Bekker et al., 2010; Konhauser et al., 2017). This influx of hydrothermal Fe(II) into the oceans inundated the marine oxygen and sulfate reservoirs of the deep ocean (Rasmussen et al., 2012). Another hypothesis involves a trigger caused by a decrease in atmospheric O_2 levels and a resulting limited oxidative weathering of the continents, inferred from a decrease in the oceanic U reservoir as recorded by IFs and black shales (Partin et al., 2013a, 2013b), and from the absence of positive Cr-isotope fractionation in the ca. 1.88 Ga Gunflint IF (Frei et al., 2009). A lower oxidizing potential of the atmosphere would have hampered the weathering of sulfide minerals on land and restricted sulfate delivery to the oceans, and thus permitted the development of ferruginous conditions in mid- to deep-water

environments. Both hypotheses invoke global, or at least regional, processes, and thus additional constraints that may be provided by the Sokoman IF are important to further testing these ideas.

1.3 Iron formations as tracers of ancient seawater composition

The intrinsic ability of IFs to track changes in ocean redox and element supply in the Precambrian ocean has been well documented (Robbins et al., 2016). Among the various marine sedimentary rocks capable of recording aspects of ocean chemistry at the time of deposition, IFs are especially favourable because the geochemical signatures they preserve can be discerned by studying adsorption reactions that occur at the surfaces of Fe(III)-oxyhydroxides in the modern environment and by relating those to compositionally similar precursor phases from which the IFs originally precipitated (Bjerrum and Canfield, 2002; Konhauser et al., 2007). By studying trace-element scavenging in modern Fe(III)-oxyhydroxides, models can be generated to relate the concentration of elements in the precipitate (IF) to the dissolved concentration of those in seawater at the time of IF deposition (Konhauser et al., 2009).

1.3.1 Barriers to extracting marine signatures from IFs

Despite the demonstrated utility of IFs, there are still several notable barriers to extracting marine signatures from these deposits. First, the original minerals that precipitated from seawater are not always known and as a result will change the inferred scavenging potential of different trace elements and isotopic signatures (Klein, 2005). For example, early studies posit that hydrous ferric or mixed ferro-ferric oxides (**Fig. 1.3**), derived from the oxidation of ferrous iron in the photic zone, were the original precursors to IF minerals (e.g., Cloud, 1968; Morris, 1993). However, many recent experimental and petrographic studies have proposed other primary

precipitates including Fe-silicates (Johnson et al., 2018; Muhling and Rasmussen, 2020; Rasmussen et al., 2013, 2014, 2016, 2017, 2021; Tosca et al., 2016), Fe-carbonates (Siahi et al., 2020), magnetite (Bauer et al., 2020), and the ferrous-ferric hydroxy salt, green rust (Halevy et al., 2017). Second, the primary Fe-rich minerals that precipitated from seawater and were deposited on the seafloor have undergone a complex sequence of diagenetic mineralogical changes, and all preserved IFs are modified further by varying degrees of metamorphic overprinting (Klein, 2005; Posth et al., 2013, 2014; Simonson, 2003). Consequently, it is not always clear from bulk-rock geochemical analyses to what extent authigenic marine signatures are retained through the various post-depositional complexities of diagenesis and metamorphism. In light of these complexities, several workers have attempted to determine phase-specific signatures in order to better understand marine signature preservation and pathways of alteration. Notably, these studies have included the use of sequential extraction strategies (Poulton and Canfield, 2005; Oonk et al., 2017, 2018), and physical isolation of distinct mineralogical-textural fractions, e.g., cutting out Si-rich (chert) and Fe-rich (Fe-oxide, Fe-carbonate) bands from the IF deposits (e.g., Baldwin et al., 2011). With respect to the physical isolation approach, the primary rationale is that relative to the Fe-rich fractions, early diagenetic chert is generally less amenable to post-depositional processes and is thus viewed as recording a purer seawater signature (Baldwin et al., 2011; Marin-Carbonne et al., 2014). However, an evident disadvantage is that relative to the Fe-rich fractions, chert has much lower trace element abundances. Consequently, chert is potentially more amenable to contamination by detrital (volcaniclastic or terrigenous) particles. In order to address this issue, Baldwin et al. (2011) demonstrated the use of exploratory laser ablation analyses to screen chert microbands and identify suitable sites (e.g., texturally

homogeneous, low detrital element abundances) for subsequent, lower-level and higher-precision, solution-based trace element analyses.

1.3.2 Rare earth elements and yttrium

Rare earth element plus yttrium (REE+Y) signatures are useful tools for tracing solute sources and understanding the depositional setting of IFs, as the unique REE+Y characteristics of modern seawater are well defined (Alibo and Nozaki, 1999; Byrne and Sholkovitz, 1996; German and Elderfield, 1990) and the preservation of these same signatures in IFs is generally agreed to record the contemporaneous seawater pattern from which they precipitated (Bau and Dulski, 1996; Bekker et al., 2010; Bolhar et al., 2004; Dymek and Klein, 1988; Kato et al., 1998; Kato et al., 2006; Konhauser et al., 2017; Planavsky et al., 2010b). Specifically, these features (**Fig. 1.4**) include (1) a relative depletion in light REE (LREE) relative to heavy REE (HREE) when normalized against the REE+Y source in a marine basin, which is often approximated as average upper continental crust due to continental weathering and riverine delivery being the primary marine REE+Y source (e.g., Nance and Taylor, 1976; Kamber et al., 2005; Pourmand et al., 2012); and (2) a series of 'anomalies' (over- or under-abundances), including positive La-Gd-Y, positive or negative Ce, and variably positive Eu, in shale-normalized REE+Y plots (Byrne and Kim, 1990; Byrne and Lee, 1993; Bolhar et al., 2004; De Baar et al., 1985). The combined La-Gd-Y anomalies are diagnostic of marine affinity, and the Ce and Eu anomalies, discussed below in detail, are useful tracers of oxygenation and hydrothermal element sources, respectively (Bolhar et al., 2004). The underpinning assumption is that negligible REE+Y fractionation exists from seawater into IFs during deposition and post-depositional alteration (Bau, 1993; Bekker et al., 2010; Haugaard et al., 2016). The marine REE+Y pattern inherited in IFs is also amenable to

modification by addition of detrital material enriched in REE+Y relative to IFs, which acts to increase the LREE/HREE ratio and dampen the aforementioned anomalies. However, this detrital contamination can be monitored with abundances of relatively insoluble elements (e.g., Al, Ti, Zr, Th, Hf, Sc) to either screen for the least-contaminated samples to use for interpretation, or to correct for the detrital influence via a two-component mixing relationship (Alexander et al., 2008). Finally, IFs extensively altered by hypogene- and/or supergene processes (e.g., Angerer et al., 2013; Conliffe, 2015, 2016) have disturbed REE+Y patterns and are generally avoided, or only used with caution, for inferring ancient marine redox conditions (Bau, 1993). The additional importance of identifying preserved marine REE+Y anomalies (LREE/HREE depletion, La-Gd-Y) in IFs arises because these anomalies are often also used as a test for the authigenic nature of other trace-element and isotopic signatures.

Large positive Eu anomalies in marine chemogenic sediments are generally used to indicate strong influence from reduced, high-temperature hydrothermal fluids (Danielson et al., 1992; German et al., 1993; Klinkhammer et al., 1994; Konhauser et al., 2017; Viehmann et al., 2015). The presence of positive Eu anomalies in modern hydrothermal vent fluids is a consequence of the breakdown of plagioclase in footwall volcanic rocks, as plagioclase exhibits greater compatibility in Eu(II) relative to other trivalent REEs (Fryer et al., 1979; Graf, 1978) and subsequent mobilization of Eu(II) at high T (>250 °C) and low pH under reducing conditions (Bau, 1991; Michard, 1989). The presence of large positive Eu anomalies in Precambrian IFs implies precipitation from seawater that incorporated a significant hydrothermal component (Alexander et al., 2008; Danielson et al., 1992). Secular changes in the magnitude of Eu anomalies in IFs generally decreased from the Archean through the Proterozoic, suggesting that hydrothermal fluids were major contributors to the REE+Y budget of Archean seawater

(Danielson et al., 1992; Derry and Jacobsen, 1990; Konhauser et al., 2017; Planavsky et al., 2010b; Viehmann et al., 2015).

Large negative Ce anomalies generally manifest in oxic marine conditions and are attributed to the oxidation of Ce(III) to Ce(IV), which greatly reduces its solubility and leads to preferential adsorption onto Mn(IV)-Fe(III) oxyhydroxides, clays, and organic matter and results in the surrounding water column being depleted in Ce (Byrne and Sholkovitz, 1996; German and Elderfield, 1990; Klein, 2005). In contrast, suboxic and anoxic waters generally lack significant negative Ce anomalies due to release of Ce during the dissolution of settling Mn(IV)-Fe(III) oxyhydroxide particles under reducing conditions (Byrne and Sholkovitz, 1996; German and Elderfield, 1990; German et al., 1991). It has been observed that many Archean and early Paleoproterozoic IFs lack pronounced Ce anomalies, which suggests that deposition took place under suboxic to anoxic conditions, whereas examples from the late Paleoproterozoic, such as the ca. 1.88 Ga Biwabik and Gunflint IFs, consistently exhibit both small negative or large positive Ce anomalies (Planavsky et al., 2010b). The occurrence of these positive Ce anomalies has been attributed to an oxide shuttle across a strong redoxcline, resulting in the reductive dissolution of Mn-oxyhydroxide particles and remobilization of REEs, especially Ce and Ho, relative to Y (Planavsky et al., 2010b). Consequently, Fe-oxyhydroxides then capture the REE+Y signatures of this process and manifest as large positive Ce anomalies, low Y/Ho ratios, and a wide range of LREE/HREE ratios, relative to those of Archean and early Paleoproterozoic IFs (**Fig. 1.4**; Planavsky et al., 2010b).

1.3.3 Redox-sensitive and nutrient-type trace elements and redox thresholds

Redox-sensitive and nutrient-type trace element (TE) enrichments, including those of Cr, V, U, Ni, Co, and Zn, are widely used as tools for reconstructing past ocean and atmosphere conditions owing to differences in aqueous behaviour as a function of many factors including, but not limited to, biological uptake, thermodynamics, solution chemistry, redox, and pH conditions (Algeo and Li, 2020; Bennett and Canfield, 2020; Tribovillard et al., 2006). Normalization of authigenic TE enrichment values is typically conducted to account for detrital effects and differences in basin composition or depositional environment (Tribovillard et al., 2006). Most studies employ the use of enrichment factors (EFs), wherein TE concentrations of a given sample are doubly normalized to both detrital element (DE) concentrations and an upper crustal average such as Post-Archean Australian Shale (PAAS) or Mud from Queensland (MuQ), as shown in **Eq. 1.1**. Samples with TE_{EF} values greater than 1 are considered enriched, whereas values less than 1 are considered depleted. In cases where local basin effects exert a strong influence on trace element compositions of contained sediments, the use of a local shale average is preferred (e.g., Albut et al., 2018).

$$\mathbf{TE_{EF} = [(TE/DE)_{sample}] / [(TE/DE)_{upper\ crustal\ average}]} \qquad \mathbf{(1.1)}$$

In determining paleoredox conditions, most geochemical studies employ the oxic-suboxic-anoxic/ferruginous/euxinic classification scheme that broadly corresponds to strong gradients in ambient oxygen levels and dominant biological respiration processes (Algeo and Li, 2020; Canfield and Thamdrup, 2009). For example, waters where oxygen levels are high and aerobic respiration is predominant are considered oxic. In contrast, waters having very low oxygen levels and where nitrate reduction, Mn-reduction, and Fe-reduction dominate, are considered suboxic. Furthermore, areas with no appreciable dissolved oxygen and where sulfate

reduction and methanogenesis are dominant are considered anoxic. Anoxic water-column conditions are further subdivided into euxinic and ferruginous conditions depending on the predominance of either H_2S and Fe(II) in solution, respectively. However, significant overlaps between these zones generate inconsistencies in the interpretation of water-column redox (see Canfield and Thamdrup, 2009). Consequently, Algeo and Li (2020), proposed a revision to this classification scheme in which the suboxic zone is subdivided into a 'truly suboxic' suboxidized zone with low dissolved oxygen and an 'anoxic-ferruginous' subreduced zone with no dissolved O_2 or H_2S. In the context of TEs evaluated in the present study, relevant redox couples are positioned within the following zones: (1) Co^{3+} to Co^{2+} and Cr^{6+} to Cr^{3+} in the suboxidized zone, (2) V^{5+} to V^{4+} and U^{6+} to U^{4+} in the upper and lower subreduced zones, respectively, and (3) Ni^{2+} to Ni^0 and Zn^{2+} to Zn^0 in the euxinic zone. Variable coupling in TE enrichments could thus be used to infer paleoredox conditions (Algeo and Liu, 2020; Tribovillard et al., 2006). For instance, strong authigenic V and U enrichments without comparable degrees of authigenic Ni and Zn enrichments may point to deposition under primarily subreduced conditions. However, inferences on water-column redox necessitate evaluation of other factors that influence the magnitude of authigenic TE enrichments such as paleoproductivity (e.g., Schoepfer et al., 2015).

1.4 Objectives and original contributions

1.4.1 New geochemical, mineralogical, and sedimentological constraints on the Sokoman IF

Research conducted on the Sokoman IF in the past decade has focused on elucidating various geochemical (Chung et al., 2015; Cunningham et al., 2012, Raye et al., 2015), mineralogical (Chung et al., 2015, Cunningham et al., 2012), and sedimentological (Edwards et al., 2012; Pufahl et al., 2014) aspects of its deposition. Earlier studies, conducted in the 1970s

and 1980s, focused on constraining the depositional environment and complex alteration pathways that led to the genesis of this IF, in light of its significance as an exceptionally well-preserved example of a continental-margin, granular-type IF (e.g., Dimroth and Chauvel, 1973; Fryer, 1977; Klein and Fink, 1976; Zajac, 1974). However, despite the pioneering and recent work on the Sokoman IF to date, this unit remains sparsely investigated relative to other ca. 1.88 Ga IFs in terms of a modern, multi-geochemical proxy strategy, such as by combining high-precision REE+Y data with results for other TEs (e.g., Cr, Mo, U, V, Ni, Co, Zn) and stable isotopes (e.g., Cr, Mo, U). These geochemical proxies are known to elucidate a number of important paleo-environmental and paleo-depositional aspects of IF genesis, and those of ancient ocean-atmosphere-lithosphere evolution. However, no recent studies have sought to establish in-depth links between the mineralogy and sedimentology of the Sokoman IF with these new geochemical proxies. Establishing these links are also hindered by the paucity of modern mineralogical data on the IF using techniques such as scanning electron microscopy-mineral liberation analysis (SEM-MLA). The development of SEM-MLA was driven, in part, by the study of iron ore (Grant et al., 2016, 2018) as a tool to rapidly assess ore grade using modal mineralogy (abundances of different oxide phases and non-oxide phases). Moreover, no publications to date have revisited the Sokoman IF using this technique to quantitatively document the mineralogical variations across IF facies; such a quantitative mineralogical baseline is especially important for texturally complex GIFs like the Sokoman IF. By contrast, the occurrence of banding in BIFs permits mineralogical-geochemical associations to be established with relative ease (e.g., Alibert, 2016; Haugaard et al., 2016).

This study aims to provide one of the first comprehensive geochemical-mineralogical-sedimentological datasets on the Sokoman IF with the aim to inform a number of targeted

scientific issues from sample- (**Section 1.4.2**) to basin- (**Section 1.4.3)** scale. New data reported here are evaluated in the geological context of the sampled drill cores and the wider basinal setting, and through comparisons with better-studied contemporaneous deposits (e.g., Animikie Basin, Lake Superior region), as well as in the context of broader constraints from other surface and marine environments of the Paleoproterozoic Earth.

1.4.2 Isolating the purest seawater signatures

Owing to the overprinting effects of post-depositional processes, it is important to select the IF samples that record the purest, authigenic marine signatures in order to focus geochemical proxies on interpretations of depositional signatures. In this study, a combined bulk sampling and sub-sampling approach is applied. Specifically, where possible, Si-rich fractions of intraformational chert are targeted for physical extraction from the bulk sample to examine their isolated geochemical signatures and compare to the bulk IF signatures. This approach is rarely undertaken on GIFs due to textural complexity and the absence of prominent microbanding as exists in BIFs. Nevertheless, the sub-sampling of intraformational chert is hypothesized to provide a test of whether specific Si-rich phases are more robust tracers of marine signatures, relative to the bulk rock, or if more Fe-rich fractions are better in GIFs. Furthermore, these subsamples target uniformly microcrystalline chert because coarsely recrystallized chert may not necessarily record primary seawater signatures (Maliva et al., 2005; van den Boorn et al., 2007). Determining which of these two fractions provides purer marine signatures will involve the use of major element data including Si (to confirm the effectiveness of physically extracting chert), and detrital element signatures (to monitor detrital contributions), as well as trace element data, specifically REE+Y.

1.4.3 Inferring basin paleoredox conditions at ca. 1.88 Ga

The presence of both small negative to large positive Ce anomalies in ca. 1.88 Ga IFs (Planavsky et al., 2010b) remains an important discovery that highlights their importance as the first IFs to preserve unambiguous evidence for Mn-Ce cycling across a (Fe/Mn) redox-stratified ocean. Evidence for an earlier occurrence of basin redox stratification owing to shallow oxygen oases (i.e., localized oxygenation of surface waters induced vertical stratification) has been proposed, based on (1) shifts in Fe-isotope values and elevated U concentrations in proximal (relative to the shelf), shallow-water BIF facies (Satkoski et al., 2015); (2) negative Ce anomalies in platform carbonates (Riding et al., 2014); (3) depth-related variations in Mo and Re concentrations and Fe_{HR}/Fe_T ratios in a carbonate platform margin (Kendall et al., 2010); (4) positive correlations between Fe/Mn ratios and Mo-isotope fractionation in BIF (Planavsky et al., 2014); and (5) Mo- and Fe-isotope fractionations, and Mn-enrichment in Fe-, Mn-, and carbonate-rich shales (Ossa Ossa et al., 2018; Planavsky et al. 2018). However, the younger Paleoproterozoic examples ideally serve to further examine some of these proxies in a basin where Ce anomalies provide direct evidence for a Mn-redoxcline, since Ce anomalies are absent in several of the aforementioned examples. Thus, one objective of this study is to better constrain the complex redox architecture of the global ocean at ca. 1.88 Ga via geochemical data on the Sokoman IF, and to compare and contrast these results with those from contemporaneous IFs and from older Proterozoic and Archean IFs in similar depositional environments. Following the approach employed by Planavsky et al. (2010b), this study makes use of REE+Y systematics, specifically Y/Ho ratios, Ce anomalies, and REE+Y patterns, in association with ratios and

enrichment factors of Fe and Mn, but also extends these data to redox-sensitive and nutrient-type trace elements found useful in IF studies (e.g., Baldwin et al., 2012).

1.4.4 Generating a baseline for understanding the evolution of IF to iron ore deposits

Given the economic importance of high-grade (> 55 wt.% Fe) iron ore deposits hosted in the Sokoman IF in the Labrador Trough (Conliffe, 2014, 2015, 2016), a further objective of this study is to establish a comprehensive mineralogical-geochemical baseline that can be used as a guide to better understand the complex alteration pathways that occurred during hypogene and/or supergene alteration of the IF. For example, in addition to the use of stratigraphic marker units and some bulk mineralogical differences between more silicate-rich (e.g., Lean Chert) vs. oxide-rich (e.g., Jasper Upper Iron Formation) stratigraphic units, it is possible that some geochemical signatures in the pristine Sokoman IF are also preserved in highly altered equivalents. For instance, high-grade iron ore deposits in the eastern Labrador Trough, which are composed of massive to laminated hematite-rich rock (Conliffe, 2015), exhibit a strong depletion in Si, Mg, Ca, and Na, and enrichment in Fe, Mn, and P, whereas Al and Ti show variable enrichment. Further analyses of other high field strength elements (HFSEs) such as Zr, Nb, Hf, Ta, and Th, can be conducted to identify the least mobile elements within the high-grade iron ore deposits, the altered IF (altered zones that surround the ore bodies), and the pristine Sokoman IF. In doing so, more robust mass balance calculations can be done to determine the relative enrichments and depletions of various trace elements in the highly altered equivalents, relative to the pristine Sokoman IF (this study). A better understanding of their enrichments and depletions could potentially be used to correlate units across imbricated fault blocks and thus act as vectors toward other high-grade iron ore deposits. In addition, many published datasets for both the

altered and pristine Sokoman IF lack results for several important elements, either due to analytical limitations or contamination caused by steel (e.g., Cr, Ni) or tungsten carbide (e.g., Co, Mo, Ta, W) milling. Thus, the new and more comprehensive data can be used to establish an initial set of observations for any future work aiming to better reconstruct the phase-specific alteration progression that occurred during Si-loss and further Fe-oxidation associated with post-depositional fluid alteration of the least-altered IF.

1.4.5 Provision of high-precision trace element data for IF reference materials (RMs)

Despite the ever-growing interest in IFs and their use as proxies for the composition and evolution of ancient oceans and atmospheres, there remains an apparent scarcity of available IF reference materials for quality assurance/quality control (QA/QC). Furthermore, the high Fe concentrations and low trace element abundances in most IFs pose an analytical challenge that necessitates the use of IF RMs to minimize analytical uncertainties, including matrix effects and inter-element interferences (Dulski, 1992). Among the few IF RMs with published trace element values, only IF-G is still commercially available. Formerly, RMs FeR-1 to FeR-4 (produced by Canada Centre for Mineral and Energy Technology, CANMET), and in particular FeR-3 and FeR-4, were used for QA/QC in IF studies (Bau and Alexander, 2009; Dulski, 1992, 2001; Govindaraju, 1994; Sampaio and Enzweiler, 2015), but have since been discontinued. The IF RM IF-G has been used in many studies, but it suffers from Co, Ta, and W contamination as a result of tungsten carbide milling (Govindaraju, 1984). This standard is also slightly heterogeneous in concentrations of these elements, generating problematic instrumental washout issues, particularly for W (e.g., see Babechuk et al., 2010) and as a result, is often avoided. Natural Resources Canada (NRCan) recently produced IOC-1, a certified iron ore RM sourced

from the Iron Ore Company of Canada's (IOC) operations in Labrador City, Newfoundland and Labrador. However, most trace element values for this RM are uncertified, still being provisional (S, V, Co, Sr, Mo), semi-quantitative (Cu, Ga, Ba, Ce), or unmeasured/unreported (e.g., Ni, Zn, Nb, Sn, Sb, Ta, W, Th, U, and REY excluding Ce). One objective of this project is to provide new trace element data for FeR-3 and FeR-4, in recognition that many laboratories may still use these RMs, as well as to report new data to better characterize IOC-1. In addition to aiding with QA/QC in the form of precision estimates for low-level trace elements in Fe-rich matrices, these new IF RM data will be compared to published or certified values in order to evaluate the method accuracy, where possible, and provide data for future inter-laboratory method evaluation.

1.5 Organization of thesis

The presented thesis is divided into three main chapters corresponding to the introduction (Chapter 1), main findings (Chapter 2), and synthesis of the study (Chapter 3). Chapter 1 provides a brief overview of IFs, their genetic and textural classifications, spatio-temporal distribution, and importance in reconstructing past ocean-atmosphere redox conditions and biogeochemical cycles. This chapter also outlines several important paleo-redox proxies as applied to IFs, and their consequent implications to the interpretation of ancient seawater composition. Importantly, the significance of ca. 1.88 Ga IFs, specifically the Sokoman IF in the Labrador Trough, is presented in this chapter, together with the objectives and the original contributions that stem from this study.

The contents of Chapter 2 are written as a manuscript entitled "**Shallow-ocean and atmospheric redox signatures preserved in the ca. 1.88 Ga Sokoman iron formation, Labrador Trough, Canada**", to be submitted to *Precambrian Research*, and is co-authored

with Dr. Michael Babechuk, Dr. James Conliffe, Dr. John Slack. Dr. Carolina Rosca, and Dr. Ronny Schoenberg. Specific contributions to this manuscript are outlined in **Section 1.6**. This manuscript presents a novel and comprehensive mineralogical-geochemical-sedimentological dataset on previously uninvestigated occurrences of the Sokoman IF. The implications of this new dataset are discussed in the context of existing data from other localities, with extended comparisons to correlative sequences within the Labrador Trough, and in the Animikie Basin, Lake Superior region.

Chapter 3 summarizes the overall thesis and lays out the many future potential avenues of research that can be taken to build upon this study, thereby refining our understanding of oceanic and atmospheric conditions at ca. 1.88 Ga.

1.6 Co-Authorship Statement

The first author (thesis author) was responsible and involved with all stages of the project including manuscript writing, literature review, fieldwork, sample collection and preparation, and mineralogical and geochemical analyses. The first author's supervisor, Dr. Babechuk, conceived the research and provided primary funding to the project through his NSERC Discovery Grant. The first author's supervisory committee (Dr. Babechuk, Dr. Conliffe, Dr. Slack) provided invaluable assistance with fieldwork, sample collection, and most importantly, feedback and supervision. Dr. Rosca and Dr. Schoenberg supplied the means to conduct major and ultra-trace element geochemical work at the University of Tübingen, Germany, by providing access to their lab resources and instruments. Dr. Rosca also aided with geochemical analyses and subsequent data reduction. All listed co-authors contributed to the formal review and editing process of the manuscript.

1.7 References Cited

Albut, G., Babechuk, M.G., Kleinhanns, I.C., Benger, M., Beukes, N.J., Steinhilber, B., Smith, A.J.B., Kruger, S.J., Schoenberg, R., 2018. Modern rather than Mesoarchaean oxidative weathering responsible for the heavy stable Cr isotopic signatures of the 2.95 Ga old Ijzermijn Iron Formation (South Africa). Geochimica et Cosmochimica Acta 228, 157–189. https://doi.org/10/gdb3mg

Alexander, B.W., Bau, M., Andersson, P., Dulski, P., 2008. Continentally-derived solutes in shallow Archean seawater: rare earth element and Nd isotope evidence in iron formation from the 2.9 Ga Pongola Supergroup, South Africa. Geochimica et Cosmochimica Acta 72, 378–394. https://doi.org/10/dfz4xm

Algeo, T.J., and Li, C., 2020. Redox classification and calibration of redox thresholds in sedimentary systems. Geochimica et Cosmochimica Acta 287, 8–26. https://doi.org/10.1016/j.gca.2020.01.055

Algeo, T.J., Liu, J., 2020. A re-assessment of elemental proxies for paleoredox analysis. Chemical Geology 540, 119549. https://doi.org/10.1016/j.chemgeo.2020.119549

Alibert, C., 2016. Rare earth elements in Hamersley BIF minerals. Geochimica et Cosmochimica Acta 184, 311–328. https://doi.org/10/gfvwd4

Alibo, D.S., Nozaki, Y., 1999. Rare earth elements in seawater: particle association, shale-normalization, and Ce oxidation. Geochimica et Cosmochimica Acta 63, 363–372. https://doi.org/10/bdn54n

Angerer, T., Hagemann, S.G., Danyushevsky, L., 2013. High-grade iron ore at Windarling, Yilgarn Craton: a product of syn-orogenic deformation, hypogene hydrothermal alteration and supergene modification in an Archean BIF-basalt lithostratigraphy. Mineralium Deposita 48, 697–728. https://doi.org/10/gfvtsw

Babechuk, M.G., Kamber, B.S., Greig, A., Canil, D., Kodolányi, J., 2010. The behaviour of tungsten during mantle melting revisited with implications for planetary differentiation time scales. Geochimica et Cosmochimica Acta 74, 1448–1470. https://doi.org/10.1016/j.gca.2009.11.018

Baldwin, G.J., Thurston, P.C., Kamber, B.S., 2011. High-precision rare earth element, nickel, and chromium chemistry of chert microbands pre-screened with in-situ analysis. Chemical Geology 285, 133–143. https://doi.org/10.1016/j.chemgeo.2011.03.019

Baldwin, G.J., Turner, E.C., Kamber, B.S., 2012. A new depositional model for glaciogenic Neoproterozoic iron formation: insights from the chemostratigraphy and basin configuration of the Rapitan Iron Formation. Canadian Journal of Earth Sciences 49, 455–476. https://doi.org/10/gfkw5s

Baldwin, G.J., Turner, E.C., Kamber, B.S., 2016. Tectonic controls on distribution and stratigraphy of the Cryogenian Rapitan Iron Formation, northwestern Canada. Precambrian Research 278, 303–322. https://doi.org/10.1016/j.precamres.2016.03.014

Bau, M., 1991. Rare-earth element mobility during hydrothermal and metamorphic fluid-rock interaction and the significance of the oxidation state of europium. Chemical Geology 93, 219–230. https://doi.org/10.1016/0009-2541(91)90115-8

Bau, M., 1993. Effects of syn-and post-depositional processes on the rare-earth element distribution in Precambrian iron-formations. European Journal of Mineralogy 5, 257–267.

Bau, M., Dulski, P., 1996. Distribution of yttrium and rare-earth elements in the Penge and Kuruman iron-formations, Transvaal Supergroup, South Africa. Precambrian Research 79, 37–55.

Bau, M., Alexander, B.W., 2009. Distribution of high field strength elements (Y, Zr, REE, Hf, Ta, Th, U) in adjacent magnetite and chert bands and in reference standards FeR-3 and FeR-4 from the Temagami Iron-Formation, Canada, and the redox level of the Neoarchean ocean. Precambrian Research 174, 337–346. https://doi.org/10/c9v65n

Bauer, K.W., Byrne, J.M., Kenward, P., Simister, R.L., Michiels, C.C., Friese, A., Vuillemin, A., Henny, C., Nomosatryo, S., Kallmeyer, J., Kappler, A., Smit, M.A., Francois, R., Crowe, S.A., 2020. Magnetite biomineralization in ferruginous waters and early Earth evolution. Earth and Planetary Science Letters 549, 116495. https://doi.org/10.1016/j.epsl.2020.116495

Bekker, A., Slack, J.F., Planavsky, N., Krapež, B., Hofmann, A., Konhauser, K.O., Rouxel, O.J., 2010. Iron formation: the sedimentary product of a complex interplay among mantle, tectonic, oceanic, and biospheric processes. Economic Geology 105, 467–508.

Bekker, A., Planavsky, N.J., Krapež, B., Rasmussen, B., Hofmann, A., Slack, J.F., Rouxel, O.J., Konhauser, K.O., 2014. Iron formations: their origins and implications for ancient seawater chemistry, In: Treatise on Geochemistry. Elsevier, vol. 9, pp. 561–628. https://doi.org/10.1016/B978-0-08-095975-7.00719-1

Bekker, A., Kovalick, A., 2020. Ironstones, iron formations, and iron ore, in: Reference Module in Earth Systems and Environmental Sciences. Elsevier, p. B9780081029084002000. https://doi.org/10.1016/B978-0-08-102908-4.00199-5

Bennett, W.W., Canfield, D.E., 2020. Redox-sensitive trace metals as paleoredox proxies: a review and analysis of data from modern sediments. Earth-Science Reviews 204, 103175. https://doi.org/10.1016/j.earscirev.2020.103175

Bjerrum, C.J., Canfield, D.E., 2002. Ocean productivity before about 1.9 Gyr ago limited by phosphorus adsorption onto iron oxides. Nature 417, 159–162. https://doi.org/10/b9ffh6

Bolhar, R., Kamber, B.S., Moorbath, S., Fedo, C.M., Whitehouse, M.J., 2004. Characterisation of Early Archaean chemical sediments by trace element signatures. Earth and Planetary Science Letters 222, 43–60. https://doi.org/10/d84tp5

Byrne, R.H., Kim, K.-H., 1990. Rare earth element scavenging in seawater. Geochimica et Cosmochimica Acta 54, 2645–2656.

Byrne, R.H., Lee, J.H., 1993. Comparative yttrium and rare earth element chemistries in seawater. Marine Chemistry 44, 121–130.

Byrne, R.H., Sholkovitz, E.R., 1996. Chapter 158. Marine chemistry and geochemistry of the lanthanides, In: Handbook on the Physics and Chemistry of Rare Earths. Elsevier, Amsterdam, pp. 497–593. https://doi.org/10.1016/S0168-1273(96)23009-0

Canfield, D.E., Thamdrup, B., 2009. Towards a consistent classification scheme for geochemical environments, or, why we wish the term 'suboxic' would go away. Geobiology 7, 385–392.

Chung, D., Zhou, M.-F., Gao, J.-F., Chen, W.T., 2015. In-situ LA–ICP-MS trace elemental analyses of magnetite: the late Palaeoproterozoic Sokoman Iron Formation in the Labrador Trough, Canada. Ore Geology Reviews 65, 917–928. https://doi.org/10.1016/j.oregeorev.2014.09.030

Cloud, P., 1968. Atmospheric and hydrospheric evolution on the primitive Earth. Science 160, 729–736.

Condie, K.C., Des Marais, D.J., Abbott, D., 2000. Geologic evidence for a mantle superplume event at 1.9 Ga. Geochemistry, Geophysics, Geosystems, 1, 1-25.

Conliffe, J. 2014. The Sawyer Lake iron-ore deposit, western Labrador: potential for future high-grade iron-ore deposits in the Labrador Trough. Newfoundland and Labrador Department

of Natural Resources. Geological Survey Report 14-1, 1-14.

Conliffe, J., 2015. Geological setting and genesis of high-grade iron-ore deposits in the eastern Labrador Trough. Newfoundland and Labrador Department of Natural Resources. Geological Survey Report 15-1, 1-25.

Conliffe, J., 2016. Geology and geochemistry of high-grade iron-ore deposits in the Kiviviv, Timmins and Ruth Lake areas, western Labrador. Newfoundland and Labrador Department of Natural Resources. Geological Survey Report 16, 1–26.

Cox, G.M., Halverson, G.P., Minarik, W.G., Le Heron, D.P., Macdonald, F.A., Bellefroid, E.J., Strauss, J.V., 2013. Neoproterozoic iron formation: an evaluation of its temporal, environmental and tectonic significance. Chemical Geology 362, 232–249. https://doi.org/10/f5jmsn

Crockford, P.W., Kunzmann, M., Bekker, A., Hayles, J., Bao, H., Halverson, G.P., Peng, Y., Bui, T.H., Cox, G.M., Gibson, T.M., Wörndle, S., Rainbird, R., Lepland, A., Swanson-Hysell, N.L., Master, S., Sreenivas, B., Kuznetsov, A., Krupenik, V., Wing, B.A., 2019. Claypool continued: extending the isotopic record of sedimentary sulfate. Chemical Geology 513, 200–225. https://doi.org/10/gf4gxr

Cunningham, L.C., Page, F.Z., Simonson, B.M., Kozdon, R., Valley, J.W., 2012. Ion microprobe analyses of $\delta^{18}O$ in early quartz cements from 1.9 Ga granular iron formations (GIFs): a pilot study. Precambrian Research 214–215, 258–268. https://doi.org/10/gft5rz

Danielson, A., Möller, P., Dulski, P., 1992. The europium anomalies in banded iron formations and the thermal history of the oceanic crust. Chemical Geology 97, 89–100.

De Baar, H.J., Brewer, P.G., Bacon, M.P., 1985. Anomalies in rare earth distributions in seawater: Gd and Tb. Geochimica et Cosmochimica Acta 49, 1961–1969.

Derry, L.A., Jacobsen, S.B., 1990. The chemical evolution of Precambrian seawater: evidence from REEs in banded iron formations. Geochimica et Cosmochimica Acta 54, 2965–2977.

Dimroth, E., Chauvel, J.-J., 1973. Petrography of the Sokoman Iron Formation in part of the central Labrador Trough, Quebec, Canada. Geological Society of America Bulletin 84, 111–134. https://doi.org/10/btdc56

Dulski P., 1992. Determination of minor and trace elements in four Canadian iron formation standard samples FeR-1, FeR-2, FeR-3 and FeR-4 by INAA and ICP-MS. Geostandards

Newsletter, 16, 325–332.

Dulski, P., 2001. Reference materials for geochemical studies: new analytical data by ICP-MS and critical discussion of reference values. Geostandards Newsletter 25, 87–125.

Dymek, R.F., Klein, C., 1988. Chemistry, petrology and origin of banded iron-formation lithologies from the 3800 Ma Isua supracrustal belt, West Greenland. Precambrian Research 39, 247–302.

Edwards, C.T., Pufahl, P.K., Hiatt, E.E., Kyser, T.K., 2012. Paleoenvironmental and taphonomic controls on the occurrence of Paleoproterozoic microbial communities in the 1.88 Ga Ferriman Group, Labrador Trough, Canada. Precambrian Research 212–213, 91–106. https://doi.org/10/gft5np

Frei, R., Dahl, P.S., Duke, E.F., Frei, K.M., Hansen, T.R., Frandsson, M.M., Jensen, L.A., 2008. Trace element and isotopic characterization of Neoarchean and Paleoproterozoic iron formations in the Black Hills (South Dakota, USA): assessment of chemical change during 2.9–1.9 Ga deposition bracketing the 2.4–2.2 Ga first rise of atmospheric oxygen. Precambrian Research 162, 441–474. https://doi.org/10/cgbg6h

Frei, R., Gaucher, C., Poulton, S.W., Canfield, D.E., 2009. Fluctuations in Precambrian atmospheric oxygenation recorded by chromium isotopes. Nature 461, 250–253. https://doi.org/10.1038/nature08266

Fryer, B.J., 1977. Trace element geochemistry of the Sokoman Iron Formation. Canadian Journal of Earth Sciences 14, 1598–1610. https://doi.org/10/df9wgq

Fryer, B.J., Fyfe, W.S., Kerrich, R., 1979. Archaean volcanogenic oceans. Chemical Geology 24, 25–33.

German, C.R., Elderfield, H., 1990. Application of the Ce anomaly as a paleoredox indicator: the ground rules. Paleoceanography 5, 823–833. https://doi.org/10/c4x8d5

German, C.R., Higgs, N.C., Thomson, J., Mills, R., Elderfield, H., Blusztajn, J., Fleer, A.P., Bacon, M.P., 1993. A geochemical study of metalliferous sediment from the TAG hydrothermal mound, 26°08′N, Mid-Atlantic Ridge. Journal of Geophysical Research 98, 9683–9692. https://doi.org/10/cxgfrb

German, C.R., Holliday, B.P., Elderfield, H., 1991. Redox cycling of rare earth elements in the suboxic zone of the Black Sea. Geochimica et Cosmochimica Acta 55, 3553–3558.

Gole, M.J., Klein, C., 1981. Banded iron-formations through much of Precambrian time. The

Journal of Geology 89, 169–183. https://doi.org/10/bcst7d

Govindaraju K., 1984. Report (1984) on two GIT-IWG geochemical reference samples – albites from Italy, AL-I and iron formation sample from Greenland, IF-G. Geostandards Newsletter 8, 63–113.

Govindaraju, K., 1994. 1994 compilation of working values and sample descriptions for 383 geostandards. Geostandards Newsletter 18, 1–158

Gourcerol, B., Thurston, P.C., Kontak, D.J., Côté-Mantha, O., Biczok, J., 2016. Depositional setting of Algoma-type banded iron formation. Precambrian Research 281, 47–79. https://doi.org/10.1016/j.precamres.2016.04.019

Graf, J.L., 1978. Rare earth elements, iron formations and sea water. Geochimica et Cosmochimica Acta 42, 1845–1850.

Grant, D.C., Goudie, D.J., Shaffer, M., Sylvester, P., 2016. A single-step trans-vertical epoxy preparation method for maximising throughput of iron-ore samples via SEM-MLA analysis. Applied Earth Science 125, 57–62. https://doi.org/10/gfv463

Grant, D.C., Goudie, D.J., Voisey, C., Shaffer, M., Sylvester, P., 2018. Discriminating hematite and magnetite via Scanning Electron Microscope–Mineral Liberation Analyzer in the −200 mesh size fraction of iron ores. Applied Earth Science 127, 30–37. https://doi.org/10/gfv46n

Gross, G.A., 1980. A classification of iron-formation based on depositional environments. Canadian Mineralogist 18, 215–222.

Gross, G.A., 1983. Tectonic systems and the deposition of iron-formation. Precambrian Research 20, 171–187.

Gumsley, A.P., Chamberlain, K.R., Bleeker, W., Söderlund, U., de Kock, M.O., Larsson, E.R., Bekker, A., 2017. Timing and tempo of the Great Oxidation Event. Proceedings of the National Academy of Sciences 114, 1811–1816. https://doi.org/10/f9scjw

Halevy, I., Alesker, M., Schuster, E.M., Popovitz-Biro, R., Feldman, Y., 2017. A key role for green rust in the Precambrian oceans and the genesis of iron formations. Nature Geoscience 10, 135–139. https://doi.org/10.1038/ngeo2878

Haugaard, R., Pecoits, E., Lalonde, S., Rouxel, O., Konhauser, K., 2016. The Joffre banded iron formation, Hamersley Group, Western Australia: assessing the palaeoenvironment through detailed petrology and chemostratigraphy. Precambrian Research 273, 12–37.

https://doi.org/10/f784fx

Holland, H.D., 2002. Volcanic gases, black smokers, and the great oxidation event. Geochimica et Cosmochimica Acta 66, 3811–3826. https://doi.org/10/bzns2c

Holland, H.D., 2006. The oxygenation of the atmosphere and oceans. Philosophical Transactions of the Royal Society of London B: Biological Sciences 361, 903–915. https://doi.org/10.1098/rstb.2006.1838

Isley, A.E., 1995. Hydrothermal plumes and the delivery of iron to banded iron formation. The Journal of Geology 103, 169–185. https://doi.org/10/cw3hvm

Isley, A.E., Abbott, D.H., 1999. Plume-related mafic volcanism and the deposition of banded iron formation. Journal of Geophysical Research: Solid Earth 104, 15461–15477. https://doi.org/10/cvgbdb

Johnson, J.E., Muhling, J.R., Cosmidis, J., Rasmussen, B., Templeton, A.S., 2018. Low-Fe(III) greenalite was a primary mineral from Neoarchean oceans. Geophysical Research Letters 45, 3182–3192. https://doi.org/10/gdr3zv

Kamber, B.S., Greig, A., Collerson, K.D., 2005. A new estimate for the composition of weathered young upper continental crust from alluvial sediments, Queensland, Australia. Geochimica et Cosmochimica Acta 69, 1041–1058. https://doi.org/10/dh9qcq

Kato, Y., Ohta, I., Tsunematsu, T., Watanabe, Y., Isozaki, Y., Maruyama, S., Imai, N., 1998. Rare earth element variations in mid-Archean banded iron formations: implications for the chemistry of ocean and continent and plate tectonics. Geochimica et Cosmochimica Acta 62, 3475–3497. https://doi.org/10/fkr46h

Kato, Y., Yamaguchi, K.E., Ohmoto, H., 2006. Rare earth elements in Precambrian banded iron formations: secular changes of Ce and Eu anomalies and evolution of atmospheric oxygen, In: Evolution of Early Earth's Atmosphere, Hydrosphere, and Biosphere - Constraints from Ore Deposits. Geological Society of America Memoir 198, 269–289. https://doi.org/10.1130/2006.1198(16)

Kendall, B., Reinhard, C.T., Lyons, T.W., Kaufman, A.J., Poulton, S.W., Anbar, A.D., 2010. Pervasive oxygenation along Late Archaean ocean margins. Nature Geoscience 3, 647–652. https://doi.org/10/cb6f2n

Klein, C., 2005. Some Precambrian banded iron-formations (BIFs) from around the world: their

age, geologic setting, mineralogy, metamorphism, geochemistry, and origins. American Mineralogist 90, 1473–1499. https://doi.org/10/fwgmpx

Klein C., Fink, R.P., 1976. Petrology of the Sokoman Iron Formation in the Howells River area, at the western edge of the Labrador Trough. Economic Geology 71, 453–487.

Klinkhammer, G.., Elderfield, H., Edmond, J.., Mitra, A., 1994. Geochemical implications of rare earth element patterns in hydrothermal fluids from mid-ocean ridges. Geochimica et Cosmochimica Acta 58, 5105–5113. https://doi.org/10/ddmzwj

Konhauser, K.O., Lalonde, S.V., Amskold, L., Holland, H.D., 2007. Was there really an Archean phosphate crisis? Science 315, 1234–1234. https://doi.org/10/cw7shg

Konhauser, K.O., Pecoits, E., Lalonde, S.V., Papineau, D., Nisbet, E.G., Barley, M.E., Arndt, N.T., Zahnle, K., Kamber, B.S., 2009. Oceanic nickel depletion and a methanogen famine before the Great Oxidation Event. Nature 458, 750–753. https://doi.org/10.1038/nature07858

Konhauser, K.O., Lalonde, S.V., Planavsky, N.J., Pecoits, E., Lyons, T.W., Mojzsis, S.J., Rouxel, O.J., Barley, M.E., Rosìere, C., Fralick, P.W., Kump, L.R., Bekker, A., 2011. Aerobic bacterial pyrite oxidation and acid rock drainage during the Great Oxidation Event. Nature 478, 369–373. https://doi.org/10/fc57tn

Konhauser, K.O., Robbins, L.J., Pecoits, E., Peacock, C., Kappler, A., Lalonde, S.V., 2015. The Archean nickel famine revisited. Astrobiology 15, 804–815. https://doi.org/10/f7w8f3

Konhauser, K.O., Planavsky, N.J., Hardisty, D.S., Robbins, L.J., Warchola, T.J., Haugaard, R., Lalonde, S.V., Partin, C.A., Oonk, P.B.H., Tsikos, H., Lyons, T.W., Bekker, A., Johnson, C.M., 2017. Iron formations: a global record of Neoarchaean to Palaeoproterozoic environmental history. Earth-Science Reviews 172, 140–177. https://doi.org/10.1016/j.earscirev.2017.06.012

Lyons, T.W., Reinhard, C.T., Planavsky, N.J., 2014. The rise of oxygen in Earth's early ocean and atmosphere. Nature 506, 307–315. https://doi.org/10.1038/nature13068

Maliva, R.G., Knoll, A.H., Simonson, B.M., 2005. Secular change in the Precambrian silica cycle: insights from chert petrology. Geological Society of America Bulletin 117, 835–845. https://doi.org/10/c7w5c3

Marin-Carbonne, J., Robert, F., Chaussidon, M., 2014. The silicon and oxygen isotope

compositions of Precambrian cherts: a record of oceanic paleo-temperatures? Precambrian Research 247, 223–234. https://doi.org/10.1016/j.precamres.2014.03.016

Michard, A., 1989. Rare earth element systematics in hydrothermal fluids. Geochimica et Cosmochimica Acta 53, 745–750. https://doi.org/10.1016/0016-7037(89)90017-3

Morris, R.C., 1993. Genetic modelling for banded iron-formation of the Hamersley Group, Pilbara Craton, Western Australia. Precambrian Research 60, 243–286. https://doi.org/10.1016/0301-9268(93)90051-3

Muhling, J.R., Rasmussen, B., 2020. Widespread deposition of greenalite to form banded iron formations before the Great Oxidation Event. Precambrian Research 339, 105619. https://doi.org/10.1016/j.precamres.2020.105619

Nance, W.B., Taylor, S.R., 1976. Rare earth element patterns and crustal evolution—I. Australian post-Archean sedimentary rocks. Geochimica et Cosmochimica Acta 40, 1539–1551.

Oonk, P.B.H., Tsikos, H., Mason, P.R.D., Henkel, S., Staubwasser, M., Fryer, L., Poulton, S.W., Williams, H.M., 2017. Fraction-specific controls on the trace element distribution in iron formations: implications for trace metal stable isotope proxies. Chemical Geology 474, 17–32. https://doi.org/10.1016/j.chemgeo.2017.10.018

Oonk, P.B.H., Mason, P.R.D., Tsikos, H., Bau, M., 2018. Fraction-specific rare earth elements enable the reconstruction of primary seawater signatures from iron formations. Geochimica et Cosmochimica Acta 238, 102–122. https://doi.org/10/gfvjmb

Ossa Ossa, F., Hofmann, A., Wille, M., Spangenberg, J.E., Bekker, A., Poulton, S.W., Eickmann, B., Schoenberg, R., 2018. Aerobic iron and manganese cycling in a redox-stratified Mesoarchean epicontinental sea. Earth and Planetary Science Letters 500, 28–40. https://doi.org/10/gfdpwj

Partin, C.A., Lalonde, S.V., Planavsky, N.J., Bekker, A., Rouxel, O.J., Lyons, T.W., Konhauser, K.O., 2013a. Uranium in iron formations and the rise of atmospheric oxygen. Chemical Geology 362, 82–90. https://doi.org/10.1016/j.chemgeo.2013.09.005

Partin, C.A., Bekker, A., Planavsky, N.J., Scott, C.T., Gill, B.C., Li, C., Podkovyrov, V., Maslov, A., Konhauser, K.O., Lalonde, S.V., Love, G.D., Poulton, S.W., Lyons, T.W., 2013b. Large-scale fluctuations in Precambrian atmospheric and oceanic oxygen levels from the

record of U in shales. Earth and Planetary Science Letters 369–370, 284–293. https://doi.org/10.1016/j.epsl.2013.03.031

Planavsky, N.J., Rouxel, O.J., Bekker, A., Lalonde, S.V., Konhauser, K.O., Reinhard, C.T., Lyons, T.W., 2010a. The evolution of the marine phosphate reservoir. Nature 467, 1088–1090. https://doi.org/10/drs9x9

Planavsky, N., Bekker, A., Rouxel, O.J., Kamber, B., Hofmann, A., Knudsen, A., Lyons, T.W., 2010b. Rare earth element and yttrium compositions of Archean and Paleoproterozoic Fe formations revisited: new perspectives on the significance and mechanisms of deposition. Geochimica et Cosmochimica Acta 74, 6387–6405. https://doi.org/10/fj558k

Planavsky, N.J., McGoldrick, P., Scott, C.T., Li, C., Reinhard, C.T., Kelly, A.E., Chu, X., Bekker, A., Love, G.D., Lyons, T.W., 2011. Widespread iron-rich conditions in the mid-Proterozoic ocean. Nature 477, 448–451. https://doi.org/10/ckq7pb

Planavsky, N.J., Asael, D., Hofmann, A., Reinhard, C.T., Lalonde, S.V., Knudsen, A., Wang, X., Ossa Ossa, F., Pecoits, E., Smith, A.J.B., Beukes, N.J., Bekker, A., Johnson, T.M., Konhauser, K.O., Lyons, T.W., Rouxel, O.J., 2014. Evidence for oxygenic photosynthesis half a billion years before the Great Oxidation Event. Nature Geoscience 7, 283–286. https://doi.org/10.1038/ngeo2122

Planavsky, N. J., Slack, J. F., Cannon, W. F., O'Connell, B., Isson, T. T., Asael, D., Jackson, J. C., Hardisty, D. S., Lyons, T. W., and Bekker, A., 2018, Evidence for episodic oxygenation in a weakly redox-buffered deep mid-Proterozoic ocean: Chemical Geology, 483, 581–594.

Posth, N.R., Köhler, I., D. Swanner, E., Schröder, C., Wellmann, E., Binder, B., Konhauser, K.O., Neumann, U., Berthold, C., Nowak, M., Kappler, A., 2013. Simulating Precambrian banded iron formation diagenesis. Chemical Geology 362, 66–73. https://doi.org/10.1016/j.chemgeo.2013.05.031

Posth, N.R., Canfield, D.E., Kappler, A., 2014. Biogenic Fe(III) minerals: from formation to diagenesis and preservation in the rock record. Earth-Science Reviews 135, 103–121. https://doi.org/10/f589j4

Poulton, S.W., Canfield, D.E., 2005. Development of a sequential extraction procedure for iron: implications for iron partitioning in continentally derived particulates. Chemical Geology 214, 209–221. https://doi.org/10/cs754b

Poulton, S.W., Canfield, D.E., 2011. Ferruginous conditions: a dominant feature of the ocean through Earth's history. Elements 7, 107–112. https://doi.org/10.2113/gselements.7.2.107

Poulton, S.W., Bekker, A., Cumming, V.M., Zerkle, A.L., Canfield, D.E., Johnston, D.T., 2021. A 200-million-year delay in permanent atmospheric oxygenation. Nature 592, 232–236. https://doi.org/10.1038/s41586-021-03393-7

Pourmand, A., Dauphas, N., Ireland, T.J., 2012. A novel extraction chromatography and MC-ICP-MS technique for rapid analysis of REE, Sc and Y: revising CI-chondrite and Post-Archean Australian Shale (PAAS) abundances. Chemical Geology 291, 38–54. https://doi.org/10/bwz489

Pufahl, P.K., 2010. Bioelemental sediments, In: James, N.P., Dalrymple, R.W. (eds.), Facies Models, fourth ed. Geological Association of Canada, pp. 477-503.

Pufahl, P.K., Hiatt, E.E., 2012. Oxygenation of the Earth's atmosphere–ocean system: a review of physical and chemical sedimentologic responses. Marine and Petroleum Geology 32, 1–20. https://doi.org/10/bvvcd9

Pufahl, P.K., Anderson, S.L., Hiatt, E.E., 2014. Dynamic sedimentation of Paleoproterozoic continental margin iron formation, Labrador Trough, Canada: paleoenvironments and sequence stratigraphy. Sedimentary Geology 309, 48–65. https://doi.org/10.1016/j.sedgeo.2014.05.006

Rasmussen, B., Fletcher, I.R., Bekker, A., Muhling, J.R., Gregory, C.J., Thorne, A.M., 2012. Deposition of 1.88-billion-year-old iron formations as a consequence of rapid crustal growth. Nature 484, 498–501. https://doi.org/10/gfvcnf

Rasmussen, B., Meier, D.B., Krapež, B., Muhling, J.R., 2013. Iron silicate microgranules as precursor sediments to 2.5-billion-year-old banded iron formations. Geology 41, 435–438. https://doi.org/10/f4vrhs

Rasmussen, B., Krapež, B., Muhling, J.R., 2014. Hematite replacement of iron-bearing precursor sediments in the 3.46-b.y.-old Marble Bar Chert, Pilbara Craton, Australia. Geological Society of America Bulletin 126, 1245–1258. https://doi.org/10/f6m34p

Rasmussen, B., Muhling, J.R., Suvorova, A., Krapež, B., 2016. Dust to dust: evidence for the formation of "primary" hematite dust in banded iron formations via oxidation of iron silicate nanoparticles. Precambrian Research 284, 49–63. https://doi.org/10.1016/j.precamres.2016.07.003

Rasmussen, B., Muhling, J.R., Suvorova, A., Krapež, B., 2017. Greenalite precipitation linked to the deposition of banded iron formations downslope from a Late Archean carbonate platform. Precambrian Research 290, 49–62. https://doi.org/10/f9vsz7

Rasmussen, B., Muhling, J.R., Krapež, B., 2021. Greenalite and its role in the genesis of early Precambrian iron formations – A review. Earth-Science Reviews 217, 103613. https://doi.org/10.1016/j.earscirev.2021.103613

Raye, U., Pufahl, P.K., Kyser, T.K., Ricard, E., Hiatt, E.E., 2015. The role of sedimentology, oceanography, and alteration on the δ^{56} Fe value of the Sokoman Iron Formation, Labrador Trough, Canada. Geochimica et Cosmochimica Acta 164, 205–220. https://doi.org/10/f7jw64

Reddy, S.M., Evans, D.A.D., 2009. Palaeoproterozoic supercontinents and global evolution: correlations from core to atmosphere. Geological Society of London Special Publication 323, 1–26. https://doi.org/10/bstd2x

Riding, R., Fralick, P., Liang, L., 2014. Identification of an Archean marine oxygen oasis. Precambrian Research 251, 232–237. https://doi.org/10/tsq

Robbins, L.J., Lalonde, S.V., Saito, M.A., Planavsky, N.J., Mloszewska, A.M., Pecoits, E., Scott, C., Dupont, C.L., Kappler, A., Konhauser, K.O., 2013. Authigenic iron oxide proxies for marine zinc over geological time and implications for eukaryotic metallome evolution. Geobiology 11, 295–306. https://doi.org/10/f48wtj

Robbins, L.J., Lalonde, S.V., Planavsky, N.J., Partin, C.A., Reinhard, C.T., Kendall, B., Scott, C., Hardisty, D.S., Gill, B.C., Alessi, D.S., Dupont, C.L., Saito, M.A., Crowe, S.A., Poulton, S.W., Bekker, A., Lyons, T.W., Konhauser, K.O., 2016. Trace elements at the intersection of marine biological and geochemical evolution. Earth-Science Reviews 163, 323–348. https://doi.org/10.1016/j.earscirev.2016.10.013

Sampaio, G.M.S., and Enzweiler, J., 2015. New ICP-MS results for trace elements in five iron-formation reference materials. Geostandards and Geoanalytical Research 39, 105–119. https://doi.org/10/f6zsjs

Satkoski, A.M., Beukes, N.J., Li, W., Beard, B.L., Johnson, C.M., 2015. A redox-stratified ocean 3.2 billion years ago. Earth and Planetary Science Letters 430, 43–53. https://doi.org/10/f7v2ng

Schoepfer, S.D., Shen, J., Wei, H., Tyson, R.V., Ingall, E., Algeo, T.J., 2015. Total organic

carbon, organic phosphorus, and biogenic barium fluxes as proxies for paleomarine productivity. Earth-Science Reviews 149, 23–52. https://doi.org/10/f7txpj

Siahi, M., Tsikos, H., Rafuza, S., Oonk, P.B.H., Mhlanga, X.R., van Niekerk, D., Mason, P.R.D., Harris, C., 2020. Insights into the processes and controls on the absolute abundance and distribution of manganese in Precambrian iron formations. Precambrian Research 350, 105878. https://doi.org/10.1016/j.precamres.2020.105878

Simonson, B.M., 2003. Origin and evolution of large Precambrian iron formations, In: Extreme Depositional Environments: Mega End Members in Geologic Time. Geological Society of America Special Paper 370, pp. 231–244. https://doi.org/10.1130/0-8137-2370-1.231

Slack, J.F., Cannon, W.F., 2009. Extraterrestrial demise of banded iron formations 1.85 billion years ago. Geology 37, 1011–1014. https://doi.org/10/dhgwtn

Swanner, E.D., Planavsky, N.J., Lalonde, S.V., Robbins, L.J., Bekker, A., Rouxel, O.J., Saito, M.A., Kappler, A., Mojzsis, S.J., Konhauser, K.O., 2014. Cobalt and marine redox evolution. Earth and Planetary Science Letters 390, 253–263. https://doi.org/10/f5x2pr

Tosca, N.J., Guggenheim, S., Pufahl, P.K., 2016. An authigenic origin for Precambrian greenalite: implications for iron formation and the chemistry of ancient seawater. Geological Society of America Bulletin 128, 511–530. https://doi.org/10.1130/B31339.1

Trendall, A., 2012. Iron formation: the sedimentary product of a complex interplay among mantle, tectonic, oceanic, and biospheric processes: a discussion. Economic Geology 107, 377–378. https://doi.org/10/gfvjmk

Tribovillard, N., Algeo, T.J., Lyons, T., Riboulleau, A., 2006. Trace metals as paleoredox and paleoproductivity proxies: an update. Chemical Geology 232, 12–32. https://doi.org/10/bp6kr3

van den Boorn, S.H.J.M., van Bergen, M.J., Nijman, W., Vroon, P.Z., 2007. Dual role of seawater and hydrothermal fluids in Early Archean chert formation: evidence from silicon isotopes. Geology 35, 939–942. https://doi.org/10/dgmdhj

Viehmann, S., Bau, M., Hoffmann, J.E., Münker, C., 2015. Geochemistry of the Krivoy Rog banded iron formation, Ukraine, and the impact of peak episodes of increased global magmatic activity on the trace element composition of Precambrian seawater. Precambrian Research 270, 165–180. https://doi.org/10/f7zm4g

Zajac, I.S., 1974. The stratigraphy and mineralogy of the Sokoman Formation in the Knob Lake area, Quebec and Newfoundland. Bulletin of the Geological Survey of Canada 220, 159 p.

1.8 Figures

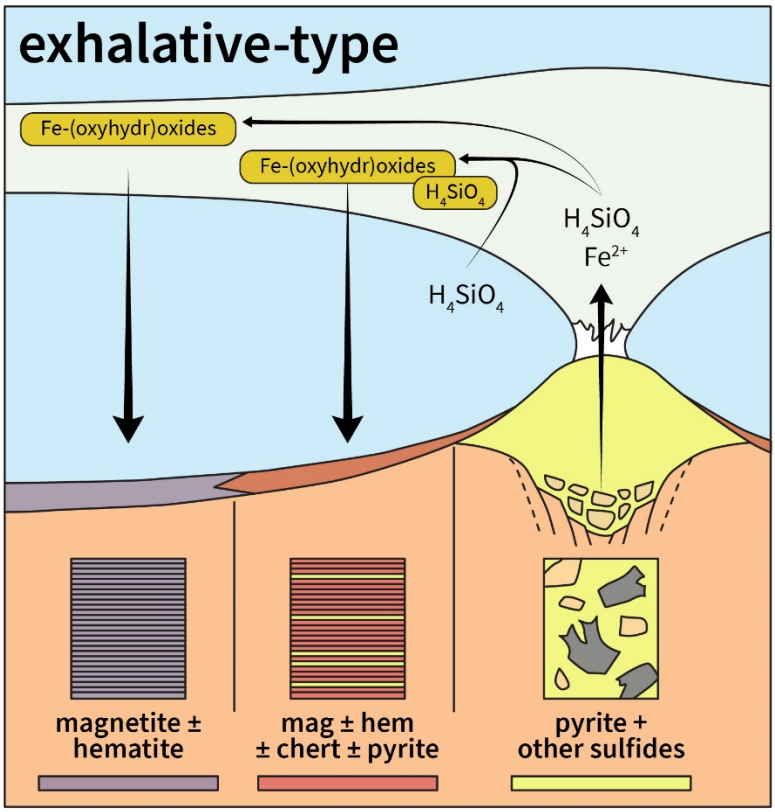
exhalative-type
Fe-(oxyhydr)oxides
Fe-(oxyhydr)oxides
H_4SiO_4
H_4SiO_4
Fe^{2+}
H_4SiO_4
magnetite ± hematite
mag ± hem ± chert ± pyrite
pyrite + other sulfides

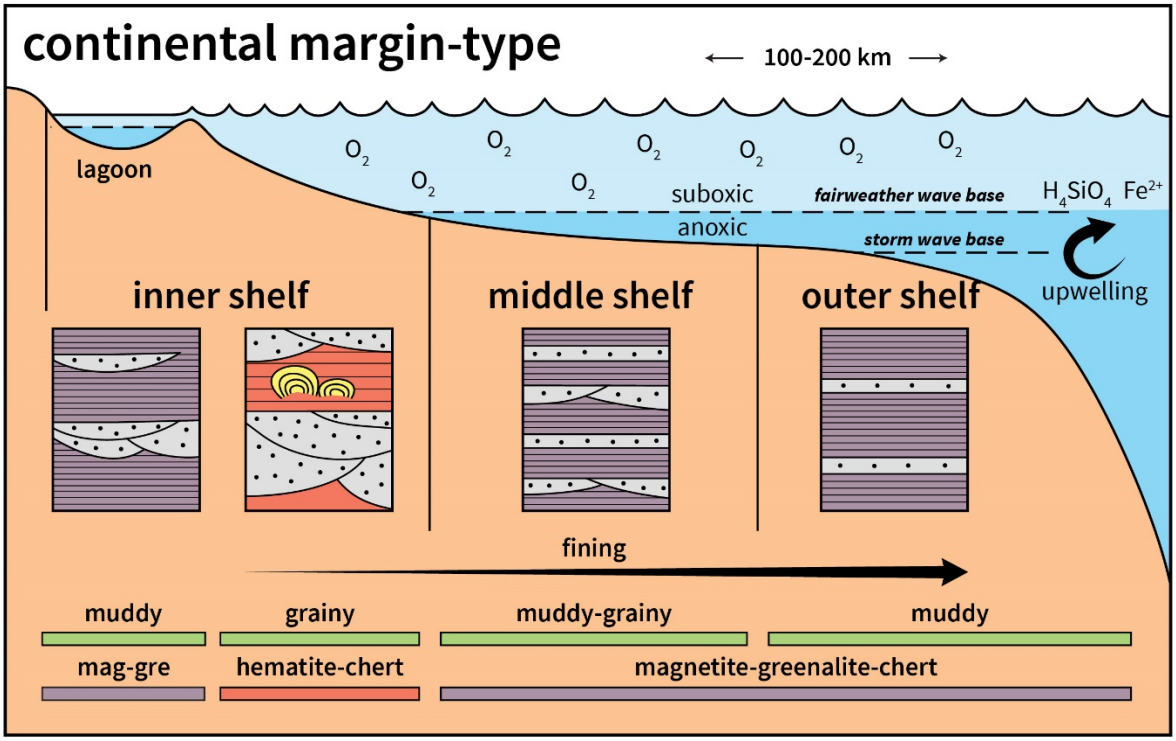
continental margin-type
100-200 km
lagoon
O_2
O_2
O_2
O_2
O_2
O_2
O_2
O_2
suboxic
anoxic
fairweather wave base
H_4SiO_4 Fe^{2+}
storm wave base
upwelling
inner shelf
middle shelf
outer shelf
fining
muddy
grainy
muddy-grainy
muddy
mag-gre
hematite-chert
magnetite-greenalite-chert

Figure 1.1. Depositional schematic of exhalative- and continental margin-type iron formations (modified from Pufahl, 2010). In exhalative-type IFs, lateral gradational facies develop due to the mixing of acidic, hydrothermal vent fluids and alkaline, deep-ocean seawater. Brecciation and precipitation of the volcanogenic massive sulfide (VMS) system occur at the vent. Deposition of Fe-(oxyhydr)oxides occurs as the hydrothermal plume disperses, and depending on bottom ocean redox conditions, magnetite and/or hematite laminae form. In continental margin-type IFs, upwelling of deep-water Fe and Si and their subsequent precipitation due to stratified water column conditions (i.e., shallow suboxic waters vs. deep anoxic waters) result in lateral and vertical gradational facies of IFs. These are characterized by low-energy, Fe(II)-rich lagoonal deposits that grade into high-energy, commonly stromatolitic, Fe(III)-rich inner shelf deposits, and into low-energy, granular to laminated, Fe(II)-rich middle to outer shelf deposits.

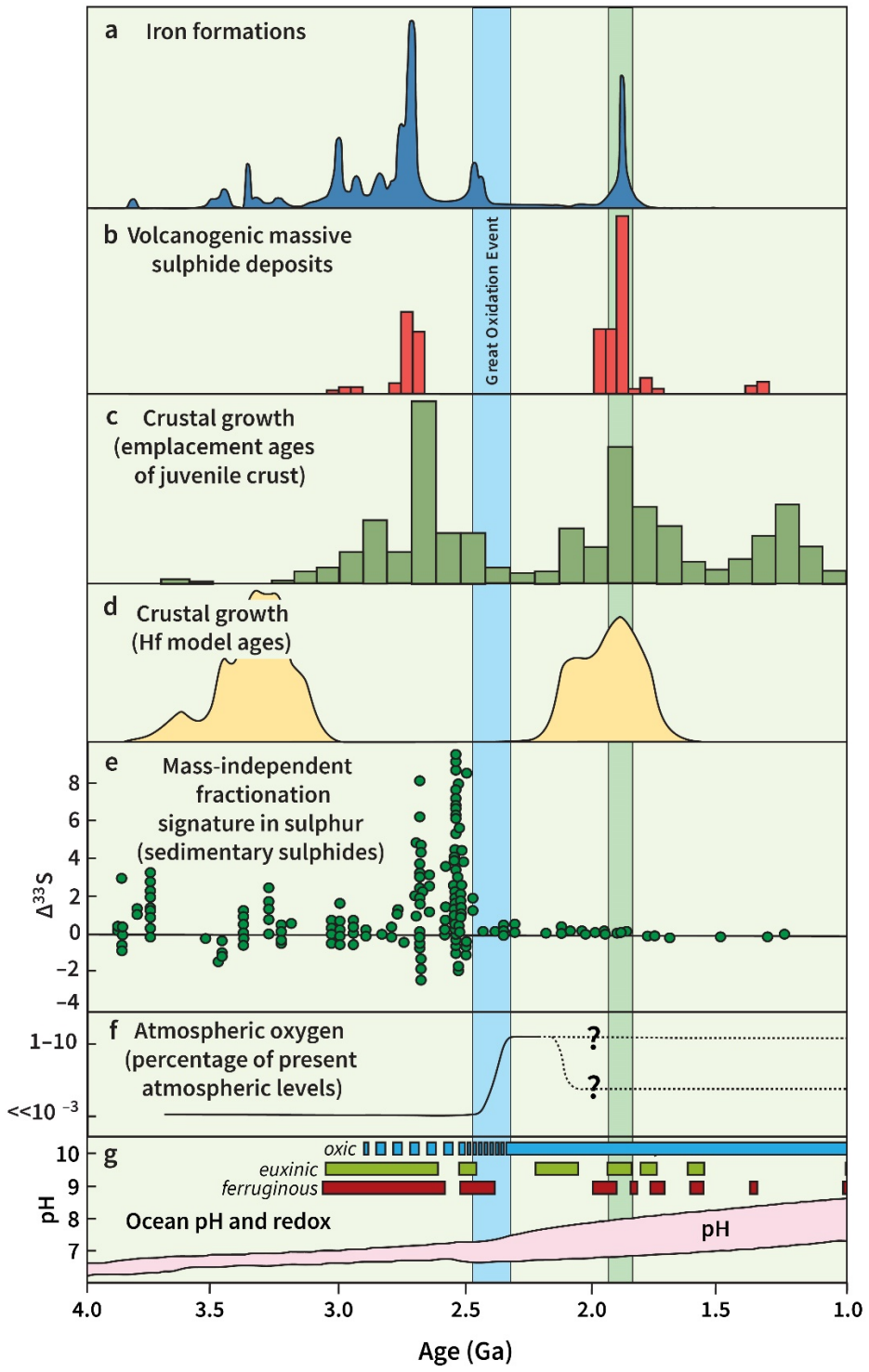

Figure 1.2. Age distribution and secular trends in (A) iron formations, (B) VMS deposits, (C) U–Pb zircon ages for juvenile crust, (D) Gaussian probability distribution of Hf model ages for zircons, (E) $\Delta^{33}S$ data from sedimentary sulfides, (F) inferred ranges of atmospheric oxygen concentrations, and (G) inferred redox and pH conditions in the shallow to deep global ocean (modified from Crockford et al., 2019; Rasmussen et al., 2012).

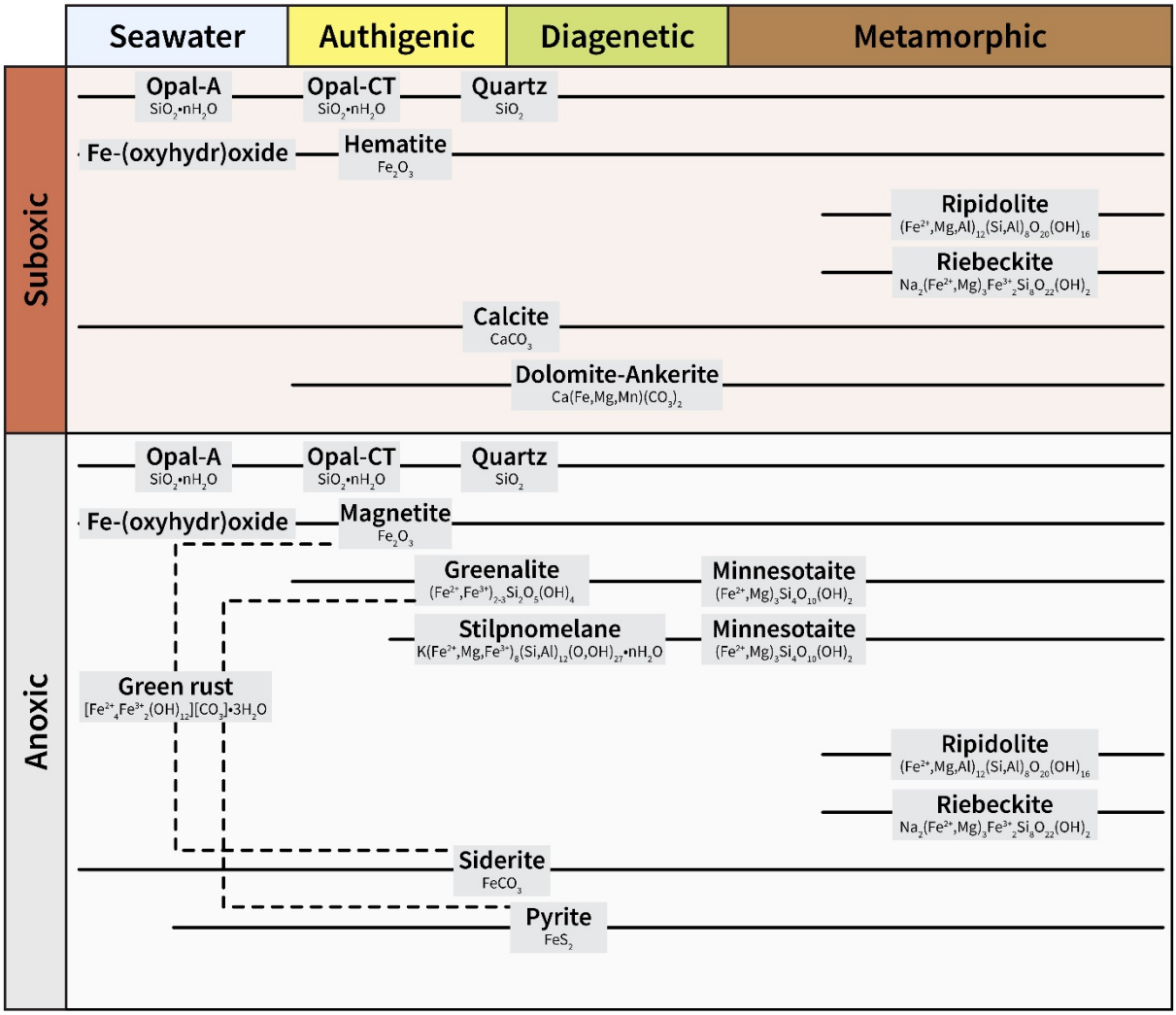

Figure 1.3. Generalized mineral paragenesis of iron formations under suboxic and anoxic pathways (modified from Klein, 2005; Pufahl and Hiatt, 2012).

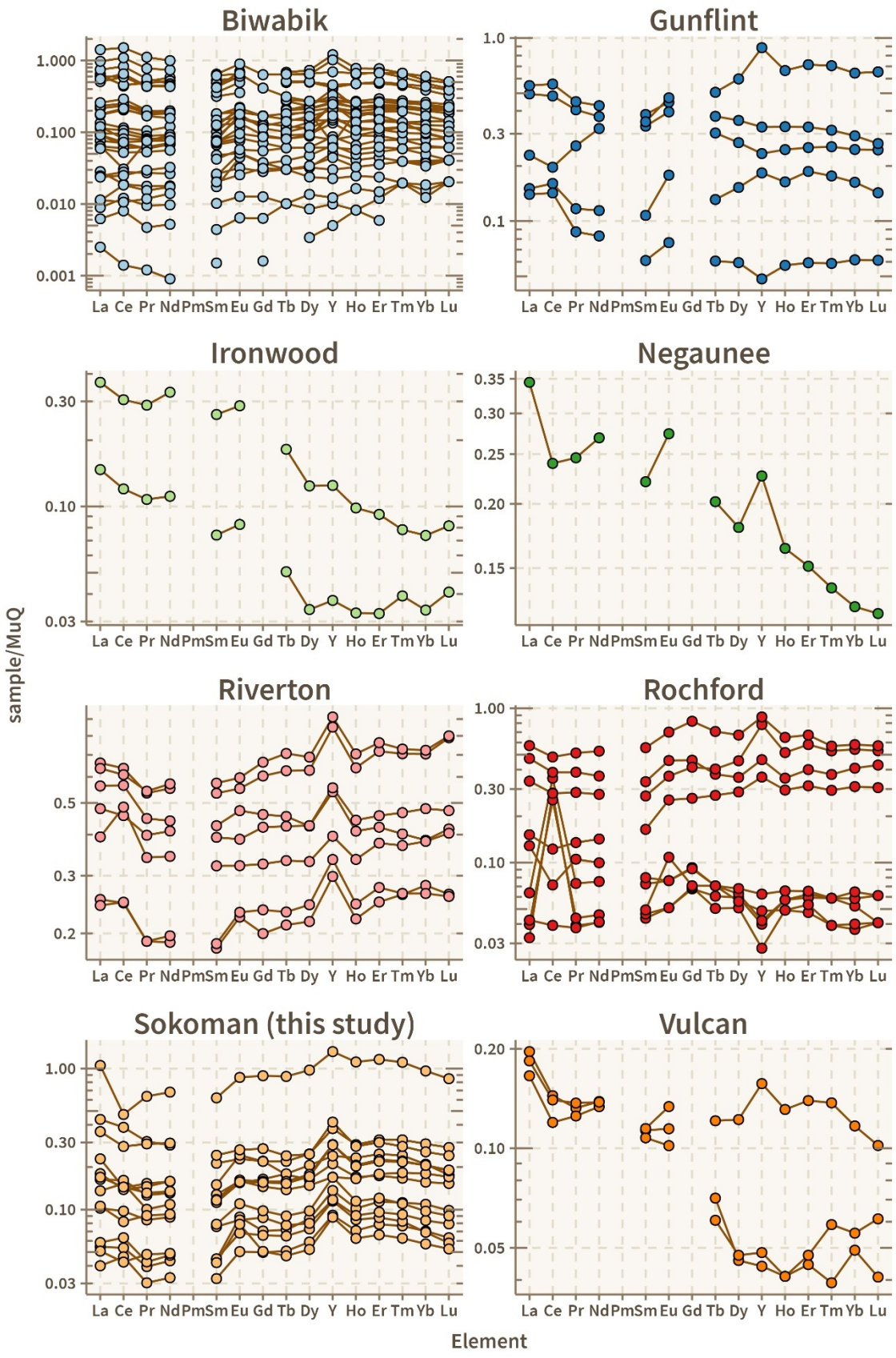
Biwabik
Gunflint
Ironwood
Negaunee
Riverton
Rochford
Sokoman (this study)
Vulcan
sample/MuQ
La Ce Pr Nd Pm Sm Eu Gd Tb Dy Y Ho Er Tm Yb Lu
Element

Figure 1.4. Mud from Queensland (MuQ)-normalized rare earth element and yttrium (REE+Y) profiles for a suite of Paleoproterozoic iron formations. Note the prominence of positive La, positive Eu, and both positive and negative Ce anomalies in these patterns. Data are compiled Frei et al. (2008), and Planavsky et al. (2010b, 2018).

CHAPTER 2: SHALLOW-OCEAN AND ATMOSPHERIC REDOX SIGNATURES PRESERVED IN THE CA. 1.88 GA SOKOMAN IRON FORMATION, LABRADOR TROUGH, CANADA

Abstract

Detailed mineral-chemical analysis of drill core samples from three previously unstudied localities (Sheps Lake, Lac Ritchie, Hayot Lake) of the ca. 1.88 Ga Sokoman continental margin-type iron formation (IF) was undertaken to better understand tectonically stable, shallow-marine environments during the late Paleoproterozoic. Suboxic (Fe-oxide-rich including paragenetically early hematite) and anoxic (Fe-silicate/carbonate-rich) mineral paragenetic pathways operated during IF deposition; post-depositional alteration beyond late diagenesis/metamorphism was negligible. We present new high-precision trace-element data for the Sokoman IF that are resolvable to low abundances (ppb levels), as illustrated with ratios of data for IF/iron ore reference materials (IOC-1, FeR-3, FeR-4). The rare earth element and yttrium (REE+Y) signature of the Sokoman IF is confirmed to have developed during deposition/early diagenesis through a comparison of geochemical signatures of chert (jasper) intraclasts and surrounding bulk IF. A previously published sequence-stratigraphic framework is integrated with chemostratigraphic variations in detrital-element, REE+Y, and other trace-element (TEs: Cr, V, U, Ni, Co, Zn) parameters of the Sokoman IF. This approach elucidates important aspects of the combined influence of base-level fluctuations, terrigenous input, basin redox stratification, and microbial activity captured within the mineralogically and textually complex units of the Sokoman IF. Detritus-poor samples record highly fractionated Nb/Ta and Zr/Hf ratios (w/w; Nb/Ta up to 679.7; Zr/Hf up to 409.4) that exceed those observed in the modern hydrosphere,

interpreted to reflect greater interaction of these elements with marine Fe/Mn particulates; both ratios approach crustal values with increasing element abundance. The REE+Y in the Sokoman IF, like contemporaneous IF localities elsewhere, were supplied predominantly by terrestrial sources and have patterns reminiscent of modern seawater (LREE-depletion, small negative Ce anomalies, small positive La, Gd, and Y anomalies), but in some cases also strong positive Ce anomalies. The REE+Y analysis suggests that distally transported hydrothermal Fe and Mn reaching the continental shelf was oxidized above a very shallow and likely spatially dynamic redoxcline, producing spatially close, but distinct, Mn- and Fe-oxide shuttles controlled by cyanobacteria and photoferrotrophs, respectively. The low magnitude and limited range of authigenic enrichments in redox-sensitive and nutrient-type TEs in the Sokoman IF are similar to those of other ca. 1.88 Ga IF localities, suggesting that both collectively capture evidence for similar low-O_2 Earth surface conditions, in contrast to preceding time intervals in the Paleoproterozoic. However, a coupled authigenic proxy and sequence-stratigraphic analysis of the various Sokoman IF units reveals variable input/scavenging of different TEs and provides a template for better understanding the geochemical signatures in these deposits. Authigenic TE enrichment is more readily captured in deeper, suboxic to anoxic units relative to shallower, nearshore units where even low amounts of continental detritus can obscure low-magnitude, authigenic redox signatures. Overall, our new inferences from the Sokoman IF echo those of other studies in indicating that atmosphere-ocean oxygenation and microbial ecosystems were linked via continental weathering of predominantly felsic Archean rocks under an oxygen-poor atmosphere (and aided locally by arid conditions). These conditions limited the terrestrial supply of redox-sensitive and nutrient-type elements into the ocean, largely restricting the spatial extent of primary productivity to the photic zone of coastal regions.

2.1 Introduction

Continental-margin iron formations ('Superior-type' IF) are marine chemogenic sedimentary rocks composed predominantly of chert and Fe-rich minerals that were deposited in tectonically stable, shallow and nearshore shelf environments (Gole and Klein, 1981; Gross, 1980; Pufahl, 2010; Pufahl and Hiatt, 2012). Major occurrences of continental-margin IF deposition ($\geq 10^3$ Gt; Bekker et al., 2010, 2014) temporally coincide with periods of extensive shelf development and enhanced hydrothermal activity in the lead-up to the ca. 2.45-2.32 Ga Great Oxidation Event (GOE), before reaching a second conspicuous and temporary resurgent peak at ca. 1.88 Ga (Bekker et al., 2010, 2014; Reddy and Evans, 2009). The latter peak coincides with crustal growth and tonnages of volcanogenic massive sulfide (VMS) deposits (Bekker et al., 2010; Isley and Abbott, 1999; Konhauser et al., 2017; Rasmussen et al., 2012). Thus, it has been argued that ferruginous marine conditions were developed from extensive amounts of hydrothermal Fe vented into the oceans during intense mantle plume activity (Bekker et al., 2010; Condie et al., 2000; Isley and Abbott, 1999; Reddy and Evans, 2009) with enhanced contributions from VMS hydrothermal fluids (Bau et al., 1997; Beukes and Gutzmer, 2008; Isley, 1995), all leading to inundation of the marine oxygen and sulfate reservoirs. Alternatively, the peak in IF deposition could be related to a decrease in atmospheric O_2 levels and consequent limited oxidative weathering of the continents, as inferred on the basis of subdued element mobilization in paleosols (e.g., Sindol et al., 2020), decreasing oceanic trace element inventories (Partin et al., 2013a, 2013b), and the absence of large positive Cr-isotope fractionation in contemporaneous marine deposits (Frei et al., 2009). An atmosphere with a lower oxidizing potential would have hampered the weathering of sulfide minerals on land and restricted sulfate delivery to the oceans, thus permitting the development of ferruginous conditions in shallow

water environments. It is probable that both atmospheric and marine factors played significant roles in triggering IF deposition, but each invokes global-, or at least regional-scale, processes. Therefore, better understanding of the late Paleoproterozoic atmosphere-hydrosphere systems benefits from a further analysis of the redox structure of the contemporaneous shallow and deep ocean.

Continental margin-type IFs offer a nearshore perspective on continental solute delivery and shallow marine redox conditions that has significantly aided understanding of Precambrian ocean-atmosphere oxygenation (e.g., Konhauser et al., 2017; Pufahl and Hiatt, 2012 and references therein), largely through detailed studies of the abundance and isotopic ratios of redox-sensitive elements (paleo-redox proxies). By the late Paleoproterozoic, the presence of oxygen in shallow marine settings is a widely accepted concept (Bellefroid et al., 2018; Kipp et al., 2017, 2018; Poulton and Canfield, 2011), but the spatio-temporal extent of water-column oxygenation and the redox structure of the deep ocean remain points of contention. Many studies implicate restricted euxinic conditions in productive continental margins and a largely ferruginous and anoxic deep ocean, but there is also evidence to support the presence of at least some deep-marine suboxic environments (Kipp et al., 2020; Planavsky et al., 2018; Slack et al., 2007, 2009).

Earlier inferences on the redox structure of the late Paleoproterozoic global ocean were derived from marine deposits of the Animikie Group in the Lake Superior region in North America (e.g., Planavsky et al., 2009, 2010a, 2018; Poulton et al., 2004, 2010). One of the premier paleo-redox proxies applied is the development of Ce anomalies (separation of Ce from other LREE) via Ce(III)-Ce(IV) redox transformation. The occurrence of both small negative to large positive Ce anomalies in ca. 1.88 Ga IFs remains an important discovery that highlights

their importance in capturing coupled Mn-Ce cycling across a (Fe/Mn) redox-stratified ocean (Fryer, 1977a, 1977b; Kato et al., 2006; Planavsky et al., 2009, 2010a). Evidence has now accumulated for inferring a similar basin redox stratification in earlier marine strata based on the presence of shallow oxygen oases as old as the Mesoarchean (e.g., Kendall et al., 2010; Ossa Ossa et al., 2018; Ostrander et al., 2019; Planavsky et al., 2014; Riding et al., 2014; Satkoski et al., 2015), but these examples generally do not show any Ce anomalies. As such, the redox threshold for shallow-marine Ce(III) oxidation was unlikely to have been readily reached in the oceans, or at the very least preserved, until younger Paleoproterozoic Mn-redoxcline development, thus making the ca. 1.88 Ga IFs an important suite of deposits to understand late Paleoproterozoic atmosphere-hydrosphere redox dynamics. However, much of our information on this age of IF deposition is still largely extracted from low-resolution geochemical sampling that lacks full interpretative integration with stratigraphic and mineralogical information.

Most studies on IFs involving redox-sensitive element geochemistry are underpinned by the assumption that Fe- ± Mn-(oxyhydr)oxides were involved in some capacity together with Fe-silicates in marine-particulate shuttling as part of element delivery to sediments (e.g., Fischer and Knoll, 2009; Planavsky et al., 2009, 2010a; Severmann et al., 2008). However, post-depositional oxidation (secondary origin of hematite) rather than primary seawater (oxyhydr)oxide development has been advocated for several Archean IFs (e.g., Rasmussen et al., 2014, 2016), and also recently for the ca. 1.88 Ga Gunflint IF (Rasmussen and Muhling, 2020). If assumptions of primary marine oxide shuttling are incorrect, then significant implications exist for Fe(II) oxidation mechanisms, as well as for several linked element tracers that can challenge prevailing interpretations of paleo-environmental conditions from IF geochemical signatures. It is also being increasingly appreciated that even purportedly robust paleo-redox proxies like Ce

anomalies can be disturbed by post-depositional processes (Bonnand et al., 2020; Planavsky et al., 2020). The convergence of Ce anomalies being vital to interpretations of a seawater redoxcline (Planavsky et al., 2010a) with reports of secondary Fe-oxidation among the suite of different ca. 1.88 Ga IFs (Petrash et al., 2016; Rasmussen and Muhling, 2020; Shapiro and Konhauser, 2015), makes it timely to re-evaluate the REE+Y systematics and inferred marine paleo-redox conditions of these deposits.

The present study focuses on the ca. 1.88 Ga Sokoman Formation in the Labrador Trough, Canada—one of the oldest sedimentologically and geochemically documented Paleoproterozoic granular-type IFs (GIFs) deposited on a continental margin (e.g., Dimroth and Chauvel, 1973; Fryer, 1977a; Klein and Fink, 1976; Zajac, 1974). More recent research conducted on the Sokoman IF has elucidated various geochemical, mineralogical, and sedimentological aspects of its deposition (e.g., Conliffe, 2019; Chung et al., 2015; Cunningham et al., 2012; Edwards et al., 2012; Pufahl et al., 2014; Raye et al., 2015). However, this formation has remained sparsely investigated relative to other ca. 1.88 Ga IFs in terms of applying modern geochemical proxies. Here, we report new high-precision, ultra-trace element data on drill core of the Sokoman IF from three previously unsampled localities (Lac Ritchie, Sheps Lake, and Hayot Lake) that complement the comprehensive work done in other areas (Howells Lake, Howells River). Our targeted sampling areas of the Sokoman IF (excepting Hayot Lake) are in parautochthonous tectonic zones lying directly on the paleo-Superior continental margin. Data quality is demonstrated with analyses of three IF reference materials from the Natural Resources Canada (NRCan)/Canada Centre for Mineral and Energy Technology (CANMET), FeR-3 and FeR-4 (Archean oxide-silicate facies IF from Temagami, Ontario; now discontinued) and IOC-1 (iron ore sourced from the Iron Ore Company of Canada's operations in Labrador City,

Newfoundland and Labrador). The ultra-trace element data include REE+Y and several other detrital trace elements (e.g., Zr, Hf, Nb, Th, Ta) and redox-sensitive/nutrient-type trace elements (e.g., Cr, V, U, Ni, Co, Zn). We also undertake a comparative geochemical test of physically subsampled intraformational chert with bulk IF in order to better evaluate effects from post-depositional processes and the fidelity of preserved seawater signatures. This strategy follows earlier studies that have applied sequential chemical extraction techniques (Oonk et al., 2017, 2018; Poulton and Canfield, 2005), sub-sampled early diagenetic chert (Baldwin et al., 2011), and compared geochemical signatures of IFs between bulk vs. laser ablation analyses (Robbins et al., 2019). The strategy employed by Baldwin et al. (2011), however, has only been thoroughly tested in Archean examples where microbanding is prominent, but is rarely undertaken on GIFs due to inherent textural complexity (e.g., Raye et al., 2015). Specifically, this study addresses the paragenesis of hematite formation in the Sokoman IF relative to other mineral phases and for the first time integrates recently constructed sequence-stratigraphic models with multiple geochemical proxies. This approach provides more refined insights into the preservation of seawater signatures in the IF, the relationship of the overall basin redox with nearshore sea-level dynamics, the flux of continentally derived redox-sensitive elements into the basin and their redox-controlled sequestration in the IF, as well as P enrichments and their relationship to previously documented microbial signatures (e.g., Edwards et al., 2012).

2.2 Regional geology

The collision and amalgamation of several Archean cratons and oceanic blocks at ca. 1.85 Ga led to the development of the Paleoproterozoic Trans-Hudson Orogen (THO) during formation of the supercontinent Columbia (Darbyshire et al., 2017; Hoffman, 1988). Within the

THO, the New Québec Orogen (NQO) serves as one of the best-preserved supracrustal belts and is a critical suture zone between the Superior Craton and the 'Core Zone' microcontinent (**Fig. 2.1**; Henrique-Pinto et al., 2017; Konstantinovskaya et al., 2019; Wardle et al., 2002). The Labrador Trough, which constitutes the foreland of the NQO, is an elongate, NW-SE-trending, supracrustal fold-and-thrust belt that stretches over 1100 km, from near the mouth of Ungava Bay in the north to south of the Grenville Front where highly metamorphosed and deformed equivalents of the Labrador Trough rocks predominate (Baragar and Scoates, 1981; Machado et al., 1989, 1997; Neal, 2000; Skulski et al., 1993; Wardle and Van Kranendonk, 1996; Wardle et al., 2002).

The Labrador Trough is broadly divided into several lithotectonic zones bounded by major thrust faults. The westernmost zones are characterized by platform sedimentary rocks that are autochthonous to parautochthonous (Bérard, Cambrien, and Tamarack zones) and allochthonous (Schefferville zone) in origin (**Fig. 2.1**; Clark and Wares, 2005). Strata of the Labrador Trough are mainly composed of sedimentary and volcanic rocks of the Kaniapiskau Supergroup, which overlie Archean basement composed primarily of granitic gneiss (Le Gallais and Lavoie, 1982; Wardle and Bailey, 1981). The Kaniapiskau Supergroup records three cycles of sedimentation and volcanism that reflect the tectonic evolution of the Labrador Trough, from rifting to drifting and eventual oblique collision of the Superior and Nain Provinces during formation of the NQO (**Fig. 2.2**; Wardle and Bailey, 1981). Within the west-central Labrador Trough, onset of the first cycle is marked by the deposition of immature sandstone and conglomerate (Seward Group) in fluvial to shallow marine settings, contemporaneous with mafic volcanism (Rohon et al., 1993). The accumulation of terrigenous clastic sediments of the Seward Group at ca. 2.17 to 2.14 Ga (Clark and Wares, 2005) is attributed to rifting between the

Superior and Nain Provinces (Machado et al., 1997). Seward Group rocks subsequently grade upward into passive-margin and shallow-marine sediments of the Swampy Bay and Attikamagen groups. Rifting that led to the deposition of the first-cycle rocks is constrained to have initiated before 2169 ± 4 Ma based on U–Pb zircon ages for a granophyre dike within a gabbro sill that intrudes the base of the Seward Group (Rohon et al., 1993), and persisted until at least ca. 2142 +4/-2 Ma based on the U–Pb zircon age of a rhyolite dike that cuts the upper section of the Swampy Bay Group (Clark, 1984; Clark and Wares, 2005).

The second cycle of sedimentation is marked by onset of a transgressive sequence of lagoonal platform sediments (Ferriman Group) that include sandstone and black chert (Wishart Formation) and iron formation (Sokoman Formation) (Chauvel and Dimroth, 1974; Simonson, 1984). The Sokoman Formation reflects deposition in a wave-dominated, shelf environment characterized by coastal upwelling of hydrothermal Fe and Si (Pufahl et al., 2014). Alkalic volcanism (Nimish Formation), dated at 1877.8 ± 1.3 Ma from a syenite cobble in a polymictic conglomerate within the Nimish Formation, was coeval with deposition of rocks of the Wishart and Sokoman formations (Findlay et al., 1995). Nimish volcanic rocks are largely confined to the Schefferville zone in the south-central Labrador Trough near the Dyke Lake-Astray Lake areas (Findlay et al., 1995; Wardle and Bailey, 1981; Zajac, 1974). The second cycle of sedimentation ends with foundering of the platform as reflected by the deposition of distal, euxinic black shale and turbidite of the Menihek Formation (Clark and Wares, 2005; Wardle and Bailey, 1981). In the central part of the Labrador Trough, encompassing the Wakuach Lake and Lac Ritchie areas, the Purdy Dolomite overlies the Sokoman Formation and is conformably overlain by the Menihek Formation (Baragar, 1967; Frarey and Duffell, 1964). However, the current status of the Purdy Dolomite as a formal stratigraphic subdivision remains uncertain. The deposition of

the Ferriman Group reflects continued passive-margin development and subsequent shortening of the margin during the nascent stages of the Torngat Orogen at ca. 1.87 Ga. as the 'Core Zone' microcontinent and the Nain Province collided (Clark and Wares, 2005). Sedimentary sequences farther to the east (Doublet, Koksoak, Le Moyne groups) show stratigraphic correlations with the Wishart-Sokoman-Menihek sequence and are considered deeper-water counterparts of the Ferriman Group (Clark and Wares, 2005). In the south-central Labrador Trough, the Ferriman Group, specifically the Menihek Formation, correlates with the Doublet Group that is composed of pyroclastics and basalt of the Murdoch Formation, shale and oxide-facies IF of the Thompson Lake Formation, and basalt of the Willbob Formation (Baragar, 1967; Findlay et al., 1995; Clark and Wares, 2005). In the central Labrador Trough, voluminous mafic to ultramafic sills, traditionally referred to as the Montagnais sills or the Montagnais Group, intruded on the first- and second-cycle rocks of the Kaniapiskau Supergroup (Baragar, 1967; Butler, 2020; Conliffe et al., 2019; Frarey and Duffell, 1964). Emplacement of these intrusions occurred during two discrete stages, at ca. 2.17 Ga and ca. 1.88 Ga (Bleeker and Kamo, 2018; Findlay et al., 1995; Rohon et al., 1993). Geochronological constraints for these intrusive suites are based on U–Pb zircon ages of (1) 2169 ± 2 Ma obtained on a felsic differentiate of a gabbro sill that intruded the Seward Group (Rohon et al., 1993), and (2) 1878.5 ± 0.8 Ma for a glomeroporphyritic gabbro sill that intruded the Menihek Formation (Bleeker and Kamo, 2018; Findlay et al., 1995). Bilodeau and Caron-Côté (2018) proposed use of the terms Wakuach Intrusive Suite and Gerido Intrusive Suite to refer to the mafic and ultramafic sills that intruded first- and second-cycle rocks, respectively; these terms are adopted in the present study. Emplacement of the Wakuach Intrusive Suite is interpreted to be associated with initial rifting of the Superior Craton at ca. 2.2 Ga (Wardle and Bailey, 1981). In contrast, the tectonomagmatic setting of the Gerido Intrusive

Suite is less well understood, but may be related to (1) development of pull-apart rift basins owing to pre-collisional, oblique convergence of the 'Core Zone' and the Superior Craton (Skulski et al., 1993); (2) extension in a back-arc basin (Corrigan et al., 2016; Rohon et al., 1993; van Rooyen et al., 2019); or (3) magma derived from a single deep-seated mantle plume under the Superior continent (Ciborowski et al., 2017).

The third cycle of sedimentation that resulted from the onset of the Torngat Orogen is characterized by emergence of red-bed arkose and conglomerate of the Chioak (north) and Tamarack River (south) formations, which have been interpreted as fluvial-deltaic, synorogenic molasse deposits (Wardle et al., 2002).

Major deformation and shortening in the western section of the Labrador Trough occurred as the Superior Province and its marginal cover obliquely collided with the western 'Core Zone' between 1.82 and 1.77 Ga (James and Dunning, 2000) leading to development of the NQO (Clark and Wares, 2005). Dextral transpressional deformation along its western section formed the west-verging fold-and-thrust belt, the Labrador Trough (Clark and Wares, 2005). Although assemblages from the western Labrador Trough have undergone extensive diagenesis, metamorphic overprinting is relatively low, restricted to prehnite-pumpellyite facies (Baragar, 1967; Klein and Fink, 1976; Klein, 1978), with metamorphic grade increasing towards the east (Baragar and Scoates, 1981). In contrast, the southern Labrador Trough exhibits higher metamorphic grades (greenschist to granulite facies) south of the ca. 1.0 Ga Grenville front (Klein, 1978; Wardle et al., 2002).

2.3 Lithostratigraphy and depositional framework

2.3.1 Sampled localities

Three key localities – Sheps Lake, Lac Ritche, and Hayot Lake – that best capture the least-metamorphosed and unaltered IF were chosen for this study (**Figs. 2.1–2.2, A2.1–A2.3**). The Sheps Lake and Lac Ritchie areas are situated within autochthonous to parautochthonous tectonic zones (Tamarack and Cambrien zones, respectively), and thus encompass sedimentary cover sequences on the Superior Craton. Previous sequence stratigraphic work on the Sokoman IF focused on the Howells Lake and Howells River areas (Edwards et al., 2012; Pufahl et al., 2014; Raye et al., 2015), the latter situated roughly 12 km NW of the Sheps Lake area. The Hayot Lake area is within the allochthonous Schefferville zone, which was thrust over the autochthonous to parautochthonous tectonic zones (Clark and Wares, 2005). This area thus records deposition in a more 'distal' sense relative to areas (e.g., Lac Ritchie) where second-cycle sediments noncomformably overlie granitic gneiss of the Superior margin.

2.3.2 Stratigraphic uncertainties at the base of the Sokoman Formation

The present contribution expands on the existing stratigraphic framework (Klein and Fink, 1976) using field and petrographic observations from the newly evaluated localities. These observations lead to the following proposed revisions: (1) inclusion of the Ruth Slate (RTH) within the Sokoman Formation, and (2) redefinition of this unit as a formal stratigraphic subdivision, namely the Ruth Slate Member of the Sokoman Formation (**Fig. 2.3**). To accomplish this goal, it is also imperative that the stratigraphic nature of the underlying unit, the Basal Chert member, be described.

In the Sheps Lake and Lac Ritchie localities, the Ruth Slate Member is underlain by the Basal Chert member (BC), which is an extensive but discontinuous unit that sharply overlies quartz arenite of the Wishart Formation in the west-central Labrador Trough (Baragar, 1967; Zajac, 1974). In the present study, drill core samples of the BC (**Fig. 2.4A–B**) are defined by massive black chert and are petrographically characterized by microcrystalline (<20 μm) chert granules cemented by drusy to blocky mesocrystalline quartz with subordinate siderite granules and disseminated pyrite (**Fig. 2.4C–D**). Thicknesses of this member are highly variable, generally ranging between 1 and 25 m in drill core in the Sheps Lake and Lac Ritchie areas based on company logs. In drill core 11-LR-1020D, the lower 20 cm of the RTH is marked by an increase in pyrite and the contact with the BC is relatively sharp (**Fig. A2.2**). Massive black chert occurrences were not documented in detailed sedimentological and petrographic studies on the Wishart Formation in the allochthonous Schefferville zone (Simonson, 1984, 1985), consistent with the absence of the BC in the Hayot Lake drill core. The formal stratigraphic status of the BC remains unclear, with several workers having included it as an informal member within the Wishart Formation (e.g., Baragar, 1967; Klein and Fink, 1976; Lesher, 1978), based on the absence of strong recrystallization features within the BC, which contrast to some of the Fe-carbonate- and Fe-silicate-rich units of the Sokoman Formation (Klein and Fink, 1976). In the uppermost part of the Wishart Formation in the Howells Lake and Howells River areas, locally autobrecciated massive chert with subaerial exposure surfaces was also documented (Edwards et al., 2012; their Facies F3). However, other studies reported similar mineralogical and textural features between the BC and several units of the Sokoman Formation (Chauvel and Dimroth, 1974; Dimroth, 1972; Harrison, 1952; Zajac, 1974). Evaluation of the formal stratigraphic status of the BC is beyond the scope of the present study and is not discussed in detail; nonetheless, its

proximity to the RTH may be useful for inferring paleo-environmental conditions during deposition in supratidal/lagoonal settings.

The Ruth Slate Member (RTH) constitutes the base of the Sokoman Formation (**Figs. 2.5C–D; 2.12A**) and its contact with the underlying Wishart Formation varies from conformable in the western Labrador Trough to disconformable towards the east (Baragar, 1967; Zajac, 1974). The upper contact of the RTH with the overlying members of the Sokoman Formation is gradational and conformable in Lac Ritchie drill core, consistent with previous observations in the Knob Lake, Howells Lake, and Howells River areas (Edwards et al., 2012; Pufahl et al., 2014; Zajac, 1974). The RTH is characterized by finely laminated, dark grey to dark green, pyritic and ferruginous shale that includes minor tuffaceous units (Zajac, 1974). Prevalence of pyritic laminae and grains of francolite (carbonate fluorapatite) have been attributed to bacterial sulfate reduction in shallow coastal lagoons (Edwards et al., 2012; Pufahl et al., 2014). Earlier investigations in the Labrador Trough commonly regard the Ruth Formation as a distinct formation, separate from the Sokoman Formation (Frarey and Duffell, 1964; Harrison, 1952; Dimroth, 1972), but inconsistencies in its usage across various areas in the Labrador Trough were reported by Zajac (1974). Importantly, it is now apparent that the ferruginous shale of the RTH composes part of a stratigraphically equivalent and lateral gradational facies that range from oxide- and silicate-dominated in the west, proximal to the Superior margin, to carbonate- and silicate-sulfide-dominated to the east (Zajac, 1974). Furthermore, we note that the RTH is distinctly enriched in Fe and depleted in both Ca and Na relative to the Early and Middle Proterozoic shale composites of Condie (1993), reflecting its feldspar-poor and Fe-silicate- and Fe-carbonate-rich mineralogical composition (**Fig. 2.3**). Although the ferruginous shale of the RTH is not IF *sensu stricto*, its Fe-rich mineralogical and geochemical composition and close

genetic association with the Sokoman Formation warrants inclusion within the latter, in agreement with previous studies (Klein and Fink, 1976; Lesher, 1978; Zajac, 1974). We therefore agree with the early proposal by Zajac (1974) to redefine the Ruth Formation as the Ruth Slate Member of the Sokoman Formation.

2.3.3 Mineralogical facies and depositional framework

Several units are recognized within the Sokoman Formation (e.g., Chauvel and Dimroth, 1974; Klein and Fink, 1976; Zajac, 1974). Herein, we adopt the classification scheme outlined by Klein and Fink (1976) based on the facies classification initially outlined by James (1954) with several revisions. This scheme is ideal given its basis on the extensive characterization of units in the Howells River area, which is located in the west-central Labrador Trough in close proximity to the localities evaluated in this study. Furthermore, this classification scheme represents the culmination of decades of work on redefining the stratigraphy of the Sokoman Formation and remains actively used by mining and exploration companies in the area.

The Klein and Fink (1976) work in the Howells River area outlined four distinct mineralogical facies comprising nine units, namely: (1) sulfide facies (Ruth Slate Member); (2) silicate facies (Lower Iron Formation, Lean Chert); (3) magnetite-carbonate facies (Lower Red Green Chert, Pink Grey Chert, Green Chert, Jasper Upper Iron Formation); and (4) hematite-carbonate facies (Lower Red Chert, Upper Red Chert).

In the present contribution, four distinct facies are outlined based on dominant mineral assemblages (**Fig. 2.3**). Three revisions to the original Klein and Fink (1976) classification scheme are made herein: (1) abandonment of the former sulfide facies, (2) revision of the original silicate facies into the silicate-carbonate facies, and (3) addition of a new hematite-

magnetite facies. It is important to note that chert and/or quartz are ubiquitous among all of these facies. Supplementary drill core and outcrop photographs of the units described below are also provided in **Figures 2.5–2.11**.

The Ruth Slate Member (RTH) constitutes the former sulfide facies (**Fig. 2.12A**). In Lac Ritchie drill core, the RTH grades into hematite-magnetite facies as represented by the Jaspilite facies (JSP; **Fig. 2.12B**). The lower contact with the RTH is generally marked by numerous water-escape structures and by euhedral pyrite. The JSP is defined by red, granular to oolitic grainstone containing abundant jasper intraclasts and interbeds of hematite and magnetite. Gradation of the RTH with the JSP was interpreted by Zajac (1974) as evidence for an elevated nearshore ridge that partially isolated the lagoon from the main basin.

The Lower Iron Formation (LIF) and Lean Chert (LC), which mainly comprise Fe-silicates (greenalite, stilpnomelane, minnesotaite), Fe-carbonate, and magnetite, represent the silicate-carbonate facies. Both units may appear massive but microbands are observed at the microscopic scale (Klein and Fink, 1976). The LIF consists of finely laminated to brecciated IF with pervasive stylolites (**Figs. 2.12C, 2.13A**). The LC is characterized by grey-green, thin- to thick-bedded chert and magnetite with subordinate Fe-silicate-rich granular intervals (**Figs. 2.12D, 2.13B**). Stromatolites defined by magnetite-rich bands are common in the upper sections of the Sheps Lake and Hayot Lake drill core. Prominent parallel to wavy interbeds of muddy and granular intervals are interpreted to record deposition in a deeper subtidal setting below the fairweather wave base (FWWB), but above the storm wave base (SWB) (Edwards et al., 2012; Pufahl et al., 2014).

The Lower Red-Green Chert (LRGC), Pink-Grey Chert (PGC), Green Chert (GC), and Jasper Upper Iron Formation (JUIF) constitute the magnetite-carbonate facies. The LRGC is

defined by thin-bedded IF with minor cross-laminations that grades upwards into pinkish, granular to oolitic grainstone (**Figs. 2.12E, 2.13C**). Domal stromatolites are most evident in Hayot Lake drill core. The PGC is composed of grey to grey-green and locally pinkish, granular grainstone with rare ooliths and subordinate intervals of massive to weakly banded IF (**Figs. 2.12F, 2.13D**). This unit generally exhibits a mottled texture with abundant coarse-grained ankerite overprints. Prominent cross-beds in granular intervals and the absence of hematite in banded IF are attributed to sediment reworking and transport by fair-weather currents towards deeper, subtidal settings (Pufahl et al., 2014). The GC is characterized by green, massive to thick-bedded chert with disseminated Fe-carbonate and magnetite and subordinate granular intervals (**Figs. 2.12G, 2.13E**). Occurrence of desiccation cracks and phosphatized microbial laminae are interpreted to record deposition in supratidal to intertidal settings (Pufahl et al., 2014). The JUIF is composed of alternating intervals of dark-grey, massive to weakly banded, magnetite-dominated IF and red-pink, granular to oolitic, hematite-rich grainstone (**Figs. 2.12H, 2.13F–G**). Spherulitic siderite and rip-up clasts of magnetite and jasper are relatively common. Domal stromatolites are widespread in Lac Ritchie drill core.

The Upper Red Chert (URC; **Figs. 2.12I, 2.13H**) and Lower Red Chert (LRC; **Fig. 2.12J**) make up the hematite-carbonate facies. These units, mineralogically and texturally similar, are defined by alternating, discontinuous, thin to thick bands of magnetite and ankerite, and granular to oolitic, hematite-bearing grainstone. Like the JUIF, rip-up clasts of magnetite and jasper are common. The ubiquity of coated grains, lithoclasts, and cross-stratified intervals within these units are interpreted to reflect deposition in a high-energy, subtidal environment above the FWWB (Edwards et al., 2012; Pufahl et al., 2014).

Sequence stratigraphy of the Sokoman IF has outlined two relative sea-level cycles based on stacking patterns of seven distinct lithofacies that delineate two depositional sequences (**Fig. 2.3**; Edwards et al., 2012; Pufahl et al., 2014; Raye et al., 2015). Mineralogical and textural observations on lithofacies from these studies compare well with those outlined here. The first sequence comprises (1) lowstand deposits of lagoonal black shale (RTH) and peritidal, flaser-bedded chert grainstone (LIF, part of LRGC); (2) transgressive deposits of shallow to deep subtidal, cross-stratified hematitic chert grainstone (part of LRGC, LRC) and cross-bedded magnetite-rich packstone (PGC); and (3) highstand deposits of shallow, cross-stratified hematitic chert grainstone (URC). The second sequence comprises (1) lowstand deposits of supratidal chert (GC) and peritidal chert grainstone (part of JUIF), and (2) transgressive deposits of cross-stratified hematitic chert grainstone (part of JUIF) and laminated magnetite-rich chert grainstone (LC). Subsequent erosion led to the incomplete preservation of transgressive deposits of the second sequence (Pufahl et al., 2014). A notable difference between our study and these previous ones (Edwards et al., 2012; Pufahl et al., 2014; Raye et al., 2015) is the absence of JSP in the Howells River and Howells Lake drill cores. In the present study, the JSP is observed exclusively in Lac Ritchie drill core, reflecting its limited spatial extent (Zajac, 1974).

Collectively, the sedimentological and stratigraphic changes, as expressed by variable mineralogy across units of the Sokoman IF, are largely controlled by both basin hydrodynamics and ocean redox (Pufahl et al., 2014). These variations indicate an overall shift from lagoonal (RTH) to deeper subtidal (PGC, JUIF, LC) settings punctuated by deposition within intertidal (LIF, GC) to shallow subtidal (JSP, LRC, URC, JUIF) environments.

2.4 Methods

2.4.1 Sample collection and preparation

Sample extraction encompassed 11 drill holes across three properties drilled by New Millennium Iron Corp. (Sheps Lake: 12-SL-1005D, 12-SL-1011D, 12-SL-1017D, 12-SL-1018D; Lac Ritchie: 11-LR, 1005D, 11-LR-1010D, 11-LR-1012D, 11-LR-1020D, 11-LR-1029D) and by Labec Century Iron Ore Inc. (Hayot Lake: HAY-11-07, HAY-11-29).

Drill core sampling targeted representative pristine sections, away from fracture and alteration zones. The same sections were sampled for both bulk geochemical analysis and thin section preparation, where feasible. Eleven irregular (e.g., **Fig. 2.12H**) intraformational chert rip-up clast subsamples (JUIF: 4; URC: 2; PGC: 1; LRGC: 1; JSP: 3) were isolated for geochemistry for comparison with bulk data obtained on the surrounding IF. Individual samples were cut with a diamond-tipped saw into ~1-cm-thick flat slabs and were subsequently polished with aluminum oxide grit using a grinding wheel to remove saw marks and polish off the outermost edges of the drill core surface. These slabs were immediately washed with ethanol and ultrapure water in an ultrasonic bath and dried prior to crushing in a plastic bag via a steel hammer. The coarsely crushed (~3–5 mm) chips were sequentially washed once with ethanol and twice with ultrapure water in an ultrasonic bath and dried. These chips were then screened under a binocular microscope and picked through using plastic tweezers to reject any remaining pieces that showed evidence of metal transfer. Cleaned and picked chips were sent to Geoscience Laboratories (Geo Labs) of the Ontario Geological Survey in Sudbury, Ontario, for agate milling (code: SAM-AGM).

2.4.2 Scanning electron microscopy and mineral liberation analysis (SEM-MLA)

Scanning electron microscopy (SEM) and subsequent mineral classification by proprietary mineral liberation analysis (MLA) software by the Field Electron and Ion (FEI) Company was conducted at the Microanalysis Facility (MAF) within the Core Research Equipment and Instrument Training (CREAIT) Network at Memorial University of Newfoundland. Samples were analyzed using a FEI MLA 650F equipped with 5th generation, dual Bruker XFLash SDD X-ray detectors. Mineral liberation analysis was done with a high voltage of 25 kV, spot size of 5.37 μm, X-ray acquisition time of 12 ms, and step size of 10 pixels. Measurements on polished thin sections were conducted in grain-based X-ray mapping (GXMAP) mode (Fandrich et al., 2007; Gu, 2003; Sylvester, 2012), following the procedure outlined in Sindol et al. (2020).

2.4.3 Major elements, loss on ignition (LOI), and ferrous iron

Major-element concentrations were measured at the Department of Geosciences at Eberhard-Karls University in Tübingen, Germany, following protocols outlined in previous studies (e.g., Albut et al., 2018; Babechuk et al., 2019). Fused glass beads were prepared by mixing 1.5 g of sample powder and 7.5 g of MERCK Spectromelt A12 (66% $Li_2B_4O_7$, 34% $LiBO_2$), then fused at 1050 °C using an Oxiflux system from CRB Analyse Service GmbH. X-ray fluorescence (XRF) analysis was conducted using a wavelength-dispersive Bruker AXS Pioneer S4 (Rh-tube at 4 kW) instrument, with calibration based on 32 well-characterized geological reference materials (RMs) (Potts and Web, 1992). Mean concentrations and 1 relative standard deviation (1rsd) for the RMs FeR-3, FeR-4, and IOC-1 (n = 2 for all RMs) are reported in **Table A6.1**. The percent bias calculation relative to NRCan/CANMET-certified values for

most elements with concentrations >1 oxide wt.% is within ±10%, and better for more abundant elements (Fe and Si), generally within ±3%. For the Sokoman IF samples, concentrations of several elements were commonly below (Al, Na, K) or near to (Ti) the XRF method detection limits.

For all samples, total LOI (LOI_T) was measured using 1 g aliquots of dried sample powder ignited at 1050 °C for 2 h. For a smaller selection (but still covering major textural and mineralogical variations among all units), sequential four-step LOI measurements were conducted at Geo Labs (code: LOI-4ST). Sequential four-step LOI (105 °C, 371 °C, 500 °C, 1000 °C) analyses were made on 2 g aliquots of dried sample powder as described in more detail in previous studies (e.g., Turner and Kamber, 2012). Briefly, the main component reactions at specific temperature thresholds are listed as follows: (1) loss of mineral surface moisture (105 °C); (2) loss of free organic C (105–371 °C); (3) loss of organic C (371–500 °C); and (4) carbonate decomposition, metal oxidation, and loss of structural water (500–1000 °C). Quality control data for the sequential four-step LOI measurements show that with respect to the in-house reference material RAFT-2, values are precise (1rsd) within ±2%, ±6%, ±1%. ±17%, and ±0.5% for $LOI_{(105\ °C)}$, $LOI_{(105\text{-}371\ °C)}$, $LOI_{(371\text{-}500\ °C)}$, $LOI_{(500\text{-}1000\ °C)}$, and cumulative sequential four-step LOI total ($LOI_{(0\text{-}1000\ °C)}$), respectively (**Table A6.2**). Percent bias of the $LOI_{0\text{-}1000\ °C}$ value relative to the NRCan/CANMET-provisional total LOI value for stream sediment RM STSD-1 is –2.5%. For the IF samples, there is excellent agreement between LOI_T values and $LOI_{0\text{-}1000\ °C}$ values (R^2 = 0.99) as determined at the separate facilities.

Ferrous iron measurements were conducted at Geo Labs (FEO-ION) on 1 g aliquots of dried sample powder via potentiometric titration using a standardized permanganate solution as previously described (Sindol et al., 2020). Quality control data for ferrous iron determination

were published by Hargreaves (2019) and show that long-term (2012-2019) precision for IF RMs FeR-1 (n=59), FeR-2 (n=76), and FeR-3 (n=269), are all within 0.44% (1rsd). Percent bias relative to NRCan/CANMET provisional values (in parentheses) are within ±1.5% for FeR-2 (15.24) and FeR-3 (13.63) (**Table A6.3**).

2.4.4 Trace elements

Trace element data for 101 bulk samples and 11 intraformational chert subsamples were measured at the Department of Geosciences at Eberhard-Karls University in Tübingen, Germany. Samples were binned into two batches based on chert abundance (batch 1: chert-rich, batch 2: chert-poor). Approximately 100 mg aliquots of sample and reference material powders were digested inside screw-cap Savillex Teflon® beakers using HF-HNO_3 (3:1) on a hotplate at 120 °C for 60–72 h, and subsequently dried down at 95 °C. The residues were each reacted once with 1 mL aliquots of concentrated HNO_3 and twice with 2 mL aliquots of 50% HNO_3 with evaporation in between. Residues were dissolved in 3 M HNO_3 and then diluted to 0.3 M HNO_3 'stock' solutions with gravimetric dilution factors of ~250 and ~1000 for batch 1 and 2 samples, respectively. For analysis, solutions were further diluted to a gravimetric dilution factor ranging from 5000 (intraformational chert) to 60000 (shale) depending on the sample type, and mixed with an internal standard comprising ^{6}Li (~3 ppb), In (~1 ppb), Re (~1 ppb), and Bi (~1 ppb).

Trace elements were measured using a ThermoFisher Scientific iCap-Qc quadrupole inductively coupled plasma-mass spectrometer (ICP-MS) in standard mode, following an identical procedure as Albut et al. (2018), as adapted from Eggins et al. (1997). Samples were stationed into an Elemental Scientific SC-2 DX autosampler and injected into the ICP-MS from a 4 mL Teflon loop via the peristaltic pump at 40 rpm. Data were collected in batches of 20 to 25

samples over 11 experiments where internal standard, blanks, calibration standards, and quality control standards were run prior to the sample unknowns, and monitor samples were run after every five sample unknowns. Signal intensity corrections, including for blank, two-step internal and external drift corrections, oxide/dimer corrections based on daily tuning conditions, and final calibration using a rock reference material, were conducted offline as described in previous studies (Eggins et al., 1997; Ulrich et al., 2010). Final calibration of corrected signal intensities used a preferred composition of USGS reference material W-2a, as outlined in **Table A6.4**. A method detection limit filter of 3 × background equivalent concentration (BEC) was applied for all elements, and a more stringent filter (30 × BEC) was applied specifically to Zr (<5.26 ppb), Hf (<0.12 ppb), Nb (<0.85 ppb), and Ta (<0.18 ppb) to eliminate potential spuriously high inter-element ratios of these elements. The latter filter resulted in the exclusion of data from five samples having the lowest Ta concentrations (JUIF121C, JUIF124, JUIF127, LC260, LC227).

Iron formation (FeR-3, FeR-4), iron ore concentrate (IOC-1), and shale (OU-6) RMs were measured alongside unknowns to estimate method accuracy (quantified as a percent bias of compiled means from this study relative to certified or literature values) and precision under repeatability conditions during the timeframe of the study. For the Fe-rich RMs, an additional test using 200 mg aliquot digests was undertaken to compare with data from 100 mg aliquot digests. The mean concentrations and 1rsd of FeR-3 (n = 8), FeR-4 (n = 8), IOC-1 (n = 8), and OU-6 (n = 2) measured during this study are reported in **Table A6.4**. Certified concentrations are available for OU-6 and for selected elements in IOC-1, whereas FeR-3 and FeR-4 (now discontinued) have data available for comparison from previous studies.

The percent bias relative to certified values of OU-6 (Potts and Kane, 2005) is within ±5% for most elements except Cu (+17%), Zr (–13%), and Hf (–11%). Most trace element

values for IOC-1 remain uncertified, with many reported by NRCan/CANMET still being provisional (S, V, Co, Sr, Mo), semi-quantitative (Cu, Ga, Ba, Ce), or unmeasured/unreported (i.e., Ni, Zn, Nb, Sn, Sb, Ta, W, Th, U, and REE+Y excluding Ce). The percent bias relative to provisional and semi-quantitative values of IOC-1 is within ±3% and ±6%, respectively. This study provides one of the first published datasets to characterize a wide suite of trace elements in IOC-1. The percent bias of FeR-3 and FeR-4 relative to tabletop digests in Sampaio and Enzweiler (2015) is within ±10% and better (±5%) for the REE+Y.

Overall, the compiled precision (1rsd) for most elements in the RMs is within ±5% except for some elements at very low abundances in the specific material (e.g., Be, Sc, Cs, Nb, Cd). In more detail, it is apparent that the 1rsd of the mean of repeated measurements of individual digests of IF/iron ore concentrate RM is lower than the 1rsd of the compiled mean from measurements of all digests; small but repeatable biases for some elements are found between the means of measurements from separate digests. The inter-digest bias is less apparent between measurements of separate 200 mg aliquot digests, resulting in a lower compiled 1rsd from measurements of all 200 mg aliquot digests, when compared to data from the 100 mg aliquot digests (**Table A6.5**). These observations are tentatively interpreted to reflect the higher density of the Fe-rich material compared to other sample matrices, such that effects from minor powder heterogeneities are amplified in digests of the 100 mg relative to the 200 mg aliquots. Accordingly, a recommendation of digesting the higher aliquot mass (≥200 mg) of well-shaken/homogenized powder is proposed for future studies dealing with Fe-rich IF. Intermediate method precision assessed at the University of Tübingen has been demonstrated to be excellent (<1–3% 1rsd for all but a select few elements having ultra-low abundances and those heterogeneous in the reference materials) for different matrices, including another trace element-

depleted IF RM, IF-G (Albut et al., 2018). This precision compares well with similar applications of this drift-corrected, rock-calibration method as described for other laboratories (Kamber, 2009; Marx et al., 2010; Rosca et al., 2018; Babechuk et al., 2019).

2.5 Results

2.5.1 Iron formation petrography and mineralogy

An overview of the mineralogical and petrographic characteristics of the Sokoman IF (i.e., excluding the RTH) is provided here (**Figs. 2.13–2.19**). More detailed characterizations are laid out in previous studies (e.g., Dimroth and Chauvel, 1973; Klein, 1974; Klein and Fink, 1976; Maliva et al., 2005; Simonson, 1987; Zajac, 1974).

2.5.1.1 Intraformational chert and quartz cements

Intraformational chert clasts targeted for subsampling in this study are composed of equigranular microcrystalline (<20 μm) quartz interspersed with fine-grained, disseminated, 'dusty' hematite and subordinate anhedral, 'spongy' hematite (**Figs. 2.12H, 2.14A–B**). Many workers consider rocks composed of microcrystalline quartz with fine-grained hematite disseminations to be jasper (e.g., Simonson, 1987). Similar textural features are observed within the interiors of coated grains (ooids). The most common intergranular quartz cements are generally of four types: (1) microcrystalline mosaic chert in which crystals are equant and randomly oriented (**Fig. 2.14C–D**); (2) microcrystalline domain chert that also contains crystals that are equant, but exhibit internal sweeping extinction; (3) blocky mesocrystalline (>20 μm) quartz with equant, randomly oriented crystals (**Fig. 2.14E**); and (4) drusy mesocrystalline quartz for which crystals are variably aligned normal to granule surfaces and the crystal size coarsens

from the edges of granules towards the pore centres (**Fig. 2.14F**). In the present study, it is noted that as per Maliva et al. (2005), although mesocrystalline quartz and megaquartz are both characterized by grain sizes greater than 20 μm, but the latter tends to exhibit unit extinction and planar grain boundaries.

2.5.1.2 Fe-silicates

The dominant Fe-silicate phase in granular intervals is greenalite that occurs as uniform, very fine- to fine-grained, ellipsoidal granules that commonly exhibit shrinkage cracks (**Figs. 2.15A–C, 2.19A–C**). These granules are typically coated with quartz, siderite, or other Fe-silicate phases, and are cemented with either drusy to blocky mesocrystalline quartz, siderite, or a combination thereof. In some cases, greenalite granules display sieve-like textures that appear to preserve intragranular porosity (**Fig. 2.19B**). Granular occurrences of greenalite are generally restricted to the silicate-carbonate facies and to a lesser extent the magnetite-carbonate facies. Stilpnomelane typically appears either as networks of radial sheaves, individual blades, or prismatic sections; granular occurrences are rare (**Figs. 2.15D–E, 2.19D–E**). Stilpnomelane is generally replaced by magnetite and less commonly by minnesotaite. The abundance of stilpnomelane is not directly correlated with variations in mineral assemblages as it is present across all facies, but appears to be most abundant within the LIF. In banded intervals, minnesotaite is more abundant and occurs either as well-formed, randomly oriented, acicular aggregates that exhibit radial ‘bowtie’ textures (**Figs. 2.15A–B, 2.15F, 2.19C, 2.19H**), or as disseminated platy crystals. Crosscutting relationships and overgrowth textures show that minnesotaite formed later than both greenalite and stilpnomelane.

2.5.1.3 Carbonates

Siderite is generally the predominant carbonate mineral among all units excluding the hematite-carbonate facies and the PGC unit within the magnetite-carbonate facies. Siderite commonly forms granules, thin laminae associated with carbonaceous material, or medium- to coarse-grained, subhedral to euhedral rhombs (**Figs. 2.16A–D, 2.19F–G**). Siderite laminae and microgranular siderite are most common in the silicate-carbonate facies, whereas coarse granular and rhombohedral forms are more prevalent in the magnetite-carbonate facies. Specifically, coarse granular occurrences of siderite are typical of the GC samples and are characterized by medium to very coarse, sand-sized (up to 2 mm) granules cemented by drusy to blocky mesocrystalline quartz and partially replaced by coarse-grained ankerite (**Fig. 2.19F**). Ankerite occurrences are typically present either as disseminated, coarse-grained, subhedral to euhedral rhombs, or as fine-grained, poorly crystallized forms within fine laminae associated with siderite and Fe-oxides, as well as overgrowth rims on some granules (**Figs. 2.16C–F**). Coarse-grained ankerite occurrences are commonly observed as pervasive mottled overprints in the PGC unit, whereas fine-grained, poorly crystalline occurrences are characteristic of banded intervals in the magnetite-carbonate facies. In some samples, sieve-like textures are also present (**Fig. 2.19G**). Importantly, within the hematite-carbonate facies, ankerite is the predominant carbonate phase. Calcite was not identified petrographically, but BSE imaging and MLA classification indicate its presence in one LC sample (**Fig. 2.19H**). This calcite occurrence is texturally homogeneous without a well-defined habit or cleavage. Chert inclusions and crosscutting siderite and minnesotaite suggest an early paragenesis for the calcite, after chert but prior to siderite and minnesotaite formation.

2.5.1.4 Oxides

Magnetite is the predominant Fe-oxide phase among most units excluding those of the hematite-carbonate and hematite-magnetite facies. Typical forms are very fine- to very coarse-grained (10–500 μm), subhedral to euhedral octahedra (**Figs. 2.17, 2.18A–B, 2.19D–E, 2.19H**). Within banded intervals, magnetite octahedra are generally parallel to bedding. However, crosscutting relationships show that many aggregates also cut bedding, suggesting multiple generations of magnetite. In granular intervals, magnetite commonly forms replacement rims and overgrowth textures around granules. Hematite occurrences are generally of three types: (1) fine-grained (1–10 μm), anhedral, 'spongy' hematite (**Figs. 2.14A–B, 2.17C–D, 2.17F**, **2.18A–D**); (2) very fine-grained (<1 μm), microcrystalline material, referred to as 'hematite dust' (**Figs. 2.14A–B, 2.17C–D, 2.18A–D**); and (3) fine-grained (5–20 μm), anhedral to subhedral, elongated to microplaty/flaky aggregates (**Figs. 2.18E–F, 2.19I–J**). Hematite dust is generally observed within intraformational chert and oolith cores, whereas 'spongy' and microplaty hematite are more common in the cortical layers of the ooliths and in the rims of chert granules. Microplaty/flaky hematite is also the least common textural variety observed. Crosscutting relationships and inclusions of hematite within coarse subhedral and euhedral magnetite octahedra suggest an earlier paragenesis for hematite relative to magnetite within the hematite-magnetite, hematite-carbonate, and magnetite-carbonate facies.

2.5.1.5 Accessory phases

Apatite occurs mainly as very fine-grained (10–60 μm), subhedral to euhedral, tabular to prismatic grains that typically form aggregates. Apatite aggregates appear to replace greenalite granules in some samples (**Fig. 2.19K–L**). Inclusions of apatite within surrounding ankerite

indicate an earlier paragenesis, specifically prior to ankerite but after greenalite and chert, based on the presence of the latter two minerals as inclusions within the apatite aggregates. In general, apatite is most commonly associated with siderite and ankerite.

Pyrite is rare within the Sokoman IF but is locally present in some units within the magnetite-carbonate (GC) and silicate-carbonate facies (LC, LIF). In these units, pyrite grains are very fine- to coarse-grained (10–150 μm), subhedral to euhedral, and are commonly disseminated. Pyrite grains, together with minor chalcopyrite, were also noted to concentrate within some stylolite seams, as observed in one LC sample (**Fig. 2.19M**) A coarse-grained, subhedral scheelite grain was also observed within this pyrite-rich interval of the same LC sample (**Fig. 2.19N**).

Albite and orthoclase were not identified petrographically, but BSE imaging and MLA classification indicate that these minerals are mostly present in the magnetite-carbonate facies, specifically within the LRGC, PGC, and JUIF. The documented feldspar phases are fine-grained, anhedral to subhedral, and considered to be authigenic (**Fig. 2.19O**).

2.5.2 Major elements and LOI

Chemostratigraphic patterns in major element data are congruous with changes in the dominant mineral assemblages across lithofacies (**Figs. 2.20–2.30**). Bulk chemical ranges obtained in this study are comparable with those reported for the Sokoman IF in the Howells River area (Klein and Fink, 1976). High SiO_2 and Fe_2O_{3T} concentrations are observed among all units, but large intra-unit variations likely represent textural heterogeneity inherent to IFs (e.g., sampling Fe-carbonate/Fe-oxide-rich bands vs. chert-rich granular intervals) (**Fig. 2.20A, 2.20C**). The high modal abundances of chert and quartz in the JSP and GC are reflected by the

highest SiO_2 contents [mean ± 1s, JSP: 63.2 ± 22.1 (wt.%); GC: 57.6 ± 25.2 [(wt.%)], but also some of the lowest Fe_2O_{3T} concentrations [JSP: 28.2 ± 20.5 (wt.%); GC: 25.2 ± 14.3 (wt.%)]. Concentrations of FeO are highest in the silicate-carbonate [LIF: 21.8 ± 6.9 (wt.%); LC: 20.1 ± 8.2 (wt.%)] and magnetite-carbonate [LRGC: 18.8 ± 10.2 (wt.%)] facies, consistent with the abundance of Fe(II)-bearing carbonates and silicates within these units. In contrast, the lowest FeO contents are in the hematite-magnetite facies [JSP: 0.51 ± 0.39 (wt.%)] and consequently, JSP samples also have the highest molar Fe(III)/Fe(II) ratios (59.6 ± 4.4). Excluding the JSP, limited variation exists in molar Fe(III)/Fe(II) ratios among other units, but intra-unit variations are greater in hematite-rich units (e.g., URC: 5.02 ± 4.53) relative to hematite-poor units (e.g., LC: 0.69 ± 0.78).

Inter-unit variations in CaO, MgO, and MnO contents are small and are not diagnostic of changes in mineralogical facies (**Fig. 2.20H, 2.20K–L**). Concentrations of these oxides show very strong positive correlations with each other and collectively (calculated as molar CaO+MnO+MgO) have a very strong association with LOI_T values (e.g., PGC: $r = 0.94$, $p < 0.001$; GC: $r = 0.95$, $p < 0.001$) and $LOI_{(500\text{-}1000\ °C)}$ values (e.g., PGC: $r = 0.99$, $p < 0.01$; JUIF: $r = 0.86$, $p < 0.001$), suggesting that Ca, Mg, and Mn abundances are all controlled by Fe-silicate and carbonate abundances (Dean, 1974; Heiri et al., 2000). Concentrations of K_2O, Na_2O, and P_2O_5 are generally low among all units with a mean ± 1s of 0.06 ± 0.09 [wt.%] ($n = 21$), 0.14 ± 0.12 [wt.%] ($n = 83$), and 0.03 ± 0.03 [wt.%] ($n = 108$), respectively. In comparison, RTH samples have higher K_2O, Na_2O, and P_2O_5 contents [$n = 3$, 7.21 ± 0.43 (wt.%), 0.51 ± 0.22 (wt.%), 0.07 ± 0.003 (wt.%), respectively].

Trends in major element composition across units can also be visualized using a molar SiO_2-Fe_2O_{3T}-(CaO+MnO+MgO) ternary plot (**Fig. 2.31A**). In this figure, data for chert-

dominated units (JSP, GC) plot near the SiO_2 apex, those for Fe-oxide-rich units (JUIF, LRGC) trend toward the Fe_2O_{3T} apex, and data for Fe-carbonate-rich units trend toward the CaO+MnO+MgO (LC, LIF) apex. Data plotted in the same ternary compositional space also effectively demonstrate the more consistent and Si-rich compositions (proximal to the SiO_2 apex) of the extracted intraformational chert subsamples compared to the more variable mineral composition (i.e., more oxide- and/or carbonate-rich) of their corresponding bulk sample counterparts (**Fig. 2.31B**). The size of the sample bubble in **Fig. 2.31** tracks Ti abundance and documents the (1) overall low detrital element abundances in all IF samples relative to the RTH, (2) minimal inter-unit variation apart from a tendency towards higher values in selected samples of the LRGC and JUIF units, and (3) lower detrital element abundances in intraformational chert subsamples relative to corresponding bulk samples (**Section 2.5.3**).

Enrichments in Fe, Mn, and P are determined from normalization to Zr (w/w), and P is further evaluated using the enrichment factor (EF) approach, as discussed in detail in **Section 2.5.5**. Chemostratigraphic trends in ΣFe/Zr, Mn/Zr, P/Zr, and P_{EF} (**Figs. 2.32–2.41**) are generally antithetic to those of detrital elements (**Section 2.5.3**). Enrichments in Fe and Mn are elevated across all units relative to the RTH (**Fig. 2.20F, 2.20I**; mean ± 1s, ΣFe/Zr = 918.4 ± 175.5; Mn/Zr = 41.9 ± 47.5) and the highest mean Fe and Mn enrichments are in the URC (1.18×10^5 ± 8.32×10^4; 2354.2 ± 1926.3), PGC (1.25×10^5 ± 9.84×10^4; 5390.7 ± 9205.6), and LC (7.89×10^4 ± 5.51×10^4; 3832.8 ± 4337.8). Similarly, P/Zr ratios (w/w) and P_{EF} are lowest in the RTH (**Fig. 2.20O–P**; mean ± 1s, P/Zr = 3.30 ± 0.48; P_{EF} = 0.84 ± 0.12) and increase upsection from the JSP (27.2 ± 18.6; 6.89 ± 4.70) and LIF (51.2 ± 35.8; 13.0 ± 9.1). High values are observed in the PGC (46.7 ± 28.4; 11.8 ± 7.2) and URC (59.0 ± 66.9; 15.0 ± 16.9) and return to slightly lower values in the JUIF (24.7 ± 22.1; 6.3 ± 5.6), before increasing again in the LC (45.8 ± 25.2; 11.6 ±

6.4). On a unit-specific basis, molar Mn/ΣFe ratios overlap across units but higher ratios are generally observed in both JUIF (mean ± 1s, 0.046 ± 0.042) and LC (0.040 ± 0.024) (**Fig. 2.20J**). Although elevated Mn/ΣFe ratios are also observed in some GC and JSP samples, these appear to be a consequence of greater chert content and associated lower Fe_2O_{3T} rather than true Mn-enrichments. Molar P/ΣFe ratios (**Fig. 2.20Q**) are highest in the RTH (0.0066 ± 0.0003) and LIF (0.0019 ± 0.0011) and gradually decrease upsection before reaching a minimum in the URC (0.00080 ± 0.00050). An increase is observed in the overlying GC (0.0014 ± 0.0009) followed by slightly lower values in the JUIF (0.0011 ± 0.0005) and LC (0.0013 ± 0.0011). It is noted that chemostratigraphic trends in P/ΣFe ratios exhibit broad positive correlations with detrital element abundances in select intervals including: (1) LIF towards bottom-mid LRGC, and (2) GC towards bottom-middle of the JUIF.

2.5.3 Detritally sourced elements

Elements typically resident in detrital minerals (detrital elements; DE) (Al_2O_3, Ga, Hf, Nb, Sc, Ta, Th, Ti, Zr) have very low abundances in all units of the Sokoman IF, especially when compared against the RTH. For example, median concentrations of Al_2O_3, Hf, Th, Ti, and Zr in the Sokoman IF are 0.14 wt.%, 0.0447 ppm, 0.0513 ppm, 27.66 ppm, and 4.26 ppm, respectively, whereas for the same components the RTH samples have median concentrations of 13.86 wt.%, 2.47 ppm, 9.10 ppm, 3302 ppm, and 90.8 ppm, respectively. Strong positive correlations of Zr with Hf, Ga, Nb, Ta, and Th, and Ti with Ta and Sc are evident (**Fig. 2.42**). However, a slight decoupling and resulting weaker positive correlation exist between Ti and Zr in some samples.

Chemostratigraphic trends in DE abundances outline cyclical patterns (irregular sinusoidal) across all facies of the Sokoman IF (**Figs. 2.32–2.41**). Detrital element abundances increase upsection from the LIF-LRGC contact towards mid-LRGC (Sheps Lake, Hayot Lake) and from the base of the JSP towards its mid-section (Lac Ritchie). This trend is followed by an overall decrease towards the PGC-URC contact and a slight increase towards the URC-GC contact. From the GC, values increase towards the base of the JUIF before returning to lower levels in the upper JUIF/mid-LC. This pattern is followed by another increase upsection towards the upper LC or MS-LC contact, where present.

Elevated Zr/Hf and Nb/Ta ratios (w/w) are present among all samples (Zr/Hf = 42.9–409.4, median: 97.8; Nb/Ta = 15.5–679.7, median: 56.4) relative to average upper crustal composites [e.g., UCC (36.7, 13.4; Rudnick and Gao, 2003); MuQ (36.9, 13.8; Kamber et al., 2005)] except for the RTH (Zr/Hf = 36.9 ± 0.13; Nb/Ta = 14.4 ± 0.97). Although inter-unit overlaps are present, both Zr/Hf and Nb/Ta ratios increase upsection from the LIF (mean ± 1s, Zr/Hf = 60.9 ± 22.2; Nb/Ta = 49.4 ± 55.5) towards the LC (138.1 ± 57.1; 124.2 ± 75.8). Chemostratigraphic Zr/Hf and Nb/Ta trends show identical patterns, but both are broadly antithetic to DE abundances with the highest ratios occurring generally in samples having lower Nb-Ta-Zr-Hf abundances (**Figs. 2.32–2.41**). The elevated Zr/Hf and Nb/Ta ratios in the Sokoman IF exceed the ratios in the dissolved load of modern river waters such as those of the Ottawa River basin (32.5 ± 5.1, 25.1 ± 7.7; Babechuk et al., 2020) and are instead closer in magnitude to those of modern seawater (e.g., Pacific Ocean: 45–350, 14–85; Firdaus et al., 2011). In terms of Zr/Hf, examples from older IFs including microdrilled samples of the ~2.7 Ga Carajás IF [$(Zr/Hf)_{Fe\text{-}bands}$ = 35–80, $(Zr/Hf)_{Si\text{-}bands}$ = 50–64; Justo et al., 2020)], and the 2.74 Ga Temagami IF [$(Zr/Hf)_{Fe\text{-}bands}$ = 39–55, $(Zr/Hf)_{Si\text{-}bands}$ = 17–48; Bau and Alexander, 2009)] show

an overlap, albeit more limited, with those in the Sokoman IF. As such, it appears that shifts towards greater fractionation with higher Nb/Ta and Zr/Hf constitutes an additional monitor of decreasing detrital particle influence at the expense of progressively detecting an authigenic/seawater signature in the residual Nb-Ta-Zr-Hf budget of the IF.

2.5.4 Rare earth element systematics (REE+Y) and Ce anomalies

2.5.4.1 Overall and unit-specific REE+Y patterns

The REE+Y data are normalized to the average composition of the local shale (Ruth Slate mean, RTH, $n = 3$) for reporting trends in the Sokoman, to the modern alluvial sediment composite MuQ (Mud from Queensland, Australia; Kamber et al., 2005) when comparing with other ca. 1.88 Ga IFs, and to CI-chondrite (Barrat et al., 2012) for separate calculations of Eu anomalies and tetrad effects.

The RTH and average upper crustal normalizers both have negligible Ce anomalies and similar Y/Ho mass ratios of 27.5 and 26.2, respectively. The MuQ normalization produces very similar trends to those of Post-Archean Australian Shale (PAAS; e.g., Pourmand et al. 2012). Normalizing to the RTH offers two key advantages: (1) it represents a better approximation of the local siliciclastic composition (i.e., more felsic compared to MuQ); and (2) it highlights local basin-specific effects on the soluble REE+Y load. The main difference arising in REE+Y patterns of IF due to normalization with RTH over MuQ is in the LREE/HREE slope (e.g., $[Pr/Yb]_{SN}$) due to the more LREE-enriched pattern in the former; only very minor differences are observed in REE+Y anomalies (La, Gd, Eu, Y) and other ratios that define pattern architecture, which do not change major interpretations (**Fig. 2.43**). The primary MuQ-normalized features are also retained after correction of the IF samples to a detrital-free composition using the RTH

mean composite and assuming that the detritus is represented by different elements (e.g., Hf, Ta, Th), following **Eq. 2.1** where DE = detrital element and Ln = lanthanide.

$$\mathbf{Ln_{(detritus\text{-}free)} = Ln_{(sample)} - Ln_{(RTH\ mean)} \cdot [DE_{(sample)} / DE_{(RTH\ mean)}]} \qquad \mathbf{(2.1)}$$

In general, this correction results in normalized REE+Y patterns that are nearly parallel to those of the uncorrected (original) composition and only minor shifts in calculated anomalies. As such, the original data (i.e., not detrital-free) are used here in all subsequent plots and calculations.

Normalized REE+Y patterns of the Sokoman IF show several features strikingly reminiscent of modern seawater, including (1) LREE depletion relative to HREE, (2) small negative Ce anomalies, and (3) small positive La, Gd, and Y anomalies (**Figs. 2.44–2.46**; Bau and Dulski, 1996; Bolhar et al., 2004). However, unlike modern seawater, many Sokoman samples also display varying degrees of positive Ce and Eu anomalies, similar to those of other contemporaneous IFs from the Animikie Basin (Kato et al., 2006; Planavsky et al., 2010a, 2018). In the present study, REE+Y anomalies are calculated using the geometric projection of Lawrence et al. (2006), as outlined in **Eqs. 2.2–2.6** unless otherwise stated.

$$\mathbf{La^*_N = Pr_N \cdot (Pr_N/Nd_N)^2} \qquad \mathbf{(2.2)}$$

$$\mathbf{Ce^*_N = Pr \cdot (Pr_N/Nd_N)} \qquad \mathbf{(2.3)}$$

$$\mathbf{Eu^*_N = Sm_N \cdot (Sm_N/Nd_N)^{0.5}} \qquad \mathbf{(2.4)}$$

$$\mathbf{Gd^*_N = Tb_N \cdot (Tb_N/Dy_N)} \qquad \mathbf{(2.5)}$$

$$\mathbf{Lu^*_N = Yb_N \cdot (Yb_N/Tm_N)} \qquad \mathbf{(2.6)}$$

The Sokoman IF exhibits a wide range of Ce anomalies (**Figs. 2.48C, 2.49**) from small negative to large positive values [$(Ce/Ce^*)_{SN}$ = 0.77–1.84; mean ± 1s = 1.20 ± 0.26; *n* = 109]. The largest positive Ce anomalies are observed in samples of the LC [mean ± 1s: $(Ce/Ce^*)_{SN}$ =

1.40 ± 0.18, n = 17] and the JUIF (1.39 ± 0.28, n = 30), whereas the most negative values occur in samples of the URC (0.95 ± 0.15, n = 10) and the LIF (1.00 ± 0.18, n = 6). When normalized to MuQ, the observed range of Ce anomalies [$(Ce/Ce^*)_{MuQ}$ = 0.80–1.89; mean ± 1s = 1.24 ± 0.27; n = 109] is comparable to those of samples from previous studies of the Sokoman IF as well as of other ca. 1.88 Ga IFs [$(Ce/Ce^*)_{MuQ}$ = 0.51–1.85; mean ± 1s = 1.17 ± 0.22; n = 75; Frei et al., 2008; Planavksy et al., 2010a, 2018; Raye et al., 2015]. When plotted on the Ce-Pr anomaly cross-plot, as per Bau and Dulski (1996), the Sokoman IF samples (**Fig. 2.49A**), together with other ca. 1.88 Ga IF (**Fig. 2.49B**), outline hyperbolic trends that encompass both true positive and true negative Ce anomaly fields. Note that on the latter end of the hyperbolic trend, there are only five Sokoman samples from this study (URC133B, URC133C, URC148B, URC148C, PGC276) for which data consistently plot in the true negative Ce anomaly field [i.e., $(Pr/Pr^*)_{SN} > 1.05$], after using different normalizers (RTH, MuQ) and attempting variable detrital corrections.

Samples of the Sokoman IF generally have moderate to large positive La [$(La/La^*)_{SN}$ = 1.07–2.08; mean ± 1s = 1.55 ± 0.24) and Gd [$(Gd/Gd^*)_{SN}$ = 0.85–1.20; mean ± 1s = 1.08 ± 0.05) anomalies (**Figs. 2.48B, 2.48E**), and muted Lu [$(Lu/Lu^*)_{SN}$ = 0.83–1.10; mean ± 1s = 1.00 ± 0.04) anomalies (**Fig. 2.48F**). Lanthanum anomalies broadly increase from the LIF [$(La/La^*)_{SN}$ = 1.32 ± 0.24] towards the LC [$(La/La^*)_{SN}$ = 1.55 ± 0.24], whereas unit-specific trends in Gd and Lu anomalies are less well defined. The IF has Y/Ho ratios (23.5–42.9; mean ± 1s: 33.3 ± 4.0) that exceed the average upper crustal value (**Fig. 2.48G**) and those of the RTH samples (27.0-28.1; mean ± 1s: 27.5 ± 0.55). The mean Y/Ho ratios of each unit overlap within their respective standard deviations, but a general decrease in magnitude exists from samples of JSP (35.4 ± 5.3, n = 8) towards JUIF (31.2 ± 3.3, n = 30) before returning to higher levels in LC samples (33.3 ±

3.1, n = 17). The $(Pr/Yb)_{SN}$ ratios among all IF units range from 0.10 to 0.92 with a mean of 0.28 ± 0.13 (**Fig. 2.48H**), indicating variable depletion in the LREE > HREE relative to RTH. Moreover, an overall decrease exists in the magnitude of this ratio from LIF [$(Pr/Yb)_{SN}$ = 0.40 ± 0.14] towards LC [$(Pr/Yb)_{SN}$ = 0.28 ± 0.22]. The Sokoman IF exhibits positive Eu anomalies [$(Eu/Eu^*)_{SN}$ = 0.97–2.42; mean ± 1s = 1.48 ± 0.27] (**Fig. 2.48D**) with the highest mean values observed in JSP and LIF samples [$(Eu/Eu^*)_{SN}$ = 1.44 ± 0.29 and 1.72 ± 0.40, respectively]. Europium anomalies in IF are often reported with CI-chondrite normalization (e.g. Viehmann et al. 2015); this normalization shifts all RTH-normalized Eu anomalies of the Sokoman samples to slightly lower values [$(Eu/Eu^*)_{CN}$ = 0.77–1.92; mean ± 1s = 1.18 ± 0.21] by avoiding the slight negative CI-chondrite normalized Eu anomalies of the RTH [$(Eu/Eu^*)_{CN}$ = 0.75–0.84; mean ± 1s = 0.80 ± 0.04].

An additional feature of the Sokoman IF REE+Y patterns, best observed with CI-chondrite normalization, is expression of the W-type lanthanide tetrad effect (Bau, 1999; Ernst and Bau, 2021; Masuda and Ikeuchi, 1979). This tetrad pattern effect, in four groups [La-Nd, (Pm)-Gd, Gd-Ho, Er-Lu], can exist with either a convex (W-shape) or concave (M-shape) geometry, which is quantified here using tetrad coefficients, presented as tau (τ) values, calculated using the BLambdaR software (Anenburg, 2020). Negative τ values correspond to convex geometry, whereas positive τ values correspond to concave geometry. In the Sokoman IF, the fourth (Er–Lu) (τ_4) and third (Gd–Ho) (τ_3) tetrads are best developed (**Fig. 2.47**). With respect to τ_3 values (**Fig. 2.48I**), a gradual increase occurs upsection from JSP (median = –0.1693) towards URC (–0.1029) before returning to slightly lower values towards LC (–0.1315). A similar increasing trend upsection is observed for τ_4 (**Fig. 2.48J**) wherein values increase from LIF (–0.1348) towards JUIF (–0.0354) and subsequently drop slightly in LC (–0.0606). Strong

negative correlations are also observed between τ_4 and Y/Ho ratios ($r = -0.79$, $p < 0.001$), as well as between τ_4 and Gd and Lu anomalies ($r = -0.70$, $r = -0.83$, respectively; $p < 0.001$ for both).

Chemostratigraphic trends in ΣREE+Y follow similar irregular sinusoidal trajectories as that outlined for DE abundances (**Figs. 2.32–2.41**). However, these cyclical patterns are less evident for $(La/La^*)_{SN}$, $(Eu/Eu^*)_{SN}$, $(Gd/Gd^*)_{SN}$, $(Lu/Lu^*)_{SN}$, Y/Ho, and $(Pr/Yb)_{SN}$ such that the aforementioned parameters are instead only loosely correlated with DE abundances. Minimal correlation between REE+Y parameters and DE abundances is observed in intervals where the latter progressively increase upsection, specifically (1) near the LIF-LRGC contact towards the middle LRGC, and (2) from the GC towards the bottom middle section of JUIF in both Sheps Lake and Hayot Lake drill core. Observations from Lac Ritchie drillcore are similar, but the first interval spans the base of JSP towards the bottom middle section of LRGC instead. Chemostratigraphic trends in $(Ce/Ce^*)_{SN}$ are also somewhat decoupled from those of $(Gd/Gd^*)_{SN}$, $(Lu/Lu^*)_{SN}$, Y/Ho, and $(Pr/Yb)_{SN}$. Instead, $(Ce/Ce^*)_{SN}$ shows a consistent shift towards more positive values from the base of LIF and peak at PGC, before returning to lower values in URC and GC. This pattern is subsequently followed by a sharp increase in $(Ce/Ce^*)_{SN}$ values from the GC-JUIF contact towards the middle JUIF before gradually decreasing towards the LC-MS contact. In Lac Ritchie drill core, the $(Ce/Ce^*)_{SN}$ values progressively increase from the base of JSP and peak towards the middle to top sections of JSP, but are otherwise similar to those seen in Sheps Lake and Hayot Lake drill core. Chemostratigraphic trends in τ_3, and τ_4 notably display antithetic patterns to those of $(Gd/Gd^*)_{SN}$, $(Lu/Lu^*)_{SN}$, and Y/Ho among all units, such that negative τ values (W-shape) are matched by elevated Y/Ho, $(Gd/Gd^*)_{SN}$, and $(Lu/Lu^*)_{SN}$ values.

2.5.4.2 Bulk vs. chert REE + Y signatures

Intraformational chert REE+Y patterns are generally nearly parallel to their bulk IF counterparts, albeit being uniformly lower in total REE+Y contents (**Fig. 2.45**). Scatterplots of bulk and chert REE+Y signatures (**Fig. 2.50**) reveal that the RTH-normalized anomalies in the cherts for Ce (0.81–1.82), Gd (0.96–1.19), and Lu (0.83–1.10), as well as Y/Ho ratios (26.9–42.9), lack significant deviations from the bulk IF values, typically ranging within ±20% of the 1:1 line for all samples. Among these parameters, Ce anomalies and Y/Ho ratios are very similar between both fractions, evident by the well-defined linear trends (R^2 = 0.94 and 0.70, respectively) and close proximity of data to the 1:1 line in the scatterplots.

2.5.4.3 Detrital effects on REE+Y

The evaluated REE+Y parameters display poor correlations with Ti concentrations (**Fig. 2.51**) and with other detrital input monitors such as Ga, Zr, Hf, and Th (**Figs. 2.52–2.56**). However, minor detrital element admixtures can be discerned by the presence of hyperbolic 'tails' on ratio-element plots. These relationships can be modeled using mixing curves between detrital-poor ('pure') and detrital-rich endmembers (**Fig. 2.51**), the latter being well represented by data for RTH samples (**Section 2.6.2**). Nonetheless, selecting a 'pure' endmember is not always straightforward owing to greater variability in the low-DE end, suggesting that no single mixing line can truly represent all variations in the REE+Y as a function of detrital mixtures. Simple mixing models of DE abundances between the mean of the 10 'purest' Sokoman IF samples with the lowest DE abundances (Ti, Zr, Ga, Nb) and the RTH mean demonstrate that the vast majority of data for the Sokoman IF samples lie between 0% and 5% along the mixing lines. This result, therefore, illustrates that although some variation in the REE+Y can be attributed to

detrital admixtures, other processes (e.g., particle scavenging, dissolution) played a more significant role in influencing REE+Y variability, especially at the lowermost end of the DE concentration range.

2.5.5 Trace element (Cr, V, U, Ni, Co, Zn) patterns

Authigenic enrichments of other trace elements (TEs) are expressed as enrichment factors (EFs), as per Tribovillard et al. (2006) and are calculated as $EF = [(X/Zr)_{sample}] / [(X/Zr)_{MuQ}]$, where X is the concentration of the selected element and MuQ is taken as an independent upper crustal composite for the detrital baseline composition. Normalization to the RTH mean tends to shift EFs for most TEs to lower values relative to normalization to MuQ, but the latter approach is preferred due to variability in the abundance of some TEs (e.g., Co, Zn) observed among the three RTH samples. Although EFs are traditionally normalized using Al or Ti, the use of Zr is preferred here due to the low Al concentrations in the IF samples, commonly below the XRF detection limit. Our use of Zr as a detrital monitor is validated by the strong positive correlations between Zr and other immobile trace elements including Ga, Hf, Nb, Ta, and Th (**Section 2.5.3**). Zirconium is also preferred over Ti owing to a slight decoupling between these elements and because normalization to Ti over Zr tends to inflate EF values in samples of the Sokoman IF. For example, $Cr_{EF–Zr}$ has a more limited range of values (0.05–7.81) when compared to $Cr_{EF–Ti}$ (0.19–34.84). However, despite differences in the absolute Zr- or Ti-normalized EF values or changes to the applied detrital baseline (RTH vs. MuQ), relative inter-sample and stratigraphic enrichment trends are similar. The means and ranges of enrichment factors of Cr, V, U, Ni, Co, and Zn of the various Sokoman IF units and RTH are listed in **Table 2.1**. In conjunction with

EFs, TE enrichments are also evaluated as Fe- and Ti-normalized ratios, where relevant, to more directly compare with the values published in IF compilation studies (**Table 2.2**).

Enrichment factors of Cr, V, U, Ni, Co, and Zn overlap across the Sokoman IF and do not exhibit strong inter-unit variations (**Fig. 2.57**). Significant overlaps in values between the Sokoman IF and RTH are also evident for all TEs except Cr, which appears to be more enriched in the latter unit. In general, the highest mean and median TE EFs are in the LC, LIF, LRGC, PGC, and URC. Relative to other ca. 1.88 Ga IFs, evolving crust-normalized molar Cr/Ti ratios (i.e., normalized to molar Cr/Ti ratios of upper continental crust according to the restoration model of Condie (1993)) in the Sokoman IF are comparable, whereas evolving crust-normalized molar U/Ti and molar Co/Ti ratios are both slightly elevated and cover a wider range of values. In contrast, molar TE/ΣFe ratios in the Sokoman IF are comparable but trend towards the lower range of values relative to the compilation of other 1.88 Ga IFs (U, Ni, Co, Zn).

Chemostratigraphic trends in TE abundances (ppm) and their respective molar TE/ΣFe ratios are variably correlated with those of DE abundances (**Figs. 2.58–2.67**). Among these, Cr and U exhibit the strongest positive correlations across all units, followed by V and Ni. The weakest positive correlations are observed for Co and Zn. In contrast, TE EFs show chemostratigraphic patterns that are only weakly similar to TE (ppm) and molar TE/ΣFe ratios, but certain intervals have pronounced antithetic patterns, including (1) the base of LIF towards the bottom middle LRGC, and (2) near the URC-GC contact towards the bottom middle JUIF. An exception is the JSP for which molar TE EFs are coupled with molar TE/ΣFe ratios, and are collectively antithetic to TE (ppm). When molar TE/ΣFe ratios are plotted against TE EFs, two main endmember trendlines are apparent: (1) high TE/ΣFe–low TE_{EF} samples (TE/ΣFe >> TE_{EF}) with high DE abundances defined by samples from GC, uppermost LIF, lower JUIF, and

bottommost LRGC; and (2) low TE/ΣFe–high TE_{EF} (TE_{EF} >> TE/ΣFe) samples with low DE abundances defined by samples from LRC, URC, PGC, upper LRGC, upper JUIF, and bottom to mid-LC.

2.6 Discussion

2.6.1 Mineral paragenesis and early origin of hematite

The preserved mineral assemblages in the Sokoman IF represent the dehydrated and recrystallized products of the original sedimentary precursors, including Fe-(oxyhydr)oxides, amorphous Fe-Si gels, and/or carbonate oozes (**Fig. 2.68**; Klein, 2005; Konhauser et al., 2017; Pufahl, 2010). Reconstructing geochemical signatures of coeval seawater from IF depends on understanding the nature of these primary precipitates and their pathways of mineral transformation during subsequent diagenetic and metamorphic reactions (e.g., Posth et al., 2013, 2014; Tosca et al., 2016). Previous work on the Sokoman IF in the Howells River area outlined two main paragenetic pathways: (1) an anoxic pathway characterized by magnetite, chert, and greenalite, which were all deposited either in coastal regions distal from shallow oxygen oases or in deeper, anoxic sections of the shelf; and (2) a suboxic pathway defined by hematite- and chert-rich assemblages that were deposited within or near shallow oxygen oases (Raye et al., 2015). In the present study, we establish that the anoxic pathway most closely corresponds to the silicate-carbonate facies, whereas the suboxic pathway is represented most closely by the hematite-carbonate, hematite-magnetite, and magnetite-carbonate facies.

In the anoxic pathway, microcrystalline chert, greenalite, siderite, and fabric-retentive magnetite are interpreted to be the earliest phases. These phases share a similar set of features including fine-grain size and propensity to retain primary sedimentary fabrics including bedding,

laminations, and framework grains. Microcrystalline chert, occurring both as framework grains and interstitial cements, is ubiquitous among all Sokoman IF units; its subsequent recrystallization to coarser-grained mesocrystalline and megaquartz is attributed to late diagenetic to early metamorphic reactions (Dimroth and Chauvel, 1973; Simonson, 1987). Greenalite and stilpnomelane represent the oldest Fe-silicate phases, with the former having crystallized earlier based on a smaller grain size, lesser degree of crystallinity, and prevalence as framework grains. The crosscutting nature of minnesotaite and its common occurrence as overgrowth rims, in contrast attest to a late origin, consistent with previous petrogenetic observations that suggest formation during late diagenesis to early metamorphism (Klein, 1974, 2005). Siderite represents the earliest carbonate phase as it is commonly fabric-retentive, and the wide array of textural varieties observed (microgranular, granular, rhombohedral, laminated) indicates that multiple generations are present. Although poorly crystalline ankerite-siderite associations are observed in some finely laminated intervals, fabric-destructive ankerite having strong recrystallization features is more common, indicating the prevalence of ankerite growth during late diagenesis. Laminated, subhedral fabric-retentive magnetite is likely authigenic to early diagenetic, whereas the more prevalent coarser-grained, euhedral, fabric-destructive magnetite is a product of late-stage recrystallization. All of these petrographic features are consistent with the lower and overall similar Fe(III)/Fe(II) ratios in the Sokoman IF units for which this anoxic pathway dominates (**Fig. 2.20E**).

The suboxic pathway resembles the anoxic pathway with respect to inferred late diagenetic to early metamorphic phases but differs mainly in terms of hematite being a paragenetically early phase. Following Sun et al. (2015), paragenetically early hematite herein refers to hematite that inherited the original Fe(III) from precursor Fe(III)-(oxyhydr)oxides.

Based on textural relationships, hematite ‘dust’ is interpreted to be the earliest iron oxide phase form followed by ‘spongy’ hematite and microplaty/flaky hematite aggregates. In samples of the hematite-carbonate and hematite-magnetite facies, fine-grained hematite ‘dust’ is a common constituent occurring in the interiors of oolith cores and intraformational chert clasts, whereas ‘spongy’ and microplaty/flaky hematite aggregates typically compose the cortical layers and/or rims of these granules. Several textural characteristics point to a paragenetically early origin for hematite, including: (1) the very fine-grain size, especially the hematite ‘dust;’ (2) preferential alignment of hematite occurrences following sedimentary fabrics (e.g., bedding, oolith cortices); (3) greater abundance of generally microcrystalline forms (i.e., hematite ‘dust’ and ‘spongy’ hematite are more abundant than microplaty hematite); and (4) paucity of hematite-bearing assemblages that cut, replace, and overgrow other paragenetically early phases. These textural features are consistent with the higher Fe(III)/Fe(II) ratios overall in the hematite/jasper-bearing units, but more notably with the localized Fe(III)/Fe(II) increases in the most hematitic samples of these units relative to adjacent carbonate- and/or magnetite-rich intervals (**Fig. 2.20E**).

The observed increases in Fe(III)/Fe(II) are decoupled from any clearly distinguishable pattern that implies horizontal or stratiform, post-depositional alteration (e.g., a groundwater oxidation front). Instead, these increases typically occur in the middle of thick deposits of IF, and tend to correspond to the aforementioned hematite textures interpreted here as being paragenetically early. The hematite occurrences observed in this study are clearly texturally different from those of both oxidized IF and high-grade hematite ore deposits in the eastern Labrador Trough (Conliffe, 2014, 2015). Such deposits feature abundant crosscutting hematite and quartz-filled microfractures that are unambiguously secondary and also include evidence of secondary porosity and collapse breccias. Furthermore, hematite within these highly altered

equivalents exclusively occurs as microplaty to patchy aggregates and replaces original sedimentary fabrics. Overall, the combined petrographic and Fe-based geochemical evidence from the areas of the Sokoman IF evaluated here are suggestive of a paragenetically early origin for the hematite.

2.6.2 Intraformational chert REE+Y data and primary seawater signatures in granular IF

The potential overprinting effects on IF geochemical and mineralogical features, from diagenesis to metamorphism to later chemical weathering, have recently motivated applications of phase-specific geochemical analysis to extract the purest, primary marine signatures (e.g., Baldwin et al., 2011; Haugaard et al., 2016a; Oonk et al., 2017, 2018; Poulton and Canfield, 2005). An emerging observation is that early diagenetic microcrystalline chert (avoiding coarsely recrystallized quartz; Maliva et al., 2005; van den Boorn et al., 2007) in IF is generally less susceptible to post-depositional processes relative to the oxide, carbonate, and Fe-silicate fractions. As such, this chert is viewed as recording a purer seawater signature despite having lower trace-element abundances that are more challenging to measure and more amenable to contamination by detrital (volcaniclastic or terrigenous) particles captured in the chert.

Analysis of the intraformational chert samples physically extracted from multiple units of the Sokoman IF represent, to the best of our knowledge, the first attempt to do this from texturally complex granular IF using an ultra-trace element geochemical comparison between both fractions. In this study, geochemical focus is given to REE+Y patterns, and especially Ce anomalies, for two main reasons. First, Ce anomalies in ca. 1.88 Ga IF are adopted as a critical line of evidence for a Ce redox cycle across Mn-redoxclines (e.g., Fryer, 1977b; Kato et al., 2006; Planavsky et al., 2010a). Second, most studies of IF have tacitly assumed that Ce

anomalies in bulk IF samples are not significantly influenced by post-depositional processes due to relative immobility of the REE and greater REE content of bulk sediments compared to fluids (e.g., Bau, 1993; Kato et al., 2006). However, there is now growing evidence for post-depositional disruption to REE+Y signatures in some IFs (e.g., Albut et al., 2018; Bonnand et al., 2020). Accordingly, even though samples from our study were extracted from drill core, the geochemical composition of the intraformational chert provides additional evidence atop petrographic examination (**Section 2.6.1**) that the chert preserves primary seawater features (in line with inferred early hematite formation in the chert), and that the IF geochemical signatures overall are not obviously disturbed from their depositional/early diagenetic states.

Within the intraformational cherts, the influence of detritus on REE+Y parameters is relatively minor (**Figs. 2.51–2.56**; **Section 2.5.4.3**). Also, the chert REE+Y parameters are very similar to those of the surrounding bulk IF (**Fig. 2.45**), including identical Ce anomalies and near-identical Y/Ho ratios (**Fig. 2.50**). Accordingly, data for the bulk IF-chert pairs both include all REE+Y features linked to seawater chemistry (**Section 2.5.4**) and the preservation of positive and negative Ce anomalies. Two main possibilities that may explain the matching REE+Y patterns are (1) post-depositional assimilation of chemical signatures across IF mineralogy and intraclasts, by either diagenetic, meteoric, or metamorphic fluids; and (2) preservation of similar primary/early diagenetic signatures in both reservoirs that reflect the ambient seawater chemistry at the same or similar water depth.

The first possibility, the post-depositional assimilation of REE+Y signatures during interaction with late diagenetic, meteoric, or metamorphic fluids, is deemed improbable. Such fluids would need to fortuitously possess and/or not fully erase the REE+Y parameters consistent with those of seawater. Also, variations in the REE+Y signatures are evident within intra-unit

samples extracted from the same drill hole, even for closely spaced samples, suggesting negligible homogenization of chemical signatures over significant depths of IF. For example, samples JUIF230 and JUIF231 from drill core 12-SL-1017D show notable differences in REE+Y parameters [e.g., JUIF230: $(Ce/Ce^*)_{SN}$ = 1.33; Y/Ho = 30.7 vs. JUIF231: $(Ce/Ce^*)_{SN}$ = 0.93; Y/Ho = 34.2], despite their proximity to each other (~3 m). Post-depositional processes, especially if pervasive, would arguably shift primary REE+Y signatures towards a unidirectional and more extreme signature (i.e., more positive or more negative values) and produce correlations with monitors of alteration. For instance, Albut et al. (2018) showed that outcrop samples of the ca. 2.95 Ga Izjermin IF in South Africa, overprinted by oxidative weathering as recognized by lower LOI (chiefly loss of carbonate) values and higher Fe(III)/Fe(II) ratios, have signatures trending towards true negative Ce anomalies, whereas drill core samples of the same IF do not (their Fig. 5). Such signatures are absent in the Sokoman IF and no links between hematite (and Fe(III)/Fe(II) ratios) and REE+Y parameters including ΣREE+Y (ppm), $(Ce/Ce^*)_{SN}$, and Y/Ho are found that could collectively point towards oxidative overprinting and the breakdown of Fe-silicates or Fe-carbonates to hematite. Finally, although oxygen isotope analysis of the Sokoman IF was not undertaken in this study, published data for quartz and magnetite separates from similar units suggest temperatures during late diagenetic to early metamorphic reactions of 140 to 310 °C ($\delta^{18}O_{mag}$ = –2.4‰ to 3‰; $\delta^{18}O_{qtz}$ = 17.1‰ to 23.9‰) and indicate a relatively closed-system exchange between IF minerals and fluids under low fluid/rock ratios (Raye et al., 2015).

More probable is the second possibility, that both bulk and intraformational chert REE+Y chemistry records seawater signatures at the same water depth throughout the integrated timeframe of IF precipitation and clastic input. Models for the genesis of intraformational chert

suggest that some early silica cementation occurred near the sediment-water interface within reach of erosion (Simonson, 1987; Cunningham et al., 2012). It follows that whereas intraclasts undergo varying degrees of transport from original source(s), seawater-specific signatures are locked in at the time of IF precipitation from contemporaneous seawater and sediment pore water. Such a process better describes the inter-unit variations observed in chert $(Ce/Ce^*)_{SN}$ values that closely follow those of bulk IF trends in the stratigraphy (e.g., –ve Ce in the URC and +ve Ce in the LC; **Fig. 2.49A**), and implies that the chert intraclasts were locally sourced. In other words, the dominant minerals controlling the REE+Y signatures in the cherts inherited the same patterns as the more diverse and volumetrically significant minerals present in the surrounding bulk IF. In terms of intraclast mineralogy, moderate to strong positive covariations between ΣREE+Y and molar CaO+MnO+MgO ($r = 0.78$, $p < 0.005$, $n = 11$), molar Mn/Ti ratios ($r = 0.80$, $p < 0.005$), and LOI ($r = 0.63$, $p < 0.05$), suggest that carbonate minerals captured in the chert had a dominant control on chert REE+Y concentrations even if these minerals only constitute a minor fraction of overall chert modes (**Fig. 2.31B**). A similar carbonate control on total REE+Y concentrations has also been demonstrated by laser ablation and sequential extraction data on the Griquatown and Kuruman IFs of South Africa for which higher REE+Y concentrations occur in the carbonate/acetate fraction relative to the oxide and silicate fractions (Oonk et al., 2018).

Overall, the effects of syn- (detrital contamination) and post-depositional (diagenesis, metamorphism, weathering) processes had an insignificant influence on the different REE+Y patterns of bulk and chert samples, hence implicating a primary control from water-depth-related redox variations. Our observations confirm that similar REE+Y patterns can be found between the different Si-rich and Fe-rich mineral phases within these granular IFs, thus validating the use

of bulk sampling in such detrital-poor granular IF devoid of obvious post-depositional overprinting. These observations can also constitute supporting evidence that the REE+Y patterns and hematite abundances/distributions (**Section 2.6.1**) both reflect primary basin redox and Fe-oxidation dynamics, rather than post-depositional redox changes.

2.6.3 Basin sediment composition and detrital contamination

The lithology of rocks undergoing continental weathering plays a central role in defining the clastic sediment composition and soluble flux to the marine realm and the redox-sensitive and nutrient-type element enrichments possibly captured within marine sediment. For example, mafic igneous rocks are more enriched in several redox-sensitive and nutrient-type TEs including Co, Cr, Cu, Fe, Mn, Ni, P, and Se, relative to felsic igneous rocks, which are more enriched in high-field strength elements (HFSEs: e.g., Nb, REE+Y, Ta, U, Zr), large-ion lithophile elements (LILEs: e.g., Ba, K, Rb), and Mo (e.g., Large et al., 2018). Deposition of continental-margin IFs is generally indicative of a starved siliciclastic sediment supply, but episodic surges in continental sediment deposition or even contemporaneous volcanism may result in certain intervals within the IF having a more detritally influenced signature.

Effects of detrital contamination on the geochemical signatures of the Sokoman IF benefit from an evaluation of the composition of both the bounding shales [Ruth Slate Member (RTH), Menihek Formation (MS)] and intercalated volcanic sequences (Nimish Formation). Both the RTH and MS show similar overall patterns to those of average upper continental crust (UCC; Rudnick and Gao, 2003) in extended normalized trace element plots **(Figs. 2.69–2.70**). However, there are some deviations that include enrichment in U in MS samples and an enrichment in Ba and depletion in Pb and Sr in RTH samples. Excluding some element

deviations possibly affected by authigenesis, the composition of the MS sample obtained in this study is similar to previously reported data (Cameron and Garrels, 1980). Given that UCC is composed predominantly of felsic igneous and metasedimentary lithologies (Condie, 1993; Rudnick and Gao, 2003), similarities in the composition of the RTH and MS with UCC points to a felsic rock-dominated sediment source. In order to provide a more robust provenance assessment, we also use several well-established binary element ratios including Th/Sc, Th/Co, La/Sc, and Cr/Th, where Th-La and Sc-Co-Cr are proxies for more felsic and mafic sources, respectively. Furthermore, we compare these ratios to those of shale composites and possible source rock data where available (**Table 2.3**). In the following discussion, data for sample MS005 are omitted due to effects of post-depositional silicification.

The Th-La-Sc-Co-Cr binary element ratios are comparable in both the RTH and MS samples. These results point to felsic-dominated sources when compared against the Early and Middle Proterozoic shale composites of Condie (1993). However, lower Th/Co and higher Cr/Th values in RTH samples relative to both MS and early and middle Paleoproterozoic shale composites appear to reflect the incorporation of minor mafic components. The sedimentary cover sequences of the Kaniapiskau Supergroup directly overly Archean basement rocks in parautochthonous zones such that it is reasonable to hypothesize that intermittent clastic input at the time of IF deposition, although not substantial, was dominated by sediments derived from these Archean sources. To test this, Zr-Hf-Th-Ga element ratios in the RTH and MS are evaluated and compared against those of the Ashuanipi Complex—a granulite-grade subprovince of the eastern Archean Superior Province situated west of the Sheps Lake area and composed mainly of metasedimentary rocks intruded by an adakitic plutonic suite of mainly intermediate to felsic composition with potential minor mafic components (Guernina and Sawyer, 2003;

Percival, 2003; van Nostrand, 2017; van Nostrand and Bradford, 2014). The ratios in the RTH are most similar to those of metagreywacke, paragneiss, migmatitic paragneiss, biotite-rich paragneiss, biotite granite, tonalite gneiss, and diorite-gabbro in the Ashuanipi Complex (**Table 2.3**). Ratios in the MS sample also overlap largely with those of the latter potential source rocks with small deviation towards higher Zr/Hf and Zr/Ga ratios. These comparisons further support the premise that these rocks, including a metasedimentary component, may be good proxies for the specific prevailing sediment source across the timeframe of Sokoman IF deposition. The felsic-dominated sediment sources inferred here are also supported by U-Pb detrital zircon data from meta-sandstones of the Baby Formation (Koksoak Group), which together with the Doublet and Le Moyne groups, are considered deep-water correlatives to the Ferriman Group (Henrique-Pinto et al., 2017). The greatest proportion of dated zircon grains are Neoarchean (2.8–2.5 Ga), and trace element and Nd-isotope analyses of their host rock suggests sediment derivation from sources of Archean age (3.2–2.7 Ga) that were mostly felsic based on high Th/Sc ratios of 0.71 to 4.74 (Henrique-Pinto et al., 2019).

Intermediate-composition to mafic volcanic and volcaniclastic rocks of the Nimish Formation are interbedded with the Sokoman Formation in the Dyke Lake-Astray Lake areas (**Section 2**) and may represent another potential source of clastic input. High stilpnomelane abundances in IF, including the Sokoman, have been linked to enhanced supply of K-Al (e.g., volcanic ash or other locally derived detritus) from alkalic volcanism (Beukes, 1984; Haugaard et al., 2016b; Zajac, 1974). In the Knob Lake area, Zajac (1974) noted that stilpnomelane occurrences in the Sokoman IF were most common in the Dyke Lake-Astray Lake areas. The Hayot Lake samples analyzed in this study are located ~90 km NW of these areas, but both are part of the same allochthonous tectonic zone. No obvious difference in stilpnomelane

abundances was noted petrographically among the Hayot Lake and Lac Ritchie and Sheps Lake localities, but a tendency towards higher K occurs in the Hayot Lake samples [median ± 1s: K_2O = 0.066 ± 0.096 (wt.%), *n* = 8] in comparison to Lac Ritchie [K_2O = 0.022 ± 0.024 (wt.%), *n* = 8] and Sheps Lake [K_2O = 0.038 ± 0.13 (wt.%), *n* = 5]. These differences may be consistent with a comparatively greater volcanic input in the Hayot Lake samples, but confidence is limited by the few samples analyzed from the Hayot Lake locality and even fewer examined in petrographic detail, as well as by the low stilpnomelane abundance and greater number of samples with K contents below XRF detection limits.

In summary, evidence suggests that at the time of Sokoman IF deposition, episodic inputs of continental detritus were derived predominantly from Archean felsic and metasedimentary sources of which the RTH is a good approximation, thus validating its use as an endmember for detritus admixture calculations. Detrital material from Nimish volcanism appears to have been more significant in the Dyke Lake-Astray Lake areas but was largely outpaced by terrigenous supply in the evaluated localities.

2.6.4 Sequence-stratigraphic relationships with chemostratigraphic trends

Previous sequence-stratigraphic work on the Sokoman IF in the Howells River area outlined two relative sea-level cycles based on changes in dominant mineral assemblages and sedimentary features among all units (**Fig. 2.3**) that document shifts in sediment supply and relative sea level in the depositional environment (Edwards et al., 2012; Pufahl et al., 2014). Each depositional sequence is further subdivided into systems tracts: lowstand systems tract (LST), transgressive systems tract (TST), highstand systems tract (HST), and falling-stage systems tract (FSST). The component lithofacies defined above for these two depositional

sequences (**Section 2.3.3**) and their corresponding systems tracts are (1) [Sequence 1: LST (RTH, LIF, part of LRGC), TST (part of LRGC, LRC, PGC), HST (URC), FSST (not developed/not preserved)]; and (2) [Sequence 2: LST (GC, part of JUIF), TST (upper JUIF, LC), HST and FSST (not preserved)]. Integration of this sequence stratigraphy with geochemical data is currently limited to Fe-isotopes (Raye et al., 2015). Our study is the first to further test this sequence stratigraphic framework with DE abundances and relative inter-element fractionations, REE+Y trends, and other paleo-redox and paleo-productivity proxies. Importantly, linking geochemical trends to sequence stratigraphy requires continuous sampling (e.g., LaGrange et al., 2020). Several key drillholes from this study including 12-SL-1018D, 12-SL-1017D, and 11-LR-1012D fit this requirement, whereas others, although lacking complete sampling (e.g., 11-LR-1005D), record a similar continental-margin position along strike and are used in order to link to the other drill holes.

Owing to the shallow depositional setting of the Sokoman IF, detritus-bound element signatures (Al, Ga, Hf, Nb, Sc, Ta, Th, Ti, Zr) are arguably most sensitive to changes in the composition and supply of terrigenous sediment into the basin whereby such changes reflect fluctuations in base-level rise and fall (Catuneanu 2006; LaGrange et al., 2020; Nichols, 2009). The bounding surfaces and systems tracts of the Sokoman IF (Pufahl et al., 2014) indeed show a strong link with chemostratigraphic patterns in DE abundances, via the recognition of inflection points (local minima and maxima) within irregular sinusoidal patterns (**Fig. 2.32F–H**). The evolution of DE abundances and Zr/Hf and Nb/Ta ratios across systems tracts are summarized in **Fig. 2.71**. During the LST, higher rates of sediment supply relative to sea-level rise are matched by an increase in DE abundances that generally peak at or near the transgressive surface (TS), and are also matched by Zr/Hf and Nb/Ta ratios closer to crustal values, as well as by low P/Zr,

ΣFe/Zr, and Mn/Zr ratios. For the ensuing TST, relative sea-level rise outpaced the rate of sediment supply, resulting in a consequent drop in DE abundances and a local minimum at the maximum flooding surface (MFS). This trend is matched by gradually increasing Zr/Hf and Nb/Ta ratios, as well as by higher P/Zr, ΣFe/Zr, and Mn/Zr. Following this interval, terrigenous influx increased during the early the stages of the HST as the rate of sea-level rise falls below the rate of sediment supply. Like the LST, the progressive increase in the rate of sediment supply in the HST is paired with an increase in DE abundances and both are similarly matched by a drop in P/Zr, ΣFe/Zr, and Mn/Zr ratios. During periods of relatively high sea level (i.e., late TST, early HST), DE abundances are at lowest and the fractionation of Zr-Hf and Nb-Ta are most pronounced, thus pointing to the budget of these elements within the IF recording greater authigenic/marine fractionation effects relative to other intervals. The wide range of Zr/Hf and Nb/Ta ratios observed in the Sokoman IF, with values typically exceeding those of modern seawater (**Section 2.5.3**), are attributed to the greater sorption of Hf > Zr and Nb > Ta on Fe/Mn-(oxyhydr)oxide surfaces, which in our model were produced during the mixing of upwelled, Fe(II)-rich, anoxic deep waters with oxic surface waters. These fractionation effects are more readily captured in areas distal to the paleoshoreline due to the smaller detrital HFSE load. Earlier studies of other IF successions have similarly documented the occurrence of irregular sinusoidal patterns in DE abundances, wherein TST and early HST intervals are characterized by higher ΣFe/Al and Mn/Al ratios relative to those of LST and HST intervals (e.g., Schröder et al., 2011; Warchola et al., 2018). Following earlier studies, the aforementioned trends are attributed to the combination of reduced terrigenous input during landward migration of the shoreline and a greater upwelling of hydrothermal Fe and Mn.

Chemostratigraphic trends of REE+Y parameters [$(La/La^*)_{SN}$, $(Ce/Ce^*)_{SN}$, $(Eu/Eu^*)_{SN}$, $(Gd/Gd^*)_{SN}$, $(Lu/Lu^*)_{SN}$, Y/Ho, $(Pr/Yb)_{SN}$, and tetrad development] lack well-expressed sinuosity (**Section 2.5.4.1**) but show broad correlations with DE abundances during LST intervals. On REE+Y anomaly vs. DE mixing plots, samples from units comprising LST intervals (i.e., LIF, GC, bottom LRGC, bottom JUIF) typically fall along early sections of hyperbolic mixing lines (**Fig. 2.51**) with RTH, suggesting a slightly greater control of the REE+Y signatures by detritus within these samples. In contrast, decreasing detrital input during TST intervals should result in progressive decoupling between the aforementioned REE+Y parameters and DE abundances. However, the observed response in REE+Y parameters during these intervals is variable. For example, within the TST of Sequence 1, some parameters increase upsection [$(La/La^*)_{SN}$, $(Ce/Ce^*)_{SN}$, $(Eu/Eu^*)_{SN}$], whereas others show a slight to negligible decrease [$(Gd/Gd^*)_{SN}$, $(Lu/Lu^*)_{SN}$, $(Pr/Yb)_{SN}$, Y/Ho] as DE abundances progressively fall. Positive coupling between $(Gd/Gd^*)_{SN}$, $(Lu/Lu^*)_{SN}$, and Y/Ho is strongest within late TST intervals where detrital input is at a minimum. For example, Gd anomalies ($(Gd/Gd^*)_{SN}$) and Y/Ho ratios show strong to very strong positive correlations in TST intervals (e.g., PGC: $r = 0.81$, $p < 0.005$; LC: $r = 0.62$, $p < 0.01$; JUIF: $r = 0.60$, $p < 0.001$) but weak to moderate positive correlations in LST and HST intervals (e.g., LIF: $r = 0.36$, $p = 0.49$; URC: $r = 0.16$; $p = 0.66$).

The variable response in chemostratigraphic REE+Y trends across sequences is posited to reflect the many factors at play within the highly dynamic shallow shelf environment of the Sokoman IF. Most prominent are particle scavenging and dissolution processes associated with crossing a redoxcline that seaparated suboxic upper waters from anoxic deeper waters (discussed in further detail in **Section 2.6.5**). Evidence for this crossing of redox boundaries is best preserved in late LST to early TST intervals, and best expressed in Sequence 2 where evaporitic

chert of the LST (GC) and hematite-rich, granular peritidal facies of the early TST (JUIF) transition towards deeper, magnetite- and Fe-silicate-dominated facies of the late TST (LC) (Pufahl et al., 2014). For example, in drill hole 12-SL-1017D, Ce anomalies display a sharp increase from the base of the JUIF [JUIF231: $(Ce/Ce^*)_{SN} = 0.93$] towards the top of the JUIF [JUIF228: $(Ce/Ce^*)_{SN} = 1.78$] across an interval spanning ~7 m. Within the same interval, increasing Ce anomalies are matched by overall decreases in La (1.97 to 1.77), Gd (1.08 to 1.04), and Lu (0.98 to 0.95) anomalies as well as by $(Pr/Yb)_{SN}$ (0.23 to 0.19), Y/Ho (34.2 to 29.0) and molar Mn/ΣFe ratios (0.144 to 0.015), and by an increase in τ_3 (–0.14 to –0.11) and τ_4 (–0.082 to –0.023) values. This short interval likely represents the impingement of a redoxcline across the shallow shelf environment in which Fe- and Mn-(oxyhydr)oxides underwent variable reductive dissolution upon transport to deeper suboxic-anoxic waters (**Section 2.6.5**).

Chemostratigraphic trends of other TEs, most notably those of Cr, V, and Ni, are influenced by variable terrigenous influx as evidenced by broad positive correlations with DE abundances (**Section 2.5.5**). The strongest positive correlation with DE abundances occurs in LST to earliest TST intervals, whereas decoupling is observed in late TST to early HST intervals. This observation indicates that TE enrichments in LST to earliest TST intervals can be accommodated mainly by detritus, whereas those in late TST to early HST intervals more closely represent true authigenic enrichment (**Section 2.6.6)**. Similarly, chemostratigraphic analysis reveals that P enrichments during LST intervals are more closely linked to detritus, whereas those in late TST to early HST reflect greater soluble P flux and/or authigenic enrichment (**Section 2.6.7**).

Overall, the geochemical trends presented here can be interpreted within the sequence stratigraphic framework of Pufahl et al. (2014). The periodicity in chemostratigraphic trends of

DE abundances is intimately linked with changes to terrigenous influx as a function of base-level fluctuations. Chemostratigraphic trends in REE+Y are more complex, revealing an additional control by redox gradients in the shallow shelf environment. The very low overall enrichments of several TEs are also highly amenable to overprinting of the terrigenous influx, even if the detrital addition is not quantitatively significant, thus emphasizing that importance of the overall sequence stratigraphic framework for discerning authigenic trends in the Sokoman IF.

2.6.5 Dynamic shallow-water redox stratification

The production of marine Fe-(oxyhydr)oxides is widely considered to transcend the secular record of Precambrian IF deposition, but coupled Fe/Mn-redox stratification is inferred for the late Paleoproterozoic ocean based on constraints from ca. 1.88 Ga IFs (Klein, 2005; Planavsky et al., 2010a; Poulton and Canfield, 2011). This model draws on Ce anomaly constraints whereby insoluble CeO_2 is produced during the oxidation of Ce(III) to Ce(IV) in an upper, oxygenated water column (Elderfield, 1988), possibly having started in terrestrial environments (e.g., Schier et al., 2020) as a precursor to produce a negative Ce anomaly in marine waters. This process is further catalyzed by the adsorption of Ce(III) and its partial oxidation on highly reactive surfaces of Mn-(oxyhydr)oxides (De Carlo et al., 1997; Ohta and Kawabe, 2001), and to a lesser extent Fe-(oxyhydr)oxides (Bau, 1999; Bau and Koschinsky, 2009). Relative to Ce, however, scavenging of other REE(III) (LREE > HREE) and Ho (relative to its geochemical twin, Y) are substantially less efficient, as evidenced by higher bulk distribution coefficients for Ce (Bau, 1999). Upon reaching deeper and more reducing waters, Fe/Mn-(oxyhydr)oxides undergo reductive dissolution, resulting in the reduction of Ce(IV) to Ce(III) and its subsequent remobilization together with other REE(III) (De Baar et al., 1988; De

Carlo and Green, 2002; German and Elderfield, 1989) that generates a neutral or positive Ce anomaly. However, positive Ce anomalies are not uniformly recorded in these reducing waters and there is now evidence that admixtures with sediment pore waters may significantly affect the recorded water-column Ce signatures (e.g., Adebayo et al., 2020).

The occurrence of small negative Ce anomalies (**Fig. 2.49A**) in some URC and PGC samples provides evidence for at least a partially oxygenated water column during IF deposition. Conversely, the ubiquity of large positive Ce anomalies in many samples of the LC and JUIF implicate the scavenging of REE+Y from waters after reductive dissolution of Fe/Mn-(oxyhydr)oxides under more reducing water-column conditions that dominated in deeper subtidal settings across the middle shelf. The hyperbolic trends in Ce/Ce*-Pr/Pr* plots (**Fig. 2.49A, C–D**) defined by all Sokoman IF samples require true changes to Ce anomalies (i.e., not developed with changing La anomalies exclusively), but can also be accommodated by progressively changing both La+Ce anomalies (with greater change in Ce than La). In order to demonstrate that the overall range from small negative to large positive Ce anomalies in the Sokoman IF records Ce anomaly changes via soluble REE+Y interaction with marine Fe/Mn-(oxyhydr)oxides, we fit a simple model (**Fig. 2.49C)** to the data using the Lu-normalized apparent oxide-seawater partition coefficients $(K_D^{\text{REY-oxide /REY-SW}})_{Lu}$ from Bau and Koschinsky (2009). Starting from sample URC148B (negative Ce anomaly) as an endpoint representing the REE+Y signature of dissolved seawater above the redoxcline, proportionally releasing REE+Y according to oxide-seawater partition coefficients and adding these released REE+Y to the URC148B pattern produces a strong fit to all of the remaining Sokoman IF sample data. This result successfully models the Ce >> La anomaly development associated with crossing a redoxcline that dissolves oxides, with either Fe- or Mn oxides producing nearly identical trends,

and liberates the oxide REE+Y budget back into the water column prior to subsequent scavenging and incorporation into the IF. We also demonstrate how this hyperbolic trend survives through variable admixture of detrital material (**Fig. 2.49D**). This is demonstrated by assuming that all points along the modelled Mn-oxide trend start with an average REE+Y abundance equivalent to the mean of the 10 IF samples with the lowest Zr (<1 ppm), i.e., representative detritus-poor IFs, and then mixing different percentages of detritus having the REE composition of the RTH mean. This model illustrates the greater susceptibility of the small negative Ce anomalies to being erased (shifted to $Pr/Pr^* < 1.05$) by detritus addition (≥5%), compared to the positive Ce anomalies that can survive (measurable with $Pr/Pr^* < 0.95$ and $Ce/Ce^* > 1.05$) with 20 to 50% detritus addition, depending on the magnitude of the starting positive Ce anomaly.

Overall, the presence of basin redox stratification as inferred from Ce anomalies in the Sokoman IF is consistent with proposed depth-dependent suboxic vs. anoxic Fe-mineral pathways, as well as with observations from the ca. 1.88 Ga Biwabik, Riverton, Gunflint, Frere, and Rochford IFs that collectively also display predominantly true positive Ce anomalies and less commonly, true negative Ce anomalies (**Fig. 2.49B**). Basin redox stratification for such IFs is also reflected by a depositional transition from hematite-rich assemblages in shallow subtidal settings to laminated magnetite-rich assemblages in deeper subtidal settings (Akin et al., 2013; Frei et al., 2008; Planavksy et al., 2009). There is further evidence from the Sokoman IF that the Mn-redoxcline was sharp and shallow (within the zone of wave abrasion), as suggested by Ce/Ce^* inversions during early TST intervals (**Section 2.6.4**) together with sedimentological features such as poorly deformed chert and hematite intraclasts and ooids (e.g., JUIF231 to JUIF228 in 12-SL-1017D). Pufahl et al. (2014) argued for a shallow oxygen chemocline that

extended no deeper than the FWWB and that wave mixing was effective down to a water depth of about 20 m, based on the sharp transition from hematite-rich peritidal grainstone towards shore-distal, laminated Fe-silicate- and magnetite-dominated chemical mudstone. In a similar manner, the prevalence of hematite-rich siliceous stromatolites that lack negative Ce anomalies vs. shallow-water Mn-rich oncoids with prominent negative Ce anomalies in the Biwabik IF was interpreted as evidence for a shallow redoxcline (Planavsky et al., 2009).

Three main observations, in contrast, point to a more complicated scenario of Fe-Mn-Ce redox cycling during Sokoman IF deposition. First, although unit-specific analysis shows that strong positive Ce anomalies are matched by higher molar Mn/ΣFe ratios compared to units with negative or no Ce anomalies (**Figs. 2.20J, 2.48C**), there are no strong covariations between bulk-rock Ce anomalies and either Mn- or Fe-enrichments that would suggest a straightforward and persistent redoxcline architecture, relative to the shoreline. This lack of covariation also lowers the probability that samples with large positive Ce anomalies are explainable by the direct delivery of Mn-(oxyhydr)oxides (with +Ce anomalies) to the IF sediment. Second, the positive Ce anomalies are not directly matched by negative Y anomalies or LREE-enriched REE+Y slopes, which contrasts with data for modern ferromanganese crusts and nodules (e.g., Bau and Koschinsky, 2009) and the expectation of full REE+Y release from the dissolution of oxides below a redoxcline (Planavsky et al. 2010a). The decoupling between Ce anomalies and other REE+Y parameters is also recognized in the Biwabik and Gunflint IFs, although negative Y anomalies are more common at these localities (Planavsky et al., 2009, 2010a). Third, the presence of both positive and negative Ce anomalies in hematite/jasper-bearing units of the Sokoman IF that formed via the suboxic mineral pathway reflects Fe-(oxyhydr)oxide development above and below an independent redoxcline responsible for controlling the Ce

anomalies. Here, we show that the various observed complications in the REE+Y, Fe, and Mn data can be explained through the separation of a shallow Mn-redoxcline from a slightly deeper and more diffuse Fe-redoxcline (**Fig. 2.73B**), both of which existed within the photic zone.

The upwelling of anoxic, Fe(II)- and REE+Y-charged deep waters from the middle shelf (below the Mn- and Fe-redoxclines) towards oxic shallow waters triggered the precipitation of Fe(III)-(oxyhydr)oxides. In shallow surface waters, the greater availability of sunlight is favourable for oxygenic photosynthesis, such that cyanobacterial O_2 input promoted the direct oxidation of Fe and Mn (e.g., Dick et al., 2018; Pufahl and Hiatt, 2012). Surface water mixing across the shallow Mn-redoxcline probably caused rapid recycling of Mn- and, to a much lesser extent, Fe-(oxyhydr)oxide particles across the interface, resulting in the wide range of observed Ce anomalies across inferred sharp redox gradients (e.g., JUIF231 to JUIF228 in 12-SL-1017D). However, the insufficient release of other REE+Y from oxide particles due to vigorous oxide recycling prevented the co-occurrence of negative Y anomalies, normalized REE+Y patterns with LREE > HREE, and more pronounced weakening of the W-type lanthanide tetrad effect (i.e., τ_3 and τ_4 values closer to 0) in samples having positive Ce anomalies. Above the Mn-redoxcline, in areas of high cyanobacterial activity, waters may have been sufficiently oxygenated to facilitate direct Ce(III) to Ce(IV) oxidation without the involvement of Mn-oxide surfaces. Concomitantly, the constant supply of Fe(II) and lower light availability across the Fe-redox boundary provide the necessary conditions for anoxygenic photoferrotrophy to proliferate (e.g., Edwards et al., 2012; Schad et al., 2019), resulting in local Fe(III)-(oxyhydr)oxide precipitation in an otherwise transitional Fe(III)-Fe(II)-dominated zone. The presence of paragenetically early hematite in intraformational chert clasts and the occurrence of identical Ce anomalies between bulk IF samples and intraformational chert subsamples (**Section 2.6.2**)

collectively suggest a decoupling between redox-driven REE+Y cycling and Fe-oxidation mechanisms, as previously suggested for other Precambrian IFs (Planavsky et al., 2010a). It is posited that for the Sokoman IF, direct Fe-oxidation above the Mn-redoxcline was rapid, whereas biogenic Fe-oxidation persisted between the Mn- and Fe-redox transition zones, albeit at slower rates, consistent with the model of Raye et al. (2015).

2.6.6 Trace-element proxies of element sources and paleo-environmental conditions

Many factors in continental environments affect the delivery of elements to the marine realm, including source lithology, climate (influencing weathering rate), surface oxygenation, and soluble vs. detritus-bound pathways. All of these factors can be more important in controlling the geochemical signatures of continental-margin IFs compared to deep-water Algoma-type and exhalative IFs (cf. Bekker et al., 2010). Once in the marine realm in dissolved form, some redox-sensitive trace elements can inform paleoredox conditions owing to variable enrichments in depositional systems under differing redox conditions, i.e., oxic-suboxic-anoxic-euxinic (e.g., Bennett and Canfield, 2020; Liu and Algeo, 2020). For the Sokoman IF, trends in Cr-U-V-Ni-Co-Zn-Eu are examined in terms of element sources and paleo-environmental controls within the outlined sequence stratigraphic framework (**Section 2.6.4**). Chromium, U, V, and Ni are delivered in soluble form primarily from continental sources, and in the case of Cr, V, and U, have a solubility that is dictated primarily by atmospheric/surface water oxygen levels. In contrast, hydrothermal sources are equally as important as continental sources in contributing the soluble budgets of Co, Zn, and the REE (monitored with the Eu anomaly) (Robbins et al., 2013; Swanner et al., 2014). With the exception of Eu, two main endmember trendlines related to base-level changes are recorded in the Sokoman IF stratigraphy. These trendlines are revealed with a

cross-plot of molar TE/ΣFe ratios (recording enrichment above Fe applied due to close association of many elements with marine Fe cycling; Tribovillard et al., 2006) vs. TE_{EF} (recording enrichment above detrital budgets of the TE, using Zr as a monitor), with DE abundances indicated for each sample by bubble size populations (**Section 2.5.5**; **Fig. 2.72**). The first trendline, characterized by TE/ΣFe >> TE_{EF} and high DE abundances (defined by samples from the GC, uppermost LIF, lower JUIF, and bottommost LRGC) corresponds to units deposited during LST to earliest TST intervals and indicates a detritus-dominated control. The second trendline, with TE_{EF} >> TE/ΣFe and low DE abundances (defined by samples from the LRC, URC, PGC, upper LRGC, upper JUIF, and bottom to mid-LC), reflects units deposited during late TST to early HST intervals and where authigenic enrichment is most prominent. Notably, the latter trend requires a more coupled increase of TE with Fe. Data for several samples fall between these endmember trends and suggest a mixture of the above controls, and for some elements (Co, Zn) the trends are not defined or only one endmember trend is dominant.

2.6.6.1 Cr-V-U systematics support limited chemical weathering under a low-O_2 atmosphere

In the sequence-stratigraphic framework, the shore-proximal units (lagoonal, intertidal to shallow subtidal) are the most likely to capture any authigenic Cr originating from a soluble continental flux via rivers or groundwater, whether it be Cr(VI) formed in soils after Cr(III) oxidation (Oze et al., 2007; Frei et al., 2009; Fralick et al., 2017) or a soluble load of ligand-complexed Cr(III) (Babechuk et al., 2017; Saad et al., 2017). The same logic applies to any soluble V(IV)/V(V) generated from V(III) during oxidative continental weathering (Huang et al., 2015; Wanty and Goldhaber, 1992). However, these depositional environments are also at the unfortunate coincidence (in terms of detecting authigenic Cr or V) of receiving the greatest input

of detritus. It is shown in the present study that distinguishing between authigenic vs. detrital controls on both of these elements is possible using TE/ΣFe vs. TE_{EF} plots.

For both Cr and V, the shore-proximal (LST and earliest TST) units with the highest DE abundances define a steep positive trend of increasing TE/ΣFe >> TE_{EF} (**Fig. 2.72A–B**). This trend could hypothetically capture a mixture of authigenic and detrital Cr and V. However, a very tight individual correlation of Cr (e.g., with Zr, LIF: $r = 0.96$, $p < 0.005$; LC: $r = 0.72$, $p < 0.001$) abundance (and V to a lesser extent) with numerous detritally sourced element abundances (e.g., Ga, Hf, Nb, Sc, Ta, Th, Ti, Zr) strongly supports evidence that the Cr-V budget is dominantly from Cr-/V-bearing detritus, with the small shift in increasing V_{EF} and Cr_{EF} arising from minor differences in source-rock lithology or Cr-/V-bearing mineral chemistry relative to the MuQ normalizer. Both elements have an affinity for structural incorporation into clay minerals such as illite and smectite in their reduced state (Huang et al., 2015), such that a strong correlation with low-solubility elements associated predominantly with detritus is expected.

The slightly more shore-distal units (late TST and HST) with low DE abundances define a shallower positive trend of increasing TE_{EF} >> TE/ΣFe for both Cr and V (**Fig. 2.72A–B**) and indicate that an authigenic trend involving soluble elements is still detectable in the IF. For this soluble element budget, any solutes entering marine waters as Cr(VI) or V(IV)/V(V) and crossing below the Mn-redoxcline into regions with higher dissolved Fe(II) was reduced and scavenged as Cr(III) or V(III) into the IF (Frei et al., 2009). The TE_{EF} >> TE/ΣFe trend suggests that this reductive scavenging process is either more efficient and/or more readily detectable in the more distal, suboxic-anoxic IF depositional environments compared to nearer-shore, more detrital-rich environments. It is also possible that some of this authigenic pool, most notably involving Cr(III), was sourced from distally transported hydrothermal fluids (Koschinsky et al.,

2002; Sander and Koschinsky, 2000). Data for several samples fall between the two main trends on the TE_{EF} vs. TE/ΣFe plots, suggesting a mixture of Cr and V that reflects both detrital and authigenic processes. The magnitude of Cr_{EF} is low and exceeded by V_{EF}, but the TE_{EF} vs. TE/ΣFe trends are more clearly defined for Cr than V. The low authigenic Cr enrichment can be partly attributed to the dominantly felsic (low-Cr) rocks (**Section 2.6.2**) that were exposed to weathering and erosion, and thus the low supply of Cr-bearing detritus or soluble Cr transported to the continental margin; the higher V authigenic enrichment may indicate a higher V source. Alternatively, the data could reflect the lower threshold for continental V oxidation relative to that for Cr (requiring the development of Mn-oxides), or that the mechanism for scavenging authigenic V (Huang et al., 2015; Wanty and Goldhaber, 1992) into the IF is more efficient than for Cr.

In contrast to Cr, the causes of the low authigenic U enrichment in the Sokoman IF must arise independently of the inferred U-rich, felsic-rock dominated continental source (**Section 2.6.2**). A trend of increasing U/ΣFe in detritus-influenced samples is less evident on the U/ΣFe vs. U_{EF} plot (**Fig. 2.72C**) compared to Cr, but samples from shore-proximal units show a subtle but distinct trend of increasing U/ΣFe together with Zr abundance. Following a similar logic as per Cr, part of the authigenic U enrichment can be ascribed to detritus that was transported to the IF depositional environment. Some of this detrital correlation could record the coincidence of finer-grained clay detritus containing more weathering-resistant U-rich minerals (e.g., monazite or zircon), or U adsorbed onto and directly associated with clay mineral surfaces (e.g., Sylwester et al., 2000).

Minor authigenic U enrichment ($U_{EF} < 3$) is recorded in detritus-poor samples. The near-crustal values indicate a low overall soluble U(VI) contribution from continental sources after

oxidative weathering—the dominant source of soluble U to the oceans (Partin et al., 2013a; Suhr et al., 2018; Tribovillard et al., 2006). Rare occurrences of slightly higher U enrichment (U_{EF} > 4–5, with high U/ΣFe) decoupled from Zr are defined by three samples of the GC and one of the LIF. This pattern suggests that a minor continental flux of soluble U had already started to be removed in intertidal-lagoonal environments, presumably through reductive scavenging, possibly involving organic matter (Edwards et al., 2012; Pufahl et al., 2014). The remaining slightly higher U enrichments (U_{EF} = 3–5) occur in local samples of more shore-distal units that are either hematite-bearing (URC272 and PGC276 with Fe^{3+}/Fe^{2+} of 1.5 and 7.2, respectively), or more reduced with stromatolitic features (LC166; Fe^{3+}/Fe^{2+}: 0.01). The presence of the more-oxidized (high Fe^{3+}/Fe^{2+}) and hematitic examples suggest a possible mechanism of soluble U scavenged by Fe-(oxyhydr)oxides via adsorption or structural incorporation (Partin et al., 2013a). However, in the Sokoman IF, there is no consistent mechanism that explains the locally higher U enrichment overall, such as (1) sampling effects (e.g., higher chert proportions amplifying U enrichment over detrital background); or (2) that a slightly more soluble U supply to the continental margin, above a more consistent background, was episodic or possibly localized from the marine environment (e.g., oxidative weathering of U-rich detrital minerals and transport directly into nearshore marine settings). Regardless, independent supporting evidence for soluble U in marine environments at the time can be inferred from the U abundance in the Menihek Formation that overlies the IF (**Fig. 2.70**; Cameron and Garrels, 1980).

Separate studies that have evaluated secular trends of authigenic Cr (Konhauser et al., 2011) and U (Partin et al. 2013a) enrichment in IF are important proxy records of atmospheric oxygenation in the Precambrian. Collectively, these studies suggest that variable authigenic enrichment in Cr-U, including very low levels in late Paleoproterozoic IFs compared to older

examples, can be explained by varying atmospheric O_2 and restrictions on continental supply. The Cr-U results from this study largely overlap with the data reported for other ca. 1.88 Ga IFs (**Table 2.2**; Konhauser et al. 2011; Partin et al., 2013a) and are interpreted as supporting evidence that the low authigenic enrichment of these two elements in the Sokoman IF reflects a limited soluble continental supply coupled to low levels of atmospheric O_2. This overlap comes with two possible implications. First, it would support a model in which paleo-environmental conditions restricting continental delivery of several solutes was a more global feature than expressed within any individual ca. 1.88 Ga depositional locality. Second, this overlap could provide an important context for previous data compilations, because it can be tacitly assumed that these data are not influenced by secondary oxidation of Fe minerals, because such effects were carefully evaluated in our study. However, a drawback of using single geochemical proxy data and/or trends on a compilation-style basis is that these do not necessarily capture the spatio-temporal complexities preserved in each deposit. Whereas the previous arguments for a low atmospheric O_2 control on redox-sensitive TE supply appear robust (Konhauser et al., 2011; Partin et al., 2013a), climatic, and possibly tectonic, factors are likely to have played a compounding role in restricting soluble TE delivery during the deposition of the Sokoman IF. An arid climate that curtailed fluvial activity and restricted continental weathering, thereby limiting both terrigenous input and solute delivery, is thought to have enhanced Sokoman IF deposition (Edwards et al. 2012; Pufahl et al., 2014). Several lines of sedimentological evidence for this arid climate include the ubiquity of desiccation cracks in chert mudstone, the presence of evaporitic chert, and the absence of riverine and deltaic sediments in both the Sokoman Formation and the underlying Wishart Formation (Edwards et al., 2012, Pufahl et al., 2014). Orogenic quiescence has also been linked to subdued weathering fluxes in Earth's history, especially during the mid-

Proterozoic (Tang et al., 2021), as high rates of physical and chemical denudation can be triggered by mountainous topography (e.g., Larsen et al., 2014). Although difficult to fully evaluate for the Sokoman IF, it is possible that the elevation of the eastern Superior margin was relatively low at ca. 1.88 Ga given that its oblique convergence with the 'Core Zone' microcontinent leading to the New Québec Orogen occurred later, from 1.82 to 1.77 Ga (Clark and Wares, 2005; James and Dunning, 2000), after the deposition of the Sokoman IF.

2.6.6.2 Eu, Ni, Co, and Zn evidence for a complex mixture of continental vs. hydrothermal sources

Preservation of a seawater-like REE+Y pattern in IF implies that most of these elements were sourced and processed across the continent-to-marine transition, but the selective and large enrichments of Eu constitute one of the most commonly applied proxies (together with the source of Fe and Mn) for derivation from reduced, high-temperature hydrothermal fluids (Alexander et al., 2008; Danielson et al., 1992; Derry and Jacobsen, 1990; Fryer, 1977b; German et al., 1993; Klinkhammer et al., 1994; Viehmann et al., 2015). The resultant positive Eu anomaly is tied to breakdown of Eu(II)-bearing plagioclase in volcanic rocks underlying the hydrothermal vents (Fryer et al., 1979; Graf, 1978), and to subsequent mobilization of Eu(II) relative to REE(III) at high T (>250 °C) and low pH under reducing conditions (Bau, 1991; Michard, 1989; Sverjensky, 1984). The common occurrence of positive Eu anomalies in ca. 1.88 Ga continental-margin IFs, including the Sokoman, although smaller in magnitude than those of Archean IFs, has been atrributed to long-distance transport of Fe and Mn from distal hydrothermal sources (Raye et al., 2015; Viehmann et al., 2015).

The $(Eu/Eu^*)_{CN}$ values of the Sokoman IF determined in this study are similar to those reported previously for the Sokoman and other ca. 1.88 Ga IFs (Justo et al., 2020; Viehmann et al., 2015). However, no systematic unit-to-unit or intra-unit trend is observed in the Sokoman IF that is explainable within the sequence stratigraphic framework (**Section 2.6.4**). Moreover, there is no clear shift to larger positive Eu anomalies in shore-distal, deeper-water units relative to shore-proximal, shallow-water units; also, most of the full range in $(Eu/Eu^*)_{CN}$ values occurs within specific areas of the sequence stratigraphic divisions (e.g., JUIF: 0.77–1.64; URC: 0.81–1.67; ĹIF: 1.05–1.92). Thus, there is no means to attribute the Sokoman IF Eu anomalies exclusively to Eu supply from distal hydrothermal fluids, outside of conventional inferences from other IF studies. The influence of detritus on the IF REE+Y pattern was evaluated above to be minimal (**Section 2.5.4.3**). Nevertheless, it is evident that the most detrital-rich samples (highest Zr or Ti) tend to have $(Eu/Eu^*)_{CN}$ values in the lower end of the full Sokoman IF range (e.g., LRGC055 = 0.90; JUIF116 = 0.96). This result is consistent with the lower $(Eu/Eu^*)_{CN}$ values obtained for some of the probable source rocks (e.g., mean ± 1s: 1.19 ± 0.28, n = 31, from metagreywackes of the Ashuanipi Complex reported by Guernina and Sawyer, 2003; 0.63–1.05, n = 10), or from intruding adakite (dioritic to tonalitic sills) of the same complex reported by Percival et al. (2003) that could have provided detritus. Because some of the high $(Eu/Eu^*)_{CN}$ values can be found in the very shore-proximal and shallow-water units above the Mn-redoxcline and without any significant detrital budget (e.g., GC147 = 1.56; LIF063 = 1.51), it is also possible that some Eu anomaly variability arises from incongruent leaching of Eu(II)-bearing plagioclase during subaerial chemical weathering, prior to its oxidation and transport together with transport of other REE(III) from the continents to the marine realm (Babechuk et al., 2019).

Some of the ambiguity in confidently fingerprinting a hydrothermal element source from Eu anomalies also applies to Ni, as evidenced by a plot of Ni/ΣFe vs. Ni_{EF} (**Fig. 2.72D**) that yields population trends similar to those of Cr and V. Shore-proximal units of the IF show a shallow positive trend of increasing Ni/ΣFe >> Ni_{EF} coupled to increasing DE abundances; it is probable that this Ni budget is directly associated with detritus given the compatibility of Ni in clay minerals (Koppelman and Dillard, 1977). In contrast, another population for which Ni_{EF} >> Ni/ΣFe indicates that any soluble Ni derived from continental weathering (Konhauser et al., 2009) is preferentially scavenged in deeper water, more shore-distal units, or that some of the Ni budget could be associated with hydrothermal sources (Douville et al., 2002).

In the case of Co and Zn, the magnitude of TE_{EF} is higher than for other TEs, and there are no TE/ΣFe >> TE_{EF} trends pointing towards a strong detrital-controlled enrichment over Fe (**Fig. 2.72D–E**). Nearly all of the authigenic enrichment is focused in more shore-distal units (i.e., shallow positive or flat trend of TE_{EF} >> TE/ΣFe). Collectively, these observations are best explained by Co and Zn being sourced primarily from distally transported hydrothermal fluids (e.g., modern fluids are typically enriched in Fe, Mn, Co, Ni, Cu, Zn, Cd, Pb, and REE+Y: Douville et al., 2002; German and Seyfried, 2014; Haalboom et al., 2020) and/or from hydrothermally derived particulate Fe and Mn (e.g., >4,000 km from vent sources on the southern East Pacific Rise; Fitzsimmons et al., 2017), as noted previously for the Sokoman IF (Raye et al., 2015). Cobalt enrichments in the Sokoman IF that overlap with those for compiled data from other ca. 1.88 Ga IFs are also in line with inferred high marine Co levels (Swanner et al., 2014), due to enhanced mantle plume-related hydrothermal activity during this time period (Ernst and Jowitt, 2013; Isley and Abbott, 1999; Rasmussen et al., 2012). Interestingly, the $(Eu/Eu^*)_{CN}$ values are not strongly correlated with either Co or Zn enrichment proxies (as EFs

and Fe-normalized ratios), which indicates that the element sources are likely decoupled, thus supporting the hypothesis of a greater soluble continental supply for Eu (with minor effects from detrital contamination). The greater Co and Zn enrichments observed in slightly more shore-distal units, especially in samples deposited below the Mn-redoxcline, (**Section 2.6.5**) can also be related, in part, to localized release of any marine hydrothermally or continentally sourced elements that were adsorbed onto Fe-/Mn-(oxyhydr)oxides above the redoxcline (e.g., Viollier et al., 1995). Examination of unit-specific trends of strong positive covariations between ΣFe/Zr, Mn/Zr ratios, and Co and Zn EFs in TST and early HST intervals suggests that there was either a substantial hydrothermal contribution of Co and Zn, or enhanced local (oxyhydr)oxide dissolution that released Co and Zn. In our model, both possibilities can be explained by the shoreward migration of the Fe- and Mn-redoxclines and the greater extent of upwelling ferruginous deep waters along the shallow shelf (**Fig. 2.73**).

2.6.7 Limited continental P supply restricted paleoproductivity and phosphogenesis

On geological timescales, primary productivity in the oceans is thought to be largely controlled by marine P concentrations, which is directly tied to continental weathering and recycling within the ocean (Bjerrum and Canfield, 2002; Canfield et al., 2020; Hao et al., 2020a, 2020b; Reinhard et al., 2017). In shallow marine environments of the late Paleoproterozoic, Fe-redox pumping is interpreted to have played an important role in the release of adsorbed P during Fe/Mn-(oxyhydr)oxide dissolution in suboxic to anoxic waters, thereby concentrating P in pore waters and enhancing the precipitation of authigenic P phases (Edwards et al., 2012; Hiatt et al., 2015; Nelson et al., 2010; Pufahl, 2010). Indeed, P-bearing phases within the Sokoman IF are typically present as sedimentary apatite (francolite), occurring as phosphatic crusts in microbial

laminae, *in situ* peloids in shaly intervals, or less commonly as reworked intraclasts within grainstone intervals (Edwards et al., 2012; Pufahl et al., 2014). Similar to the evaluation of TE distributions (**Section 2.6.6**), P enrichments in the Sokoman IF studied here are evaluated using the coupled P/ΣFe vs. P_{EF} plot (**Fig. 2.72G**), in order to discern enrichments relative to detrital background and to evaluate whether inferred primary Fe-(oxyhydr)oxides were efficient P scavengers (Bjerrum and Canfield, 2002; Filippelli, 2008). The sequence stratigraphic variations in P/ΣFe are discussed above (**Section 2.6.2**), but the aforementioned plot reveals important controls on the P supply and sediment incorporation via two endmember trendlines that are similar to some of those exhibited by the TEs.

A steep positive trend of P/ΣFe >> P_{EF} is defined largely by samples containing greater amounts of detritus (high DE abundances) in shore-proximal units, reminiscent of the distribution of Cr, V, and Ni. However, unlike these latter TEs, P is not readily incorporated into clay mineral structures and generally resides in both detrital and authigenic phosphate minerals (Canfield et al., 2020). This mineral distribution suggests that the correlation of increasing P/ΣFe with higher Zr (and other detrital-bound elements) is either coincidental (i.e., co-addition of detrital phosphate and clay minerals, or greater authigenic enrichment in shore-proximal units due to other environmental factors such as proximity to soluble continental supply), or that P has an indirect but close association with detritus. A paucity of detrital phosphate grains is observed in the Sokoman IF, with apatite occurrences being principally authigenic and commonly associated with greenalite, siderite, and ankerite (**Section 2.5.1.5**). Thus, direct addition of detrital phosphate is unlikely, leading us to propose an indirect relationship of P with detritus entering the shallow marine environment (e.g., soluble P adsorbed to clay mineral surfaces under low pH conditions; Edzwald et al., 1976; Hao et al., 2021), prior to being released and becoming

bioavailable in shallow-marine waters and sediment. After release from the initial form of P, authigenic Fe-silicates, organic matter, and Fe-(oxyhydr)oxides then became the dominant pathways by which P was incorporated into the marine sediment (Schoepfer et al., 2015).

A second, less-steep positive trend of P_{EF} >> P/ΣFe defined largely by more shore-distal units and samples having low detrital contents, including LC and PGC with the highest median P_{EF} values, points to existence of a minor but soluble pool of P in deeper and more suboxic-anoxic waters. In these cases, the P is attributed to a higher soluble budget arising from P that was released from (oxyhydr)oxides after crossing the redoxcline, and from a greater budget of recycled and upwelled P from deeper marine environments (Pufahl and Hiatt, 2012).

Data for several samples fall between the two main trendlines and include a limited number of localized samples (most notably LRGC197B, LRGC198, and LIF212) that have large P enrichments expressed in both P_{EF} and P/ΣFe. These three bulk-rock IF samples are all from Hayot Lake drill core where occurrences of domal stromatolitic laminae are very common relative to core from Sheps Lake and Lac Ritchie. This pattern is consistent with the intimate association typically reported between phosphatic phases and microbial accretionary structures (e.g., stromatolites), in turn implicating a crucial link between microbial activity and phosphogenesis (Caird et al., 2017; Papineau et al., 2013; Shiraishi et al., 2019) including within the Sokoman IF (Edwards et al., 2012).

Independent of the details of P distribution in the Sokoman IF, the full range of molar P/ΣFe ratios observed here is generally small and congruous with those reported for other ca. 1.88 Ga shallow-marine IFs (**Fig. 2.20Q**; Planavsky et al., 2010b). These data suggest a P-limited environment compared to those captured in other Precambrian IFs. Given the nearshore setting of the Sokoman IF, P delivery into the shallow ocean would have likely been more

sensitive to fluxes from continental weathering than to upwelling of open-marine deep waters. The low P supply to the Sokoman IF is atttibuted to the felsic-dominated source lithology (since P concentrations are higher in mafic rocks), and to compounding effects of more limited chemical weathering under the arid and low atmospheric O_2 conditions inferred for this environment (**Section 2.6.6**). Such conditions would result in an overall contraction of the marine phosphate reservoir, to the detriment of marine microbial ecosystems such that primary productivity became spatially restricted to intertidal to shallow subtidal settings (where microbial accretionary features in the Sokoman IF are common). These observations are consistent with the documentation of Gunflint-type microfossil assemblages in other ca. 1.88 Ga IFs, generally interpreted to represent the remains of either oxygenic photosynthetic bacteria (e.g., Lepot et al., 2017) or Fe(II)-oxidizing bacteria (e.g., Edwards et al., 2012; Planavsky et al., 2009), both being commonly restricted to shallow-water microbial mats within late Paleoproterozoic IFs (see Javaux and Lepot, 2018, for review). Conversely, the minimal expression of microfossil evidence in sediments from deeper waters can be taken as indirect support for limited nutrient availability in the latter setting. However, several studies have shown that the contrasting microfossil abundance in sediments deposited between shallow and deep waters stems from preservational bias. These biases are generated by processes such as enhanced silicification and phosphatization due to nearshore evaporation and Fe-redox pumping, respectively, in shallow waters (Edwards et al., 2012), and by post-depositional alteration involving oxic groundwaters (Shapiro and Konhauser, 2015).

2.6.8 Wider implications of Sokoman IF data for the Paleoproterozoic Earth system

It is generally accepted that shallow-marine environments were oxygenated in the time window of ~2.0–1.8 Ga (Bellefroid et al., 2018; Kipp et al., 2017; 2018). In contrast, the deep oceans then were generally anoxic and ferruginous, mirroring much of the wider Proterozoic (Beukes and Gutzmer, 2008; Lyons et al., 2014), with spatially local or temporally restricted intervals of more extensive marine euxinia in mid-depth waters (Poulton et al., 2010; Poulton and Canfield, 2011) and of deeper marine oxygenation (e.g., Planavsky et al., 2018). Ferruginous conditions extending from deep to mid- and shallow-depth waters at ca. 1.88 Ga, as recorded by the resurgence of massive GIFs along cratonic margins (Bekker et al., 2010; Rasmussen et al., 2012), remain anomalous within this time window and require either enhanced marine Fe(II) fluxes (providing greater competition with O_2 sources) from magmatism/hydrothermal activity, or reduced fluxes of sulfate from terrestrial environments caused by lower atmospheric O_2 and/or lower topographic relief, or a combination of both.

The multiple geochemical proxies discussed in this study arguing for low atmospheric O_2 (**Section 2.6.6.1**) are internally consistent with several parameters. These include (1) accumulation of soluble Fe(II) in shallow marine waters; (2) restricted supply of sulfate to the basin inferred from the rarity of sulfidic units; and (3) existence of a very shallow but spatially dynamic Mn-redoxcline (**Section 2.6.5**), as also outlined in earlier studies (Planavsky et al., 2009; Pufahl et al., 2014). In this sense, our study contributes to a growing body of evidence for a more protracted interval of lower atmospheric O_2 in the late Paleoproterozoic (e.g., Sindol et al., 2020), in contrast to comparatively higher levels of O_2 inferred for the aftermath of the ca. 2.3–2.1 Ga Lomagundi-Jatuli Event (LJE) (e.g., Fralick et al., 2017; Kreitsmann et al., 2020; Mänd et al., 2020; Steadman et al., 2020). Data for the Sokoman IF (**Sections 2.6.6–2.6.7**) also

contribute new support for P-limited and continental supply-dominated shallow-marine environments in the late Paleoproterozoic. Marine primary productivity is inferred to have collapsed by the end of the LJE (Crockford et al., 2019; Hodgskiss et al., 2019; Laakso and Schrag, 2014, 2018), and the scarcity of oxidants in the mid-Proterozoic ocean is believed to have promoted efficient burial of organic C and slower P recycling, thereby limiting productivity and oxygen production (Kipp and Stüeken, 2017). Such environmental conditions would have contributed to a feedback of low atmospheric O_2 by restricting the spatial extent of areas with higher rates of primary productivity and oxygen production to the photic zone of coastal regions. Within an overall Earth surface framework of low atmospheric O_2 and nutrient limitation in shallow marine environments at ca. 1.88 Ga, the overprinting effects of enhanced marine Fe(II) fluxes (Isley and Abbott, 1999; Rasmussen et al., 2012) could have easily tipped the scales towards even lower atmospheric O_2 and thus nearly fully restricted euxinia that promoted a punctuated interval of shallow-marine ferruginous conditions, until excess Fe(II) was either consumed or the supply waned. In other words, the resurgence of IF deposition at ca. 1.88 Ga is considered here to reflect a one-two punch of low oxygen levels and enhanced magmatism/hydrothermal activity.

2.7 Summary

Here, we present new high-precision geochemical (major elements, REE+Y, TEs, Fe(II), and sequential four-step LOI) and mineralogical (SEM-MLA) data on IF/iron ore reference materials (IOC-1, FeR-3, FeR-4) and on the ca. 1.88 Ga Sokoman iron formation in the Labrador Trough. Our new data on the Sokoman IF is integrated with previously defined mineralogical, sedimentological, and sequence stratigraphic constraints (**Fig. 2.73**). We demonstrate that proper

interpretation of the new IF geochemical data in the context of these geological frameworks is imperative for distinguishing syn-depositional (detrital, seawater) vs. post-depositional (diagenesis, metamorphism, late-stage alteration) signatures as recorded in the IF.

Careful evaluation of the Sokoman IF geochemistry within a mineral paragenetic, continental-source rock, and sequence-stratigraphic framework reveals several important trends. First, recognition of primary signature preservation hinges on detailed analysis of the IF mineralogy and geochemistry. Increasing numbers of reports of secondary oxidation effects in IFs make this step especially important (e.g., Bonnand et al., 2020; Rasmussen and Muhling, 2020). Second, the primary signatures preserved in the Sokoman IF are captured over the integrated timeframe of IF deposition, indicating that understanding the syn-depositional processes that operated in the shallow-marine environment is crucial. Third, Ce-anomaly evidence, in tandem with paragenetically early hematite occurrences, define distinct Mn- and Fe-redoxclines promoted by cyanobacteria and photoferrotrophs, respectively, which had contrasting depths and apparent sharpness. Fourth, some elemental variations (TE/ΣFe or TE_{EF}) can be accounted for by detritus, even at very low overall DE abundances; careful screening with consideration of specific sediment composition and supply dynamics is important. Fifth, sedimentological context and unit-specific evaluation within the broad classification of continental margin-type IF is essential in targeting the best samples for extracting authigenic TE information; counterintuitively, the most shore-proximal units of the Sokoman IF are identified as being unfavourable for recording authigenic information of continentally derived solutes. This result is due to the greater influence of detritus in the shore-proximal units relative to more distal, suboxic-anoxic units that better capture reductive scavenging together with significantly lower detrital contributions. Overall, these considerations show how the authigenic TE enrichments of

a single IF locality can vary as a function of source rock, and sedimentological and climatic factors, in addition to atmospheric oxygenation and distance from both continental and hydrothermal element sources.

2.8 Acknowledgements

This research was primarily funded through Natural Sciences and Engineering Research Council of Canada (NSERC) Discovery Grant #RGPIN-2017-05028 to MGB and an NSERC CGS-M Scholarship and Society of Economic Geologists (SEG) Graduate Student Fellowship to GPS. The authors thank Bernd Steinhilber, Heinrich Taubald, and Gülüm Albut for assistance with solution ICP-MS and XRF analyses. Dylan Goudie and David Grant assisted with SEM-MLA analyses. The Geological Survey of Newfoundland and Labrador (GSNL) provided logistical support. New Millennium Iron Corp. and Labec Century Iron Ore Inc. are thanked for permitting access to and sampling of drill cores.

2.9 References Cited

Adebayo, S.B., Cui, M., Hong, T., Akintomide, O., Kelly, R.P., Johannesson, K.H., 2020. Rare earth element cycling and reaction path modeling across the chemocline of the Pettaquamscutt River estuary, Rhode Island. Geochimica et Cosmochimica Acta 284, 21–42. https://doi.org/10.1016/j.gca.2020.06.001

Akin, S.J., Pufahl, P.K., Hiatt, E.E., Pirajno, F., 2013. Oxygenation of shallow marine environments and chemical sedimentation in Palaeoproterozoic peritidal settings: Frere Formation, Western Australia. Sedimentology 60, 1559–1582. https://doi.org/10.1111/sed.12038

Albut, G., Babechuk, M.G., Kleinhanns, I.C., Benger, M., Beukes, N.J., Steinhilber, B., Smith, A.J.B., Kruger, S.J., Schoenberg, R., 2018. Modern rather than Mesoarchaean oxidative weathering responsible for the heavy stable Cr isotopic signatures of the 2.95 Ga old Ijzermijn iron formation (South Africa). Geochimica et Cosmochimica Acta 228, 157–189. https://doi.org/10/gdb3mg

Alexander, B.W., Bau, M., Andersson, P., Dulski, P., 2008. Continentally-derived solutes in shallow Archean seawater: rare earth element and Nd isotope evidence in iron formation from the 2.9 Ga Pongola Supergroup, South Africa. Geochimica et Cosmochimica Acta 72, 378–394. https://doi.org/10/dfz4xm

Anenburg, M., 2020. Rare earth mineral diversity controlled by REE pattern shapes. Mineralogical Magazine 84, 629–639. https://doi.org/10.1180/mgm.2020.70

Babechuk, M.G., Kleinhanns, I.C., Schoenberg, R., 2017. Chromium geochemistry of the ca. 1.85 Ga Flin Flon paleosol. Geobiology 15, 30–50. https://doi.org/10.1111/gbi.12203

Babechuk, M.G., Weimar, N.E., Kleinhanns, I.C., Eroglu, S., Swanner, E.D., Kenny, G.G., Kamber, B.S., Schoenberg, R., 2019. Pervasively anoxic surface conditions at the onset of the Great Oxidation Event: new multi-proxy constraints from the Cooper Lake paleosol. Precambrian Research 323, 126–163. https://doi.org/10/gft2ff

Babechuk, M.G., O'Sullivan, E.M., McKenna, C.A., Rosca, C., Nägler, T.F., Schoenberg, R., Kamber, B.S., 2020. Ultra-trace element characterization of the central Ottawa River basin using a rapid, flexible, and low-volume ICP-MS method. Aquatic Geochemistry 26, 327–374. https://doi.org/10.1007/s10498-020-09376-w

Baldwin, G.J., Thurston, P.C., Kamber, B.S., 2011. High-precision rare earth element, nickel,

and chromium chemistry of chert microbands pre-screened with in-situ analysis. Chemical Geology 285, 133–143. https://doi.org/10/ddzspd

Baragar, W.R.A., 1967. Wakuach Lake map area, Quebec-Labrador. Geological Survey of Canada Memoir 344, 174 p. https://doi.org/10.4095/123960

Baragar, W.R.A., Scoates, R.F.J., 1981. The circum-Superior belt: a Proterozoic plate margin? In: Developments in Precambrian Geology 4, 297–330. https://doi.org/10.1016/S0166-2635(08)70017-3

Barrat, J.A., Zanda, B., Moynier, F., Bollinger, C., Liorzou, C., Bayon, G., 2012. Geochemistry of CI chondrites: major and trace elements, and Cu and Zn isotopes. Geochimica et Cosmochimica Acta 83, 79–92. https://doi.org/10.1016/j.gca.2011.12.011

Bau, M., 1991. Rare-earth element mobility during hydrothermal and metamorphic fluid-rock interaction and the significance of the oxidation state of europium. Chemical Geology 93, 219–230. https://doi.org/10.1016/0009-2541(91)90115-8

Bau, M., 1993. Effects of syn- and post-depositional processes on the rare-earth element distribution in Precambrian iron-formations. European Journal of Mineralogy 5, 257–268. https://doi.org/10/gft2fh

Bau, M., 1999. Scavenging of dissolved yttrium and rare earths by precipitating iron oxyhydroxide: experimental evidence for Ce oxidation, Y-Ho fractionation, and lanthanide tetrad effect. Geochimica et Cosmochimica Acta 63, 67–77. https://doi.org/10/bwdqg9

Bau, M., Alexander, B.W., 2009. Distribution of high field strength elements (Y, Zr, REE, Hf, Ta, Th, U) in adjacent magnetite and chert bands and in reference standards FeR-3 and FeR-4 from the Temagami Iron-Formation, Canada, and the redox level of the Neoarchean ocean. Precambrian Research 174, 337–346. https://doi.org/10/c9v65n

Bau, M., Dulski, P., 1996. Distribution of yttrium and rare-earth elements in the Penge and Kuruman iron-formations, Transvaal Supergroup, South Africa. Precambrian Research 79, 37–55.

Bau, M., Koschinsky, A., 2009. Oxidative scavenging of cerium on hydrous Fe oxide: evidence from the distribution of rare earth elements and yttrium between Fe oxides and Mn oxides in hydrogenetic ferromanganese crusts. Geochemical Journal 43, 37–47. https://doi.org/10.2343/geochemj.1.0005

Bau, M., Hohndorf, A., Dulski, P., Beukes, N.J., 1997. Sources of rare-earth elements and iron in Paleoproterozoic iron formations from the Transvaal Supergroup, South Africa: evidence from neodymium isotopes. The Journal of Geology 105, 121–129.

Bekker, A., Planavsky, N.J., Krapež, B., Rasmussen, B., Hofmann, A., Slack, J.F., Rouxel, O.J., Konhauser, K.O., 2014. Iron formations: their origins and implications for ancient seawater chemistry. In: Mackenzie, F.T. (Ed.), Sediments, Diagenesis and Sedimentary Rocks. Treatise on Geochemistry. Elsevier, vol. 9, pp. 561–628. https://doi.org/10.1016/B978-0-08-095975-7.00719-1

Bekker, A., Slack, J.F., Planavsky, N., Krapež, B., Hofmann, A., Konhauser, K.O., Rouxel, O.J., 2010. Iron formation: the sedimentary product of a complex interplay among mantle, tectonic, oceanic, and biospheric processes. Economic Geology 105, 467–508. https://doi.org/10.2113/gsecongeo.105.3.467

Bellefroid, E.J., Hood, A.v.S., Hoffman, P.F., Thomas, M.D., Reinhard, C.T., Planavsky, N.J., 2018. Constraints on Paleoproterozoic atmospheric oxygen levels. Proceedings of the National Academy of Sciences 115, 8104–8109. https://doi.org/10/gd4gxk

Bennett, W.W., Canfield, D.E., 2020. Redox-sensitive trace metals as paleoredox proxies: a review and analysis of data from modern sediments. Earth-Science Reviews 204, 103175. https://doi.org/10.1016/j.earscirev.2020.103175

Beukes, N.J., 1984. Sedimentology of the Kuruman and Griquatown iron-formations, Transvaal Supergroup, Griqualand West, South Africa. Precambrian Research 24, 47–84. https://doi.org/10.1016/0301-9268(84)90069-X

Beukes, N.J., Gutzmer, J., 2008. Origin and paleoenvironmental significance of major iron formations at the Archean-Paleoproterozoic boundary. Reviews in Economic Geology 15, 5–47.

Bilodeau, C., Caron-Côté, E., 2018. Géologie de la région de la rivière Arnaud, provinces du Supérieur (Minto) et de Churchill (Fosse du Labrador), secteur de Kangirsuk, Nunavik, Québec, Canada. Ministère de l'Énergie et des Ressources naturelles, Québec, Bulletin Géologique. http://gq.mines.gouv.qc.ca/bulletins-geologiques_en/riviere-arnaud_en/

Bjerrum, C.J., Canfield, D.E., 2002. Ocean productivity before about 1.9 Gyr ago limited by phosphorus adsorption onto iron oxides. Nature 417, 159–162. https://doi.org/10/b9ffh6

Bleeker, W., Kamo, S.L., 2018. Extent, origin, and deposit-scale controls of the 1883 Ma circum-Superior large igneous province, northern Manitoba, Ontario, Québec, Nunavut and Labrador. In: Rogers, N. (Ed.), Targeted Geoscience Initiative: 2017 Report of Activities. Geological Survey of Canada Open File 8373, vol. 3, pp. 5–14.

Bolhar, R., Kamber, B.S., Moorbath, S., Fedo, C.M., Whitehouse, M.J., 2004. Characterisation of Early Archaean chemical sediments by trace element signatures. Earth and Planetary Science Letters 222, 43–60. https://doi.org/10/d84tp5

Bonnand, P., Lalonde, S.V., Boyet, M., Heubeck, C., Homann, M., Nonnotte, P., Foster, I., Konhauser, K.O., Köhler, I., 2020. Post-depositional REE mobility in a Paleoarchean banded iron formation revealed by La-Ce geochronology: a cautionary tale for signals of ancient oxygenation. Earth and Planetary Science Letters 547, 116452. https://doi.org/10.1016/j.epsl.2020.116452

Butler, J.P., 2020. Major- and trace-element geochemistry of mafic sills and dykes from the New Québec Orogen, western Labrador. In: Current Research. Government of Newfoundland and Labrador, Department of Natural Resources, Geological Survey Report 20-1, 29–48.

Caird, R.A., Pufahl, P.K., Hiatt, E.E., Abram, M.B., Rocha, A.J.D., Kyser, T.K., 2017. Ediacaran stromatolites and intertidal phosphorite of the Salitre Formation, Brazil: phosphogenesis during the Neoproterozoic Oxygenation Event. Sedimentary Geology 350, 55–71. https://doi.org/10.1016/j.sedgeo.2017.01.005

Cameron, E.M., Garrels, R.M., 1980. Geochemical compositions of some Precambrian shales from the Canadian Shield. Chemical Geology 28, 181–197.

Canfield, D.E., Bjerrum, C.J., Zhang, S., Wang, H., Wang, X., 2020. The modern phosphorus cycle informs interpretations of Mesoproterozoic Era phosphorus dynamics. Earth-Science Reviews 208, 103267. https://doi.org/10.1016/j.earscirev.2020.103267

Catuneanu, O., 2006. Principles of sequence stratigraphy. Elsevier, Amsterdam, 386 p.

Chauvel, J., Dimroth, E., 1974. Facies types and depositional environment of the Sokoman Iron Formation, central Labrador Trough, Quebec, Canada. Journal of Sedimentary Petrology 44, 299–327.

Chung, D., Zhou, M.-F., Gao, J.-F., Chen, W.T., 2015. In-situ LA-ICP-MS trace elemental

analyses of magnetite: the late Palaeoproterozoic Sokoman Iron Formation in the Labrador Trough, Canada. Ore Geology Reviews 65, 917–928. https://doi.org/10.1016/j.oregeorev.2014.09.030

Ciborowski, T.J.R., Minifie, M.J., Kerr, A.C., Ernst, R.E., Baragar, B., Millar, I.L., 2017. A mantle plume origin for the Palaeoproterozoic Circum-Superior Large Igneous Province. Precambrian Research 294, 189–213. https://doi.org/10.1016/j.precamres.2017.03.001

Clark, T., 1984. Géologie et minéralisations de la région du lac Cambrien, Territroire du Nouveau-Québec. Ministère de L'Énergie et des Ressources, Québec, ET 83–02, 71 p.

Clark, T., Wares, M., 2005. Lithotectonic and metallogenic synthesis of the New Québec Orogen (Labrador Trough). Ministère des Ressources Naturelles, Québec, MM 2005–01, 175 p.

Condie, K.C., 1993. Chemical composition and evolution of the upper continental crust: contrasting results from surface samples and shales. Chemical Geology 104, 1–37.

Condie, K.C., Des Marais, D.J., Abbott, D., 2000. Geologic evidence for a mantle superplume event at 1.9 Ga. Geochemistry, Geophysics, Geosystems 1, 1–25.

Conliffe, J., 2014. The Sawyer Lake iron-ore deposit, western Labrador: potential for future high-grade iron-ore deposits in the Labrador Trough. In: Current Research. Newfoundland and Labrador Department of Natural Resources, Geological Survey Report 14–1, 1–14.

Conliffe, J., 2015. Geological setting and genesis of high-grade iron-ore deposits in the eastern Labrador Trough. In: Current Research. Government of Newfoundland and Labrador, Department of Natural Resources, Geological Survey Report 15–1, 1–25.

Conliffe, J., 2019, Iron-ore deposits of southwestern Labrador. Government of Newfoundland and Labrador, Department of Natural Resources, Geological Survey, Occasional Paper 2019–01, 210 p.

Conliffe, J., Smith, A., Wilton, D., 2019. Petrographic, geochemical, and sulphur isotope studies of gabbro sills, Labrador Trough: implications for Ni–Cu–PGE exploration. In: Current Research. Government of Newfoundland and Labrador, Department of Natural Resources, Geological Survey Report 19–1, 1–21.

Corrigan, D., Van Rooyen, D., Morin, A., Houlé, M.G., Bédard, M.P., 2016. Report of activities

for the Core Zone and Bounding Orogens: Recent observations from the New Quebec Orogen in the Schefferville area, Quebec and Labrador, GEM-2 Hudson-Ungava Project.

Crockford, P.W., Kunzmann, M., Bekker, A., Hayles, J., Bao, H., Halverson, G.P., Peng, Y., Bui, T.H., Cox, G.M., Gibson, T.M., Wörndle, S., Rainbird, R., Lepland, A., Swanson-Hysell, N.L., Master, S., Sreenivas, B., Kuznetsov, A., Krupenik, V., Wing, B.A., 2019. Claypool continued: extending the isotopic record of sedimentary sulfate. Chemical Geology 513, 200–225. https://doi.org/10/gf4gxr

Cunningham, L.C., Page, F.Z., Simonson, B.M., Kozdon, R., Valley, J.W., 2012. Ion microprobe analyses of $\delta^{18}O$ in early quartz cements from 1.9 Ga granular iron formations (GIFs): a pilot study. Precambrian Research 214–215, 258–268. https://doi.org/10/gft5rz

Danielson, A., Möller, P., Dulski, P., 1992. The europium anomalies in banded iron formations and the thermal history of the oceanic crust. Chemical Geology 97, 89–100.

Darbyshire, F.A., Bastow, I.D., Petrescu, L., Gilligan, A., Thompson, D.A., 2017. A tale of two orogens: crustal processes in the Proterozoic Trans-Hudson and Grenville orogens, eastern Canada. Tectonics 36, 1633–1659. https://doi.org/10.1002/2017TC004479

De Baar, H.J.W., German, C.R., Elderfield, H., van Gaans, P., 1988. Rare earth element distributions in anoxic waters of the Cariaco Trench. Geochimica et Cosmochimica Acta 52, 1203–1219. https://doi.org/10.1016/0016-7037(88)90275-X

De Carlo, E.H., Green, W.J., 2002. Rare earth elements in the water column of Lake Vanda, McMurdo Dry Valleys, Antarctica. Geochimica et Cosmochimica Acta 66, 1323–1333. https://doi.org/10.1016/S0016-7037(01)00861-4

De Carlo, E. H., Wen, X. Y., Irving, M., 1997. The influence of redox reactions on the uptake of dissolved Ce by suspended Fe and Mn oxide particles. Aquatic Geochemistry 3, 357–389. https://doi.org/10.1023/A:1009664626181

Dean, W.E., 1974. Determination of carbonate and organic matter in calcareous sediments and sedimentary rocks by loss on ignition: comparison with other methods. Journal of Sedimentary Petrology 44, 242–248.

Derry, L.A., Jacobsen, S.B., 1990. The chemical evolution of Precambrian seawater: evidence from REEs in banded iron formations. Geochimica et Cosmochimica Acta 54, 2965–2977.

Dick, G.J., Grim, S.L., Klatt, J.M., 2018. Controls on O_2 production in cyanobacterial mats and

implications for Earth's oxygenation. Annual Review of Earth and Planetary Sciences 46, 123–147. https://doi.org/10.1146/annurev-earth-082517-010035

Dimroth, E., 1972. Stratigraphy of part of the central Labrador Trough. Ministère de l'Énergie et des Ressources, Québec. DP–154, 304 p.

Dimroth, E., Chauvel, J.-J., 1973. Petrography of the Sokoman Iron Formation in part of the central Labrador Trough, Quebec, Canada. Geological Society of America Bulletin 84, 111–134. https://doi.org/10/btdc56

Douville, E., Charlou, J.L., Oelkers, E.H., Bienvenu, P., Colon, C.F.J., Donval, J.P., Fouquet, Y., Prieur, D., Appriou, P., 2002. The Rainbow vent fluids (36°14' N, MAR): the influence of ultramafic rocks and phase separation on trace metal content in Mid-Atlantic Ridge hydrothermal fluids. Chemical Geology 184, 37–48. https://doi.org/10.1016/S0009-2541(01)00351-5

Edwards, C.T., Pufahl, P.K., Hiatt, E.E., Kyser, T.K., 2012. Paleoenvironmental and taphonomic controls on the occurrence of Paleoproterozoic microbial communities in the 1.88 Ga Ferriman Group, Labrador Trough, Canada. Precambrian Research 212–213, 91–106. https://doi.org/10/gft5np

Edzwald, J.K., Toensing, D.C., Leung, M.C.-Yew., 1976. Phosphate adsorption reactions with clay minerals. Environmental Science and Technology 10, 485–490. https://doi.org/10.1021/es60116a001

Eggins, S.M., Woodhead, J.D., Kinsley, L.P.J., Mortimer, G.E., Sylvester, P., McCulloch, M.T., Hergt, J.M., Handler, M.R., 1997. A simple method for the precise determination of ≥40 trace elements in geological samples by ICPMS using enriched isotope internal standardisation. Chemical Geology 134, 311–326. https://doi.org/10.1016/S0009-2541(96)00100-3

Elderfield, H., 1988. The oceanic chemistry of the rare-earth elements. Philosophical Transactions of the Royal Society of London. Series A, Mathematical and Physical Sciences 325, 105–126.

Ernst, D.M., Bau, M., 2021. Banded iron formation from Antarctica: the 2.5 Ga old Mt. Ruker BIF and the antiquity of lanthanide tetrad effect and super-chondritic Y/Ho ratio in seawater. Gondwana Research 91, 97–111. https://doi.org/10.1016/j.gr.2020.11.011

Ernst, R.E., Jowitt, S.M., 2013. Large Igneous Provinces (LIPs) and metallogeny. In: Colpron,

M., Bissig, T., Rusk, B.G., Thompson, J.F.H. (Eds.), Teconics, Metallogeny, and Discovery: The North American Cordillera and Similar Accretionary Settings. Society of Economic Geologists, Inc., Littleton, Colorado, Special Publication 17, pp. 17–51.

Fandrich, R., Gu, Y., Burrows, D., Moeller, K., 2007. Modern SEM-based mineral liberation analysis. International Journal of Mineral Processing 84, 310–320. https://doi.org/10.1016/j.minpro.2006.07.018

Filippelli, G.M., 2008. The global phosphorus cycle: past, present, and future. Elements 4, 89–95. https://doi.org/10/bh2sdn

Findlay, J.M., Parrish, R.R., Birkett, T.C., Watanabe, D.H., 1995. U–Pb ages from the Nimish Formation and Montagnais glomeroporphyritic gabbro of the central New Québec Orogen, Canada. Canadian Journal of Earth Sciences 32, 1208–1220. https://doi.org/10/dzsd6t

Firdaus, M.L., Minami, T., Norisuye, K., Sohrin, Y., 2011. Strong elemental fractionation of Zr–Hf and Nb–Ta across the Pacific Ocean. Nature Geoscience 4, 227–230. https://doi.org/10.1038/ngeo1114

Fischer, W.W., Knoll, A.H., 2009. An iron shuttle for deepwater silica in Late Archean and early Paleoproterozoic iron formation. Geological Society of America Bulletin 121, 222–235. https://doi.org/10.1130/B26328.1

Fitzsimmons, J.N., John, S.G., Marsay, C.M., Hoffman, C.L., Nicholas, S.L., Toner, B.M., German, C.R., Sherrell, R.M., 2017. Iron persistence in a distal hydrothermal plume supported by dissolved-particulate exchange. Nature Geoscience 10, 195–201. https://doi.org/10/f9vfph

Fralick, P., Planavsky, N., Burton, J., Jarvis, I., Addison, W.D., Barrett, T.J., Brumpton, G.R., 2017. Geochemistry of Paleoproterozoic Gunflint Formation carbonate: implications for hydrosphere-atmosphere evolution. Precambrian Research 290, 126–146. https://doi.org/10/f9v556

Frarey, M.J., Duffell, S., 1964. Revised stratigraphic nomenclature for the central part of the Labrador Trough. Geological Survey of Canada Paper 64–25, 13 p. https://doi.org/10.4095/123909

Frei, R., Dahl, P.S., Duke, E.F., Frei, K.M., Hansen, T.R., Frandsson, M.M., Jensen, L.A., 2008. Trace element and isotopic characterization of Neoarchean and Paleoproterozoic iron

formations in the Black Hills (South Dakota, USA): assessment of chemical change during 2.9–1.9 Ga deposition bracketing the 2.4–2.2 Ga first rise of atmospheric oxygen. Precambrian Research 162, 441–474. https://doi.org/10/cgbg6h

Frei, R., Gaucher, C., Poulton, S.W., Canfield, D.E., 2009. Fluctuations in Precambrian atmospheric oxygenation recorded by chromium isotopes. Nature 461, 250–253. https://doi.org/10.1038/nature08266

Fryer, B.J., 1977a. Trace element geochemistry of the Sokoman Iron Formation. Canadian Journal of Earth Sciences 14, 1598–1610. https://doi.org/10/df9wgq

Fryer, B.J., 1977b. Rare earth evidence in iron-formations for changing Precambrian oxidation states. Geochimica et Cosmochimica Acta 41, 361–367. https://doi.org/10/dpq4fn

Fryer, B.J., Fyfe, W.S., Kerrich, R., 1979. Archaean volcanogenic oceans. Chemical Geology 24, 25–33.

German C.R., Elderfield, H., 1989. Rare earth elements in Saanich Inlet, British Columbia, a seasonally anoxic basin. Geochimica Cosmochimica Acta 53, 2561–2571.

German, C.R., Seyfried, W.E., 2014. Hydrothermal Processes. In: Mottl, M.J., Elderfield, H. (Eds.), The Oceans and Marine Geochemistry. Treatise on Geochemistry, second ed. Elsevier, Oxford, pp. 191–233. https://doi.org/10.1016/B978-0-08-095975-7.00607-0

German, C.R., Higgs, N.C., Thomson, J., Mills, R., Elderfield, H., Blusztajn, J., Fleer, A.P., Bacon, M.P., 1993. A geochemical study of metalliferous sediment from the TAG hydrothermal mound, 26°08′N, Mid-Atlantic Ridge. Journal of Geophysical Research 98, 9683. https://doi.org/10/cxgfrb

Gole, M.J., Klein, C., 1981. Banded iron-formations through much of Precambrian time. The Journal of Geology 89, 169–183. https://doi.org/10/bcst7d

Graf, Jr., J.L., 1978. Rare earth elements, iron formations and sea water. Geochimica et Cosmochimica Acta 42, 1845–1850.

Gross G.A., 1980. A classification of iron formations based on depositional environments. Canadian Mineralogist 18(2), 215–222.

Gu, Y., 2003. Automated scanning electron microscope based mineral liberation analysis: an

introduction to JKMRC/FEI mineral liberation analyser. Journal of Minerals and Materials Characterization and Engineering 2, 33–41. https://doi.org/10.4236/jmmce.2003.21003

Guernina, S., Sawyer, E.W., 2003. Large-scale melt-depletion in granulite terranes: an example from the Archean Ashuanipi subprovince of Quebec. Journal of Metamorphic Geology 21, 181–201. https://doi.org/10.1046/j.1525-1314.2003.00436.x

Haalboom, S., Price, D.M., Mienis, F., van Bleijswijk, J.D.L., de Stigter, H.C., Witte, H.J., Reichart, G.-J., Duineveld, G.C.A., 2020. Patterns of (trace) metals and microorganisms in the Rainbow hydrothermal vent plume at the Mid-Atlantic Ridge. Biogeosciences 17, 2499–2519. https://doi.org/10.5194/bg-17-2499-2020

Hao, J., Knoll, A.H., Huang, F., Hazen, R.M., Daniel, I., 2020a. Cycling phosphorus on the Archean Earth: Part I. Continental weathering and riverine transport of phosphorus. Geochimica et Cosmochimica Acta 273, 70–84. https://doi.org/10.1016/j.gca.2020.01.027

Hao, J., Knoll, A.H., Huang, F., Schieber, J., Hazen, R.M., Daniel, I., 2020b. Cycling phosphorus on the Archean Earth: Part II. Phosphorus limitation on primary production in Archean ecosystems. Geochimica et Cosmochimica Acta 280, 360–377. https://doi.org/10.1016/j.gca.2020.04.005

Hao, W., Mänd, K., Li, Y., Alessi, D.S., Somelar, P., Moussavou, M., Romashkin, A.E., Lepland, A., Kirsimäe, K., Planavsky, N.J., Konhauser, K.O., 2021. The kaolinite shuttle links the Great Oxidation and Lomagundi events. Nature Communications 12, 2944. https://doi.org/10.1038/s41467-021-23304-8

Hargreaves, J.C., 2019. Summary of quality control data for the Geosciences Laboratories methods FEO-ION, IAW-200, ICW-100, IRC-100, IRW-H2O and TOC-100. In: Summary of Field Work and Other Activities 2019. Ontario Geological Survey Open File Report 6360, 25–1 to 25–6.

Harrison, J.M., 1952. The Quebec-Labrador iron belt, Quebec and Newfoundland. Canada Geological Survey Special Paper 52–20, 21 p. https://doi.org/10.4095/123923

Haugaard, R., Ootes, L., Creaser, R.A., Konhauser, K.O., 2016a. The nature of Mesoarchaean seawater and continental weathering in 2.85 Ga banded iron formation, Slave Craton, NW Canada. Geochimica et Cosmochimica Acta 194, 34–56.

https://doi.org/10.1016/j.gca.2016.08.020

Haugaard, R., Pecoits, E., Lalonde, S., Rouxel, O., Konhauser, K., 2016b. The Joffre Banded Iron Formation, Hamersley Group, Western Australia: assessing the palaeoenvironment through detailed petrology and chemostratigraphy. Precambrian Research 273, 12–37. https://doi.org/10/f784fx

Heiri, O., Lotter, A.F., Lemcke, G., 2001. Loss on ignition as a method for estimating organic and carbonate content in sediments: reproducibility and comparability of results. Journal of Paleolimnology 25, 101–110.

Henrique-Pinto, R., Guilmette, C., Bilodeau, C., McNicoll, V., 2017. Evidence for transition from a continental forearc to a collisional pro-foreland basin in the eastern Trans-Hudson Orogen: detrital zircon provenance analysis in the Labrador Trough, Canada. Precambrian Research 296, 181–194. https://doi.org/10/gbktd6

Henrique-Pinto, R., Guilmette, C., Bilodeau, C., Stevenson, R., Carvalho, B.B., 2019. Petrography, geochemistry, and Nd isotope systematics of metaconglomerates and matrix-rich metasedimentary rocks: implications for the provenance and tectonic setting of the Labrador Trough, Canada. Canadian Journal of Earth Sciences 56, 672–687. https://doi.org/10.1139/cjes-2018-0187

Hiatt, E.E., Pufahl, P.K., Edwards, C.T., 2015. Sedimentary phosphate and associated fossil bacteria in a Paleoproterozoic tidal flat in the 1.85 Ga Michigamme Formation, Michigan, USA. Sedimentary Geology 319, 24–39. https://doi.org/10.1016/j.sedgeo.2015.01.006

Hodgskiss, M.S.W., Crockford, P.W., Peng, Y., Wing, B.A., Horner, T.J., 2019. A productivity collapse to end Earth's Great Oxidation. Proceedings of the National Academy of Sciences 201900325. https://doi.org/10/gf6dcj

Hoffman, P.F., 1988. United Plates of America, the birth of a craton: Early Proterozoic assembly and growth of Laurentia. Annual Review of Earth and Planetary Sciences 16, 543–603.

Huang, J.-H., Huang, F., Evans, L., Glasauer, S., 2015. Vanadium: global (bio)geochemistry. Chemical Geology 417, 68–89. https://doi.org/10/f7znff

Isley, A.E., 1995. Hydrothermal plumes and the delivery of iron to banded iron formation. The Journal of Geology 103, 169–185. https://doi.org/10/cw3hvm

Isley, A.E., Abbott, D.H., 1999. Plume-related mafic volcanism and the deposition of banded iron formation. Journal of Geophysical Research: Solid Earth 104, 15461–15477. https://doi.org/10/cvgbdb

James, D.T., Dunning, G.R., 2000. U–Pb geochronological constraints for Paleoproterozoic evolution of the Core Zone, southeastern Churchill Province, northeastern Laurentia. Precambrian Research 103, 31–54. https://doi.org/10/b6v59w

James, H.L., 1954, Sedimentary facies of iron-formation. Economic Geology 49, 235-293.

Javaux, E.J., Lepot, K., 2018. The Paleoproterozoic fossil record: implications for the evolution of the biosphere during Earth's middle-age. Earth-Science Reviews 176, 68–86. https://doi.org/10.1016/j.earscirev.2017.10.001

Justo, A.P., Dantas, E.L., Bau, M., Freitas-Silva, F.H., Santos, R.V., Schorscher, J.H.D., 2020. Paleobasinal to band-scale REE + Y distribution in iron formations from Carajás, Amazon Craton, Brazil. Ore Geology Reviews 127, 103750. https://doi.org/10.1016/j.oregeorev.2020.103750

Kamber, B.S., 2009. Geochemical fingerprinting: 40 years of analytical development and real world applications. Applied Geochemistry 24, 1074–1086. https://doi.org/10.1016/j.apgeochem.2009.02.012

Kamber, B.S., Greig, A., Collerson, K.D., 2005. A new estimate for the composition of weathered young upper continental crust from alluvial sediments, Queensland, Australia. Geochimica et Cosmochimica Acta 69, 1041–1058. https://doi.org/10/dh9qcq

Kato, Y., Yamaguchi, K.E., Ohmoto, H., 2006. Rare earth elements in Precambrian banded iron formations: secular changes of Ce and Eu anomalies and evolution of atmospheric oxygen. In: Kesler, S.E., Ohmoto, H. (Eds.), Evolution of Early Earth's Atmosphere, Hydrosphere, and Biosphere—Constraints from Ore Deposits. Geological Society of America Memoir 198, pp. 269–289. https://doi.org/10.1130/2006.1198(16)

Kendall, B., Reinhard, C.T., Lyons, T.W., Kaufman, A.J., Poulton, S.W., Anbar, A.D., 2010. Pervasive oxygenation along Late Archaean ocean margins. Nature Geoscience 3, 647–652. https://doi.org/10/cb6f2n

Kipp, M.A., Stüeken, E.E., 2017. Biomass recycling and Earth's early phosphorus cycle. Science Advances 3, eaao4795. https://doi.org/10/gcnsrx

Kipp, M.A., Stüeken, E.E., Bekker, A., Buick, R., 2017. Selenium isotopes record extensive

marine suboxia during the Great Oxidation Event. Proceedings of the National Academy of Sciences 114, 875–880. https://doi.org/10.1073/pnas.1615867114

Kipp, M.A., Stüeken, E.E., Yun, M., Bekker, A., Buick, R., 2018. Pervasive aerobic nitrogen cycling in the surface ocean across the Paleoproterozoic Era. Earth and Planetary Science Letters 500, 117–126. https://doi.org/10.1016/j.epsl.2018.08.007

Kipp, M.A., Lepland, A., Buick, R., 2020. Redox fluctuations, trace metal enrichment and phosphogenesis in the ~2.0 Ga Zaonega Formation. Precambrian Research 343, 105716. https://doi.org/10.1016/j.precamres.2020.105716

Klein, C., 1974. Greenalite, stilpnomelane, minnesotaite, crocidolite and carbonates in a very low-grade metamorphic Precambrian iron-formation. Canadian Mineralogist 12, 475–498.

Klein, C., 1978. Regional metamorphism of Proterozoic iron-formation. Labrador Trough, Canada, American Mineralogist 63, 898–912.

Klein, C., 2005. Some Precambrian banded iron-formations (BIFs) from around the world: their age, geologic setting, mineralogy, metamorphism, geochemistry, and origins. American Mineralogist 90, 1473–1499. https://doi.org/10/fwgmpx

Klein C., Fink, R.P., 1976. Petrology of the Sokoman Iron Formation in the Howells River area, at the western edge of the Labrador Trough. Economic Geology 71, 453–487.

Klinkhammer, G., Elderfield, H., Edmond, J., Mitra, A., 1994. Geochemical implications of rare earth element patterns in hydrothermal fluids from mid-ocean ridges. Geochimica et Cosmochimica Acta 58, 5105–5113. https://doi.org/10/ddmzwj

Konhauser, K.O., Pecoits, E., Lalonde, S.V., Papineau, D., Nisbet, E.G., Barley, M.E., Arndt, N.T., Zahnle, K., Kamber, B.S., 2009. Oceanic nickel depletion and a methanogen famine before the Great Oxidation Event. Nature 458, 750–753. https://doi.org/10/cnqbmj

Konhauser, K.O., Planavsky, N.J., Hardisty, D.S., Robbins, L.J., Warchola, T.J., Haugaard, R., Lalonde, S.V., Partin, C.A., Oonk, P.B.H., Tsikos, H., Lyons, T.W., Bekker, A., Johnson, C.M., 2017. Iron formations: a global record of Neoarchaean to Palaeoproterozoic environmental history. Earth-Science Reviews 172, 140–177. https://doi.org/10.1016/j.earscirev.2017.06.012

Konstantinovskaya, E., Ivanov, G., Feybesse, J.-L., Lescuyer, J.-L., 2019. Structural features of

the central Labrador Trough: a model for strain partitioning, differential exhumation and late normal faulting in a thrust wedge under oblique shortening. Geoscience Canada 46, 5–30. https://doi.org/10/gf9xqt

Koppelman, M.H., Dillard, J.G., 1977. A study of the adsorption of Ni(II) and Cu(II) by clay minerals. Clays and Clay Minerals 25, 457–462.

Koschinsky, A., Seifert, R., Halbach, P., Bau, M., Brasse, S., de Carvalho, L.M., Fonseca, N.M., 2002. Geochemistry of diffuse low-temperature hydrothermal fluids in the North Fiji Basin. Geochimica et Cosmochimica Acta 66, 1409–1427. https://doi.org/10.1016/S0016-7037(01)00855-9

Kreitsmann, T., Lepland, A., Bau, M., Prave, A., Paiste, K., Mänd, K., Sepp, H., Martma, T., Romashkin, A.E., Kirsimäe, K., 2020. Oxygenated conditions in the aftermath of the Lomagundi-Jatuli Event: the carbon isotope and rare earth element signatures of the Paleoproterozoic Zaonega Formation, Russia. Precambrian Research 347, 105855. https://doi.org/10.1016/j.precamres.2020.105855

Laakso, T.A., Schrag, D.P., 2014. Regulation of atmospheric oxygen during the Proterozoic. Earth and Planetary Science Letters 388, 81–91. https://doi.org/10/f5rtvk

Laakso, T.A., Schrag, D.P., 2018. Limitations on limitation. Global Biogeochemical Cycles 32, 486–496. https://doi.org/10.1002/2017GB005832

LaGrange, M.T., Konhauser, K.O., Catuneanu, O., Harris, B.S., Playter, T.L., Gingras, M.K., 2020. Sequence stratigraphy in organic-rich marine mudstone successions using chemostratigraphic datasets. Earth-Science Reviews 203, 103137. https://doi.org/10.1016/j.earscirev.2020.103137

Large, R.R., Mukherjee, I., Zhukova, I., Corkrey, R., Stepanov, A., Danyushevsky, L.V., 2018. Role of upper-most crustal composition in the evolution of the Precambrian ocean–atmosphere system. Earth and Planetary Science Letters 487, 44–53. https://doi.org/10.1016/j.epsl.2018.01.019

Larsen, I.J., Montgomery, D.R., Greenberg, H.M., 2014. The contribution of mountains to global denudation. Geology 42, 527–530. https://doi.org/10.1130/G35136.1

Lawrence, M.G., Greig, A., Collerson, K.D., Kamber, B.S., 2006. Rare earth element and yttrium variability in south east Queensland waterways. Aquatic Geochemistry 12, 39–72. https://doi.org/10/dtw2t3

Le Gallais, C.J., Lavoie, S., 1982. Basin evolution of the Lower Proterozoic Kaniapiskau Supergroup central Labrador miogeocline (trough), Quebec. Bulletin of Canadian Petroleum Geology 30, 150–166.

Lepot, K., Addad, A., Knoll, A.H., Wang, J., Troadec, D., Béché, A., Javaux, E.J., 2017. Iron minerals within specific microfossil morphospecies of the 1.88 Ga Gunflint Formation. Nature Communications 8, 14890. https://doi.org/10/f9wvvf

Lesher, C.M., 1978. Mineralogy and petrology of the Sokoman Iron Formation near Ardua Lake, Quebec. Canadian Journal of Earth Sciences 15, 480–500. https://doi.org/10.1139/e78-056

Liu, J., Algeo, T.J., 2020. Beyond redox: control of trace-metal enrichment in anoxic marine facies by watermass chemistry and sedimentation rate. Geochimica et Cosmochimica Acta 287, 296–317. https://doi.org/10.1016/j.gca.2020.02.037

Lyons, T.W., Reinhard, C.T., Planavsky, N.J., 2014. The rise of oxygen in Earth's early ocean and atmosphere. Nature 506, 307–315. https://doi.org/10/s2c

Machado, N., Goulet, N., Gariépy, C., 1989. U–Pb geochronology of reactivated Archean basement and of Hudsonian metamorphism in the northern Labrador Trough. Canadian Journal of Earth Sciences 26, 1–15. https://doi.org/10/fb22cz

Machado, N., Clark, T., David, J., Goulet, N., 1997. U–Pb ages for magmatism and deformation in the New Quebec Orogen. Canadian Journal of Earth Sciences 34, 716–723. https://doi.org/10/d72xx4

Maliva, R.G., Knoll, A.H., Simonson, B.M., 2005. Secular change in the Precambrian silica cycle: insights from chert petrology. Geological Society of America Bulletin 117, 835–845.

Mänd, K., Lalonde, S.V., Robbins, L.J., Thoby, M., Paiste, K., Kreitsmann, T., Paiste, P., Reinhard, C.T., Romashkin, A.E., Planavsky, N.J., Kirsimäe, K., Lepland, A., Konhauser, K.O., 2020. Palaeoproterozoic oxygenated oceans following the Lomagundi–Jatuli Event. Nature Geoscience 13, 302–306. https://doi.org/10.1038/s41561-020-0558-5

Marx, S.K., Kamber, B.S., McGowan, H.A., Zawadzki, A., 2010. Atmospheric pollutants in alpine peat bogs record a detailed chronology of industrial and agricultural development on the Australian continent. Environmental Pollution 158, 1615–1628. https://doi.org/10/br8h6d

Masuda, A., Ikeuchi, Y., 1979. Lanthanide tetrad effect observed in marine environment. Geochemical Journal 13, 19–22. https://doi.org/10.2343/geochemj.13.19

Michard, A., 1989. Rare earth element systematics in hydrothermal fluids. Geochimica et Cosmochimica Acta 53, 745–750. https://doi.org/10.1016/0016-7037(89)90017-3

Neal, H.E., 2000. Iron deposits of the Labrador Trough. Exploration and Mining Geology 9, 113–121. https://doi.org/10.2113/0090113

Nelson, G.J., Pufahl, P.K., Hiatt, E.E., 2010. Paleoceanographic constraints on Precambrian phosphorite accumulation, Baraga Group, Michigan, USA. Sedimentary Geology 226, 9–21. https://doi.org/10.1016/j.sedgeo.2010.02.001

Nichols, G., 2009. Sedimentology and stratigraphy. Wiley-Blackwell, Oxford, 432 p.

Ohta, A., Kawabe, I., 2001. REE(III) adsorption onto Mn dioxide (δ-MnO_2) and Fe oxyhydroxide: Ce(III) oxidation by δ-MnO_2. Geochimica et Cosmochimica Acta 65, 695–703.

Oonk, P.B.H., Tsikos, H., Mason, P.R.D., Henkel, S., Staubwasser, M., Fryer, L., Poulton, S.W., Williams, H.M., 2017. Fraction-specific controls on the trace element distribution in iron formations: implications for trace metal stable isotope proxies. Chemical Geology 474, 17–32. https://doi.org/10/gft2fm

Oonk, P.B.H., Mason, P.R.D., Tsikos, H., Bau, M., 2018. Fraction-specific rare earth elements enable the reconstruction of primary seawater signatures from iron formations. Geochimica et Cosmochimica Acta 238, 102–122. https://doi.org/10/gfvjmb

Ossa Ossa, F., Hofmann, A., Wille, M., Spangenberg, J.E., Bekker, A., Poulton, S.W., Eickmann, B., Schoenberg, R., 2018. Aerobic iron and manganese cycling in a redox-stratified Mesoarchean epicontinental sea. Earth and Planetary Science Letters 500, 28–40. https://doi.org/10/gfdpwj

Ostrander, C.M., Nielsen, S.G., Owens, J.D., Kendall, B., Gordon, G.W., Romaniello, S.J., Anbar, A.D., 2019. Fully oxygenated water columns over continental shelves before the Great Oxidation Event. Nature Geoscience 12, 186–191. https://doi.org/10/ggc8n6

Oze, C., Bird, D.K., Fendorf, S., 2007. Genesis of hexavalent chromium from natural sources in soil and groundwater. Proceedings of the National Academy of Sciences 104, 6544–6549. https://doi.org/10.1073/pnas.0701085104

Papineau, D., Purohit, R., Fogel, M.L., Shields-Zhou, G.A., 2013. High phosphate availability as

a possible cause for massive cyanobacterial production of oxygen in the Paleoproterozoic atmosphere. Earth and Planetary Science Letters 362, 225–236. https://doi.org/10.1016/j.epsl.2012.11.050

Partin, C.A., Lalonde, S.V., Planavsky, N.J., Bekker, A., Rouxel, O.J., Lyons, T.W., Konhauser, K.O., 2013a. Uranium in iron formations and the rise of atmospheric oxygen. Chemical Geology 362, 82–90. https://doi.org/10.1016/j.chemgeo.2013.09.005

Partin, C.A., Bekker, A., Planavsky, N.J., Scott, C.T., Gill, B.C., Li, C., Podkovyrov, V., Maslov, A., Konhauser, K.O., Lalonde, S.V., Love, G.D., Poulton, S.W., Lyons, T.W., 2013b. Large-scale fluctuations in Precambrian atmospheric and oceanic oxygen levels from the record of U in shales. Earth and Planetary Science Letters 369–370, 284–293. https://doi.org/10.1016/j.epsl.2013.03.031

Percival, J.A., Stern, R.A., Rayner, N., 2003. Archean adakites from the Ashuanipi Complex, eastern Superior Province, Canada: geochemistry, geochronology and tectonic significance. Contributions to Mineralogy and Petrology 145, 265–280. https://doi.org/10.1007/s00410-003-0450-5

Petrash, D.A., Robbins, L.J., Shapiro, R.S., Mojzsis, S.J., Konhauser, K.O., 2016. Chemical and textural overprinting of ancient stromatolites: timing, processes, and implications for their use as paleoenvironmental proxies. Precambrian Research 278, 145–160. https://doi.org/10.1016/j.precamres.2016.03.010

Planavsky, N., Rouxel, O., Bekker, A., Shapiro, R., Fralick, P., Knudsen, A., 2009. Iron-oxidizing microbial ecosystems thrived in late Paleoproterozoic redox-stratified oceans. Earth and Planetary Science Letters 286, 230–242. https://doi.org/10/crzgkv

Planavsky, N., Bekker, A., Rouxel, O.J., Kamber, B., Hofmann, A., Knudsen, A., Lyons, T.W., 2010a. Rare earth element and yttrium compositions of Archean and Paleoproterozoic Fe formations revisited: new perspectives on the significance and mechanisms of deposition. Geochimica et Cosmochimica Acta 74, 6387–6405. https://doi.org/10/fj558k

Planavsky, N.J., Rouxel, O.J., Bekker, A., Lalonde, S.V., Konhauser, K.O., Reinhard, C.T., Lyons, T.W., 2010b. The evolution of the marine phosphate reservoir. Nature 467, 1088–1090. https://doi.org/10/drs9x9

Planavsky, N.J., Asael, D., Hofmann, A., Reinhard, C.T., Lalonde, S.V., Knudsen, A., Wang, X., Ossa Ossa, F., Pecoits, E., Smith, A.J.B., Beukes, N.J., Bekker, A., Johnson, T.M.,

Konhauser, K.O., Lyons, T.W., Rouxel, O.J., 2014. Evidence for oxygenic photosynthesis half a billion years before the Great Oxidation Event. Nature Geoscience 7, 283–286. https://doi.org/10.1038/ngeo2122

Planavsky, N.J., Slack, J.F., Cannon, W.F., O'Connell, B., Isson, T.T., Asael, D., Jackson, J.C., Hardisty, D.S., Lyons, T.W., Bekker, A., 2018. Evidence for episodic oxygenation in a weakly redox-buffered deep mid-Proterozoic ocean. Chemical Geology 483, 581–594. https://doi.org/10/gdfwdr

Planavsky, N.J., Robbins, L.J., Kamber, B.S., Schoenberg, R., 2020. Weathering, alteration and reconstructing Earth's oxygenation. Interface Focus 10, 20190140. https://doi.org/10.1098/rsfs.2019.0140

Posth, N.R., Köhler, I.D., Swanner, E., Schröder, C., Wellmann, E., Binder, B., Konhauser, K.O., Neumann, U., Berthold, C., Nowak, M., Kappler, A., 2013. Simulating Precambrian banded iron formation diagenesis. Chemical Geology 362, 66–73. https://doi.org/10.1016/j.chemgeo.2013.05.031

Posth, N.R., Canfield, D.E., Kappler, A., 2014. Biogenic Fe(III) minerals: from formation to diagenesis and preservation in the rock record. Earth-Science Reviews 135, 103–121. https://doi.org/10/f589j4

Potts, P.J., Kane, J.S., 2005. International Association of Geoanalysts Certificate of Analysis: Certified Reference Material OU-6 (Penrhyn Slate). Geostandards and Geoanalytical Research 29, 233–236. https://doi.org/10.1111/j.1751-908X.2005.tb00895.x

Potts, P.J., Webb, P.C., 1992. X-ray fluorescence spectrometry. Journal of Geochemical Exploration 44, 251–296.

Poulton, S.W., Canfield, D.E., 2005. Development of a sequential extraction procedure for iron: implications for iron partitioning in continentally derived particulates. Chemical Geology 214, 209–221. https://doi.org/10/cs754b

Poulton, S.W., Canfield, D.E., 2011. Ferruginous conditions: a dominant feature of the ocean through Earth's history. Elements 7, 107–112. https://doi.org/10.2113/gselements.7.2.107

Poulton, S.W., Fralick, P.W., Canfield, D.E., 2004. The transition to a sulphidic ocean ~1.84 billion years ago. Nature 431, 173–177. https://doi.org/10.1038/nature02912

Poulton, S.W., Fralick, P.W., Canfield, D.E., 2010. Spatial variability in oceanic redox structure 1.8 billion years ago. Nature Geoscience 3, 486–490. https://doi.org/10/dzw3rg

Pourmand, A., Dauphas, N., Ireland, T.J., 2012. A novel extraction chromatography and MC-ICP-MS technique for rapid analysis of REE, Sc and Y: revising CI-chondrite and Post-Archean Australian Shale (PAAS) abundances. Chemical Geology 291, 38–54. https://doi.org/10/bwz489

Pufahl, P.K., 2010. Bioelemental sediments. In: James, N.P., Dalrymple, R.W. (Eds.), Facies Models, fourth ed. Geological Association of Canada, pp. 477–503.

Pufahl, P.K., Hiatt, E.E., 2012. Oxygenation of the Earth's atmosphere–ocean system: a review of physical and chemical sedimentologic responses. Marine and Petroleum Geology 32, 1–20. https://doi.org/10/bvvcd9

Pufahl, P.K., Anderson, S.L., Hiatt, E.E., 2014. Dynamic sedimentation of Paleoproterozoic continental margin iron formation, Labrador Trough, Canada: paleoenvironments and sequence stratigraphy. Sedimentary Geology 309, 48–65. https://doi.org/10.1016/j.sedgeo.2014.05.006

Rasmussen, B., Muhling, J.R., 2020. Hematite replacement and oxidative overprinting recorded in the 1.88 Ga Gunflint Iron Formation, Ontario, Canada. Geology 48, 688–692. https://doi.org/10.1130/G47410.1

Rasmussen, B., Fletcher, I.R., Bekker, A., Muhling, J.R., Gregory, C.J., Thorne, A.M., 2012. Deposition of 1.88-billion-year-old iron formations as a consequence of rapid crustal growth. Nature 484, 498–501. https://doi.org/10/gfvcnf

Rasmussen, B., Krapež, B., Muhling, J.R., 2014. Hematite replacement of iron-bearing precursor sediments in the 3.46-b.y.-old Marble Bar Chert, Pilbara Craton, Australia. Geological Society of America Bulletin 126, 1245–1258. https://doi.org/10/f6m34p

Rasmussen, B., Muhling, J.R., Suvorova, A., Krapež, B., 2016. Dust to dust: evidence for the formation of "primary" hematite dust in banded iron formations via oxidation of iron silicate nanoparticles. Precambrian Research 284, 49–63. https://doi.org/10.1016/j.precamres.2016.07.003

Raye, U., Pufahl, P.K., Kyser, T.K., Ricard, E., Hiatt, E.E., 2015. The role of sedimentology, oceanography, and alteration on the δ^{56}Fe value of the Sokoman Iron Formation, Labrador Trough, Canada. Geochimica et Cosmochimica Acta 164, 205–220. https://doi.org/10/f7jw64

Reddy, S.M., Evans, D.A.D., 2009. Palaeoproterozoic supercontinents and global evolution:

correlations from core to atmosphere. Geological Society of London Special Publication 323, 1–26. https://doi.org/10/bstd2x

Reinhard, C.T., Planavsky, N.J., Gill, B.C., Ozaki, K., Robbins, L.J., Lyons, T.W., Fischer, W.W., Wang, C., Cole, D.B., Konhauser, K.O., 2017. Evolution of the global phosphorus cycle. Nature 541, 386–389. https://doi.org/10/f9kcpg

Riding, R., Fralick, P., Liang, L., 2014. Identification of an Archean marine oxygen oasis. Precambrian Research 251, 232–237. https://doi.org/10/tsq

Robbins, L.J., Lalonde, S.V., Saito, M.A., Planavsky, N.J., Mloszewska, A.M., Pecoits, E., Scott, C., Dupont, C.L., Kappler, A., Konhauser, K.O., 2013. Authigenic iron oxide proxies for marine zinc over geological time and implications for eukaryotic metallome evolution. Geobiology 11, 295–306. https://doi.org/10/f48wtj

Robbins, L.J., Konhauser, K.O., Warchola, T.J., Homann, M., Thoby, M., Foster, I., Mloszewska, A.M., Alessi, D.S., Lalonde, S.V., 2019. A comparison of bulk versus laser ablation trace element analyses in banded iron formations: insights into the mechanisms leading to compositional variability. Chemical Geology 506, 197–224. https://doi.org/10/gfvjmg

Rohon, M.-L., Vialette, Y., Clark, T., Roger, G., Ohnenstetter, D., Vidal, P., 1993. Aphebian mafic-ultramafic magmatism in the Labrador Trough (New Quebec): its age and the nature of its mantle source. Canadian Journal of Earth Sciences 30, 1582–1593. https://doi.org/10/gft5m8

Rosca, C., Tomlinson, E.L., Geibert, W., McKenna, C.A., Babechuk, M.G., Kamber, B.S., 2018. Trace element and Pb isotope fingerprinting of atmospheric pollution sources: a case study from the east coast of Ireland. Applied Geochemistry 96, 302–326. https://doi.org/10/gd5q7m

Rudnick, R., Gao, S., 2003. Composition of the continental crust. In: Rudnick, R.L. (Ed.), The Crust. Treatise on Geochemistry, The Crust, vol. 3. Elsevier Pergamon, Oxford, pp. 1–64.

Saad, E.M., Wang, X., Planavsky, N.J., Reinhard, C.T., Tang, Y., 2017. Redox-independent chromium isotope fractionation induced by ligand-promoted dissolution. Nature Communications 8, 1590. https://doi.org/10/gcmv6t

Sampaio, G.M.S., Enzweiler, J., 2015. New ICP-MS results for trace elements in five iron-formation reference materials. Geostandards and Geoanalytical Research 39, 105–

119. https://doi.org/10/f6zsjs

Sander, S., Koschinsky, A., 2000. Onboard-ship redox speciation of chromium in diffuse hydrothermal fluids from the North Fiji Basin. Marine Chemistry 71, 83–102.

Satkoski, A.M., Beukes, N.J., Li, W., Beard, B.L., Johnson, C.M., 2015. A redox-stratified ocean 3.2 billion years ago. Earth and Planetary Science Letters 430, 43–53. https://doi.org/10/f7v2ng

Schad, M., Konhauser, K.O., Sánchez-Baracaldo, P., Kappler, A., Bryce, C., 2019. How did the evolution of oxygenic photosynthesis influence the temporal and spatial development of the microbial iron cycle on ancient Earth? Free Radical Biology and Medicine 140, 154–166. https://doi.org/10/ggm83c

Schier, K., Bau, M., Smith, A.J.B., Beukes, N.J., Coetzee, L.L., Viehmann, S., 2020. Chemical evolution of seawater in the Transvaal Ocean between 2426 Ma (Ongeluk Large Igneous Province) and 2413 Ma ago (Kalahari Manganese Field). Gondwana Research 88, 373–388. https://doi.org/10.1016/j.gr.2020.09.001

Schoepfer, S.D., Shen, J., Wei, H., Tyson, R.V., Ingall, E., Algeo, T.J., 2015. Total organic carbon, organic phosphorus, and biogenic barium fluxes as proxies for paleomarine productivity. Earth-Science Reviews 149, 23–52. https://doi.org/10/f7txpj

Schröder, S., Bedorf, D., Beukes, N.J., Gutzmer, J., 2011. From BIF to red beds: sedimentology and sequence stratigraphy of the Paleoproterozoic Koegas Subgroup (South Africa). Sedimentary Geology 236, 25–44. https://doi.org/10.1016/j.sedgeo.2010.11.007

Severmann, S., Lyons, T.W., Anbar, A., McManus, J., Gordon, G., 2008. Modern iron isotope perspective on the benthic iron shuttle and the redox evolution of ancient oceans. Geology 36, 487–490. https://doi.org/10.1130/G24670A.1

Shapiro, R.S., Konhauser, K.O., 2015. Hematite-coated microfossils: primary ecological fingerprint or taphonomic oddity of the Paleoproterozoic? Geobiology 13, 209–224. https://doi.org/10.1111/gbi.12127

Shiraishi, F., Ohnishi, S., Hayasaka, Y., Hanzawa, Y., Takashima, C., Okumura, T., Kano, A., 2019. Potential photosynthetic impact on phosphate stromatolite formation after the Marinoan glaciation: paleoceanographic implications. Sedimentary Geology 380, 65–82. https://doi.org/10.1016/j.sedgeo.2018.11.014

Simonson, B.M., 1984. High energy shelf-deposit; early Proterozoic Wishart Formation,

northeastern Canada. Society of Economic Paleontologists and Mineralogists Special Publication 34, 251–268.

Simonson, B.M., 1985. Sedimentology of cherts in the Early Proterozoic Wishart Formation, Quebec-Newfoundland, Canada. Sedimentology 32, 23–40. https://doi.org/10.1111/j.1365-3091.1985.tb00490.x

Simonson, B.M., 1987. Early silica cementation and subsequent diagenesis in arenites from four Early Proterozoic iron formations of North America. Journal of Sedimentary Petrology 57, 494–511.

Sindol, G.P., Babechuk, M.G., Petrus, J.A., Kamber, B.S., 2020. New insights into Paleoproterozoic surficial conditions revealed by 1.85 Ga corestone-rich saprolith. Chemical Geology 545, 119621. https://doi.org/10.1016/j.chemgeo.2020.119621

Skulski, T., Wares, R.P., Smith, A.D., 1993. Early Proterozoic (1.88–1.87 Ga) tholeiitic magmatism in the New Québec Orogen. Canadian Journal of Earth Sciences 30, 1505–1520. https://doi.org/10/fm9kz5

Slack, J.F., Grenne, T., Bekker, A., Rouxel, O.J., Lindberg, P.A., 2007. Suboxic deep seawater in the late Paleoproterozoic: evidence from hematitic chert and iron formation related to seafloor-hydrothermal sulfide deposits, central Arizona, USA. Earth and Planetary Science Letters 255, 243–256. https://doi.org/10/fv8vtd

Slack, J.F., Grenne, T., Bekker, A., 2009. Seafloor-hydrothermal Si-Fe-Mn exhalites in the Pecos greenstone belt, New Mexico, and the redox state of ca. 1720 Ma deep seawater. Geosphere 5, 302–314. https://doi.org/10/dfnw7q

Steadman, J.A., Large, R.R., Blamey, N.J., Mukherjee, I., Corkrey, R., Danyushevsky, L.V., Maslennikov, V., Hollings, P., Garven, G., Brand, U., Lécuyer, C., 2020. Evidence for elevated and variable atmospheric oxygen in the Precambrian. Precambrian Research 343, 105722. https://doi.org/10.1016/j.precamres.2020.105722

Suhr, N., Widdowson, M., McDermott, F., Kamber, B.S., 2018. Th/U and U series systematics of saprolite: importance for the oceanic ^{234}U excess. Geochemical Perspectives Letters 6, 17–22. https://doi.org/10.7185/geochemlet.1803

Sun, S., Konhauser, K.O., Kappler, A., Li, Y.-L., 2015. Primary hematite in Neoarchean to Paleoproterozoic oceans. Geological Society of America Bulletin 127, 850–861. https://doi.org/10.1130/B31122.1

Sverjensky, D.A., 1984. Europium redox equilibria in aqueous solution. Earth and Planetary Science Letters 67, 70–78. https://doi.org/10.1016/0012-821X(84)90039-6

Swanner, E.D., Planavsky, N.J., Lalonde, S.V., Robbins, L.J., Bekker, A., Rouxel, O.J., Saito, M.A., Kappler, A., Mojzsis, S.J., Konhauser, K.O., 2014. Cobalt and marine redox evolution. Earth and Planetary Science Letters 390, 253–263. https://doi.org/10/f5x2pr

Sylvester, P.J., 2012. Use of the Mineral Liberation Analyzer (MLA) for mineralogical studies of sediments and sedimentary rocks. Mineralogical Association of Canada Short Course Series 42, 1–16.

Sylwester, E.R., Hudson, E.A., Allen, P.G., 2000. The structure of uranium (VI) sorption complexes on silica, alumina, and montmorillonite. Geochimica et Cosmochimica Acta 64, 2431–2438.

Tang, M., Chu, X., Hao, J., Shen, B., 2021. Orogenic quiescence in Earth's middle age. Science 371, 728–731. https://doi.org/10.1126/science.abf1876

Tosca, N.J., Guggenheim, S., Pufahl, P.K., 2016. An authigenic origin for Precambrian greenalite: implications for iron formation and the chemistry of ancient seawater. Geological Society of America Bulletin 128, 511–530. https://doi.org/10.1130/B31339.1

Tribovillard, N., Algeo, T.J., Lyons, T., Riboulleau, A., 2006. Trace metals as paleoredox and paleoproductivity proxies: an update. Chemical Geology 232, 12–32. https://doi.org/10/bp6kr3

Turner, E.C., Kamber, B.S., 2012. Arctic Bay Formation, Borden Basin, Nunavut (Canada): basin evolution, black shale, and dissolved metal systematics in the Mesoproterozoic ocean. Precambrian Research 208–211, 1–18. https://doi.org/10.1016/j.precamres.2012.03.006

Ulrich, T., Kamber, B.S., Woodhead, J.D., Spencer, L.A., 2010. Long-term observations of isotope ratio accuracy and reproducibility using Quadrupole ICP-MS. Geostandards and Geoanalytical Research 34, 161–174. https://doi.org/10/fmj59x

van den Boorn, S.H.J.M., van Bergen, M.J., Nijman, W., Vroon, P.Z., 2007. Dual role of seawater and hydrothermal fluids in Early Archean chert formation: evidence from silicon isotopes. Geology 35, 939–942. https://doi.org/10/dgmdhj

van Nostrand, T.S., 2017. Geochemical data from the Archean Ashuanipi Complex, western Labrador (NTS map sheets 23J/02, 03, 04, 05, 06, 07, 10, 11 and 14). Government of

Newfoundland and Labrador, Department of Natural Resources, Geological Survey Open File 023J/0396, 10 p.

van Nostrand, T., Bradford, W., 2014. Geology of the northeastern Ashuanipi Complex, western Labrador (Parts of 1:50 000-scale NTS map areas 23J/06, 07, 10, 11 and 14 and 23O/03). In: Current Research. Government of Newfoundland and Labrador, Department of Natural Resources, Geological Survey Report 14–1, 189–216.

van Rooyen, D., Corrigan, D., McNicoll, V., Rayner, N. 2019. Tectonic evolution of the New Quebec Orogen: new insights from field mapping and U-Pb geochronology in the Kuujjuaq area. GAC-MAC-IAH Québec 2019.

Viehmann, S., Bau, M., Hoffmann, J.E., Münker, C., 2015. Geochemistry of the Krivoy Rog banded iron formation, Ukraine, and the impact of peak episodes of increased global magmatic activity on the trace element composition of Precambrian seawater. Precambrian Research 270, 165–180. https://doi.org/10/f7zm4g

Viollier, E., Michard, G., Jézéquel, D., Pèpe, M., Sarazin, G., 1997. Geochemical study of a crater lake: Lake Pavin, Puy de Dôme, France. Constraints afforded by the particulate matter distribution in the element cycling within the lake. Chemical Geology 142, 225–241.

Wanty, R.B., Goldhaber, M.B., 1992. Thermodynamics and kinetics of reactions involving vanadium in natural systems: accumulation of vanadium in sedimentary rocks. Geochimica et Cosmochimica Acta 56, 1471–1483. https://doi.org/10.1016/0016-7037(92)90217-7

Warchola, T., Lalonde, S.V., Pecoits, E., von Gunten, K., Robbins, L.J., Alessi, D.S., Philippot, P., Konhauser, K.O., 2018. Petrology and geochemistry of the Boolgeeda Iron Formation, Hamersley Basin, Western Australia. Precambrian Research 316, 155–173. https://doi.org/10.1016/j.precamres.2018.07.015

Wardle, R.J., 1982a. Map 1, Geology of the south-central Labrador Trough. Government of Newfoundland and Labrador, Department of Mines and Energy, Mineral Development Division, Map 82-5, scale 1:100,000.

Wardle, R.J., 1982b: Map 2, Geology of the south-central Labrador Trough. Government of Newfoundland and Labrador, Department of Mines and Energy, Mineral Development Division, Map 82-6, scale 1:100,000.

Wardle, R.J., Bailey, D.G., 1981. Early Proterozoic sequences in Labrador. In: Campbell, F. H.A. (Ed.) Proterozoic basins of Canada. Geological Survey of Canada Paper 81–10, 331–359.

Wardle, R.J., Van Kranendonk, M.J., 1996. The Palaeoproterozoic southeastern Churchill Province of Labrador-Quebec, Canada: orogenic development as a consequence of oblique collision and indentation. Geological Society of London Special Publication 112, 137–153. https://doi.org/10/b5cvws

Wardle, R.J., James, D.T., Scott, D.J., Hall, J., 2002. The southeastern Churchill Province: synthesis of a Paleoproterozoic transpressional orogen. Canadian Journal of Earth Sciences 39, 639–663. https://doi.org/10/cvx6mt

Zajac, I.S., 1974. The stratigraphy and mineralogy of the Sokoman Formation in the Knob Lake area, Quebec and Newfoundland. Bulletin of the Geological Survey of Canada 220, 159 p.

2.10 Figures

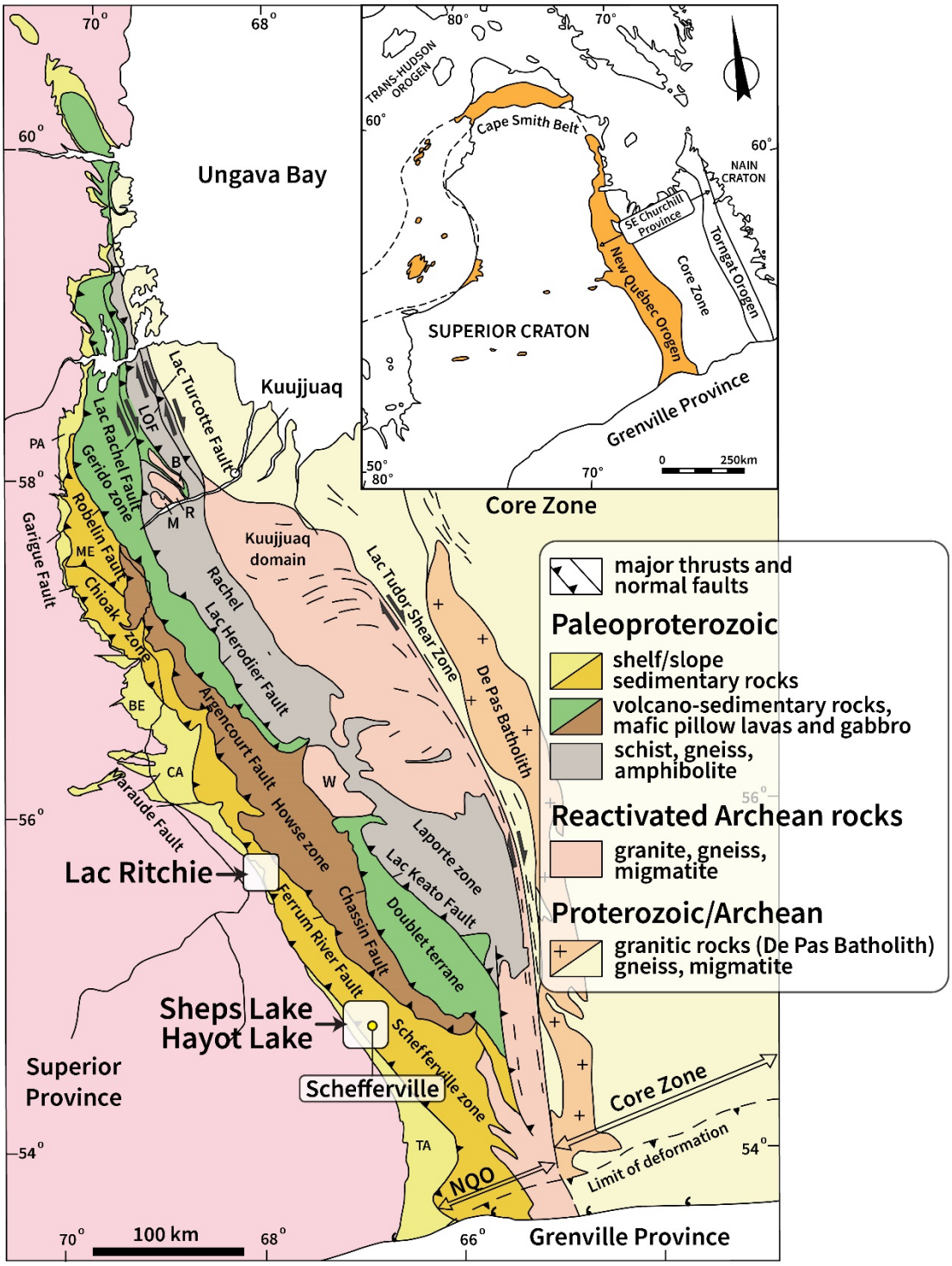

Figure 2.1. Regional geological map of the New Québec Orogen outlining major features and lithotectonic zones (modified from Konstantinovskaya et al., 2019). The evaluated localities are bounded by the black boxes.

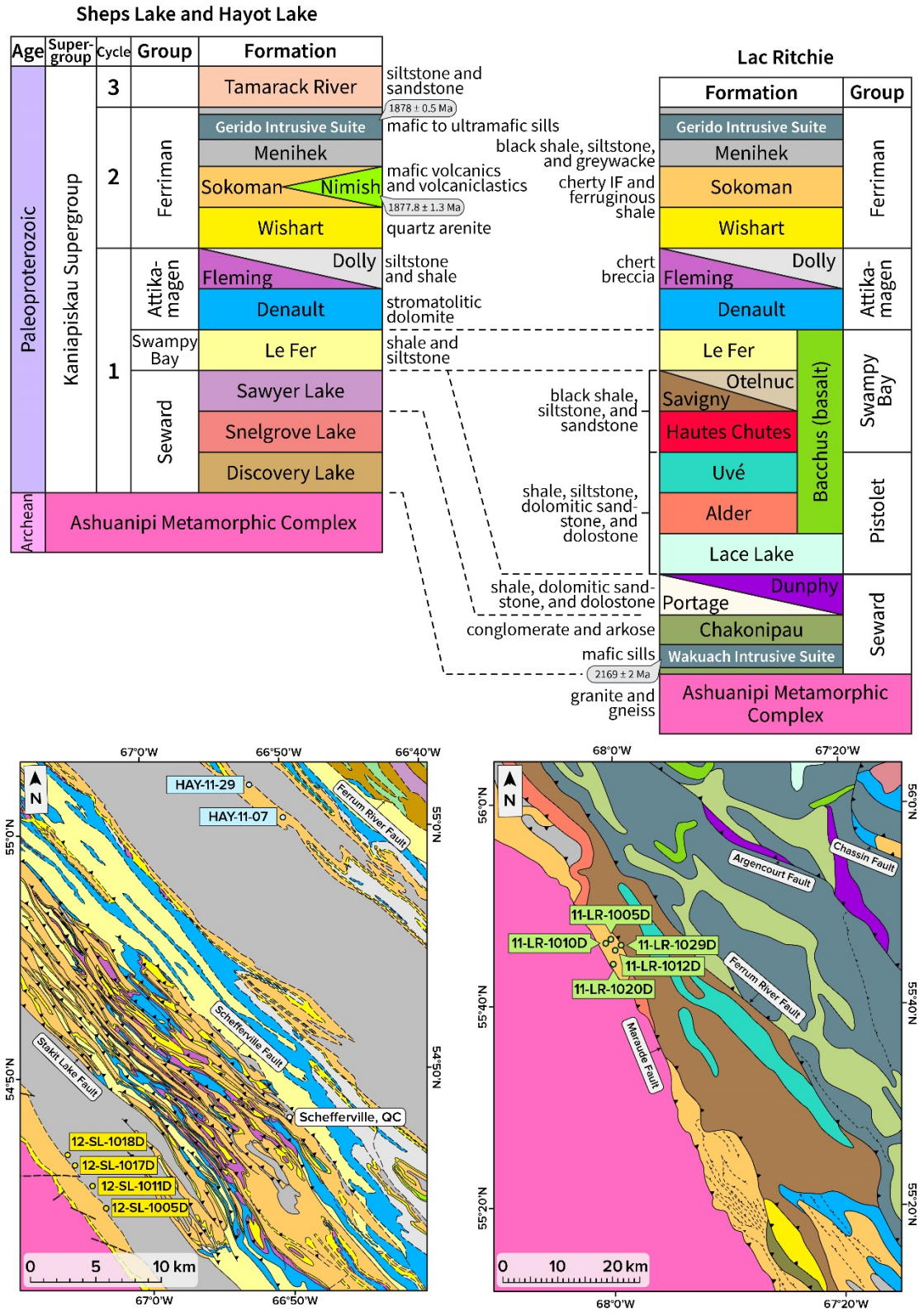

Figure 2.2. Simplified stratigraphy and geological maps of the evaluated localities indicating the location of sampled drillholes. Maps are modified from Wardle (1982a, 1982b) and the SIGÉOM (Système d'information géominière du Québec) database. http://sigeom.mines.gouv.qc.ca)

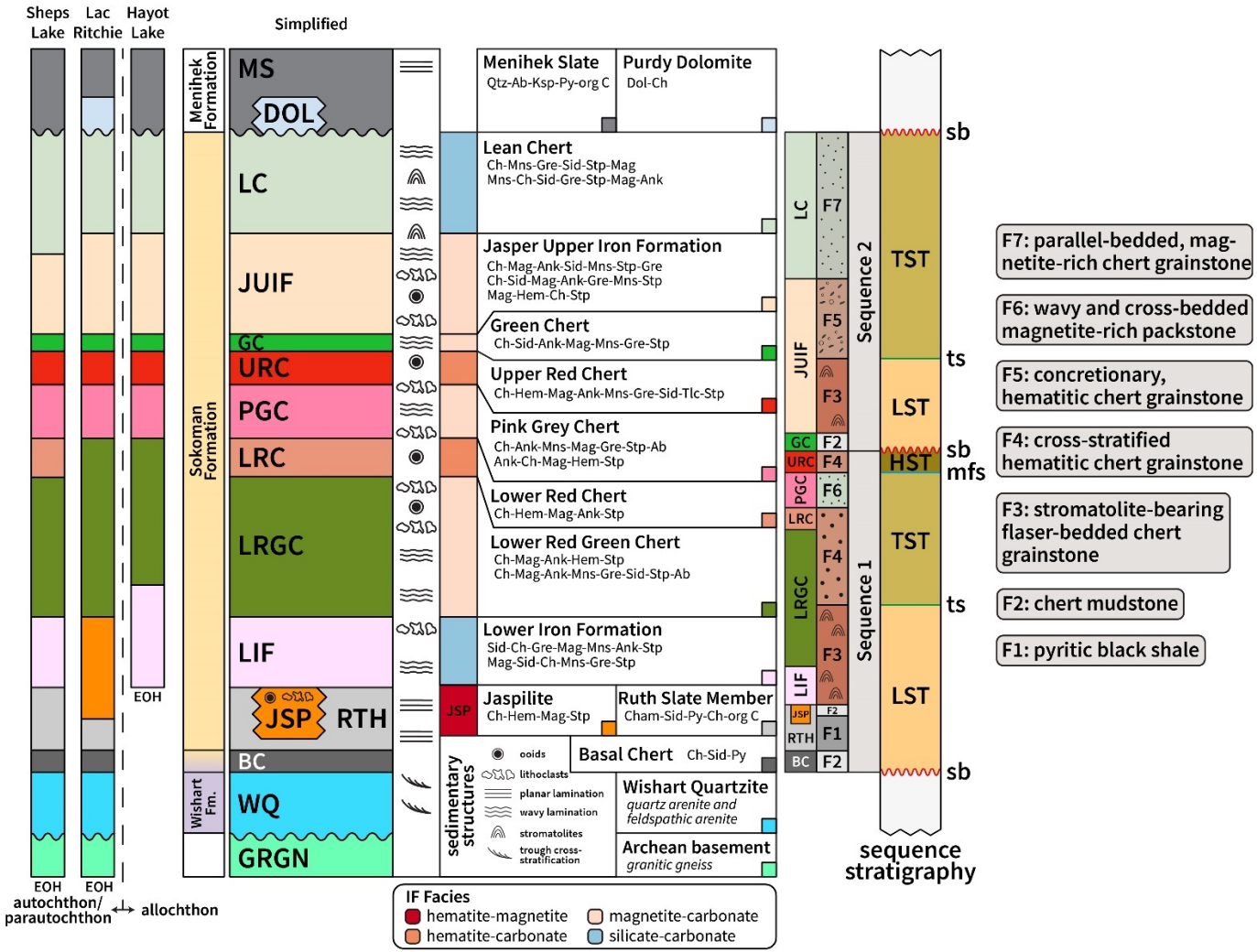

Figure 2.3. Simplified stratigraphy of the Sokoman Iron Formation with common mineral assemblages and sedimentary features. The mineralogical facies classification is modified from Klein and Fink (1976) to include the hematite-magnetite facies and exclude the silicate-sulfide facies. The outlined IF units are correlated with lithofacies defined by sequence stratigraphy (Pufahl et al., 2014). LST = lowstand systems tract; TST = transgressive systems tract; HST = highstand systems tract; sb = sequence boundary; ts = transgressive surface; mfs = maximum flooding surface

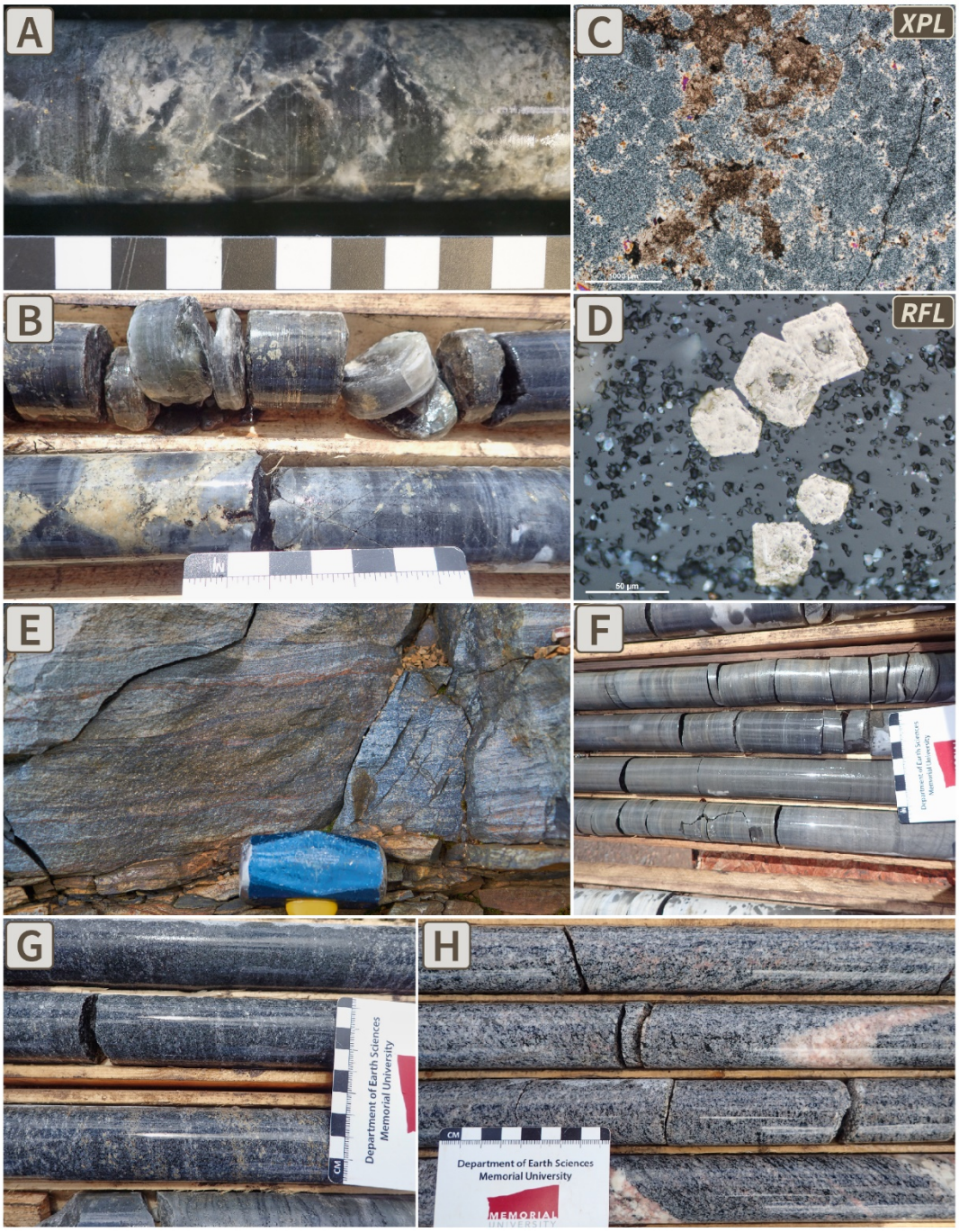

Figure 2.4. Drillcore and outcrop photos and photomicrographs of the Basal Chert member (BC), Wishart Formation (WQ), and Archean basement (GRGN). (A–B) Brecciated to conglomeratic massive black chert of the BC; (C) Photomicrographs of the BC showing microcrystalline chert granules cemented by drusy to blocky mesocrystalline quartz with subordinate siderite granules and rare siderite rims; (D) Disseminated pyrite grains present in the BC; (E–F) Typical quartzite of the Wishart Formation characterized by well-bedded, fine- to medium-grained sandstone (quartz arenite) with thin silty interbeds; (G) Coarse-grained Wishart Formation sandstone with large carbonate grains; (H) Archean basement rocks (tonalitic gneiss and granitic pegmatites) underlying the Sokoman Formation in the Lac Ritchie area.

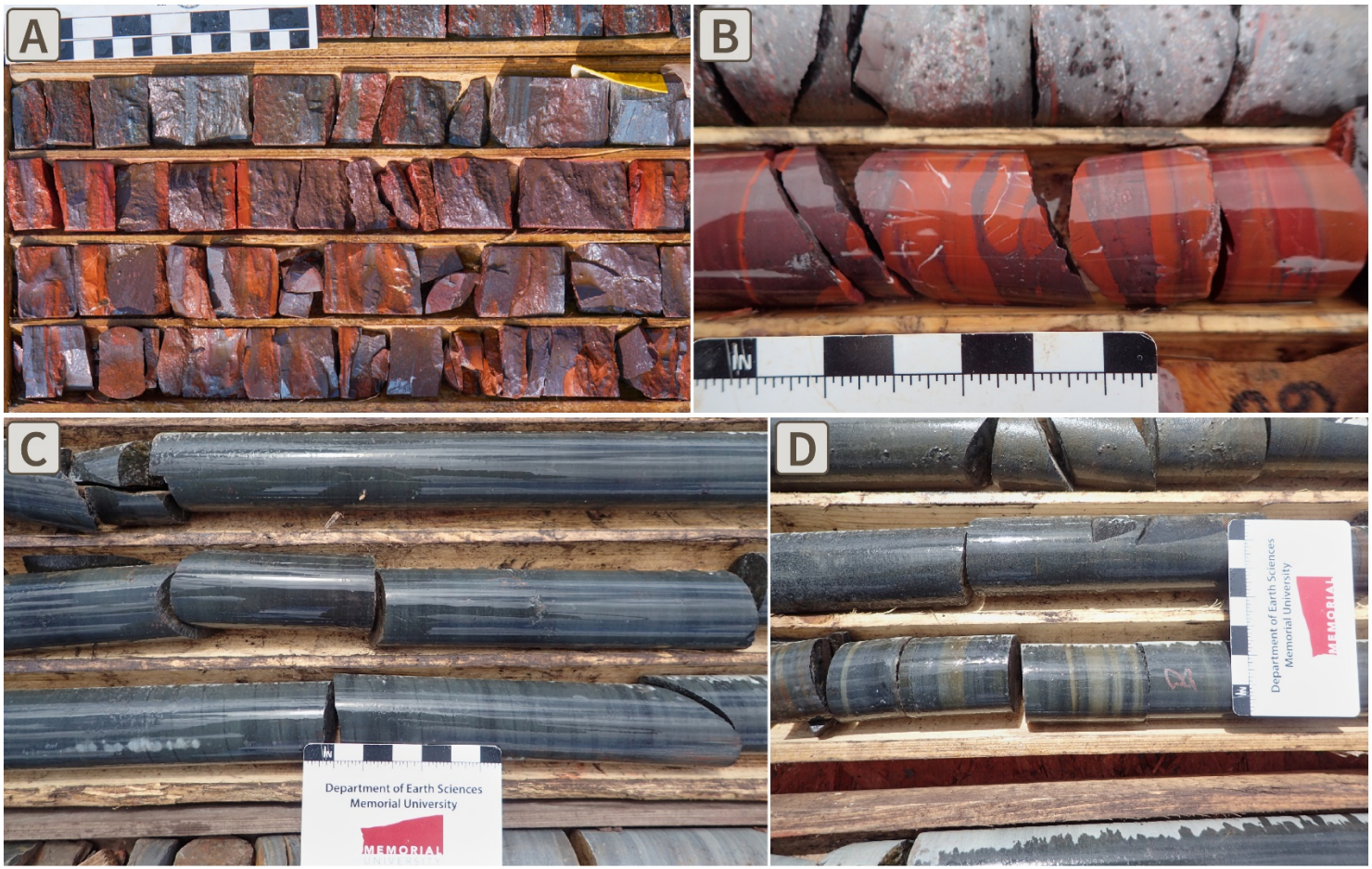

Figure 2.5. Drillcore photos of the Jaspilite (JSP) and the Ruth Slate Member (RTH) of the Sokoman Formation. (A–B) Granular to oolitic jaspilite with subordinate red jasper and grey oxide bands (hematite >> magnetite); (C) Massive grey-green shale and fine-grained siltstone of the Ruth Slate Member; (D) Ruth Slate Member with carbonate interbands.

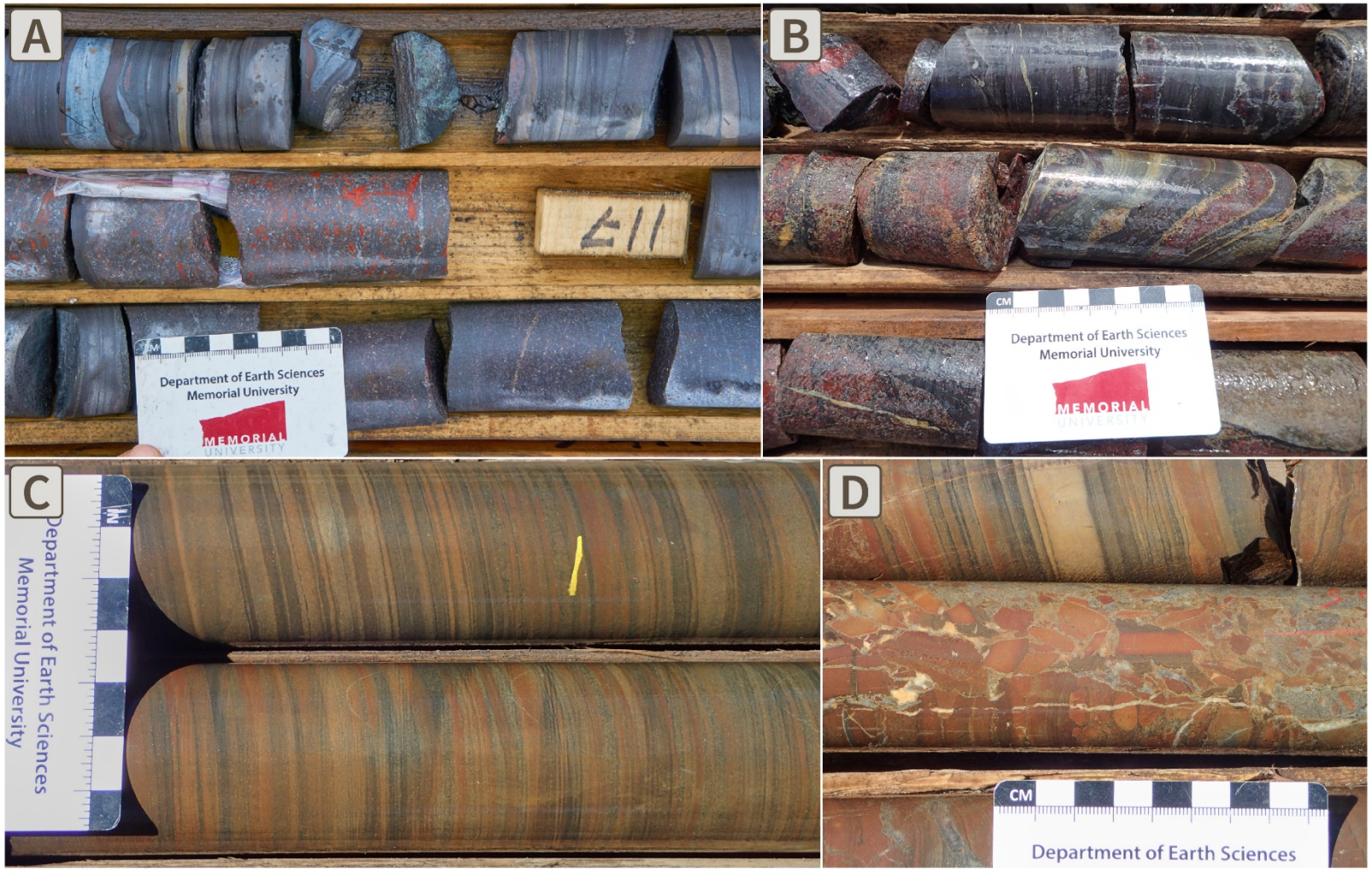

Figure 2.6. Drillcore photos of the Lower Red Green Chert (LRGC) and Lower Iron Formation (LIF) units of the Sokoman Formation. (A) Typical banded to granular IF of the LRGC; (B) Stromatolitic laminations in the LRGC defined mainly by chert and oxide (magnetite > hematite) bands; (C) Typical finely laminated siderite and Fe-silicate rich intervals of the LIF; (D) Brecciated LIF with abundant subangular to angular clasts of Fe-carbonate with a quartz-rich matrix.

Figure 2.7. Drillcore photos of the Pink Grey Chert (PGC) and Lower Red Chert (LRC) units of the Sokoman Formation. (A–B) Typical grey to pinkish granular to oolitic IF of the PGC with abundant cream-coloured late diagenetic ankerite mottles; (C-D) Typical granular to oolitic IF with abundant jasper clasts and less carbonate overprints.

Figure 2.8. Drillcore photos of the Green Chert (GC) and Upper Red Chert (URC) units of the Sokoman Formation. (A–B) Typical grey-green chert of the GC with common siderite and magnetite granules. Late diagenetic ankerite mottles common in some intervals but are not pervasive; (C–D) Typical granular to oolitic IF of the URC with abundant jasper bands and clasts, as well as discontinuous oxide bands.

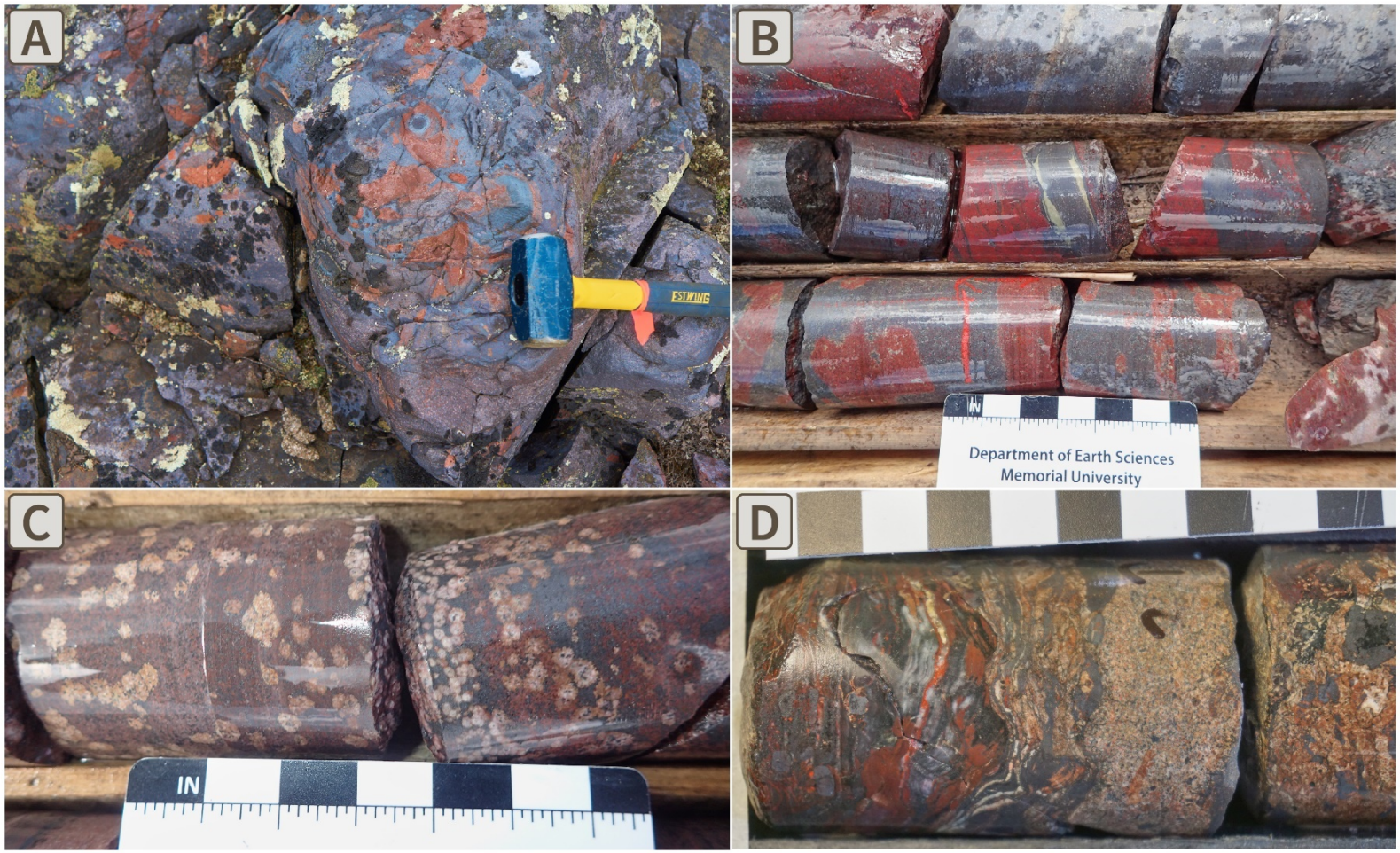

Figure 2.9. Drillcore and outcrop photos of the Jasper Upper Iron Formation (JUIF) unit of the Sokoman Formation. (A–B) Outcrop and drillcore photos of typical JUIF with abundant red jasper clasts and discontinuous grey oxide bands (magnetite > hematite); (C) Pervasive late diagenetic ankerite mottles in JUIF; Stromatolitic laminations in JUIF defined primarily by chert and red jasper bands.

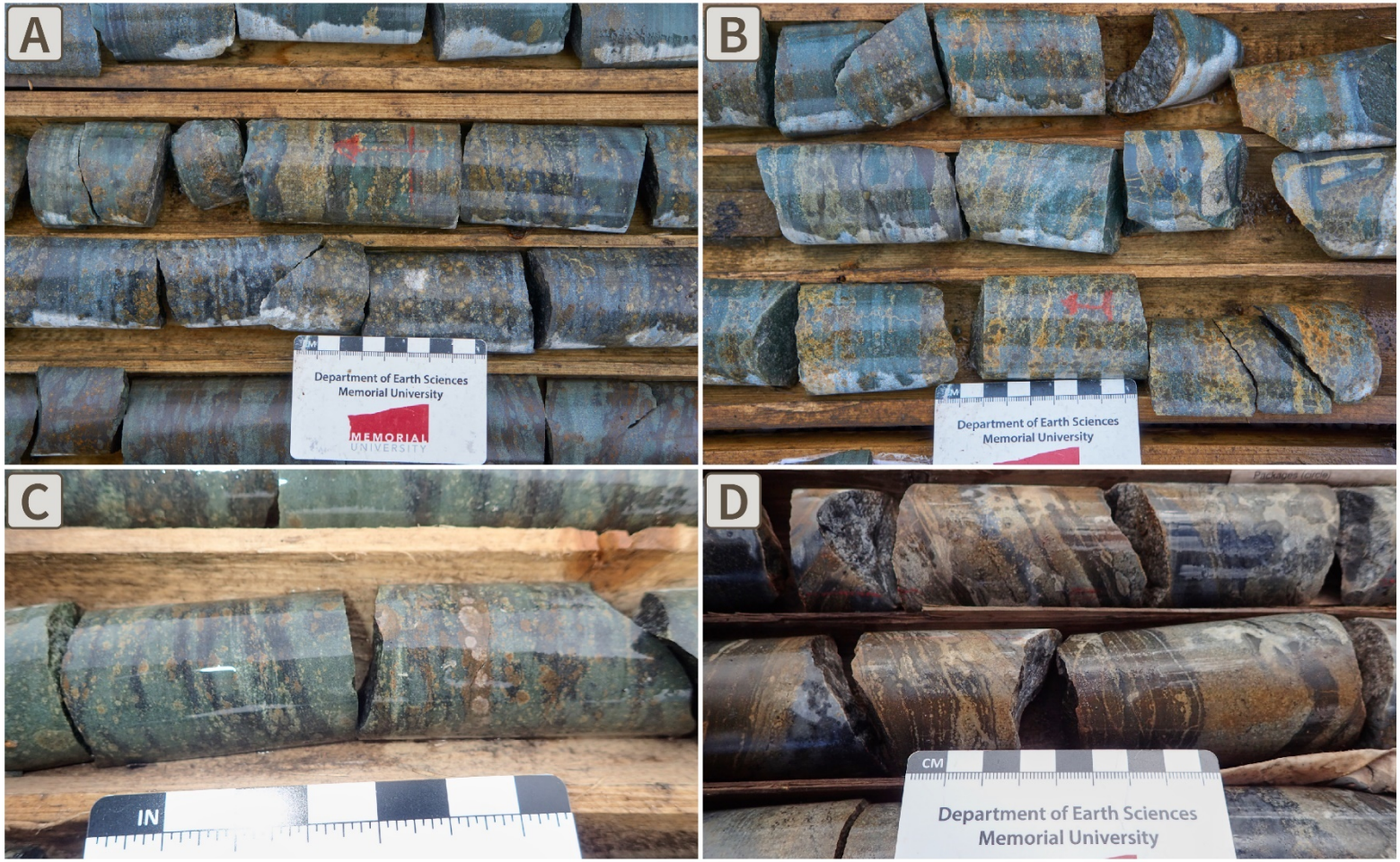

Figure 2.10. Drillcore photos of the Lean Chert (LC) unit of the Sokoman Formation. (A–C) Typical LC characterized by green to clear chert with pervasive yellowish to dark brown minnesotaite-siderite mottles and thin grey magnetite bands; (D) Stromatolitic laminations in the LC defined primarily by Fe-silicates (minnesotaite >> greenalite) and siderite.

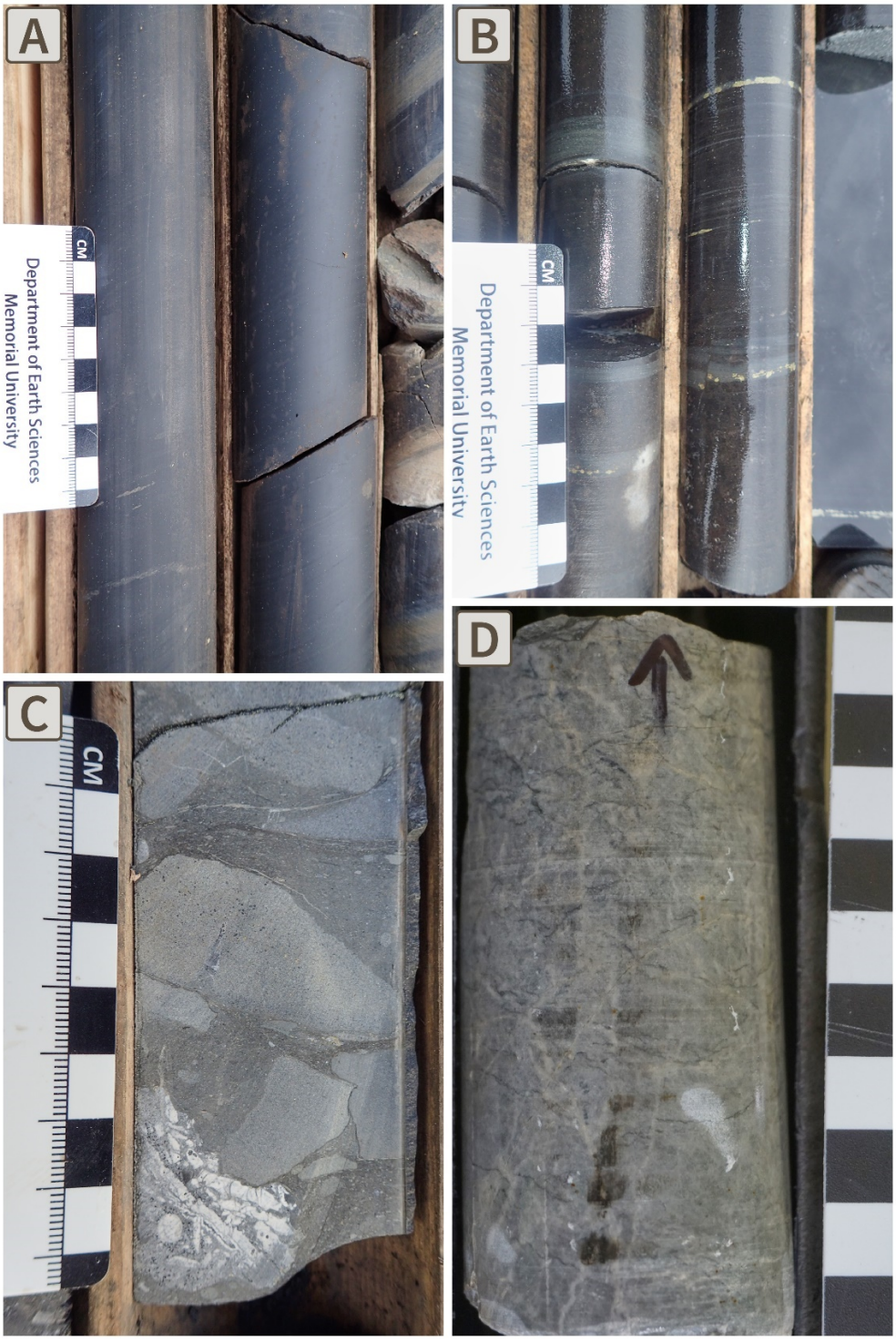

Figure 2.11. Drillcore photos of the Menihek Formation (MS) and the Purdy Dolomite (DOL). (A) Typical finely laminated black shale of the MS; (B) Euhedral pyrite overgrowths in siltstone interbeds of the MS; (C) Poorly sorted, matrix-supported (carbonate-rich sand) conglomerate at the base of the MS; (D) Typical massive cherty dolomite of the Purdy Dolomite with common stylolites.

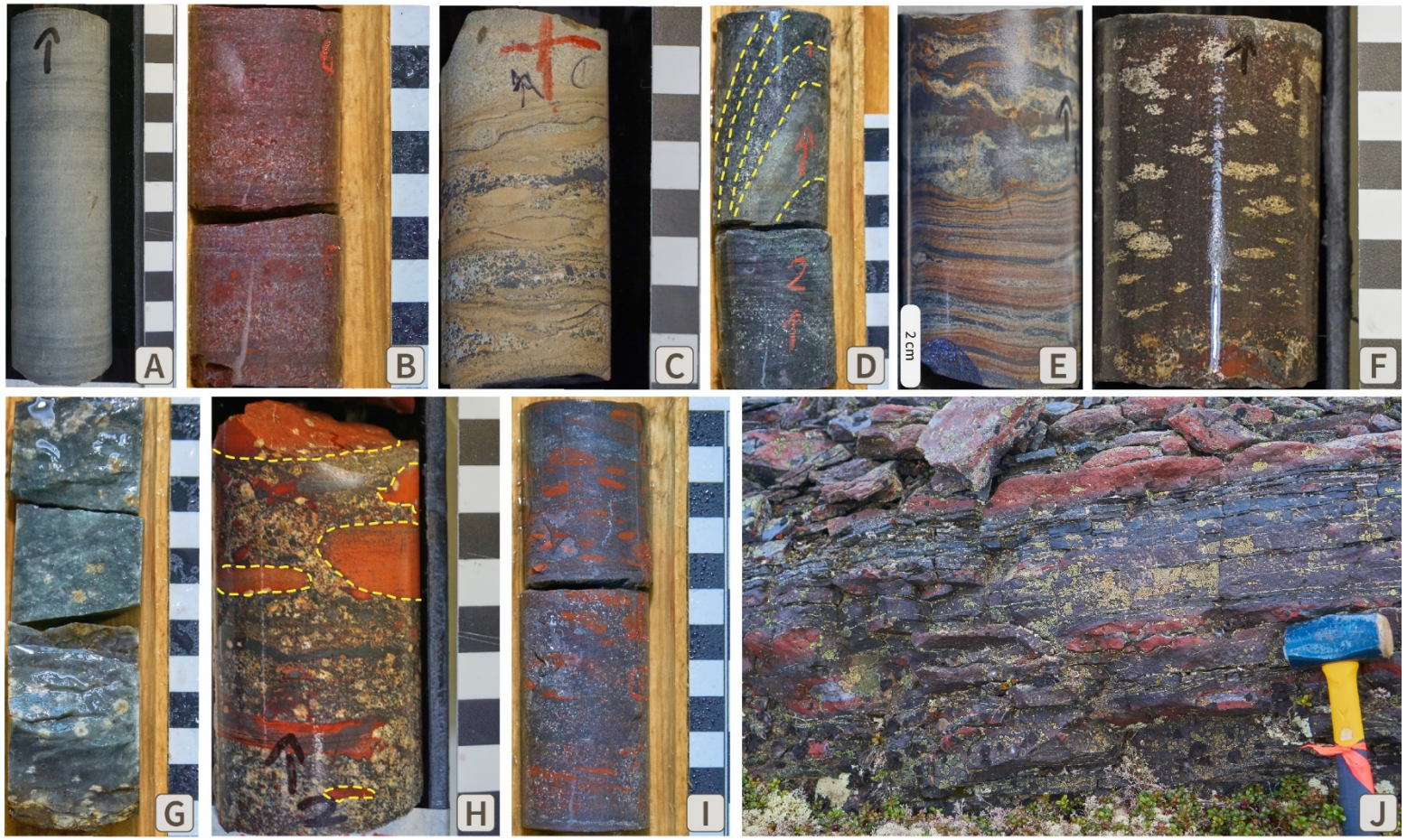

Figure 2.12. Representative samples depicting the various mineralogical facies within the Sokoman IF. (A) silicate-sulfide: RTH; (B) hematite-magnetite: JSP; (C–D) silicate-carbonate: LIF, LC; (E–H) magnetite-carbonate: LRGC, PGC, GC, JUIF; (I–J) hematite-magnetite: URC, LRC. Domal stromatolites in the LC are typically defined by magnetite and chert bands as shown by the yellow dashed lines (D). Examples of intraformational chert subsamples targeted in this study are illustrated by the yellow dashed lines (H).

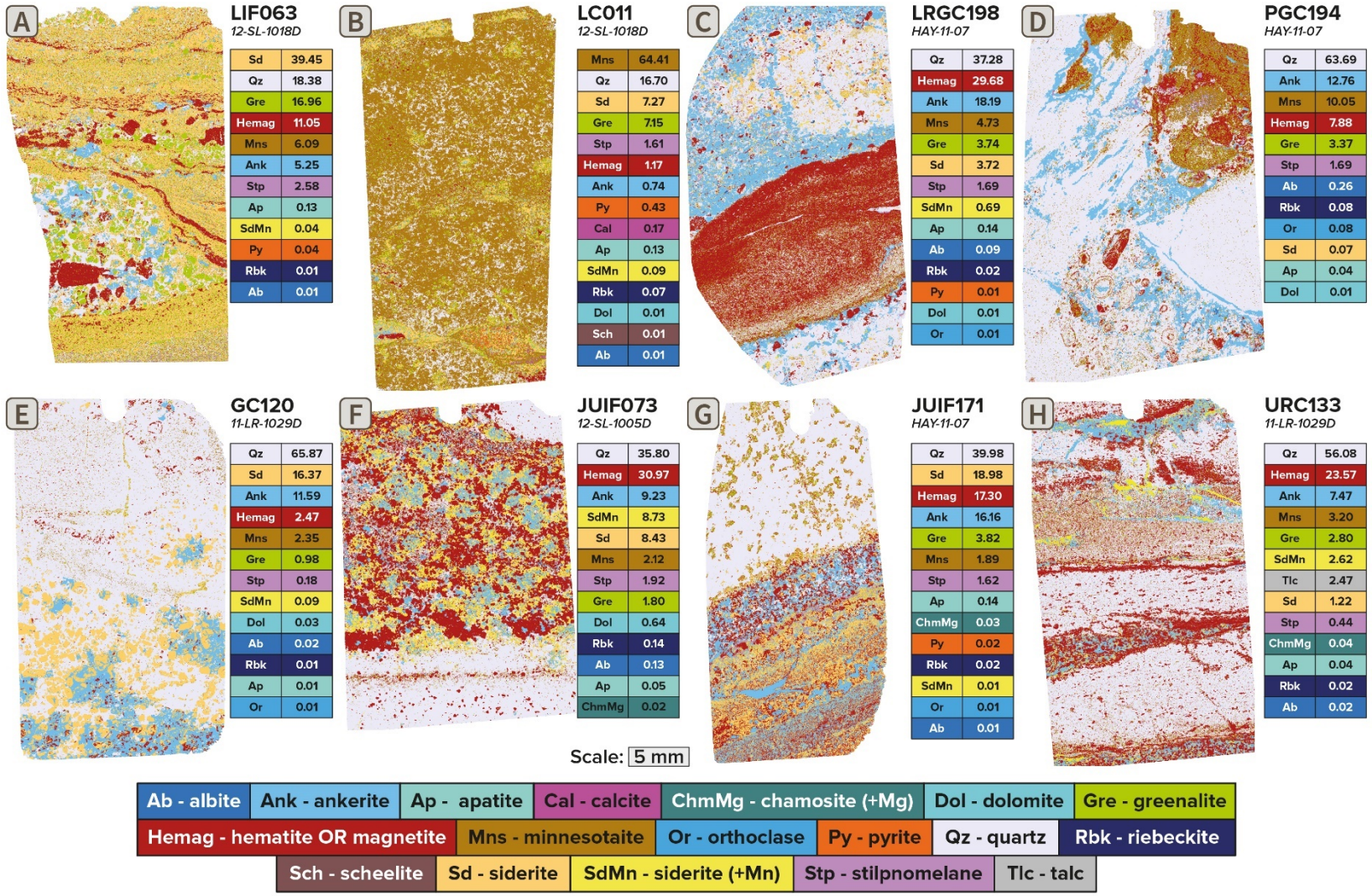

Figure 2.13. False-colour MLA maps of several representative sections of various units in the Sokoman IF. Modal mineralogical distributions (area %) for each section are listed below their respective sample ID and drillhole.

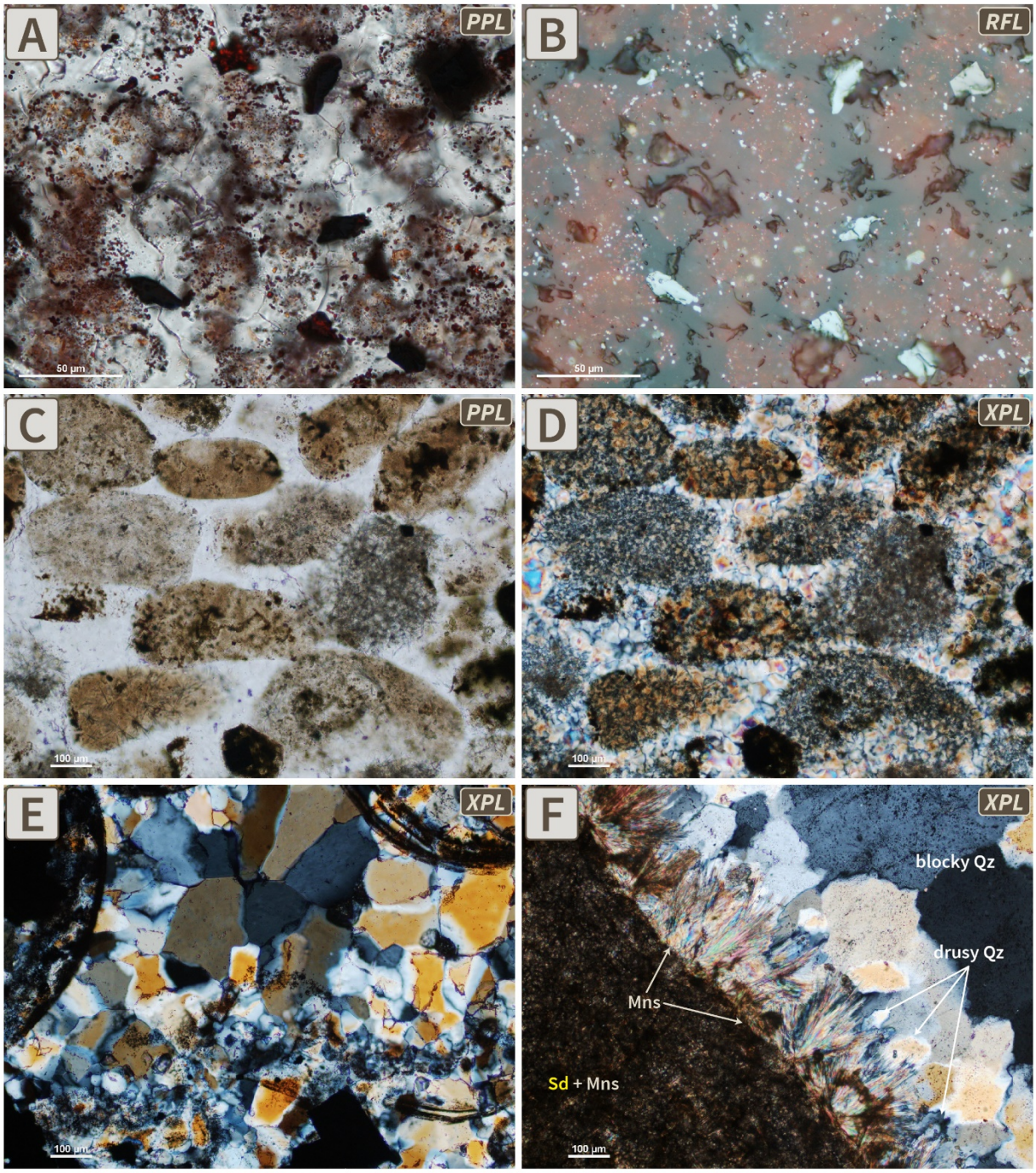

Figure 2.14. Textural characteristics of intraformational chert and intergranular quartz cements. (A–B) Granules of equigranular microcrystalline quartz (<20 µm) interspersed with fine-grained, disseminated, 'dusty' hematite and generally rimmed by anhedral, 'spongy' hematite; (C–D) Loosely compacted granules of 'dusty' microcrystalline chert with greenalite microspheroids and stilpnomelane sheaves cemented by interstitial mosaic chert; (E) Blocky mesocrystalline quartz (<20 µm) cement surrounding relict ooliths; (F) Drusy to blocky mesocrystalline quartz cement surrounding a minnesotaite-rimmed siderite granule. Mns = minnesotaite, Sd = siderite

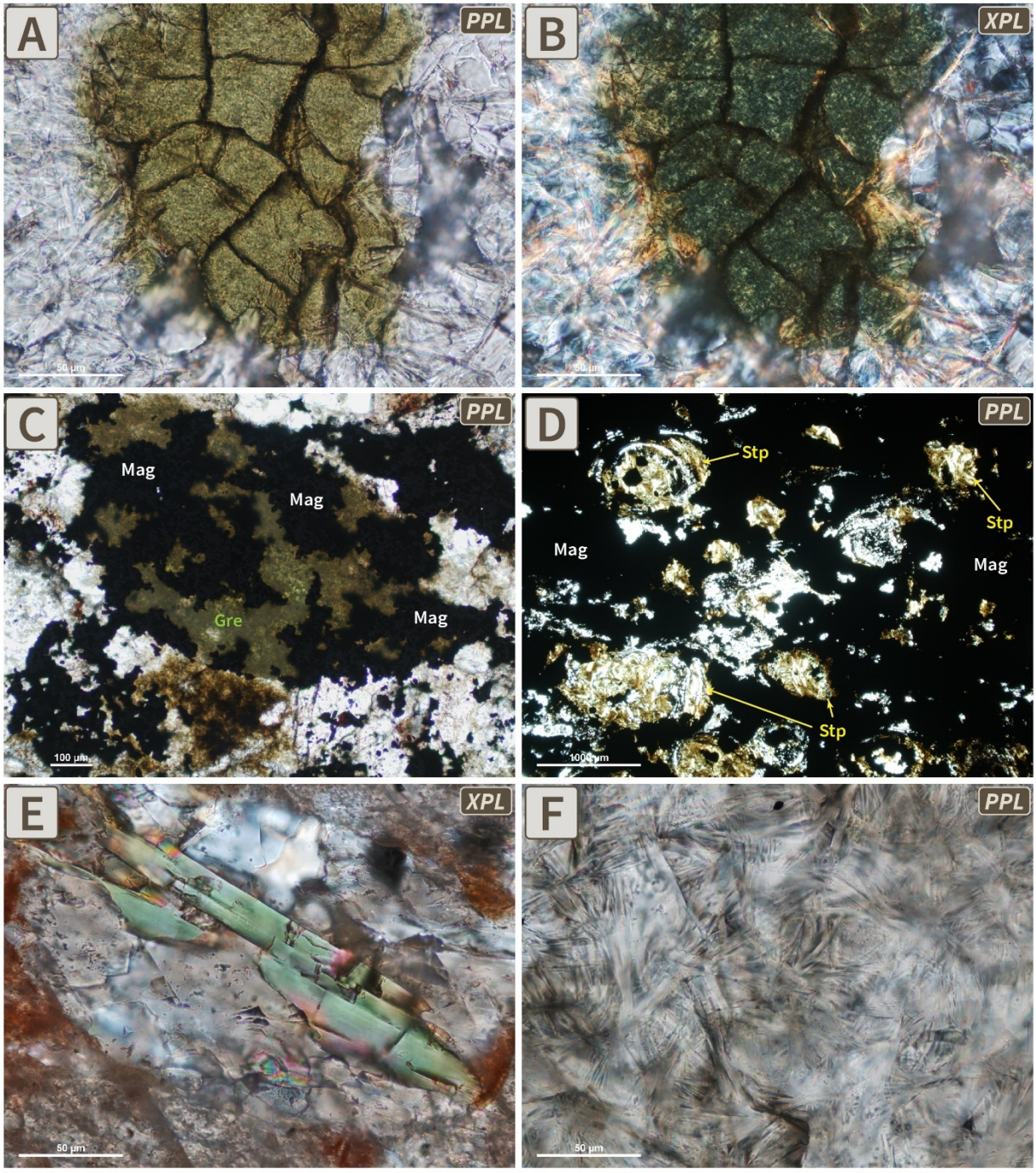

Figure 2.15. Textural characteristics of Fe-silicates. (A–B) Greenalite granule with shrinkage cracks in a minnesotaite-rich matrix; (C) Magnetite euhedra replacing greenalite; (D) Stilpnomelane granules rimmed by coarse-grained magnetite euhedra; (E) Individual stilpnomelane plate showing third-fourth order birefringence; (F) radial 'bowtie' aggregates of minnesotaite. Gre = greenalite, Mag = magnetite, Stp = stilpnomelane

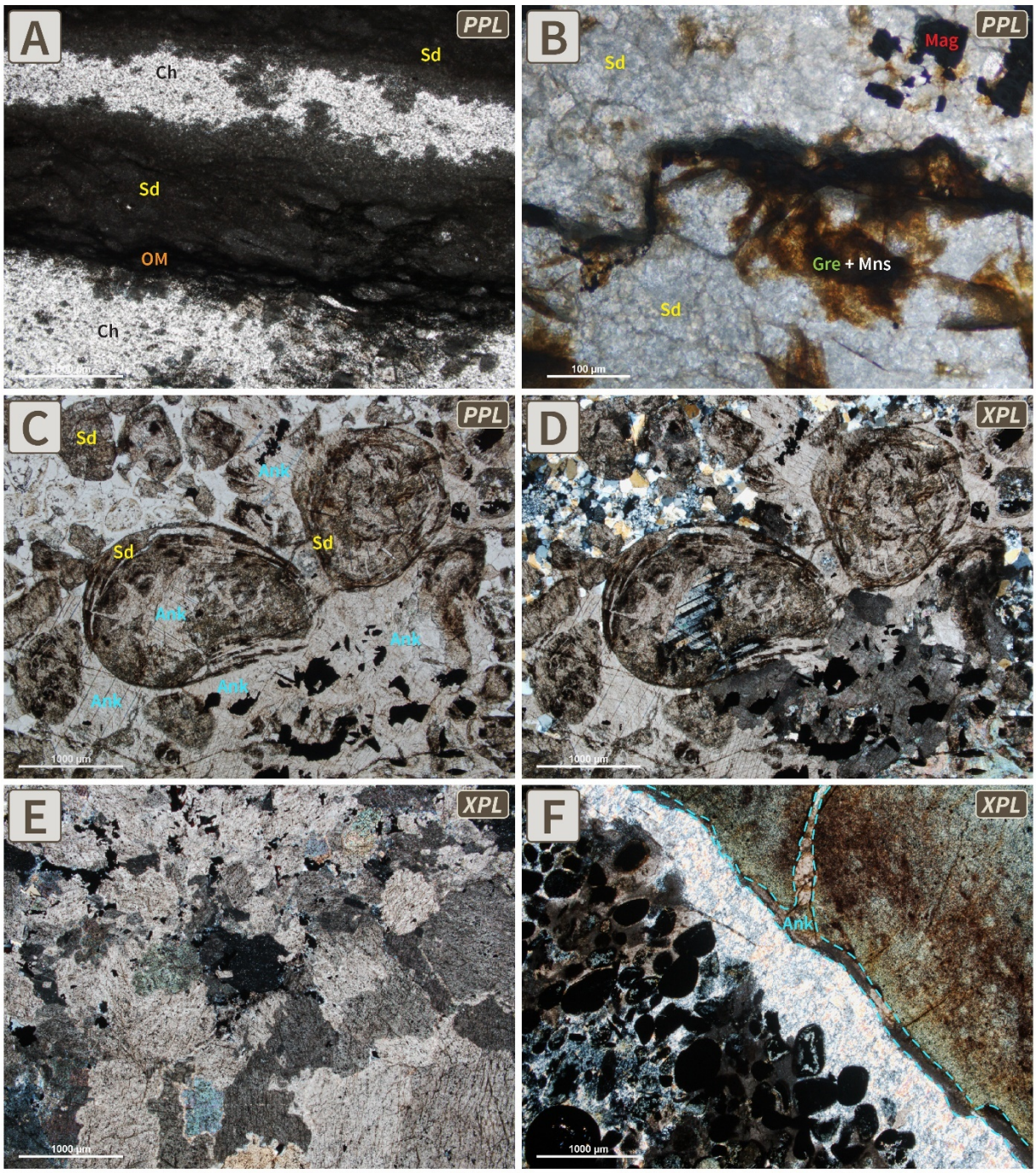

Figure 2.16. Textural characteristics of carbonates. (A) Alternating bands of chert and siderite interspersed with carbonaceous material; (B) Stylolite seam cutting across band of microgranular siderite with common greenalite-minnesotaite sheaves and disseminated magnetite grains; (C–D) Coarse siderite granules cemented by drusy to blocky mesocrystalline quartz and overprinted by coarse-grained ankerite; (E) Mottled, coarse-grained ankerite overprints typically seen in the PGC; (F) Overgrowth rim of poorly crystalline ankerite around a chert fragment. Ch = chert; Sd = siderite; OM = organic matter; Ank = ankerite

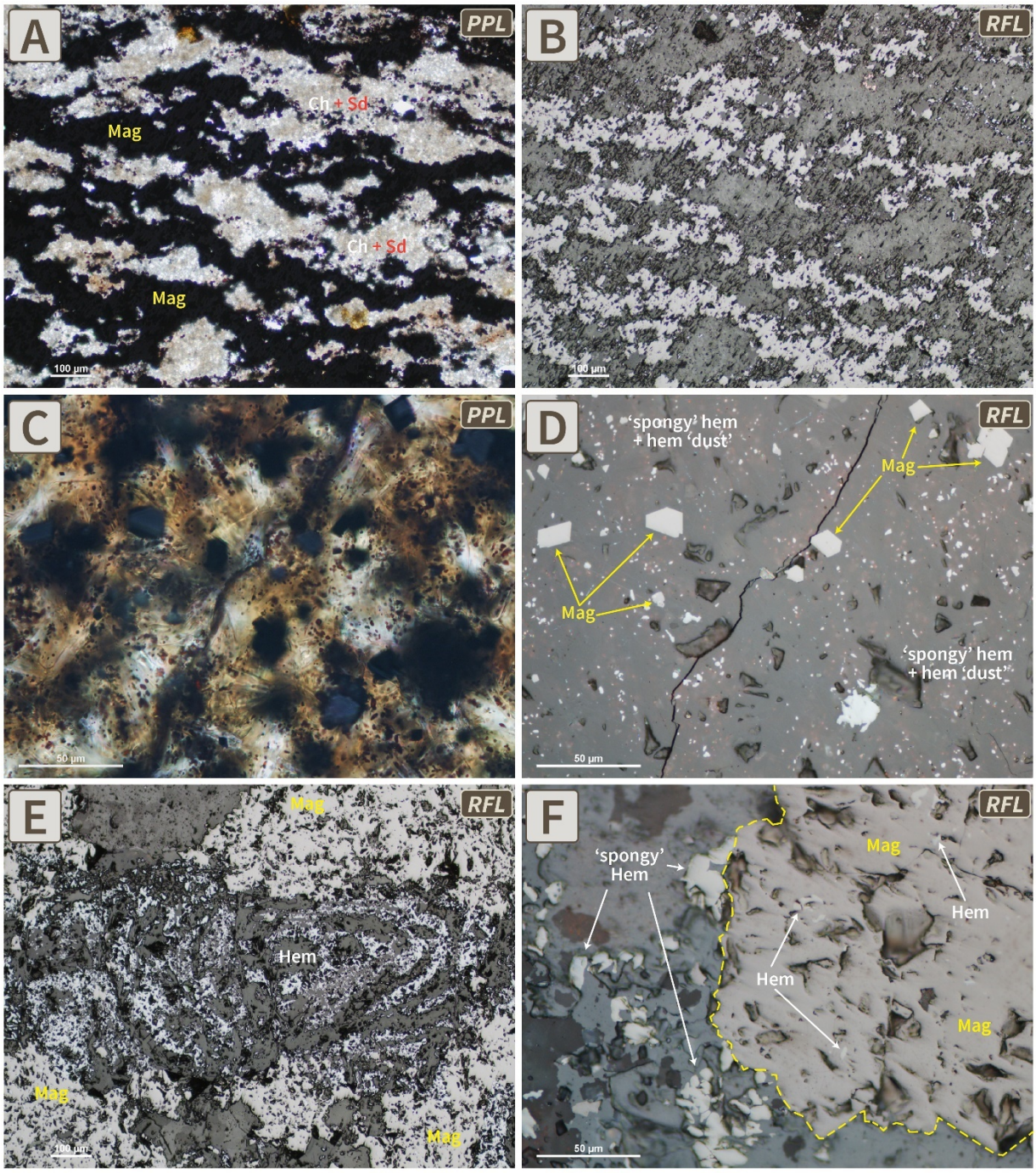

Figure 2.17. Textural characteristics of Fe-oxides. (A–B) Magnetite-siderite-chert laminae oriented parallel to sedimentary bedding; (C–D) Disseminated magnetite and aggregates of 'spongy' hematite and hematite 'dust' within stilpnomelane granule. Note that the Fe-oxides do not show any preferential alignment with respect to the fracture cutting across in the middle; (E) Compacted chert-hematite oolith rimmed by subhedral magnetite octahedra. Note that the cortices are primarily made up of 'spongy' and microplaty hematite aggregates; (F) 'Spongy' hematite inclusions within coarse-grained magnetite grain. Hem = hematite; Mag = magnetite

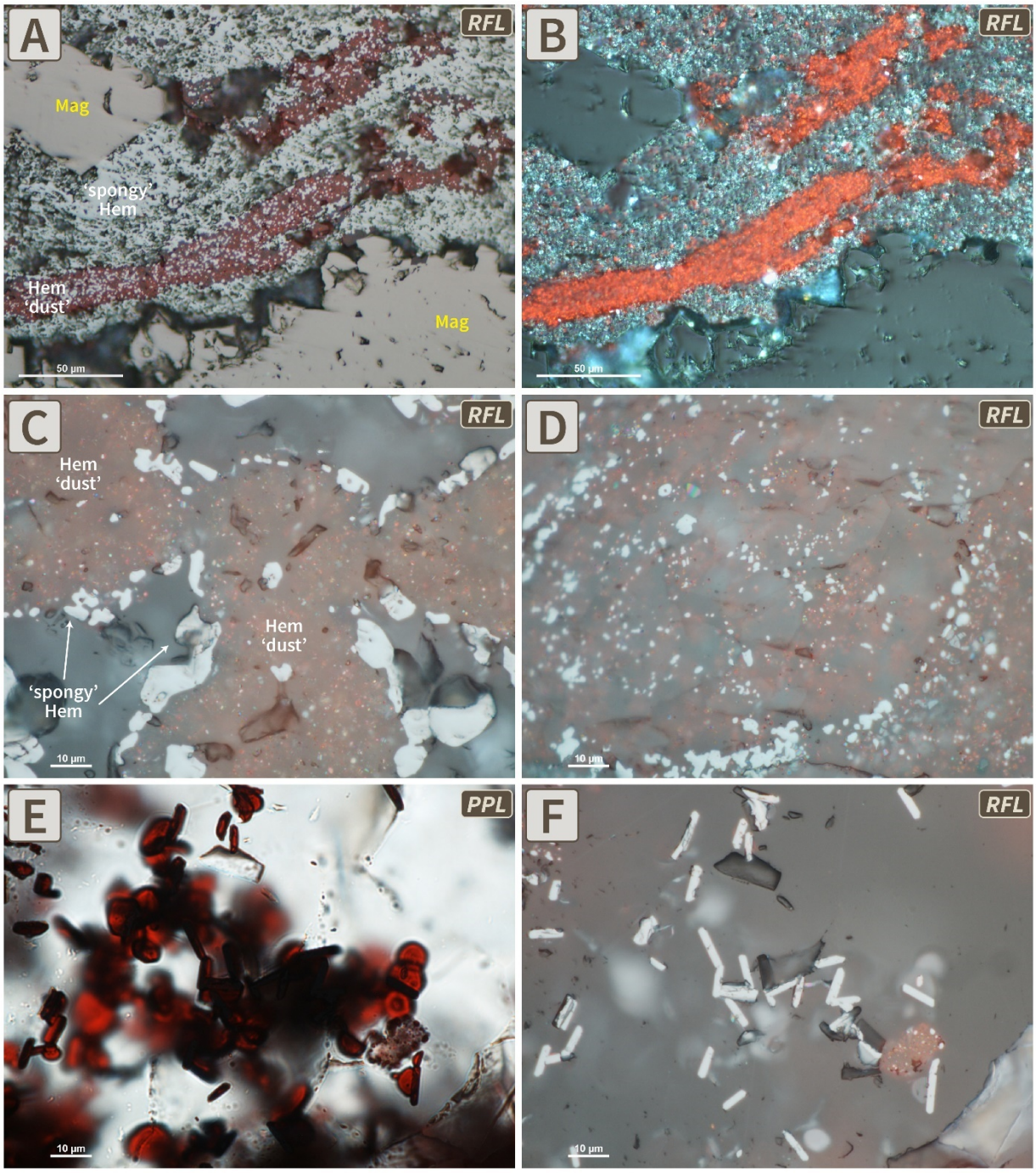

Figure 2.18. Textural characteristics of Fe-oxides. (A–B) Hematite 'dust' and 'spongy' hematite laminae wrapping around magnetite peloids. Note that these peloids do not contain hematite inclusions; (C) Rims of 'spongy' hematite surrounding jasper granules; (D) Oolith core with prevalent hematite 'dust' and cortices with predominantly 'spongy' hematite; (E–F) Microplaty hematite aggregates within chert matrix. Hem = hematite, Mag = magnetite

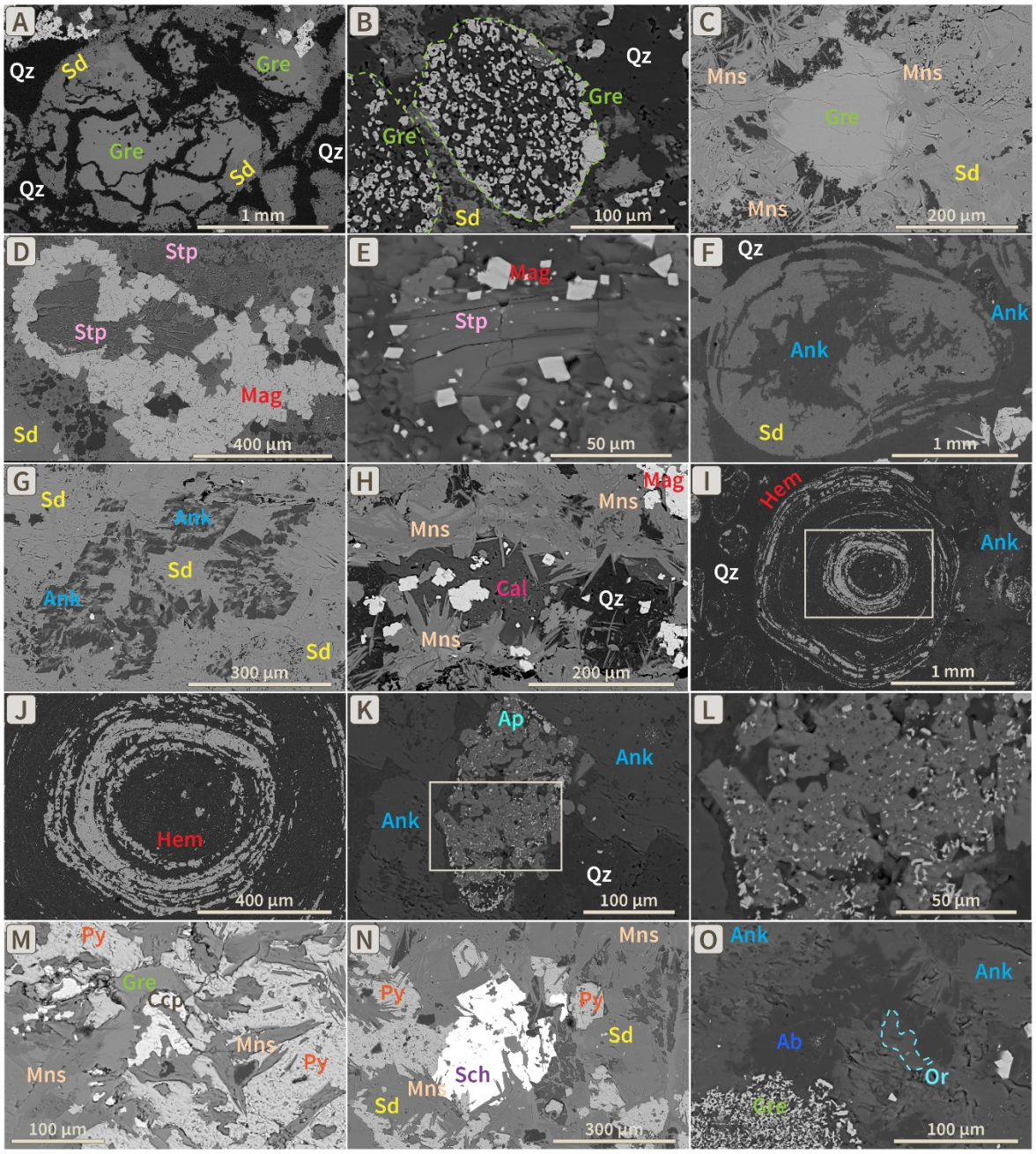

Figure 2.19. BSE images of common mineralogical textures in the Sokoman IF. (A–C) Greenalite granules are cemented by drusy to blocky mesocrystalline quartz and often replaced by siderite and minnesotaite. These commonly exhibit shrinkage cracks (A) and sieve-like textures (B); (D–E) Stilpnomelane occurrences replaced by magnetite octahedra; (F–G) Siderite occurrences replaced by late diagenetic ankerite rhombs; (H) Early diagenetic calcite crosscut by siderite and minnesotaite; (I–J) Microplaty hematite aggregates within ooidal cortices that envelop a chert-rich, 'dusty hematite' core; (K–L) Prismatic apatite aggregates with sieve-like textures after greenalite; (M–N) Subhedral to euhedral pyrite, chalcopyrite, and scheelite grains within a siderite-minnesotaite-rich stylolite seam; (O) Authigenic albite and orthoclase in an ankerite-rich matrix.

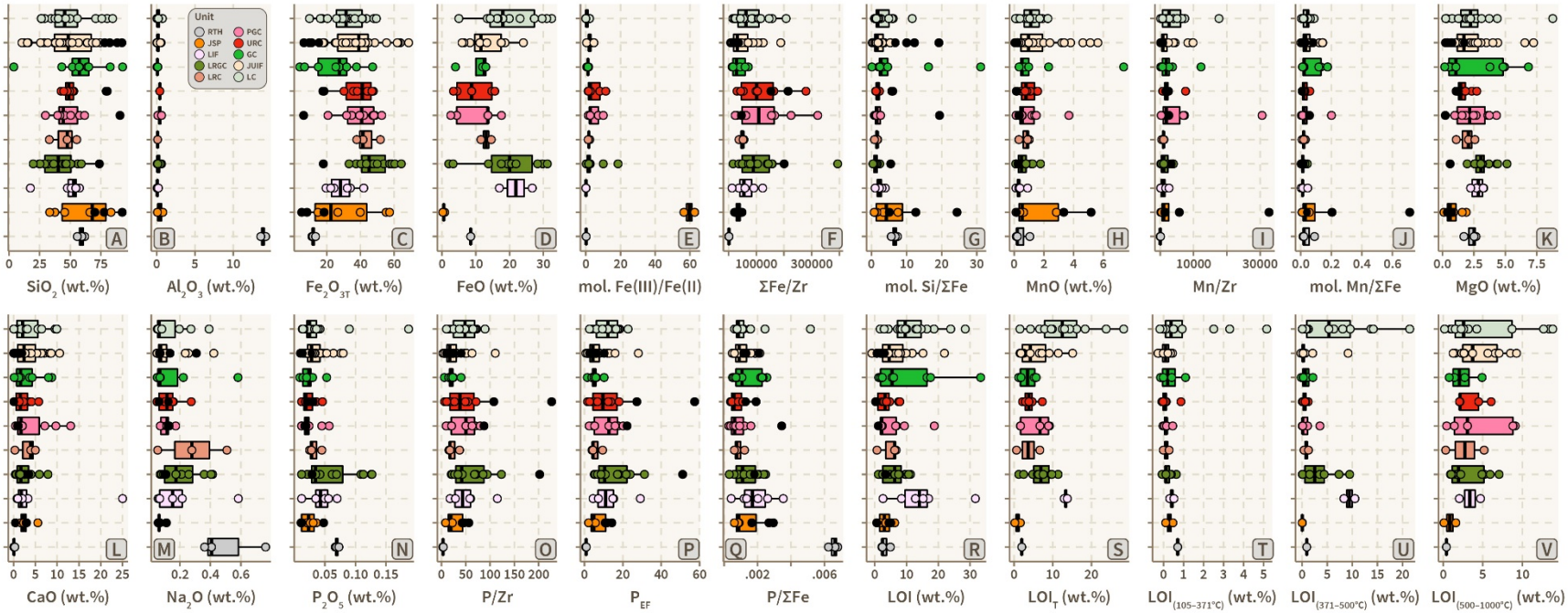

Figure 2.20. Unit-specific boxplots of major element abundances, major element ratios, and sequential 4-step LOI.

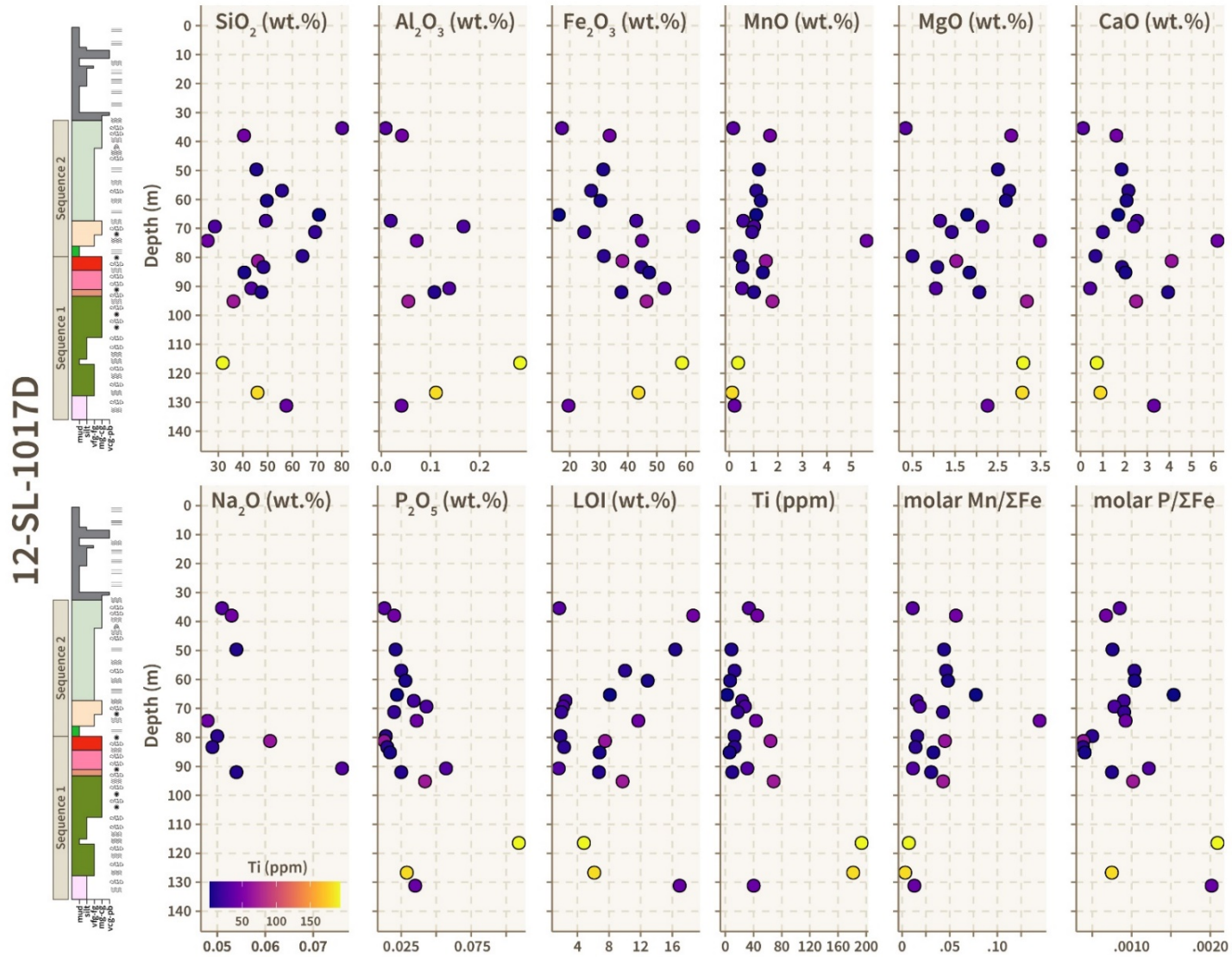

Figure 2.21. Chemostratigraphic variations in major element data and LOI in drillhole 12-SL-1017D. Note that the colour of the dots corresponds to Ti (ppm) concentrations. The range in Ti (ppm) concentrations vary across the evaluated drill holes.

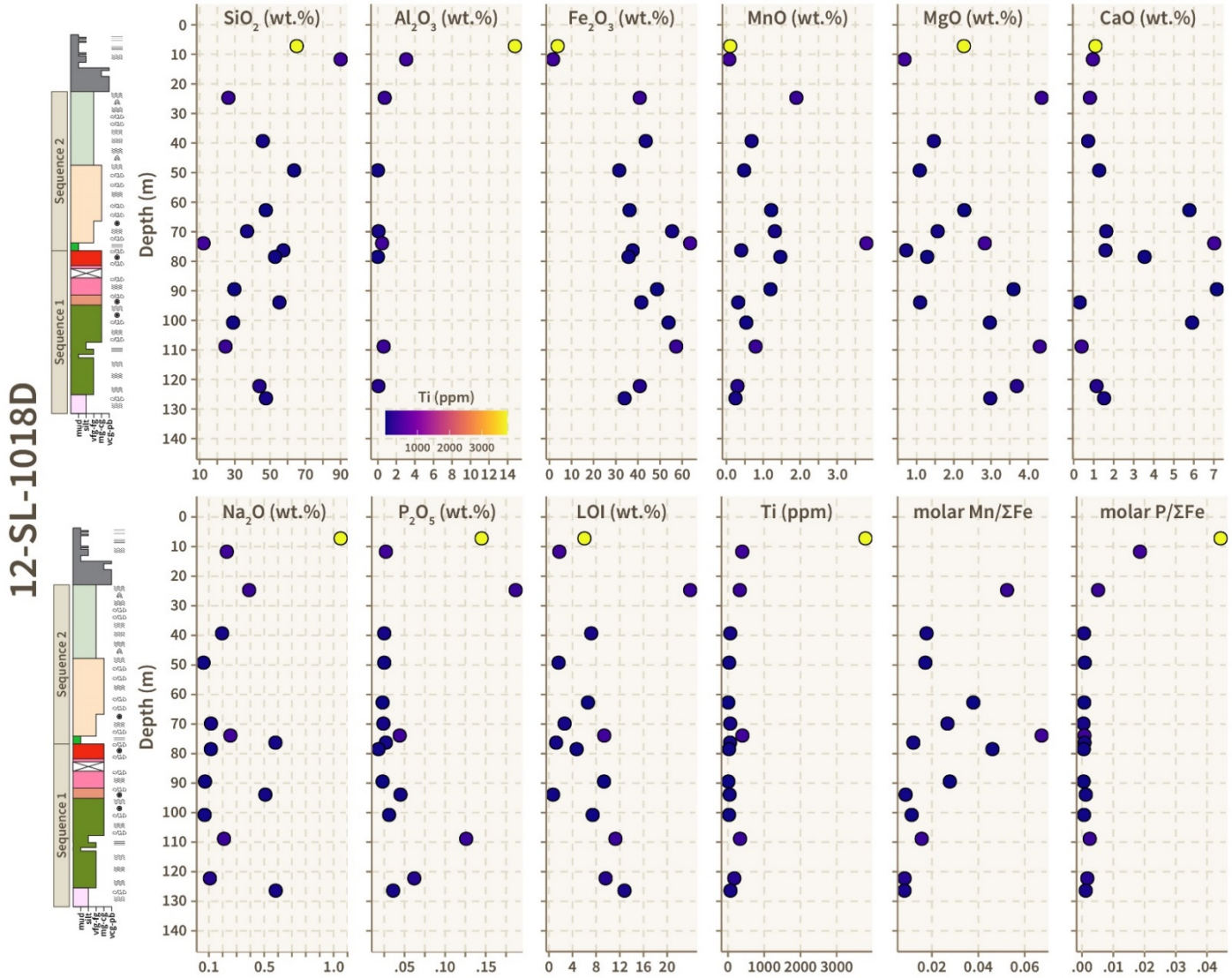

Figure 2.22. Chemostratigraphic variations in major element data and LOI in drillhole 12-SL-1018D. Note that the colour of the dots corresponds to Ti (ppm) concentrations. The range in Ti (ppm) concentrations vary across the evaluated drill holes.

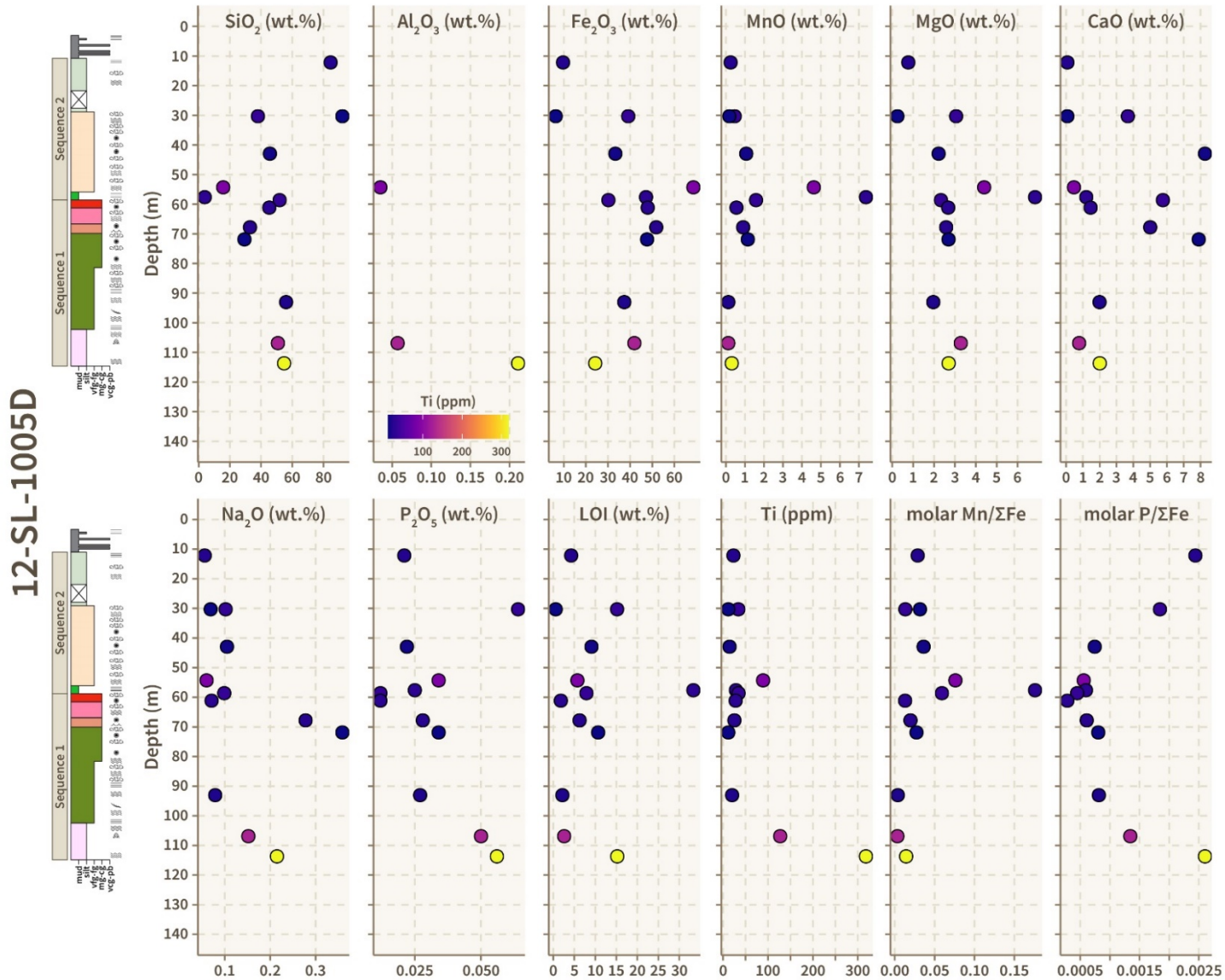

Figure 2.23. Chemostratigraphic variations in major element data and LOI in drillhole 12-SL-1005D. Note that the colour of the dots corresponds to Ti (ppm) concentrations. The range in Ti (ppm) concentrations vary across the evaluated drill holes.

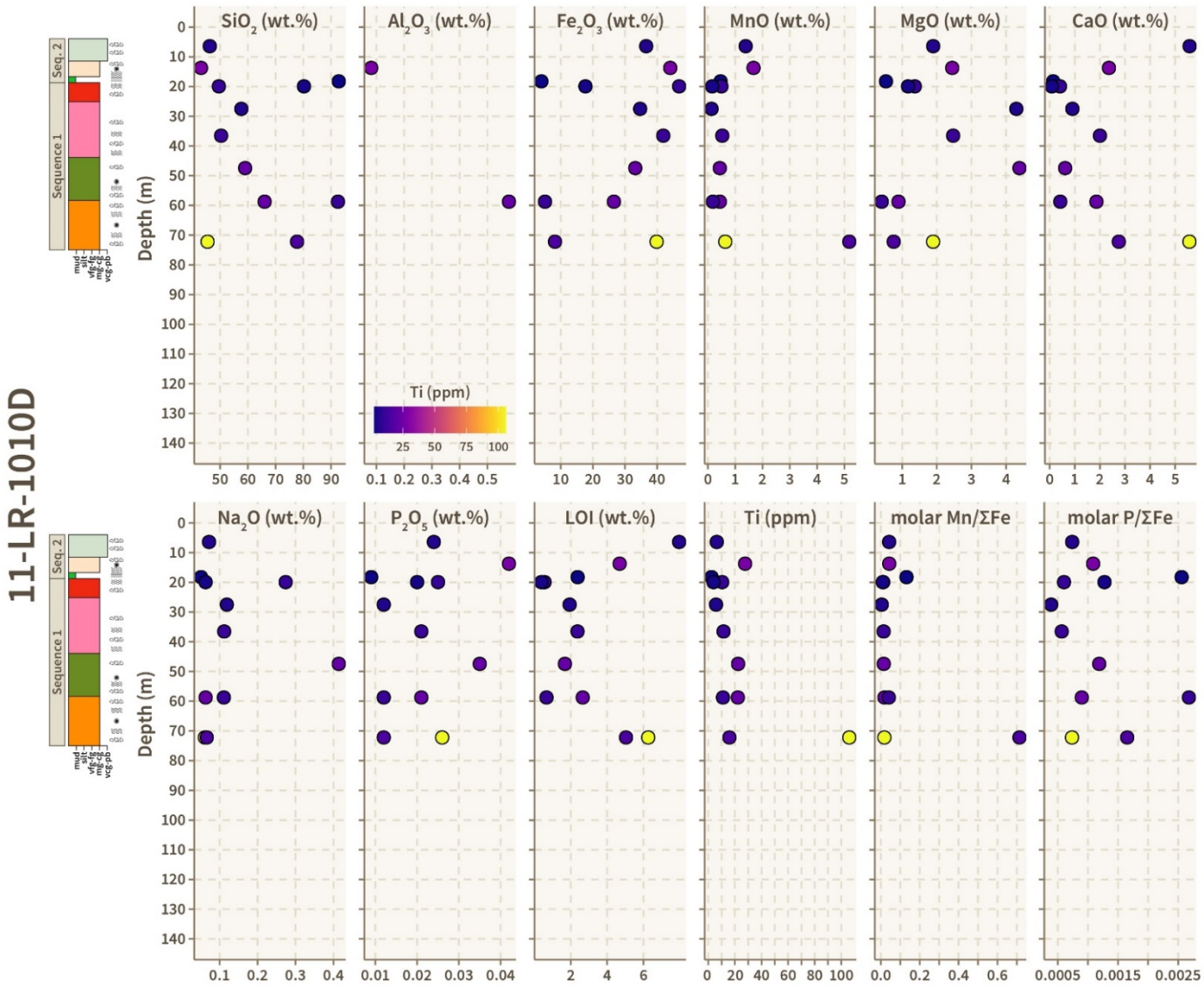

Figure 2.24. Chemostratigraphic variations in major element data and LOI in drillhole 11-LR-1010D. Note that the colour of the dots corresponds to Ti (ppm) concentrations. The range in Ti (ppm) concentrations vary across the evaluated drill holes.

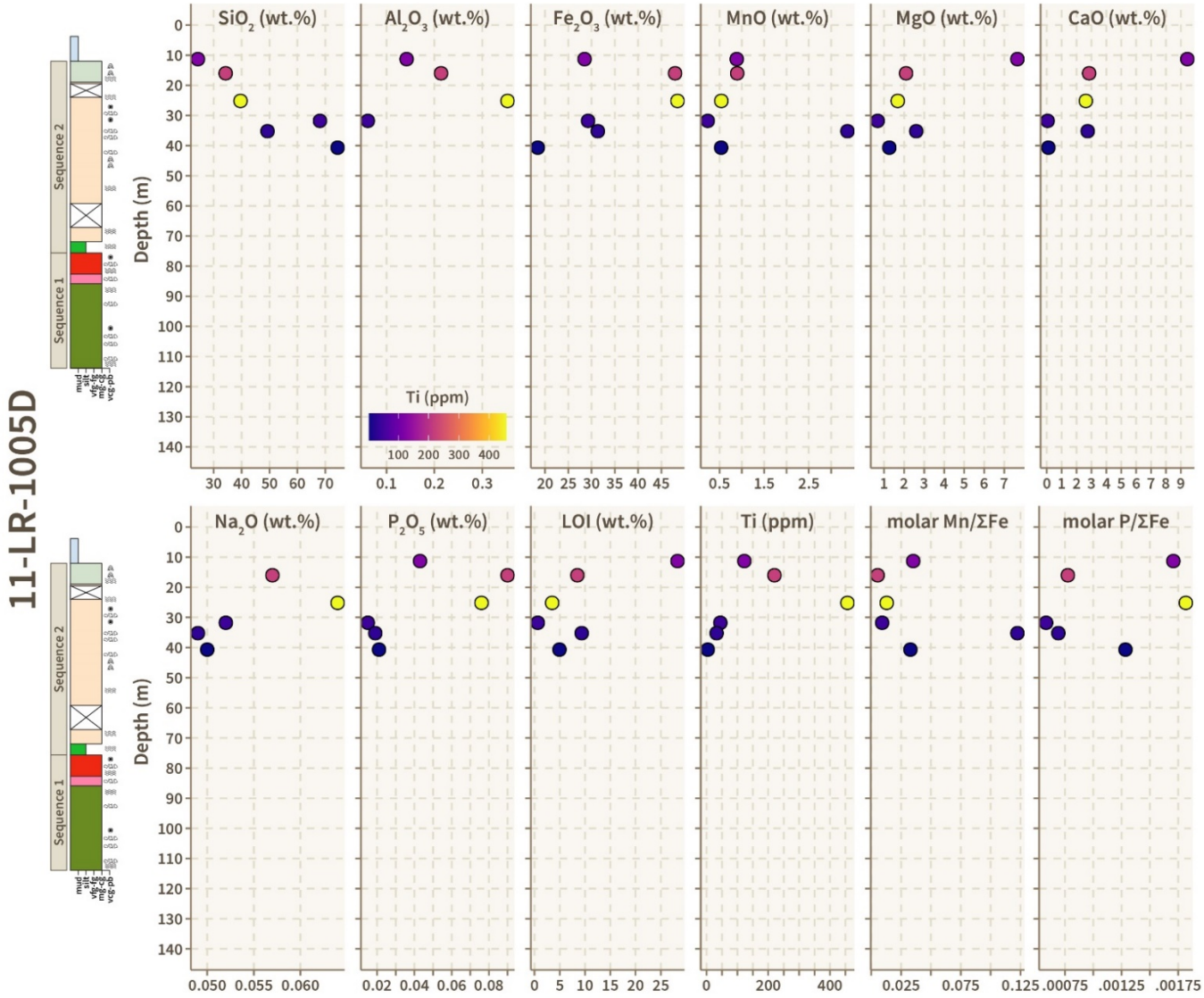

Figure 2.25. Chemostratigraphic variations in major element data and LOI in drillhole 11-LR-1005D. Note that the colour of the dots corresponds to Ti (ppm) concentrations. The range in Ti (ppm) concentrations vary across the evaluated drill holes.

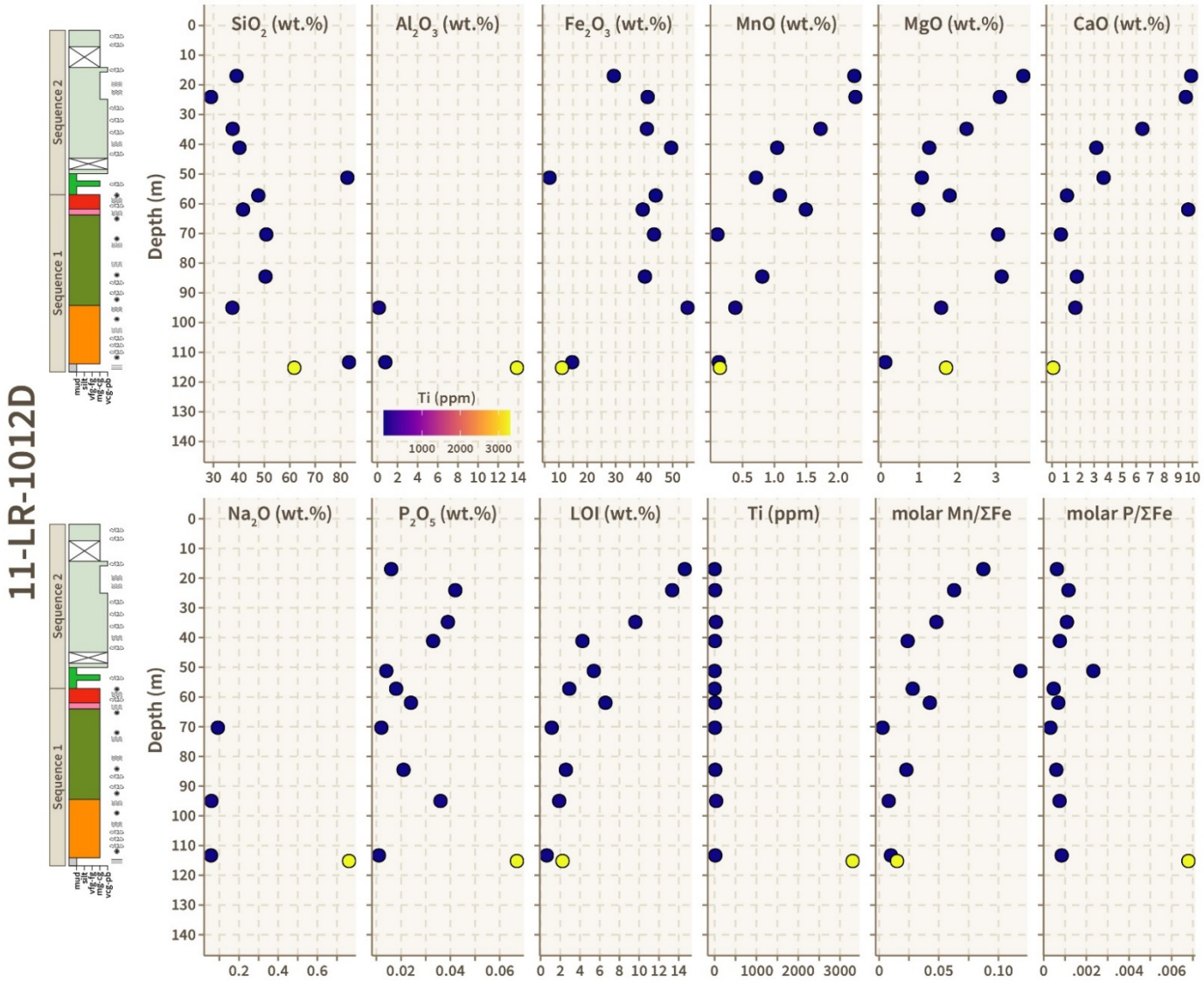

Figure 2.26. Chemostratigraphic variations in major element data and LOI in drillhole 11-LR-1012D. Note that the colour of the dots corresponds to Ti (ppm) concentrations. The range in Ti (ppm) concentrations vary across the evaluated drill holes.

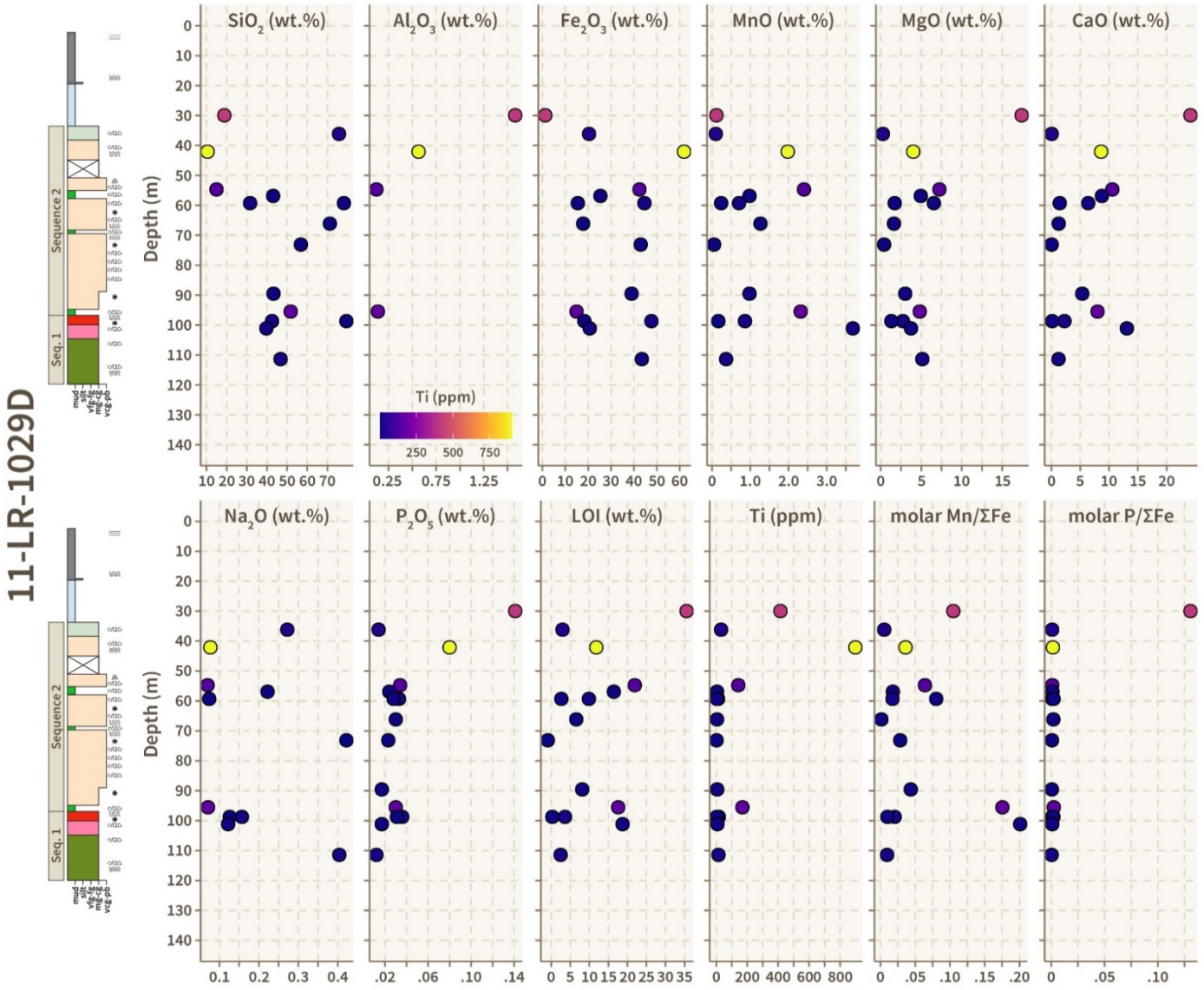

Figure 2.27. Chemostratigraphic variations in major element data and LOI in drillhole 11-LR-1029D. Note that the colour of the dots corresponds to Ti (ppm) concentrations. The range in Ti (ppm) concentrations vary across the evaluated drill holes.

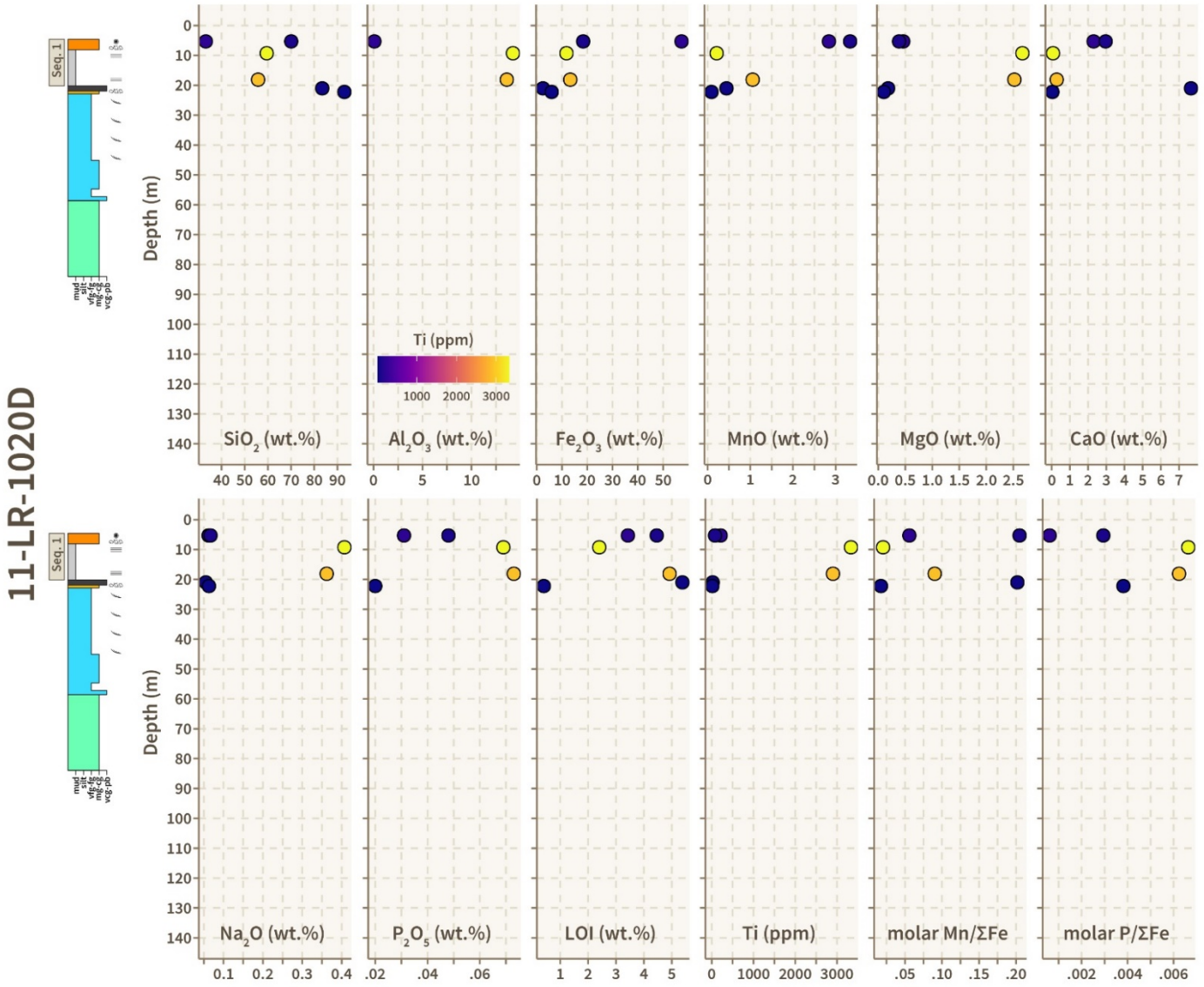

Figure 2.28. Chemostratigraphic variations in major element data and LOI in drillhole 11-LR-1020D. Note that the colour of the dots corresponds to Ti (ppm) concentrations. The range in Ti (ppm) concentrations vary across the evaluated drill holes.

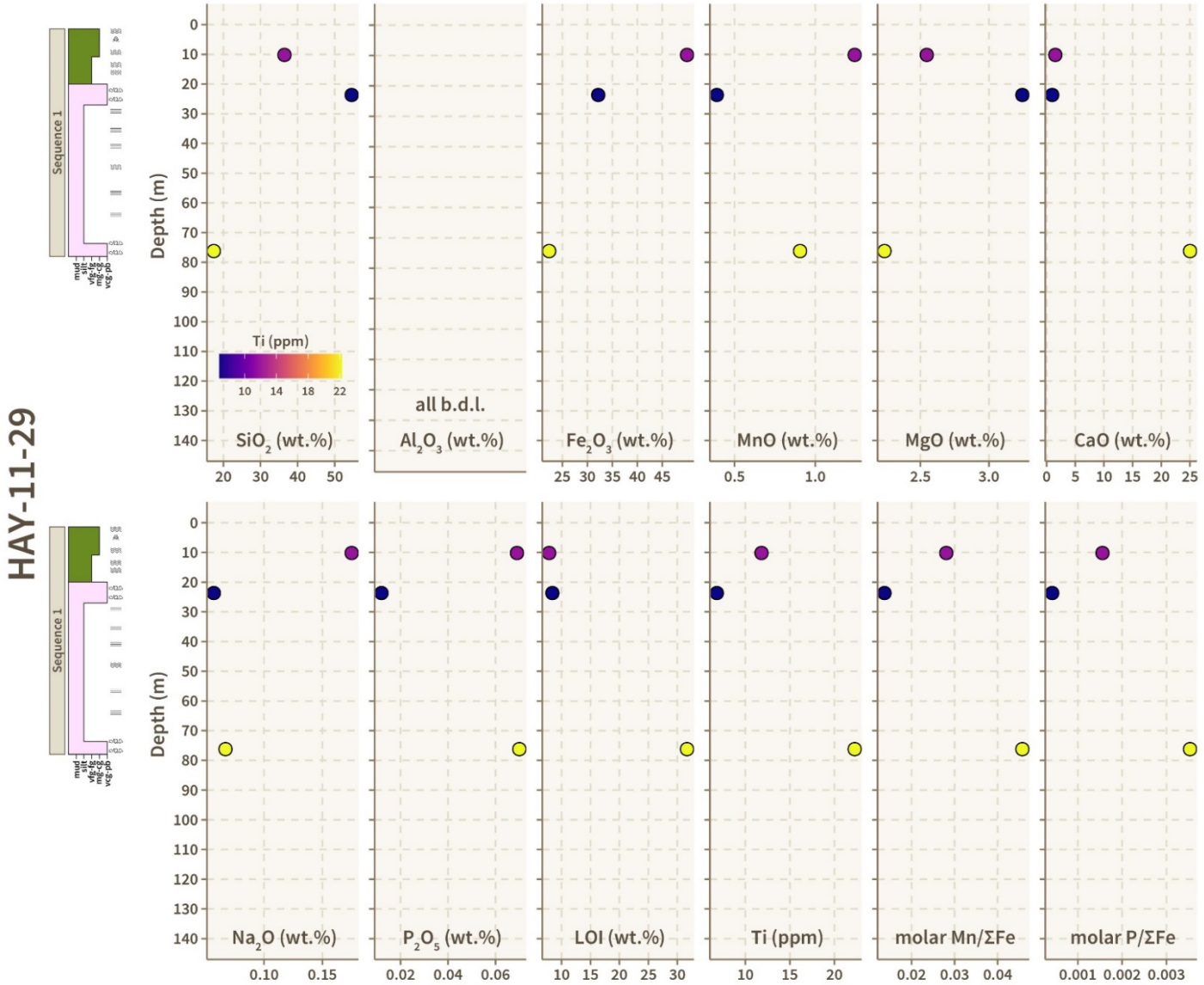

Figure 2.29. Chemostratigraphic variations in major element data and LOI in drillhole HAY-11-29. Note that the colour of the dots corresponds to Ti (ppm) concentrations. The range in Ti (ppm) concentrations vary across the evaluated drill holes.

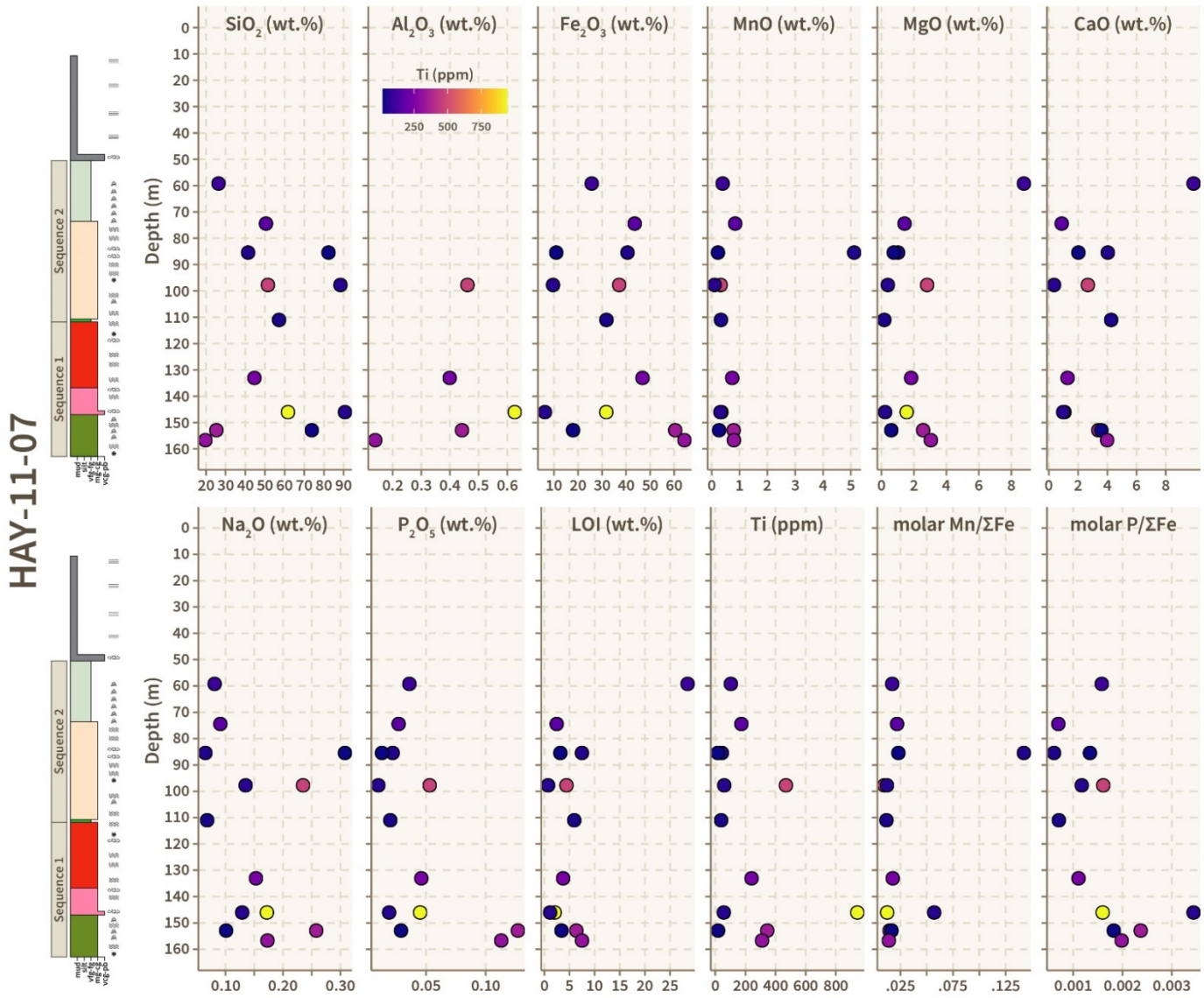

Figure 2.30. Chemostratigraphic variations in major element data and LOI in drillhole HAY-11-07. Note that the colour of the dots corresponds to Ti (ppm) concentrations. The range in Ti (ppm) concentrations vary across the evaluated drill holes.

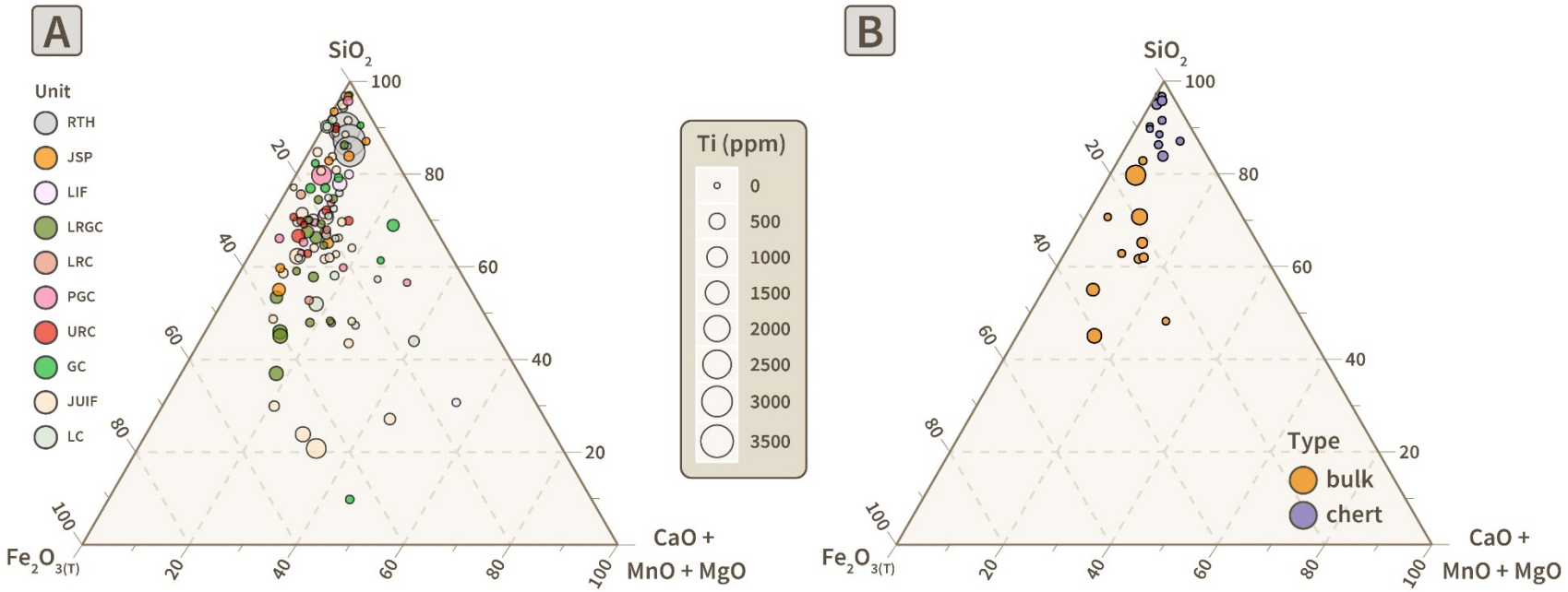

Figure 2.31. Molar ternary SiO_2–Fe_2O_{3T}–(CaO+MnO+MgO) plot showing (A) mineralogical variations across IF units and (B) between bulk IF and intraformational chert sample pairs.

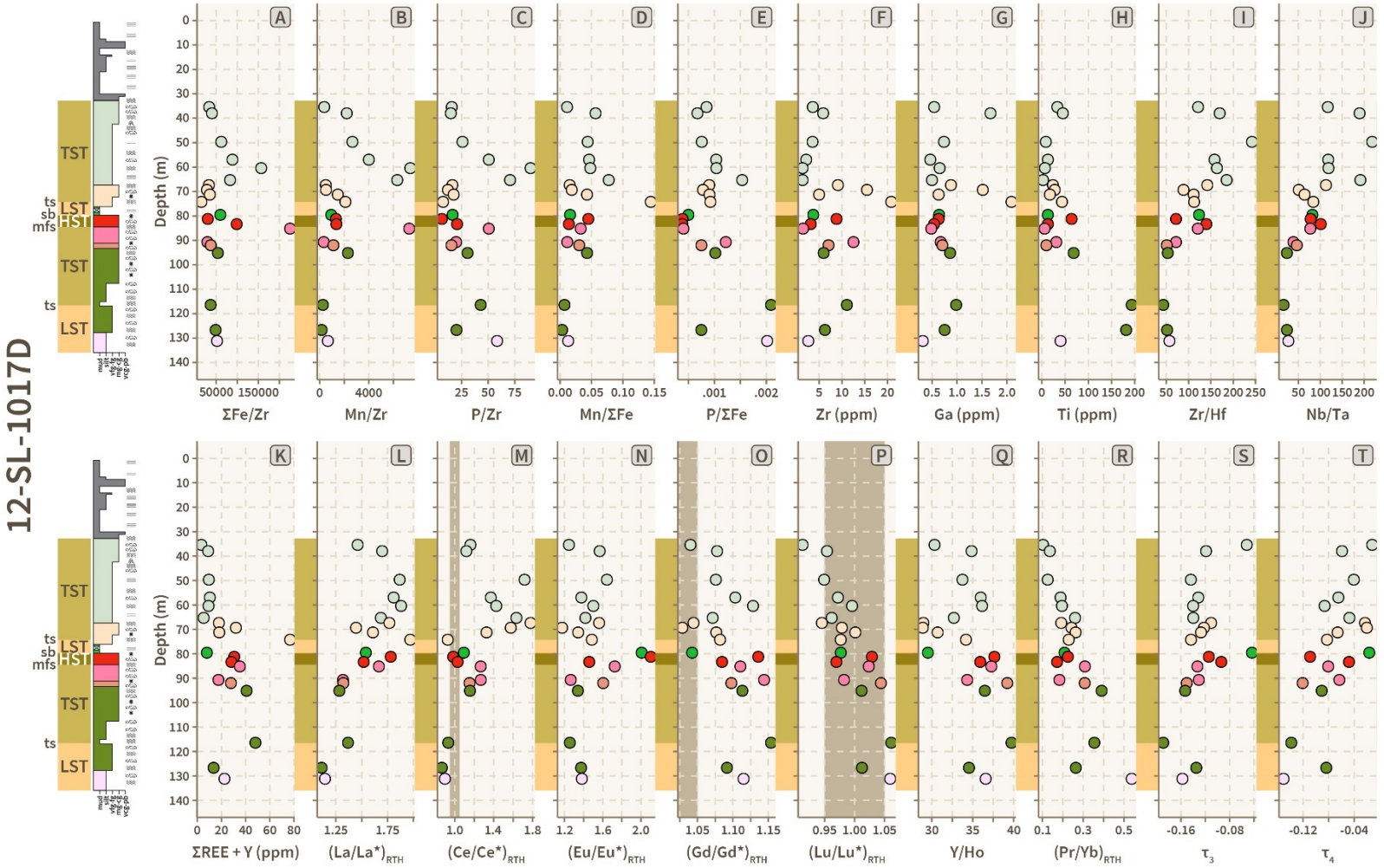

Figure 2.32. Chemostratigraphic variations in major element ratios (Fe, Mn, P), detrital element abundances (Zr, Ga, Ti) and Ruth mean slate-normalized REE + Y anomalies and ratios for drillhole 12-SL-1017D correlated with depositional sequences. Shaded brown fields indicate the ranges within analytical uncertainty. LST – lowstand systems tract; TST – transgressive systems tract; HST – highstand systems tract; ts – transgressive surface; mfs – maximum flooding surface; sb – sequence boundary

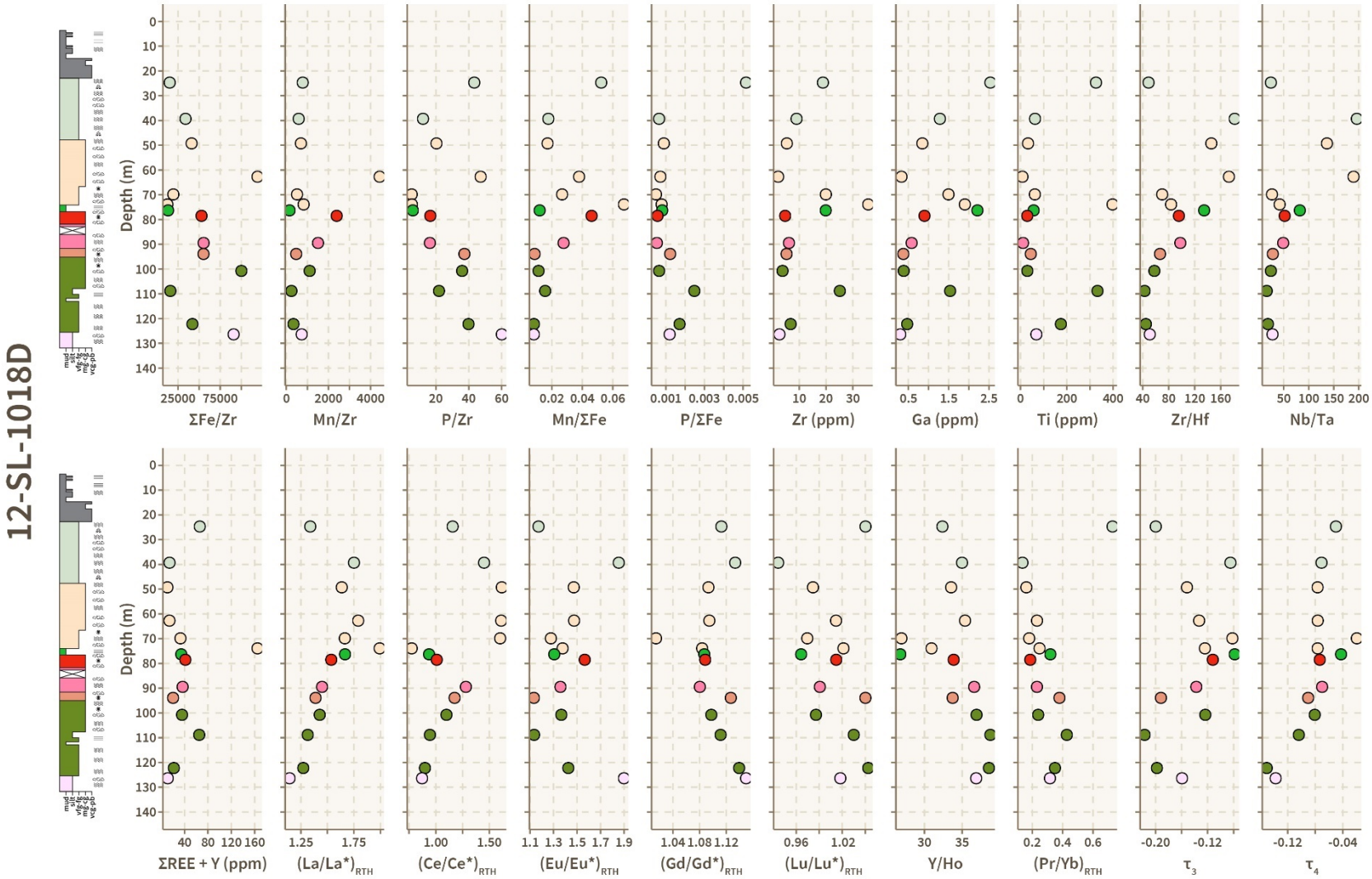

Figure 2.33. Chemostratigraphic variations in major element ratios (ΣFe/Zr, Mn/Zr, P/Zr) and REE+Y anomalies and ratios in drillhole 12-SL-1018D. Note that the colors of the individual points denote their unit.

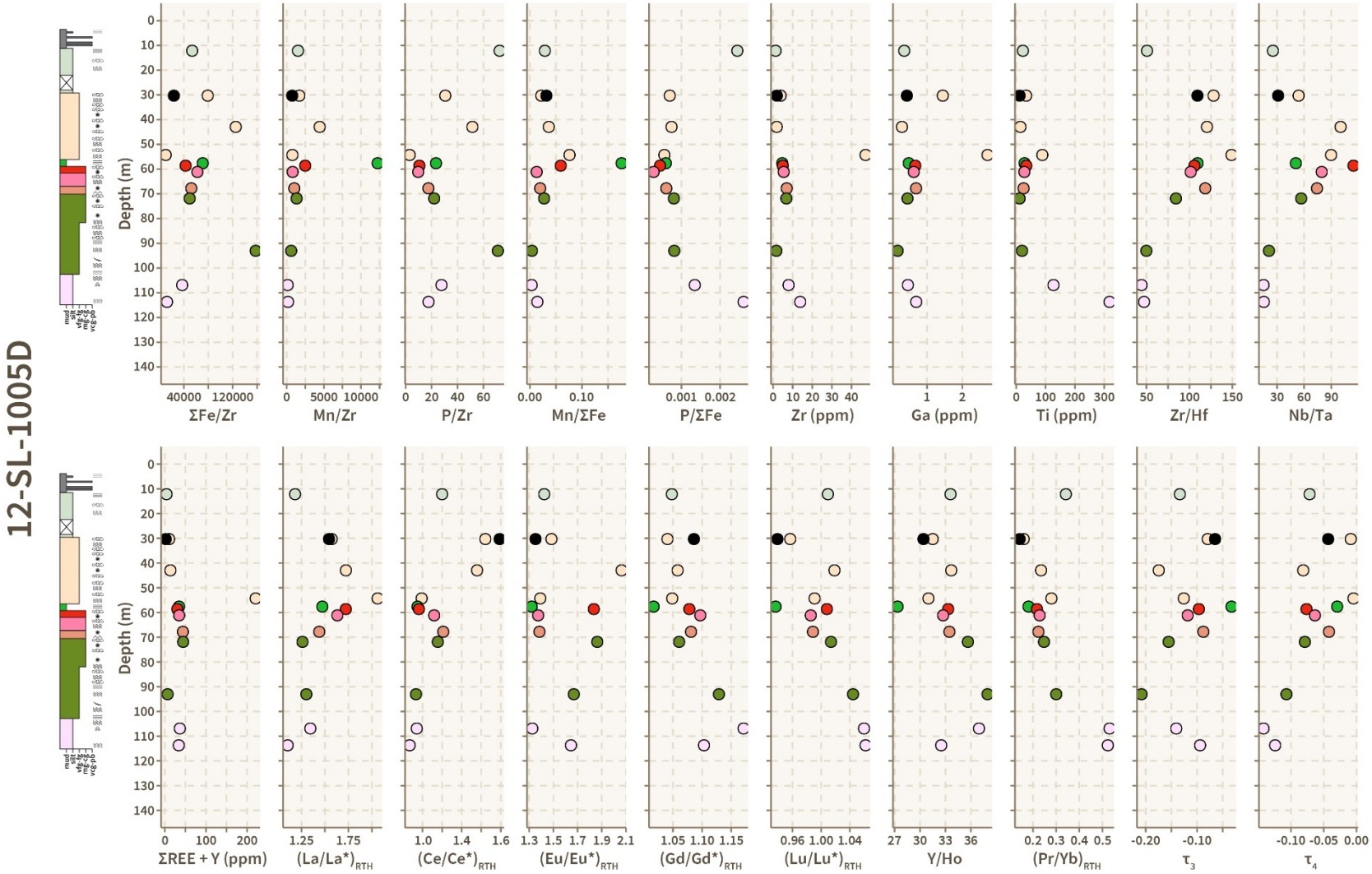

Figure 2.34. Chemostratigraphic variations in major element ratios (ΣFe/Zr, Mn/Zr, P/Zr) and REE+Y anomalies and ratios in drillhole 12-SL-1005D. Note that the colors of the individual points denote their unit. Black dots correspond to chert subsamples.

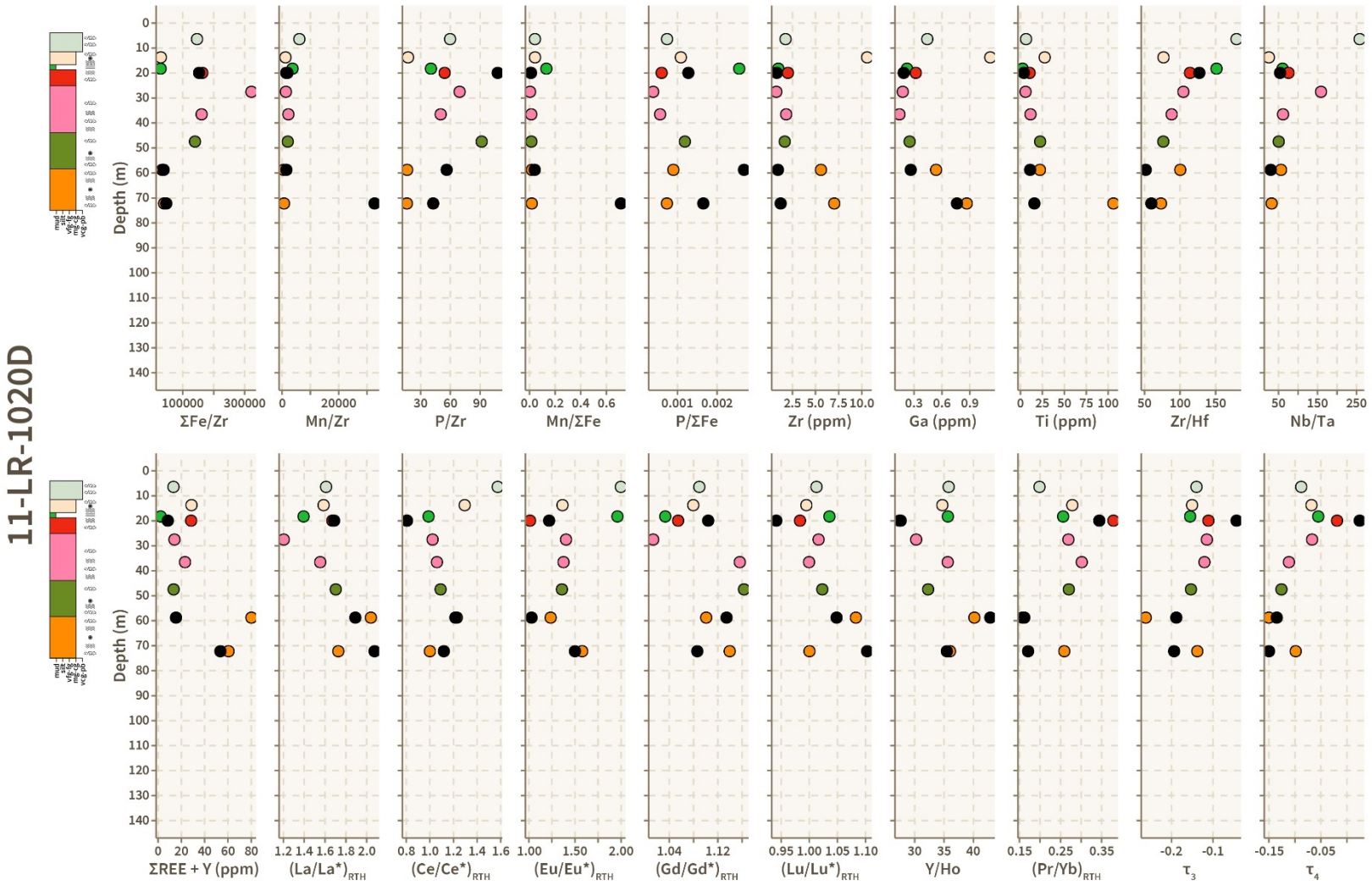

Figure 2.35. Chemostratigraphic variations in major element ratios (ΣFe/Zr, Mn/Zr, P/Zr) and REE+Y anomalies and ratios in drillhole 11-LR-1010D. Note that the colors of the individual points denote their unit. Black dots correspond to chert subsamples.

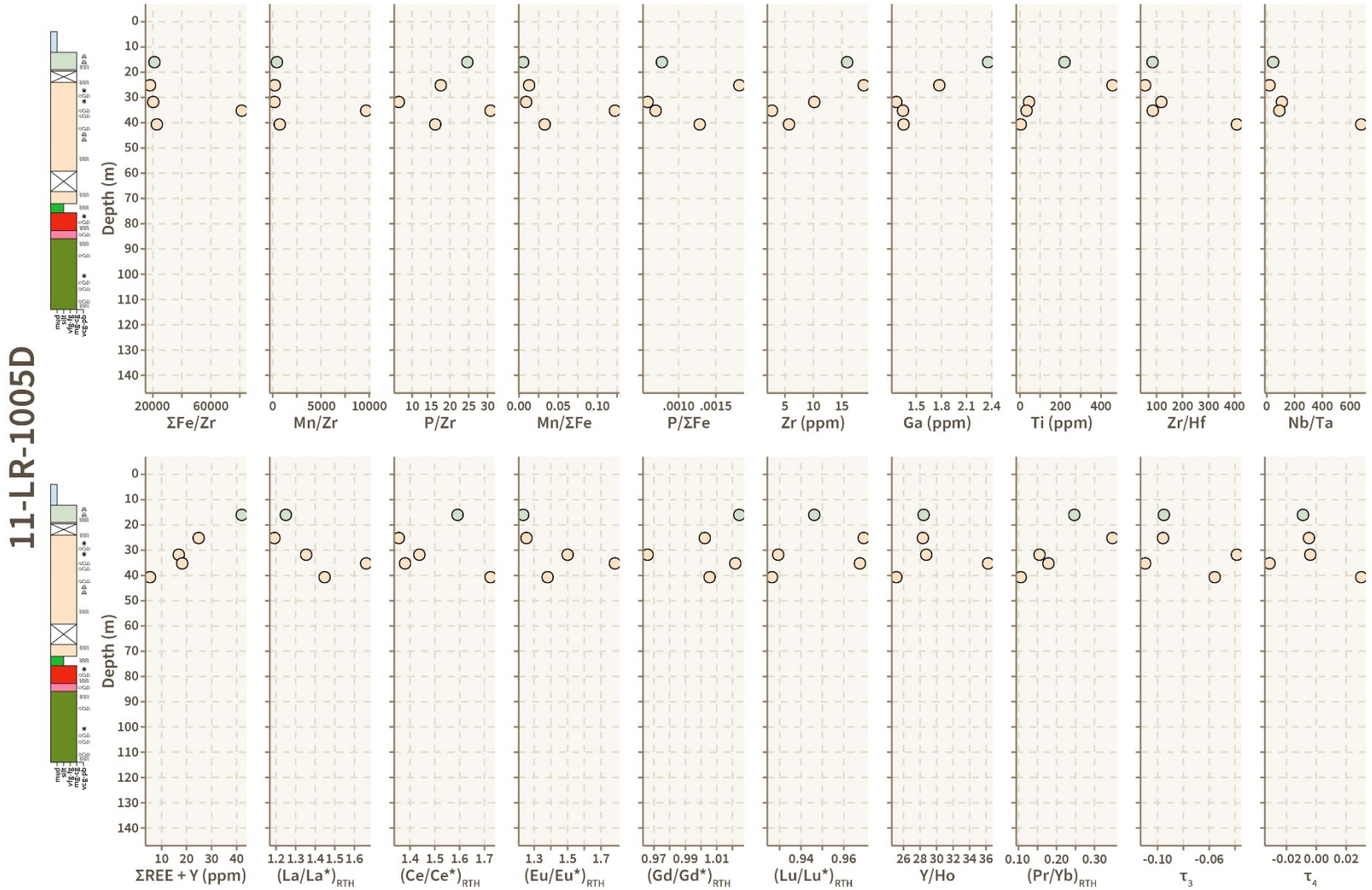

Figure 2.36. Chemostratigraphic variations in major element ratios (ΣFe/Zr, Mn/Zr, P/Zr) and REE+Y anomalies and ratios in drillhole 11-LR-1005D. Note that the colors of the individual points denote their unit.

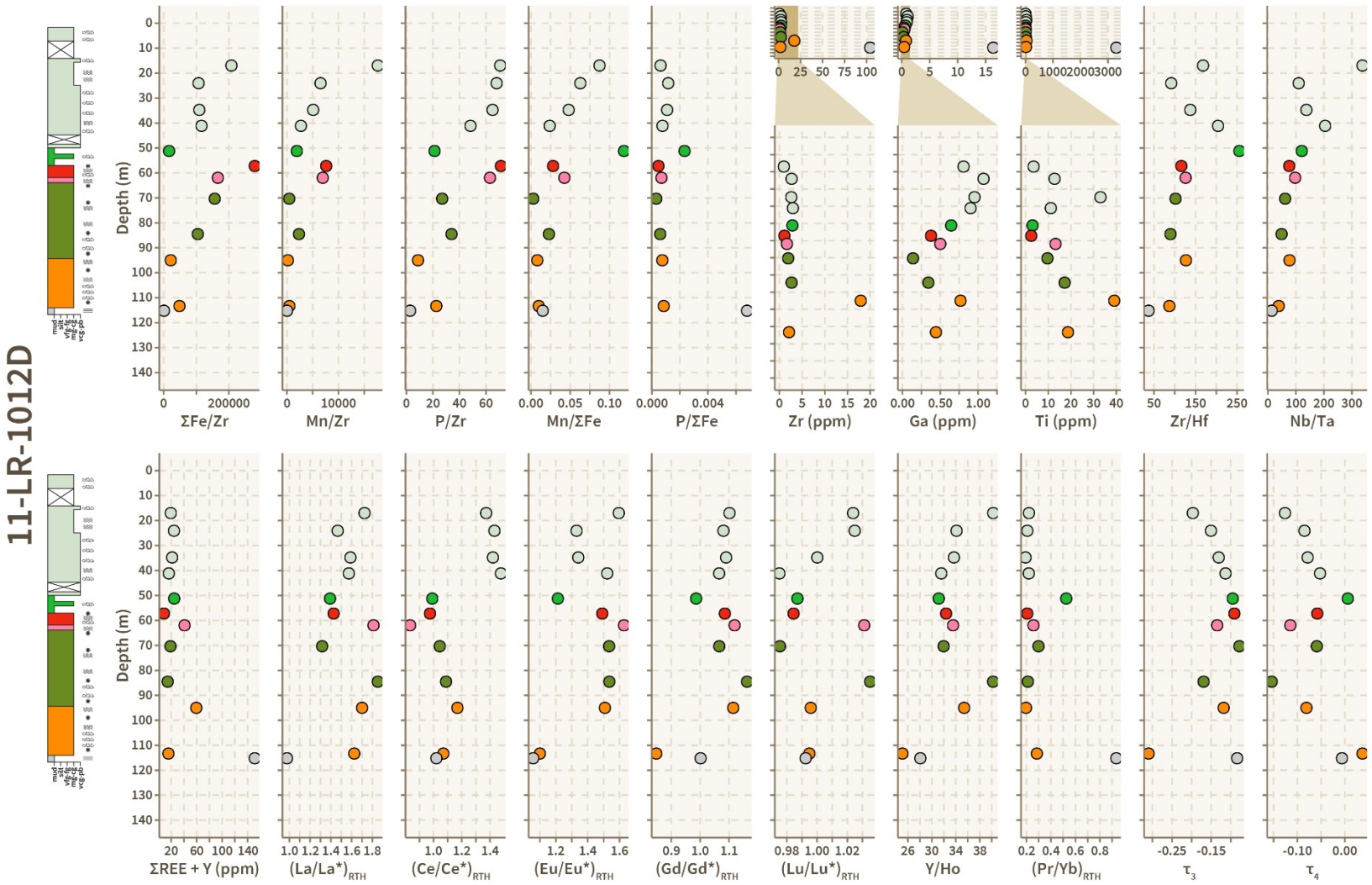

Figure 2.37. Chemostratigraphic variations in major element ratios (ΣFe/Zr, Mn/Zr, P/Zr) and REE+Y anomalies and ratios in drillhole 11-LR-1012D. Note that the colors of the individual points denote their unit.

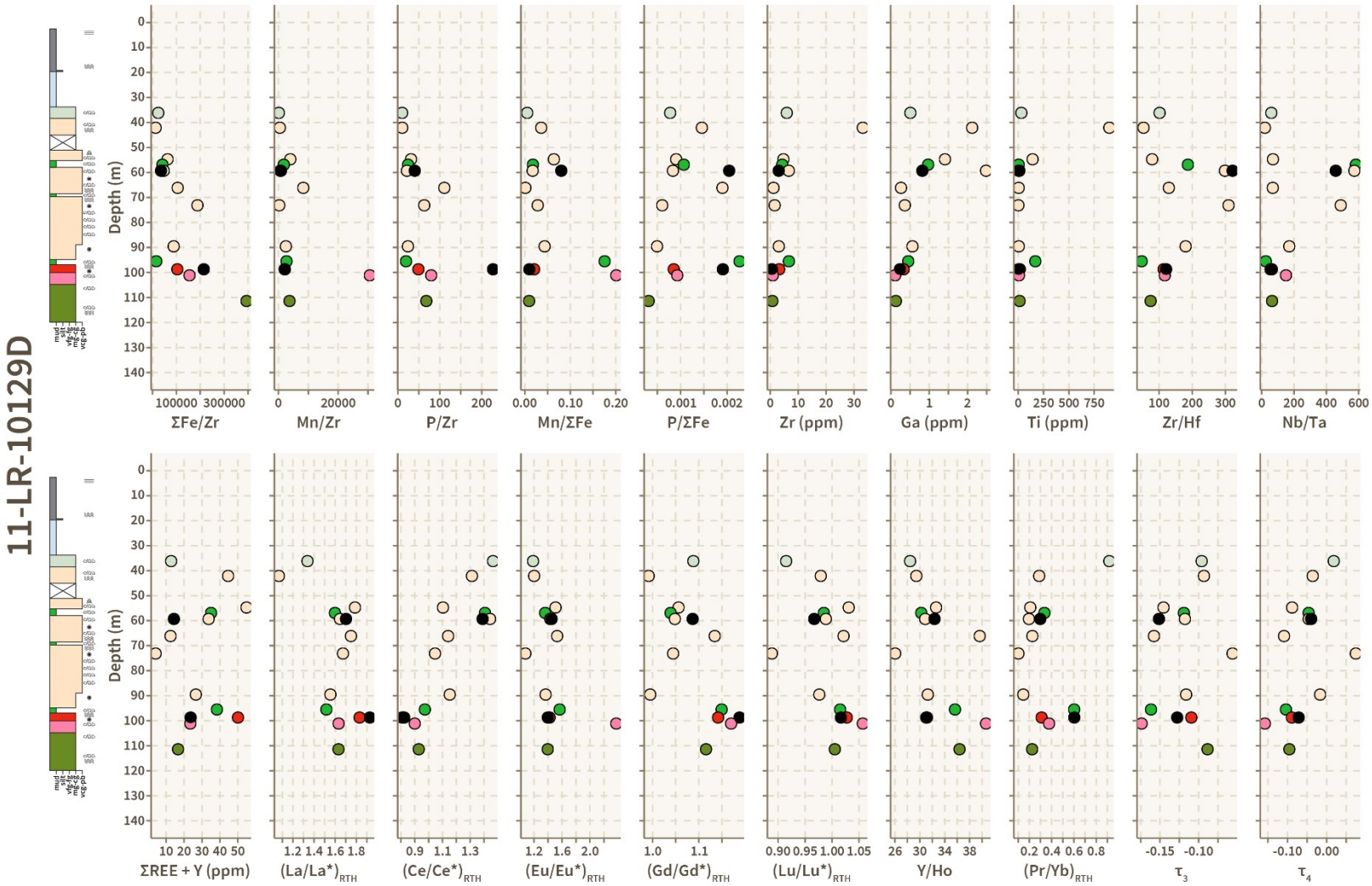

Figure 2.38. Chemostratigraphic variations in major element ratios (ΣFe/Zr, Mn/Zr, P/Zr) and REE+Y anomalies and ratios in drillhole 11-LR-1029D. Note that the colors of the individual points denote their unit. Black dots correspond to chert subsamples.

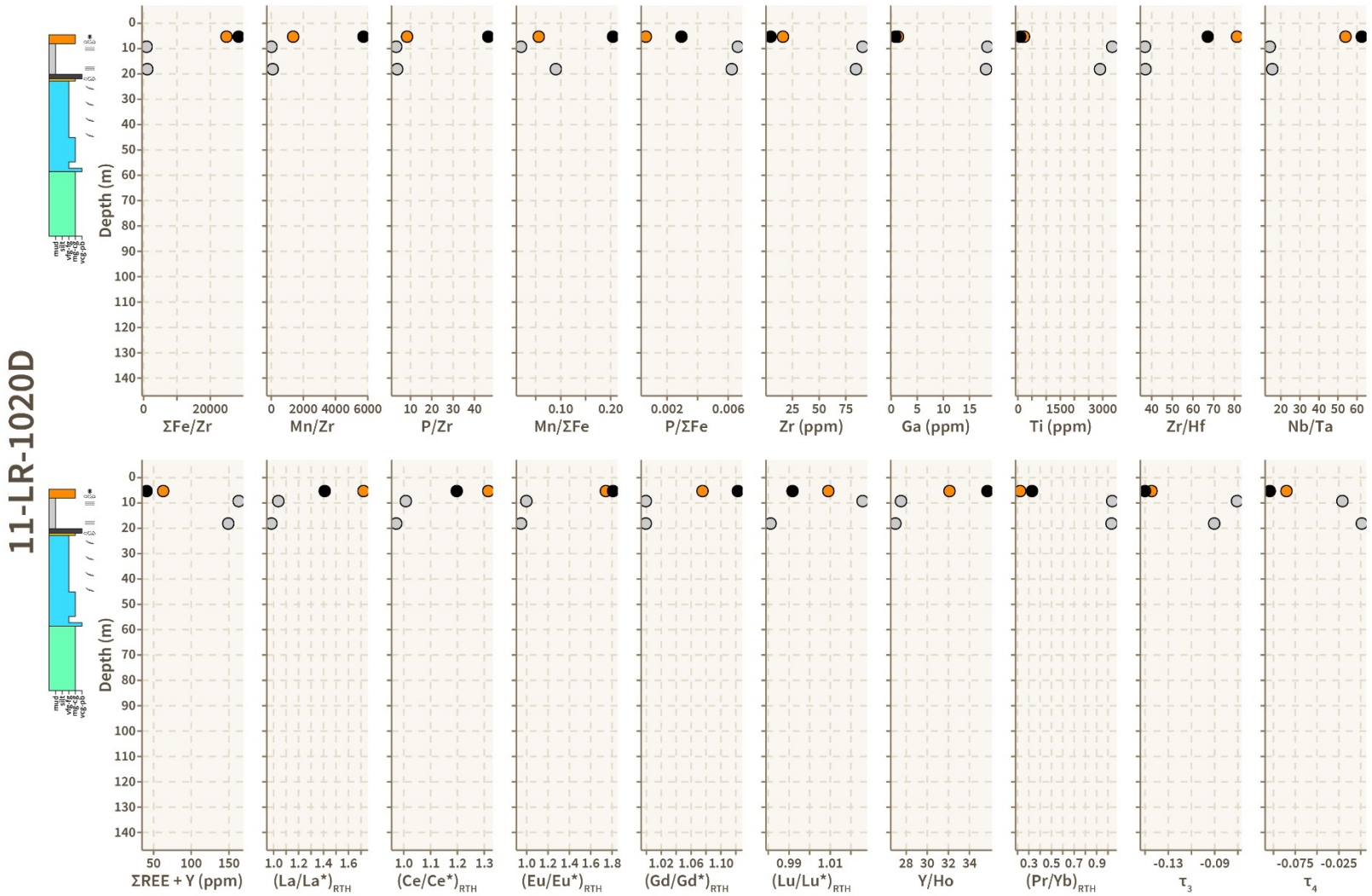

Figure 2.39. Chemostratigraphic variations in major element ratios (ΣFe/Zr, Mn/Zr, P/Zr) and REE+Y anomalies and ratios in drillhole 11-LR-1020D. Note that the colors of the individual points denote their unit. Black dots correspond to chert subsamples.

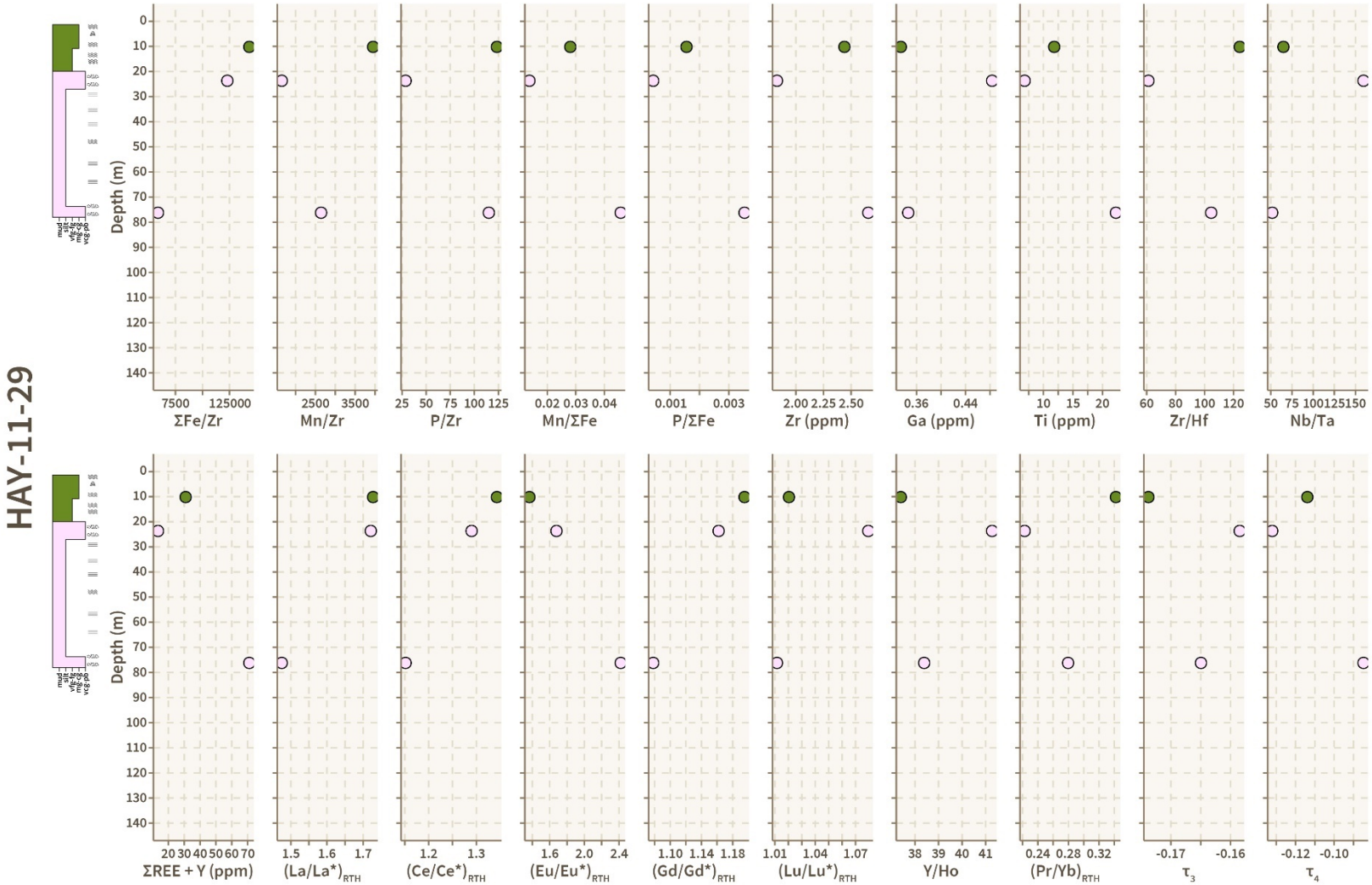

Figure 2.40. Chemostratigraphic variations in major element ratios (ΣFe/Zr, Mn/Zr, P/Zr) and REE+Y anomalies and ratios in drillhole HAY-11-29. Note that the colors of the individual points denote their unit.

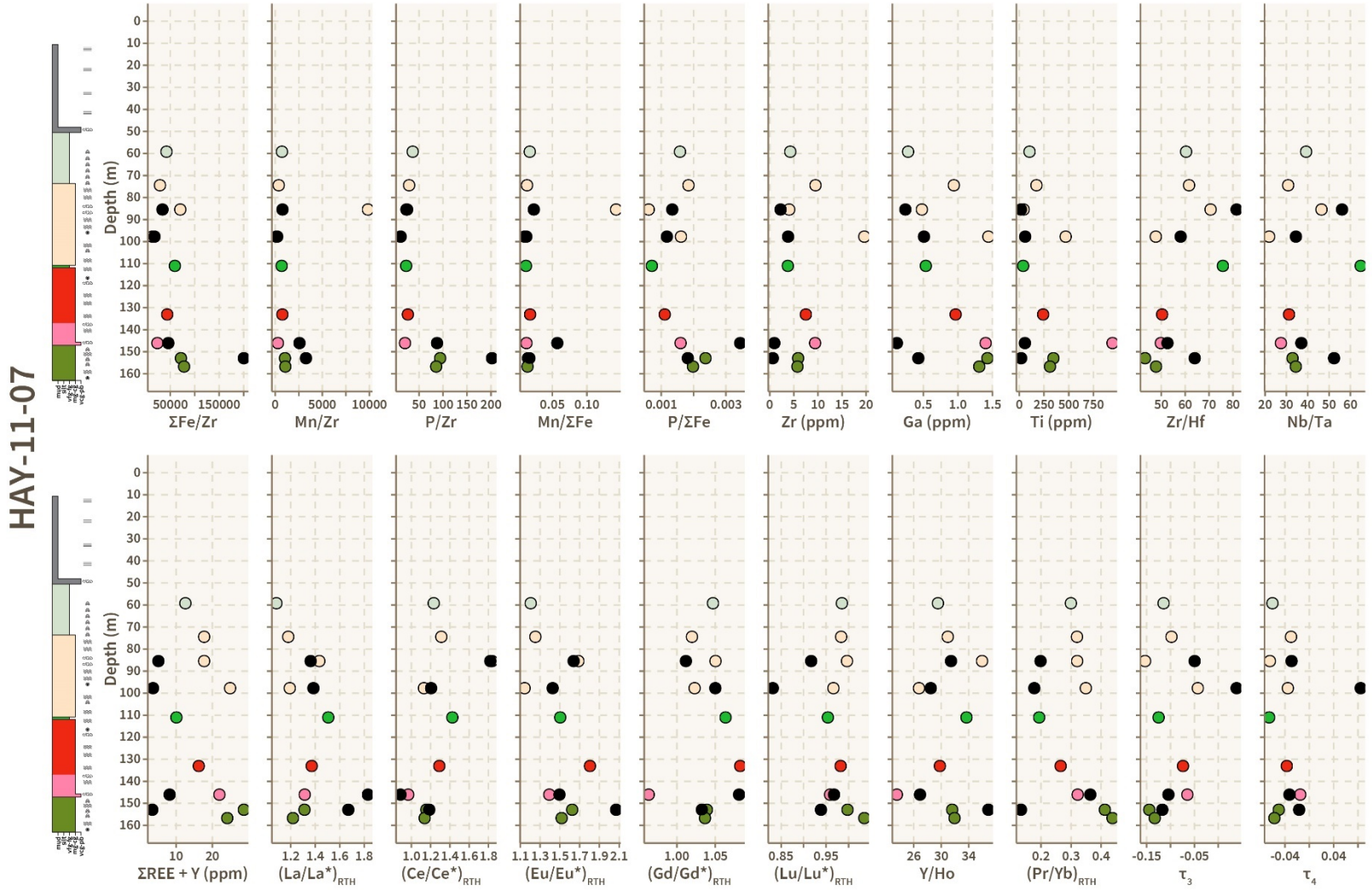

Figure 2.41. Chemostratigraphic variations in major element ratios (ΣFe/Zr, Mn/Zr, P/Zr) and REE + Y anomalies and ratios in drillhole HAY-11-07. Note that the colors of the individual points denote their unit. Black dots correspond to chert subsamples.

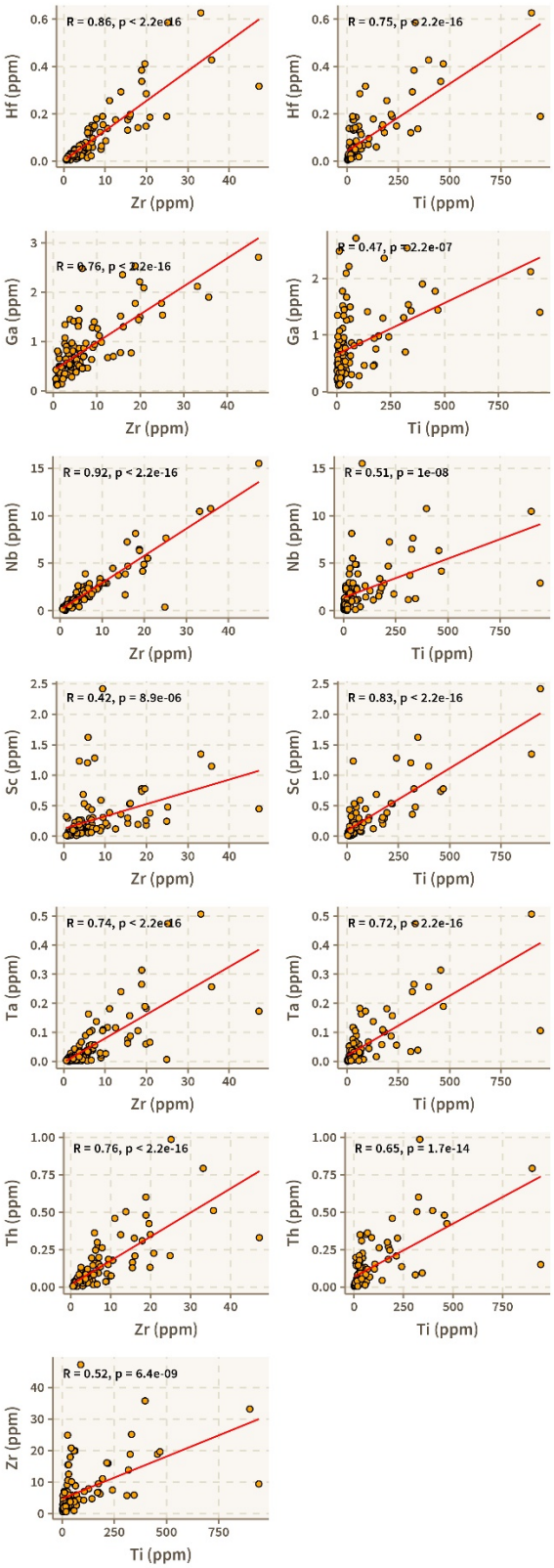

Figure 2.42. Cross-plots of Ti and Zr concentrations (ppm) against other detrital monitors (Ga, Hf, Nb, Sc, Ta, Th).

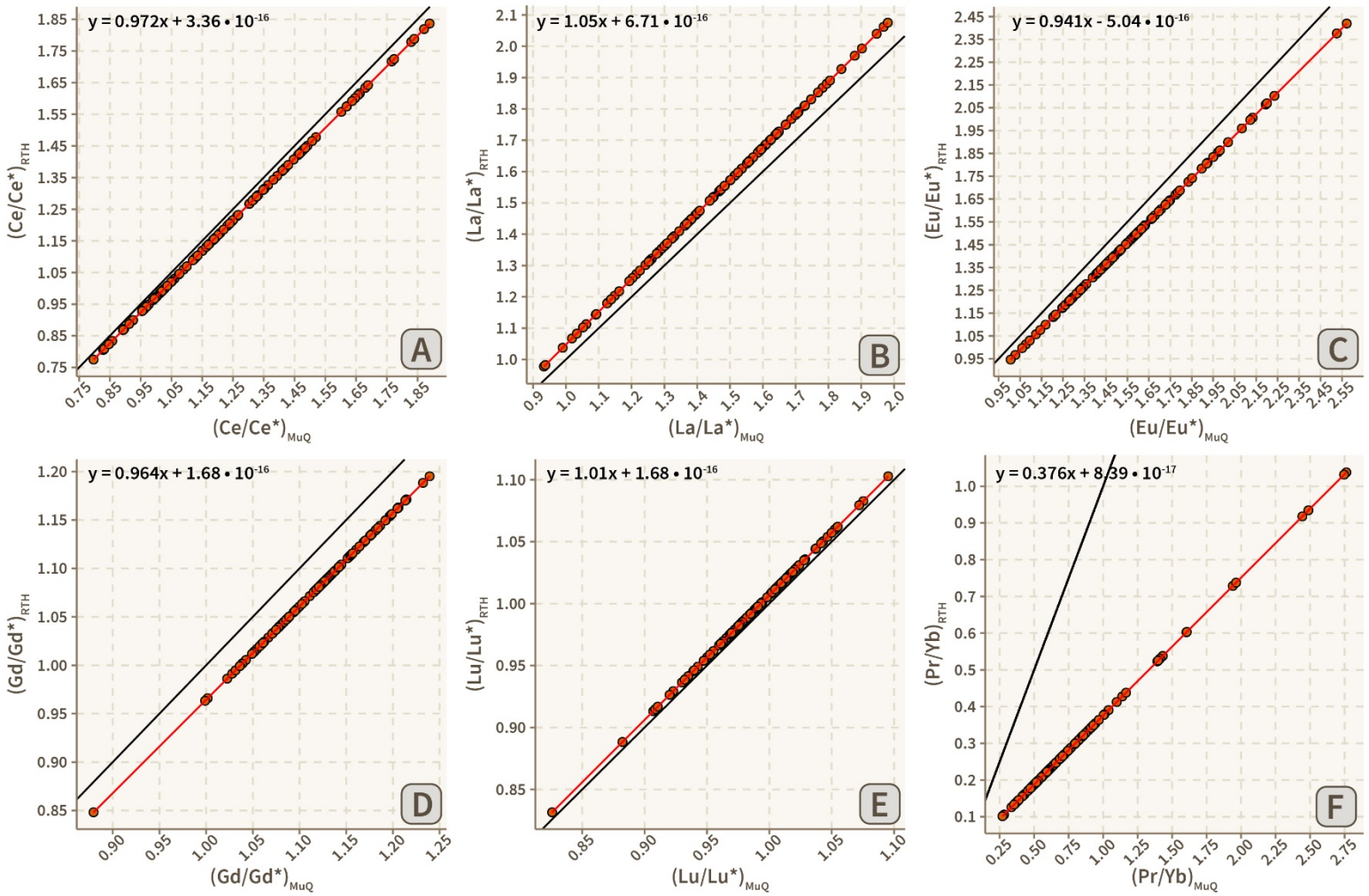

Figure 2.43. Anomaly and ratio comparison between Mud from Queensland (MuQ)- and Ruth slate mean (RTH)- normalized values. The solid black defines the 1:1 line. Note that a significant deviation (~62% difference) is observed in Pr/Yb ratios.

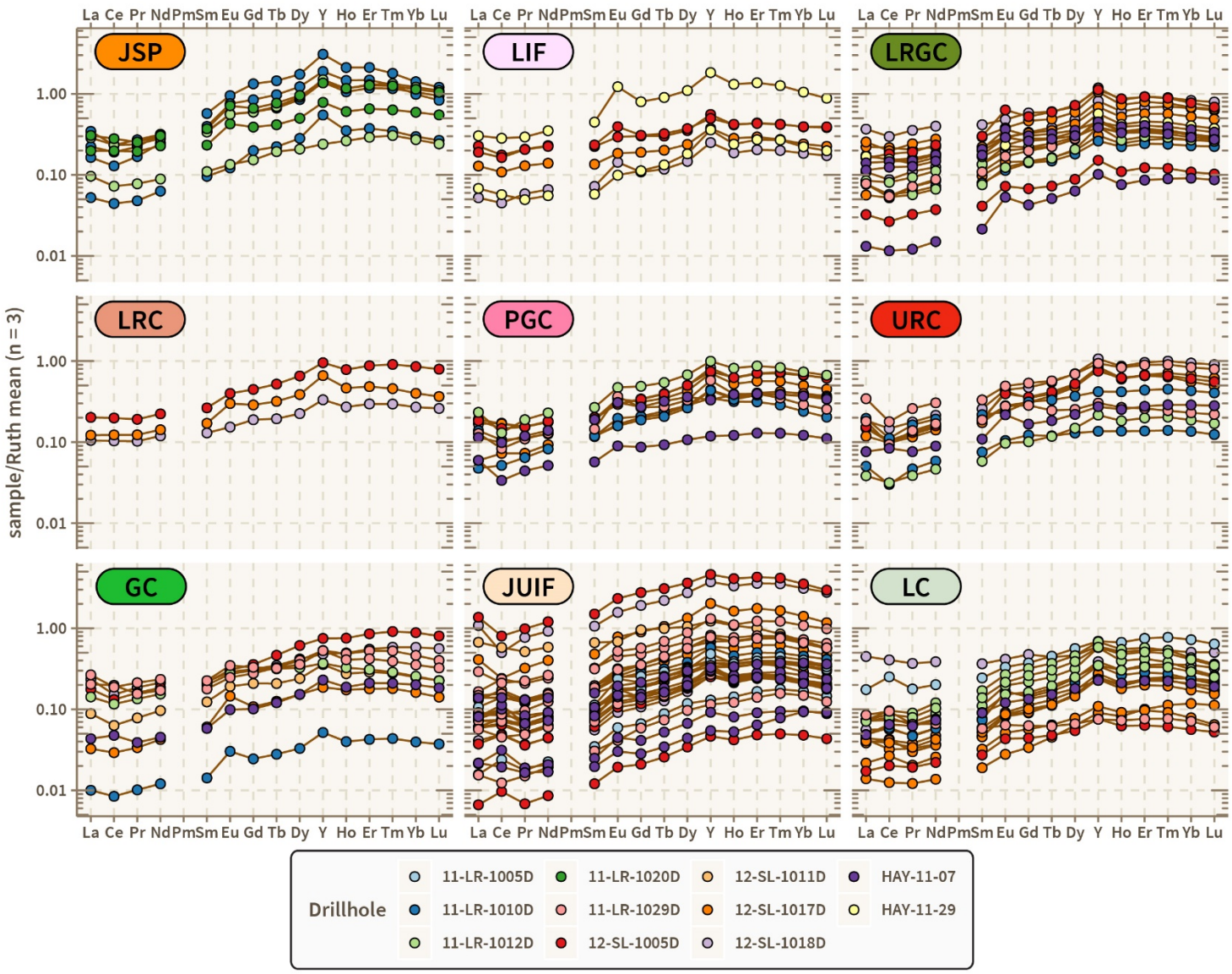

Figure 2.44. Unit-specific RTH mean-normalized REE+Y patterns.

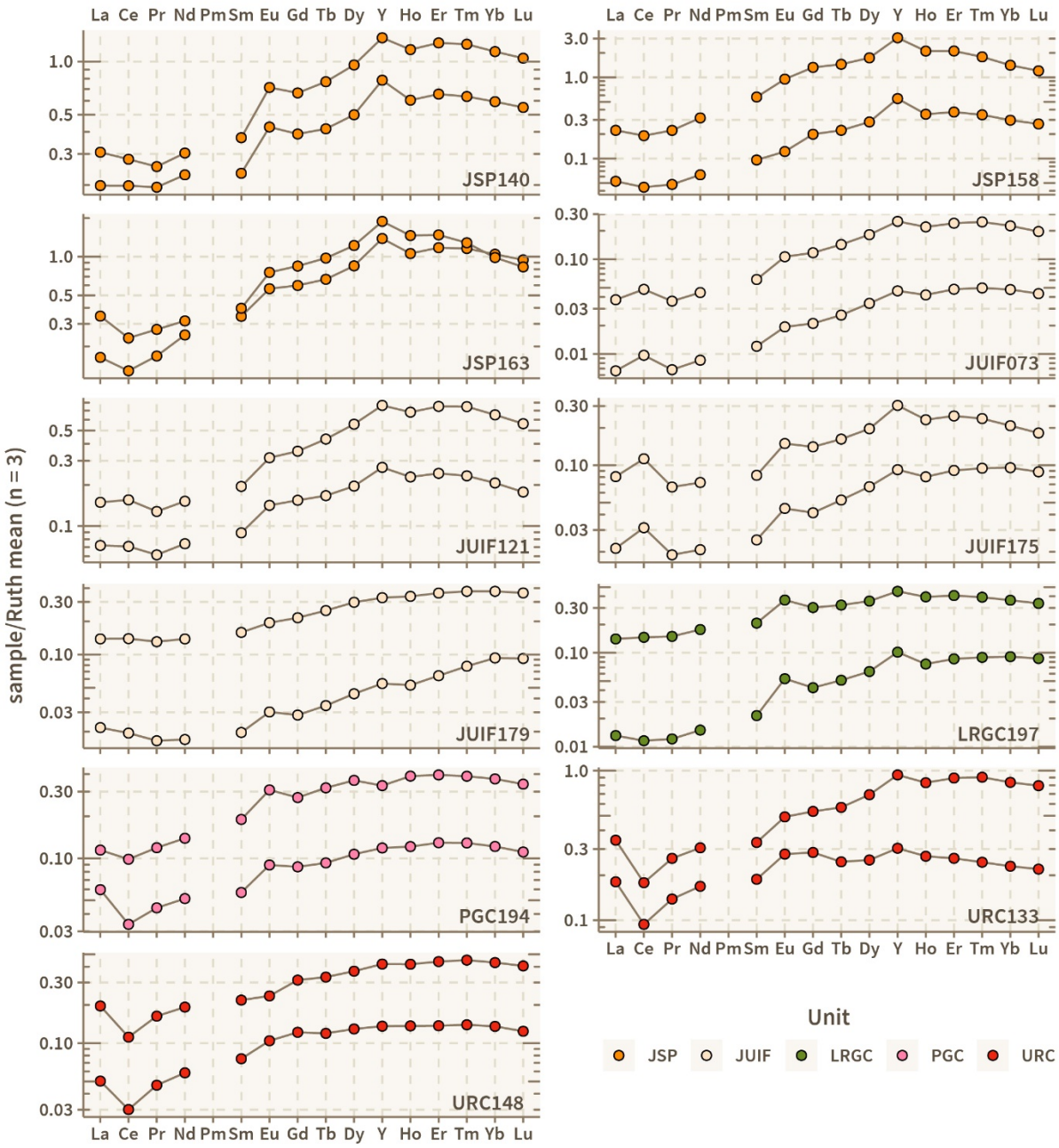

Figure 2.45. Comparison of REE+Y patterns between bulk and intraformational chert samples. Note the similarity in the magnitude of Ce anomalies. In contrast, large but unsystematic differences in the LREE/HREE slope are observed.

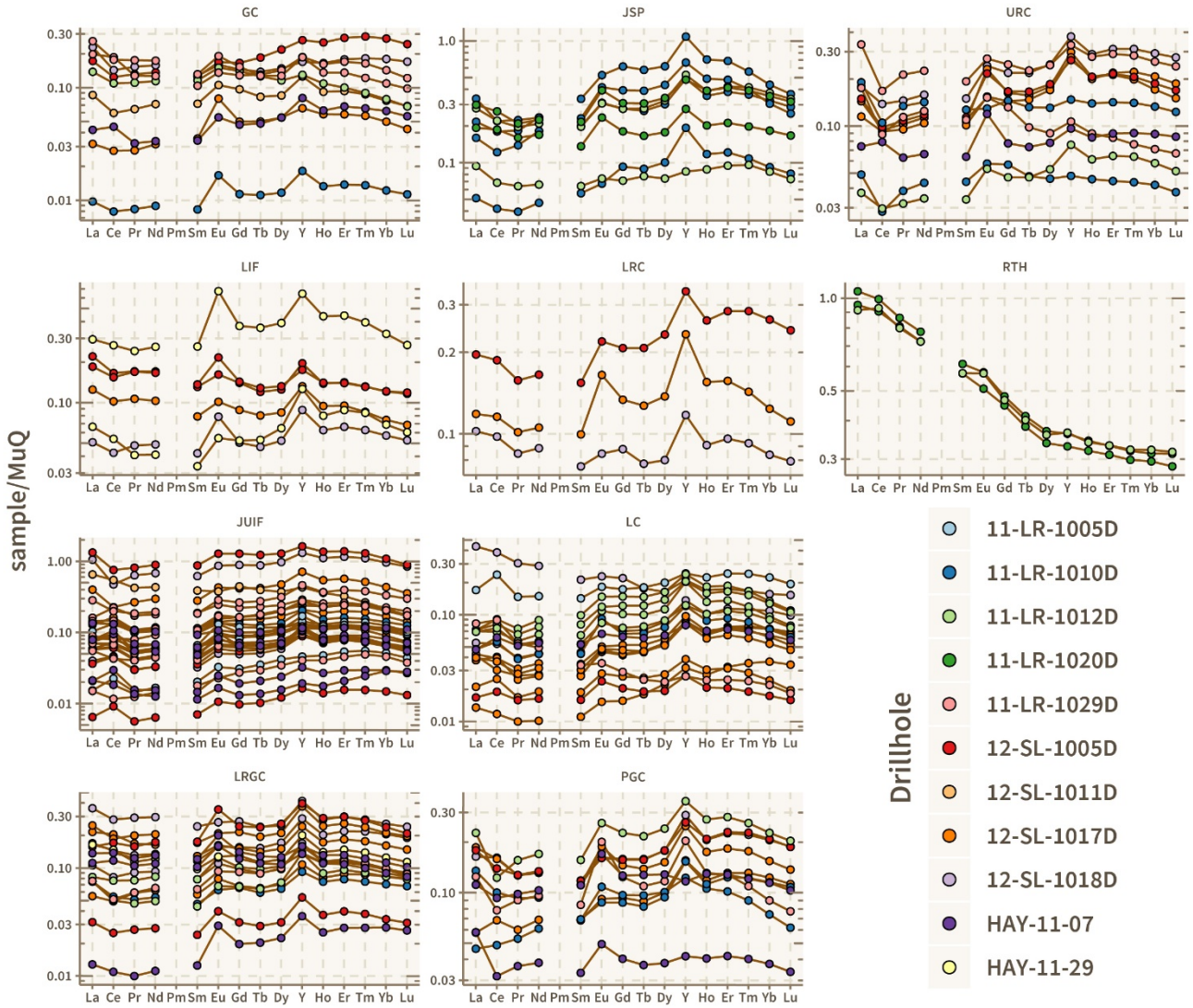

Figure 2.46. Unit-specific REE+Y patterns normalized to Mud from Queensland (MuQ).

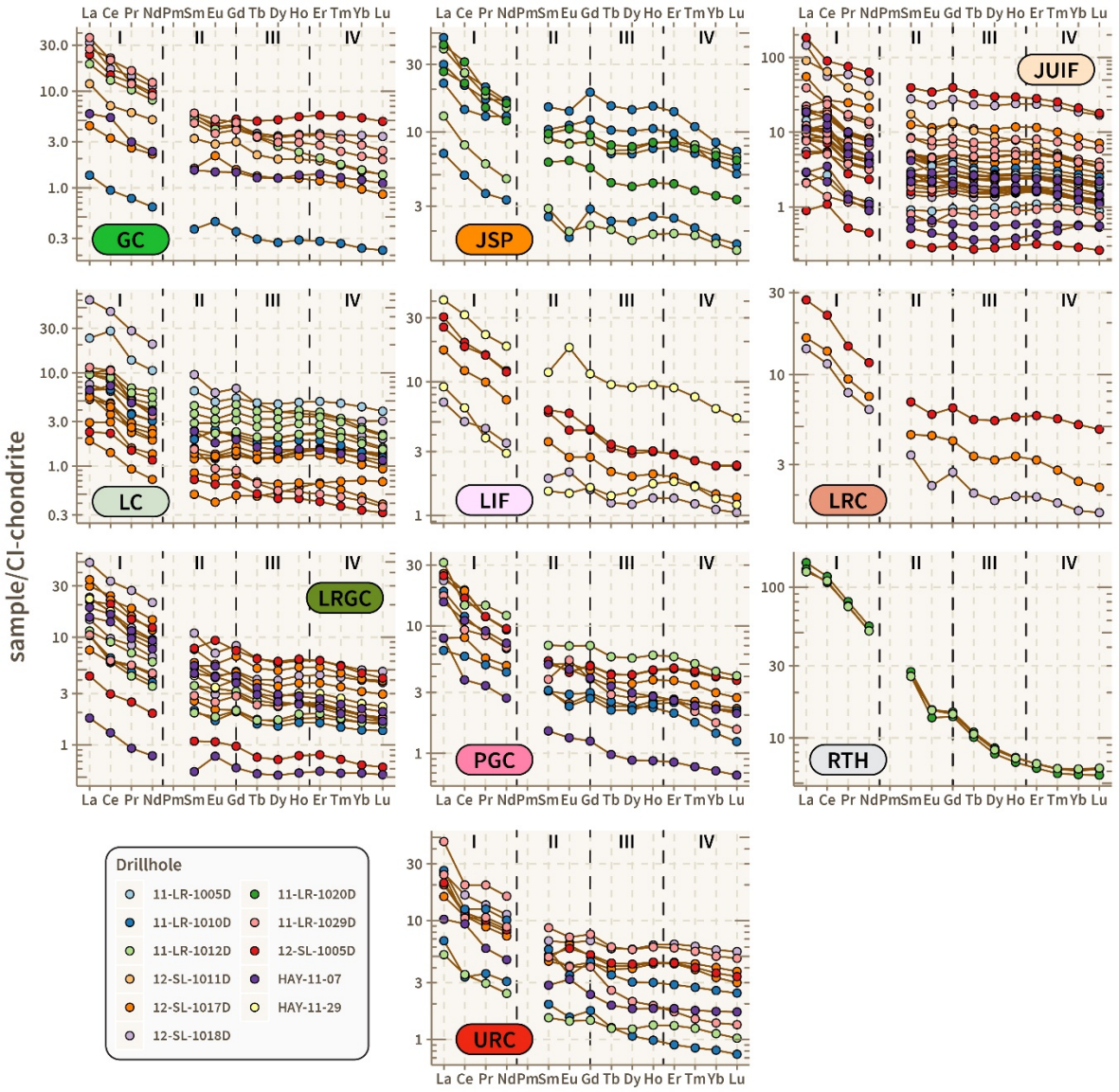

Figure 2.47. Unit-specific REE patterns normalized to CI-chondrite.

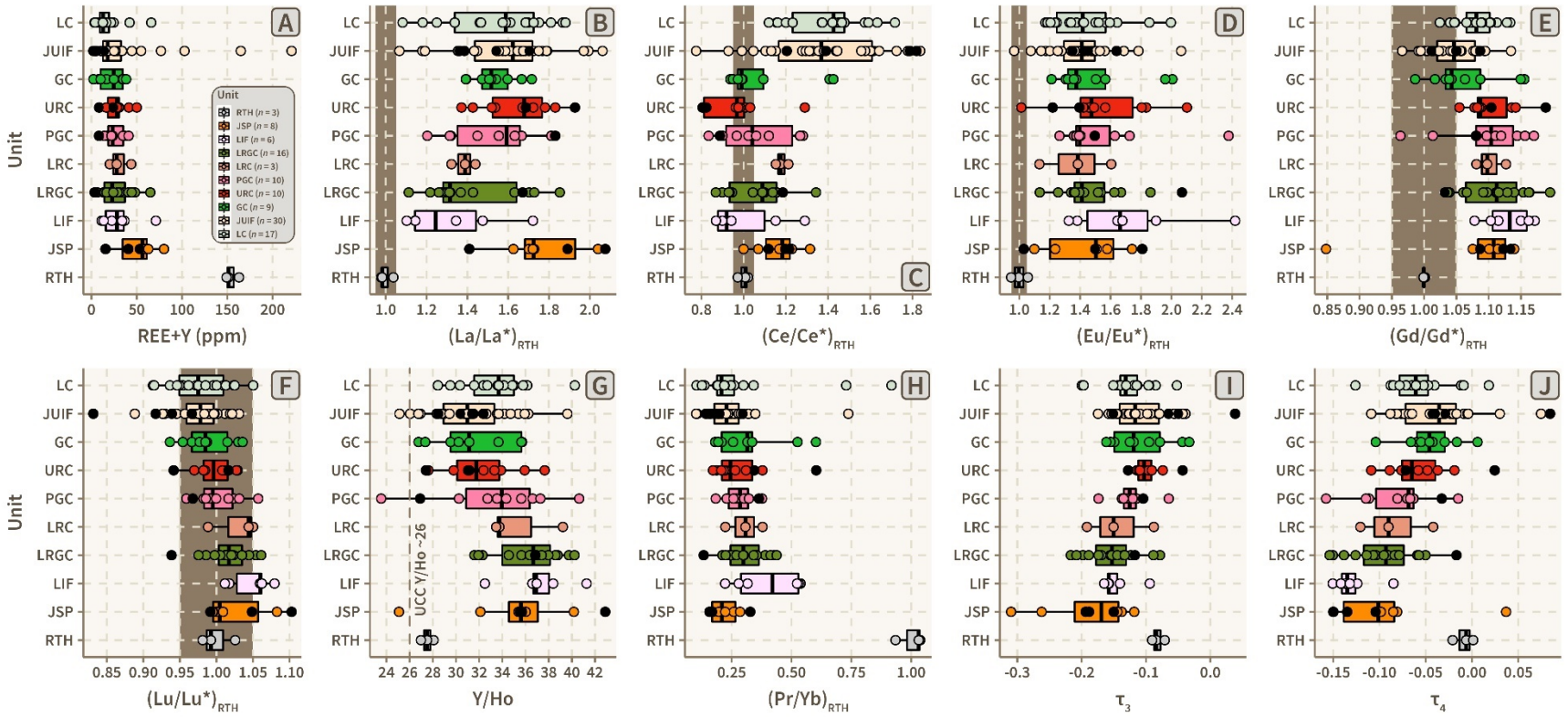

Figure 2.48. Boxplots of RTH mean-normalized REE+Y anomalies and ratios subdivided by unit. Shaded brown fields indicate the ranges within analytical uncertainty. Dashed line in (G) denotes the upper crustal Y/Ho value ~26.

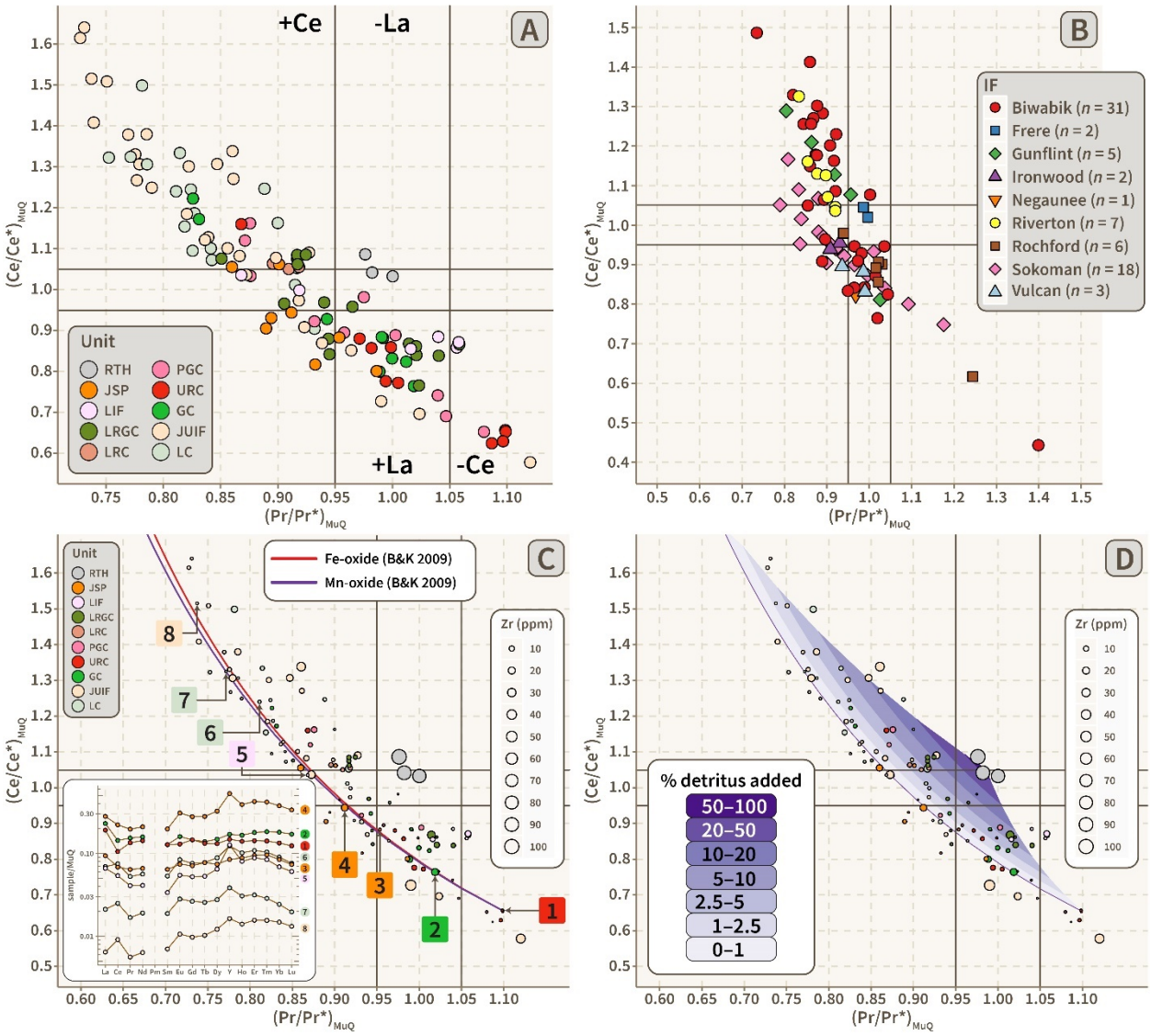

Figure 2.49. Ce-Pr anomaly bubble cross-plots. (A) Samples from this study and (B) other ca. 1.88 Ga IF as per Bau and Dulski (1996). The bubble size in (A) corresponds to Ti (ppm) concentrations. The IF dataset plotted in (B) are derived from Frei et al. (2008); Planavsky et al. (2010a, 2018); Raye et al. (2015). Note the hyperbolic trends that span both true negative and true positive Ce anomaly fields; (C–D) Modeling IF trends in the Ce-Pr anomaly cross-plot. (C) Hyperbolic trends in the IF data are best reconstructed by emulating the release of sorbed REE+Y using Lu-normalized apparent oxide-seawater partition coefficients $(K_D^{\text{REY-oxide /REY-SW}})_{Lu}$, as those derived by Bau and Koschinsky (2009), that are further normalized to the apparent oxide-seawater partition coefficient for Ce $(K_D^{\text{Ce-oxide /Ce-SW}})_{Lu}$. Here an endmember plotting in the true negative Ce anomaly field (URC148B) was chosen to simulate REE+Y release from Fe- and Mn-oxides as a function of water depth relative to the redoxcline. The resulting model curves for Fe- and Mn-oxides are depicted by solid red and purple lines, respectively. (D) With the addition of detrital material, represented by the RTH mean, hyperbolic trends are retained. However, the addition of at least 5% detritus is sufficient to erase the presence of slight negative Ce anomalies.

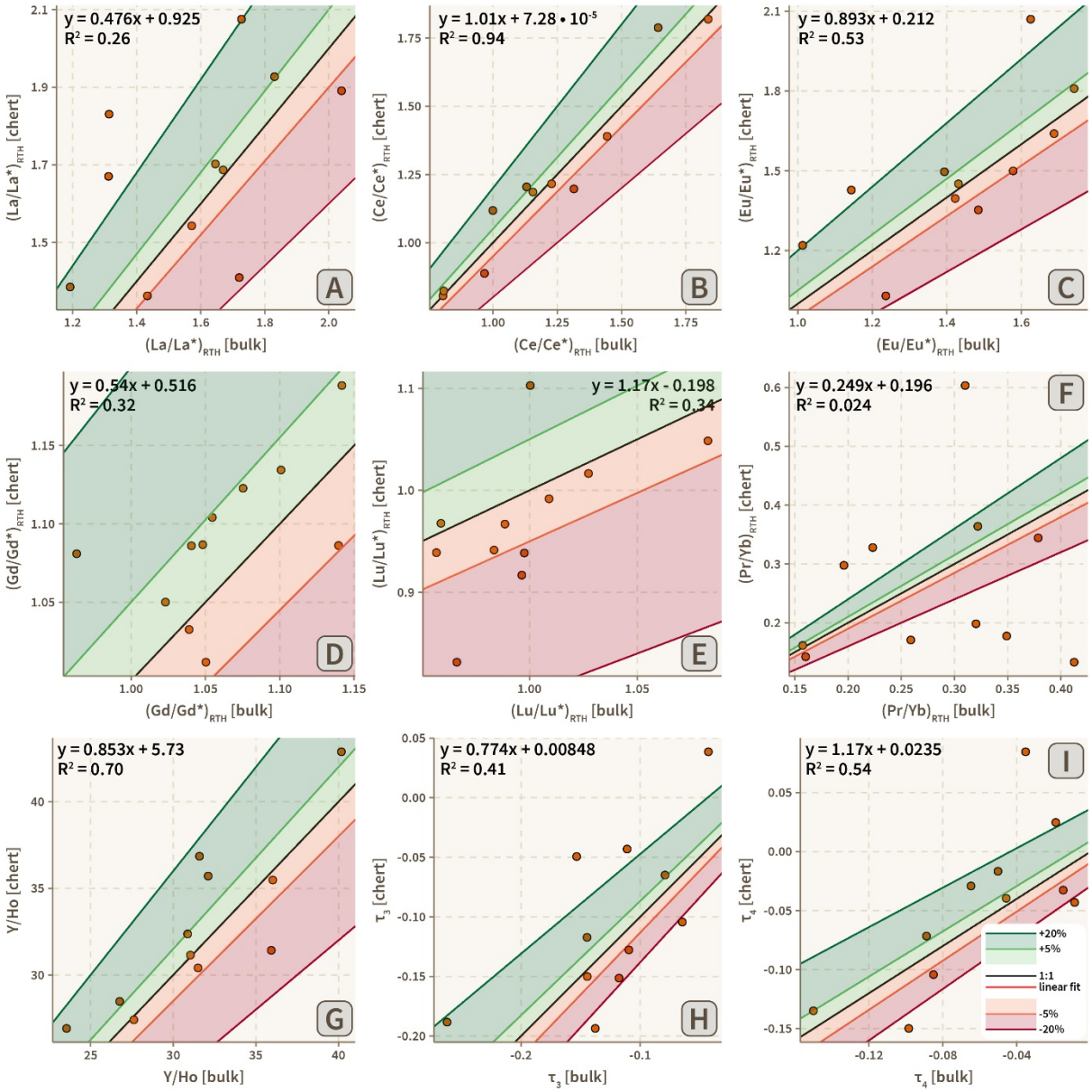

Figure 2.50. Scatterplots comparing REE+Y anomalies and ratios between bulk vs. intraformational chert samples. The 1:1, ±5%, and ±20% control lines are illustrated above.

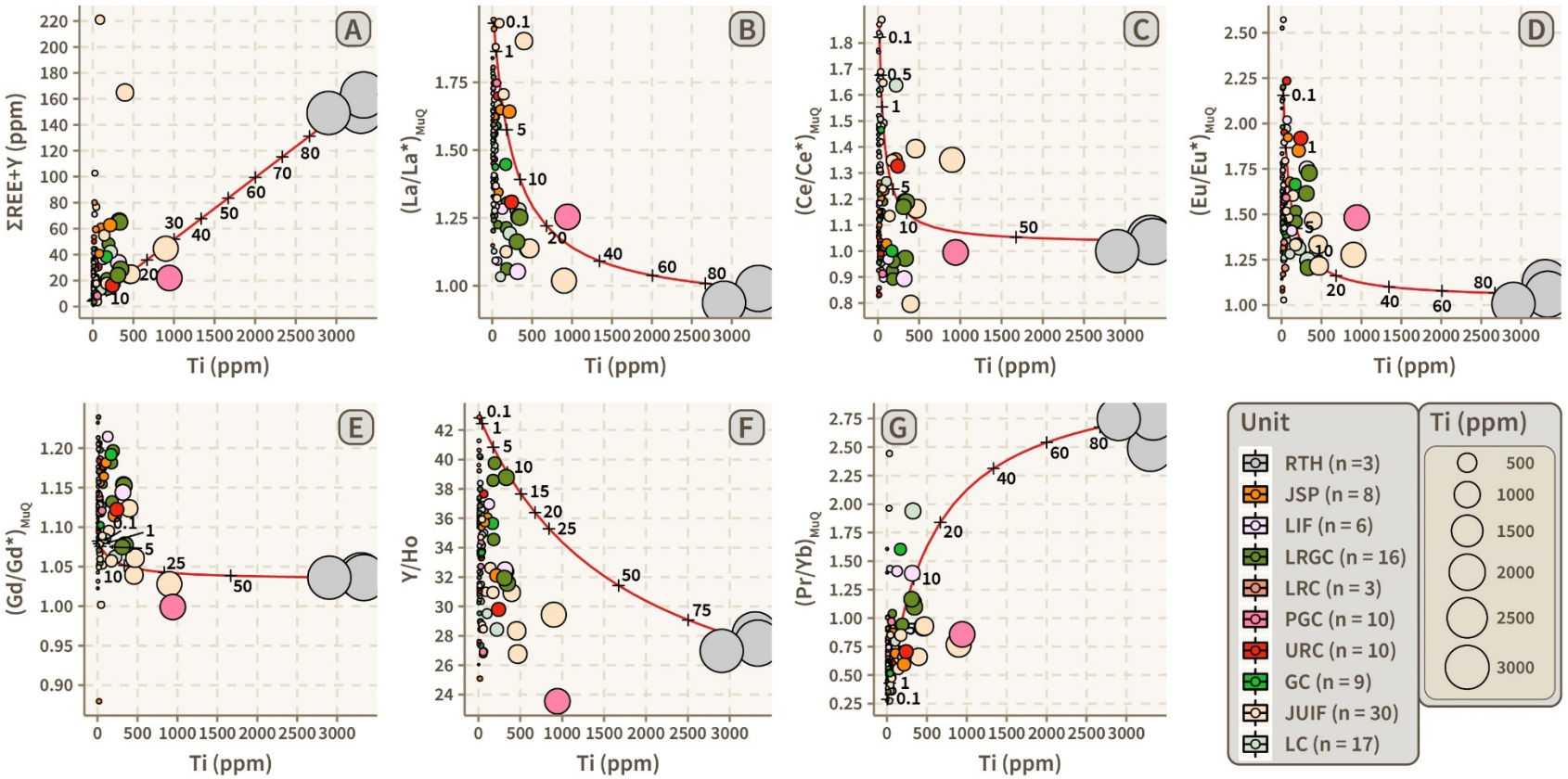

Figure 2.51. Bubble cross-plots of Ti (ppm) against REE+Y anomalies and ratios. Bubble sizes and gradients correspond to Ti (ppm) concentrations. Poor correlations indicate minimal detrital influence, but the presence of hyperbolic 'tails' suggests the effect of minor detrital element admixtures for some units.

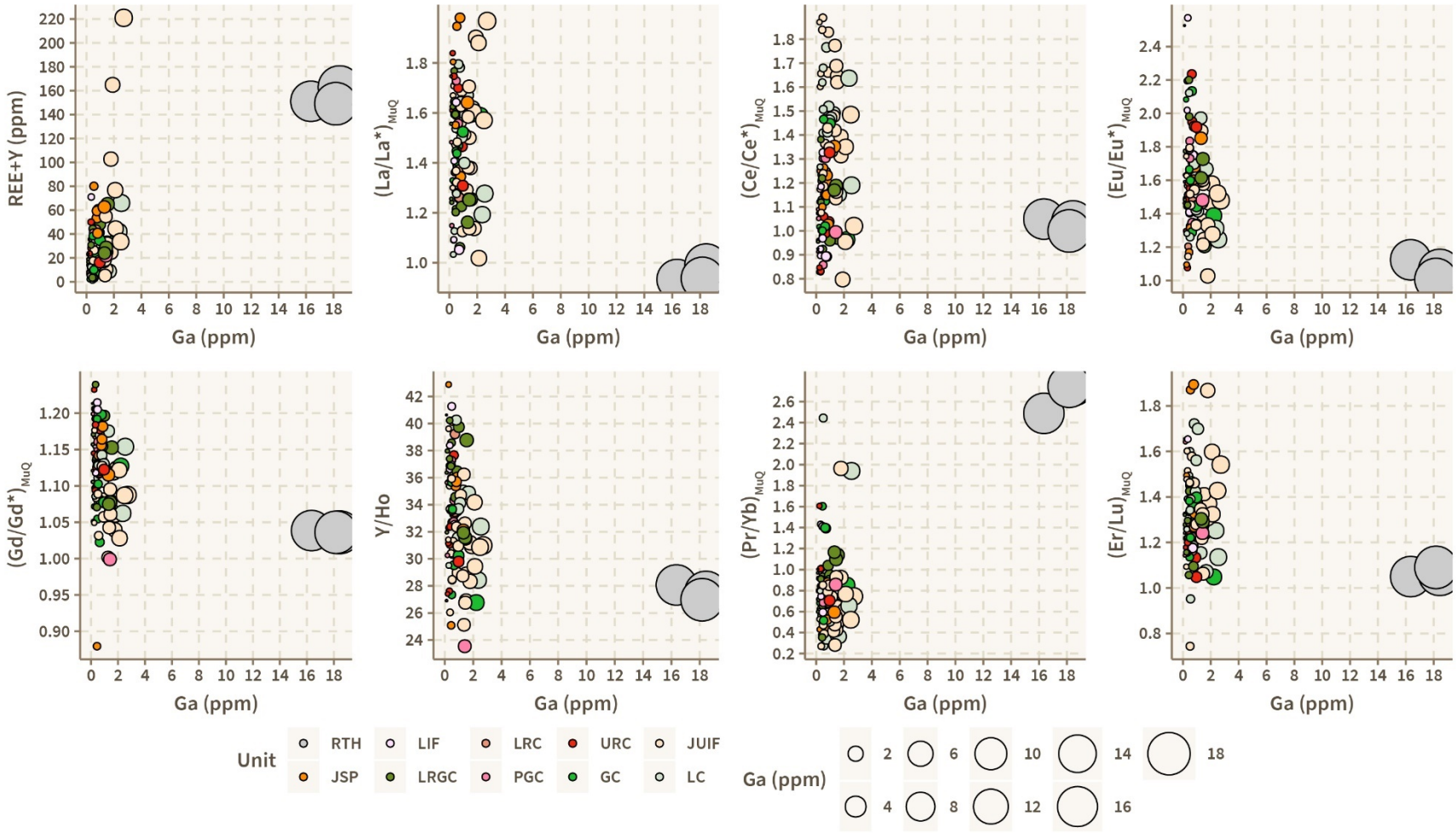

Figure 2.52. Scatterplots of REE+Y anomalies and ratios against Ga (ppm). Correlations are generally poor, but minor detrital element admixtures are indicated by hyperbolic 'tails' trending towards the detrital endmembers (RTH).

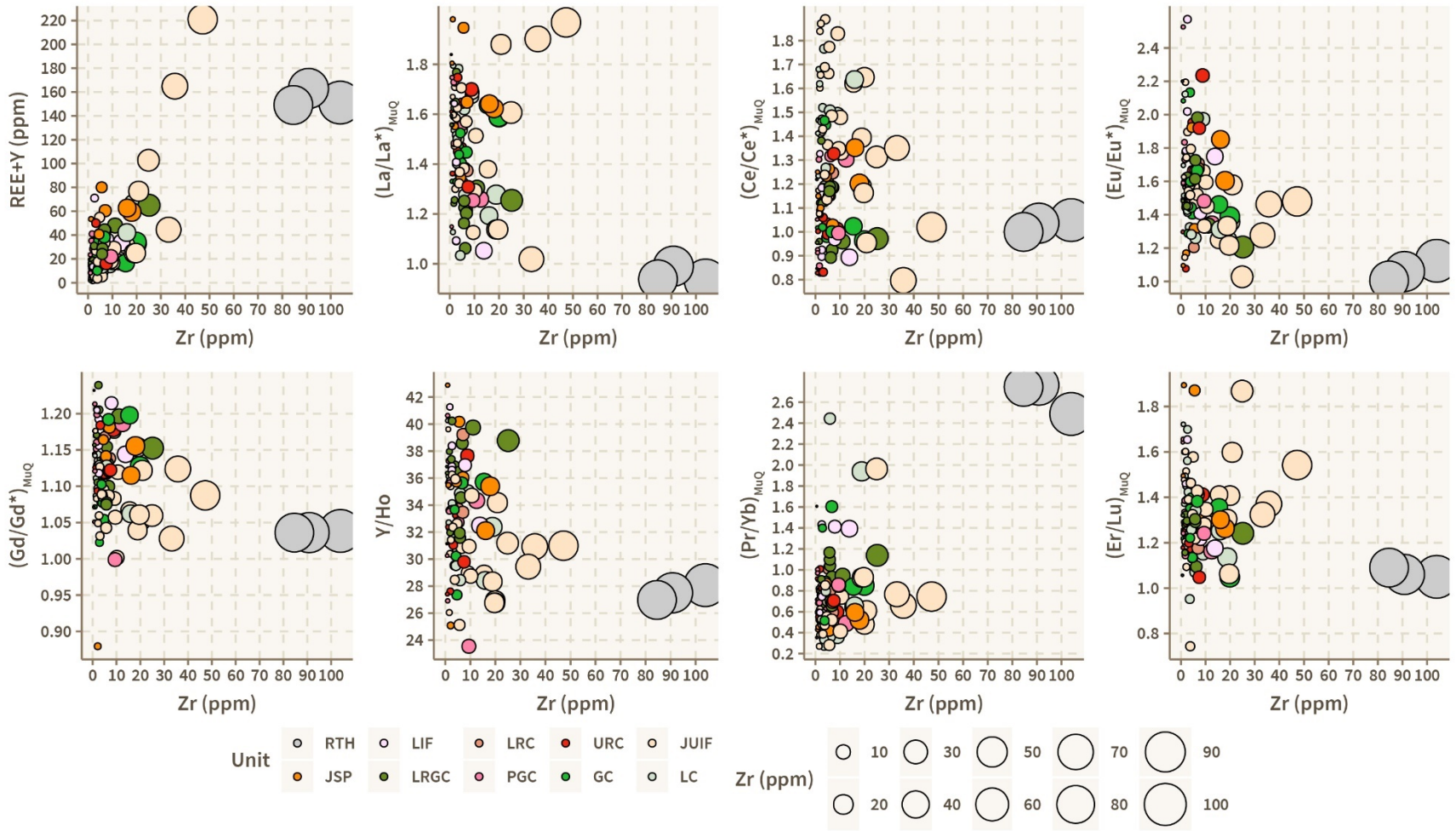

Figure 2.53. Scatterplots of REE+Y anomalies and ratios against Zr (ppm). Correlations are generally poor, but minor detrital element admixtures are indicated by hyperbolic 'tails' trending towards the detrital endmembers (RTH).

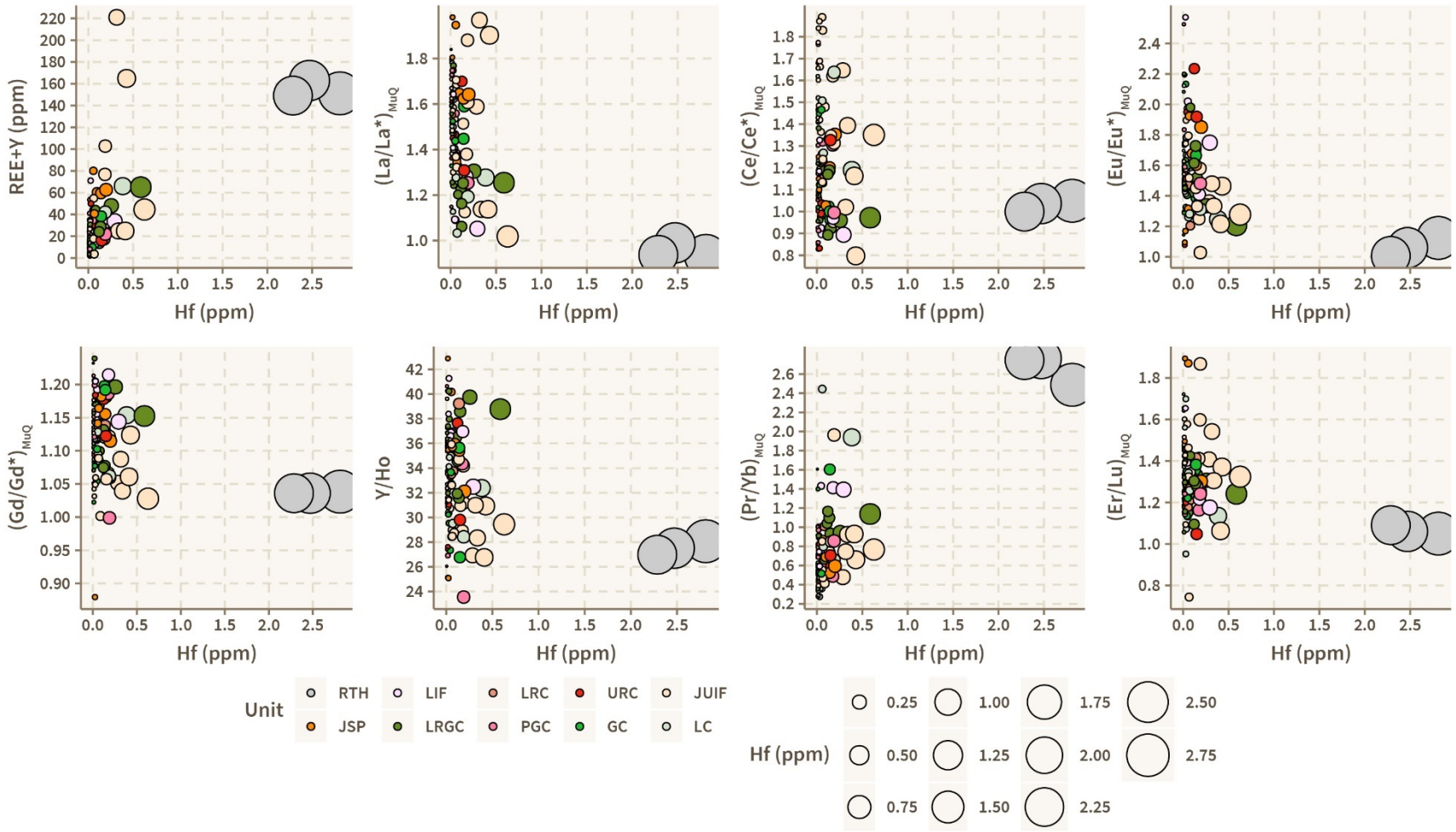

Figure 2.54. Scatterplots of REE+Y anomalies and ratios against Hf (ppm). Correlations are generally poor, but minor detrital element admixtures are indicated by hyperbolic 'tails' trending towards the detrital endmembers (RTH).

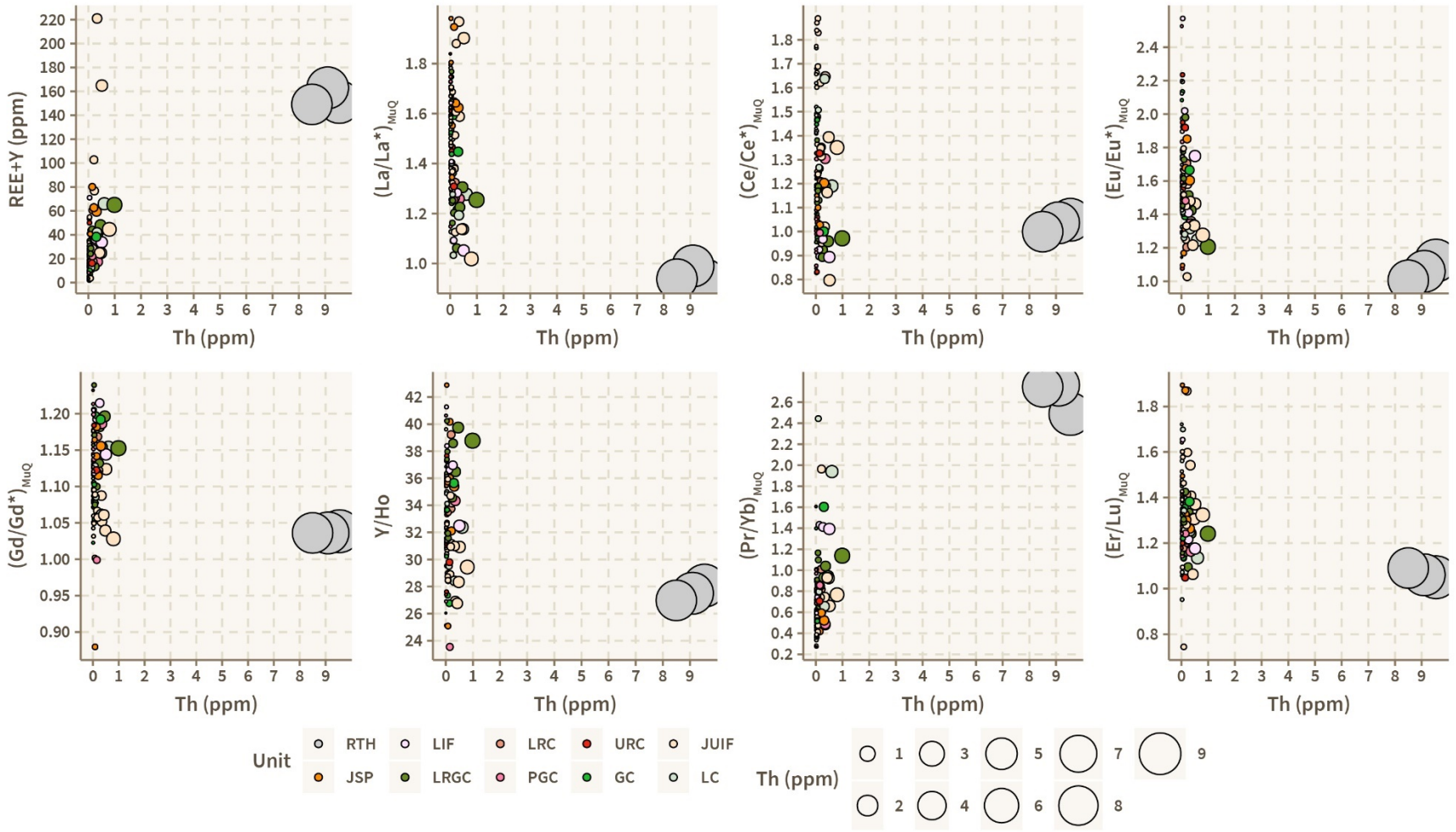

Figure 2.55. Scatterplots of REE+Y anomalies and ratios against Th (ppm). Correlations are generally poor, but minor detrital element admixtures are indicated by hyperbolic 'tails' trending towards the detrital endmembers (RTH).

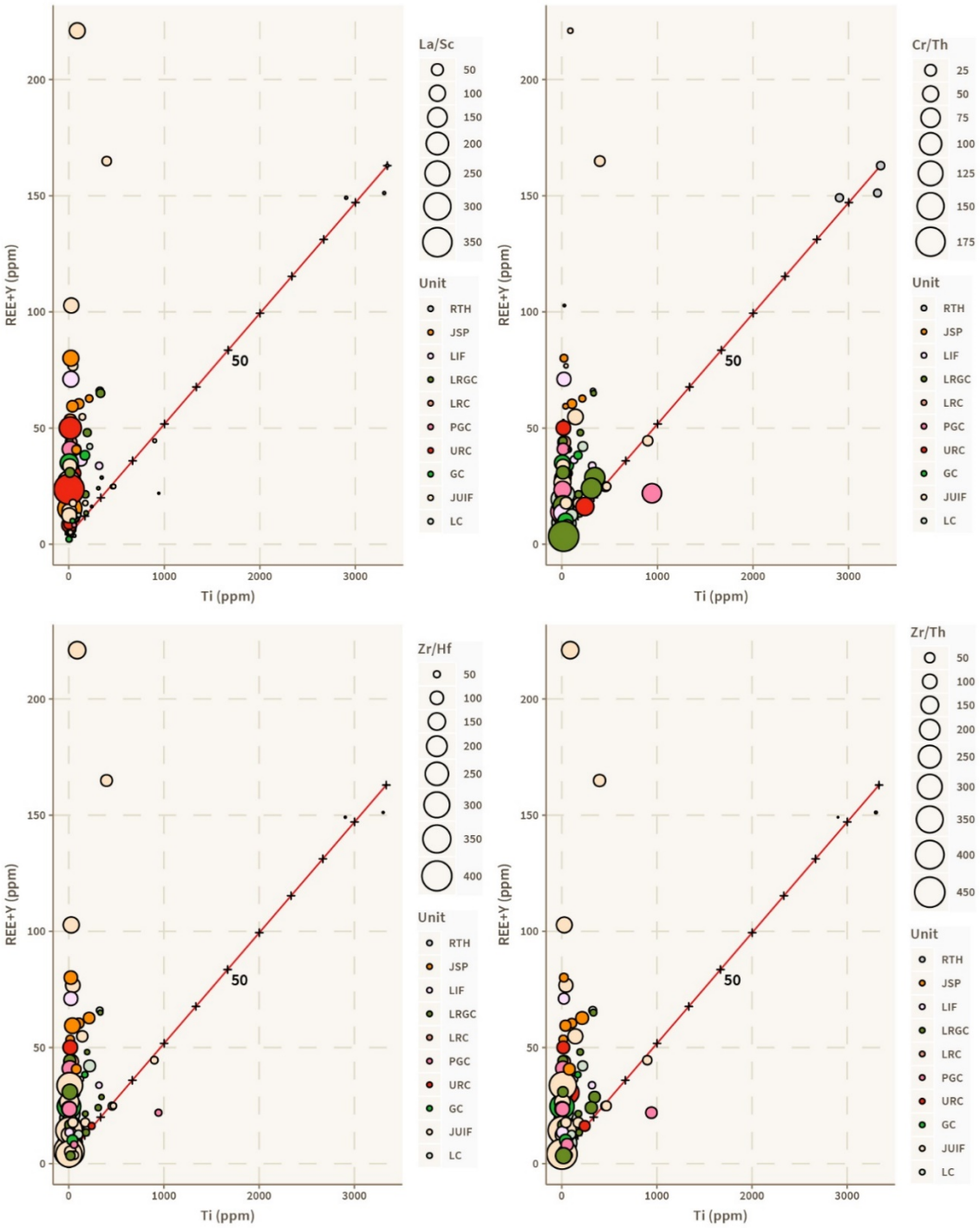

Figure 2.56. Bubble cross-plots of Ti (ppm) against REE+Y (ppm) with bubble sizes representing a suite of binary immobile element ratios. Note that mixing lines are modeled from the detritus-poor JUIF037 towards the detritus-rich RTH141. The mixing relationships show that binary element ratios decrease along the linear path towards RTH141, suggesting that the RTH represents a good approximation of the clastic detritus contaminating the IF samples.

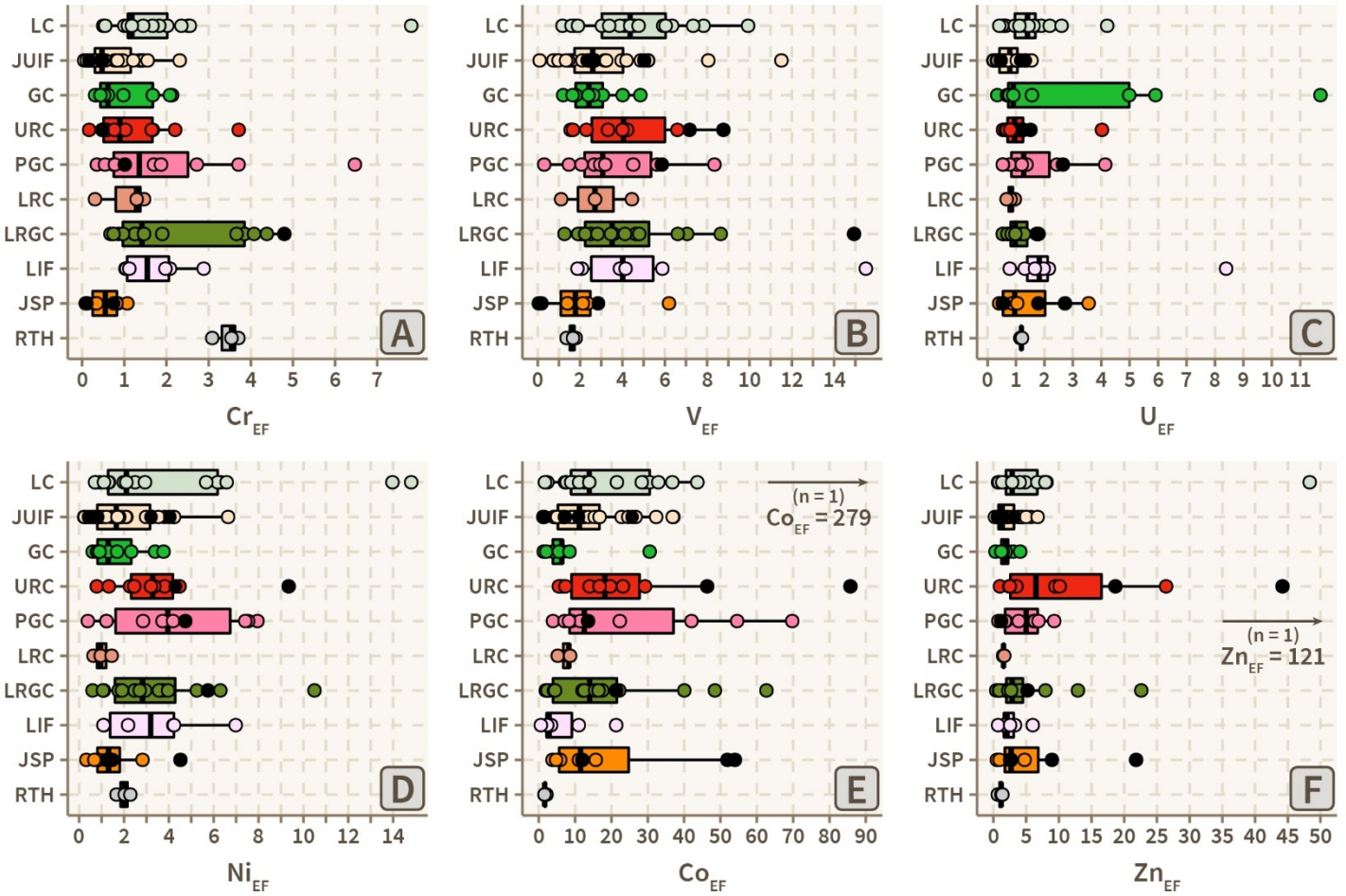

Figure 2.57. Boxplots of Cr, V, U, Ni, Co, and Zn enrichment factors (EFs) subdivided by unit. Note the overall modest authigenic enrichment (EFs < 10) in Cr, V, U, and Ni. and moderate enrichment in Co and Zn.

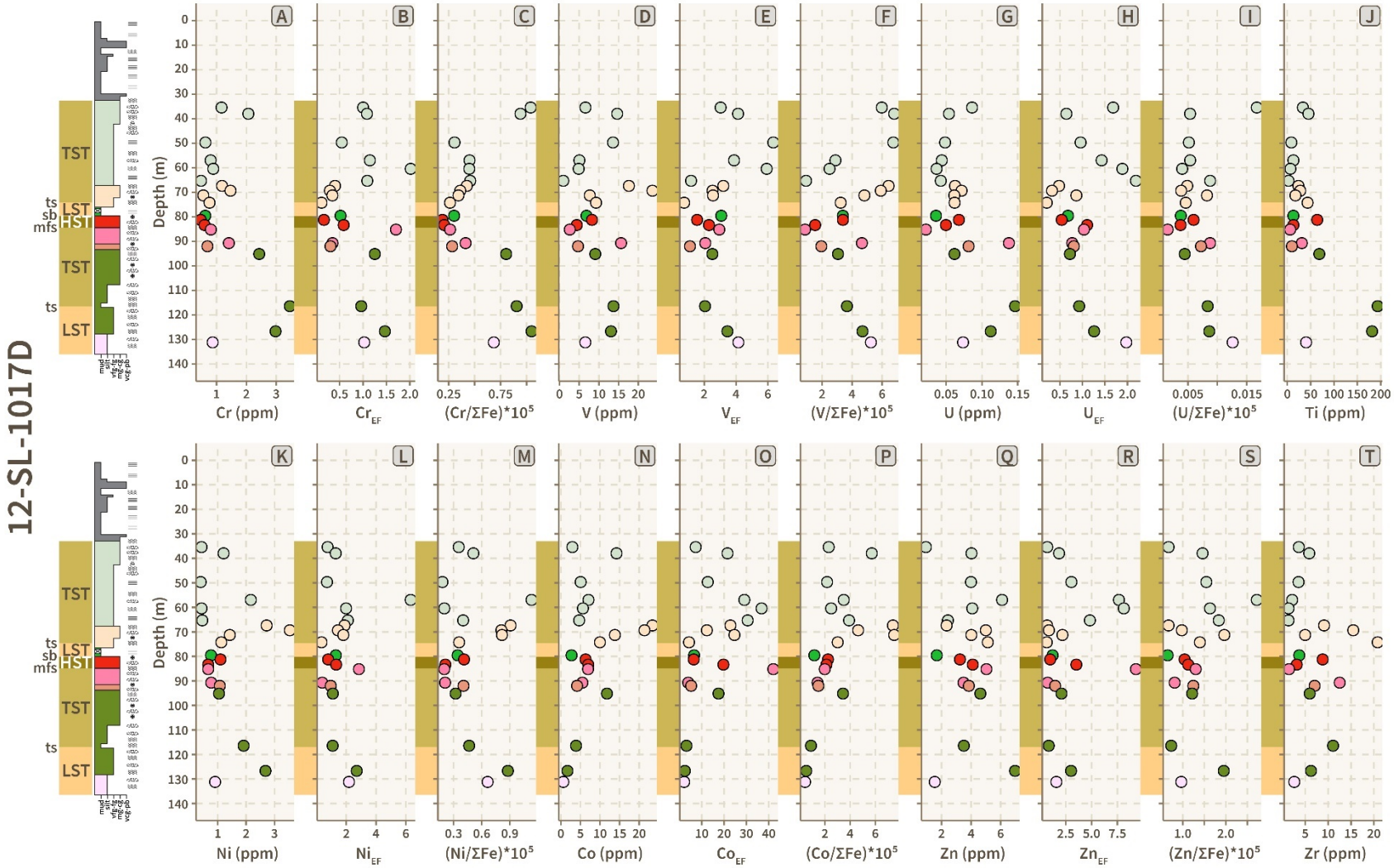

Figure 2.58. Chemostratigraphic variations in redox-sensitive trace element abundances, Fe-normalized ratios, and enrichment factors for drillhole 12-SL-1017D.

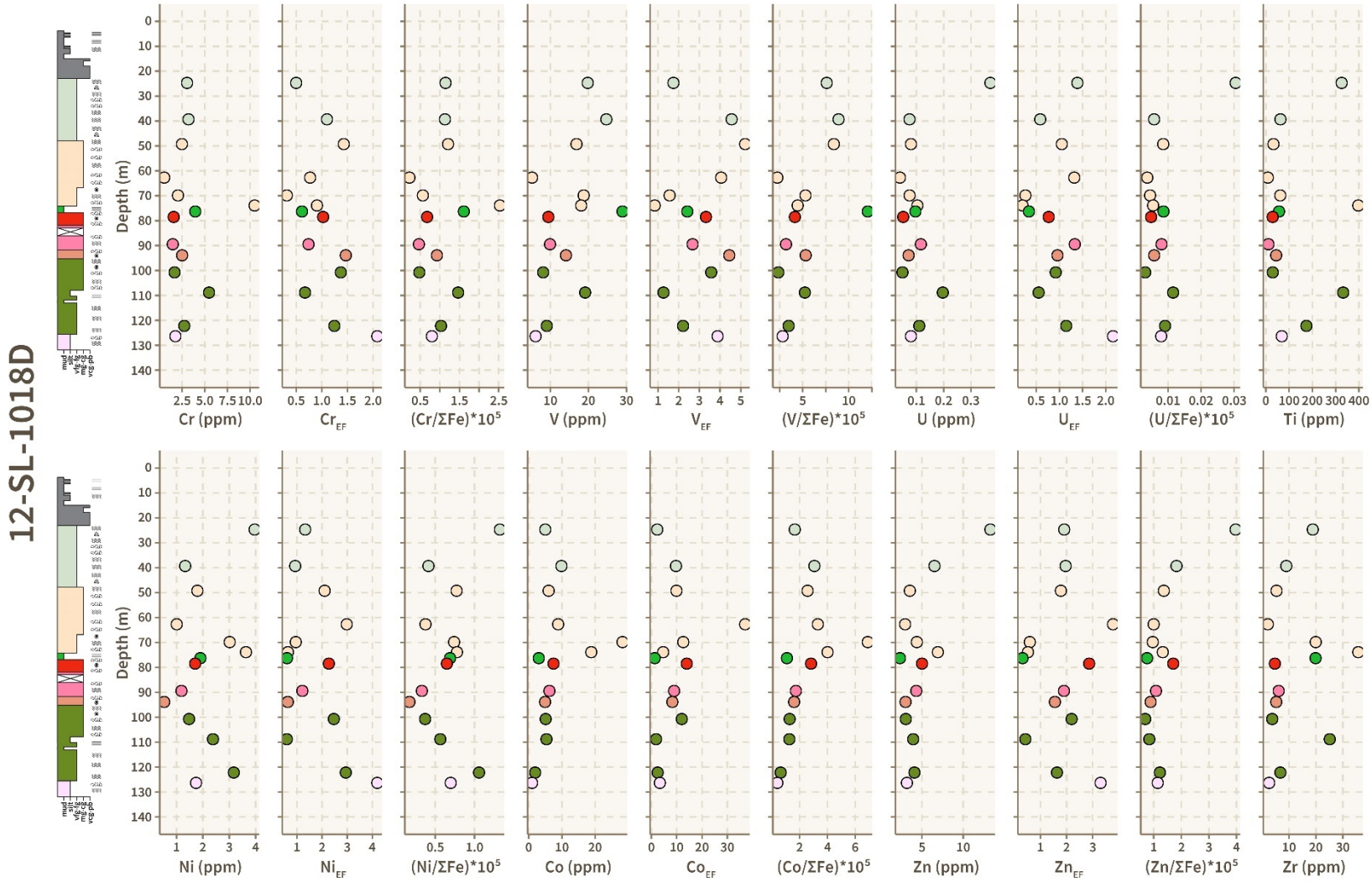

Figure 2.59. Chemostratigraphic variations in redox-sensitive trace element abundances, Fe-normalized ratios, and enrichment factors for drillhole 12-SL-1018D.

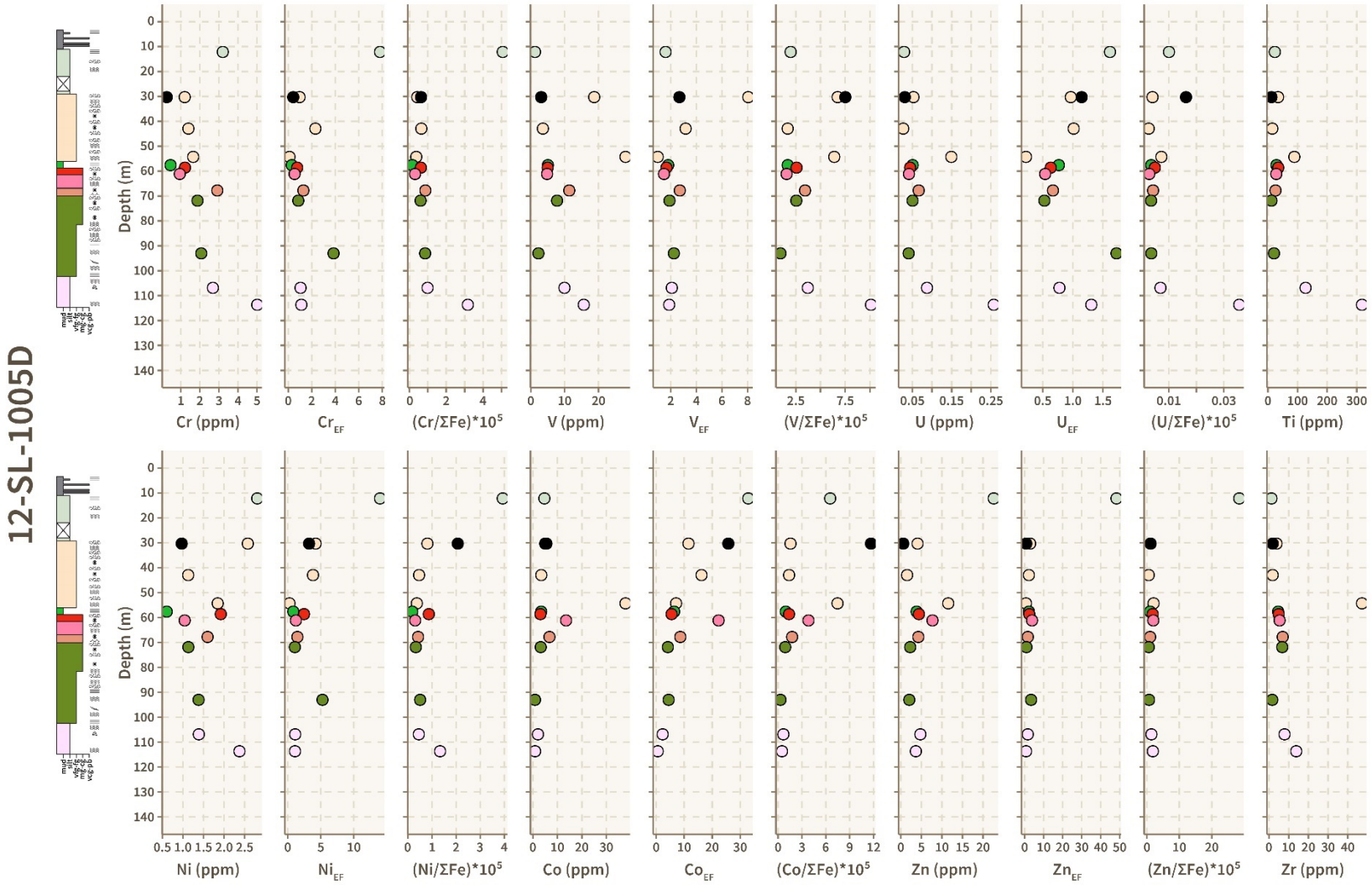

Figure 2.60. Chemostratigraphic variations in redox-sensitive trace element abundances, Fe-normalized ratios, and enrichment factors for drillhole 12-SL-1005D. Black dots correspond to chert subsamples.

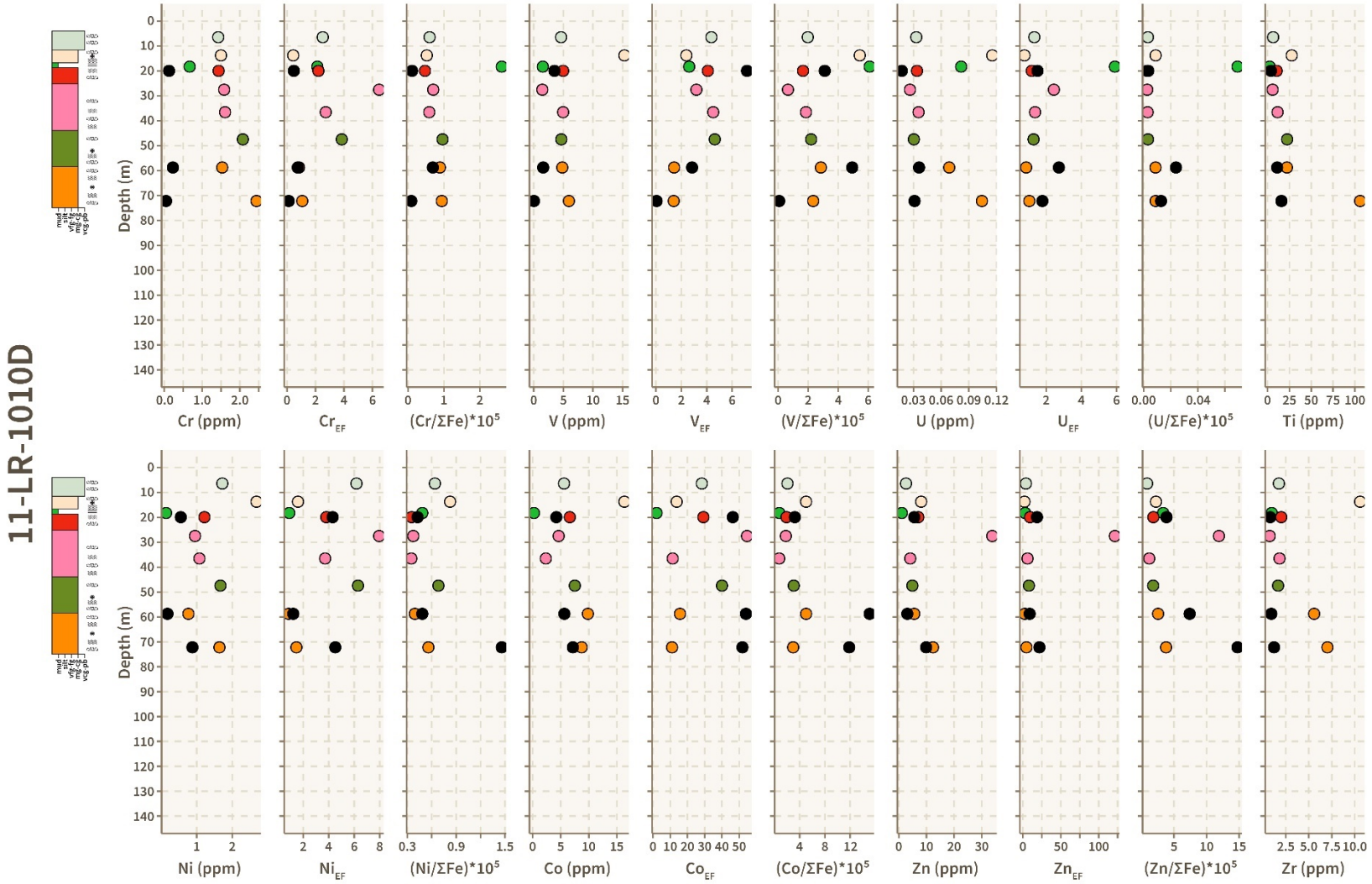

Figure 2.61. Chemostratigraphic variations in redox-sensitive trace element abundances, Fe-normalized ratios, and enrichment factors for drillhole 11-LR-1010D. Black dots correspond to chert subsamples.

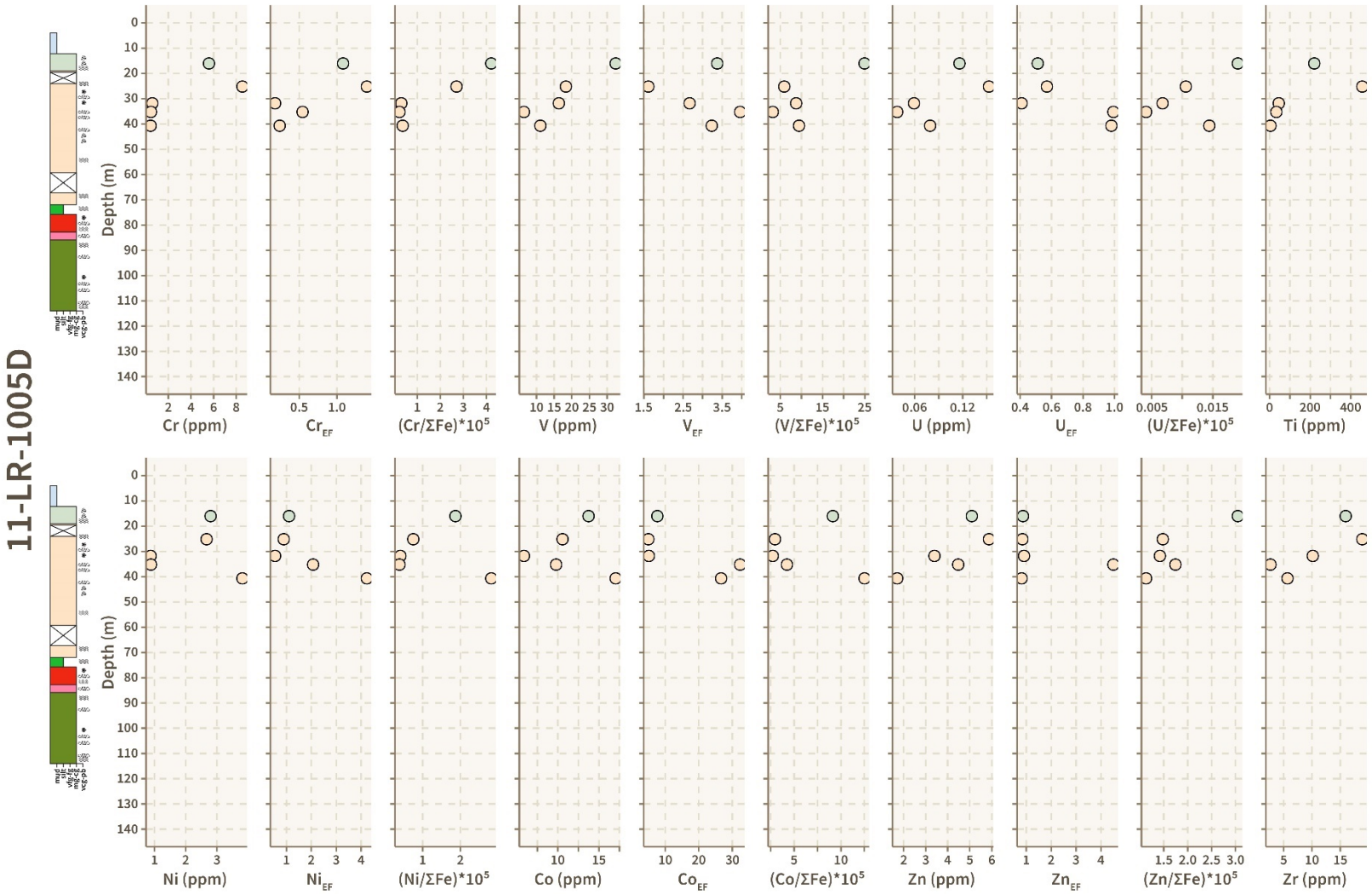

Figure 2.62. Chemostratigraphic variations in redox-sensitive trace element abundances, Fe-normalized ratios, and enrichment factors for drillhole 11-LR-1005D.

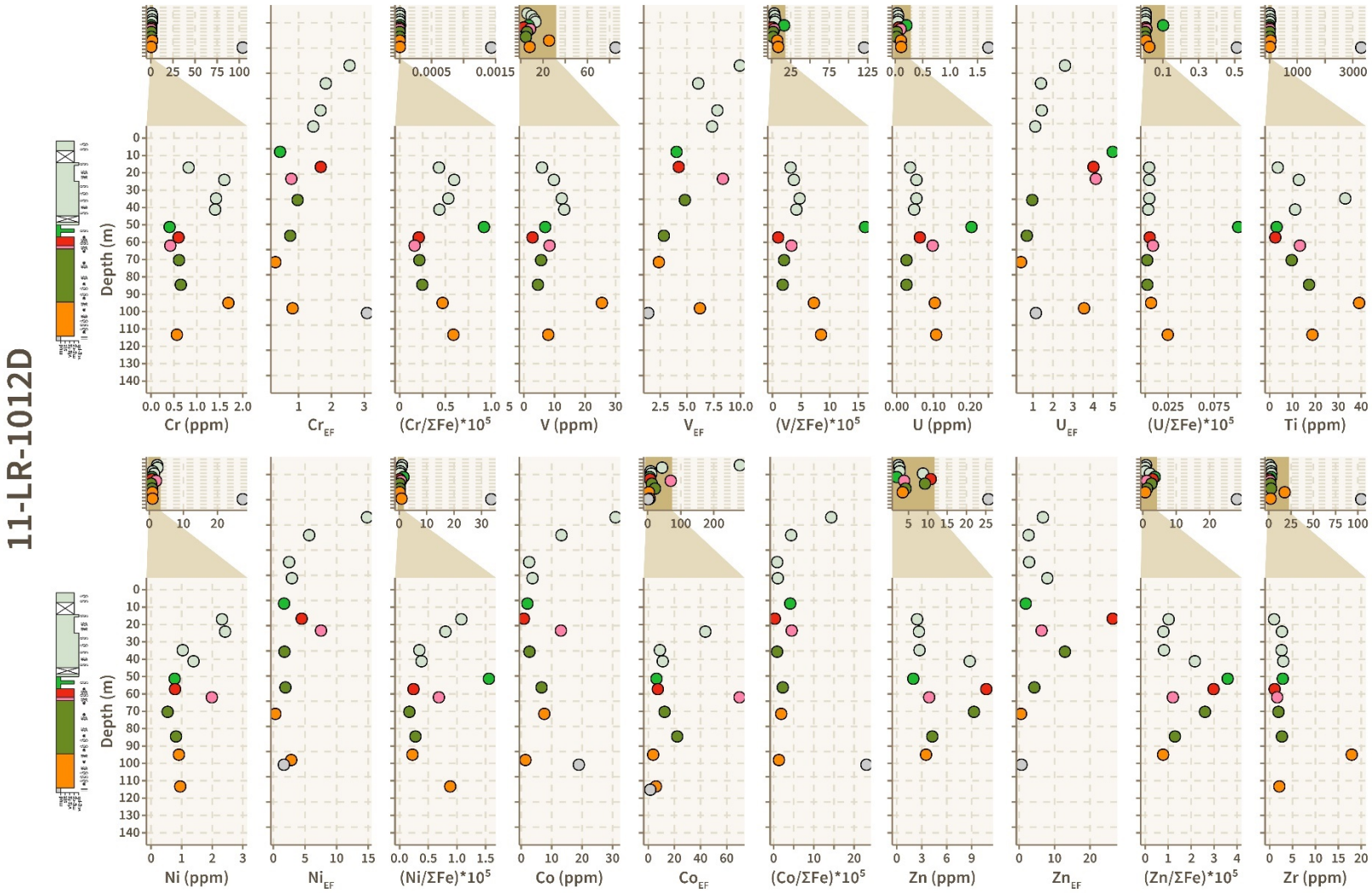

Figure 2.63. Chemostratigraphic variations in redox-sensitive trace element abundances, Fe-normalized ratios, and enrichment factors for drillhole 11-LR-1012D.

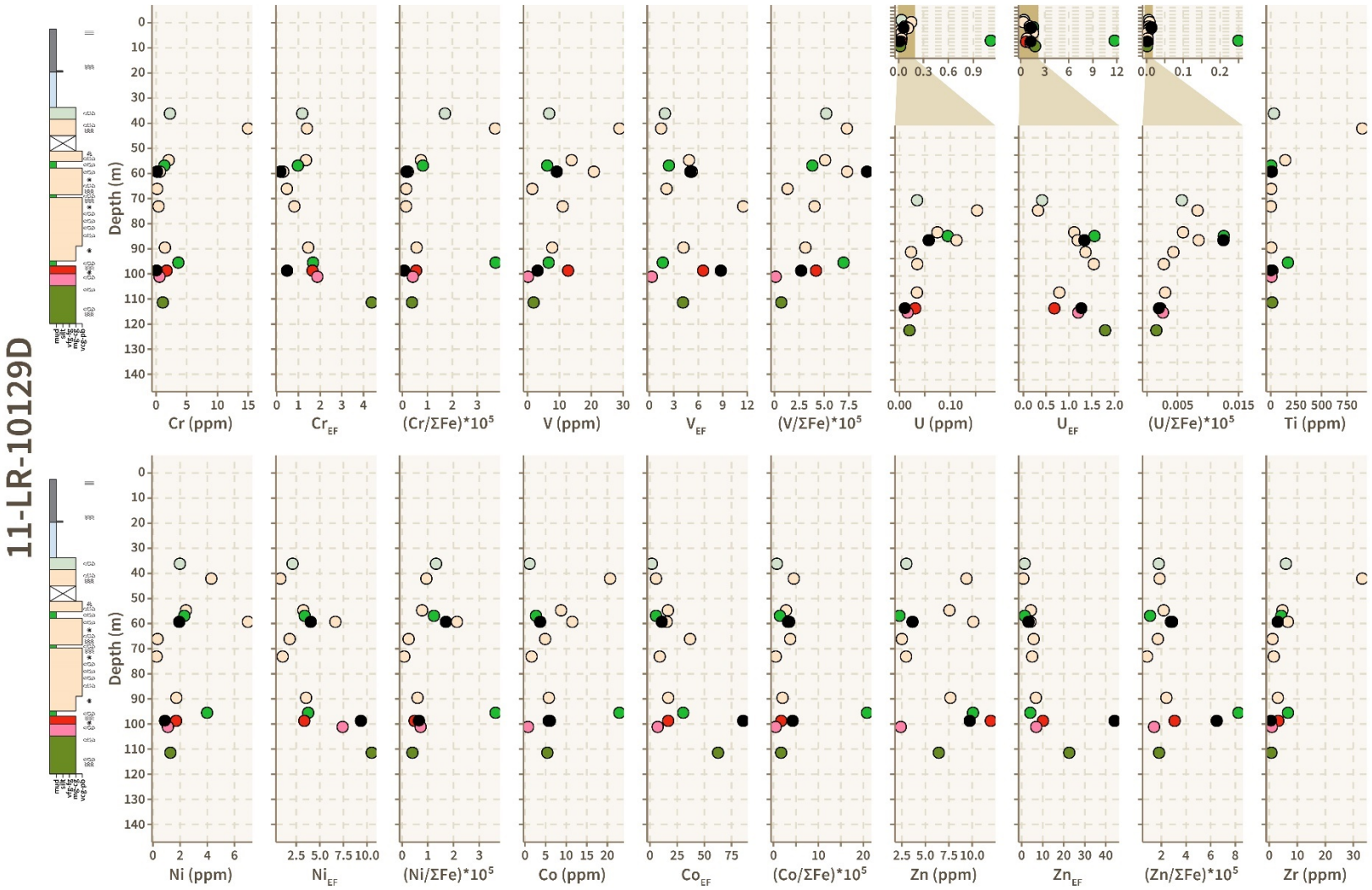

Figure 2.64. Chemostratigraphic variations in redox-sensitive trace element abundances, Fe-normalized ratios, and enrichment factors for drillhole 11-LR-1029D. Black dots correspond to chert subsamples.

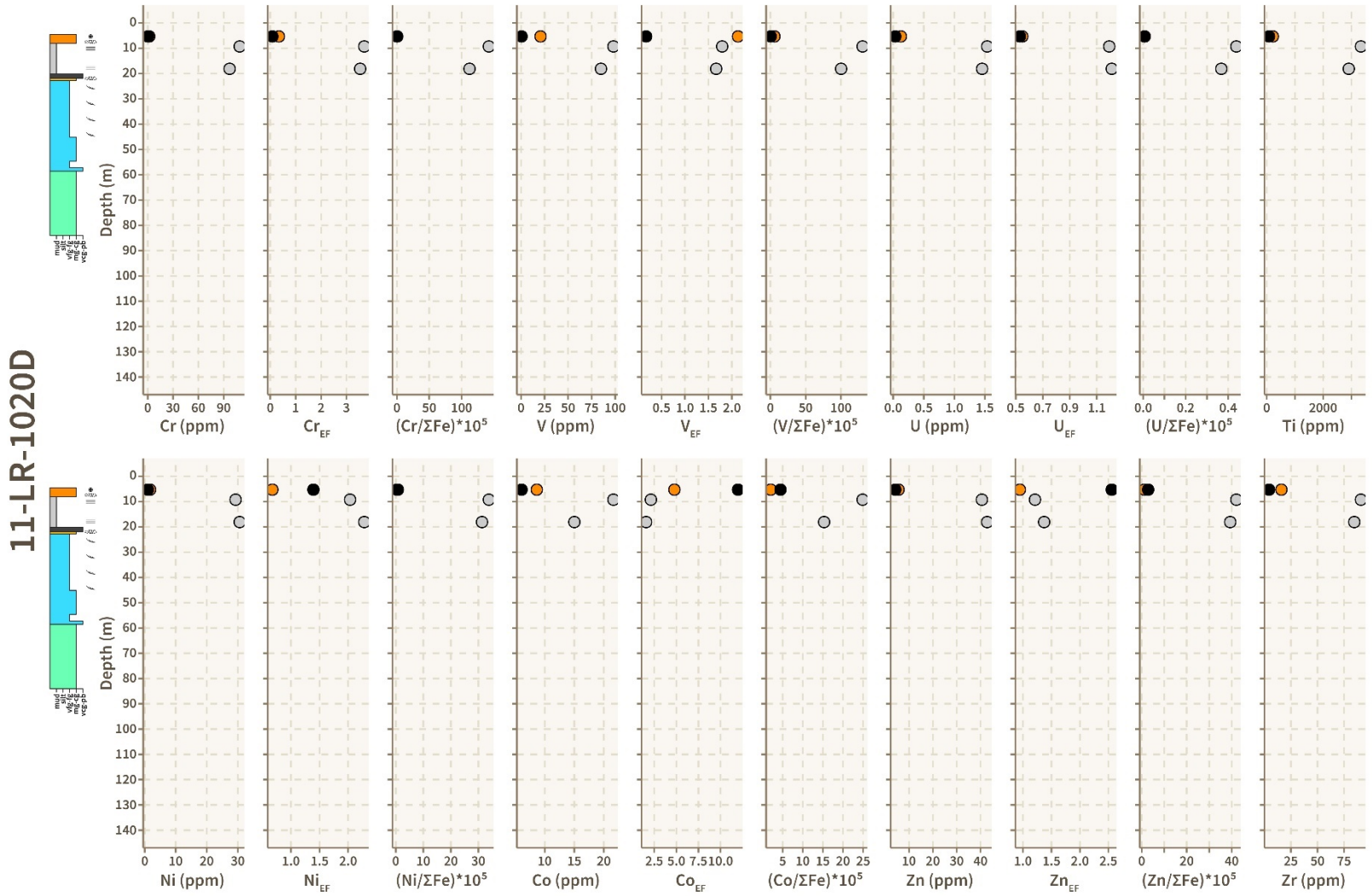

Figure 2.65. Chemostratigraphic variations in redox-sensitive trace element abundances, Fe-normalized ratios, and enrichment factors for drillhole 11-LR-1020D. Black dots correspond to chert subsamples.

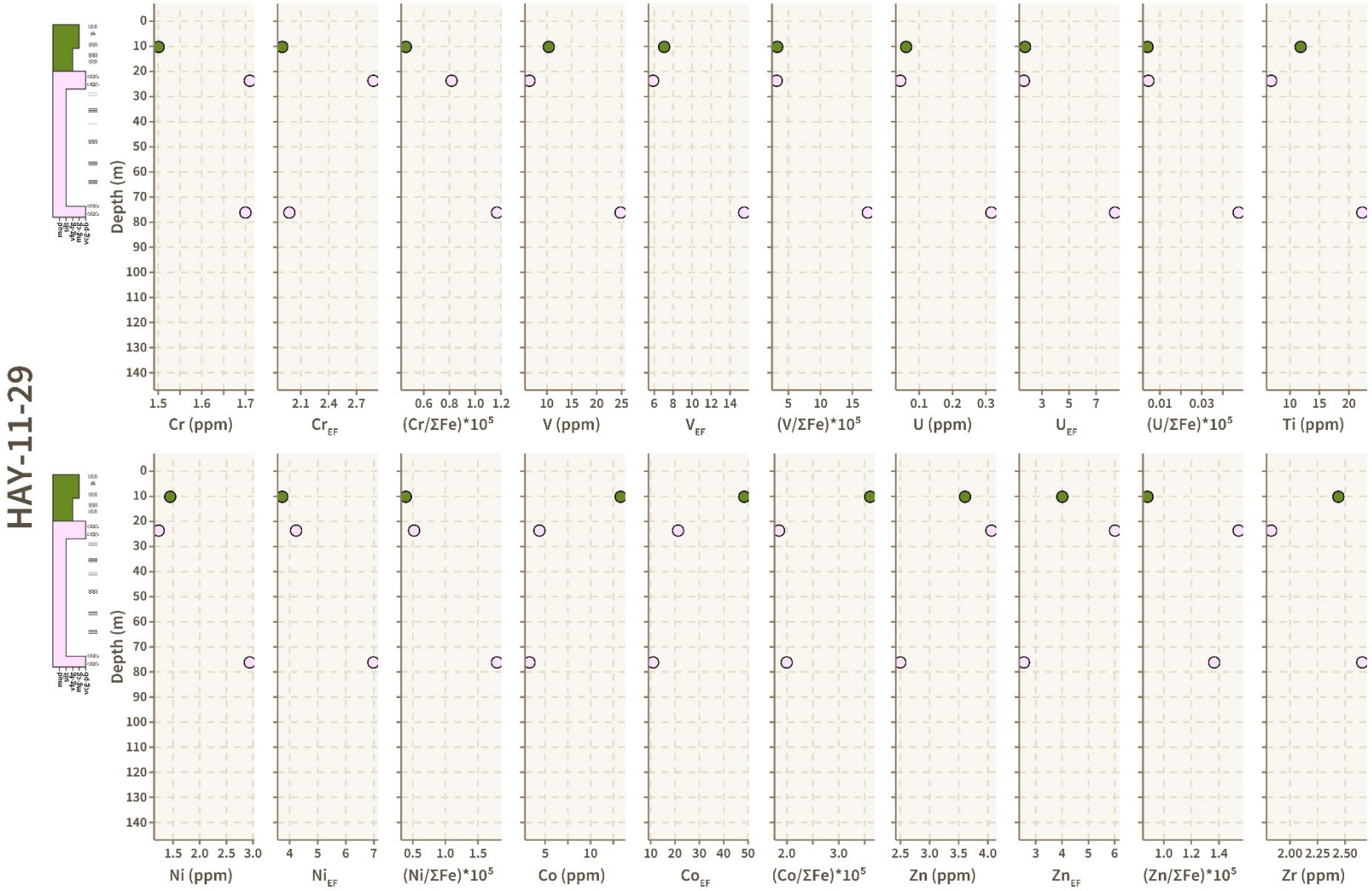

Figure 2.66. Chemostratigraphic variations in redox-sensitive trace element abundances, Fe-normalized ratios, and enrichment factors for drillhole HAY-11-29.

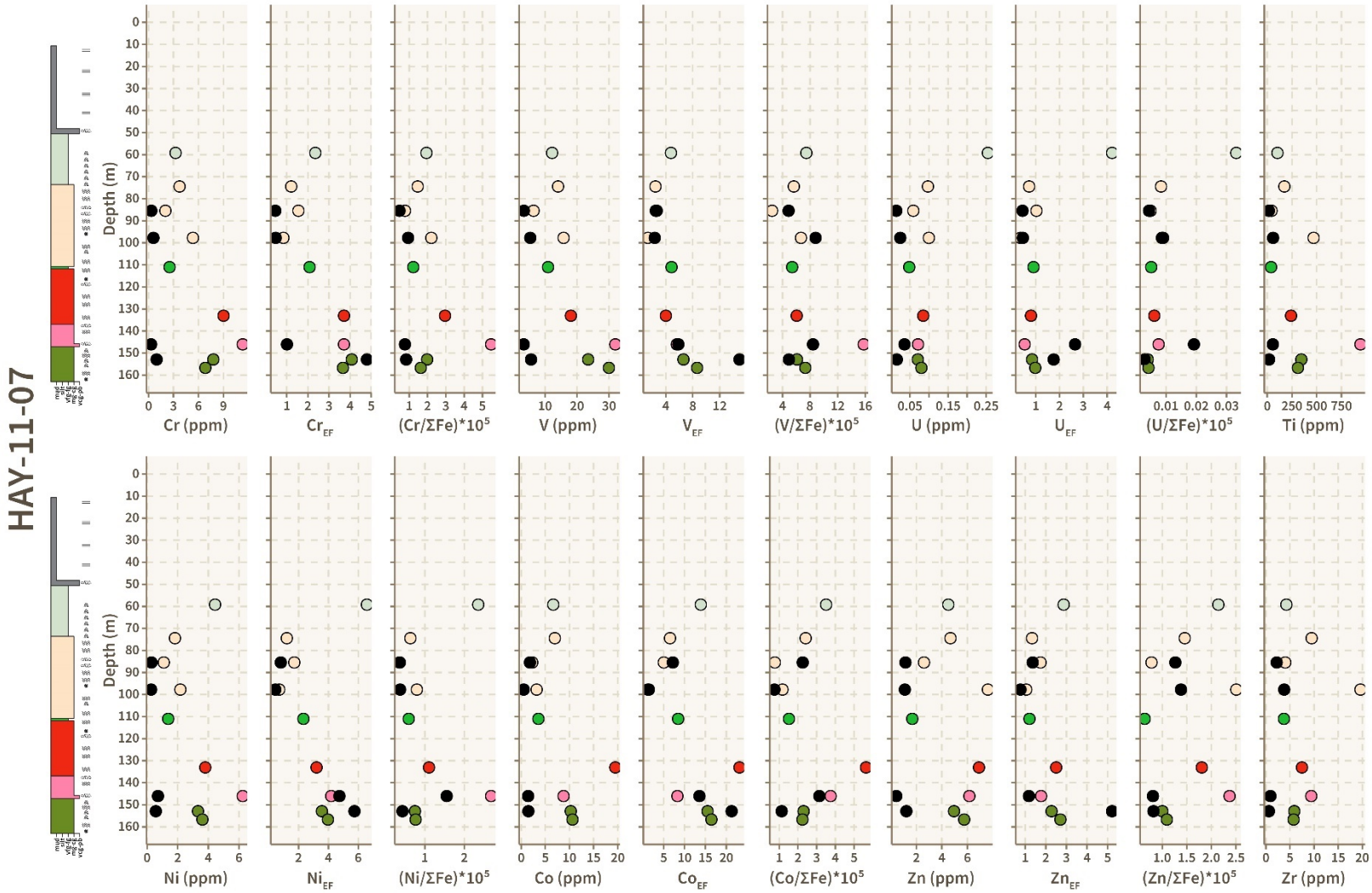

Figure 2.67. Chemostratigraphic variations in redox-sensitive trace element abundances, Fe-normalized ratios, and enrichment factors for drillhole HAY-11-07. Black dots correspond to chert subsamples.

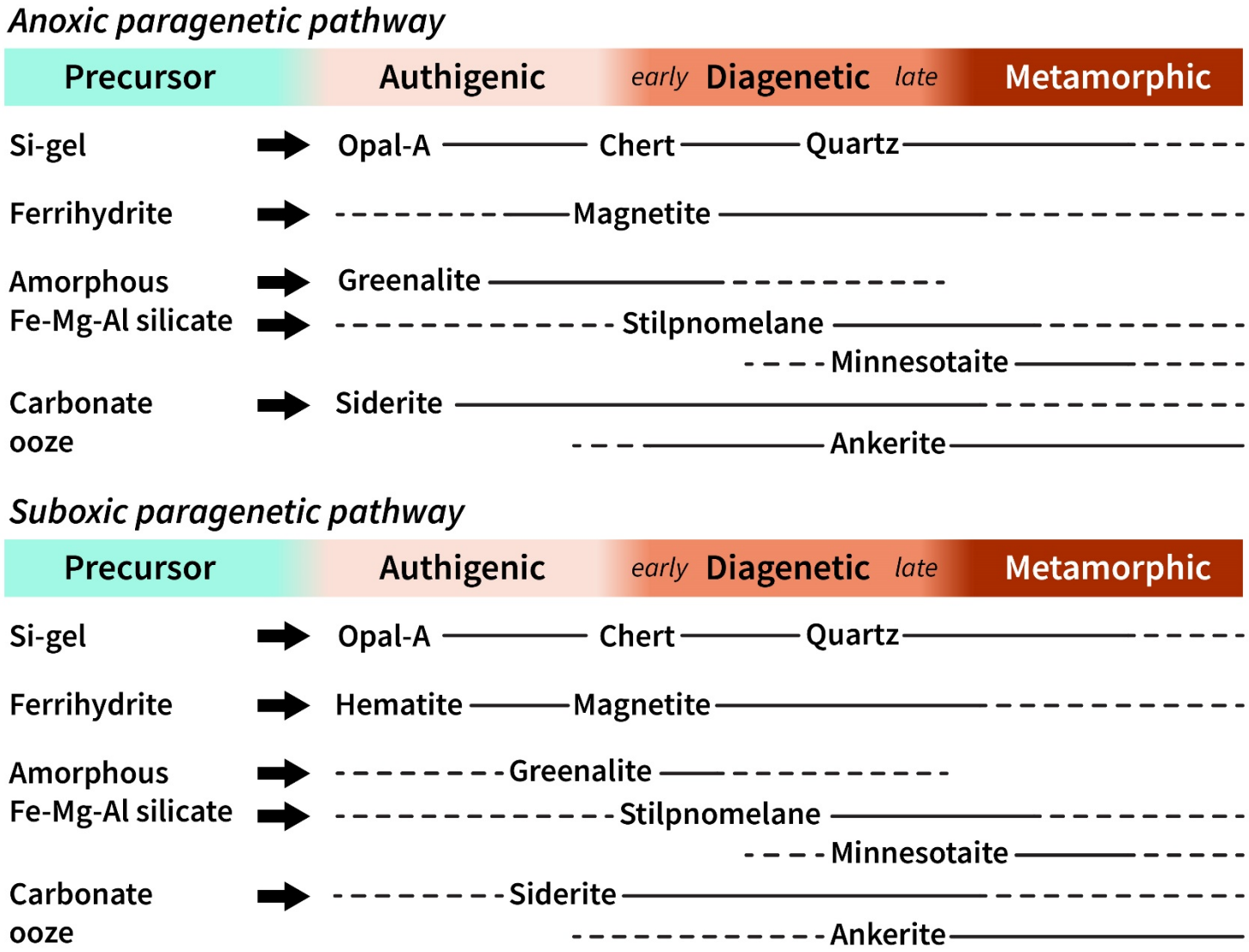

Figure 2.68. Inferred pathways for anoxic and suboxic paragenesis. The silicate-carbonate facies follow the former, whereas the hematite-magnetite, hematite-carbonate, and magnetite-carbonate facies follow the latter.

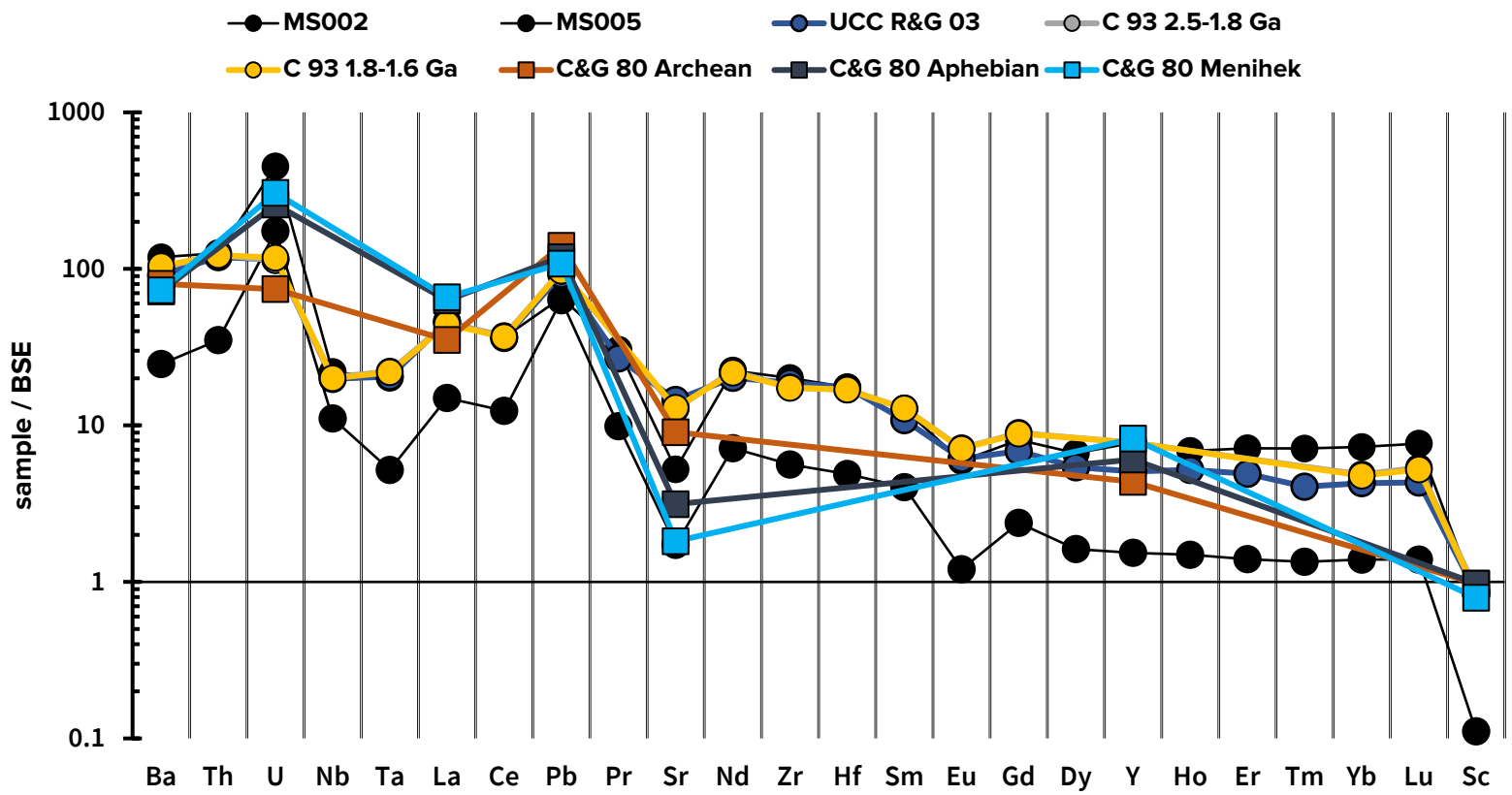

Figure 2.69. Extended normalized trace element diagrams of the Menihek Slate (MS) relative to UCC (Rudnick and Gao, 2003), and Archean and Proterozoic shale composites of Condie (1993) and Cameron and Garrels (1980). Values are normalized to Bulk Silicate Earth (BSE).

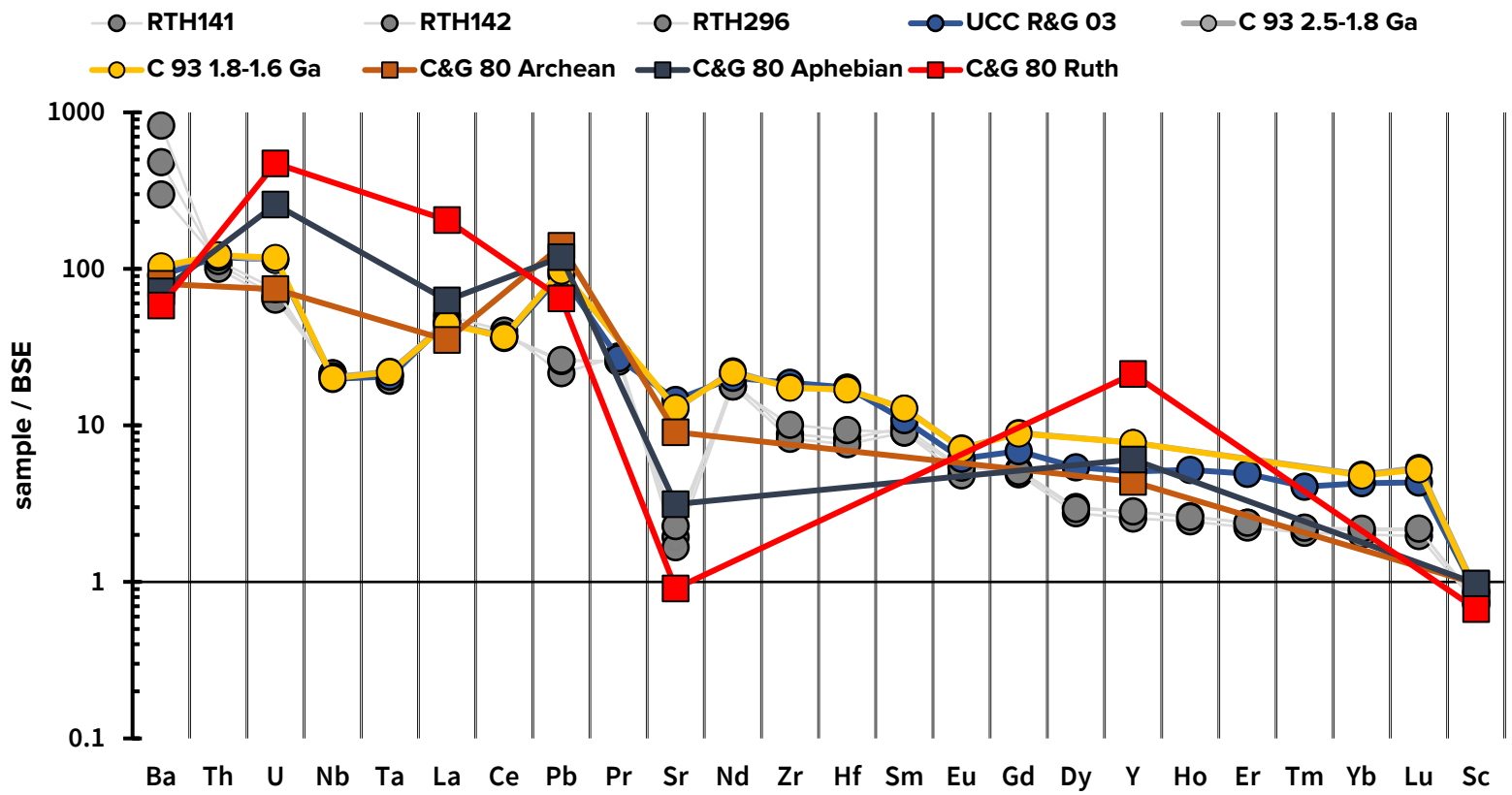

Figure 2.70. Extended normalized trace element diagrams of the Ruth Slate Member (RTH) relative to UCC (Rudnick and Gao, 2003), and Archean and Proterozoic shale composites of Condie (1993) and Cameron and Garrels (1980). Values are normalized to Bulk Silicate Earth (BSE).

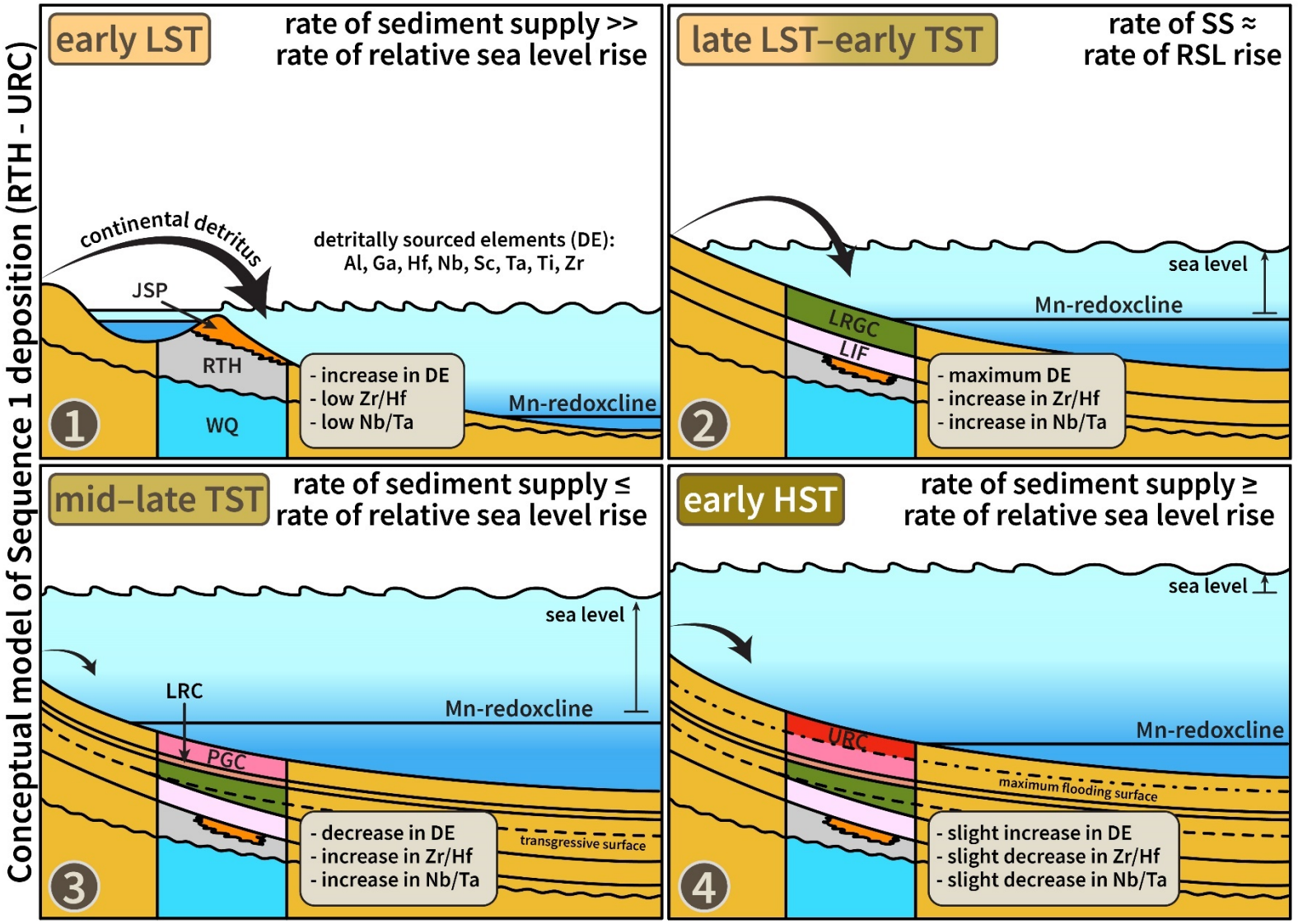

Figure 2.71. Conceptual model of Sequence 1 deposition encompassing early LST to early HST strata (RTH to URC) and corresponding changes in detrital element (DE) abundances and ratios, sea level, and redoxcline depth.

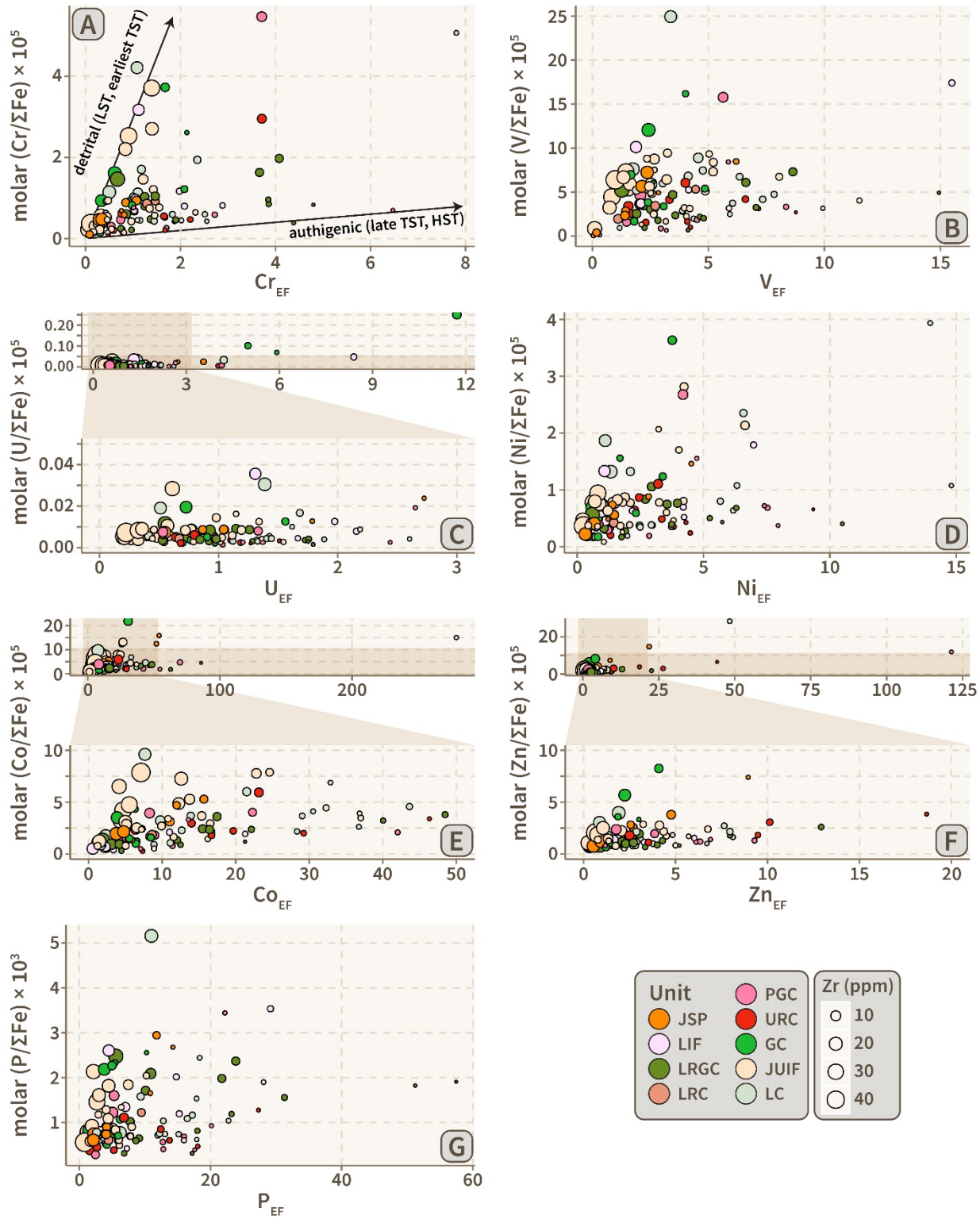

Figure 2.72. Bivariate plots of TE and P EFs against their respective Fe-normalized ratios.

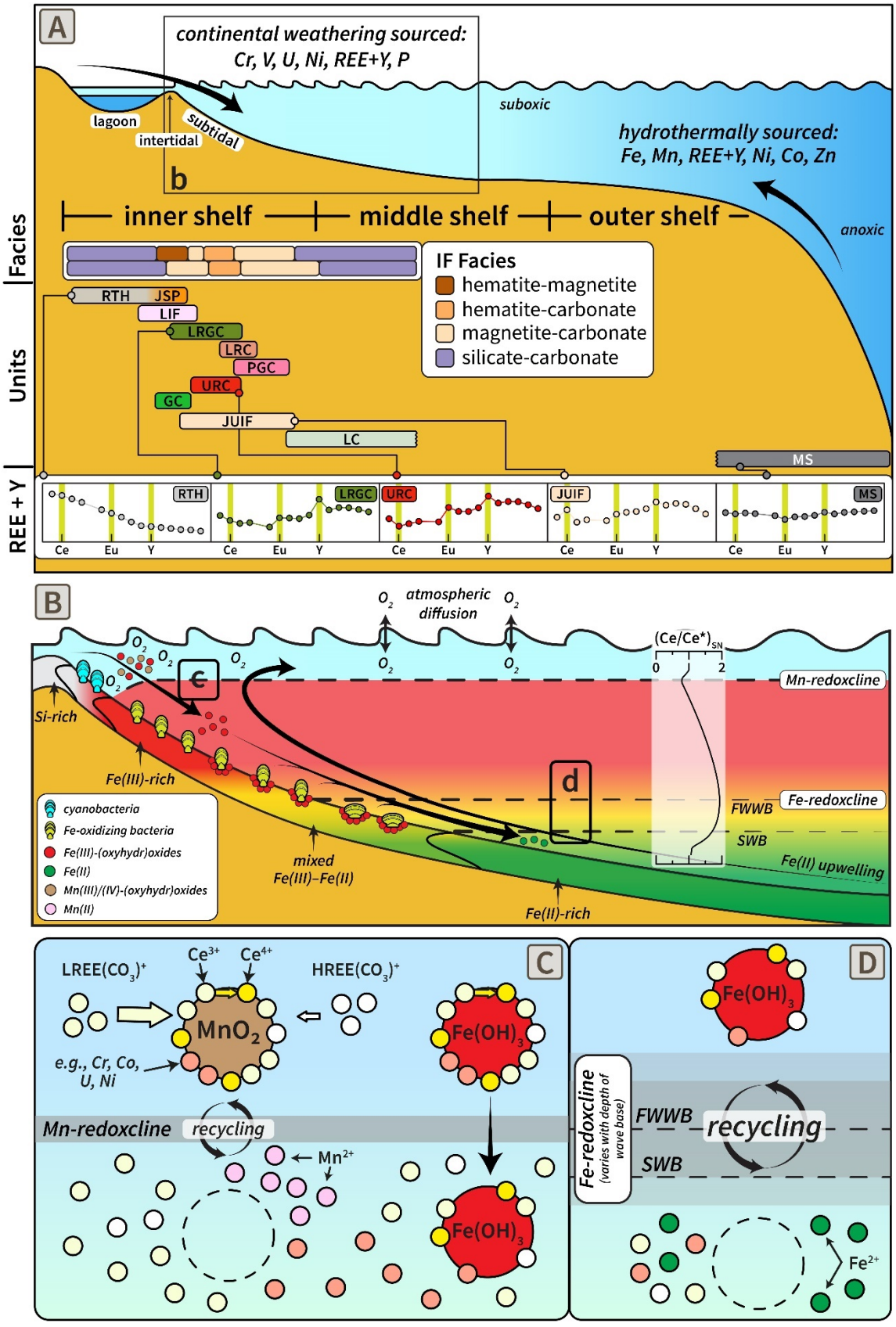
A
continental weathering sourced:
Cr, V, U, Ni, REE+Y, P
lagoon
intertidal
subtidal
b
suboxic
hydrothermally sourced:
Fe, Mn, REE+Y, Ni, Co, Zn
anoxic
inner shelf
middle shelf
outer shelf
Facies
Units
REE + Y
IF Facies
hematite-magnetite
hematite-carbonate
magnetite-carbonate
silicate-carbonate
RTH
JSP
LIF
LRGC
LRC
PGC
URC
GC
JUIF
LC
MS
Ce
Eu
Y
B
atmospheric diffusion
(Ce/Ce*)SN
0
2
Mn-redoxcline
Fe-redoxcline
FWWB
SWB
Fe(II) upwelling
Si-rich
Fe(III)-rich
c
d
mixed Fe(III)–Fe(II)
Fe(II)-rich
cyanobacteria
Fe-oxidizing bacteria
Fe(III)-(oxyhydr)oxides
Fe(II)
Mn(III)/(IV)-(oxyhydr)oxides
Mn(II)
C
LREE(CO3)+
Ce3+
Ce4+
HREE(CO3)+
MnO2
Fe(OH)3
e.g., Cr, Co, U, Ni
Mn-redoxcline
recycling
Mn2+
D
Fe-redoxcline
(varies with depth of wave base)
FWWB
SWB
recycling
Fe2+

Figure 2.73. Summary figure illustrating the depositional, mineralogical, and geochemical trends deciphered from the Sokoman IF. (A) Depositional model, element sources, and variations in mineralogical facies and REE+Y patterns across the shallow shelf system (modified from Pufahl, 2010); (B) Conceptual model of redox stratification with spatially close, but distinct Mn- and Fe-redoxclines that collectively lie within the photic zone. Greater light intensities and nutrient availability in shallow surface waters are conducive to photosynthetic oxygen production, resulting in the precipitation of Mn- and Fe-(oxyhydr)oxides above a shallow Mn-redoxcline. Across the Mn-redox interface, Mn-(oxyhydr)oxides are rapidly dissolved, thereby generating positive Ce/Ce* in the ambient seawater with increasing depth. In slightly deeper waters, lower light intensities and a more consistent upwelling flux of Fe(II) are more conducive to photoferrotrophy, resulting in Fe-oxidation in a dominantly mixed Fe(II)-Fe(III) substrate. The vertical extent of the Fe-redoxcline is diffuse and is largely affected by the depth of the wave bases; (C–D) Precipitation and dissolution of Mn- and Fe-(oxyhydr)oxides across their respective redox boundaries. The LREE, especially Ce, and Ho (relative to Y) are preferentially scavenged from oxic seawater, along with many redox-sensitive trace elements (e.g., Cr, Co, U, Ni). Upon reductive dissolution, these elements are released back into the water column and are either recycled or transported into the sediment pile.

2.11 Tables

Table 2.1. Mean redox-sensitive and nutrient-type trace element enrichment factors plus 1 standard deviation (1s) and range of values across the Sokoman Formation.

		RTH	JSP	LIF	LRGC	LRC	PGC	URC	GC	JUIF	LC
TE	n	3	8	6	16	3	10	10	9	30	17
Cr_{EF}	mean ± 1s	3.44 ± 0.32	0.54 ± 0.37	1.69 ± 0.75	2.25 ± 1.53	1.02 ± 0.62	1.99 ± 1.90	1.27 ± 1.08	1.00 ± 0.75	0.72 ± 0.56	1.82 ± 1.67
	range	3.09–3.70	0.08-1.07	1.03-2.88	0.67–4.80	0.30–1.47	0.35–6.47	0.16–3.71	0.31–2.13	0.05–2.31	0.50–7.81
V_{EF}	mean ± 1s	1.61 ± 0.22	2.07 ± 1.94	5.56 ± 5.09	4.55 ± 3.46	2.75 ± 1.67	3.70 ± 2.40	4.37 ± 2.43	2.67 ± 1.16	3.17 ± 2.29	4.58 ± 2.43
	range	1.36-1.79	0.05-6.20	1.88-15.50	1.26–14.94	1.10–4.45	0.31–8.35	1.55–8.77	1.20–4.85	0.09–11.51	1.17–9.93
U_{EF}	mean ± 1s	1.18 ± 0.03	1.43 ± 1.16	2.71 ± 2.83	1.12 ± 0.44	0.81 ± 0.14	1.60 ± 1.15	1.25 ± 1.02	3.07 ± 3.83	0.77 ± 0.40	1.49 ± 0.92
	range	1.15-1.21	0.41-3.55	0.78-8.39	0.53–1.79	0.67–0.96	0.53–4.14	0.54–4.02	0.34–11.71	0.20–1.54	0.41–4.21
Ni_{EF}	mean ± 1s	1.99 ± 0.31	1.66 ± 1.37	3.30 ± 2.29	3.42 ± 2.56	1.01 ± 0.41	4.12 ± 2.79	3.53 ± 2.37	1.73 ± 1.18	1.97 ± 1.55	4.19 ± 4.36
	range	1.66-2.28	0.32-4.52	1.08-6.98	0.60–10.49	0.64–1.45	0.39–7.95	0.78–9.34	0.60–3.76	0.22–6.64	0.71–14.81
Co_{EF}	mean ± 1s	1.77 ± 0.30	19.88 ± 20.80	6.77 ± 8.01	17.94 ± 17.98	7.38 ± 1.89	24.19 ± 23.06	25.41 ± 24.54	7.90 ± 8.78	13.60 ± 10.20	33.93 ± 64.42
	range	1.58-2.12	2.77-53.98	0.57-21.29	1.89–62.64	5.20–8.63	3.90–69.75	5.52–85.75	1.35–30.51	1.23–37.01	1.69–278.96
Zn_{EF}	mean ± 1s	1.08 ± 0.37	6.04 ± 7.51	2.63 ± 1.88	4.78 ± 5.68	1.56 ± 0.09	15.95 ± 37.14	12.12 ± 13.97	1.96 ± 1.11	2.11 ± 1.77	6.34 ± 11.11
	range	0.67-1.37	0.53-21.82	0.71-6.01	0.42–22.60	1.48–1.66	0.75–121.33	1.00–44.19	0.32–4.09	0.24–6.76	0.71–48.35

Table 2.2. Comparison of redox-sensitive and nutrient-type trace element enrichments between the Sokoman IF and those of data compiled from ca. 1.9–1.8 Ga IFs

Parameter and Reference	IF	Sokoman bulk (this study)	Biwabik bulk	Gunflint bulk	Riverton bulk	Negaunee laser
EC-norm molar Cr/Ti	mean	3.99	4.17	n.d.	2.42	n.d.
Konhauser et al. (2011)	1s	3.91	10.3	n.d.	0.29	n.d.
	min	0.091	0.25	n.d.	2.11	n.d.
	max	16.24	62.88	n.d.	2.75	n.d.
	n	109	36	n.d.	4	n.d.
molar U/ΣFe	mean	1.18×10^{-7}	4.07×10^{-7}	5.33×10^{-7}	1.92×10^{-6}	1.47×10^{-7}
Partin et al. (2013a)	1s	2.65×10^{-7}	2.61×10^{-7}	5.12×10^{-7}	9.35×10^{-7}	7.17×10^{-8}
	min	1.52×10^{-7}	6.35×10^{-8}	8.30×10^{-8}	1.22×10^{-6}	4.13×10^{-8}
	max	2.50×10^{-6}	8.43×10^{-7}	1.49×10^{-6}	3.39×10^{-6}	3.25×10^{-7}
	n	109	21	11	5	22
EC-norm molar U/Ti	mean	5.97	1.15	2.79	6.04	n.d.
Partin et al. (2013a)	1s	10.64	1.07	3.56	2.08	n.d.
	min	0.1	0.196	0.42	3.26	n.d.
	max	88.1	4.28	8.03	8.31	n.d.
	n	109	20	4	5	n.d.
molar Ni/ΣFe	mean	7.63×10^{-6}	n.d.	1.49×10^{-5}	4.91×10^{-5}	1.30×10^{-5}
Konhauser et al. (2009)	1s	6.73×10^{-5}	n.d.	9.54×10^{-7}	2.47×10^{-5}	1.75×10^{-7}
	min	8.45×10^{-7}	n.d.	1.43×10^{-5}	2.59×10^{-5}	1.93×10^{-6}
	max	3.94×10^{-5}	n.d.	1.63×10^{-5}	7.73×10^{-5}	5.97×10^{-5}
	n	109	n.d.	4	5	26
molar Co/ΣFe	mean	3.27×10^{-5}	2.79×10^{-4}	3.32×10^{-5}	4.21×10^{-5}	7.70×10^{-6}
Swanner et al. (2014)	1s	3.32×10^{-5}	5.36×10^{-4}	2.95×10^{-5}	1.75×10^{-5}	6.47×10^{-6}
	min	2.81×10^{-6}	4.68×10^{-6}	1.30×10^{-6}	2.04×10^{-5}	1.19×10^{-6}
	max	2.08×10^{-4}	5.36×10^{-4}	7.70×10^{-5}	6.16×10^{-5}	2.06×10^{-5}
	n	109	7	9	5	11
EC-norm molar Co/Ti	mean	51.6	61.7	14.3	2.61	n.d.
Swanner et al. (2014)	1s	106.4	138.7	24.3	0.55	n.d.
	min	0.306	0.363	0.365	2.11	n.d.
	max	958.1	451.6	50.5	3.33	n.d.
	n	109	13	13	5	n.d.
molar Zn/ΣFe	mean	2.23×10^{-5}	1.98×10^{-4}	4.94×10^{-5}	2.66×10^{-4}	5.20×10^{-5}
Robbins et al. (2013)	1s	3.26×10^{-5}	3.49×10^{-4}	4.38×10^{-5}	1.93×10^{-4}	7.97×10^{-5}
	min	5.58×10^{-6}	1.76×10^{-5}	5.33×10^{-6}	9.19×10^{-5}	7.85×10^{-6}
	max	2.85×10^{-4}	1.66×10^{-3}	1.21×10^{-4}	5.88×10^{-4}	2.14×10^{-4}
	n	108	22	7	5	6

n.d. = no data; EC = evolving upper continental crust based on the restoration model of Condie (1993)

Table 2.3. Summary of binary element ratios used for determining the composition and provenance of detritus to the Sokoman IF**.**

			Shale Composite		Ashuanipi Complex						
	MS	RTH	Early Prot. (2.5–1.8 Ga)	Middle Prot. (1.8–1.6 Ga)	migmatitic paragneiss	biotite-rich paragneiss	biotite granite	tonalite gneiss	diorite-gabbro	paragneiss (average)	meta-greywacke
n	1	3			16	1	1	2	5	10	31
Reference	this study	this study	Condie (1993)		van Nostrand (2017)					Percival (2003)	Guernina and Sawyer (2003)
Th/Sc	0.80	0.74 ± 0.04	0.72	0.74	0.52 ± 0.23	1.00	0.67	0.52 ± 0.57	0.51 ± 0.57	-	0.57 ± 0.37
Th/Co	1.04	0.50 ± 0.07	0.69	0.69	0.41 ± 0.47	0.69	0.29	0.24 ± 0.24	0.18 ± 0.19	0.42	0.49 ± 0.33
La/Sc	2.39	2.60 ± 0.12	2.13	2.15	1.56 ± 1.04	3.02	3.36	1.87 ± 1.93	0.42 ± 0.39	-	2.08 ± 0.95
Cr/Th	5.07	11.44 ± 0.55	5.67	5.29	17.50 ± 5.60	7.86	1.06	32.64 ± 30.61	10.49 ± 9.03	18.70	20.04 ± 10.94
Zr/Hf	39.16	36.90 ± 0.13	35.29	35.1	37.40 ± 1.92	40.71	30.00	39.57 ± 5.32	36.85 ± 2.91	39.07	33.39 ± 2.56
Zr/Ga	10.59	5.31 ± 0.91	-	-	5.29 ± 2.19	12.67	2.25	4.79 ± 2.45	6.07 ± 0.62	7.60	7.14 ± 1.09
Zr/Th	19.32	10.28 ± 0.54	17.31	17.21	20.42 ± 9.23	11.07	11.49	17.21 ± 1.92	22.72 ± 9.41	16.52	18.38 ± 8.77
Al_2O_3/TiO_2	22.55	24.80 ± 1.77	25.69	25.59	25.48 ± 10.89	24.98	29.21	27.12 ± 16.31	9.67 ± 2.13	27.26	30.55 ± 4.23

CHAPTER 3: SUMMARY, CONCLUSIONS, AND FUTURE WORK

3.1 Summary and Conclusions

In this contribution, we present new high-precision geochemical (major elements, REE+Y, trace elements, Fe(II), and sequential four-step LOI) and mineralogical (SEM-MLA) data on IF reference materials (IOC-1, FeR-3, FeR-4) and the ca. 1.88 Ga Sokoman Formation in the Labrador Trough. Results for the latter are integrated with previously defined mineralogical, sedimentological, and sequence stratigraphic constraints. The Sokoman IF is divided into four distinct mineralogical facies that encompass the following units, as follows: (1) silicate-carbonate facies: LIF, LC; (2) magnetite-carbonate facies: LRGC, PGC, GC, JUIF; (3) hematite-carbonate facies: LRC, URC; and (4) hematite-magnetite facies: JSP. Our mineralogical observations show that the silicate-carbonate facies reflects an anoxic paragenetic pathway, whereas the magnetite-carbonate, hematite-carbonate, and hematite-magnetite facies collectively reflect a suboxic paragenetic pathway.

Careful evaluation of geochemical proxies on a unit-specific and sequence stratigraphic basis reveals the presence of trends potentially masked by collective sample treatment. For example, minor detrital element admixtures are observed preferentially in specific units based on modeled mixing relationships between REE+Y parameters and detrital element (DE) abundances (e.g., Ga, Hf, Nb, Sc, Ta, Th, Ti, and Zr). The interpretation of chemostratigraphic trends within a sequence stratigraphic framework (Pufahl et al., 2014) show that DE abundances exhibit irregular sinusoidal patterns that can be linked to base-level fluctuations. We observe high DE and low P/Zr, ΣFe/Zr, and Mn/Zr during the lowstand systems tract (LST: RTH, LIF, bottom LRGC, bottom JUIF) and highstand systems tract (HST: URC). In contrast, low DE and high

P/Zr, ΣFe/Zr, and Mn/Zr characterize the transgressive systems tract (TST: upper LRGC, LRC, PGC, upper JUIF, LC).

Chemostratigraphic REE+Y trends show broad correlations with DE and are strongest in LST intervals. However, REE+Y trends in TST and HST intervals are less uniform with $(La/La^*)_{SN}$, $(Ce/Ce^*)_{SN}$, and $(Eu/Eu^*)_{SN}$ commonly exhibiting trends that are decoupled from $(Gd/Gd^*)_{SN}$, $(Lu/Lu^*)_{SN}$, Y/Ho, τ_3, and τ_4 due to the effects of particle scavenging and basin redox stratification. During TST intervals, $(Gd/Gd^*)_{SN}$, $(Lu/Lu^*)_{SN}$, and Y/Ho values show the strongest positive correlation with each other, suggesting that TST deposits more clearly record marine signatures relative to LST and HST deposits. Sharp redox gradients are observed across late LST to early TST intervals based on continuous increases in $(Ce/Ce^*)_{SN}$, τ_3, and τ_4, which are collectively matched by overall decreases in $(La/La^*)_{SN}$, $(Gd/Gd^*)_{SN}$, $(Lu/Lu^*)_{SN}$, Y/Ho, and Mn/ΣFe. These redox gradients are interpreted to represent impingement of the Mn-redoxcline across the shallow shelf during a marine transgression. The REE+Y data for the Sokoman IF display a hyperbolic trend spanning true small negative Ce and true large positive Ce anomaly fields that can be modelled effectively by oxide shuttling across distinct Mn- and Fe-redoxclines with minimal detrital overprinting. The dearth of negative Y anomalies and LREE-enriched slopes in samples having true positive Ce anomalies are reconciled through insufficient REE+Y release owing to enhanced recycling across a shallow Mn-redox interface that was strongly influenced by surface water mixing. Identical Ce anomalies are observed between bulk samples and their respective intraformational chert subsamples, and are most parsimoniously explained by a primary control from water depth-related redox variations rather than detrital contamination and/or modification by post-depositional processes.

Chemostratigraphic trends for TEs (Cr, V, U, Ni, Co, Zn) trends also show broad positive correlations with DE that are strongest for Cr, U, V, and Ni. Weaker positive correlations with respect to Co and Zn are inferred to record a significant hydrothermal contribution for these elements. Bivariate plots of molar TE/ΣFe and P/ΣFe against their respective EFs outline two endmember trendlines that are effective in distinguishing between the purest authigenic enrichments vs. detrital-influenced signatures. Samples from late TST to early HST intervals represent the former, whereas samples from LST to earliest TST intervals constitute the latter. Muted authigenic enrichments of TEs including Cr, V, U, and Ni (EFs < 10), even in late TST to early HST intervals, are interpreted as evidence for low atmospheric O_2 levels, especially considering the composition of the inferred continental source (enriched in U and relatively enriched in mafic-associated TEs). Among the continentally derived redox-sensitive trace elements evaluated here (Cr, V, U), a higher V enrichment contrasts with muted Cr-U enrichments, suggesting either a V-rich continental source or that soluble V was generated more readily than soluble Cr or U under the existing surface redox conditions. Aridity and orogenic quiescence are also inferred to have compounded the effects of low atmospheric O_2 levels, thereby limiting continental weathering and solute delivery to the oceans. A general decrease in molar P/ΣFe from LST to HST intervals may represent a reduction in bioavailable P with increasing distance from the paleoshoreline. Several stromatolite-rich samples from LST intervals are characterized by both high P_{EF} and high P/ΣFe, which might indicate elevated biological P utilization in intertidal to shallow subtidal environments.

Collectively, the present study on the Sokoman IF demonstrates that detailed evaluation of sedimentological-mineralogical-geochemical datasets within geological (sedimentological and

sequence stratigraphic) frameworks is imperative for ascertaining syn-depositional (detrital, seawater) vs. post-depositional (diagenesis, metamorphism, late-stage alteration) signatures.

3.2 Recommendations for Future Work

The present study provides one of the first combined mineralogical-geochemical-sedimentological datasets on the Sokoman IF for the Lac Ritchie, Sheps Lake, and Hayot Lake localities. Despite contributing to a better understanding of shallow marine conditions at ca 1.88 Ga, many opportunities for future investigations of the Sokoman IF remain.

3.2.1 Investigating the timing of hematite formation

Recent investigations into the ca. 1.88 Ga Gunflint IF using petrography and high-resolution imaging techniques (TEM, HAADF) have challenged the traditional view of hematite having a primary depositional origin (Rasmussen and Muhling, 2020). In their work, hematite is shown to infill intergranular fractures and display overgrowth textures around Fe-silicate granules. These lines of evidence were used to invoke a post-depositional oxidative origin for hematite. Similar post-depositional hematite growth was observed in stromatolites of the Gunflint and Biwabik IFs (Shapiro and Konhauser, 2015). The similarity in bulk-rock REE+Y signatures in siderite/hematite-bearing stromatolites (Planavsky et al., 2009) vs. ankerite/pyrite-bearing stromatolites (Petrash et al., 2016) of the lower Gunflint Formation also calls into question the syngenicity of recorded geochemical signatures. If true, these findings argue against microbially-mediated oxidation of Fe(II), as well as the presence of oxygen in the seafloor and pore waters at the time of IF precipitation. However, recent hydrogeological modeling by Robbins et al. (2019) shows that basin-scale, post-depositional oxidation of Fe(II)-precursor

phases was implausible as it required steep hydraulic gradients, high permeability conditions, and significantly high dissolved O_2 fluxes. In light of these contrasting arguments regarding primary vs. post-depositional oxidation signatures, future studies on the Sokoman IF should employ a similar, combined high-resolution mineralogical-geochemical approach in an attempt to either support or refute these observations and interpretations based on other Proterozoic IFs.

3.2.2 Sequential extraction for determining fraction-specific trace element distributions

Interpretations of redox-sensitive trace element data from the Sokoman IF will benefit from employing a sequential extraction scheme, as shown recently for the Griquatown and Kuruman IFs (Oonk et al., 2017, 2018). Akin to the bulk-rock trends shown in the present study, their work reveals a complex association between most elements and the principal mineral fractions (Fe-carbonate, Fe-oxide, Fe-silicate). However, the approach of these authors eliminates the influence of minor detrital element admixtures and permits the evaluation of certain TEs bound in a specific fraction. Such an approach is promising for the application of future isotopic investigations, as highly variable mineralogical compositions are more likely to compromise bulk-rock isotopic signatures.

3.2.3 Integration of other paleo-redox proxies

Interpretations of shallow marine redox based on REE+Y parameters and authigenic TE enrichments (Cr, V, U, Ni, Co, Zn) can be reinforced through the evaluation of other TEs, such as Mo and Re, as well as via the application of stable isotopes. For example, Mo exhibits aqueous solubility under oxic marine conditions as the tetrahedrally coordinated molybdate oxyanion, (MoO_4^{2-}), which weakly coordinates with other environmentally common ligands such

as chloride (Cl^-) and hydroxide (OH^-) (Morford and Emerson, 1999). Importantly, Mo is efficiently adsorbed by Fe/Mn-(oxyhydr)oxides, resulting in its enrichment in pelagic Fe-Mn nodules and crusts (Barling and Anbar, 2004; Goldberg et al., 2009). Large Mo isotopic ($\delta^{98}Mo$) fractionations are associated with this process (Barling and Anbar, 2004).

Under more reducing conditions, adsorbed Mo can be re-released into the water column during the reductive dissolution of Fe/Mn-(oxyhydr)oxides at the sediment-water interface (Morford and Emerson, 1999; Tribovillard et al., 2006). Under sulfidic and reducing conditions, Mo is readily sequestered from the water column and undergoes a series of transformations to become particle-reactive oxythiomolybdates. Ultimately, these species are incorporated into Fe-Mo-S phases and organic matter (Bertine, 1972; Emerson and Huested, 1991).

Under weakly euxinic conditions, the incomplete conversion of molybdate to thiomolybdate species yields a diverse range of Mo-isotopic values (Neubert et al., 2008). In contrast, under strongly euxinic conditions, the quantitative conversion of molybdate to particle-reactive thiomolybdate species can be attained, resulting in minimal isotopic fractionation between sediments and the overlying euxinic water column (Neubert et al., 2008; Vorlicek et al., 2004).

Coupled high $\delta^{98}Mo$ values and elevated Mo concentrations should therefore indicate strong euxinic conditions. In contrast, low $\delta^{98}Mo$ values and high Mo concentrations indicate deposition in weakly euxinic environments, since isotopically lighter (i.e., lower, more negative) $\delta^{98}Mo$ values reflect isotopic fractionations (towards lighter values) arising from the incomplete conversion of molybdate to thiomolybdate species. Additionally, interpretation of Mo enrichment and isotopic composition benefits from the integration of data from other tracers such as Re, U, and TOC. For instance, low sedimentary enrichments of Mo and U, coupled with

modest Re enrichment and low δ^{98}Mo values, collectively point to predominantly oxic conditions (Baldwin et al., 2013).

3.2.4 Sampling deeper correlative sequences

Evaluation of deeper water equivalents to the Sokoman IF, namely the middle member of the Baby Formation, may provide the data necessary to build a more refined understanding of deep ocean redox at ca. 1.88 Ga, and therefore a better picture of shallow-deep ocean dynamics during this time period. A similar approach was done for the Stambaugh Formation, the deep-water equivalent to the Gunflint and Biwabik IFs, which revealed highly variable marine ocean redox conditions characterized by predominantly ferruginous and euxinic conditions with transient suboxic/oxic episodes (Planasvky et al., 2018).

3.3 References Cited

Baldwin, G.J., Nägler, T.F., Greber, N.D., Turner, E.C., Kamber, B.S., 2013. Mo isotopic composition of the mid-Neoproterozoic ocean: an iron formation perspective. Precambrian Research 230, 168–178. https://doi.org/10/gft2fg

Barling, J., and Anbar, A. D., 2004, Molybdenum isotope fractionation during adsorption by manganese oxides. Earth and Planetary Science Letters 217, 315–329.

Bertine, K. K., 1972. The deposition of molybdenum in anoxic waters: Marine Chemistry 1, 43–53.

Cunningham, L.C., Page, F.Z., Simonson, B.M., Kozdon, R., Valley, J.W., 2012. Ion microprobe analyses of $\delta^{18}O$ in early quartz cements from 1.9 Ga granular iron formations (GIFs): a pilot study. Precambrian Research 214–215, 258–268. https://doi.org/10/gft5rz

Dimroth, E., Chauvel, J.-J., 1973. Petrography of the Sokoman Iron Formation in part of the central Labrador Trough, Quebec, Canada. Geological Society of America Bulletin 84, 111–134. https://doi.org/10/btdc56

Edwards, C.T., Pufahl, P.K., Hiatt, E.E., Kyser, T.K., 2012. Paleoenvironmental and taphonomic controls on the occurrence of Paleoproterozoic microbial communities in the 1.88 Ga Ferriman Group, Labrador Trough, Canada. Precambrian Research 212–213, 91–106. https://doi.org/10/gft5np

Emerson, S.R., Huested, S.S., 1991, Ocean anoxia and the concentrations of molybdenum and vanadium in seawater. Marine Chemistry, 34, 177–196.

Fryer, B.J., 1977. Trace element geochemistry of the Sokoman Iron Formation. Canadian Journal of Earth Sciences 14, 1598–1610. https://doi.org/10/df9wgq

Goldberg, T., Archer, C., Vance, D., Poulton, S.W., 2009. Mo isotope fractionation during adsorption to Fe (oxyhydr)oxides: Geochimica et Cosmochimica Acta 73, 6502–6516.

Klein C., Fink, R.P., 1976. Petrology of the Sokoman Iron Formation in the Howells River area, at the western edge of the Labrador Trough. Economic Geology 71, 453–487.

Morford, J.L., Emerson, S., 1999. The geochemistry of redox sensitive trace metals in sediments. Geochimica et Cosmochimica Acta 63, 1735–1750.

Neubert, N., Nägler, T.F., Böttcher, M.E., 2008. Sulfidity controls molybdenum isotope fractionation into euxinic sediments: evidence from the modern Black Sea. Geology 36,

775–778. https://doi.org/10.1130/G24959A.1

Oonk, P.B.H., Tsikos, H., Mason, P.R.D., Henkel, S., Staubwasser, M., Fryer, L., Poulton, S.W., Williams, H.M., 2017. Fraction-specific controls on the trace element distribution in iron formations: implications for trace metal stable isotope proxies. Chemical Geology 474, 17–32. https://doi.org/10/gft2fm

Oonk, P.B.H., Mason, P.R.D., Tsikos, H., Bau, M., 2018. Fraction-specific rare earth elements enable the reconstruction of primary seawater signatures from iron formations. Geochimica et Cosmochimica Acta 238, 102–122. https://doi.org/10/gfvjmb

Petrash, D.A., Robbins, L.J., Shapiro, R.S., Mojzsis, S.J., Konhauser, K.O., 2016. Chemical and textural overprinting of ancient stromatolites: timing, processes, and implications for their use as paleoenvironmental proxies. Precambrian Research 278, 145–160. https://doi.org/10.1016/j.precamres.2016.03.010

Planavsky, N., Rouxel, O., Bekker, A., Shapiro, R., Fralick, P., Knudsen, A., 2009. Iron-oxidizing microbial ecosystems thrived in late Paleoproterozoic redox-stratified oceans. Earth and Planetary Science Letters 286, 230–242. https://doi.org/10/crzgkv

Planavsky, N., Bekker, A., Rouxel, O.J., Kamber, B., Hofmann, A., Knudsen, A., Lyons, T.W., 2010. Rare earth element and yttrium compositions of Archean and Paleoproterozoic Fe formations revisited: new perspectives on the significance and mechanisms of deposition. Geochimica et Cosmochimica Acta 74, 6387–6405. https://doi.org/10/fj558k

Planavsky, N.J., Slack, J.F., Cannon, W.F., O'Connell, B., Isson, T.T., Asael, D., Jackson, J.C., Hardisty, D.S., Lyons, T.W., Bekker, A., 2018. Evidence for episodic oxygenation in a weakly redox-buffered deep mid-Proterozoic ocean. Chemical Geology 483, 581–594.

Poulton, S.W., Fralick, P.W., Canfield, D.E., 2004. The transition to a sulphidic ocean ~1.84 billion years ago. Nature 431, 173–177. https://doi.org/10.1038/nature02912

Poulton, S.W., Fralick, P.W., Canfield, D.E., 2010. Spatial variability in oceanic redox structure 1.8 billion years ago. Nature Geoscience 3, 486–490. https://doi.org/10/dzw3rg

Pufahl, P.K., Anderson, S.L., Hiatt, E.E., 2014. Dynamic sedimentation of Paleoproterozoic continental margin iron formation, Labrador Trough, Canada: paleoenvironments and sequence stratigraphy. Sedimentary Geology 309, 48–65. https://doi.org/10/f592gh

Rasmussen, B., Muhling, J.R., 2020. Hematite replacement and oxidative overprinting recorded

in the 1.88 Ga Gunflint iron formation, Ontario, Canada. Geology 48, 688–692. https://doi.org/10.1130/G47410.1

Raye, U., Pufahl, P.K., Kyser, T.K., Ricard, E., Hiatt, E.E., 2015. The role of sedimentology, oceanography, and alteration on the δ^{56}Fe value of the Sokoman Iron Formation, Labrador Trough, Canada. Geochimica et Cosmochimica Acta 164, 205–220. https://doi.org/10/f7jw64

Robbins, L.J., Funk, S.P., Flynn, S.L., Warchola, T.J., Li, Z., Lalonde, S.V., Rostron, B.J., Smith, A.J.B., Beukes, N.J., de Kock, M.O., Heaman, L.M., Alessi, D.S., Konhauser, K.O., 2019. Hydrogeological constraints on the formation of Palaeoproterozoic banded iron formations. Nature Geoscience 12, 558–563. https://doi.org/10/gf3czc

Shapiro, R.S., Konhauser, K.O., 2015. Hematite-coated microfossils: primary ecological fingerprint or taphonomic oddity of the Paleoproterozoic? Geobiology 13, 209–224. https://doi.org/10.1111/gbi.12127

Tribovillard, N., Algeo, T.J., Lyons, T., Riboulleau, A., 2006. Trace metals as paleoredox and paleoproductivity proxies: an update. Chemical Geology 232, 12–32. https://doi.org/10/bp6kr3

Vorlicek, T.P., Kahn, M.D., Kasuya, Y., Helz, G.R., 2004. Capture of molybdenum in pyrite-forming sediments: role of ligand-induced reduction by polysulfides: Geochimica et Cosmochimica Acta 68, 547–556.

Zajac, I.S., 1974. The stratigraphy and mineralogy of the Sokoman Formation in the Knob Lake area, Quebec and Newfoundland. Bulletin of the Geological Survey of Canada 220, 159 p.

APPENDIX 1: DRILL HOLE COLLARS

Table A1.1. Drill hole collar coordinates, orientation, total length, and locality names.

Drillhole	*Property*	*Tectonic Zone*	*NAD83; UTM Zone 19N*		*Length (m)*	*Azimuth*	*Dip*
			Easting	*Northing*			
12-SL-1018D	Sheps Lake	Tamarack	622324	6071788	132	0	-90
12-SL-1017D	Sheps Lake	Tamarack	622882	6070992	132	0	-90
12-SL-1011D	Sheps Lake	Tamarack	624221	6069441	129	0	-90
12-SL-1005D	Sheps Lake	Tamarack	625277	6067725	114	0	-90
11-LR-1010D	Lac Ritchie	Cambrien	561349	6181042	75	0	-90
11-LR-1005D	Lac Ritchie	Cambrien	562295	6181795	127.5	0	-90
11-LR-1012D	Lac Ritchie	Cambrien	563100	6179797	117	0	-90
11-LR-1029D	Lac Ritchie	Cambrien	564189	6180709	120	0	-90
11-LR-1020D	Lac Ritchie	Cambrien	562777	6177220	84	0	-90
HAY-11-07	Hayot Lake	Schefferville (east)	638762	6097614	163	0	-90
HAY-11-29	Hayot Lake	Schefferville (east)	636175	6100101	78	0	-90

APPENDIX 2: GRAPHIC LOGS OF SAMPLED DRILL HOLES

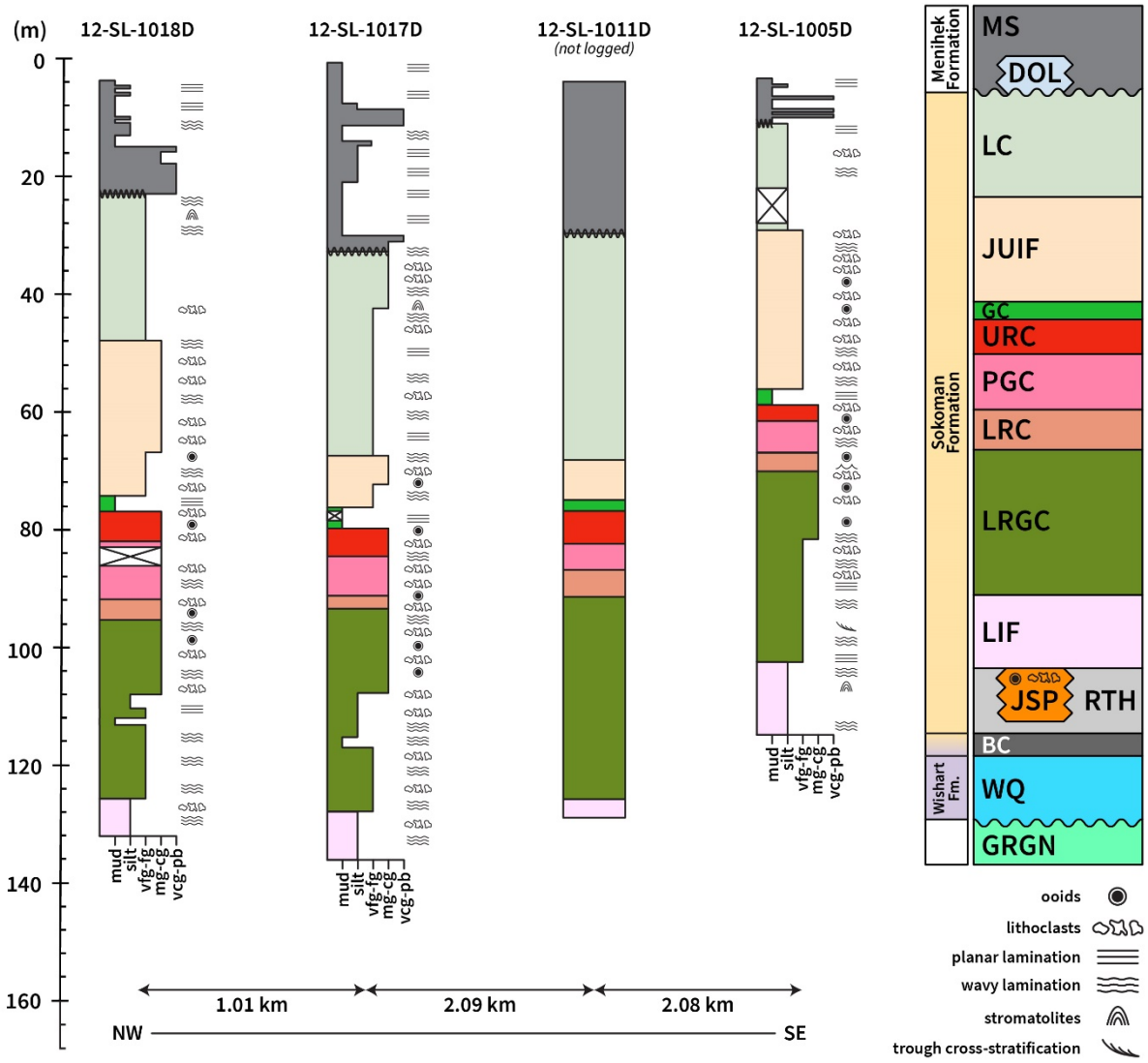

Figure A2.1. Stratigraphic logs of the sampled drill holes in the Sheps Lake area. Crosshatched boxes indicate intervals of missing core.

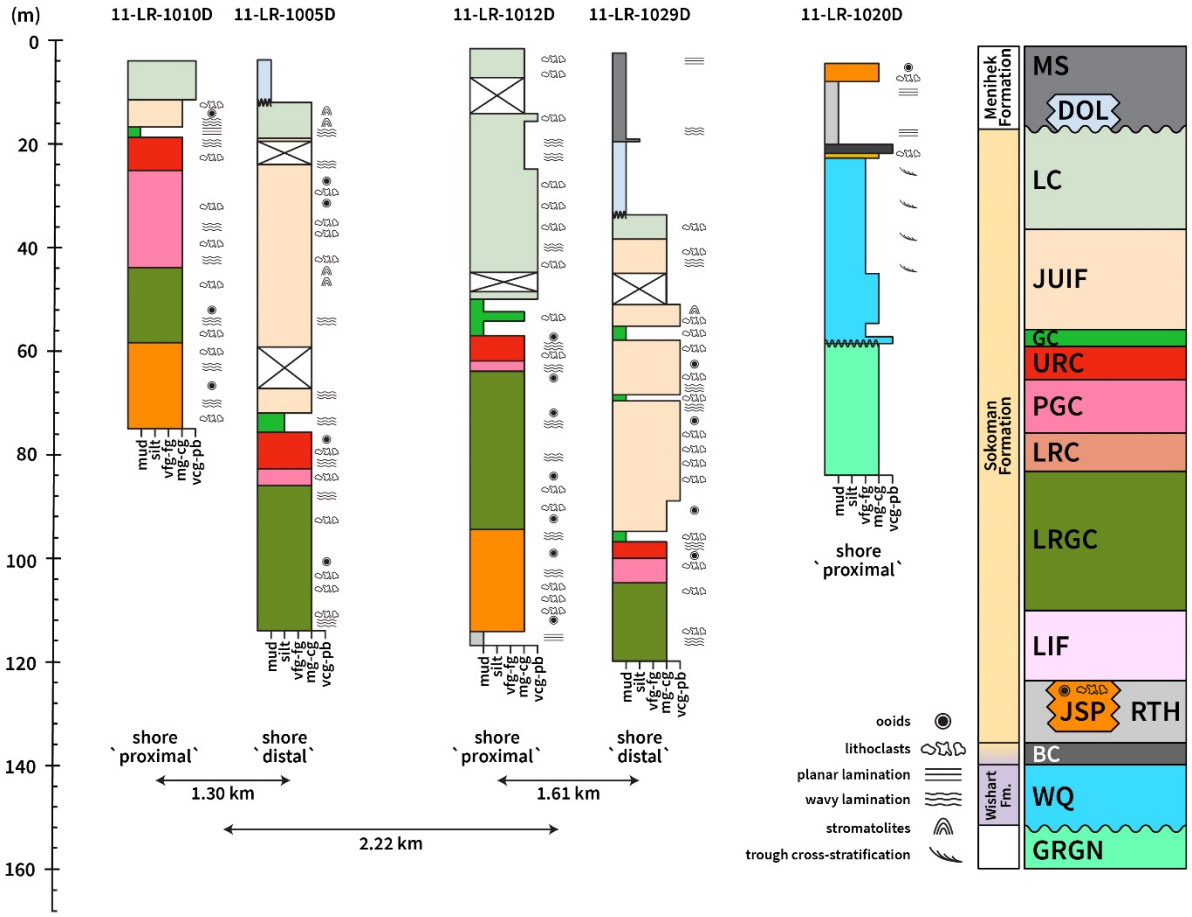

Figure A2.2. Stratigraphic logs of the sampled drill holes in the Lac Ritchie area. Crosshatched boxes indicate intervals of missing core.

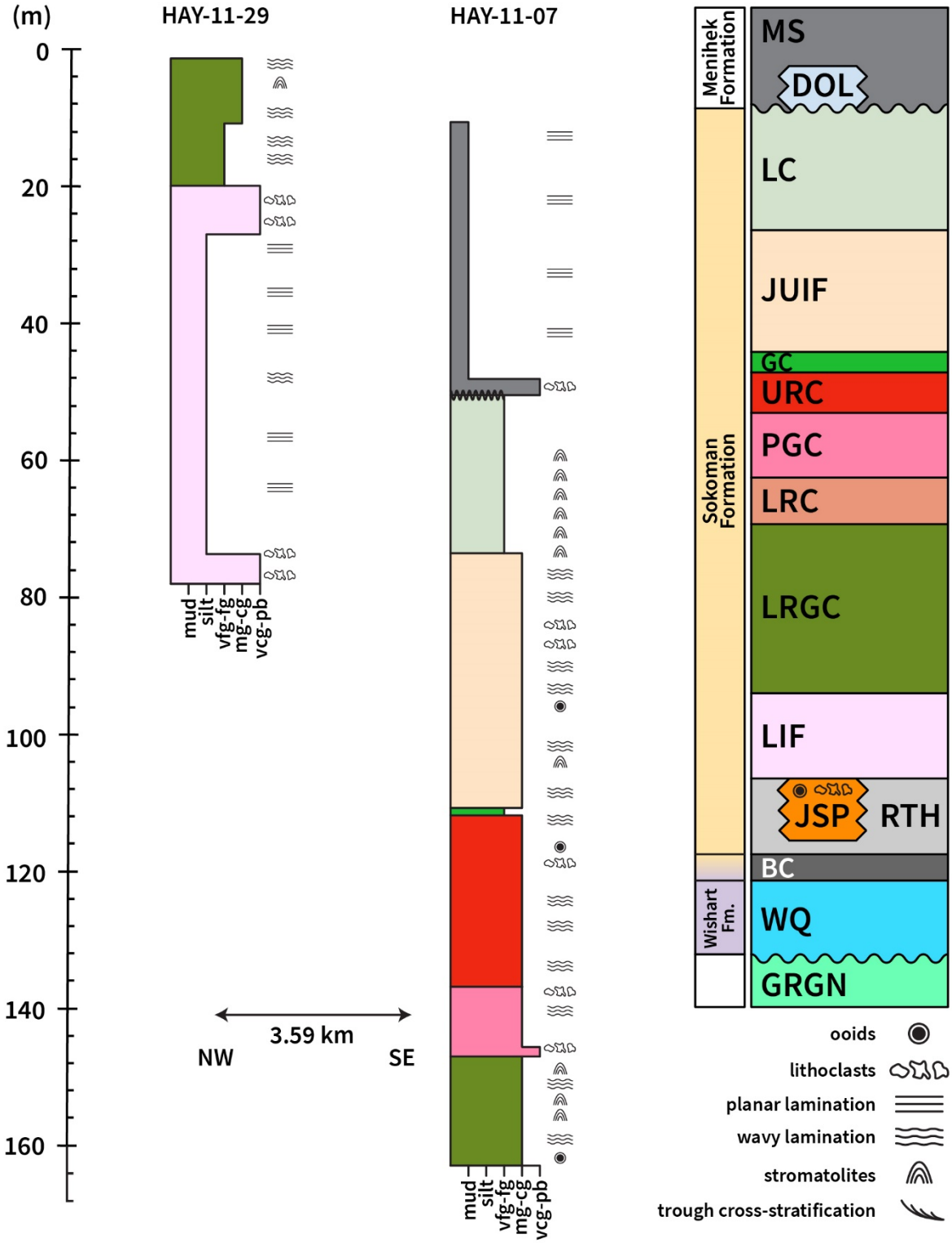

Figure A2.3. Stratigraphic logs of the sampled drill holes in the Hayot Lake area.

APPENDIX 3: DRILL CORE LOGS

Table A3.1. Descriptive logs of evaluated drill holes across Sheps Lake, Lac Ritchie, and Hayot Lake localities.

Area	*Drillhole*	*From (m)*	*To (m)*	*Lithology*	*Description*
Sheps Lake	12-SL-1018D	0.00	3.60	**OB**	overburden
Sheps Lake	12-SL-1018D	3.60	11.13	**MS**	finely laminated black shale, with mm-scale grey-green silty interbeds; shale coarsens to fine-grained siltstone over lower 20 cm; silty units contain small euhedral pyrite grains
Sheps Lake	12-SL-1018D	11.13	11.73	**MS**	intraclastic breccia with subangular chert and shale fragments; breccia interbedded with fine-grained siltstone; interval with unusual crenulated laminations close to end of unit
Sheps Lake	12-SL-1018D	11.73	15.20	**MS**	interbedded black shale and fine-grained siltstone; shale is massive to finely laminated; siltstone coarsens upwards into fine-grained sandstone in individual beds
Sheps Lake	12-SL-1018D	15.20	19.20	**MS**	interbedded conglomerate, coarse sandstone and black shale beds; conglomerate is matrix-supported with coarse sandy matrix and shale clasts (clasts up to 2 cm, some clasts replaced by pyrite)
Sheps Lake	12-SL-1018D	19.20	22.77	**MS**	conglomerate with minor coarse-grained sandstone units; conglomerate is poorly sorted and matrix-supported with large clasts up to 10 cm and most clasts < 3 cm; clasts are rounded to angular, and brecciation is highly chaotic in places; matrix of conglomerate is carbonate sand
Sheps Lake	12-SL-1018D	22.77	25.13	**LC**	unconformable contact between overlying unit and grey sandstone that grades into Fe-silicate and Fe-carbonate rich sandstone with brown weathering; abundant evidence for stromatolites evidenced by many curved and discontinuous laminations

Table A3.1. *(continued)*

Sheps Lake	12-SL-1018D	25.13	47.82	**LC**	highly variable unit, with upper contact marked by first appearance of green chert, with stromatolites over upper 3 m; consists of layers of green chert and of granular Fe-silicate and Fe-carbonate sand; unit is non-magnetic to 31.4 m, after this magnetite bands and disseminated magnetite become common, increasing in proportion towards base; distinctive brown magnetite-rich unit from 43.7 to 44.14 m, followed by possible stromatolite with wavy laminations of magnetite in green chert; rare other possible stromatolites noted
Sheps Lake	12-SL-1018D	47.82	55.80	**JUIF**	upper contact of JUIF marked by first appearance of red jasper, but appears gradational over 30 cm; variable unit with discontinuous bands of red jasper and grey magnetite, and granular grainstones with peloids and ooliths; granular bands consist of chert+mag±hem±carb and have characteristic mottled texture and weak bands of magnetite; overgrowths of Fe-carbonate common in magnetite layers
Sheps Lake	12-SL-1018D	55.80	67.52	**JUIF**	similar to overlying JUIF, but jasper and magnetite bands are rare and unit is dominantly mottled pink grainstone; occasional rip-up clasts with elongate jasper clasts
Sheps Lake	12-SL-1018D	67.52	74.15	**JUIF**	dominantly red jasper and grey magnetite layers (discontinuous) with minor grainstone
Sheps Lake	12-SL-1018D	74.15	76.81	**GC**	green chert with minor jasper over upper 20 cm; composed predominantly of green chert with disseminated Fe-carbonate; magnetite disseminate in chert and rare over upper 1.5 m but increase significantly after this interval with associated increase in Fe-carbonate
Sheps Lake	12-SL-1018D	76.81	82.00	**URC**	discontinuous bands of magnetite and red jasper interbedded with granular mag-chert-Fe-carb grainstone; common subrounded magnetite clasts surrounded by red jasper in grainstones

Table A3.1. *(continued)*

Sheps Lake	12-SL-1018D	82.00	87.00	**PGC**	missing core but logged as PGC in company logs
Sheps Lake	12-SL-1018D	87.00	91.70	**PGC**	pink to grey mag-chert-Fe-carb-jasper grainstone with mottled texture and large overprinting Fe-carbonates; from 89.43 to 89.55 m, predominantly cherty grainstone with large secondary magnetite blebs
Sheps Lake	12-SL-1018D	91.70	95.20	**LRC**	gradational upper contact with PGC, but boundary marked by first appearance of jasper bands; LRC consists of minor jasper and magnetite bands, and is dominantly grainstone with large ooliths (up to 2 mm around jasper clast); graded bedding recorded in some beds
Sheps Lake	12-SL-1018D	95.20	125.60	**LRGC**	gradational contact with LRC, but no jasper bands; dominantly pink grainstone to 102 m with intervals of grey-green grainstone and cherty iron formation; overall, the unit has a mottled appearance, with abundant ooliths, disseminated magnetite, chert, Fe-sil, Fe-carb ± hem; bands of carbonate (yellow weathering) common to 107.5 m and after 117 m; magnetite content decreases with depth and base of unit marked by final magnetite band; well-laminated green siltstone from 108 to 109.5 m; distinctive black chert recorded from 112.9 to 113.1 m
Sheps Lake	12-SL-1018D	125.60	EOH (132)	**LIF**	green LIF with carbonate bands; similar in appearance to overlying unit, but generally fine-grained Fe-sil-rich siltstone with no magnetite
Sheps Lake	12-SL-1017D	0.00	0.50	**OB**	overburden
Sheps Lake	12-SL-1017D	0.50	32.55	**MS**	finely laminated black shale, typical MS; silicified horizons from 9.6 to 10.2 m

Table A3.1. *(continued)*

Sheps Lake	12-SL-1017D	32.55	34.15	**LC**	grey-green LC dominated by mm- to cm-scale bands of mag and Fe-sil; interval is strongly magnetic, but with a relatively clean (cherty) non-magnetic horizon from 33.40 to 33.55 m
Sheps Lake	12-SL-1017D	34.15	34.50	**LC**	weakly to non-magnetic horizons characterized by bands of Fe-carbonate and Fe-silicate; stylolitization pervasive throughout this interval
Sheps Lake	12-SL-1017D	34.50	34.85	**LC**	same as above, but with occurrence of black, weakly magnetic, graphitic bands
Sheps Lake	12-SL-1017D	34.85	35.80	**LC**	weakly magnetic horizons characterized by appearance of reddish to greenish clasts of jasper
Sheps Lake	12-SL-1017D	35.80	39.75	**LC**	nonmagnetic interval with pervasive, coarse-grained diagenetic Fe-carb (sid) and lesser Fe-sil
Sheps Lake	12-SL-1017D	39.75	42.10	**LC**	same as above, but with distinct horizons of mag-rich bands that are strongly magnetic; potentially stromatolitic
Sheps Lake	12-SL-1017D	42.10	67.20	**LC**	nonmagnetic to weakly magnetic interval characterized by cleaner (chertier) horizons
Sheps Lake	12-SL-1017D	67.20	72.40	**JUIF**	alternating bands of mag and jasper with abundant Fe-carbonate overprints; bands are typically 1-2 cm in thickness with granular to oolitic intervals from 71 m onwards
Sheps Lake	12-SL-1017D	72.40	76.10	**JUIF**	finer bands of mag; sparse jasper clasts and disappearance of mottled, late sid/ank overprints; no evidence of potential stromatolites
Sheps Lake	12-SL-1017D	79.20	79.60	**GC**	core missing from 76.10 to 79.20 m; weakly magnetic interval with primarily green chert and siderite; stylolites pervasive throughout this section
Sheps Lake	12-SL-1017D	79.60	84.10	**URC**	alternating bands of mag and hem with abundant jasper clasts; calcite veins prominent from 79.9 to 80.8 m; strongly magnetic

Table A3.1. *(continued)*

Sheps Lake	12-SL-1017D	84.10	90.95	**PGC**	alternating bands of mag with common thin, sub-mm bands and a thin interval (85.4 to 86.0 m) characterized by the absence of jsp clasts; pinkish ank common throughout the measured unit
Sheps Lake	12-SL-1017D	90.95	93.20	**LRC**	predominantly granular to oolitic IF characterized by mag and hem granules interspersed with jsp clasts; spherulitic siderite/ankerite common from 91.6 to 92.0 m
Sheps Lake	12-SL-1017D	93.20	99.51	**LRGC**	gradational contact with LRC over a span of ~0.25 m, marked by the disappearance of jsp clasts; fine, alternating bands of mag and Fe-carb + chert with very rare jsp clasts; Fe-carb typically occur as bands rather than discrete carb overprints; strongly magnetic throughout this interval
Sheps Lake	12-SL-1017D	99.51	107.90	**LRGC**	same as above, but marked by the disappearance of jsp-rich bands; Fe-carb bands common, but spherultic siderite/ankerite overprints also present throughout this section; punctuated by thin granular to oolitic intervals
Sheps Lake	12-SL-1017D	107.90	115.30	**LRGC**	predominantly mag-rich siltstone; carb bands less common, as well as carb overprints; bands of Fe-sil are more common; jsp clasts and bands not present
Sheps Lake	12-SL-1017D	115.30	122.90	**LRGC**	muddier, mag-rich, carb-poor interval with abundant jsp ooliths and granules; minor occurrences of black-gray chert between 115.30 and 116.85 m

Table A3.1. *(continued)*

Sheps Lake	12-SL-1017D	122.90	127.60	**LRGC**	predominantly finely laminated mag + Fe-carb + Fe-sil; no jsp clasts/bands/granules; green-grey chert abundant from 126.0 to 126.4 m
Sheps Lake	12-SL-1017D	127.60	136.00	**LIF**	typical LIF, alternating bands of Fe-carb, Fe-sil, mag, and green chert; stylolites common throughout sequence
Sheps Lake	12-SL-1011D	70.90	72.70	**JUIF**	alternating bands of mag and hem; abundant jasper clasts and sub-mm laminae of Fe-carb; mottled late Fe-carbonate absent
Sheps Lake	12-SL-1011D	72.70	74.71	**JUIF**	jasper restricted to thin bands; predominantly granular (mag) and progressively increasing chert abundance towards GC contact
Sheps Lake	12-SL-1011D	74.71	77.00	**GC**	grey-green chert with abundant wavy mag bands; abundant sulfide (py) blebs at 76.2 to 76.5 m; core missing from 77.0 m downhole
Sheps Lake	12-SL-1005D	0.00	2.50	**OB**	overburden
Sheps Lake	12-SL-1005D	2.50	10.20	**MS**	dominantly fine-grained massive to laminated black shale with lesser < 1 cm silty units (with pyrite); matrix-supported conglomerate with chert and shale clasts from 7.63 to 7.85 m, 8.45 to 9.00 m and 9.10 to 9.30 m; lower contact sharp with underlying LC, probably erosional contact
Sheps Lake	12-SL-1005D	10.20	17.30	**LC**	finely laminated grey-green mudstone and siltstone layers, rarely up to fine-grained sandstone; mineralogy difficult to determine due to fine grain size, but likely chert-carb-Fe-silicates; minor pyrite in sandstone layers; occasional stylolites throughout the unit; no stromatolites observed

Table A3.1. *(continued)*

Sheps Lake	12-SL-1005D	17.30	22.20	**LC**	similar to overlying LC, but magnetite bands and disseminated magnetite throughout, increasing with depth.
Sheps Lake	12-SL-1005D	22.20	28.20	**LC**	missing core but logged as LC in company logs
Sheps Lake	12-SL-1005D	28.20	40.90	**JUIF**	upper contact of JUIF marked by first appearance of red jasper; variable unit with discontinuous bands of red jasper and grey magnetite, and mottled IF with fine-grained magnetite, pink chert and large overprinting carbonates
Sheps Lake	12-SL-1005D	40.90	47.59	**JUIF**	mottled pink to grey JUIF with no jasper bands and rare magnetite bands; mineralogy dominantly magnetite and pink chert, with large overprinting carbonates
Sheps Lake	12-SL-1005D	47.59	55.25	**JUIF**	JUIF with common discontinuous jasper and magnetite bands and granular mottled pink interbeds (chert + mag); after 51.5 m, abundant grey-green granular bands with lesser jasper; sharp lower contact with glassy GC
Sheps Lake	12-SL-1005D	55.25	58.00	**GC**	upper 55 cm glassy green chert with disseminated magnetite; after 55.45 m, magnetite bands are more common; following this interval, GC is granular and laminated with only minor green chert; dominantly granular carbonates, Fe-silicates, chert and minor disseminated mag; disseminated euhedral pyrite associated with black-brown shaly units and rare stylolites
Sheps Lake	12-SL-1005D	58.00	60.72	**URC**	no URC recorded in company logs, but this unit has abundant jasper and magnetite bands (discontinuous) and oolitic pink grainstone consisting of chert, hem and mag; large overprinting carbonates locally common; gradational lower contact marked by disappearance of jasper bands

Table A3.1. *(continued)*

Sheps Lake	12-SL-1005D	60.72	66.00	**PGC**	oolitic mottled pink-grey grainstone with disseminated mag and chert and large overprinting carbonates; rare jasper clasts throughout, likely rip-up clasts; rare magnetite bands also recorded
Sheps Lake	12-SL-1005D	66.00	69.16	**LRC**	gradational contact with PGC marked by first appearance of jasper bands and abundant discontinuous magnetite bands; grainstone interbeds similar to PGC, but less late carbonate
Sheps Lake	12-SL-1005D	69.16	81.30	**LRGC**	highly variable unit with gradational contact with LRC marked by appearance of green chert layers; consists of layered bands of green chert, red jasper, yellow carbonate and grey magnetite, with grainstone interbeds
Sheps Lake	12-SL-1005D	81.30	101.64	**LRGC**	granular to fine-grained LRGC with numerous carbonate bands; disseminated magnetite throughout and common ooliths; carbonate banding more common over lower 2 m
Sheps Lake	12-SL-1005D	101.64	114.00	**LIF**	well laminated LIF with bands of fine-grained siltstone, magnetite, chert, carbonate and Fe-silicates (generally < 1 cm); possible stromatolites from 106.64 to 106.92 m; magnetite out at 111.10 m, but rest of core is similar to overlying section
Sheps Lake	11-LR-1010D	0.00	4.00	**OB**	overburden
Lac Ritchie	11-LR-1010D	4.00	11.54	**LC**	grey to green granular iron formation and iron formation breccia with high magnetite content (strongly magnetic); breccia consists of angular to sub-rounded chert clasts, matrix-supported with sandy matrix; common evidence of syn-sedimentary slumping and micro-faults

Table A3.1. *(continued)*

Lac Ritchie	11-LR-1010D	11.54	16.78	**JUIF**	purple to grey, granular to oolitic iron formation; massive to banded, rare jasper clasts and discontinuous bands throughout; strongly magnetic with abundant disseminated magnetite and magnetite bands; increase in carbonate content, abundance of ooliths, and abundance of thin green chert bands with increasing depth
Lac Ritchie	11-LR-1010D	16.78	18.69	**GC**	green chert with Fe-carb-rich, weakly banded units with disseminated magnetite over upper and lower 40 cm (rare magnetite bands)
Lac Ritchie	11-LR-1010D	18.69	25.20	**URC**	highly variable iron formation with bands of oolitic grainstone and granular iron formation, and abundant jasper bands and clasts; common magnetite/hematite-rich intervals with disseminated magnetite
Lac Ritchie	11-LR-1010D	25.20	27.00	**PGC**	granular, grey to purple massive granular iron formation; strongly to moderately magnetic with disseminated magnetite; rare jasper bands and clasts and rare ooliths in some intervals
Lac Ritchie	11-LR-1010D	27.00	43.87	**PGC**	similar to overlying unit, but only weakly magnetic (hematite >> magnetite); dominantly consists of chert and hematite grains with rare jasper clasts; graded and wavy laminations observed, as well as possible thin channel sandstones
Lac Ritchie	11-LR-1010D	43.87	58.37	**LRGC**	red to grey oolitic grainstone and granular iron formation with abundant jasper clasts and grains; rare jasper bands, green chert bands and hematite bands also recorded; jasper clasts commonly have purple oxide-rich cores surrounded by red jasper; abundance of jasper increases with depth; non-magnetic to weakly magnetic interval

Table A3.1. *(continued)*

Lac Ritchie	11-LR-1010D	58.37	75.00	**JSP**	red jasper-rich unit with abundant clean jasper bands, jasper clasts and grains and granular jasper-rich iron formation with rare ooliths; weakly magnetic with some hematite rich bands
Lac Ritchie	11-LR-1005D	0.00	3.80	**OB**	overburden
Lac Ritchie	11-LR-1005D	3.80	11.97	**DOL**	take way-up with a pinch of salt, as core pieces are highly fragmented; grey-beige dolomite unit with common greenish-clear chert inclusions; no dominant structures; nonmagnetic over measured interval; lower contact with LC marked by appearance of cleaner green chert; contact relatively sharp; stylolites common, but not pervasive
Lac Ritchie	11-LR-1005D	11.97	18.90	**LC**	green to clear chert with abundant mag bands; increasing jsp content towards JUIF contact over a span of ~ 1 m; stromatolitic from 13.55 to 18.90 m defined by wavy bands of chert and magnetite
Lac Ritchie	11-LR-1005D	18.90	40.64	**JUIF**	core missing from 19 to 25 m; granular to oolitic IF with abundant jasper clasts with sparse intervals of Fe-oxide bands and occasional spherulitic siderite/ankerite
Lac Ritchie	11-LR-1005D	40.64	41.96	**JUIF**	thin interval of green chert with abundant overprinting siderite/ankerite; rip-up clasts of jasper common; overall, interval is mag-poor

Table A3.1. *(continued)*

Lac Ritchie	11-LR-1005D	41.96	59.87	**JUIF**	mag-rich granular to oolitic JUIF with considerably lower abundance of jsp clasts; potential stromatolites over a span of 6 m from upper contact with GC; interval is characterized by more abundant siderite/ankerite overprints relative to JUIF interval from above; microfaults pervasive from ~48 to 59.87 m
Lac Ritchie	11-LR-1005D	59.87	66.86	**JUIF**	missing core but logged as JUIF in company logs
Lac Ritchie	11-LR-1005D	66.86	72.00	**JUIF**	primarily oolitic to banded JUIF with sparser jasper intraclasts; hem ooliths distinct in certain intervals, but Fe-oxides are dominated by mag; no evidence for stromatolites across the interval; lower contact with GC is marked by appearance of green chert and progressive increase in Fe-carb bands and mottles
Lac Ritchie	11-LR-1005D	72.00	75.75	**GC**	grey-green chert predominantly ch+mag+Fe-carb+Fe-sil; mottled Fe-carb present throughout interval with several horizons of non- to weakly magnetic, chert-rich areas
Lac Ritchie	11-LR-1005D	75.75	82.80	**URC**	contact with GC marked by the appearance of abundant jasper clasts; predominantly granular to oolitic IF and relatively homogeneous unit overall; banding increases from ~82 to 82.80 m; spherulitic siderite/ankerite most common from ~77 to 79 m
Lac Ritchie	11-LR-1005D	82.80	86.00	**PGC**	appearance-wise, relatively similar to URC and LRGC units above and below it, but is characterized by lower mag abundance relative to LRGC, and occurrence of mottled carbonate; more oxide (mag)-rich than URC; texturally granular to oolitic with hem-rich bands
Lac Ritchie	11-LR-1005D	86.00	114.00	**LRGC**	granular to oolitic IF; jasper clasts and bands increase in abundance downhole from 104.55 m

Table A3.1. *(continued)*

Lac Ritchie	11-LR-1012D	0.00	1.50	**OB**	overburden
Lac Ritchie	11-LR-1012D	1.50	7.00	**LC**	interval is rich in jasper ooliths and granules with abundant mottled siderite scattered throughout; granules of Fe-oxides, predominantly mag, common throughout; overall appearance is quite similar to JUIF, although distinct intervals of grey-green chert differentiate it
Lac Ritchie	11-LR-1012D	7.00	13.88	**LC**	missing core, but likely similar as above (present from 7.5 to 8.5 m)
Lac Ritchie	11-LR-1012D	13.88	15.48	**LC**	conglomeratic horizon of LC with abundant grey (tan weathering) chert and yellow-orange weathering Fe-carb; matrix is dominated by mag; highly magnetic over this interval
Lac Ritchie	11-LR-1012D	15.48	25.95	**LC**	mineralogically similar to previous interval, but is distinctly more banded, and stylolites are common
Lac Ritchie	11-LR-1012D	25.95	39.05	**LC**	return to conglomerate; microfaulting and limonite alteration present throughout unit but is most pervasive from about 30.20 to 32.90 m
Lac Ritchie	11-LR-1012D	39.05	45.50	**LC**	reappearance of jasper clasts, common throughout interval; fracture and microfaults evident from 44.0 to 45.5 m
Lac Ritchie	11-LR-1012D	45.50	48.70	**LC**	missing core
Lac Ritchie	11-LR-1012D	48.70	52.37	**GC**	primarily green chert with clasts of grey chert; calcite veins pervasive from 51.78 to 51.97 m; stylolites common and mottled Fe-carb present from 51 m downhole; overall, interval is mag-poor

Table A3.1. *(continued)*

Lac Ritchie	11-LR-1012D	52.37	54.70	**GC**	appearance of jasper clasts and mag ooliths and granules; relative decrease in grey-green chert from previous interval
Lac Ritchie	11-LR-1012D	54.70	57.10	**GC**	disappearance of jasper clasts; return to cleaner green chert with several horizons of late diagenetic ankerite; interval is nonmagnetic; calcite veins pervasive from 55.60 to 56.00 m
Lac Ritchie	11-LR-1012D	57.10	61.87	**URC**	oolitic grainstone with abundant jasper clasts; abundant siderite from 57.10 to 57,47 m and from 58.66 to 60.00 m
Lac Ritchie	11-LR-1012D	61.87	64.01	**PGC**	similar to URC interval above, but with considerably less jasper clasts and mottled siderite
Lac Ritchie	11-LR-1012D	64.01	94.50	**LRGC**	oolitic grainstone and predominantly mag-rich; increasing abundance of jasper ooliths towards JSP contact; overall, texturally and mineralogically homogeneous
Lac Ritchie	11-LR-1012D	94.50	114.28	**JSP**	granular to oolitic grainstone with abundant jasper clasts and hem+mag bands; weakly magnetic throughout, but increases towards contact with RTH shale over a span of 0.20 m; lower contact is strongly magnetic with abundant water escape structures and euhedral pyrite; predominantly rich in hem granules and ooliths
Lac Ritchie	11-LR-1012D	114.28	117.00	**RTH**	massive grey-green shale unit with pyrite overgrowths most prominent along tops/bottoms of drill core sections where they break
Lac Ritchie	11-LR-1029D	0.00	2.40	**OB**	overburden

Table A3.1. *(continued)*

Lac Ritchie	11-LR-1029D	2.40	19.50	**MS**	finely laminated black shale with silty units over lower 50 cm; strongly deformed and altered along laminations
Lac Ritchie	11-LR-1029D	19.50	33.76	**DOL**	massive grey-beige crystalline dolomite with no internal structure; numerous narrow calcite veinlets throughout; remobilized magnetite and thin magnetite layers over lower 20 cm; lower contact marked by minor breccia but appears gradational with lower chert unit
Lac Ritchie	11-LR-1029D	33.76	38.39	**LC**	grey, granular chert with disseminated magnetite and Fe-silicates and minor carbonate in places; gradational lower contact marked by appearance of jasper clasts
Lac Ritchie	11-LR-1029D	38.39	45.50	**JUIF**	grey magnetite-rich granular IF with rare jasper bands and clasts
Lac Ritchie	11-LR-1029D	45.50	51.50	**JUIF**	missing core
Lac Ritchie	11-LR-1029D	51.50	55.25	**JUIF**	grey to pink granular IF with lesser carbonate-rich bands; abundant bands of coarser-grained material with clasts of jasper and lesser magnetite clasts (rip up clasts) and common brecciation; stromatolites observed at 54.67 m followed by chaotic brecciation with magnetite fragments in a carbonate matrix for 35 cm after this; some other possible stromatolites also observed below this unit
Lac Ritchie	11-LR-1029D	55.25	57.90	**GC**	green unit with overall granular texture and discontinuous bands or clasts of chert; dominated by chert-carb-Fe-silicates with only minor disseminated magnetite and rare magnetite bands
Lac Ritchie	11-LR-1029D	57.90	65.30	**JUIF**	grey to pink, granular, and massive to banded chert (mag-chert-hem) with interbeds of breccia and conglomerate (matrix-supported with large jasper and magnetite clasts up to 5 cm); overprinting Fe-carbonates common in some areas

Table A3.1. *(continued)*

Lac Ritchie	11-LR-1029D	65.30	68.44	**JUIF**	similar to overlying unit, but with a greater abundance of conglomerate and breccia units (> 50% of the core) and common carbonate banding; common evidence of syn-sedimentary deformation (e.g., microfaults, slumps); matrix of conglomerate is generally pink chert; abundant disseminated magnetite and magnetite bands
Lac Ritchie	11-LR-1029D	68.44	69.70	**GC**	similar to GC interval from 55.25 to 57.9 m.
Lac Ritchie	11-LR-1029D	69.70	89.70	**JUIF**	similar to JUIF interval from 65.3 to 68.44 m; massive granular magnetite-rich section from 72.95 to 73.60 m; after 79 m, matrix of conglomerates becomes grey-green in colour, and abundance of jasper decreases; gradational lower contact marked by last conglomerate bed
Lac Ritchie	11-LR-1029D	89.70	94.87	**JUIF**	grey to pink granular IF; generally massive with minor banding in places; bands composed of disseminated magnetite, chert, hem and Fe-carbonate; ooliths common in some sections; hematite content decreases with increasing depth
Lac Ritchie	11-LR-1029D	94.87	96.86	**GC**	green unit composed of bands and clasts of glassy green chert in a granular matrix; mineralogy dominantly green chert-carb-Fe-sil, with minor disseminated magnetite in places; banding increases over lower 50 cm, and lower contact is gradational, marked by first appearance of red jasper and abundant ooliths
Lac Ritchie	11-LR-1029D	96.86	100.18	**URC**	interbedded oolitic grainstone with common jasper clasts, and jasper and magnetite bands.

Table A3.1. *(continued)*

Lac Ritchie	11-LR-1029D	100.18	104.97	**PGC**	dominantly pink to grey granular and oolitic IF bands with abundant overprinting carbonates in places; jasper clasts (rip-up clasts) observed throughout, but less abundant than in the overlying unit; magnetite content highly variable
Lac Ritchie	11-LR-1029D	104.79	120.00	**LRGC**	dominantly grey to pink/red granular IF; varies throughout from grey IF with abundant disseminated magnetite to pink/red units with low magnetite content; rare jasper clasts and bands seen throughout; carbonate almost completely absent from this unit
Lac Ritchie	11-LR-1020D	0.00	4.50	**OB**	overburden
Lac Ritchie	11-LR-1020D	4.50	7.94	**JSP**	granular to oolitic red to white chert jaspilite with lesser red jasper and grey oxide bands; generally only weakly magnetic; rare magnetite bands; lower contact marked by numerous water escape structures from underlying shales (with euhedral pyrite overgrowths)
Lac Ritchie	11-LR-1020D	7.94	20.11	**RTH**	generally massive grey-green shale and fine-grained siltstone; banding more common after 13.5 m; sharp lower contact and marked by sharp increase in pyrite over lower 20 cm
Lac Ritchie	11-LR-1020D	20.11	21.90	**BC**	massive to conglomeratic black chert; conglomeratic sections contain clasts of angular to subrounded black chert in carbonate matrix; lower contact gradational with chert fragments in granular IF
Lac Ritchie	11-LR-1020D	21.90	22.54	**IF**	grey to red granular IF with chert, hematite and minor disseminated magnetite; minor carbonates and some ooliths; sharp lower contact
Lac Ritchie	11-LR-1020D	22.54	45.00	**WQ**	massive to well-bedded fine-grained to medium-grained sandstone with thin shale interbeds; common cross-laminations and thin channel structures; dominantly quartz-rich sandstone with minor feldspar

Table A3.1. *(continued)*

Lac Ritchie	11-LR-1020D	45.00	54.09	**WQ**	interbedded fine-grained to medium-grained sandstone and coarse-grained sandstone with abundant carbonate
Lac Ritchie	11-LR-1020D	54.09	56.92	**WQ**	generally coarse-grained sandstone with large carbonate grains (up to 3 mm) and red sandy matrix
Lac Ritchie	11-LR-1020D	56.20	58.50	**WQ**	fine-grained, well-bedded sandstone with conglomerate at base
Lac Ritchie	11-LR-1020D	58.50	84.00	**GRGN**	Archean basement, composed mainly of tonalite gneiss and granitic pegmatites
Hayot Lake	HAY-11-29	0.00	1.20	**OB**	overburden
Hayot Lake	HAY-11-29	1.20	5.66	**LRGC**	variable unit with magnetite bands (undulating, possible stromatolites) and interbeds of granular iron formation with lesser carbonate-Fe-silicate bands; moderately to strongly magnetic
Hayot Lake	HAY-11-29	5.66	11.44	**LRGC**	laminated, brown to beige weathering iron formation mudstone, with numerous thin < 1 cm, generally < 5 mm) bands of magnetite, carbonate, Fe-silicates and granular iron formation; laminations often wavy with some cross-laminations observed; strongly magnetic throughout
Hayot Lake	HAY-11-29	11.44	19.70	**LRGC**	green, finely laminated iron formation mudstone with lesser granular interbeds and rare breccia beds; mudstone composed of fine laminations of Fe-silicates and carbonates with lesser magnetite laminations; weakly magnetic throughout

Table A3.1. *(continued)*

Hayot Lake	HAY-11-29	19.70	27.00	**LIF**	interbedded finely laminated, Fe-silicate rich iron formation and iron formation breccia with angular fragments of iron formation in a dominantly quartz-rich matrix; breccia units linked by quartz veins; nonmagnetic throughout
Hayot Lake	HAY-11-29	27.00	73.80	**LIF**	finely laminated Fe-silicate rich iron formation mudstone with rare granular interbeds; nonmagnetic throughout
Hayot Lake	HAY-11-29	73.80	78.00	**LIF**	laminated to brecciated iron formation; laminated sections similar to overlying unit; breccia at top of the interval is characterized by angular to subrounded clasts of iron formation in a sand matrix; minor pyrite in matrix; breccias commonly with stylolites at margins; breccias at the base of the interval is characterized by angular fragments in crystalline calcite matrix and abundant quartz-carbonate veining; nonmagnetic throughout
Hayot Lake	HAY-11-07	0.00	10.50	**OB**	overburden
Hayot Lake	HAY-11-07	10.50	41.65	**MS**	well-banded MS with black shale beds and grey silty beds;shale beds commonly grade downwards into silty beds, but have sharp tops, potentially indicating that these represent DE turbidite beds; oily over lower 2 m; lower contact is sharp with abundant to massive framboidal pyrite over the lower 10 cm
Hayot Lake	HAY-11-07	41.65	48.24	**MS**	massive, organic-rich MS black shale with no obvious bedding and oily sheen on core surface
Hayot Lake	HAY-11-07	48.24	50.31	**MS**	interbedded massive, organic-rich MS and conglomerate with large chert clasts; quartz veining common over lower 1 m, with core broken up; lower contact not seen, but interpreted as a tectonic contact

Table A3.1. *(continued)*

Hayot Lake	HAY-11-07	50.31	73.54	**LC**	cherty IF with intervals of glassy, green to transparent chert and abundant stromatolitic units (composed of finely laminated, domal structures composed of carb-Fe-silicate); oxide content is low, but section becomes more magnetic after 71.9 m, with stromatolite layers replaced by magnetite and disseminated in rare sandy intervals; minor late diagenetic carbonate in cherty layers; lower contact is gradational, with gradual increase in granular bands and magnetite content, marked by first appearance of red jasper-rich granular iron formation
Hayot Lake	HAY-11-07	73.54	82.25	**JUIF**	variable unit with red granular jasper-rich iron formation interbedded with lesser carb- and mag-rich finely laminated intervals with domal structures (probable stromatolites); moderately to strongly magnetic
Hayot Lake	HAY-11-07	82.25	105.88	**JUIF**	grey to pink granular iron formation interbedded with lesser carb- and mag-rich finely laminated bands (< 5% of total interval); granular iron formation coarse-grained in places, with numerous grains of red jasper and magnetite. no evidence of stromatolites; moderately to strongly magnetic
Hayot Lake	HAY-11-07	105.88	109.17	**JUIF**	massive to weakly banded, hematite-rich granular iron formation with rare carbonate bands; lower 15 cm brecciated with large (up to 3 cm) angular to subrounded jasper clasts; weakly magnetic
Hayot Lake	HAY-11-07	109.17	110.79	**JUIF**	variable unit, carbonate-magnetite bands common over upper 50 cm; beds of massive and granular IF predominant with abundant disseminated magnetite; moderately to strongly magnetic
Hayot Lake	HAY-11-07	110.79	111.55	**GC**	green chert with significant disseminated magnetite and carbonate and common moderate amplitude stylolites

Table A3.1. *(continued)*

Hayot Lake	HAY-11-07	111.55	120.55	**URC**	massive to weakly banded hematite-rich granular iron formation; lower contact marked by first appearance of jasper bands; weakly to nonmagnetic
Hayot Lake	HAY-11-07	120.55	136.80	**URC**	dominantly grey granular iron formation with red jasper bands and rare white chert bands; no ooliths recorded, most of the interval is weakly magnetic, but some short strongly magnetic intervals recorded
Hayot Lake	HAY-11-07	136.80	147.00	**PGC**	purple, massive to weakly banded hematite-rich granular iron formation; chaotic breccia from 145.9 to 146.3 m; weakly to nonmagnetic; sharp lower contact marked by increase in magnetite content and appearance of stromatolites
Hayot Lake	HAY-11-07	147.00	157.86	**LRGC**	interbedded pink grainstone and banded domal structures interpreted as stromatolites; pink grainstones have abundant jasper and magnetite grains and rare oolitic sections, moderately magnetic; stromatolites replaced by magnetite and carbonate and highly magnetic; laminations range from parallel to perpendicular to core axis
Hayot Lake	HAY-11-07	157.86	160.15	**LRGC**	green, well-banded unit with alternating bands of magnetite and chert-Fe-silicates; evidence of folding seen throughout; strongly magnetic
Hayot Lake	HAY-11-07	160.15	163.00	**LRGC**	red to grey oolitic grainstone; coarse-grained in places and weakly magnetic

APPENDIX 4: THIN SECTION DESCRIPTIONS

Table A4.1. Petrographic observations characterizing dominant mineralogical assemblages and textures across various units of the Sokoman IF.

Drillhole	*Unit*	*ID*	*Depth (m)*	*Comments*
12-SL-1018D	MS	MS002	7.2	black shale with fine laminae and mm-scale silt interbeds; bands of subhedral to euhedral pyrite grains are generally parallel to bedding
12-SL-1018D	MS	MS005	11.7	silicified black shale with crenulated laminations; thin section captures part of intraclastic breccia composed of subangular chert and shale fragments
12-SL-1018D	LC	LC066	24.7	wavy and discontinuous bands composed primarily of blocky megaquartz within massive siderite-minnesotaite; relict stromatolitic laminae preserved within these bands
12-SL-1018D	LC	LC011	39.3	Fe-silicate and Fe-carbonate grainstone with subordinate siderite bands that are locally pyrite-rich; scheelite grain is noted within this locally pyrite-rich interval; greenalite granules commonly exhibit overgrowth rims of siderite and minnesotaite; rare magnetite peloids
12-SL-1018D	LC	LC016	44.3	banded magnetite-siderite interval with subordinate chert grainstone; microcrystalline chert granules cemented by interstitial mosaic chert; stylolites evident around or near the margins of the banded horizons
12-SL-1018D	JUIF	JUIF018	49.3	jasper-rich grainstone with discontinuous bands of granular chert+magnetite+hematite+siderite; Fe-carbonate mottles common around banded intervals
12-SL-1018D	JUIF	JUIF022	57.8	jasper-rich grainstone with distinct magnetite-rich interval containing abundant elongated microcrystalline chert peloids with numerous minnesotaite and greenalite inclusions
12-SL-1018D	JUIF	JUIF025	62.7	jasper-rich grainstone with coarse-grained siderite-ankerite mottles

Table A4.1. *(continued)*

12-SL-1018D	JUIF	JUIF026	65.2	similar as JUIF026, but with more pronounced mottling; the boundaries of the mottles often crosscut relict ooliths indicating its late diagenetic origin
12-SL-1018D	JUIF	JUIF032	69.9	jasper-rich grainstone with discontinuous magnetite bands
12-SL-1018D	JUIF	JUIF037	73.9	compacted stilpnomelane-hematite oolith-rich interval within predominantly discontinuous magnetite-rich bands
12-SL-1018D	GC	GC038	74.4	microcrystalline chert granules cemented by drusy to blocky mesocrystalline quartz with subordinate siderite granules; rare Fe-oxides
12-SL-1018D	GC	GC039	76.3	bedded microcrystalline chert with fine laminations of siderite and minnesotaite interspersed with chert peloids that variably coarsen outwards; magnetite disseminated in upper chert interval
12-SL-1018D	URC	URC040	77.8	interbedded jasper-rich grainstone and magnetite-ankerite grainstone; granules cemented by drusy to blocky mesocrystalline quartz; abundant intraformational jasper clasts
12-SL-1018D	URC	URC041	78.5	same as URC040, but with more intraformational jasper clasts as well as subrounded magnetite peloids
12-SL-1018D	URC	URC042	79.5	same as URC040 and URC041, but encompasses more of the magnetite-ankerite-rich interval; late crosscutting quartz veins oriented perpendicular to bedding
12-SL-1018D	PGC	PGC045	89.5	very coarse-grained ankerite mottles within chert magnetite grainstone
12-SL-1018D	LRC	LRC047	93.9	jasper-rich grainstone; poorly compacted grains are cemented by drusy to blocky mesocrystalline quartz; some granules exhibit stilpnomelane cores
12-SL-1018D	LRGC	LRGC051	100.8	jasper-rich grainstone interbedded with magnetite-rich bands; jasper peloid in central section exhibits prominent shrinkage cracks

Table A4.1. *(continued)*

12-SL-1018D	LRGC	LRGC055	108.8	finely laminated chert-magnetite-siderite with massive chert band across lower section
12-SL-1018D	LRGC	LRGC061	122.2	banded chert-siderite with subordinate granular intervals of greenalite granules cemented by interstitial domain to mosaic chert; granules exhibit prominent shrinkage cracks and commonly display siderite overgrowth rims
12-SL-1018D	LIF	LIF063	126.4	wavy-bedded siderite-magnetite with subordinate granular intervals composed of magnetite peloids and greenalite granules cemented by drusy to block mesocrystalline quartz; granules commonly display siderite and ankerite overgrowth rims
12-SL-1017D	LC	LC216	35.4	chert grainstone characterized by microcrystalline chert granules cemented by domain to mosaic microcrystalline chert and locally by drusy to blocky mesocrystalline quartz; magnetite overgrowths common; jasper peloid in lower left section; little to no carbonate overprinting
12-SL-1017D	LC	LC226	60.4	chert-siderite-greenalite grainstone with granules cemented by domain to mosaic microcrystalline chert with abundant 'bowtie' minnesotaite aggregates; large siderite/ankerite spherulitic mottles encapsulating grainstone bounded by magnetite rims
12-SL-1017D	GC	GC232	79.6	chert-minnesotaite-magnetite grainstone with microcrystalline chert granules cemented by drusy to blocky mesocrystalline quartz; common magnetite peloids
12-SL-1005D	LC	LC069	12.2	finely laminated siltstone with predominantly microcrystalline chert and subordinate 'bowtie' minnesotaite aggregates; rare siderite and disseminated magnetite and pyrite blebs; several crosscutting veins composed of blocky mega- to mesocrystalline quartz noted

Table A4.1. *(continued)*

12-SL-1005D	JUIF	JUIF073	30.3	Fe-oxide (both magnetite and hematite) and chert grainstone bounded by intraformational chert clasts in the uppermost and lowermost sections; original granular fabric difficult to discern due to pervasive siderite and ankerite mottles; spongy and microplaty hematite aggregates commonly crosscut by coarse magnetite euhedra; intraformational chert clasts are jaspilitic where microcrystalline chert granules with hematite 'dust' are cemented by domain to mosaic microcrystalline chert; rare minnesotaite and stilpnomelane flakes but disseminated throughout section
12-SL-1005D	JUIF	JUIF079	42.9	chert grainstone with abundant microcrystalline chert granules cemented by drusy to blocky mesocrystalline quartz; common magnetite peloids and overgrowths on chert granules; siderite-ankerite mottles common
12-SL-1005D	JUIF	JUIF083	54.3	bands of moderately compacted chert-magnetite granules with siderite/ankerite overprints in upper section
12-SL-1005D	GC	GC084	55.3	poorly compacted grainstone defined by siderite granules with common ankerite overgrowths and cemented drusy to blocky mesocrystalline quartz; granules commonly exhibit shrinkage cracks; rare magnetite grains; homogeneous section overall
12-SL-1005D	GC	GC085	57.6	Fe-carbonate grainstone defined by siderite granules set in a siderite/ankerite matrix; rare interstitial microcrystalline chert
12-SL-1005D	URC	URC086	58.6	oolitic grainstone with abundant jasper ooliths and peloids cemented by drusy to block meso- to mega-crystalline quartz; oolith cores are typically jaspilitic containing hematite 'dust' and variable recrystallized quartz; cortices are dominated by spongy and microplaty hematite aggregates with subordinate magnetite; late diagenetic, coarse-grained ankerite mottles noted

Table A4.1. *(continued)*

12-SL-1005D	URC	URC087	59.9	similar as URC086, but incorporates more jasper peloids; stilpnomelane sheaves noted in some oolith cores
12-SL-1005D	PGC	PGC088	61.2	chert-magnetite grainstone with partial jaspilitic interval in the lowermost section; granules cemented by drusy to blocky mesocrystalline quartz; magnetite and ankerite overgrowth rims common
12-SL-1005D	LRC	LRC092	67.8	alternating jasper bands and chert-magnetite grainstone interbeds; ankerite mottles common
12-SL-1005D	LRGC	LRGC094	71.9	similar to LRC092, but is notably more abundant in siderite, ankerite, and magnetite; siderite overgrowth rims and late diagenetic ankerite mottles are more common
12-SL-1005D	LRGC	LRGC103	93.0	chert-magnetite grainstone with microcrystalline chert granules cemented predominantly by domain to mosaic microcrystalline chert and drusy to blocky mesocrystalline quartz in some areas; late diagenetic ankerite mottles not observed; siderite-magnetite bands with ankeritic margins run across the central section
12-SL-1005D	LIF	LIF109	106.9	intraformational chert blocks within finely laminated magnetite-chert banded interval; in the leftmost section, blocks are cemented by drusy to blocky megacrystalline quartz
12-SL-1005D	LIF	LIF112	113.7	finely laminated carbonaceous siltstone primarily composed of siderite and microcrystalline chert laminae; stylolite seams common near the margins of siderite laminae
11-LR-1010D	LC	LC145	6.4	chert-magnetite-minnesotaite grainstone cemented by drusy to blocky mesocrystalline quartz; offset fragments of chert-minnesotaite band running across the leftmost section interpreted as microfaults

Table A4.1. *(continued)*

11-LR-1010D	URC	URC148	19.9	oolitic chert-hematite grainstone with fine hematite-jasper laminae and occasional magnetite peloids; intraformational chert clast in lowermost section composed of microcrystalline chert and spongy and microplaty hematite aggregates
11-LR-1010D	PGC	PGC150	27.5	chert-hematite grainstone cemented by drusy to blocky mesocrystalline quartz; granules commonly have hematite 'dust' cores with rims composed of spongy and microplaty hematite aggregates; coarse-grained magnetite euhedra typically crosscut granule boundaries; occasional late diagenetic ankerite rosettes
11-LR-1010D	PGC	PGC152	36.5	chert-hematite-magnetite grainstone cemented by drusy to blocky mesocrystalline quartz; intercalated with thin hematitic jaspilite bands
11-LR-1010D	LRGC	LRGC154	47.4	chert-minnesotaite grainstone cemented by drusy to blocky mesocrystalline quartz; hematite-magnetite bands present in upper- and lowermost sections; hematite and magnetite peloids common
11-LR-1010D	JSP	JSP158	58.8	thin section captures discontinuous band of jasper with hematite-rich oolitic grainstone interval in the uppermost section
11-LR-1005D	LC	LC301	14.1	bands of Fe-silicate grainstone cemented by domain to mosaic microcrystalline chert; abundant greenalite granules with common magnetite and minnesotaite overgrowth rims
11-LR-1012D	LC	LC267	41.2	bands of chert-magnetite grainstone cemented by domain to mosaic microcrystalline chert with several hematite and microcrystalline chert peloids

Table A4.1. *(continued)*

11-LR-1012D	JSP	JSP294	113.3	oolitic chert-hematite grainstone cemented by domain to mosaic microcrystalline chert; granules are composed of hematite 'dust' cores and cortical layers of spongy to microplaty hematite aggregates; rare magnetite
11-LR-1029D	DOL	DOL113	30.0	massive cherty dolomite with thin crosscutting quartz veinlets; pyrite grains common along stylolite margins
11-LR-1029D	LC	LC114	36.2	chert grainstone with abundant granules of microcrystalline chert, siderite, and magnetite; granules cemented by drusy to blocky mesocrystalline quartz
11-LR-1029D	JUIF	JUIF116	42.1	oolitic jasper-rich horizon within bands of granular magnetite-siderite-stilpnomelane-rich intervals; the jasper-rich horizon is less compacted than the surrounding granular bands
11-LR-1029D	JUIF	JUIF119	54.7	stromatolitic horizon in upper section overlying chaotic breccia; stromatolites are defined by microcrystalline chert with jaspilitic and ankeritic encrustations between mats; brecciated interval includes many sideritic and magnetite granules within an ankeritic matrix
11-LR-1029D	GC	GC120	56.9	chert grainstone with numerous microcrystalline chert and siderite granules cemented by drusy to blocky mesocrystalline quartz; granular siderite with prominent shrinkage cracks are abundant in the lower section; granules commonly overprinted by late diagenetic ankerite; many rip-up clasts of microcrystalline chert
11-LR-1029D	JUIF	JUIF121	59.3	oolitic grainstone with abundant jasper-rich ooliths cemented by drusy to blocky mesocrystalline quartz; partial overgrowth rims of ankerite and magnetite common; section captures large intraformational chert clasts characterized by microcrystalline chert with hematite 'dust' and spongy hematite aggregates

Table A4.1. *(continued)*

11-LR-1029D	JUIF	JUIF124	66.1	interbedded massive chert with abundant disseminated magnetite euhedra; numerous microfaults across section; ankeritic mottles appear to propagate from the highly fractured upper section
11-LR-1029D	JUIF	JUIF127	73.1	oolitic grainstone with normal grading; numerous jaspilitic ooliths and magnetite and hematite peloids cemented by drusy to blocky mesocrystalline quartz; minimal Fe-carbonate overprinting
11-LR-1029D	JUIF	JUIF131	89.5	oolitic chert grainstone; most granules are rimmed by spongy to microplaty heamtite aggregates and replaced by euhedral magnetite; intergranular cements dominantly drusy to blocky mesocrystalline quartz, but domain to mosaic microcrystalline chert present in some areas; granule cores are primarily recrystallized with variable ankerite overprints
11-LR-1029D	GC	GC132	95.5	relatively homogeneous bands of granular, domain to mosaic mesocrystalline chert with occasional microcrystalline chert peloids; margins of chert peloid in upper right section delineated by stylolites; coarse-grained ankerite mottles common in lower section; magnetite disseminate throughout the section
11-LR-1029D	URC	URC133	98.7	interbedded jasper bands and oolitic grainstone with numerous jasper clasts; microfaults commonly infilled by blocky mesocrystalline quartz and occasionally by siderite and ankerite; cements in grainstone interval pervasively overprinted by ankerite
11-LR-1029D	PGC	PGC135	101.1	chert grainstone with common intraformational microcrystalline chert and magnetite peloids; late ankerite mottles common throughout section

Table A4.1. *(continued)*

11-LR-1029D	LRGC	LRGC138	111.4	chert-magnetite grainstone cemented by drusy to blocky mesocrystalline quartz; several late diagenetic ankerite mottles in lower section; stylolite seams divide the upper oxide-rich section from the lower chertier section
11-LR-1020D	JSP	JSP140	5.3	oolitic grainstone with abundant jasper-rich ooliths; granules are notably hematite-rich; upper section defined by jaspilite and hematite bands (hematite > magnetite); intergranular cement optically challenging to discern due to high oxide content (very opaque), but appears to be domain to mosaic microcrystalline chert
11-LR-1020D	RTH	RTH141	9.3	finely laminated shale with numerous fine-grained crystals of chamosite and blotchy pyrite grains in a carbonaceous-siderite-ankerite-chert matrix
11-LR-1020D	RTH	RTH142	18.1	thin section cut perpendicular to core axis; similar to RTH141, but appears to be slightly more carbonaceous
11-LR-1020D	BC	BC143	21.0	microcrystalline chert granules cemented by drusy to blocky mesocrystalline quartz with subordinate siderite granules and rare siderite rims; disseminated pyrite grains present
11-LR-1020D	IF	IF144	22.2	chert grainstone with microcrystalline chert granules cemented by domain to mosaic microcrystalline chert; rare hematite and magnetite peloids; minor Fe-carbonate
HAY-11-07	LC	LC166	59.2	domal stromatolitic laminations within a predominantly microcrystalline chert matrix; laminae are defined by fine-grained siderite and minnesotaite with subordinate greenalite; late diagenetic, coarse-grained ankerite commonly border stylolite seams

Table A4.1. *(continued)*

HAY-11-07	JUIF	JUIF171	74.4	domal stromatolitic laminations within a granular interval of microcrystalline chert cemented by drusy mesocrystalline quartz; laminae are defined by siderite and magnetite bands with abundant late diagenetic ankerite crosscutting in some areas
HAY-11-07	JUIF	JUIF179	97.7	granular IF with abundant microcrystalline chert granules and pervasive ankerite overprints, generally occluding intergranular cements; thin section includes rip-up clast of non-oolitic, jasper-rich granules cemented by drusy mesocrystalline quartz
HAY-11-07	GC	GC184	111.0	abundant microcrystalline chert granules cemented by drusy to blocky mesocrystalline quartz; chert granules commonly exhibit magnetite overgrowth rims; late diagenetic ankerite overprints notably confined between stylolite seams
HAY-11-07	URC	URC191	133.1	relatively homogeneous microcrystalline chert peloid fringed by bands of hematite-magnetite granules
HAY-11-07	PGC	PGC194	146.0	chaotic breccia of granular IF with abundant jasper ooliths and subangular microcrystalline chert peloids; common late diagenetic ankerite; rare occurrences of stilpnomelane granules partially replaced by hematite and magnetite
HAY-11-07	LRGC	LRGC197	152.9	"background" grainstone IF interbedded with domal stromatolitic laminations; grainstone predominantly composed of non-oolitic jasper and magnetite granules
HAY-11-07	LRGC	LRGC198	156.7	thin section cut perpendicular to core axis; magnetite bands set in a primarily granular interval of microcrystalline chert and greenalite cemented by drusy to blocky mesocrystalline quartz; abundance of late diagenetic ankerite highest proximal to magnetite bands

Table A4.1. *(continued)*

HAY-11-29	LRGC	LRGC201	10.2	alternating intervals of laminated minnesotaite-magnetite-chert and granular chert in a minnesotaite-rich matrix
HAY-11-29	LIF	LIF204	23.7	brecciated blocks of weakly banded siderite-minnesotaite set in a matrix of blocky megaquartz; blocks commonly exhibit acicular minnesotaite overgrowth rims
HAY-11-29	LIF	LIF212	76.2	brecciated blocks of laminated siderite-minnesotaite crosscut by late, very coarse-grained ankerite-calcite veins; pervasive stylolitization most common around the margins of brecciated blocks
Cross Ridge	FL	FL01H	outcrop	colloform chert breccia with a chert-dolomite matrix

APPENDIX 5: BULK-ROCK LITHOGEOCHEMISTRY

Table A5.1. Bulk-rock major (wt.%) and trace element (ppb) abundances, molar and mass ratios, and REE+Y ratios and anomalies (MuQ-normalized) in Sokoman IF samples.

ID		**MS002**	**MS005**	**LC066**	**LC011**	**JUIF018**
Depth (m)		7.19	11.69	24.7	39.32	49.26
Drillhole		12-SL-1018D	12-SL-1018D	12-SL-1018D	12-SL-1018D	12-SL-1018D
Unit		MS	MS	LC	LC	JUIF
SiO_2	*wt. %*	65.14	90.08	26.32	45.86	63.65
TiO_2	"	0.66	0.08	0.07	0.02	0.02
Al_2O_3	"	14.80	3.06	0.74	b.d.l.	0.00
Fe_2O_{3T}	"	3.70	1.64	40.84	43.57	31.57
FeO	"	1.84	0.65	32.46	31.01	11.24
MnO	"	0.10	0.08	1.90	0.68	0.48
MgO	"	2.27	0.68	4.36	1.46	1.09
CaO	"	1.09	0.96	0.81	0.72	1.27
Na_2O	"	1.05	0.23	0.39	0.20	0.06
K_2O	"	4.39	1.04	0.31	b.d.l.	b.d.l.
P_2O_5	"	0.15	0.03	0.19	0.03	0.03
LOI	"	6.01	1.76	23.91	7.16	1.63
Fe(III)/Fe(II)	molar	0.81	1.27	0.13	0.26	1.53
Mn/∑Fe	molar	0.031	0.054	0.052	0.018	0.017
Mn/Fe(II)	molar	0.057	0.122	0.059	0.022	0.043
Mn/Fe(III)	molar	0.070	0.096	0.449	0.085	0.028
Mn/Ti	mass	0.21	1.54	45.10	84.40	114.66
P/∑Fe	molar	0.044	0.019	0.005	0.001	0.001
P/Fe(II)	molar	0.080	0.042	0.006	0.001	0.002
P/Fe(III)	molar	0.099	0.033	0.044	0.003	0.001
P/Ti	mass	0.17	0.30	2.50	1.74	3.36
∑Fe/Ti	mass	6.83	29.20	876.53	4862.75	6795.39
Fe(II)/Ti	mass	3.77	12.84	774.21	3846.24	2689.12
Fe(III)/Ti	mass	3.06	16.36	102.32	1016.51	4106.26
Li	*ppb*	56450	21610	2430	259.9	1047
Be	"	2635	480.5	1265	16520	1211
Sc	"	13310	1823	778.2	591.45	77.87
Ti	"	3792000	393500	325900	62670	32490
V	"	218200	114800	19820	24720	16880
Cr	"	54270	11850	3047	3207	2485
Co	"	10280	6520	4972	9852	5994
Ni	"	41130	13950	3965	1328	1791
Cu	"	42750	54380	1139	11730	7850
Zn	"	36820	123900	13280	6516	3532
Ga	"	19530	4724	2535	1283	847
Rb	"	149500	35580	17090	638.1	371.9

b.d.l. = below detection limit; n.m. = not measured; n/a = not applicable

Table A5.1. *(continued)*

ID		MS002	MS005	LC066	LC011	JUIF018
Depth (m)		7.19	11.69	24.7	39.32	49.26
Drillhole		12-SL-1018D	12-SL-1018D	12-SL-1018D	12-SL-1018D	12-SL-1018D
Unit		MS	MS	LC	LC	JUIF
Sr	"	115400	37940	19690	2193	5760
Y	"	31950	6339	6732	4350	2908
Zr	"	206900	57950	18830	8991	5369
Nb	"	13070	6597	6465	2388	1460
Ag	"	562.8	301.0	27.02	18.06	4.942
Cd	"	155.7	436.1	14.88	3.331	1.965
Sn	"	2943	882.4	237.2	20.35	168.1
Sb	"	1721	1059	76.25	829.8	140.3
Cs	"	7645	1955	18340	507	143.1
Ba	"	812800	169000	32070	1233	2704
La	"	31770	10220	14180	1773	1300
Ce	"	63910	21720	27250	3806	3291
Pr	"	8068	2620	2570	333.7	256.1
Nd	"	30050	9590	9429	1427	1083
Sm	"	5503	1754	1465	305.3	223.1
Eu	"	986.3	200.5	359.1	139	79.09
Gd	"	4732	1395	1403	448.8	316.5
Tb	"	754.1	206.0	175.1	71.15	50.36
Dy	"	4815	1173	963.7	506.7	347.2
Ho	"	1098	238.3	207.9	124.3	86.69
Er	"	3346	654.7	586.5	384	265
Tm	"	525.4	99.22	85.13	57.19	39.09
Yb	"	3478	663.7	509.0	354.6	229
Lu	"	542	98.38	75.11	48.38	30.95
Hf	"	5283	1475	384.2	49.56	36.9
Ta	"	866	223.5	265.4	12.17	10.7
Pb	"	12120	11670	821.6	2110	273.3
Th	"	10710	2975	600.7	37.74	43.97
U	"	10340	3994	371.4	74.87	80.29
ΣREE+Y	"	191528	56972	65991	14129	10505
$(La/La^*)_{MuQ}$		0.94	0.90	1.28	1.67	1.56
$(Ce/Ce^*)_{MuQ}$		0.90	0.93	1.19	1.49	1.66
$(Eu/Eu^*)_{MuQ}$		0.84	0.54	1.25	1.97	1.56
$(Gd/Gd^*)_{MuQ}$		1.05	1.01	1.15	1.18	1.13
$(Lu/Lu^*)_{MuQ}$		1.00	0.94	1.04	0.93	0.98
Y/Ho		29.1	26.6	32.4	35.0	33.5
$(Pr/Yb)_{MuQ}$		0.89	1.52	1.94	0.36	0.43
$(Er/Lu)_{MuQ}$		0.90	0.97	1.14	1.15	1.24

$La^* = Pr^*(Pr/Nd)^2$; $Ce^* = Pr^*(Pr/Nd)$; $Eu^* = Sm^*(Sm/Nd)^{0.5}$; $Gd^* = Tb^*(Tb/Dy)$; $Lu^* = Yb^*(Yb/Tm)$

Table A5.1. *(continued)*

ID		JUIF025	JUIF032	JUIF037	GC039	URC041
Depth (m)		62.72	69.86	73.91	76.31	78.51
Drillhole		12-SL-1018D	12-SL-1018D	12-SL-1018D	12-SL-1018D	12-SL-1018D
Unit		JUIF	JUIF	JUIF	GC	URC
SiO_2	*wt. %*	47.60	36.94	12.19	57.58	52.86
TiO_2	"	0.02	0.02	0.08	0.02	0.02
Al_2O_3	"	b.d.l.	0.07	0.46	b.d.l.	0.00
Fe_2O_{3T}	"	36.23	55.48	63.65	37.65	35.80
FeO	"	11.52	11.19	18.66	12.92	8.77
MnO	"	1.22	1.32	3.80	0.40	1.46
MgO	"	2.28	1.57	2.83	0.72	1.29
CaO	"	5.78	1.62	7.03	1.59	3.54
Na_2O	"	b.d.l.	0.12	0.26	0.58	0.12
K_2O	"	b.d.l.	b.d.l.	0.11	0.01	0.00
P_2O_5	"	0.02	0.02	0.04	0.03	0.02
LOI	"	6.60	2.65	9.36	1.22	4.69
Fe(III)/Fe(II)	molar	1.83	3.46	2.07	1.62	2.67
Mn/∑Fe	molar	0.038	0.027	0.067	0.012	0.046
Mn/Fe(II)	molar	0.107	0.119	0.207	0.031	0.169
Mn/Fe(III)	molar	0.059	0.034	0.100	0.019	0.063
Mn/Ti	mass	1124.07	164.50	74.04	54.87	388.96
P/∑Fe	molar	0.001	0.000	0.001	0.001	0.001
P/Fe(II)	molar	0.002	0.002	0.002	0.002	0.002
P/Fe(III)	molar	0.001	0.001	0.001	0.001	0.001
P/Ti	mass	11.98	1.69	0.48	2.08	2.70
∑Fe/Ti	mass	30247.97	6268.09	1120.23	4651.95	8596.05
Fe(II)/Ti	mass	10688.24	1404.96	364.99	1774.35	2340.20
Fe(III)/Ti	mass	19559.72	4863.14	755.24	2877.60	6255.85
Li	*ppb*	1694	1250	745.3	328.4	1709
Be	"	1113	3350	4327	1068	2805
Sc	"	27.72	182.4	1147	260.9	113.3
Ti	"	8378	61910	397400	56600	29130
V	"	5196	18770	18100	28970	9482
Cr	"	531.1	2047	10490	3949	1574
Co	"	8852	28270	18840	3016	7457
Ni	"	1006	3017	3634	1906	1706
Cu	"	1727	3860	11520	1294	2325
Zn	"	2963	4382	6923	2340	5007
Ga	"	330.2	1496	1901	2213	900.4
Rb	"	167.6	993.8	6300	917.9	1315

b.d.l. = below detection limit; n.m. = not measured; n/a = not applicable

Table A5.1. *(continued)*

ID		JUIF025	JUIF032	JUIF037	GC039	URC041
Depth (m)		62.72	69.86	73.91	76.31	78.51
Drillhole		12-SL-1018D	12-SL-1018D	12-SL-1018D	12-SL-1018D	12-SL-1018D
Unit		JUIF	JUIF	JUIF	GC	URC
Sr	"	17830	9184	34030	4971	19310
Y	"	3660	7646	42030	5413	11950
Zr	"	2126	19940	35750	19880	4737
Nb	"	367.5	4856	10750	4879	1568
Ag	"	3.347	19.95	726.1	333.1	112.1
Cd	"	1.468	9.877	16.54	7.726	6.53
Sn	"	105.6	117.3	161.4	153	93.9
Sb	"	36.23	263.4	189.2	105.2	95.92
Cs	"	60.88	517.8	2639	292.5	151
Ba	"	5186	43410	41920	8550	18810
La	"	1901	4421	34220	7446	5845
Ce	"	4495	10860	33600	10180	9863
Pr	"	360.2	850.5	5376	1297	1233
Nd	"	1563	3585	22410	5205	5229
Sm	"	308.2	773.7	4264	879.2	1034
Eu	"	107.1	243.6	1359	250.4	381.9
Gd	"	418.3	1045	5658	925.9	1397
Tb	"	64.36	177.7	870.3	137.1	217.6
Dy	"	429.6	1215	5750	874.6	1462
Ho	"	103.4	284	1359	202.2	352.7
Er	"	295.8	834.9	3915	602.7	1052
Tm	"	42.16	123.4	565.2	93.16	159.3
Yb	"	224.4	681.8	3127	585.6	950.9
Lu	"	28.4	86.25	415.3	83.59	135
Hf	"	12.32	285.2	427.7	147.9	49.53
Ta	"	1.938	182.8	256.7	59.34	30.18
Pb	"	420	1424	2654	708.1	587.5
Th	"	13.84	350.7	511.1	131.1	81.14
U	"	39.93	75.2	103.8	96.56	51.8
ΣREE+Y	"	14001	32828	164919	34175	41262
$(La/La^*)_{MuQ}$		1.71	1.59	1.90	1.59	1.47
$(Ce/Ce^*)_{MuQ}$		1.66	1.65	0.80	0.96	1.04
$(Eu/Eu^*)_{MuQ}$		1.57	1.36	1.46	1.39	1.66
$(Gd/Gd^*)_{MuQ}$		1.14	1.05	1.12	1.13	1.13
$(Lu/Lu^*)_{MuQ}$		1.01	0.97	1.01	0.96	1.01
Y/Ho		35.4	26.9	30.9	26.8	33.9
$(Pr/Yb)_{MuQ}$		0.62	0.48	0.66	0.85	0.50
$(Er/Lu)_{MuQ}$		1.51	1.41	1.37	1.05	1.13

$La^* = Pr^*(Pr/Nd)^2$; $Ce^* = Pr^*(Pr/Nd)$; $Eu^* = Sm^*(Sm/Nd)^{0.5}$; $Gd^* = Tb^*(Tb/Dy)$; $Lu^* = Yb^*(Yb/Tm)$

Table A5.1. *(continued)*

ID		PGC045	LRC047	LRGC051	LRGC055	LRGC061
Depth (m)		89.465	93.9	100.75	108.845	122.23
Drillhole		12-SL-1018D	12-SL-1018D	12-SL-1018D	12-SL-1018D	12-SL-1018D
Unit		PGC	LRC	LRGC	LRGC	LRGC
SiO_2	*wt. %*	29.71	55.29	29.00	24.69	43.97
TiO_2	"	0.01	0.02	0.01	0.07	0.04
Al_2O_3	"	b.d.l.	b.d.l.	b.d.l.	0.63	0.06
Fe_2O_{3T}	"	48.68	41.54	53.87	57.32	40.86
FeO	"	13.62	11.51	13.73	29.79	28.31
MnO	"	1.20	0.32	0.54	0.79	0.30
MgO	"	3.61	1.10	2.97	4.31	3.69
CaO	"	7.16	0.30	5.92	0.39	1.14
Na_2O	"	0.07	0.51	0.07	0.21	0.11
K_2O	"	b.d.l.	b.d.l.	b.d.l.	0.04	b.d.l.
P_2O_5	"	0.02	0.05	0.03	0.13	0.06
LOI	"	9.33	0.70	7.41	11.26	9.60
Fe(III)/Fe(II)	molar	2.22	2.25	2.53	0.73	0.30
Mn/∑Fe	molar	0.028	0.009	0.011	0.016	0.008
Mn/Fe(II)	molar	0.089	0.028	0.040	0.027	0.011
Mn/Fe(III)	molar	0.040	0.013	0.016	0.037	0.036
Mn/Ti	mass	843.58	55.89	141.55	18.48	13.29
P/∑Fe	molar	0.001	0.001	0.001	0.002	0.002
P/Fe(II)	molar	0.002	0.004	0.002	0.004	0.002
P/Fe(III)	molar	0.001	0.002	0.001	0.006	0.007
P/Ti	mass	9.14	4.43	4.59	1.65	1.55
∑Fe/Ti	mass	31011.25	6551.83	12776.16	1206.05	1639.59
Fe(II)/Ti	mass	9642.04	2017.78	3619.01	696.63	1262.52
Fe(III)/Ti	mass	21369.21	4534.05	9157.15	509.42	377.07
Li	*ppb*	1093	1461	2439	1367	553.6
Be	"	1828	925.7	1383	1131	866
Sc	"	94.73	123.1	1232	478.7	200
Ti	"	10980	44340	29490	332400	174300
V	"	9914	14110	8111	19150	9055
Cr	"	1475	2503	1672	5472	2740
Co	"	6220	4914	5097	5335	1921
Ni	"	1186	531.4	1475	2383	3173
Cu	"	1035	670.7	1185	964.2	8925
Zn	"	4316	3018	3049	3943	4094
Ga	"	581.3	375.6	384.8	1536	471.3
Rb	"	292	590.1	179.8	3806	1519

b.d.l. = below detection limit; n.m. = not measured; n/a = not applicable

Table A5.1. *(continued)*

ID		PGC045	LRC047	LRGC051	LRGC055	LRGC061
Depth (m)		89.465	93.9	100.75	108.845	122.23
Drillhole		12-SL-1018D	12-SL-1018D	12-SL-1018D	12-SL-1018D	12-SL-1018D
Unit		PGC	LRC	LRGC	LRGC	LRGC
Sr	"	16510	2506	23480	4567	2878
Y	"	9223	3739	9152	13300	5401
Zr	"	6152	5261	3765	25140	6792
Nb	"	2621	2506	1335	7643	1961
Ag	"	4.469	4.205	3.028	4.843	5.781
Cd	"	3.27	2.262	1.925	9.374	2.564
Sn	"	61.06	39.83	74.97	175.2	87.68
Sb	"	48.91	40.71	44.51	27.2	61.02
Cs	"	117.8	155.2	65.38	981.5	347.4
Ba	"	279000	10720	15530	11400	1412
La	"	5325	3323	5516	11620	3440
Ce	"	11470	6940	10280	19940	5844
Pr	"	1072	715	1111	2473	768.6
Nd	"	4314	2911	4438	9744	3053
Sm	"	812.7	521.4	801.5	1671	542.1
Eu	"	254.3	132.6	246.9	416.6	172.8
Gd	"	1009	558.4	991.5	1721	624
Tb	"	157	76.74	151.8	238.5	89.24
Dy	"	1046	471	1011	1456	576.3
Ho	"	251.9	110.8	247.8	343	140
Er	"	761.3	323.4	740	1010	406.4
Tm	"	112.8	47.09	111.2	143.2	56.21
Yb	"	668.8	272.1	669.9	834.6	317.1
Lu	"	92.32	38.8	93.48	118.3	44.3
Hf	"	62.9	78.95	65.02	585.8	151.3
Ta	"	53.55	88.73	54.82	474.4	105.9
Pb	"	636.8	410.2	354.4	351.7	748.8
Th	"	159.1	194.2	111.5	986.9	268.5
U	"	116.5	71.64	49.2	197	110.7
ΣREE+Y	"	36570	20180	35562	65029	21475
$(La/La^*)_{MuQ}$		1.38	1.32	1.36	1.25	1.21
$(Ce/Ce^*)_{MuQ}$		1.32	1.21	1.13	0.97	0.92
$(Eu/Eu^*)_{MuQ}$		1.44	1.20	1.45	1.21	1.52
$(Gd/Gd^*)_{MuQ}$		1.12	1.17	1.14	1.15	1.18
$(Lu/Lu^*)_{MuQ}$		0.98	1.04	0.98	1.03	1.05
Y/Ho		36.6	33.7	36.9	38.8	38.6
$(Pr/Yb)_{MuQ}$		0.62	1.01	0.64	1.14	0.93
$(Er/Lu)_{MuQ}$		1.20	1.21	1.15	1.24	1.33

$La^* = Pr^*(Pr/Nd)^2$; $Ce^* = Pr^*(Pr/Nd)$; $Eu^* = Sm^*(Sm/Nd)^{0.5}$; $Gd^* = Tb^*(Tb/Dy)$; $Lu^* = Yb^*(Yb/Tm)$

Table A5.1. *(continued)*

ID		LIF063	LC216	LC217	LC221	LC224
Depth (m)		126.375	35.405	37.955	49.665	56.955
Drillhole		12-SL-1018D	12-SL-1017D	12-SL-1017D	12-SL-1017D	12-SL-1017D
Unit		LIF	LC	LC	LC	LC
SiO_2	*wt. %*	47.68	80.14	40.43	45.44	55.78
TiO_2	"	0.02	0.02	0.02	0.02	0.02
Al_2O_3	"	b.d.l.	0.01	0.04	b.d.l.	b.d.l.
Fe_2O_{3T}	"	33.98	17.26	33.71	31.53	27.36
FeO	"	26.72	4.98	29.63	27.34	19.91
MnO	"	0.25	0.17	1.67	1.22	1.12
MgO	"	2.98	0.34	2.81	2.50	2.77
CaO	"	1.52	0.11	1.61	1.85	2.16
Na_2O	"	0.58	0.05	0.05	0.05	b.d.l.
K_2O	"	b.d.l.	b.d.l.	b.d.l.	b.d.l.	b.d.l.
P_2O_5	"	0.04	0.01	0.02	0.02	0.03
LOI	"	12.79	1.69	18.66	16.40	10.03
Fe(III)/Fe(II)	molar	0.14	2.12	0.02	0.04	0.24
Mn/∑Fe	molar	0.008	0.011	0.056	0.044	0.046
Mn/Fe(II)	molar	0.009	0.035	0.058	0.046	0.057
Mn/Fe(III)	molar	0.065	0.016	2.443	1.215	0.241
Mn/Ti	mass	27.94	39.44	286.38	1097.38	660.69
P/∑Fe	molar	0.001	0.001	0.001	0.001	0.001
P/Fe(II)	molar	0.001	0.003	0.001	0.001	0.001
P/Fe(III)	molar	0.009	0.001	0.029	0.021	0.005
P/Ti	mass	2.29	1.70	1.93	10.64	8.35
∑Fe/Ti	mass	3470.59	3616.79	5207.95	25609.21	14643.08
Fe(II)/Ti	mass	3033.40	1159.68	5087.63	24682.53	11841.04
Fe(III)/Ti	mass	437.19	2457.12	120.32	926.68	2802.04
Li	*ppb*	494.8	1373	1995	1299	883.2
Be	"	568.9	1130	1440	2745	1226
Sc	"	72.68	265.4	479.4	72.25	79.39
Ti	"	68470	33380	45270	8610	13070
V	"	6118	6581	14630	13570	5046
Cr	"	1764	1168	2065	627.4	802
Co	"	994	2932	14220	5053	7056
Ni	"	1741	427.8	1205	398.1	2166
Cu	"	529.7	4161	2579	1589	851.9
Zn	"	3185	944.4	4028	3993	6097
Ga	"	300.6	543.2	1670	739.9	465.5
Rb	"	712.3	672.4	1038	218.5	224.7

b.d.l. = below detection limit; n.m. = not measured; n/a = not applicable

Table A5.1. *(continued)*

ID		LIF063	LC216	LC217	LC221	LC224
Depth (m)		126.375	35.405	37.955	49.665	56.955
Drillhole		12-SL-1018D	12-SL-1017D	12-SL-1017D	12-SL-1017D	12-SL-1017D
Unit		LIF	LC	LC	LC	LC
Sr	"	3543	3472	7305	8515	6012
Y	"	2815	1016	2768	2779	3091
Zr	"	2614	3601	5879	3547	2159
Nb	"	1177	917.3	1643	674.9	620.4
Ag	"	3.133	n.m.	n.m.	n.m.	n.m.
Cd	"	0.8503	1.566	3.543	2.209	1.54
Sn	"	76.18	58.89	16.69	10.53	11.96
Sb	"	39.4	121.7	77.05	57.43	99.07
Cs	"	109.1	450.1	729.5	48.19	72.41
Ba	"	955.9	9095	3847	5360	2112
La	"	1652	439.9	1353	1219	1388
Ce	"	3019	837.1	2153	2862	2784
Pr	"	407.5	84.71	227.9	209	264.2
Nd	"	1612	334.7	907.9	881	1155
Sm	"	289.6	76.29	187	183.7	238.2
Eu	"	123.7	24.09	70.6	73.15	79.01
Gd	"	321.3	99.68	266.9	273	331
Tb	"	46.57	17.88	44.19	45.27	51.67
Dy	"	307.6	132.2	312.5	320.1	352.7
Ho	"	76.33	33.48	79.39	82.33	85.89
Er	"	223.4	109.6	249.2	260	254.1
Tm	"	31.97	18	38.55	40.03	36.49
Yb	"	185.7	118.5	241.1	239.2	201.7
Lu	"	25.79	16.74	33.8	31.88	25.47
Hf	"	51.37	29.69	34.66	14.66	13.65
Ta	"	42.6	7.837	8.66	3.089	5.254
Pb	"	62.92	405.9	431.7	176.8	182.8
Th	"	118.3	20.88	26.13	19.96	15.27
U	"	80.17	86.12	53.81	48.39	43.78
ΣREE+Y	"	11137	3359	8933	9499	10338
$(La/La^*)_{MuQ}$		1.09	1.39	1.62	1.78	1.73
$(Ce/Ce^*)_{MuQ}$		0.90	1.19	1.15	1.77	1.41
$(Eu/Eu^*)_{MuQ}$		2.02	1.33	1.67	1.75	1.46
$(Gd/Gd^*)_{MuQ}$		1.19	1.08	1.12	1.12	1.14
$(Lu/Lu^*)_{MuQ}$		1.01	0.91	0.95	0.94	0.97
Y/Ho		36.9	30.3	34.9	33.8	36.0
$(Pr/Yb)_{MuQ}$		0.84	0.27	0.36	0.34	0.50
$(Er/Lu)_{MuQ}$		1.26	0.95	1.07	1.19	1.45

$La^* = Pr^*(Pr/Nd)^2$; $Ce^* = Pr^*(Pr/Nd)$; $Eu^* = Sm^*(Sm/Nd)^{0.5}$; $Gd^* = Tb^*(Tb/Dy)$; $Lu^* = Yb^*(Yb/Tm)$

Table A5.1. *(continued)*

ID		LC226	LC227	JUIF228	JUIF229	JUIF230
Depth (m)		60.415	65.3	67.37	69.335	71.26
Drillhole		12-SL-1017D	12-SL-1017D	12-SL-1017D	12-SL-1017D	12-SL-1017D
Unit		LC	LC	JUIF	JUIF	JUIF
SiO_2	*wt. %*	49.68	70.79	49.27	28.66	69.20
TiO_2	"	0.02	0.01	0.02	0.02	0.02
Al_2O_3	"	b.d.l.	b.d.l.	0.02	0.17	b.d.l.
Fe_2O_{3T}	"	30.54	16.18	42.89	62.50	24.96
FeO	"	18.01	13.90	13.26	17.50	8.28
MnO	"	1.30	1.11	0.58	1.02	0.95
MgO	"	2.69	1.79	1.15	2.14	1.42
CaO	"	2.07	1.70	2.55	2.40	1.01
Na_2O	"	b.d.l.	b.d.l.	b.d.l.	b.d.l.	b.d.l.
K_2O	"	b.d.l.	b.d.l.	b.d.l.	b.d.l.	b.d.l.
P_2O_5	"	0.03	0.02	0.03	0.04	0.02
LOI	"	12.90	8.11	2.49	2.19	1.96
Fe(III)/Fe(II)	molar	0.53	0.05	1.91	2.21	1.71
Mn/∑Fe	molar	0.048	0.077	0.015	0.019	0.043
Mn/Fe(II)	molar	0.074	0.081	0.045	0.060	0.116
Mn/Fe(III)	molar	0.140	1.714	0.023	0.027	0.068
Mn/Ti	mass	1502.36	3317.83	188.50	286.12	421.99
P/∑Fe	molar	0.001	0.002	0.001	0.001	0.001
P/Fe(II)	molar	0.002	0.002	0.003	0.003	0.002
P/Fe(III)	molar	0.003	0.034	0.001	0.001	0.001
P/Ti	mass	18.28	37.06	6.23	6.78	5.02
∑Fe/Ti	mass	31950.33	43674.56	12589.15	15787.06	10045.15
Fe(II)/Ti	mass	20938.31	41700.54	4325.28	4912.58	3703.18
Fe(III)/Ti	mass	11012.02	1974.02	8263.88	10874.49	6341.97
Li	*ppb*	781.4	429.8	474	1136	791.9
Be	"	1562	787.2	2128	1890	2319
Sc	"	55.82	38.29	144.7	212.2	90.42
Ti	"	6686	2591	23830	27690	17380
V	"	4864	961.5	17600	23570	7675
Cr	"	890.2	481.2	1184	1468	558.1
Co	"	5628	4674	23400	21370	13800
Ni	"	429.1	454.5	2722	3540	1425
Cu	"	559.2	1096	1911	659.2	1750
Zn	"	4081	2432	2346	4997	4016
Ga	"	653.1	499.2	879	1516	633
Rb	"	195.3	129.1	437.4	127.2	87.68

b.d.l. = below detection limit; n.m. = not measured; n/a = not applicable

Table A5.1. *(continued)*

ID		LC226	LC227	JUIF228	JUIF229	JUIF230
Depth (m)		60.415	65.3	67.37	69.335	71.26
Drillhole		12-SL-1017D	12-SL-1017D	12-SL-1017D	12-SL-1017D	12-SL-1017D
Unit		LC	LC	JUIF	JUIF	JUIF
Sr	"	7435	3595	18590	18880	5322
Y	"	2650	1224	3889	6672	4243
Zr	"	1361	1361	9118	15490	4984
Nb	"	310.1	114.9	2470	3859	1280
Ag	"	n.m.	n.m.	n.m.	n.m.	n.m.
Cd	"	1.401	0.8176	4.627	6.654	2.494
Sn	"	b.d.l.	b.d.l.	42.22	57.54	25.6
Sb	"	56.89	26.08	99.62	159.2	88.26
Cs	"	60.28	38.12	169.3	57.16	35.02
Ba	"	3047	1839	15090	9306	7584
La	"	1288	687.9	2426	4161	2709
Ce	"	2593	1779	6354	11570	5660
Pr	"	236.9	142.7	456.6	919.6	530.8
Nd	"	1038	628.6	1962	3872	2220
Sm	"	209.7	129.5	408.7	788	439.9
Eu	"	75.11	44.24	154.6	221.6	139.5
Gd	"	297.5	168.2	543.8	953.3	578
Tb	"	45.03	25.41	86.45	152.3	89.7
Dy	"	304.8	163	568.9	991.9	593.9
Ho	"	73.3	37.43	134.2	230.8	138.1
Er	"	217.3	106.3	395.9	675.2	394.4
Tm	"	30.94	14.64	58.65	99.1	54.96
Yb	"	174.5	79.1	342.6	547.3	291.4
Lu	"	23.03	9.659	44.46	69.52	36.35
Hf	"	8.318	7.345	64.27	174.7	44.74
Ta	"	2.614	0.5998	21.87	75.97	20.01
Pb	"	142.5	101.2	976.5	1249	386
Th	"	9.726	9.217	88.14	164.6	48.08
U	"	36.51	42.34	62.34	71.45	61.29
ΣREE+Y	"	9257	5240	17826	31924	18119
$(La/La^*)_{MuQ}$		1.79	1.61	1.69	1.38	1.54
$(Ce/Ce^*)_{MuQ}$		1.47	1.68	1.83	1.62	1.36
$(Eu/Eu^*)_{MuQ}$		1.60	1.51	1.66	1.25	1.43
$(Gd/Gd^*)_{MuQ}$		1.17	1.11	1.08	1.07	1.12
$(Lu/Lu^*)_{MuQ}$		0.99	0.96	0.94	0.97	0.99
Y/Ho		36.2	32.7	29.0	28.9	30.7
$(Pr/Yb)_{MuQ}$		0.52	0.69	0.51	0.65	0.70
$(Er/Lu)_{MuQ}$		1.37	1.60	1.29	1.41	1.58

$La^* = Pr^*(Pr/Nd)^2$; $Ce^* = Pr^*(Pr/Nd)$; $Eu^* = Sm^*(Sm/Nd)^{0.5}$; $Gd^* = Tb^*(Tb/Dy)$; $Lu^* = Yb^*(Yb/Tm)$

Table A5.1. *(continued)*

ID		JUIF231	GC232	URC233	URC235	PGC236
Depth (m)		74.24	79.55	81.23	83.345	85.19
Drillhole		12-SL-1017D	12-SL-1017D	12-SL-1017D	12-SL-1017D	12-SL-1017D
Unit		JUIF	GC	URC	URC	PGC
SiO_2	*wt. %*	25.74	64.10	46.08	48.30	40.57
TiO_2	"	0.03	0.02	0.03	0.02	0.02
Al_2O_3	"	0.07	b.d.l.	b.d.l.	b.d.l.	b.d.l.
Fe_2O_{3T}	"	44.86	31.72	38.12	44.63	47.34
FeO	"	17.55	12.03	14.75	4.42	17.60
MnO	"	5.63	0.45	1.51	0.55	1.38
MgO	"	3.49	0.50	1.53	1.08	1.84
CaO	"	6.17	0.67	4.11	1.87	2.02
Na_2O	"	0.05	0.05	0.06	0.05	b.d.l.
K_2O	"	b.d.l.	b.d.l.	b.d.l.	b.d.l.	b.d.l.
P_2O_5	"	0.04	0.01	0.01	0.02	0.02
LOI	"	11.71	1.85	7.50	2.31	6.80
Fe(III)/Fe(II)	molar	1.30	1.37	1.33	8.09	1.42
Mn/∑Fe	molar	0.144	0.016	0.045	0.014	0.033
Mn/Fe(II)	molar	0.332	0.038	0.105	0.128	0.080
Mn/Fe(III)	molar	0.255	0.028	0.079	0.016	0.056
Mn/Ti	mass	1003.66	267.12	182.25	327.43	1766.47
P/∑Fe	molar	0.001	0.000	0.000	0.000	0.000
P/Fe(II)	molar	0.002	0.001	0.001	0.003	0.001
P/Fe(III)	molar	0.002	0.001	0.001	0.000	0.001
P/Ti	mass	3.62	4.71	0.89	5.00	12.25
∑Fe/Ti	mass	7226.42	17119.84	4163.27	23864.57	54643.04
Fe(II)/Ti	mass	3141.82	7215.31	1790.34	2626.69	22579.07
Fe(III)/Ti	mass	4084.60	9904.54	2372.93	21237.88	32063.98
Li	*ppb*	1420	574.2	810	1236	1052
Be	"	2523	735.3	1737	1687	1276
Sc	"	380.3	94.31	91.77	80.97	50.94
Ti	"	43420	12960	64040	13080	6059
V	"	9267	6848	8238	4379	2610
Cr	"	765.9	622.2	469.1	600.2	810.5
Co	"	9977	2720	6313	6988	6940
Ni	"	1125	761.7	1096	662.3	663.1
Cu	"	938.7	1187	484.8	1190	1217
Zn	"	5131	1680	3248	4114	5038
Ga	"	2090	641.6	633.4	542.2	485.3
Rb	"	1079	150.8	513	367.9	98.63

b.d.l. = below detection limit; n.m. = not measured; n/a = not applicable

Table A5.1. *(continued)*

ID		JUIF231	GC232	URC233	URC235	PGC236
Depth (m)		74.24	79.55	81.23	83.345	85.19
Drillhole		12-SL-1017D	12-SL-1017D	12-SL-1017D	12-SL-1017D	12-SL-1017D
Unit		JUIF	GC	URC	URC	PGC
Sr	"	40630	2655	19620	11260	10420
Y	"	22710	2096	9485	8796	7945
Zr	"	20820	3698	8810	3158	1468
Nb	"	5515	1429	2264	1206	651.6
Ag	"	n.m.	n.m.	n.m.	n.m.	n.m.
Cd	"	9.83	2.648	5.836	1.82	1.783
Sn	"	58.08	15.7	57.29	15.53	28.27
Sb	"	132	73.79	62.83	106	49.99
Cs	"	380.1	55.71	182.7	49.29	36.04
Ba	"	17280	6313	19300	6147	3665
La	"	12990	1031	4687	3744	6044
Ce	"	16130	1957	6717	6558	11280
Pr	"	2249	234.8	869.5	806.9	1073
Nd	"	9785	1036	3723	3440	4347
Sm	"	1928	243.5	735	697.3	767.4
Eu	"	674.7	125.7	364.3	243	295.2
Gd	"	2662	318.2	1037	917.3	925.5
Tb	"	416.5	49.66	155.9	146.3	137.1
Dy	"	2794	320.2	1055	1003	893.9
Ho	"	664.4	70.97	251.9	244.8	213.1
Er	"	1920	195.8	718.6	740.9	617.4
Tm	"	263.1	28.78	101.6	113.5	90.11
Yb	"	1415	162.6	557.7	676.4	501.9
Lu	"	174.7	21.09	74.02	91.85	67.25
Hf	"	185.2	29.96	122.5	22.58	12.17
Ta	"	65.67	17.47	29.06	11.93	8.444
Pb	"	403	329.9	527	749.9	594.6
Th	"	225.2	34.95	36.09	51.65	22.92
U	"	61.73	35.73	67.71	49.6	21.59
ΣREE+Y	"	76776	7891	30533	28219	35198
$(La/La^*)_{MuQ}$		1.88	1.47	1.70	1.45	1.59
$(Ce/Ce^*)_{MuQ}$		0.95	1.13	1.01	1.06	1.30
$(Eu/Eu^*)_{MuQ}$		1.58	2.13	2.24	1.55	1.83
$(Gd/Gd^*)_{MuQ}$		1.12	1.08	1.18	1.12	1.15
$(Lu/Lu^*)_{MuQ}$		0.97	0.97	1.02	0.96	1.02
Y/Ho		34.2	29.5	37.7	35.9	37.3
$(Pr/Yb)_{MuQ}$		0.61	0.55	0.60	0.46	0.82
$(Er/Lu)_{MuQ}$		1.60	1.35	1.41	1.17	1.33

$La^* = Pr^*(Pr/Nd)^2$; $Ce^* = Pr^*(Pr/Nd)$; $Eu^* = Sm^*(Sm/Nd)^{0.5}$; $Gd^* = Tb^*(Tb/Dy)$; $Lu^* = Yb^*(Yb/Tm)$

Table A5.1. *(continued)*

ID		PGC238	LRC239	LRGC241	LRGC247	LRGC250
Depth (m)		90.705	92	95.155	116.425	126.685
Drillhole		12-SL-1017D	12-SL-1017D	12-SL-1017D	12-SL-1017D	12-SL-1017D
Unit		PGC	LRC	LRGC	LRGC	LRGC
SiO_2	*wt. %*	43.42	47.49	36.17	31.84	45.88
TiO_2	"	0.02	0.02	0.03	0.05	0.05
Al_2O_3	"	0.14	0.11	0.06	0.28	0.11
Fe_2O_{3T}	"	52.62	37.79	46.45	58.67	43.63
FeO	"	13.58	14.58	19.38	20.57	31.19
MnO	"	0.53	1.02	1.78	0.37	0.13
MgO	"	1.05	2.07	3.18	3.10	3.07
CaO	"	0.43	3.94	2.51	0.73	0.89
Na_2O	"	0.08	0.05	b.d.l.	b.d.l.	b.d.l.
K_2O	"	b.d.l.	b.d.l.	b.d.l.	b.d.l.	b.d.l.
P_2O_5	"	0.06	0.03	0.04	0.11	0.03
LOI	"	1.63	6.72	9.72	4.82	6.13
Fe(III)/Fe(II)	molar	2.49	1.33	1.16	1.57	0.26
Mn/∑Fe	molar	0.011	0.031	0.043	0.007	0.003
Mn/Fe(II)	molar	0.040	0.071	0.093	0.018	0.004
Mn/Fe(III)	molar	0.016	0.053	0.080	0.012	0.016
Mn/Ti	mass	132.60	804.03	200.65	14.81	5.38
P/∑Fe	molar	0.001	0.001	0.001	0.002	0.001
P/Fe(II)	molar	0.004	0.002	0.002	0.005	0.001
P/Fe(III)	molar	0.002	0.001	0.002	0.003	0.004
P/Ti	mass	7.99	11.14	2.68	2.46	0.70
∑Fe/Ti	mass	11823.13	26982.60	4741.75	2120.66	1681.45
Fe(II)/Ti	mass	3390.90	11569.19	2198.84	826.32	1335.77
Fe(III)/Ti	mass	8432.23	15413.41	2542.91	1294.35	345.67
Li	*ppb*	1107	686.9	876.5	4701	413
Be	"	1563	1157	1282	1026	841.5
Sc	"	120.5	101.8	149.5	385.9	295.2
Ti	"	31130	9796	68510	193500	181500
V	"	15620	4702	9071	13690	13060
Cr	"	1413	695.8	2429	3454	2977
Co	"	5499	4135	11770	3874	1677
Ni	"	770	1072	1044	1911	2683
Cu	"	577.5	614.9	1265	1510	1050
Zn	"	3489	3850	4628	3510	6976
Ga	"	673.9	707.6	862.1	983.9	752.8
Rb	"	1454	1055	543.7	175.4	2332

b.d.l. = below detection limit; n.m. = not measured; n/a = not applicable

Table A5.1. *(continued)*

ID		PGC238	LRC239	LRGC241	LRGC247	LRGC250
Depth (m)		90.705	92	95.155	116.425	126.685
Drillhole		12-SL-1017D	12-SL-1017D	12-SL-1017D	12-SL-1017D	12-SL-1017D
Unit		PGC	LRC	LRGC	LRGC	LRGC
Sr	"	10300	15520	10720	4520	4673
Y	"	4958	7437	7721	11860	3434
Zr	"	12530	7063	5990	11080	6264
Nb	"	4459	2374	3878	2882	2396
Ag	"	n.m.	n.m.	n.m.	n.m.	n.m.
Cd	"	5.304	4.276	3.022	4.004	3.322
Sn	"	68.37	74.96	88.79	144.8	82.84
Sb	"	63.29	29.78	36.84	36.8	88.14
Cs	"	541.4	403.4	177.5	40.58	538.1
Ba	"	5585	3063	8594	3424	3183
La	"	1875	3848	7011	8052	1785
Ce	"	4864	8218	14550	13290	3494
Pr	"	508.4	857.6	1423	1692	495.9
Nd	"	2265	3468	5412	6757	2054
Sm	"	470.2	684.9	888.1	1180	391.8
Eu	"	143.8	259.2	255.8	328.6	124.7
Gd	"	592.4	850.1	965.7	1372	433.3
Tb	"	87.83	125.8	139.6	193.2	64.61
Dy	"	590.4	809.9	890.4	1244	416.8
Ho	"	144.4	189.6	211.6	298.4	99.38
Er	"	441.6	529.2	621.6	871	296.1
Tm	"	66.86	72.96	90.39	121.9	44.5
Yb	"	399.8	402.4	525.9	688.2	271.2
Lu	"	55.19	54.45	72.74	96.89	39.32
Hf	"	174.4	138	112.1	255.9	120.8
Ta	"	115.7	51.19	163.1	181.3	100.8
Pb	"	712.8	385.8	869.2	588.3	255.6
Th	"	349.2	197.8	362	459.1	246
U	"	137.6	81.29	61.54	146.2	112.2
ΣREE+Y	"	17463	27807	40779	48045	13445
$(La/La^*)_{MuQ}$		1.26	1.26	1.23	1.31	1.06
$(Ce/Ce^*)_{MuQ}$		1.30	1.19	1.19	0.96	0.89
$(Eu/Eu^*)_{MuQ}$		1.34	1.71	1.42	1.34	1.46
$(Gd/Gd^*)_{MuQ}$		1.19	1.14	1.15	1.20	1.13
$(Lu/Lu^*)_{MuQ}$		0.98	1.04	1.00	1.05	1.01
Y/Ho		34.3	39.2	36.5	39.7	34.6
$(Pr/Yb)_{MuQ}$		0.49	0.82	1.04	0.94	0.70
$(Er/Lu)_{MuQ}$		1.16	1.41	1.24	1.31	1.09

$La^* = Pr^*(Pr/Nd)^2$; $Ce^* = Pr^*(Pr/Nd)$; $Eu^* = Sm^*(Sm/Nd)^{0.5}$; $Gd^* = Tb^*(Tb/Dy)$; $Lu^* = Yb^*(Yb/Tm)$

Table A5.1. *(continued)*

ID		LIF252	JUIF254	GC256	LC069	JUIF073B
Depth (m)		131.19	72.48	75.09	12.16	30.31
Drillhole		12-SL-1017D	12-SL-1011D	12-SL-1011D	12-SL-1005D	12-SL-1005D
Unit		LIF	JUIF	GC	LC	JUIF
SiO_2	*wt. %*	57.56	64.06	65.11	84.63	50.53
TiO_2	"	0.02	0.02	0.02	0.01	0.02
Al_2O_3	"	0.04	0.21	0.02	b.d.l.	b.d.l.
Fe_2O_3	"	19.54	25.52	27.45	9.70	43.56
FeO	"	16.97	n.m.	n.m.	n.m.	n.m.
MnO	"	0.22	3.21	0.53	0.25	0.84
MgO	"	2.26	1.26	3.77	0.77	1.43
CaO	"	3.31	0.91	0.69	0.08	0.88
Na_2O	"	b.d.l.	0.05	b.d.l.	0.06	0.09
K_2O	"	b.d.l.	b.d.l.	b.d.l.	b.d.l.	b.d.l.
P_2O_5	"	0.04	0.05	0.05	0.02	0.03
LOI	"	16.94	3.84	1.81	4.25	2.45
Fe(III)/Fe(II)	molar	0.0362	n/a	n/a	n/a	n/a
Mn/∑Fe	molar	0.013	0.143	0.022	0.029	0.022
Mn/Fe(II)	molar	0.013	n/a	n/a	n/a	n/a
Mn/Fe(III)	molar	0.370	n/a	n/a	n/a	n/a
Mn/Ti	mass	43.10	937.70	131.81	82.52	191.96
P/∑Fe	molar	0.002	0.002	0.002	0.002	0.001
P/Fe(II)	molar	0.002	n/a	n/a	n/a	n/a
P/Fe(III)	molar	0.058	n/a	n/a	n/a	n/a
P/Ti	mass	3.80	7.90	7.41	3.95	3.46
∑Fe/Ti	mass	3395.84	6730.56	6154.54	2926.26	8958.30
Fe(II)/Ti	mass	3277.25	n/a	n/a	n/a	n/a
Fe(III)/Ti	mass	118.59	n/a	n/a	n/a	n/a
Li	*ppb*	926.9	1906	446	430.5	3426
Be	"	483.7	919.2	943.9	1013	1791
Sc	"	143.2	245.5	299.9	69.47	39.16
Ti	"	40250	26520	31200	23180	34010
V	"	6548	1377	11220	1220	18730
Cr	"	870.6	374.4	1675	3203	1204
Co	"	612.9	11660	6763	4684	5017
Ni	"	906.1	876.7	1959	2806	2576
Cu	"	694	1252	4607	11570	2340
Zn	"	1542	2249	12780	22600	4067
Ga	"	316	1776	774.5	359.8	1448
Rb	"	1158	785.7	1548	88.43	1243

b.d.l. = below detection limit; n.m. = not measured; n/a = not applicable

Table A5.1. *(continued)*

ID		LIF252	JUIF254	GC256	LC069	JUIF073B
Depth (m)		131.19	72.48	75.09	12.16	30.31
Drillhole		12-SL-1017D	12-SL-1011D	12-SL-1011D	12-SL-1005D	12-SL-1005D
Unit		LIF	JUIF	GC	LC	JUIF
Sr	"	8067	7274	2659	1676	6642
Y	"	4223	13740	4010	854.5	2825
Zr	"	2618	24890	15460	1266	3856
Nb	"	1157	370	1660	392.7	1924
Ag	"	n.m.	n.m.	n.m.	70.67	3.053
Cd	"	1.634	9.877	7.412	76.04	1.754
Sn	"	35.84	96.09	210.5	309	92.66
Sb	"	12.57	37.22	158.8	474.3	192.8
Cs	"	259.7	345.5	373.1	208.7	444.4
Ba	"	31620	13530	503.6	715.8	6682
La	"	4063	21240	2799	546.1	1183
Ce	"	7267	38790	4238	1350	3228
Pr	"	904	3589	546	134.3	252.1
Nd	"	3399	14260	2353	539.2	1087
Sm	"	543.9	2670	495.6	109.8	245.7
Eu	"	159.5	592.5	165.9	37.45	92
Gd	"	561.9	2833	616.2	130.5	346.7
Tb	"	79.64	392.2	82.28	18.95	56.64
Dy	"	498.8	2199	503	114.3	381.6
Ho	"	115.4	440.6	112.3	25.43	89.69
Er	"	320.9	1094	315	69.36	262.8
Tm	"	43.65	135.7	44.61	9.749	39.6
Yb	"	242.5	702.2	249.5	56.67	227.1
Lu	"	33.54	85.17	33.77	7.814	29.28
Hf	"	45.82	188.9	130.9	24.99	30.1
Ta	"	42.91	6.45	61.92	15.4	35.68
Pb	"	126.5	263.7	188.4	6411	409.2
Th	"	131	209.2	128	38.55	77.02
U	"	73.5	216.4	159.7	29.11	52.99
ΣREE+Y	"	22456	102763	16564	4004	10346
$(La/La^*)_{MuQ}$		1.09	1.61	1.64	1.13	1.50
$(Ce/Ce^*)_{MuQ}$		0.92	1.31	1.02	1.23	1.69
$(Eu/Eu^*)_{MuQ}$		1.47	1.03	1.46	1.51	1.58
$(Gd/Gd^*)_{MuQ}$		1.16	1.06	1.20	1.09	1.08
$(Lu/Lu^*)_{MuQ}$		1.05	0.99	1.02	1.00	0.95
Y/Ho		36.6	31.2	35.7	33.6	31.5
$(Pr/Yb)_{MuQ}$		1.43	1.96	0.84	0.91	0.43
$(Er/Lu)_{MuQ}$		1.39	1.87	1.36	1.29	1.31

$La^* = Pr^*(Pr/Nd)^2$; $Ce^* = Pr^*(Pr/Nd)$; $Eu^* = Sm^*(Sm/Nd)^{0.5}$; $Gd^* = Tb^*(Tb/Dy)$; $Lu^* = Yb^*(Yb/Tm)$

Table A5.1. *(continued)*

ID		JUIF073C	JUIF079	JUIF083	GC085	URC086
Depth (m)		30.31	42.945	54.3	57.62	58.62
Drillhole		12-SL-1005D	12-SL-1005D	12-SL-1005D	12-SL-1005D	12-SL-1005D
Unit		JUIF	JUIF	JUIF	GC	URC
SiO_2	*wt. %*	92.19	45.66	15.71	3.85	51.91
TiO_2	"	0.01	0.01	0.07	0.02	0.02
Al_2O_3	"	b.d.l.	b.d.l.	0.04	b.d.l.	b.d.l.
Fe_2O_{3T}	"	6.39	33.35	68.62	47.21	30.20
FeO	"	n.m.	n.m.	n.m.	n.m.	n.m.
MnO	"	0.18	1.07	4.62	7.37	1.58
MgO	"	0.25	2.22	4.40	6.84	2.33
CaO	"	0.07	8.27	0.47	1.20	5.76
Na_2O	"	0.07	0.11	0.06	b.d.l.	0.10
K_2O	"	b.d.l.	b.d.l.	b.d.l.	b.d.l.	b.d.l.
P_2O_5	"	b.d.l.	0.02	0.03	0.03	0.01
LOI	"	0.58	9.10	5.74	33.35	7.89
Fe(III)/Fe(II)	molar	n/a	n/a	n/a	n/a	n/a
Mn/∑Fe	molar	0.032	0.036	0.076	0.176	0.059
Mn/Fe(II)	molar	n/a	n/a	n/a	n/a	n/a
Mn/Fe(III)	molar	n/a	n/a	n/a	n/a	n/a
Mn/Ti	mass	118.08	567.83	401.65	1986.42	354.45
P/∑Fe	molar	n/a	0.001	0.001	0.001	0.000
P/Fe(II)	molar	n/a	n/a	n/a	n/a	n/a
P/Fe(III)	molar	n/a	n/a	n/a	n/a	n/a
P/Ti	mass	n/a	6.59	1.66	3.80	1.51
∑Fe/Ti	mass	3806.35	15997.66	5382.85	11492.03	6103.29
Fe(II)/Ti	mass	n/a	n/a	n/a	n/a	n/a
Fe(III)/Ti	mass	n/a	n/a	n/a	n/a	n/a
Li	*ppb*	979.7	2015	1532	674.7	1041
Be	"	641	1012	13090	999	850.7
Sc	"	38.11	52.73	450.2	201.4	535.8
Ti	"	11740	14580	89160	28730	34610
V	"	3064	3560	27990	5053.5	4957
Cr	"	262.3	1400	1650	462.2	1218
Co	"	5506	3404	37840	3364	3065
Ni	"	971.1	1129	1845	607.1	1920
Cu	"	673	1035	4435	615.2	1351
Zn	"	575.5	1523	11530	3833.5	4396
Ga	"	434.2	295.1	2711	486.9	670.4
Rb	"	314.2	159.3	2256	309	498.7

b.d.l. = below detection limit; n.m. = not measured; n/a = not applicable

Table A5.1. *(continued)*

ID		JUIF073C	JUIF079	JUIF083	GC085	URC086
Depth (m)		30.31	42.945	54.3	57.62	58.62
Drillhole		12-SL-1005D	12-SL-1005D	12-SL-1005D	12-SL-1005D	12-SL-1005D
Unit		JUIF	JUIF	JUIF	GC	URC
Sr	"	1695	27960	9972	4088	17910
Y	"	521.4	3456	51820	8423	8430
Zr	"	1899	1867	47210	4659	4935
Nb	"	355.9	505.9	15510	1473	1467
Ag	"	1.144	3.361	10.78	0.3185	2.775
Cd	"	1.024	0.8664	16.74	7.004	2.512
Sn	"	10.4	59.96	64.02	19.02	77.96
Sb	"	154.3	68.53	106.7	7.913	41.01
Cs	"	110.1	64.63	1167	86.04	161.4
Ba	"	4849	7290	21370	6290	8197
La	"	209.9	1858	43240	5607	4871
Ce	"	649.3	4299	53750	8830	6994
Pr	"	47.59	346.9	6877	1115	916.5
Nd	"	209.7	1466	29340	4494	3887
Sm	"	48.44	306.1	6018	863.7	782
Eu	"	16.71	153.2	2013	265.3	341.4
Gd	"	62.15	413.3	8159	1056	1062
Tb	"	10.18	65.14	1220	183.5	164.9
Dy	"	71.77	430.5	7582	1285	1094
Ho	"	17.15	102.6	1672	308	253
Er	"	52.75	294.8	4680	933.9	729.7
Tm	"	7.946	40.58	663.8	145.4	105.5
Yb	"	48.26	213	3547	889	608.7
Lu	"	6.467	26.76	441.3	119.6	83.19
Hf	"	17.37	15.51	316.9	42.57	46.66
Ta	"	11.38	5.046	172.8	28.98	12.81
Pb	"	431	395.2	1058	199.6	490
Th	"	33.75	33.31	330	71.69	44.57
U	"	30.96	26.93	149.3	50.89	44.5
ΣREE+Y	"	1980	13472	221023	34518	30323
$(La/La^*)_{MuQ}$		1.47	1.64	1.97	1.40	1.64
$(Ce/Ce^*)_{MuQ}$		1.84	1.60	1.02	0.98	0.99
$(Eu/Eu^*)_{MuQ}$		1.44	2.19	1.48	1.40	1.95
$(Gd/Gd^*)_{MuQ}$		1.13	1.10	1.09	1.05	1.12
$(Lu/Lu^*)_{MuQ}$		0.93	1.01	0.98	0.93	1.00
Y/Ho		30.4	33.7	31.0	27.3	33.3
$(Pr/Yb)_{MuQ}$		0.38	0.63	0.74	0.48	0.58
$(Er/Lu)_{MuQ}$		1.19	1.60	1.54	1.14	1.28

$La^* = Pr^*(Pr/Nd)^2$; $Ce^* = Pr^*(Pr/Nd)$; $Eu^* = Sm^*(Sm/Nd)^{0.5}$; $Gd^* = Tb^*(Tb/Dy)$; $Lu^* = Yb^*(Yb/Tm)$

Table A5.1. *(continued)*

ID		PGC088	LRC092	LRGC094	LRGC103	LIF109
Depth (m)		61.155	67.79	71.875	93.04	106.885
Drillhole		12-SL-1005D	12-SL-1005D	12-SL-1005D	12-SL-1005D	12-SL-1005D
Unit		PGC	LRC	LRGC	LRGC	LIF
SiO_2	*wt. %*	45.26	32.90	29.33	56.07	50.80
TiO_2	"	0.02	0.02	0.01	0.01	0.03
Al_2O_3	"	b.d.l.	b.d.l.	b.d.l.	b.d.l.	0.06
Fe_2O_{3T}	"	47.97	51.84	47.68	37.38	41.94
FeO	"	n.m.	n.m.	n.m.	n.m.	n.m.
MnO	"	0.55	0.91	1.15	0.13	0.12
MgO	"	2.68	2.58	2.69	1.97	3.28
CaO	"	1.46	5.01	7.89	1.99	0.78
Na_2O	"	0.07	0.28	0.36	0.08	0.15
K_2O	"	b.d.l.	b.d.l.	b.d.l.	b.d.l.	0.01
P_2O_5	"	0.01	0.03	0.03	0.03	0.05
LOI	"	1.80	6.26	10.67	2.17	2.59
Fe(III)/Fe(II)	molar	n/a	n/a	n/a	n/a	n/a
Mn/∑Fe	molar	0.013	0.020	0.027	0.004	0.003
Mn/Fe(II)	molar	n/a	n/a	n/a	n/a	n/a
Mn/Fe(III)	molar	n/a	n/a	n/a	n/a	n/a
Mn/Ti	mass	152.35	276.57	755.44	48.67	7.55
P/∑Fe	molar	0.000	0.001	0.001	0.001	0.001
P/Fe(II)	molar	n/a	n/a	n/a	n/a	n/a
P/Fe(III)	molar	n/a	n/a	n/a	n/a	n/a
P/Ti	mass	1.87	4.82	12.56	5.83	1.72
∑Fe/Ti	mass	11957.11	14291.03	28235.41	12935.48	2306.19
Fe(II)/Ti	mass	n/a	n/a	n/a	n/a	n/a
Fe(III)/Ti	mass	n/a	n/a	n/a	n/a	n/a
Li	*ppb*	1712	1192	2029	1931	507.1
Be	"	1408	1473	834	533.9	584.4
Sc	"	84.08	133.6	437.2	26.32	124.4
Ti	"	28060	25370	11810	20210	127200
V	"	4795	11360	7745	2246	9929
Cr	"	945.3	2914	1876	2073	2683
Co	"	13540	6755	3175	832.8	2061
Ni	"	1043	1599	1133	1381	1387
Cu	"	821	1201	1182	958	844.6
Zn	"	7698	4255	2270	2051	4748
Ga	"	628.9	693.3	451.4	172	462.6
Rb	"	140.1	209.6	376.2	104.9	2475

b.d.l. = below detection limit; n.m. = not measured; n/a = not applicable

Table A5.1. *(continued)*

ID		PGC088	LRC092	LRGC094	LRGC103	LIF109
Depth (m)		61.155	67.79	71.875	93.04	106.885
Drillhole		12-SL-1005D	12-SL-1005D	12-SL-1005D	12-SL-1005D	12-SL-1005D
Unit		PGC	LRC	LRGC	LRGC	LIF
Sr	"	5087	12940	27030	11800	2076
Y	"	8354	10720	12630	1705	6254
Zr	"	5398	6960	6744	1659	7894
Nb	"	1790	2852	2103	583.4	2079
Ag	"	7.91	2.508	b.d.l.	0.7451	4.788
Cd	"	2.867	3.073	2.978	b.d.l.	4.42
Sn	"	57.43	132.6	90.6	101.7	158.4
Sb	"	92.97	85.77	40.73	32.09	78.22
Cs	"	41.67	55.54	88.57	38.46	584.1
Ba	"	4317	2792	4924	8889	856.3
La	"	5810	6384	5116	1024	7170
Ce	"	9891	13300	12160	1782	11810
Pr	"	1077	1333	1337	227.4	1447
Nd	"	4414	5444	5716	910.8	5615
Sm	"	808.7	1062	1206	165.6	901.5
Eu	"	252.4	344.7	547.6	62.54	254.1
Gd	"	997.6	1320	1548	199.9	893.5
Tb	"	155.3	205.6	236.2	28.75	119.2
Dy	"	1051	1372	1515	185	738.2
Ho	"	255.3	320.3	354.3	44.9	169.2
Er	"	774.2	958.2	1005	134.1	478.5
Tm	"	116.2	145.1	141	19.18	67.43
Yb	"	678.7	860	778.9	109.2	393.6
Lu	"	91.8	118.4	102.5	15.26	57.22
Hf	"	53.22	58.8	80	33.26	178.2
Ta	"	22.54	38.45	37.07	27.6	137.2
Pb	"	810.5	1057	414.9	268.8	369.3
Th	"	46.42	93.24	143.2	59.38	261.8
U	"	41.54	66.33	50.68	40.7	87.31
ΣREE+Y	"	34727	43887	44394	6614	36368
$(La/La^*)_{MuQ}$		1.56	1.37	1.20	1.24	1.28
$(Ce/Ce^*)_{MuQ}$		1.15	1.25	1.19	0.96	0.97
$(Eu/Eu^*)_{MuQ}$		1.46	1.47	1.98	1.77	1.41
$(Gd/Gd^*)_{MuQ}$		1.14	1.12	1.10	1.17	1.21
$(Lu/Lu^*)_{MuQ}$		0.98	0.98	1.01	1.04	1.05
Y/Ho		32.7	33.5	35.6	38.0	37.0
$(Pr/Yb)_{MuQ}$		0.61	0.60	0.66	0.80	1.41
$(Er/Lu)_{MuQ}$		1.23	1.18	1.43	1.28	1.22

$La^* = Pr^*(Pr/Nd)^2$; $Ce^* = Pr^*(Pr/Nd)$; $Eu^* = Sm^*(Sm/Nd)^{0.5}$; $Gd^* = Tb^*(Tb/Dy)$; $Lu^* = Yb^*(Yb/Tm)$

Table A5.1. *(continued)*

ID		LIF112	LC145	JUIF146	GC147	URC148B
Depth (m)		113.69	6.41	13.725	18.25	19.93
Drillhole		12-SL-1005D	11-LR-1010D	11-LR-1010D	11-LR-1010D	11-LR-1010D
Unit		LIF	LC	JUIF	GC	URC
SiO_2	*wt. %*	54.78	46.28	43.13	92.77	49.55
TiO_2	"	0.07	0.01	0.02	0.02	0.01
Al_2O_3	"	0.21	b.d.l.	0.08	b.d.l.	b.d.l.
Fe_2O_{3T}	"	24.25	36.62	44.12	3.95	46.88
FeO	"	n.m.	n.m.	n.m.	n.m.	n.m.
MnO	"	0.31	1.38	1.67	0.46	0.49
MgO	"	2.70	1.90	2.45	0.53	1.36
CaO	"	2.00	5.57	2.36	0.14	0.41
Na_2O	"	0.22	0.07	b.d.l.	0.05	0.27
K_2O	"	b.d.l.	b.d.l.	b.d.l.	b.d.l.	b.d.l.
P_2O_5	"	0.06	0.02	0.04	0.01	0.03
LOI	"	15.23	7.96	4.69	2.38	0.56
Fe(III)/Fe(II)	molar	n/a	n/a	n/a	n/a	n/a
Mn/∑Fe	molar	0.014	0.043	0.043	0.132	0.012
Mn/Fe(II)	molar	n/a	n/a	n/a	n/a	n/a
Mn/Fe(III)	molar	n/a	n/a	n/a	n/a	n/a
Mn/Ti	mass	7.48	1680.39	467.31	1474.56	367.52
P/∑Fe	molar	0.003	0.001	0.001	0.003	0.001
P/Fe(II)	molar	n/a	n/a	n/a	n/a	n/a
P/Fe(III)	molar	n/a	n/a	n/a	n/a	n/a
P/Ti	mass	0.77	16.43	6.63	16.12	10.48
∑Fe/Ti	mass	533.26	40180.46	11155.48	11328.07	31497.87
Fe(II)/Ti	mass	n/a	n/a	n/a	n/a	n/a
Fe(III)/Ti	mass	n/a	n/a	n/a	n/a	n/a
Li	*ppb*	3446	455.9	3211	1595	1567
Be	"	573.6	1063	1361	262.5	1556
Sc	"	359.8	39.02	179	29.6	50.63
Ti	"	318000	6374	27660	2437	10410
V	"	15650	4615	15300	1534	4958
Cr	"	5010	1427	1499	671.6	1437
Co	"	882.6	5591	16350	225	6618
Ni	"	2374	1718	2676	140.4	1216
Cu	"	2012	1341	3013	623.9	1739
Zn	"	3638	2605	8075	1077	7035
Ga	"	698.2	442.2	1119	224.3	318.8
Rb	"	112.9	161.1	1523	74.02	447.9

b.d.l. = below detection limit; n.m. = not measured; n/a = not applicable

Table A5.1. *(continued)*

ID		LIF112	LC145	JUIF146	GC147	URC148B
Depth (m)		113.69	6.41	13.725	18.25	19.93
Drillhole		12-SL-1005D	11-LR-1010D	11-LR-1010D	11-LR-1010D	11-LR-1010D
Unit		LIF	LC	JUIF	GC	URC
Sr	"	6008	38710	21800	948.4	12710
Y	"	5589	3851	6477	581.5	4711
Zr	"	13830	1753	10580	971.8	2011
Nb	"	3715	549.4	2943	298	804.7
Ag	"	6.127	21.62	n.m.	n.m.	155.1
Cd	"	3.593	25.87	7.623	1.256	b.d.l.
Sn	"	220.1	74.16	76.86	30.28	88.04
Sb	"	44.87	57.52	72.85	28.07	88.06
Cs	"	39.8	72.12	814.4	35.19	160.2
Ba	"	1949	8234	89260	8136	2435000
La	"	6018	1544	4466	317	6207
Ce	"	10980	3971	9207	565.9	7480
Pr	"	1436	325.7	881.8	70.75	1138
Nd	"	5487	1414	3676	294	4691
Sm	"	941.2	296.7	675.8	57.15	876.3
Eu	"	340.3	144	209.8	26.2	203.6
Gd	"	911.8	421.4	832.5	72.36	927.1
Tb	"	127.6	66.27	124.5	11.04	130.9
Dy	"	780.8	450	796.6	68.99	772.5
Ho	"	172	107.6	186.6	16.31	170.6
Er	"	471.9	312.6	547.6	46.54	479.5
Tm	"	67.06	43.79	78.98	6.959	71.89
Yb	"	396	236.7	456.9	39.85	433.6
Lu	"	58.36	30.45	61.79	5.554	60.44
Hf	"	293	9.763	138.2	6.424	17.65
Ta	"	239.8	2.127	116.9	4.938	10.65
Pb	"	617.8	57.72	2181	367.2	931.4
Th	"	503.5	14.74	178.3	13.58	27.19
U	"	257.2	33.07	115.4	81.67	33.86
ΣREE+Y	"	33777	13215	28679	2180	28353
$(La/La^*)_{MuQ}$		1.05	1.54	1.51	1.33	1.59
$(Ce/Ce^*)_{MuQ}$		0.89	1.62	1.33	1.02	0.83
$(Eu/Eu^*)_{MuQ}$		1.75	2.12	1.45	2.08	1.08
$(Gd/Gd^*)_{MuQ}$		1.14	1.13	1.12	1.07	1.09
$(Lu/Lu^*)_{MuQ}$		1.05	1.01	0.99	1.03	0.98
Y/Ho		32.5	35.8	34.7	35.7	27.6
$(Pr/Yb)_{MuQ}$		1.39	0.53	0.74	0.68	1.01
$(Er/Lu)_{MuQ}$		1.18	1.49	1.29	1.22	1.15

$La^* = Pr^*(Pr/Nd)^2$; $Ce^* = Pr^*(Pr/Nd)$; $Eu^* = Sm^*(Sm/Nd)^{0.5}$; $Gd^* = Tb^*(Tb/Dy)$; $Lu^* = Yb^*(Yb/Tm)$

Table A5.1. *(continued)*

ID		URC148C	PGC150	PGC152	LRGC154	JSP158B
Depth (m)		19.93	27.5	36.535	47.44	58.75
Drillhole		11-LR-1010D	11-LR-1010D	11-LR-1010D	11-LR-1010D	11-LR-1010D
Unit		URC	PGC	PGC	LRGC	JSP
SiO_2	*wt. %*	80.21	57.66	50.36	59.02	66.04
TiO_2	"	0.01	0.01	0.01	0.01	0.02
Al_2O_3	"	b.d.l.	b.d.l.	b.d.l.	b.d.l.	0.58
Fe_2O_{3T}	"	17.68	34.74	41.94	33.21	26.55
FeO	"	n.m.	n.m.	n.m.	n.m.	n.m.
MnO	"	0.16	0.13	0.53	0.44	0.44
MgO	"	1.17	4.30	2.47	4.39	0.89
CaO	"	0.09	0.91	2.00	0.62	1.86
Na_2O	"	0.06	0.12	0.11	0.41	0.06
K_2O	"	b.d.l.	b.d.l.	b.d.l.	b.d.l.	b.d.l.
P_2O_5	"	0.02	0.01	0.02	0.04	0.02
LOI	"	0.39	1.94	2.37	1.68	2.66
Fe(III)/Fe(II)	molar	n/a	n/a	n/a	n/a	n/a
Mn/∑Fe	molar	0.010	0.004	0.014	0.015	0.019
Mn/Fe(II)	molar	n/a	n/a	n/a	n/a	n/a
Mn/Fe(III)	molar	n/a	n/a	n/a	n/a	n/a
Mn/Ti	mass	309.39	177.65	355.47	150.26	151.82
P/∑Fe	molar	0.001	0.000	0.001	0.001	0.001
P/Fe(II)	molar	n/a	n/a	n/a	n/a	n/a
P/Fe(III)	molar	n/a	n/a	n/a	n/a	n/a
P/Ti	mass	22.35	9.03	8.00	6.81	4.13
∑Fe/Ti	mass	31657.94	41904.28	25598.16	10360.74	8369.52
Fe(II)/Ti	mass	n/a	n/a	n/a	n/a	n/a
Fe(III)/Ti	mass	n/a	n/a	n/a	n/a	n/a
Li	*ppb*	1509	1426	2244	2174	2213
Be	"	644.6	1033	960.1	866.9	4575
Sc	"	19.26	13.21	25.87	15.18	72.04
Ti	"	3905	5798	11460	22420	22190
V	"	3500	1451	4961	4656	4820
Cr	"	126.1	1583	1608	2078	1533
Co	"	4219	4636	2342	7510	9850
Ni	"	553.2	952.5	1076	1665	766.9
Cu	"	392.8	1362	1534	745.4	14960
Zn	"	5574	33820	4128	4897	5565
Ga	"	188.7	178.7	143.2	252.5	536.4
Rb	"	457.7	79.34	225.9	950.2	4778

b.d.l. = below detection limit; n.m. = not measured; n/a = not applicable

Table A5.1. *(continued)*

ID		URC148C	PGC150	PGC152	LRGC154	JSP158B
Depth (m)		19.93	27.5	36.535	47.44	58.75
Drillhole		11-LR-1010D	11-LR-1010D	11-LR-1010D	11-LR-1010D	11-LR-1010D
Unit		URC	PGC	PGC	LRGC	JSP
Sr	"	1616	2256	9280	4171	54460
Y	"	1529	3906	4889	2943	34600
Zr	"	809.4	755	1824	1667	5584
Nb	"	332.2	389.1	849.1	671.4	2120
Ag	"	99.12	4.297	52.46	2.438	34.56
Cd	"	b.d.l.	0.6285	2.208	0.677	1.061
Sn	"	3.285	88.27	101.3	51.27	44.66
Sb	"	42.8	39.48	36.47	30.38	91.3
Cs	"	184	25.79	98.1	629.7	3195
Ba	"	82660	6507	33820	36000	6378000
La	"	1591	1504	4384	2426	7041
Ce	"	2014	3460	7111	3857	12820
Pr	"	325.7	449.6	783.7	431	1550
Nd	"	1426	2009	3077	1766	7738
Sm	"	302.9	471.4	477.2	320.2	2301
Eu	"	90.35	170	137.2	98.28	823.1
Gd	"	360.2	615.1	554.4	417.6	3929
Tb	"	47.24	95.34	81.82	58.62	573.4
Dy	"	271.1	593.6	553.3	379.3	3651
Ho	"	55.79	129.1	137.2	91.14	861.3
Er	"	149.9	342.7	416.3	265.6	2312
Tm	"	22.28	45.8	62.38	38.19	285.9
Yb	"	136.5	241.2	375	230.3	1421
Lu	"	18.5	30.34	52.95	33.39	179.7
Hf	"	6.369	7.218	20.71	21.86	55.74
Ta	"	6.164	2.447	13.8	13.33	37.62
Pb	"	710.8	348.6	599.4	207	2487
Th	"	9.523	13.97	29.12	33.79	144.8
U	"	17.38	26.2	35.53	30.43	68.74
ΣREE+Y	"	8340	14063	23092	13356	80086
$(La/La^*)_{MuQ}$		1.61	1.15	1.48	1.63	1.95
$(Ce/Ce^*)_{MuQ}$		0.83	1.05	1.09	1.12	1.26
$(Eu/Eu^*)_{MuQ}$		1.30	1.49	1.46	1.44	1.31
$(Gd/Gd^*)_{MuQ}$		1.14	1.05	1.20	1.21	1.14
$(Lu/Lu^*)_{MuQ}$		0.94	1.01	0.99	1.02	1.08
Y/Ho		27.4	30.3	35.6	32.3	40.2
$(Pr/Yb)_{MuQ}$		0.92	0.72	0.80	0.72	0.42
$(Er/Lu)_{MuQ}$		1.18	1.64	1.14	1.16	1.87

$La^* = Pr^*(Pr/Nd)^2$; $Ce^* = Pr^*(Pr/Nd)$; $Eu^* = Sm^*(Sm/Nd)^{0.5}$; $Gd^* = Tb^*(Tb/Dy)$; $Lu^* = Yb^*(Yb/Tm)$

Table A5.1. *(continued)*

ID		JSP158C	JSP163B	JSP163C	DOL300	LC302
Depth (m)		58.75	72.21	72.21	11.295	16.005
Drillhole		11-LR-1010D	11-LR-1010D	11-LR-1010D	11-LR-1005D	11-LR-1005D
Unit		JSP	JSP	JSP	DOL	LC
SiO_2	*wt. %*	92.46	45.46	77.73	24.36	34.30
TiO_2	"	0.01	0.03	0.02	0.04	0.05
Al_2O_3	"	b.d.l.	b.d.l.	b.d.l.	0.14	0.21
Fe_2O_{3T}	"	5.07	39.87	8.19	28.50	47.97
FeO	"	n.m.	n.m.	n.m.	n.m.	n.m.
MnO	"	0.18	0.64	5.18	0.89	0.90
MgO	"	0.41	1.89	0.75	7.66	2.10
CaO	"	0.42	5.57	2.75	9.44	2.84
Na_2O	"	0.11	0.06	0.07	b.d.l.	0.06
K_2O	"	0.02	b.d.l.	0.01	0.03	b.d.l.
P_2O_5	"	0.01	0.03	0.01	0.04	0.09
LOI	"	0.67	6.26	5.04	28.30	8.48
Fe(III)/Fe(II)	molar	n/a	n/a	n/a	n/a	n/a
Mn/∑Fe	molar	0.041	0.018	0.713	0.035	0.005
Mn/Fe(II)	molar	n/a	n/a	n/a	n/a	n/a
Mn/Fe(III)	molar	n/a	n/a	n/a	n/a	n/a
Mn/Ti	mass	128.61	46.39	2526.39	56.00	3.42
P/∑Fe	molar	0.003	0.001	0.002	0.002	0.001
P/Fe(II)	molar	n/a	n/a	n/a	n/a	n/a
P/Fe(III)	molar	n/a	n/a	n/a	n/a	n/a
P/Ti	mass	4.75	1.07	3.30	1.53	0.28
∑Fe/Ti	mass	3219.79	2630.71	3609.53	1628.57	648.28
Fe(II)/Ti	mass	n/a	n/a	n/a	n/a	n/a
Fe(III)/Ti	mass	n/a	n/a	n/a	n/a	n/a
Li	*ppb*	1310	2762	2125	1682	1335
Be	"	903.6	1815	3425	5320	3137
Sc	"	7.029	305.7	94.85	324.2	532.5
Ti	"	11020	106000	15870	122400	219900
V	"	1596	5937	36.89	16680	32430
Cr	"	227.6	2439	47.4	4445	5593
Co	"	5649	8737	7166	9823	13740
Ni	"	180.4	1637	879.1	5879	2797
Cu	"	4631	710.7	129	1275	3316
Zn	"	3073	12360	9885	7393	5092
Ga	"	264.6	866.1	761.2	1902	2357
Rb	"	2799	4615	2519.5	2507	2614

b.d.l. = below detection limit; n.m. = not measured; n/a = not applicable

Table A5.1. *(continued)*

ID		JSP158C	JSP163B	JSP163C	DOL300	LC302
Depth (m)		58.75	72.21	72.21	11.295	16.005
Drillhole		11-LR-1010D	11-LR-1010D	11-LR-1010D	11-LR-1005D	11-LR-1005D
Unit		JSP	JSP	JSP	DOL	LC
Sr	"	26470	104700	48820	22590	21980
Y	"	6158	15590	21210	4080	7769
Zr	"	930.2	7027	1227	5594	15940
Nb	"	299.5	1429.25	4.445	2788	7239
Ag	"	6.322	3.485	1.017	n.m.	n.m.
Cd	"	0.3687	7.884	4.716	11.00	7.658
Sn	"	8.223	116.23	b.d.l.	39.01	60.56
Sb	"	18.8	203.1	4.061	53.73	288.3
Cs	"	1703	2600	2178	1104	1436
Ba	"	3954000	93550	40110	147200	67790
La	"	1659	10900	5192.5	2859	5535
Ce	"	2972	15590	8648.5	7786	16860
Pr	"	334.4	1892	1174.5	683.4	1244
Nd	"	1538	7718	5995	2694	4912
Sm	"	385.6	1378	1593	538.7	980.1
Eu	"	105.5	487.5	653.4	163.9	286.7
Gd	"	589.3	1767	2503	613.4	1103
Tb	"	88.06	263.9	386.15	97.13	178.9
Dy	"	591.6	1780	2564.5	614.4	1178
Ho	"	143.6	432.8	597.8	136.2	273.3
Er	"	409.2	1287	1619	381.3	820.5
Tm	"	55.22	185.2	205.3	53.49	123.5
Yb	"	298.7	1054	992.35	302.7	727.5
Lu	"	39.81	141	124.3	39.91	95.28
Hf	"	18.05	96.23	20.65	83.12	188.6
Ta	"	9.981	44.17	b.d.l.	73.77	157
Pb	"	1755	863.7	1.095	506.5	991.3
Th	"	36.15	152.8	32.49	159.5	326.5
U	"	36.05	104.2	31.17	176.8	116
ΣREE+Y	"	15368	60466	53459	21044	42087
$(La/La^*)_{MuQ}$		1.80	1.65	1.98	1.12	1.19
$(Ce/Ce^*)_{MuQ}$		1.25	1.03	1.15	1.37	1.64
$(Eu/Eu^*)_{MuQ}$		1.09	1.68	1.59	1.36	1.31
$(Gd/Gd^*)_{MuQ}$		1.18	1.18	1.13	1.05	1.06
$(Lu/Lu^*)_{MuQ}$		1.04	0.99	1.10	0.98	0.94
Y/Ho		42.9	36.0	35.5	30.0	28.4
$(Pr/Yb)_{MuQ}$		0.43	0.69	0.45	0.87	0.66
$(Er/Lu)_{MuQ}$		1.49	1.33	1.89	1.39	1.25

$La^* = Pr^*(Pr/Nd)^2$; $Ce^* = Pr^*(Pr/Nd)$; $Eu^* = Sm^*(Sm/Nd)^{0.5}$; $Gd^* = Tb^*(Tb/Dy)$; $Lu^* = Yb^*(Yb/Tm)$

Table A5.1. *(continued)*

ID		JUIF304	JUIF307	JUIF309	JUIF311	LC260
Depth (m)		25.165	31.78	35.22	40.675	16.975
Drillhole		11-LR-1005D	11-LR-1005D	11-LR-1005D	11-LR-1005D	11-LR-1012D
Unit		JUIF	JUIF	JUIF	JUIF	LC
SiO_2	*wt. %*	39.62	68.07	49.29	74.41	39.07
TiO_2	"	0.09	0.02	0.02	0.02	0.02
Al_2O_3	"	0.35	0.06	b.d.l.	b.d.l.	b.d.l.
Fe_2O_{3T}	"	48.48	29.25	31.35	18.44	29.33
FeO	"	n.m.	n.m.	n.m.	n.m.	13.38
MnO	"	0.54	0.24	3.37	0.54	2.25
MgO	"	1.68	0.68	2.60	1.26	3.72
CaO	"	2.62	0.05	2.75	0.11	9.92
Na_2O	"	0.06	0.05	0.05	0.05	b.d.l.
K_2O	"	b.d.l.	b.d.l.	b.d.l.	b.d.l.	b.d.l.
P_2O_5	"	0.08	0.02	0.02	0.02	0.02
LOI	"	3.49	0.65	9.34	4.94	14.62
Fe(III)/Fe(II)	molar	n/a	n/a	n/a	n/a	0.97
Mn/∑Fe	molar	0.013	0.009	0.122	0.033	0.087
Mn/Fe(II)	molar	n/a	n/a	n/a	n/a	0.172
Mn/Fe(III)	molar	n/a	n/a	n/a	n/a	0.177
Mn/Ti	mass	9.16	40.72	800.37	1105.78	4890.07
P/∑Fe	molar	0.002	0.001	0.001	0.001	0.001
P/Fe(II)	molar	n/a	n/a	n/a	n/a	0.001
P/Fe(III)	molar	n/a	n/a	n/a	n/a	0.001
P/Ti	mass	0.73	1.46	2.55	24.41	19.59
∑Fe/Ti	mass	742.60	4578.14	6729.17	34354.79	57541.61
Fe(II)/Ti	mass	n/a	n/a	n/a	n/a	29173.65
Fe(III)/Ti	mass	n/a	n/a	n/a	n/a	28367.95
Li	*ppb*	3995	3269	2972	1464	624.9
Be	"	2413	2428	1995	1361	1158
Sc	"	737.3	216.5	228	63.5	52.77
Ti	"	456600	44690	32580	3754	3565
V	"	18330	16330	6431	11090	5919
Cr	"	8545	592.9	475.9	445.5	817.6
Co	"	10570	5868	9787	17040	31010
Ni	"	2668	875	885.1	3816	2321
Cu	"	767.3	1362	1176	3898	1725
Zn	"	5872	3396	4475	1703	2446
Ga	"	1775	1263	1342	1349	807.5
Rb	"	1452	889.5	272.4	239.9	98.74

b.d.l. = below detection limit; n.m. = not measured; n/a = not applicable

Table A5.1. *(continued)*

ID		JUIF304	JUIF307	JUIF309	JUIF311	LC260
Depth (m)		25.165	31.78	35.22	40.675	16.975
Drillhole		11-LR-1005D	11-LR-1005D	11-LR-1005D	11-LR-1005D	11-LR-1012D
Unit		JUIF	JUIF	JUIF	JUIF	LC
Sr	"	23970	2777	6818	1642	8701
Y	"	4208	4559	5425	1461	6493
Zr	"	18860	10150	2693	5686	988
Nb	"	6330	2903	431.2	1273	333.5
Ag	"	n.m.	n.m.	n.m.	n.m.	n.m.
Cd	"	8.334	4.284	2.242	1.986	2.587
Sn	"	143.7	29.27	13.16	25.42	b.d.l.
Sb	"	335.1	237.7	116.9	145.9	178.9
Cs	"	984.2	612.2	176.8	182.4	31.77
Ba	"	75300	35960	8352	5539	7963
La	"	3363	1930	2287	498.6	2275
Ce	"	9438	5132	4964	1603	4928
Pr	"	843.9	438.7	460.9	123.2	479.4
Nd	"	3438	1813	1986	549	2153
Sm	"	713.5	394.7	454.1	139.2	442.8
Eu	"	216.2	146.6	205.5	51.34	170
Gd	"	757.5	522.2	632.9	196.2	645.8
Tb	"	115.2	96.08	101	34.88	99.07
Dy	"	696	676.8	652.7	247.1	663.5
Ho	"	148.5	158.6	149.7	58.15	161.3
Er	"	417.6	472.8	431.2	181.4	460.2
Tm	"	60.24	71.01	62.95	28.29	60.79
Yb	"	350.8	407.4	372	167.7	313.4
Lu	"	46.53	51.04	49.98	21.64	38.87
Hf	"	337.1	85.75	31.45	13.89	5.878
Ta	"	314.1	26.61	4.733	1.873	0.9876
Pb	"	1992	962.3	491.7	318.1	1858
Th	"	479.6	74.74	25.9	16.35	8.204
U	"	152.9	59.09	38.03	79.24	36.57
ΣREE+Y	"	24813	16870	18235	5361	19384
$(La/La^*)_{MuQ}$		1.14	1.29	1.58	1.38	1.65
$(Ce/Ce^*)_{MuQ}$		1.39	1.48	1.42	1.77	1.41
$(Eu/Eu^*)_{MuQ}$		1.33	1.59	1.90	1.47	1.70
$(Gd/Gd^*)_{MuQ}$		1.04	1.00	1.06	1.04	1.14
$(Lu/Lu^*)_{MuQ}$		0.96	0.92	0.96	0.92	1.02
Y/Ho		28.3	28.7	36.2	25.1	40.3
$(Pr/Yb)_{MuQ}$		0.92	0.41	0.48	0.28	0.59
$(Er/Lu)_{MuQ}$		1.30	1.35	1.25	1.22	1.72

$La^* = Pr^*(Pr/Nd)^2$; $Ce^* = Pr^*(Pr/Nd)$; $Eu^* = Sm^*(Sm/Nd)^{0.5}$; $Gd^* = Tb^*(Tb/Dy)$; $Lu^* = Yb^*(Yb/Tm)$

Table A5.1. *(continued)*

ID		LC263	LC264	LC267	GC269	URC272
Depth (m)		24.075	34.77	41.16	51.23	57.23
Drillhole		11-LR-1012D	11-LR-1012D	11-LR-1012D	11-LR-1012D	11-LR-1012D
Unit		LC	LC	LC	GC	URC
SiO_2	*wt. %*	29.02	37.54	40.22	82.67	47.62
TiO_2	"	0.02	0.02	0.02	0.02	0.02
Al_2O_3	"	b.d.l.	b.d.l.	b.d.l.	b.d.l.	b.d.l.
Fe_2O_{3T}	"	41.22	40.96	49.46	6.74	44.04
FeO	"	16.60	16.30	14.25	3.97	15.63
MnO	"	2.27	1.72	1.04	0.71	1.09
MgO	"	3.11	2.24	1.26	1.07	1.80
CaO	"	9.53	6.44	3.16	3.67	1.06
Na_2O	"	b.d.l.	b.d.l.	b.d.l.	b.d.l.	b.d.l.
K_2O	"	b.d.l.	b.d.l.	b.d.l.	b.d.l.	b.d.l.
P_2O_5	"	0.04	0.04	0.03	0.01	0.02
LOI	"	13.35	9.61	4.25	5.40	2.91
Fe(III)/Fe(II)	molar	1.23	1.26	2.12	0.53	1.54
Mn/∑Fe	molar	0.063	0.048	0.024	0.118	0.028
Mn/Fe(II)	molar	0.140	0.109	0.075	0.181	0.071
Mn/Fe(III)	molar	0.114	0.086	0.035	0.343	0.046
Mn/Ti	mass	1374.39	403.88	725.14	1782.79	3350.44
P/∑Fe	molar	0.001	0.001	0.001	0.002	0.000
P/Fe(II)	molar	0.003	0.002	0.002	0.004	0.001
P/Fe(III)	molar	0.002	0.002	0.001	0.007	0.001
P/Ti	mass	14.34	5.15	12.92	19.75	31.32
∑Fe/Ti	mass	22557.44	8675.30	31025.84	15248.16	122818.57
Fe(II)/Ti	mass	10096.51	3837.11	9934.23	9977.11	48442.41
Fe(III)/Ti	mass	12460.92	4838.19	21091.61	5271.05	74376.16
Li	*ppb*	641	675.9	2678	439	651
Be	"	1402	1633	1768	417.6	1253
Sc	"	99.48	117	106.6	49.71	32.66
Ti	"	12780	33020	11150	3093	2508
V	"	9821	12380	13200	6960	2807
Cr	"	1597	1417	1397	403.9	598.6
Co	"	13230	2624	3726	2048	911.9
Ni	"	2422	1035	1388	772.2	783.1
Cu	"	5595	754.5	1424	68400	462.4
Zn	"	2666	2731	8758	1985	10750
Ga	"	1072	952.5	900.8	643.9	377.8
Rb	"	501.7	529.9	363.4	197.3	148.8

b.d.l. = below detection limit; n.m. = not measured; n/a = not applicable

Table A5.1. *(continued)*

ID		LC263	LC264	LC267	GC269	URC272
Depth (m)		24.075	34.77	41.16	51.23	57.23
Drillhole		11-LR-1012D	11-LR-1012D	11-LR-1012D	11-LR-1012D	11-LR-1012D
Unit		LC	LC	LC	GC	URC
Sr	"	18980	11500	20790	23690	8570
Y	"	7643	6553	3915	4146	2420
Zr	"	2695	2621	2982	2876	1103
Nb	"	767	1022	1036	272.7	471.1
Ag	"	n.m.	n.m.	n.m.	n.m.	n.m.
Cd	"	7.903	5.981	28.82	20.83	8.245
Sn	"	24.65	13.98	16.61	18.54	24.42
Sb	"	109.4	126.9	131.1	63.21	39.74
Cs	"	214	248.5	112.4	95.31	61.57
Ba	"	25570	29780	171300	17810	7802
La	"	2330	2343	2250	4497	1215
Ce	"	6448	5797	5323	7782	2109
Pr	"	626.7	554.2	445.6	937.6	269.9
Nd	"	2932	2531	1853	3763	1132
Sm	"	681	558.3	366.9	798.6	233.1
Eu	"	231.6	186.5	131.9	236.6	83.71
Gd	"	942.8	772.4	480.8	893.6	299
Tb	"	145.6	120.7	76.99	125	46.53
Dy	"	963	814.7	520.7	683.4	311.5
Ho	"	224	194.5	124	133.1	74.74
Er	"	629.5	557.8	365	338.4	217.1
Tm	"	85.1	78.05	52.8	45.92	32.51
Yb	"	436.3	415.4	293.1	257.5	188.3
Lu	"	53.87	51.96	37.28	33.49	25.23
Hf	"	29.45	19.09	14.6	11.25	9.519
Ta	"	6.976	7.434	5.067	2.253	6.18
Pb	"	1582	587.2	1252	565.9	515.5
Th	"	51.31	19.44	18.59	10.06	16.81
U	"	53.84	53.79	47.47	203.8	63.12
ΣREE+Y	"	24372	21529	16236	24671	8658
$(La/La^*)_{MuQ}$		1.40	1.52	1.50	1.33	1.36
$(Ce/Ce^*)_{MuQ}$		1.47	1.46	1.52	1.02	1.00
$(Eu/Eu^*)_{MuQ}$		1.41	1.43	1.62	1.29	1.59
$(Gd/Gd^*)_{MuQ}$		1.12	1.13	1.11	1.02	1.13
$(Lu/Lu^*)_{MuQ}$		1.02	0.99	0.97	0.98	0.98
Y/Ho		34.1	33.7	31.6	31.1	32.4
$(Pr/Yb)_{MuQ}$		0.55	0.51	0.58	1.40	0.55
$(Er/Lu)_{MuQ}$		1.70	1.56	1.42	1.47	1.25

$La^* = Pr^*(Pr/Nd)^2$; $Ce^* = Pr^*(Pr/Nd)$; $Eu^* = Sm^*(Sm/Nd)^{0.5}$; $Gd^* = Tb^*(Tb/Dy)$; $Lu^* = Yb^*(Yb/Tm)$

Table A5.1. *(continued)*

ID		PGC276	LRGC280	LRGC284	JSP289	JSP294
Depth (m)		61.95	70.33	84.51	94.995	113.315
Drillhole		11-LR-1012D	11-LR-1012D	11-LR-1012D	11-LR-1012D	11-LR-1012D
Unit		PGC	LRGC	LRGC	JSP	JSP
SiO_2	*wt. %*	41.63	50.76	50.45	37.42	83.32
TiO_2	"	0.02	0.02	0.02	0.03	0.02
Al_2O_3	"	b.d.l.	b.d.l.	b.d.l.	0.15	0.79
Fe_2O_{3T}	"	39.50	43.46	40.26	55.25	14.71
FeO	"	4.33	2.00	3.28	0.78	0.23
MnO	"	1.49	0.11	0.81	0.39	0.13
MgO	"	0.98	3.06	3.15	1.57	0.12
CaO	"	9.70	0.63	1.77	1.67	b.d.l.
Na_2O	"	b.d.l.	0.09	b.d.l.	0.06	0.06
K_2O	"	b.d.l.	b.d.l.	b.d.l.	b.d.l.	b.d.l.
P_2O_5	"	0.02	0.01	0.02	0.04	0.01
LOI	"	6.58	1.13	2.57	1.89	0.63
Fe(III)/Fe(II)	molar	7.21	18.55	10.04	62.74	56.53
Mn/∑Fe	molar	0.043	0.003	0.023	0.008	0.010
Mn/Fe(II)	molar	0.349	0.056	0.253	0.513	0.569
Mn/Fe(III)	molar	0.048	0.003	0.025	0.008	0.010
Mn/Ti	mass	872.80	87.46	364.08	77.05	53.40
P/∑Fe	molar	0.001	0.000	0.001	0.001	0.001
P/Fe(II)	molar	0.006	0.006	0.007	0.047	0.049
P/Fe(III)	molar	0.001	0.000	0.001	0.001	0.001
P/Ti	mass	7.92	5.43	5.32	4.02	2.57
∑Fe/Ti	mass	20882.98	31491.02	16342.63	9883.25	5497.50
Fe(II)/Ti	mass	2544.03	1610.67	1479.73	155.06	95.55
Fe(III)/Ti	mass	18338.95	29880.35	14862.90	9728.19	5401.94
Li	*ppb*	1991	1945	2841	2946	2384
Be	"	1150	895.6	913.8	2614	489.8
Sc	"	79.48	58.58	53.31	194.3	119.7
Ti	"	13230	9652	17230	39100	18710
V	"	8370	5619	4587	25510	7958
Cr	"	418.9	609.5	648.3	1686	562
Co	"	13050	2733	6706	7605	1416
Ni	"	1987	541.1	815.6	909.8	953.8
Cu	"	847.5	713	1500	895.1	2831
Zn	"	3892	9268	4264	3513	b.d.l.
Ga	"	499.9	139.9	342.5	768.1	442.7
Rb	"	451.1	167.1	1280	5977	2515

b.d.l. = below detection limit; n.m. = not measured; n/a = not applicable

Table A5.1. *(continued)*

ID		PGC276	LRGC280	LRGC284	JSP289	JSP294
Depth (m)		61.95	70.33	84.51	94.995	113.315
Drillhole		11-LR-1012D	11-LR-1012D	11-LR-1012D	11-LR-1012D	11-LR-1012D
Unit		PGC	LRGC	LRGC	JSP	JSP
Sr	"	40330	6965	10420	17360	36620
Y	"	11170	4376	4393	16780	2694
Zr	"	1663	1943	2693	17930	2129
Nb	"	770.6	1152	1013	8136	553.9
Ag	"	n.m.	n.m.	n.m.	n.m.	n.m.
Cd	"	14.27	5.187	1.664	10.37	0.9219
Sn	"	19.65	25.93	22.05	50	73.63
Sb	"	69.01	73.19	25.19	179.8	195.1
Cs	"	70.31	258	774.3	3500	1331
Ba	"	34890	19910	90670	640700	8708000
La	"	7373	2684	2439	9088	3046
Ce	"	8721	5428	3553	15710	4863
Pr	"	1319	650.7	397.3	1659	541.9
Nd	"	5593	2738	1626	6887	2171
Sm	"	1076	541.2	303.4	1357	441.7
Eu	"	407.7	195.9	106.8	482	116.2
Gd	"	1443	647.2	427.7	1762	452.3
Tb	"	214.7	96.91	63.42	275.9	76.61
Dy	"	1417	613.1	433.2	1908	436.2
Ho	"	333	136.9	109.2	474.1	107.4
Er	"	951	380.9	324.2	1424	318.5
Tm	"	132.5	54.32	46.16	212.5	48.88
Yb	"	738.6	314.7	270.8	1220	274.2
Lu	"	99.76	41.79	38.64	163.9	35.96
Hf	"	13.19	19.08	30.02	141.3	24.49
Ta	"	7.921	18.69	20.68	105.3	14.32
Pb	"	1433	71150	597.9	3455	1853
Th	"	15.97	34.04	47.53	309	83.06
U	"	97.89	26.76	26.76	103.9	107.6
ΣREE+Y	"	40989	18900	14532	59403	15624
$(La/La^*)_{MuQ}$		1.73	1.26	1.77	1.62	1.55
$(Ce/Ce^*)_{MuQ}$		0.86	1.07	1.12	1.20	1.10
$(Eu/Eu^*)_{MuQ}$		1.73	1.63	1.63	1.60	1.17
$(Gd/Gd^*)_{MuQ}$		1.16	1.11	1.21	1.16	0.88
$(Lu/Lu^*)_{MuQ}$		1.02	0.97	1.03	0.99	0.99
Y/Ho		33.5	32.0	40.2	35.4	25.1
$(Pr/Yb)_{MuQ}$		0.69	0.79	0.56	0.52	0.76
$(Er/Lu)_{MuQ}$		1.39	1.33	1.22	1.26	1.29

$La^* = Pr^*(Pr/Nd)^2$; $Ce^* = Pr^*(Pr/Nd)$; $Eu^* = Sm^*(Sm/Nd)^{0.5}$; $Gd^* = Tb^*(Tb/Dy)$; $Lu^* = Yb^*(Yb/Tm)$

Table A5.1. *(continued)*

ID		RTH296	DOL113	DOL113-PL	LC114	JUIF116
Depth (m)		115.2	29.95	29.95	36.17	42.095
Drillhole		11-LR-1012D	11-LR-1029D	11-LR-1029D	11-LR-1029D	11-LR-1029D
Unit		RTH	DOL	DOL	LC	JUIF
SiO_2	*wt. %*	61.77	18.83	n.m.	75.76	10.54
TiO_2	"	0.58	0.10	n.m.	0.01	0.18
Al_2O_3	"	13.86	1.58	n.m.	b.d.l.	0.57
Fe_2O_{3T}	"	11.12	1.22	n.m.	20.38	61.89
FeO	"	8.49	1.42	n.m.	n.m.	n.m.
MnO	"	0.15	0.11	n.m.	0.10	1.98
MgO	"	1.70	17.40	n.m.	0.26	4.01
CaO	"	0.09	24.13	n.m.	0.04	8.62
Na_2O	"	0.76	b.d.l.	n.m.	0.27	0.08
K_2O	"	7.54	0.58	n.m.	b.d.l.	0.03
P_2O_5	"	0.07	0.14	n.m.	0.01	0.08
LOI	"	2.23	35.54	n.m.	2.96	11.83
Fe(III)/Fe(II)	molar	0.18	-0.23	n/a	n/a	n/a
Mn/∑Fe	molar	0.015	0.105	n/a	0.005	0.036
Mn/Fe(II)	molar	0.018	0.081	n/a	n/a	n/a
Mn/Fe(III)	molar	0.099	-0.354	n/a	n/a	n/a
Mn/Ti	mass	0.35	2.11	n/a	24	17
P/∑Fe	molar	0.007	0.131	n/a	0.001	0.001
P/Fe(II)	molar	0.008	0.101	n/a	n/a	n/a
P/Fe(III)	molar	0.045	-0.442	n/a	n/a	n/a
P/Ti	mass	0.09	1.48	n/a	1.95	0.39
∑Fe/Ti	mass	23.55	20.53	n/a	4546	481
Fe(II)/Ti	mass	19.99	26.60	n/a	n/a	n/a
Fe(III)/Ti	mass	3.57	-6.07	n/a	n/a	n/a
Li	*ppb*	26010	5329	1411	1169	2919
Be	"	2977	598.7	404.8	1173	2895
Sc	"	12040	1490	1352	54.26	1347
Ti	"	3302000	414900	8064	31360	899300
V	"	85470	7192	1970	6790	28840
Cr	"	103900	7584	1295	2263	14960
Co	"	18940	3045	906	1127	20660
Ni	"	27430	6839	2600	1980	4296
Cu	"	3999	4535	1193	1384	1334
Zn	"	25660	43690	25730	2969.5	9392
Ga	"	16350	2141	78.59	508.7	2119
Rb	"	352200	18300	1323	130	2283

b.d.l. = below detection limit; n.m. = not measured; n/a = not applicable

Table A5.1. *(continued)*

ID		RTH296	DOL113	DOL113-PL	LC114	JUIF116
Depth (m)		115.2	29.95	29.95	36.17	42.095
Drillhole		11-LR-1012D	11-LR-1029D	11-LR-1029D	11-LR-1029D	11-LR-1029D
Unit		RTH	DOL	DOL	LC	JUIF
Sr	"	50020	103200	99370	1022	76360
Y	"	11650	4911	3914	846.9	9215
Zr	"	103900	25480	1616	5930	33150
Nb	"	12250	1284	13.09	1836	10460
Ag	"	n.m.	45.81	9.302	18.16	28.04
Cd	"	37.61	277.2	152.2	10.03	27.1
Sn	"	1314	224.8	21.77	133.3	271.1
Sb	"	63.88	131	60.1	222.5	343
Cs	"	15470	358.2	29.58	131.3	3007
Ba	"	2046000	285400	41380	3290.5	105400
La	"	29720	5845	5485	2689	5225
Ce	"	66040	11270	10570	6332	15830
Pr	"	6768	1317	1239	456	1457
Nd	"	23790	4686	4391	1618	5921
Sm	"	3926	857.8	788.1	232.1	1296
Eu	"	894.6	199.6	177.9	55.3	386.4
Gd	"	2967	777.4	694.4	185.6	1418
Tb	"	397.9	119.1	102.9	24.44	227.1
Dy	"	2118	711.4	590.5	138.8	1429
Ho	"	415	149.4	119.8	29.78	313
Er	"	1120	411.3	309.8	83.27	884.4
Tm	"	164.2	59.79	41.66	12.24	126.1
Yb	"	1045	362	234.3	71.68	729.6
Lu	"	155.1	51.37	31.9	9.023	97.12
Hf	"	2811	631.8	37.56	58.52	627
Ta	"	901.6	88.4	0.7393	30.55	507.3
Pb	"	4846	2884	1710	473.9	1964
Th	"	9537	1379	760.2	92.08	793.1
U	"	1700	240.8	75.14	34.73	153
ΣREE+Y	"	151171	31728	28690	12784	44555
$(La/La^*)_{MuQ}$		0.93	0.97	0.96	1.28	1.02
$(Ce/Ce^*)_{MuQ}$		1.05	0.93	0.92	1.51	1.35
$(Eu/Eu^*)_{MuQ}$		1.12	1.09	1.07	1.26	1.28
$(Gd/Gd^*)_{MuQ}$		1.04	1.02	1.01	1.13	1.03
$(Lu/Lu^*)_{MuQ}$		0.99	0.99	1.02	0.91	0.97
Y/Ho		28.1	32.9	32.7	28.4	29.4
$(Pr/Yb)_{MuQ}$		2.49	1.40	2.03	2.44	0.77
$(Er/Lu)_{MuQ}$		1.05	1.16	1.41	1.34	1.32

$La^* = Pr^*(Pr/Nd)^2$; $Ce^* = Pr^*(Pr/Nd)$; $Eu^* = Sm^*(Sm/Nd)^{0.5}$; $Gd^* = Tb^*(Tb/Dy)$; $Lu^* = Yb^*(Yb/Tm)$

Table A5.1. *(continued)*

ID		JUIF119	GC120	JUIF121B	JUIF121C	JUIF124
Depth (m)		54.72	56.89	59.3	59.3	66.145
Drillhole		11-LR-1029D	11-LR-1029D	11-LR-1029D	11-LR-1029D	11-LR-1029D
Unit		JUIF	GC	JUIF	JUIF	JUIF
SiO_2	*wt. %*	14.94	43.06	31.63	78.16	71.20
TiO_2	"	0.04	0.01	0.02	0.01	0.02
Al_2O_3	"	0.12	b.d.l.	b.d.l.	b.d.l.	b.d.l.
Fe_2O_{3T}	"	42.42	25.35	44.58	15.45	17.81
FeO	"	n.m.	n.m.	n.m.	n.m.	n.m.
MnO	"	2.41	0.98	0.71	0.24	1.27
MgO	"	7.25	4.94	6.56	1.72	1.62
CaO	"	10.57	8.76	6.38	1.44	1.26
Na_2O	"	0.07	0.22	b.d.l.	0.07	b.d.l.
K_2O	"	0.03	0.00	b.d.l.	b.d.l.	b.d.l.
P_2O_5	"	0.03	0.02	0.03	0.03	0.03
LOI	"	21.94	16.44	9.89	2.65	6.58
Fe(III)/Fe(II)	molar	n/a	n/a	n/a	n/a	n/a
Mn/∑Fe	molar	0.064	0.018	0.017	0.080	0.001
Mn/Fe(II)	molar	n/a	n/a	n/a	n/a	n/a
Mn/Fe(III)	molar	n/a	n/a	n/a	n/a	n/a
Mn/Ti	mass	131	1475	477	421	1960
P/∑Fe	molar	0.001	0.001	0.001	0.002	0.002
P/Fe(II)	molar	n/a	n/a	n/a	n/a	n/a
P/Fe(III)	molar	n/a	n/a	n/a	n/a	n/a
P/Ti	mass	1.04	20.36	12.59	28.05	26.17
∑Fe/Ti	mass	2082	34463	27258	24795	24896
Fe(II)/Ti	mass	n/a	n/a	n/a	n/a	n/a
Fe(III)/Ti	mass	n/a	n/a	n/a	n/a	n/a
Li	*ppb*	2944	675.8	2050	714.7	1001
Be	"	2188	1689	5375	1979	757.2
Sc	"	685.3	50.65	62.27	28.92	21.45
Ti	"	142500	5145	11440	4357	5003
V	"	13820	6190	20830	9193	1502
Cr	"	2056	1357	641.8	166	178.8
Co	"	8759	2678	11490	3685	4896
Ni	"	2426	2304	6995	1934	335.3
Cu	"	2631	1320	803.4	41870	1103
Zn	"	7568	2238	10110	3626	2490
Ga	"	1411	971.5	2482	820.4	265.2
Rb	"	1698	324.9	443.2	114.9	76.95

b.d.l. = below detection limit; n.m. = not measured; n/a = not applicable

Table A5.1. *(continued)*

ID		JUIF119	GC120	JUIF121B	JUIF121C	JUIF124
Depth (m)		54.72	56.89	59.3	59.3	66.145
Drillhole		11-LR-1029D	11-LR-1029D	11-LR-1029D	11-LR-1029D	11-LR-1029D
Unit		JUIF	GC	JUIF	JUIF	JUIF
Sr	"	38870	12130	19260	3753	3430
Y	"	14720	5973	8581	3018	3893
Zr	"	4709	4287	6639	3030	1181
Nb	"	1119	1332	2350	799.7	91.38
Ag	"	61.32	31.44	191.2	239.3	7.679
Cd	"	4.048	3.575	4.417	1.177	1.604
Sn	"	75.19	90.32	29.73	25.17	13.33
Sb	"	226.6	173.3	338.3	216.8	40.55
Cs	"	2140	271.6	486.8	140.6	56.23
Ba	"	25890	6688	11000	4379	3948
La	"	9211	6436	4713	2278	1791
Ce	"	14150	13260	10410	4752	3045
Pr	"	1566	1082	891.1	428.9	341.6
Nd	"	6431	4177	3703	1809	1470
Sm	"	1267	716.3	782.6	357.8	282.8
Eu	"	449.7	213.8	273.2	122.5	100.7
Gd	"	1683	819.6	1043	456	390.6
Tb	"	273.1	129.5	171.1	65.91	58.8
Dy	"	1855	842.5	1166	410.3	398
Ho	"	451.3	197.6	278	93.25	98.27
Er	"	1338	574.8	821	265.6	285.6
Tm	"	194.5	83.83	119.4	37.17	40.28
Yb	"	1086	465.4	655.6	207.9	217.2
Lu	"	146.9	59.79	83.62	26.42	28.11
Hf	"	59.8	22.95	22.23	9.418	9.141
Ta	"	15.93	2.289	4.102	1.746	1.321
Pb	"	540.3	9.598	808.1	444.9	258.7
Th	"	43.52	27.59	18.5	7.781	12.87
U	"	74.65	95.11	112.5	57.7	22.87
ΣREE+Y	"	54823	35031	33692	14329	12441
$(La/La^*)_{MuQ}$		1.71	1.52	1.57	1.62	1.67
$(Ce/Ce^*)_{MuQ}$		1.14	1.45	1.49	1.43	1.17
$(Eu/Eu^*)_{MuQ}$		1.60	1.44	1.52	1.54	1.63
$(Gd/Gd^*)_{MuQ}$		1.10	1.08	1.09	1.13	1.18
$(Lu/Lu^*)_{MuQ}$		1.02	0.98	0.98	0.96	1.01
Y/Ho		32.6	30.2	30.9	32.4	39.6
$(Pr/Yb)_{MuQ}$		0.55	0.89	0.52	0.79	0.60
$(Er/Lu)_{MuQ}$		1.32	1.40	1.43	1.46	1.48

$La^* = Pr^*(Pr/Nd)^2$; $Ce^* = Pr^*(Pr/Nd)$; $Eu^* = Sm^*(Sm/Nd)^{0.5}$; $Gd^* = Tb^*(Tb/Dy)$; $Lu^* = Yb^*(Yb/Tm)$

Table A5.1. *(continued)*

ID		JUIF127	JUIF131	GC132	URC133B	URC133C
Depth (m)		73.13	89.545	95.515	98.72	98.72
Drillhole		11-LR-1029D	11-LR-1029D	11-LR-1029D	11-LR-1029D	11-LR-1029D
Unit		JUIF	JUIF	GC	URC	URC
SiO_2	*wt. %*	56.82	43.24	51.76	42.50	79.41
TiO_2	"	0.01	0.02	0.04	0.01	0.01
Al_2O_3	"	b.d.l.	b.d.l.	0.14	b.d.l.	b.d.l.
Fe_2O_{3T}	"	42.95	38.97	14.92	47.64	18.31
FeO	"	n.m.	n.m.	n.m.	n.m.	n.m.
MnO	"	0.05	0.98	2.32	0.86	0.16
MgO	"	0.41	3.02	4.81	2.73	1.31
CaO	"	0.04	5.34	8.01	2.26	0.14
Na_2O	"	0.42	b.d.l.	0.07	0.16	0.13
K_2O	"	b.d.l.	b.d.l.	0.08	b.d.l.	b.d.l.
P_2O_5	"	0.02	0.02	0.03	0.04	0.03
LOI	"	-0.91	8.14	17.58	3.61	0.28
Fe(III)/Fe(II)	molar	n/a	n/a	n/a	n/a	n/a
Mn/∑Fe	molar	0.028	0.044	0.175	0.020	0.010
Mn/Fe(II)	molar	n/a	n/a	n/a	n/a	n/a
Mn/Fe(III)	molar	n/a	n/a	n/a	n/a	n/a
Mn/Ti	mass	182	1241	106	409	370
P/∑Fe	molar	0.001	0.000	0.002	0.001	0.002
P/Fe(II)	molar	n/a	n/a	n/a	n/a	n/a
P/Fe(III)	molar	n/a	n/a	n/a	n/a	n/a
P/Ti	mass	46.21	12.13	0.77	9.64	39.41
∑Fe/Ti	mass	138311	44577	617	20457	37312
Fe(II)/Ti	mass	n/a	n/a	n/a	n/a	n/a
Fe(III)/Ti	mass	n/a	n/a	n/a	n/a	n/a
Li	*ppb*	2529	2383	1305	1621	1198
Be	"	1427	1637	710.8	2207	594.1
Sc	"	b.d.l.	12.94	267.7	54.82	15.03
Ti	"	2172	6115	169100	16290	3433
V	"	11070	7775	6630	12750	3154
Cr	"	418.2	1448	3623	1713	91.93
Co	"	1598	5789	22920	6026	5754
Ni	"	266.8	1723	3984	1703	883.9
Cu	"	1401	2237	5316	1157	1198
Zn	"	2945	7672	10080	11980	9731
Ga	"	364.1	563.8	453	332.7	237.1
Rb	"	99.25	218.7	2756	349	138.5

b.d.l. = below detection limit; n.m. = not measured; n/a = not applicable

Table A5.1. *(continued)*

ID		JUIF127	JUIF131	GC132	URC133B	URC133C
Depth (m)		73.13	89.545	95.515	98.72	98.72
Drillhole		11-LR-1029D	11-LR-1029D	11-LR-1029D	11-LR-1029D	11-LR-1029D
Unit		JUIF	JUIF	GC	URC	URC
Sr	"	891	18720	31580	13680	1660
Y	"	1293	8758	5942	10540	3407
Zr	"	1595	3075	6676	3205	596.4
Nb	"	612.4	934.5	1513.25	1148	216.3
Ag	"	6.566	37.77	136.765	324.5	52.37
Cd	"	0.9341	25.33	27.96	5.746	0.4543
Sn	"	7.726	53.4	94.14	116.4	3.918
Sb	"	123.7	133.4	92.65	110.9	39.2
Cs	"	59.97	150.1	2681	270.8	93.1
Ba	"	6171	17390	83300	14600	4032
La	"	489.3	2886	8416	10860	5716
Ce	"	828.1	5827	12600	11960	6295
Pr	"	105.2	675.7	1484	1810	967.7
Nd	"	470.1	3037	5717	7448	4118
Sm	"	122.8	742.9	906.6	1332	755.3
Eu	"	35.83	266.1	300	425.1	239.6
Gd	"	173.8	1045	975.6	1581	840.1
Tb	"	29.21	177.3	126.8	225	97.27
Dy	"	203.2	1186	750.8	1449	530.4
Ho	"	49.65	280	166.7	339.6	109.4
Er	"	153.7	816.7	459.1	977.7	283.9
Tm	"	25.13	120.4	62.42	144.5	39.03
Yb	"	149.4	669.5	355.5	842.2	231.4
Lu	"	18.54	85.41	48.29	118.5	32.77
Hf	"	5.151	17.09	141.6	28.22	4.923
Ta	"	1.253	5.466	57.4545	20.81	3.412
Pb	"	1200	829.2	913.905	759.9	296.6
Th	"	3.522	25.54	298.6	41.64	5.849
U	"	35.03	34.52	1112	31.05	10.76
ΣREE+Y	"	4147	26573	38311	50053	23663
$(La/La^*)_{MuQ}$		1.60	1.48	1.45	1.75	1.84
$(Ce/Ce^*)_{MuQ}$		1.08	1.19	1.00	0.83	0.85
$(Eu/Eu^*)_{MuQ}$		1.14	1.45	1.66	1.51	1.48
$(Gd/Gd^*)_{MuQ}$		1.08	1.03	1.19	1.18	1.23
$(Lu/Lu^*)_{MuQ}$		0.88	0.97	1.01	1.02	1.01
Y/Ho		26.0	31.3	35.6	31.0	31.1
$(Pr/Yb)_{MuQ}$		0.27	0.39	1.60	0.83	1.61
$(Er/Lu)_{MuQ}$		1.21	1.39	1.38	1.20	1.26

$La^* = Pr^*(Pr/Nd)^2$; $Ce^* = Pr^*(Pr/Nd)$; $Eu^* = Sm^*(Sm/Nd)^{0.5}$; $Gd^* = Tb^*(Tb/Dy)$; $Lu^* = Yb^*(Yb/Tm)$

Table A5.1. *(continued)*

ID		PGC135	LRGC138	JSP140B	JSP140C	RTH141
Depth (m)		101.14	111.41	5.3	5.3	9.26
Drillhole		11-LR-1029D	11-LR-1029D	11-LR-1020D	11-LR-1020D	11-LR-1020D
Unit		LRC/PGC	LRGC	JSP	JSP	RTH
SiO_2	*wt. %*	39.70	46.75	33.19	70.06	59.49
TiO_2	"	0.01	0.01	0.06	0.03	0.60
Al_2O_3	"	b.d.l.	b.d.l.	0.08	b.d.l.	14.24
Fe_2O_{3T}	"	20.68	43.44	57.30	18.39	11.78
FeO	"	n.m.	n.m.	n.m.	n.m.	n.m.
MnO	"	3.68	0.37	2.84	3.34	0.21
MgO	"	3.73	5.13	0.46	0.39	2.67
CaO	"	13.10	1.23	2.31	2.97	0.08
Na_2O	"	0.12	0.40	0.06	0.07	0.41
K_2O	"	b.d.l.	b.d.l.	0.02	0.04	7.37
P_2O_5	"	0.02	0.01	0.03	0.05	0.07
LOI	"	18.74	2.47	3.43	4.46	2.40
Fe(III)/Fe(II)	molar	n/a	n/a	n/a	n/a	n/a
Mn/∑Fe	molar	0.201	0.010	0.056	0.205	0.020
Mn/Fe(II)	molar	n/a	n/a	n/a	n/a	n/a
Mn/Fe(III)	molar	n/a	n/a	n/a	n/a	n/a
Mn/Ti	mass	3628	199	103	324	0
P/∑Fe	molar	0.001	0.000	0.001	0.003	0.007
P/Fe(II)	molar	n/a	n/a	n/a	n/a	n/a
P/Fe(III)	molar	n/a	n/a	n/a	n/a	n/a
P/Ti	mass	9.43	3.67	0.63	2.62	0.09
∑Fe/Ti	mass	18386	21294	1870	1611	25
Fe(II)/Ti	mass	n/a	n/a	n/a	n/a	n/a
Fe(III)/Ti	mass	n/a	n/a	n/a	n/a	n/a
Li	*ppb*	1678	1367	4942	6358	49910
Be	"	517.2	892.9	2302	1130	1908
Sc	"	b.d.l.	b.d.l.	539	224.5	12690
Ti	"	7865	14270	214300	79830	3335000
V	"	172.2	1917	20690	471.1	98190
Cr	"	565.3	1095	1780	122.8	109000
Co	"	743.8	5436	8651	6072	21620
Ni	"	1096	1284	1726	995.4	29280
Cu	"	880	1025	1037	464.9	28010
Zn	"	2376	6436	5616	4258	40570
Ga	"	111.9	130.7	1299	809.2	18440
Rb	"	2.986	81.27	10140	7705	321900

b.d.l. = below detection limit; n.m. = not measured; n/a = not applicable

Table A5.1. *(continued)*

ID		PGC135	LRGC138	JSP140B	JSP140C	RTH141
Depth (m)		101.14	111.41	5.3	5.3	9.26
Drillhole		11-LR-1029D	11-LR-1029D	11-LR-1020D	11-LR-1020D	11-LR-1020D
Unit		LRC/PGC	LRGC	JSP	JSP	RTH
Sr	"	27280	4761	25820	28660	42590
Y	"	6489	5074	15320	8812	11550
Zr	"	932.9	771.3	16100	4507	90790
Nb	"	275.1	318.1	4694	409.7	12750
Ag	"	0.309	2.272	5.09	3.29	71.06
Cd	"	13.51	0.9743	7.265	2.904	28.37
Sn	"	59.49	102.5	139.5	10.86	1776
Sb	"	20.3	28.46	289.7	64.63	65.26
Cs	"	30.56	50.92	7427	5587	5403
Ba	"	6860	16930	96430	57040	3293000
La	"	4043	2467	9699	6278	34250
Ce	"	5581	3650	18760	13280	70640
Pr	"	762.7	501.3	1773	1356	7307
Nd	"	3153	2150	7407	5574	25610
Sm	"	581.7	438.1	1489	936.4	4208
Eu	"	315	146.4	616.9	368.4	901.9
Gd	"	788.6	585.3	1964	1150	3052
Tb	"	108.3	88.18	303.9	164.5	409.7
Dy	"	689.7	587.4	2004	1047	2178
Ho	"	159.7	139.5	477.1	246.8	419.9
Er	"	432.2	392.4	1394	715.4	1116
Tm	"	55.81	56.63	200	101.2	162.6
Yb	"	292	321.8	1146	596.7	1016
Lu	"	37.95	43.19	155.7	81.99	153
Hf	"	7.976	10.39	198	67.12	2470
Ta	"	1.826	4.906	86.95	6.55	902.1
Pb	"	0.8446	601.3	2934	11.66	3990
Th	"	9.711	13.52	207.4	67.15	9095
U	"	15.97	19.67	125.5	33.99	1539
ΣREE+Y	"	23490	16641	62710	40708	162974
$(La/La^*)_{MuQ}$		1.56	1.56	1.64	1.35	0.99
$(Ce/Ce^*)_{MuQ}$		0.93	0.96	1.35	1.23	1.04
$(Eu/Eu^*)_{MuQ}$		2.53	1.48	1.85	1.92	1.06
$(Gd/Gd^*)_{MuQ}$		1.21	1.16	1.12	1.16	1.04
$(Lu/Lu^*)_{MuQ}$		1.05	1.00	1.00	0.98	1.02
Y/Ho		40.6	36.4	32.1	35.7	27.5
$(Pr/Yb)_{MuQ}$		1.00	0.60	0.59	0.87	2.76
$(Er/Lu)_{MuQ}$		1.66	1.32	1.30	1.27	1.06

$La^* = Pr^*(Pr/Nd)^2$; $Ce^* = Pr^*(Pr/Nd)$; $Eu^* = Sm^*(Sm/Nd)^{0.5}$; $Gd^* = Tb^*(Tb/Dy)$; $Lu^* = Yb^*(Yb/Tm)$

Table A5.1. *(continued)*

ID		RTH142	BC143	IF144	LRGC201	LIF204
Depth (m)		18.11	21.005	22.225	10.19	23.675
Drillhole		11-LR-1020D	11-LR-1020D	11-LR-1020D	HAY-11-29	HAY-11-29
Unit		RTH	BC	IF	LRGC	LIF
SiO_2	*wt. %*	55.77	83.46	93.03	36.45	54.55
TiO_2	"	0.51	0.01	0.01	0.01	0.01
Al_2O_3	"	13.61	b.d.l.	b.d.l.	b.d.l.	b.d.l.
Fe_2O_{3T}	"	13.29	2.47	5.91	49.95	32.16
FeO	"	n.m.	n.m.	n.m.	n.m.	n.m.
MnO	"	1.06	0.44	0.09	1.24	0.39
MgO	"	2.52	0.18	0.10	2.55	3.24
CaO	"	0.28	7.66	0.04	1.52	0.98
Na_2O	"	0.36	0.06	0.06	0.18	0.06
K_2O	"	6.73	0.03	0.03	b.d.l.	b.d.l.
P_2O_5	"	0.07	b.d.l.	0.02	0.07	0.01
LOI	"	4.92	5.38	0.41	7.86	8.41
Fe(III)/Fe(II)	molar	n/a	n/a	n/a	n/a	n/a
Mn/∑Fe	molar	0.090	0.202	0.018	0.028	0.014
Mn/Fe(II)	molar	n/a	n/a	n/a	n/a	n/a
Mn/Fe(III)	molar	n/a	n/a	n/a	n/a	n/a
Mn/Ti	mass	3	145	43	815	445
P/∑Fe	molar	0.006	n/a	0.004	0.002	0.000
P/Fe(II)	molar	n/a	n/a	n/a	n/a	n/a
P/Fe(III)	molar	n/a	n/a	n/a	n/a	n/a
P/Ti	mass	0.11		5.28	25.48	7.69
∑Fe/Ti	mass	32	735	2502	29559	33039
Fe(II)/Ti	mass	n/a	n/a	n/a	n/a	n/a
Fe(III)/Ti	mass	n/a	n/a	n/a	n/a	n/a
Li	*ppb*	45970	2170	1065	670.8	665.8
Be	"	2249	107.4	293.8	959.7	1257
Sc	"	11800	1646	346.3	161.5	b.d.l.
Ti	"	2904000	23530	16530	11820	6809
V	"	84930	2702	4715	10380	6496
Cr	"	97090	2896	1924	1501	1710
Co	"	15010	12240	139.2	13300	4384
Ni	"	30600	5984	735.8	1445	1228
Cu	"	26330	7097	2954	552.9	806.7
Zn	"	42790	2561	783.2	3609	4063
Ga	"	18170	206.4	377.2	334.2	483.5
Rb	"	292900	1170	2880	484.9	937.1

b.d.l. = below detection limit; n.m. = not measured; n/a = not applicable

Table A5.1. *(continued)*

ID		RTH142	BC143	IF144	LRGC201	LIF204
Depth (m)		18.11	21.005	22.225	10.19	23.675
Drillhole		11-LR-1020D	11-LR-1020D	11-LR-1020D	HAY-11-29	HAY-11-29
Unit		RTH	BC	IF	LRGC	LIF
Sr	"	36650	71600	7925	13130	7003
Y	"	10510	1579	662.6	6406	4035
Zr	"	84560	3000	4999	2439	1830
Nb	"	12830	362.1	666.3	781.6	659.8
Ag	"	105.2	355	254.7	4.095	2.527
Cd	"	29.53	11.25	0.8536	1.28	1.503
Sn	"	1806	128.6	125.4	37.57	102.7
Sb	"	105	357.9	51.94	59.28	118.2
Cs	"	4279	112.5	1739	57.15	212.8
Ba	"	5646000	185300	195200	3319	2145
La	"	30920	3675	411.9	5347	2154
Ce	"	64420	6639	1287	10470	3829
Pr	"	6851	652.9	124.9	964	345.6
Nd	"	23810	2458	537.1	4008	1353
Sm	"	3917	426.8	112.5	673.8	232.3
Eu	"	797.7	109.9	37.88	200.2	85.71
Gd	"	2851	410.8	123.2	829.4	333.1
Tb	"	378.6	45.13	16.64	111.5	52.51
Dy	"	1991	219.4	96.47	710	381.2
Ho	"	389.6	42.4	20.12	171.3	97.77
Er	"	1044	108.1	54.08	498	297.4
Tm	"	152.1	14.74	6.936	70.98	42.93
Yb	"	958.3	87.11	37.67	406.6	223.9
Lu	"	139.2	12.39	5.184	55.85	29.62
Hf	"	2286	47.1	42.4	19.63	29.89
Ta	"	829.2	6.703	5.619	12.05	4.139
Pb	"	4772	11250	536.7	318.2	79.49
Th	"	8497	203.2	202.3	45.75	26.93
U	"	1456	191.3	174	60.89	43.33
ΣREE+Y	"	149130	16481	3534	30923	13493
$(La/La^*)_{MuQ}$		0.94	1.37	1.05	1.65	1.64
$(Ce/Ce^*)_{MuQ}$		1.00	1.17	1.36	1.38	1.33
$(Eu/Eu^*)_{MuQ}$		1.01	1.24	1.47	1.45	1.78
$(Gd/Gd^*)_{MuQ}$		1.04	1.16	1.12	1.24	1.20
$(Lu/Lu^*)_{MuQ}$		0.97	1.02	1.07	1.01	1.07
Y/Ho		27.0	37.2	32.9	37.4	41.3
$(Pr/Yb)_{MuQ}$		2.75	2.88	1.27	0.91	0.59
$(Er/Lu)_{MuQ}$		1.09	1.27	1.52	1.30	1.46

$La^* = Pr^*(Pr/Nd)^2$; $Ce^* = Pr^*(Pr/Nd)$; $Eu^* = Sm^*(Sm/Nd)^{0.5}$; $Gd^* = Tb^*(Tb/Dy)$; $Lu^* = Yb^*(Yb/Tm)$

Table A5.1. *(continued)*

ID		LIF212	LC166	JUIF171	JUIF175B	JUIF175C
Depth (m)		76.22	59.215	74.435	85.45	85.45
Drillhole		HAY-11-29	HAY-11-07	HAY-11-07	HAY-11-07	HAY-11-07
Unit		LIF	LC	JUIF	JUIF	JUIF
SiO_2	*wt. %*	17.42	26.41	37.98	41.44	82.31
TiO_2	"	0.01	0.03	0.04	0.04	0.02
Al_2O_3	"	b.d.l.	b.d.l.	0.06	b.d.l.	b.d.l.
Fe_2O_3	"	22.33	25.69	39.16	40.58	10.94
FeO	"	n.m.	23.10	24.09	6.49	n.m.
MnO	"	0.91	0.39	0.46	5.12	0.22
MgO	"	2.24	8.77	3.06	1.02	0.76
CaO	"	25.02	9.90	3.68	4.03	2.02
Na_2O	"	0.07	0.08	0.10	0.07	0.31
K_2O	"	b.d.l.	b.d.l.	0.03	b.d.l.	0.00
P_2O_5	"	0.07	0.04	0.06	0.02	0.01
LOI	"	31.68	28.49	15.19	7.47	3.17
Fe(III)/Fe(II)	molar	n/a	0.0008	0.4628	4.6257	n/a
Mn/∑Fe	molar	0.046	0.017	0.013	0.142	0.023
Mn/Fe(II)	molar	n/a	0.017	0.019	0.801	n/a
Mn/Fe(III)	molar	n/a	21.131	0.042	0.173	n/a
Mn/Ti	mass	315	29	21	903	102
P/∑Fe	molar	0.004	0.002	0.002	0.001	0.001
P/Fe(II)	molar	n/a	0.002	0.003	0.003	n/a
P/Fe(III)	molar	n/a	1.940	0.006	0.001	n/a
P/Ti	mass	13.72	1.52	1.61	2.19	3.35
∑Fe/Ti	mass	7014	1736	1579	6462	4517
Fe(II)/Ti	mass	n/a	1734.87	1079.27	1148.62	n/a
Fe(III)/Ti	mass	n/a	1.41	499.46	5313.14	n/a
Li	*ppb*	2286	1567	2749	3649	1386
Be	"	557.3	653.9	1456	1402	759
Sc	"	98.53	264.8	309.4	150	99.37
Ti	"	22270	103500	173500	43920	16940
V	"	24810	12220	14080	6424	3406
Cr	"	1700	3246	3727	2026	333.6
Co	"	3288	6650	6971	2284	1820
Ni	"	2940	4441	1820	1092	287.4
Cu	"	988.9	969.6	2215	1490	2012
Zn	"	2497	4506	4674	2595	1134
Ga	"	346.3	279.1	941	477.9	239.8
Rb	"	659.4	292.4	1201	331.5	247.4

b.d.l. = below detection limit; n.m. = not measured; n/a = not applicable

Table A5.1. *(continued)*

ID		LIF212	LC166	JUIF171	JUIF175B	JUIF175C
Depth (m)		76.22	59.215	74.435	85.45	85.45
Drillhole		HAY-11-29	HAY-11-07	HAY-11-07	HAY-11-07	HAY-11-07
Unit		LIF	LC	JUIF	JUIF	JUIF
Sr	"	338300	43090	16870	61700	33790
Y	"	20560	2548	3299	3410	1033
Zr	"	2655	4256	9491	4028	2249
Nb	"	690.9	2624	3370	1174	511.1
Ag	"	45.87	80.07	13.01	16.84	10.25
Cd	"	15.08	6.095	5.353	5.348	2.169
Sn	"	30.31	58.42	172.7	87.94	5.584
Sb	"	69.42	262.4	185	160.4	85.75
Cs	"	158.7	89.5	214.3	101.4	64.11
Ba	"	7175	4282	17880	15720	4916
La	"	9604	1534	2605	2556	674.7
Ce	"	18980	4361	6719	7548	2099
Pr	"	2048	434.1	584	465	132
Nd	"	8557	1790	2237	1769	507.7
Sm	"	1798	362.2	425.2	332.7	100.2
Eu	"	1058	104.2	123.2	129.2	38.73
Gd	"	2362	395.9	455.9	415.7	122.2
Tb	"	356.8	60.04	72.32	64.16	20.7
Dy	"	2303	377.8	463.6	412.2	140.6
Ho	"	535.6	86.34	106.6	94.91	32.88
Er	"	1497	246	308	272.7	99.12
Tm	"	201.8	35.62	45.89	37.92	15.08
Yb	"	1057	209.2	263.6	209.5	96.05
Lu	"	131.6	28.44	34.99	27.1	13.18
Hf	"	25.39	70.48	154	57.01	27.58
Ta	"	13.37	66.83	109.2	25.26	9.113
Pb	"	1613	782.2	574.9	503.5	276
Th	"	45.62	119.7	184.9	77.38	39.59
U	"	316.9	254.6	97.22	58.9	14.2
ΣREE+Y	"	71050	12573	17743	17744	5125
$(La/La^*)_{MuQ}$		1.41	1.03	1.13	1.37	1.30
$(Ce/Ce^*)_{MuQ}$		1.18	1.27	1.35	1.89	1.87
$(Eu/Eu^*)_{MuQ}$		2.57	1.28	1.33	1.79	1.74
$(Gd/Gd^*)_{MuQ}$		1.12	1.09	1.06	1.09	1.05
$(Lu/Lu^*)_{MuQ}$		1.00	0.98	0.98	0.99	0.91
Y/Ho		38.4	29.5	30.9	35.9	31.4
$(Pr/Yb)_{MuQ}$		0.74	0.80	0.85	0.85	0.53
$(Er/Lu)_{MuQ}$		1.65	1.26	1.28	1.46	1.09

$La^* = Pr^*(Pr/Nd)^2$; $Ce^* = Pr^*(Pr/Nd)$; $Eu^* = Sm^*(Sm/Nd)^{0.5}$; $Gd^* = Tb^*(Tb/Dy)$; $Lu^* = Yb^*(Yb/Tm)$

Table A5.1. *(continued)*

ID		JUIF179B	JUIF179C	GC184	URC191	PGC194B
Depth (m)		97.745	97.745	111.015	133.06	146.045
Drillhole		HAY-11-07	HAY-11-07	HAY-11-07	HAY-11-07	HAY-11-07
Unit		JUIF	JUIF	GC	URC	PGC
SiO_2	*wt. %*	51.50	88.38	57.17	44.65	61.71
TiO_2	"	0.09	0.02	0.02	0.05	0.18
Al_2O_3	"	0.46	b.d.l.	b.d.l.	0.40	0.63
Fe_2O_{3T}	"	37.11	9.61	31.80	46.81	31.74
FeO	"	5.93	n.m.	12.96	3.38	2.58
MnO	"	0.32	0.10	0.33	0.74	0.35
MgO	"	2.82	0.40	0.18	1.83	1.56
CaO	"	2.67	0.35	4.26	1.28	1.07
Na_2O	"	0.24	0.14	0.07	0.15	0.17
K_2O	"	0.15	0.02	b.d.l.	0.14	0.28
P_2O_5	"	0.05	0.01	0.02	0.05	0.05
LOI	"	4.39	0.73	5.94	3.72	2.05
Fe(III)/Fe(II)	molar	4.63	n/a	1.21	11.46	10.07
Mn/∑Fe	molar	0.010	0.012	0.012	0.018	0.012
Mn/Fe(II)	molar	0.055	n/a	0.026	0.221	0.137
Mn/Fe(III)	molar	0.012	n/a	0.021	0.019	0.014
Mn/Ti	mass	5	14	65	24	3
P/∑Fe	molar	0.002	0.001	0.001	0.001	0.002
P/Fe(II)	molar	0.009	n/a	0.002	0.014	0.018
P/Fe(III)	molar	0.002	n/a	0.001	0.001	0.002
P/Ti	mass	0.49	0.73	2.22	0.83	0.21
∑Fe/Ti	mass	553	1128	5670	1358	236
Fe(II)/Ti	mass	98.28	n/a	2567.92	109.02	21.28
Fe(III)/Ti	mass	455.18	n/a	3102.23	1249.44	214.27
Li	*ppb*	11930	1652	1616	3968	13190
Be	"	1713	1670	998.2	1782	1101
Sc	"	778.1	257.5	189.1	1282	2417
Ti	"	469000	59540	39230	241000	942600
V	"	15810	5391	10950	18080	31960
Cr	"	5333	586.3	2526	9007	11310
Co	"	3207	525.4	3565	19500	8781
Ni	"	2175	263.3	1380	3802	6248
Cu	"	3458	10910	1458	17970	5186
Zn	"	7619	1086	1671	6918	6161
Ga	"	1441	508.9	535.3	966.4	1401
Rb	"	8895	1221	728	6130	22070

b.d.l. = below detection limit; n.m. = not measured; n/a = not applicable

Table A5.1. *(continued)*

ID		JUIF179B	JUIF179C	GC184	URC191	PGC194B
Depth (m)		97.745	97.745	111.015	133.06	146.045
Drillhole		HAY-11-07	HAY-11-07	HAY-11-07	HAY-11-07	HAY-11-07
Unit		JUIF	JUIF	GC	URC	PGC
Sr	"	50230	6325	27960	34820	39380
Y	"	3682	613.2	2582	3075	3720
Zr	"	19620	3802	3746	7486	9409
Nb	"	4157	1070	993.8	1747	2901
Ag	"	29.08	9.738	44.515	15.25	82.92
Cd	"	9.969	1.481	5.208	4.2	7.025
Sn	"	199.8	19.64	118.34	118.7	268
Sb	"	197.5	84.78	99.88	166	172.3
Cs	"	1949	357.8	247.5	2354	2610
Ba	"	35660	7958	8636	69170	53340
La	"	4387	687.9	1372	2410	3621
Ce	"	9349	1301	3199	5628	6604
Pr	"	911.8	115.3	271.6	531.6	830.3
Nd	"	3381	413.9	1105	2178	3395
Sm	"	637.6	78.89	233.5	437.8	761.8
Eu	"	168	26.09	85.65	188	266.8
Gd	"	637.4	83.55	298.8	493.2	804
Tb	"	99.05	13.62	47.64	72.77	126.2
Dy	"	624.1	92.4	320.1	460.6	756.3
Ho	"	137.6	21.54	76.7	103.2	158
Er	"	394.6	70.27	230.1	302.2	431.7
Tm	"	59.76	12.5	33.48	46.04	61.69
Yb	"	376.9	93.72	202.3	289.2	372.1
Lu	"	53.97	13.73	27.4	41.93	50.57
Hf	"	411.4	65.43	49.42	148.7	188.9
Ta	"	189.3	31.02	15.33	55.89	105.6
Pb	"	913.1	323.5	355.6	706	988.4
Th	"	424	83.27	54.38	135.9	150.3
U	"	99.65	24.7	48.14	84.95	71.23
ΣREE+Y	"	24900	3638	10085	16258	21959
$(La/La^*)_{MuQ}$		1.14	1.32	1.44	1.31	1.25
$(Ce/Ce^*)_{MuQ}$		1.16	1.24	1.47	1.33	0.99
$(Eu/Eu^*)_{MuQ}$		1.22	1.52	1.60	1.92	1.48
$(Gd/Gd^*)_{MuQ}$		1.06	1.09	1.10	1.12	1.00
$(Lu/Lu^*)_{MuQ}$		0.96	0.83	0.95	0.98	0.95
Y/Ho		26.8	28.5	33.7	29.8	23.5
$(Pr/Yb)_{MuQ}$		0.93	0.47	0.52	0.71	0.86
$(Er/Lu)_{MuQ}$		1.06	0.74	1.22	1.05	1.24

$La^* = Pr^*(Pr/Nd)^2$; $Ce^* = Pr^*(Pr/Nd)$; $Eu^* = Sm^*(Sm/Nd)^{0.5}$; $Gd^* = Tb^*(Tb/Dy)$; $Lu^* = Yb^*(Yb/Tm)$

Table A5.1. *(continued)*

ID		PGC194C	LRGC197B	LRGC197C	LRGC198	FL01H
Depth (m)		146.045	152.91	152.91	156.7	
Drillhole		HAY-11-07	HAY-11-07	HAY-11-07	HAY-11-07	
Unit		PGC	LRGC	LRGC	LRGC	FL
SiO_2	*wt. %*	90.67	25.30	73.80	19.74	94.43
TiO_2	"	0.02	0.08	0.01	0.06	0.05
Al_2O_3	"	b.d.l.	0.44	b.d.l.	0.14	2.79
Fe_2O_{3T}	"	6.23	60.41	17.94	64.26	0.44
FeO	"	n.m.	17.56	n.m.	21.90	n.m.
MnO	"	0.32	0.79	0.26	0.80	0.07
MgO	"	0.23	2.57	0.61	3.04	0.23
CaO	"	0.98	3.38	3.59	3.99	b.d.l.
Na_2O	"	0.13	0.26	0.10	0.17	0.06
K_2O	"	0.02	0.11	0.01	0.02	1.00
P_2O_5	"	0.02	0.13	0.03	0.11	0.02
LOI	"	1.14	6.36	3.41	7.48	0.62
Fe(III)/Fe(II)	molar	n/a	2.10	n/a	1.64	n/a
Mn/∑Fe	molar	0.057	0.015	0.017	0.014	0.168
Mn/Fe(II)	molar	n/a	0.046	n/a	0.037	n/a
Mn/Fe(III)	molar	n/a	0.022	n/a	0.023	n/a
Mn/Ti	mass	43	18	108	20	2
P/∑Fe	molar	0.003	0.002	0.002	0.002	0.054
P/Fe(II)	molar	n/a	0.007	n/a	0.005	n/a
P/Fe(III)	molar	n/a	0.003	n/a	0.003	n/a
P/Ti	mass	1.46	1.61	6.70	1.59	0.37
∑Fe/Ti	mass	765	1225	6643	1448	12
Fe(II)/Ti	mass	n/a	395.75	n/a	548.60	n/a
Fe(III)/Ti	mass	n/a	829.37	n/a	899.80	n/a
Li	*ppb*	770.2	15880	6539	9386	2457
Be	"	255.2	1118	725.4	1518	179.1
Sc	"	297.1	1622	324.7	1204	1026
Ti	"	56930	344900	18890	310300	249200
V	"	3344	23480	5640	29960	4968
Cr	"	309.7	7781	973	6824	4408
Co	"	1445	10270	1498	10630	217.3
Ni	"	710.9	3325	570.3	3616	2302
Cu	"	2026	2704	816.6	2596	1759
Zn	"	412.8	4956	1205	5753	1139
Ga	"	116.6	1427	427.4	1308	3222
Rb	"	459.7	7207	2281	4069	28700

b.d.l. = below detection limit; n.m. = not measured; n/a = not applicable

Table A5.1. *(continued)*

ID		PGC194C	LRGC197B	LRGC197C	LRGC198	FL01H
Depth (m)		146.045	152.91	152.91	156.7	
Drillhole		HAY-11-07	HAY-11-07	HAY-11-07	HAY-11-07	
Unit		PGC	LRGC	LRGC	LRGC	FL
Sr	"	20690	38330	42040	60660	1464
Y	"	1332	5076	1142	4304	6102
Zr	"	946.5	5888	626	5749	13410
Nb	"	99.97	1269	144.5	1158	638.2
Ag	"	5.11	28.61	14.34	11.71	0.7479
Cd	"	4.177	4.25	1.028	5.04	4.97
Sn	"	9.111	112.3	11.19	93.26	383.8
Sb	"	22.28	64.65	25.06	41.61	29.06
Cs	"	54.53	324.2	193.8	878.5	386.2
Ba	"	11490	43700	8549	26100	16960
La	"	1888	4446	416.4	3618	1593
Ce	"	2259	9809	776.9	8336	2285
Pr	"	308.5	1044	84.56	887.2	293.8
Nd	"	1257	4317	366.9	3612	1126
Sm	"	228.8	832.7	86.18	704.9	287
Eu	"	77.5	315.3	45.87	250.9	103.3
Gd	"	256.8	897	125.8	774.1	552.8
Tb	"	36.66	127.4	20.19	109.6	99.16
Dy	"	224.2	745.1	132.6	637.5	692.3
Ho	"	49.5	160.7	30.99	134.8	170.2
Er	"	141.3	445.2	94.28	365.4	506.2
Tm	"	20.55	62.39	14.29	51	73.57
Yb	"	122.3	365.2	91.67	292.3	432.4
Lu	"	16.55	50.11	12.97	40.74	58.62
Hf	"	18	136.3	9.78	120.3	359.4
Ta	"	2.7	38.56	2.76	33.63	43.99
Pb	"	117.2	821.9	216.9	620.6	272.7
Th	"	13.25	93.52	5.049	81.08	903.4
U	"	35.68	70.63	15.59	80.03	411.5
ΣREE+Y	"	8219	28693	3442	24118	14375
$(La/La^*)_{MuQ}$		1.75	1.25	1.59	1.16	1.37
$(Ce/Ce^*)_{MuQ}$		0.91	1.19	1.22	1.17	0.91
$(Eu/Eu^*)_{MuQ}$		1.59	1.73	2.20	1.61	1.43
$(Gd/Gd^*)_{MuQ}$		1.12	1.08	1.07	1.07	1.02
$(Lu/Lu^*)_{MuQ}$		0.96	0.99	0.93	1.03	0.97
Y/Ho		26.9	31.6	36.9	31.9	35.9
$(Pr/Yb)_{MuQ}$		0.97	1.10	0.35	1.17	0.26
$(Er/Lu)_{MuQ}$		1.24	1.29	1.06	1.30	1.26

$La^* = Pr^*(Pr/Nd)^2$; $Ce^* = Pr^*(Pr/Nd)$; $Eu^* = Sm^*(Sm/Nd)^{0.5}$; $Gd^* = Tb^*(Tb/Dy)$; $Lu^* = Yb^*(Yb/Tm)$

APPENDIX 6: DATA QUALITY

Table A6.1. Mean major element concentrations (wt.%) and 1 relative standard deviation (%) of evaluated iron formation reference materials analyzed via XRF.

FeR-3	**n = 2**			
(wt. %)	*mean*	*1rsd (%)*	*CANMET-certified*	*%bias*
SiO_2	54.01	1.77	53.61	0.8
TiO_2	0.02	8.32	0.01	70.0
Al_2O_3	0.01	n/a	0.09	-92.2
Fe_2O_{3T}	43.16	0.66	44.50	-3.0
MnO	0.10	17.0	0.08	25.0
MgO	1.09	0.65	1.02	7.3
CaO	0.83	2.04	0.84	-0.8
Na_2O	0.04	n/a	0.03	n/a
K_2O	n/a	n/a	0.03	n/a
P_2O_5	0.07	4.94	0.07	2.1
LOI	-0.15	n/a	n/a	n/a

FeR-4	**n = 2**			
(wt. %)	*mean*	*1rsd (%)*	*CANMET-certified*	*%bias*
SiO_2	50.73	1.27	50.07	1.3
TiO_2	0.08	4.62	0.07	9.3
Al_2O_3	1.55	1.14	1.70	-8.8
Fe_2O_{3T}	38.75	0.07	39.92	-2.9
MnO	0.21	4.69	0.19	11.1
MgO	1.49	0.19	1.41	5.5
CaO	2.26	1.63	2.23	1.4
Na_2O	0.08	33.17	0.05	62.0
K_2O	0.21	26.37	0.29	-28.8
P_2O_5	0.13	1.64	0.13	-0.4
LOI	3.75	0.38	n/a	n/a

IOC-1	**n = 2**			
(wt. %)	*mean*	*1rsd (%)*	*NRCan*	*%bias*
SiO_2	2.68	5.25	2.633	1.8
TiO_2	0.06	8.76	0.0429	31.7
Al_2O_3	0.08	n/a	0.184	-58.2
Fe_2O_{3T}	93.21	0.26	93.82	-0.6
MnO	0.48	3.10	0.472	1.6
MgO	1.14	3.46	1.043	9.7
CaO	1.02	2.15	0.975	4.6
Na_2O	n/a	n/a	n/a	n/a
K_2O	n/a	n/a	0.004	n/a
P_2O_5	0.03	2.18	n/a	n/a
LOI	0.90	3.14	0.863	4.3

Table A6.2. Mean sequential four-step LOI (wt.%) and 1 relative standard deviation (%) of analyzed RMs and comparison of total LOI values measured via XRF and sequential four-step LOI.

ID	*Type*		*N_2 105 °C*	*O_2 105–371 °C*	*O_2 371–500 °C*	*O_2 500–1000 °C*	*LOI_T*	*%bias*	*CANMET (provisional)*
RAFT-1	in-house standard	***mean (wt.%)***	5.46	1.51	22.39	1.27	30.63	n/a	n/a
n = 4		***1rsd***	2.04	6.24	1.00	17.35	0.45		
STSD-1	international RM	***mean (wt.%)***	4.53	1.71	22.41	2.19	30.84	-2.4	31.6
n = 1		***1rsd***	n/a	n/a	n/a	n/a	n/a		

ID	*Drillhole*	*N_2 105 °C*	*O_2 105–371 °C*	*O_2 371–500 °C*	*O_2 500–1000 °C*	*LOI_T*	*LOI_T (XRF)*
MS002	12-SL-1018D	0.17	0.20	2.89	2.54	5.80	6.01
MS005	12-SL-1018D	-0.04	0.10	0.29	1.24	1.60	1.76
LC066	12-SL-1018D	0.47	0.93	21.45	0.95	23.80	23.91
LC011	12-SL-1018D	-0.20	0.38	5.34	1.09	6.60	7.16
JUIF018	12-SL-1018D	0.01	-0.06	0.05	1.52	1.52	1.63
JUIF025	12-SL-1018D	-0.01	-0.02	-0.01	6.57	6.52	6.60
JUIF032	12-SL-1018D	-0.15	0.11	0.24	2.34	2.54	2.65
JUIF037	12-SL-1018D	0.37	0.14	0.10	8.49	9.10	9.36
GC039	12-SL-1018D	0.08	-0.15	-0.18	1.42	1.17	1.22
URC041	12-SL-1018D	0.01	0.14	0.05	4.48	4.67	4.69
PGC045	12-SL-1018D	0.07	-0.03	0.02	9.09	9.15	9.33
LRC047	12-SL-1018D	-0.05	-0.01	0.38	0.32	0.65	0.70
LRGC051	12-SL-1018D	0.13	0.08	0.24	7.06	7.51	7.41
LRGC055	12-SL-1018D	0.36	0.64	9.47	0.93	11.39	11.26
LRGC061	12-SL-1018D	0.12	0.39	7.35	1.68	9.54	9.60
LIF063	12-SL-1018D	0.10	0.31	10.52	2.04	12.96	12.79
LC216	12-SL-1017D	-0.01	0.11	1.25	0.18	1.52	1.69

Table A6.2. *(continued)*

ID	*Drillhole*	*N_2 105 °C*	*O_2 105–371 °C*	*O_2 371–500 °C*	*O_2 500–1000 °C*	*LOI_T*	*LOI_T (XRF)*
LC217	12-SL-1017D	-0.24	3.31	13.71	1.57	18.36	18.66
LC221	12-SL-1017D	-0.09	5.16	9.58	1.52	16.17	16.40
LC224	12-SL-1017D	-0.12	0.52	6.32	3.18	9.90	10.03
LC226	12-SL-1017D	-0.73	2.51	8.09	2.59	12.47	12.90
LC227	12-SL-1017D	-0.09	0.36	5.34	2.27	7.89	8.11
JUIF228	12-SL-1017D	-0.09	-0.23	-0.10	2.69	2.27	2.49
JUIF229	12-SL-1017D	-0.10	-0.28	-0.24	2.62	2.00	2.19
JUIF230	12-SL-1017D	-0.09	-0.01	0.61	1.26	1.78	1.96
JUIF231	12-SL-1017D	-0.20	0.28	2.10	9.26	11.44	11.71
GC232	12-SL-1017D	-0.01	-0.01	1.05	0.77	1.80	1.85
URC233	12-SL-1017D	-0.05	0.10	1.19	6.05	7.30	7.50
URC235	12-SL-1017D	0.00	-0.08	0.21	2.08	2.21	2.31
PGC236	12-SL-1017D	-0.11	0.17	3.55	3.07	6.69	6.80
PGC238	12-SL-1017D	0.05	0.05	1.08	0.44	1.62	1.63
LRC239	12-SL-1017D	-0.03	0.28	1.26	5.17	6.67	6.72
LRGC241	12-SL-1017D	0.12	0.11	4.33	5.21	9.77	9.72
LRGC247	12-SL-1017D	0.15	0.04	3.50	1.13	4.82	4.82
LRGC250	12-SL-1017D	0.08	0.34	4.40	1.19	6.01	6.13
LIF252	12-SL-1017D	0.21	0.52	8.33	4.71	13.76	16.94
JUIF254	12-SL-1011D	n/a	n/a	n/a	n/a	n/a	3.84
GC256	12-SL-1011D	n/a	n/a	n/a	n/a	n/a	1.81
LC069	12-SL-1005D	n/a	n/a	n/a	n/a	n/a	4.25
JUIF073B	12-SL-1005D	n/a	n/a	n/a	n/a	n/a	15.19
JUIF073C	12-SL-1005D	n/a	n/a	n/a	n/a	n/a	0.58
JUIF079	12-SL-1005D	n/a	n/a	n/a	n/a	n/a	9.10
JUIF083	12-SL-1005D	n/a	n/a	n/a	n/a	n/a	5.74
GC085	12-SL-1005D	n/a	n/a	n/a	n/a	n/a	33.35
URC086	12-SL-1005D	n/a	n/a	n/a	n/a	n/a	7.89
PGC088	12-SL-1005D	n/a	n/a	n/a	n/a	n/a	1.80
LRC092	12-SL-1005D	n/a	n/a	n/a	n/a	n/a	6.26

Table A6.2. *(continued)*

ID	*Drillhole*	*N_2 105 °C*	*O_2 105–371 °C*	*O_2 371–500 °C*	*O_2 500–1000 °C*	*LOI_T*	*LOI_T (XRF)*
LRGC094	12-SL-1005D	n/a	n/a	n/a	n/a	n/a	10.67
LRGC103	12-SL-1005D	n/a	n/a	n/a	n/a	n/a	2.17
LIF109	12-SL-1005D	n/a	n/a	n/a	n/a	n/a	2.59
LIF112	12-SL-1005D	n/a	n/a	n/a	n/a	n/a	15.23
LC145	11-LR-1010D	n/a	n/a	n/a	n/a	n/a	7.96
JUIF146	11-LR-1010D	n/a	n/a	n/a	n/a	n/a	4.69
GC147	11-LR-1010D	n/a	n/a	n/a	n/a	n/a	2.38
URC148B	11-LR-1010D	n/a	n/a	n/a	n/a	n/a	0.56
URC148C	11-LR-1010D	n/a	n/a	n/a	n/a	n/a	0.39
PGC150	11-LR-1010D	n/a	n/a	n/a	n/a	n/a	1.94
PGC152	11-LR-1010D	n/a	n/a	n/a	n/a	n/a	2.37
LRGC154	11-LR-1010D	n/a	n/a	n/a	n/a	n/a	1.68
JSP158B	11-LR-1010D	n/a	n/a	n/a	n/a	n/a	2.66
JSP158C	11-LR-1010D	n/a	n/a	n/a	n/a	n/a	0.67
JSP163B	11-LR-1010D	n/a	n/a	n/a	n/a	n/a	6.26
JSP163C	11-LR-1010D	n/a	n/a	n/a	n/a	n/a	5.04
DOL300	11-LR-1005D	n/a	n/a	n/a	n/a	n/a	28.30
LC302	11-LR-1005D	n/a	n/a	n/a	n/a	n/a	8.48
JUIF304	11-LR-1005D	n/a	n/a	n/a	n/a	n/a	3.49
JUIF307	11-LR-1005D	n/a	n/a	n/a	n/a	n/a	0.65
JUIF309	11-LR-1005D	n/a	n/a	n/a	n/a	n/a	9.34
JUIF311	11-LR-1005D	n/a	n/a	n/a	n/a	n/a	4.94
LC260	11-LR-1012D	-0.03	0.09	0.94	13.38	14.38	14.62
LC263	11-LR-1012D	-0.19	0.11	0.45	12.67	13.05	13.35
LC264	11-LR-1012D	0.13	-0.03	0.80	8.69	9.59	9.61
LC267	11-LR-1012D	0.12	-0.18	0.04	4.24	4.23	4.25
GC269	11-LR-1012D	-0.32	0.41	0.24	4.91	5.24	5.40
URC272	11-LR-1012D	0.08	-0.02	0.74	2.12	2.91	2.91
PGC276	11-LR-1012D	-0.16	0.15	0.09	8.81	8.89	6.58
LRGC280	11-LR-1012D	0.07	0.12	0.04	1.00	1.23	1.13

Table A6.2. *(continued)*

ID	*Drillhole*	*N_2 105 °C*	*O_2 105–371 °C*	*O_2 371–500 °C*	*O_2 500–1000 °C*	*LOI_T*	*LOI_T (XRF)*
LRGC284	11-LR-1012D	0.09	0.08	0.08	2.22	2.47	2.57
JSP289	11-LR-1012D	-0.50	0.47	0.05	1.60	1.63	1.89
JSP294	11-LR-1012D	-0.01	0.11	0.01	0.10	0.22	0.63
RTH296	11-LR-1012D	-0.04	0.71	0.92	0.41	2.00	2.23
DOL113	11-LR-1029D	0.12	0.19	0.50	36.15	36.95	35.54
LC114	11-LR-1029D	n/a	n/a	n/a	n/a	n/a	2.96
JUIF116	11-LR-1029D	n/a	n/a	n/a	n/a	n/a	11.83
JUIF119	11-LR-1029D	n/a	n/a	n/a	n/a	n/a	21.94
GC120	11-LR-1029D	n/a	n/a	n/a	n/a	n/a	16.44
JUIF121B	11-LR-1029D	n/a	n/a	n/a	n/a	n/a	9.89
JUIF121C	11-LR-1029D	n/a	n/a	n/a	n/a	n/a	2.65
JUIF124	11-LR-1029D	n/a	n/a	n/a	n/a	n/a	6.58
JUIF127	11-LR-1029D	n/a	n/a	n/a	n/a	n/a	-0.91
JUIF131	11-LR-1029D	n/a	n/a	n/a	n/a	n/a	8.14
GC132	11-LR-1029D	n/a	n/a	n/a	n/a	n/a	17.58
URC133B	11-LR-1029D	n/a	n/a	n/a	n/a	n/a	3.61
URC133C	11-LR-1029D	n/a	n/a	n/a	n/a	n/a	0.28
PGC135	11-LR-1029D	n/a	n/a	n/a	n/a	n/a	18.74
LRGC138	11-LR-1029D	n/a	n/a	n/a	n/a	n/a	2.47
JSP140B	11-LR-1020D	n/a	n/a	n/a	n/a	n/a	3.43
JSP140C	11-LR-1020D	n/a	n/a	n/a	n/a	n/a	4.46
RTH141	11-LR-1020D	n/a	n/a	n/a	n/a	n/a	2.40
RTH142	11-LR-1020D	n/a	n/a	n/a	n/a	n/a	4.92
BC143	11-LR-1020D	n/a	n/a	n/a	n/a	n/a	5.38
IF144	11-LR-1020D	n/a	n/a	n/a	n/a	n/a	0.41
LRGC201	HAY-11-29	n/a	n/a	n/a	n/a	n/a	7.86
LIF204	HAY-11-29	n/a	n/a	n/a	n/a	n/a	8.41
LIF212	HAY-11-29	n/a	n/a	n/a	n/a	n/a	31.68
LC166	HAY-11-07	-0.19	0.50	14.19	13.83	28.33	28.49

Table A6.2. *(continued)*

ID	*Drillhole*	*N_2 105 °C*	*O_2 105–371 °C*	*O_2 371–500 °C*	*O_2 500–1000 °C*	*LOI_T*	*LOI_T (XRF)*
JUIF171	HAY-11-07	-0.11	0.45	9.16	5.64	15.13	15.13
JUIF175B	HAY-11-07	-0.39	0.35	0.18	7.06	7.20	7.47
JUIF175C	HAY-11-07	n/a	n/a	n/a	n/a	n/a	3.17
JUIF179B	HAY-11-07	0.05	0.22	0.20	3.71	4.17	4.39
JUIF179C	HAY-11-07	n/a	n/a	n/a	n/a	n/a	0.73
GC184	HAY-11-07	-0.26	1.10	2.15	2.72	5.71	5.94
URC191	HAY-11-07	0.32	0.87	0.60	2.06	3.85	3.72
PGC194B	HAY-11-07	-0.31	0.46	0.11	1.41	1.67	2.05
PGC194C	HAY-11-07	n/a	n/a	n/a	n/a	n/a	1.14
LRGC197B	HAY-11-07	0.08	-0.07	1.44	4.90	6.35	6.36
LRGC197C	HAY-11-07	n/a	n/a	n/a	n/a	n/a	3.41
LRGC198	HAY-11-07	-0.01	0.12	1.50	5.92	7.53	7.48

Table A6.3. Mean ferrous iron concentrations (wt.%) and 1 relative standard deviation (%) of analyzed iron formation reference materials and duplicates.

ID	*Type*	*value*	*mean*	*1rsd (%)*	*%bias*	*CANMET (prov.)*	*CANMET (cert.)*	*USGS (recomm.)*
JSP294	original	0.24	0.23	9.43	n/a	n/a	n/a	n/a
JSP294	duplicate	0.21						
JUIF230	original	8.36	8.28	1.45	n/a	n/a	n/a	n/a
JUIF230	duplicate	8.19						
LC224	original	20.93	19.91	7.25	n/a	n/a	n/a	n/a
LC224	duplicate	18.89						
LC227	original	14.02	13.90	1.27	n/a	n/a	n/a	n/a
LC227	duplicate	13.77						
LRGC051	original	13.64	13.73	0.88	n/a	n/a	n/a	n/a
LRGC051	duplicate	13.81						
MS002	original	1.71	1.84	9.63	n/a	n/a	n/a	n/a
MS002	duplicate	1.96						
URC233	original	14.56	14.75	1.77	n/a	n/a	n/a	n/a
URC233	duplicate	14.93						
URC272	original	15.58	15.63	0.45	n/a	n/a	n/a	n/a
URC272	duplicate	15.68						
MRB-29	in-house standard	5.66	5.70	2.41	n/a	n/a	n/a	n/a
MRB-29	in-house standard	5.70						
MRB-29	in-house standard	5.62						
MRB-29	in-house standard	5.60						
MRB-29	in-house standard	5.94						
BIR-1A	international RM	8.29	8.29		-0.60	n/a	n/a	8.34
FER-2	international RM	15.41	15.19	1.29	-0.31	15.24	n/a	n/a
FER-2	international RM	15.03						
FER-2	international RM	15.14						
FeR-3	international RM	13.42	13.42		-1.54	13.63	n/a	n/a
FeR-4	international RM	15.55	15.55		0.06	15.54	n/a	n/a
IOC-1	international RM	22.92	22.92		10.40	n/a	20.76	n/a
SY-4	international RM	2.85	2.91	2.92	1.75	n/a	n/a	2.86
SY-4	international RM	2.97						

Table A6.4. Preferred composition of USGS reference material W-2a for calibration and mean trace element concentrations (ppb) and 1 relative standard deviation (%) of analyzed iron formation and shale reference materials via ICP-MS. n = number of digests; m = number of measurements

(ppb)	*Calibration*	*GeoReM*
Li	9158	9210
Be	617.5	672
Sc	36074	35860
Ti	6354600	6379000
V	261597	265800
Cr	92791	92000
Co	44526	44370
Ni	69993	72000
Cu	103000	105900
Zn	77000	77700
Ga	17424	17880
Rb	19803	20230
Sr	194828	195400
Y	20113	21820
Zr	87866	93300
Nb	7275	7510
Ag	77	70
Cd	77	74
Sn	1950	1920
Sb	800	809
Cs	888.2	915
Ba	169860	172800
La	10521	10630
Ce	23216	23210
Pr	3025	3018
Nd	12911	13090
Sm	3266	3300
Eu	1094	1091
Gd	3708	3713
Tb	615.1	627
Dy	3808	3806
Ho	803.3	790.8
Er	2222	2208
Tm	327.2	331.5
Yb	2058	2054
Lu	301.3	309
Hf	2356	2444
Ta	454.2	489
Pb	7528	7830
Th	2104	2179
U	505	504.8

Notes:

a *compiled from Govindaraju (1994)*

b *compiled from Dulski (2001)*

c *compiled from Bau and Alexander (2009)*

d *compiled from Sampaio and Enzweiler (2015) - bomb digest*

e *compiled from Sampaio and Enzweiler (2015) - tabletop digest*

f *compiled from Sampaio and Enzweiler (2015) - sintered*

g *certified values provided by CANMET*

h *semi-quantitative values provided by CANMET*

i *GeoReM preferred values as per Jochum et al. (2016)*

j *compiled from Albut et al. (2018)*

LOQ = limit of quantification

Table A6.4. *(continued)*

	FeR-3								
	FeR-3 this study n = 8 m = 31			[a] **Govindaraju** 1994	[b] **Dulski** 2001 *bomb*	[c] **Bau & A.** 2009 *bomb*	[d] **Sampaio & Enzweiler** 2015 *bomb*	[e] **Sampaio & Enzweiler** 2015 *tabletop*	[f] **Sampaio & Enzweiler** 2015 *sinter*
(ppb)	***mean***	***1rsd (%)***	***%bias[e]***						
Li	412.2	10.9							
Be	441.4	4.3							
Sc	370.6	20.4		600		361			
Ti	11140	7.3		60000		15100			
V	7226	1.3	20.4				8000	6000	
Cr	5139	7.6					<LOQ	<LOQ	
Co	1501	0.9	-20.2	2000		1360	1800	1880	
Ni	12000	3.0	5.3	14000		10200	13000	11400	
Cu	2441	2.6	-9.6				2600	2700	
Zn	26330	5.6	-17.7				27000	32000	
Ga	396.9	5.6	7.3				360	370	
Rb	547.4	2.1			13400	676			
Sr	33020	1.4	-13.1	31000	33600	33200	36000	38000	
Y	2464	5.1	-5.6	6000	3500	3620	3600	2610	3000
Zr	1011	4.4	-27.8	2000	1110	1180	1200	1400	
Nb	510.5	27.5	2.1				300	500	
Ag	19.26	29.9							
Cd	23.75	10.8	-66.1				50	70	
Sn	386.0	4.4	93.0				340	200	
Sb	921.3	4.6	0.1				910	920	
Cs	138.0	2.6			160	162			
Ba	7711	1.8	-6.0	11000	7800	7860	7500	8200	
La	1796	4.2	-5.5	2000	1940	1760	1800	1900	1780
Ce	2254	5.1	-9.8	2000	2320	2280	2300	2500	2160
Pr	280.6	4.8	-6.5		296	274	280	300	260
Nd	1526	4.3	-11.8		1580	1490	1600	1730	1570
Sm	531.6	5.4	-9.9	580	570	496	590	590	560
Eu	220.5	2.5	-6.6	240	242	248	260	236	221
Gd	298.1	2.4	-7.4	300	380	353	370	322	320
Tb	44.60	2.5	-3.0		54	56	59	46	49
Dy	283.4	2.7	-5.5	300	370	385	420	300	360
Ho	63.48	4.3	2.4	100	80	88.9	98	62	82
Er	181.3	5.2	-3.0		260	270	310	187	262
Tm	26.73	5.6	2.8		36	38.2	43	26	36
Yb	168.3	5.6	-1.6	200	240	246	280	171	244
Lu	26.67	5.8	-1.2	40	38	40.5	45	27	38
Hf	16.59	3.1	-46.5	7000	20	21.7	21	31	
Ta	3.865	18.0				11.2	5	<LOQ	
Pb	6012	4.3	-3.0		6300	6010	7000	6200	
Th	45.51	9.3			60	47.2	<LOQ	<LOQ	
U	260.3	10.3	-67.5	300	400	329	300	800	

Table A6.4. *(continued)*

	FeR-4								
	FeR-4 this study n = 8 m = 30			[a] **Govindaraju** 1994	[b] **Dulski** 2001 *bomb*	[c] **Bau & A.** 2009 *bomb*	[d] **Sampaio & Enzweiler** 2015 *bomb*	[e] **Sampaio & Enzweiler** 2015 *tabletop*	[f] **Sampaio & Enzweiler** 2015 *sinter*
(ppb)	***mean***	***1rsd (%)***	***%bias[e]***						
Li	7341	1.1							
Be	1178	4.6							
Sc	1119	8.0		1500		1091			
Ti	355200	2.8		420000		355000			
V	10490	2.1					12000	<LOQ	
Cr	8369	5.3	7.3				8800	7800	
Co	1949	2.3	-17.8	2000		1810	2200	2370	
Ni	6036	3.6	5.9	8000		6010	5900	5700	
Cu	8696	12.9	-3.4				10000	9000	
Zn	18750	4.7	-21.9				20000	24000	
Ga	2406	2.9	-7.5				2400	2600	
Rb	16080	0.8		16000	16100	16300			
Sr	63960	0.5	-14.7	62000	66000	64500	70000	75000	
Y	5643	3.4	0.8	9000	7900	7910	7800	5600	7100
Zr	18250	1.6	-11.4	18000	19300	18800	19000	20600	
Nb	1762	17.3	-2.1				1700	1800	
Ag	35.88	17.1							
Cd	26.57	8.0	-55.7				40	60	
Sn	716.4	5.3	27.9				650	560	
Sb	1438	6.2	-2.8				1400	1480	
Cs	647.9	0.7		700	700	634			
Ba	37360	0.8	-11.0	39000	39000	37600	38000	42000	
La	7805	1.0	-9.2	8000	8100	7820	8400	8600	7600
Ce	13100	0.9	-11.5	11000	13300	13300	14000	14800	12600
Pr	1633	1.9	-8.8	2000	1690	1600	1700	1790	1540
Nd	7397	1.4	-13.0	8000	7600	7480	8200	8500	7300
Sm	2048	2.3	-14.7	2100	2200	2090	2300	2400	1960
Eu	665.7	1.4	-8.8	740	700	696	760	730	660
Gd	1093	2.4	-5.8	1100	1220	1240	1300	1160	1150
Tb	147.7	4.2	1.2	150	173	174	190	146	161
Dy	825.7	4.9	3.2	1000	1050	1050	1100	800	1010
Ho	167.4	3.9	9.4	200	220	218	240	153	213
Er	473.7	3.5	5.3	500	650	641	710	450	630
Tm	73.02	3.4	7.4		93	94.2	99	68	90
Yb	476.5	2.8	2.7	700	630	593	660	464	582
Lu	75.12	2.6	-1.2	100	91	95.8	102	76	90
Hf	488.6	0.8	-19.9	500	520	523	560	610	
Ta	91.82	2.9	-7.3			88.1	92	99	
Pb	6565	5.0	-15.8	8000	7300	7020	7000	7800	
Th	813.5	2.4	-14.4	800	870	859	900	950	
U	494.6	11.2	-17.6	500	800	1050	600	600	

Table A6.4. *(continued)*

	IOC-1				
	IOC-1 this study n = 8 m = 28			**CANMET** *(prov.)*[g]	**CANMET** *(semi-quant.)*[h]
(ppb)	***mean***	***1rsd (%)***	***%bias***[g]		
Li	643.6	3.0			
Be	658.8	20.3			
Sc	885.2	21.1			
Ti	239200	3.1			
V	40930	1.0	0.3	40800	
Cr	168800	1.6			
Co	20560	1.2	2.9	19990	
Ni	11390	2.7			9000
Cu	7956	2.2			8000
Zn	8423	6.1			11000
Ga	1926	5.0			2000
Rb	131.3	4.0			
Sr	4520	3.7	3.2	4380	
Y	2627	4.4			3000
Zr	7072	3.7			6000
Nb	3130	2.2			3000
Ag	10.85	24.6			
Cd	7.16	33.4			
Sn	701.1	2.3			
Sb	381.5	5.6			
Cs	5.312	10.8			
Ba	25870	5.5			30000
La	6892	4.5			8000
Ce	12950	4.4			14000
Pr	1470	5.3			
Nd	5142	5.5			
Sm	685.4	5.1			
Eu	191.3	4.7			
Gd	516.1	4.2			
Tb	69.33	2.9			
Dy	384.9	2.2			
Ho	82.28	2.0			
Er	237.1	2.1			
Tm	35.47	1.6			
Yb	218.6	1.7			
Lu	30.97	1.6			
Hf	86.91	4.3			
Ta	45.39	2.7			
Pb	1478	4.6			
Th	795.1	3.6			
U	63.77	3.3			

Table A6.4. *(continued)*

	OU-6				
	OU-6 this study n = 2 m = 4			**GeoReM**[i]	**Albut et al. 2018**[j]
(ppb)	***mean***	***1rsd (%)***	***%bias***[i]		
Li	102300	2.9	7.3	95300	101700
Be	2559	2.7	1.1	2530	2458
Sc	24450	2.4	5.8	23100	23400
Ti	5963000	2.6	0.5	5934000	5765000
V	126000	2.6	-2.9	129800	123200
Cr	74680	3.4	5.6	70700	71630
Co	29840	3.5	2.2	29200	28370
Ni	40600	3.9	1.0	40200	38720
Cu	47180	13.7	16.8	40400	40220
Zn	113600	0.7	2.0	111400	109900
Ga	24440	3.3	1.1	24170	23770
Rb	125700	3.8	3.6	121300	123800
Sr	136400	4.1	3.6	131700	131300
Y	27030	3.2	-2.6	27750	25910
Zr	151300	4.5	-13.1	174200	155400
Nb	15350	4.0	5.9	14490	14460
Ag	39.28				
Cd	70.94	13.0			
Sn	2968	3.8	11.2	2670	2605
Sb	559.3	10.0	-0.1	560	521.0
Cs	8474	3.1	4.6	8100	8141
Ba	496600	3.0	3.5	480000	479400
La	34920	2.1	5.2	33200	33490
Ce	82710	2.7	7.3	77100	80810
Pr	8587	1.9	8.6	7910	8204
Nd	31860	2.3	5.5	30200	30590
Sm	6327	1.8	5.3	6010	6060
Eu	1394	2.3	2.5	1360	1347
Gd	5478	1.9	3.4	5300	5304.0
Tb	871.7	2.9	1.4	860	840.9
Dy	5199	3.0	2.7	5060	5011
Ho	1078	3.3	3.7	1040	1047
Er	3070	2.8	4.8	2930	2978
Tm	476.6	3.4	5.9	450	462.1
Yb	3138	3.7	5.3	2980	3031
Lu	468.4	3.0	4.1	450	456.0
Hf	4192	4.2	-10.8	4700	4274
Ta	991.9	3.3	-2.8	1020	951.8
Pb	28070	5.5	-2.5	28800	27130
Th	11370	3.9	0.6	11300	10940
U	2000	4.8	4.2	1920	1913

Table A6.5. Comparison of mean trace element concentrations (ppb) and 1 relative standard deviation (%) between 100 mg and 200 mg aliquots of analyzed iron formation reference materials. n = number of digests; m = number of measurements

	FeR-3 *n = 5* *100 mg*	*m = 19*	*FeR-3* *n = 3* *200 mg*	*m = 12*
(ppb)	***mean***	***1rsd (%)***	***mean***	***1rsd (%)***
Li	423.5	12.1	380.2	0.9
Be	436.5	3.7	453.9	5.8
Sc	327.7	19.1	442.1	1.3
Ti	11270	8.9	10910	4.0
V	7248	1.6	7189	0.8
Cr	5152	11.1	5126	4.5
Co	1502	1.1	1498	0.7
Ni	12070	3.6	11880	1.4
Cu	2430	0.8	2453	4.0
Zn	27900	0.4	25290	2.2
Ga	381.2	1.8	423.2	0.4
Rb	552.3	2.1	539.2	0.6
Sr	33040	1.7	32980	0.7
Y	2499	6.0	2405	1.9
Zr	1018	4.8	998.9	4.3
Nb	464.5	23.8	652.5	59.3
Cd	25.70	4.3	21.15	2.7
Sn	385.3	6.2	386.9	0.5
Sb	893.8	2.8	967.3	0.8
Cs	157.9	2.2	164.1	1.2
Ba	7762	1.8	7625	1.2
La	1819	4.0	1757	4.5
Ce	2301	5.1	2176	2.6
Pr	285.6	5.1	272.1	2.1
Nd	1543	4.7	1499	3.4
Sm	530.4	6.3	533.7	4.8
Eu	221.4	3.0	219.0	1.3
Gd	299.1	2.7	296.4	2.2
Tb	44.88	3.0	44.15	1.6
Dy	285.0	3.3	280.7	1.2
Ho	64.26	5.1	62.18	1.2
Er	184.1	6.0	176.6	1.3
Tm	27.18	6.5	25.99	1.7
Yb	170.6	6.5	164.3	3.1
Lu	27.19	6.4	25.81	3.3
Hf	16.65	1.9	16.50	5.1
Ta	3.794	19.8	4.973	21.3
Pb	5986	5.1	6057	3.2
Th	46.49	9.4	44.21	10.4
U	270.6	11.9	244.8	0.7

Table A6.5. *(continued)*

	FeR-4 n = 5 100 mg	*m = 19*	*FeR-4 n = 3 200 mg*	*m = 11*
(ppb)	***mean***	***1rsd (%)***	***mean***	***1rsd (%)***
Li	7323	1.4	7371	0.4
Be	1175	5.2	1181	4.5
Sc	1067	6.6	1206	1.3
Ti	353400	3.5	358100	1.3
V	10460	2.7	10550	0.4
Cr	8111	5.1	8713	1.8
Co	1926	2.0	1988	1.3
Ni	5960	4.3	6138	1.8
Cu	8489	12.6	9041	14.8
Zn	18780	5.8	18700	3.7
Ga	2368	2.6	2469	0.3
Rb	16030	0.9	16160	0.2
Sr	63780	0.4	64210	0.2
Y	5491	1.9	5795	1.7
Zr	18200	1.9	18340	1.2
Nb	1737	16.0	2069	26.3
Cd	27.57	8.5	25.22	2.8
Sn	744.0	12.3	728.5	3.7
Sb	1382	4.0	1532	1.7
Cs	645.2	0.3	653.5	0.2
Ba	37200	0.6	37570	0.5
La	7845	0.8	7752	1.0
Ce	13270	2.3	13040	1.1
Pr	1645	2.0	1613	1.1
Nd	7448	1.3	7328	1.1
Sm	2064	3.0	2033	1.5
Eu	665.6	1.4	666.0	1.8
Gd	1090	2.9	1097	1.6
Tb	148.1	5.2	147.0	2.3
Dy	820.5	6.7	832.6	2.2
Ho	162.5	2.1	172.3	2.6
Er	495.5	9.4	485.1	2.6
Tm	71.28	2.4	74.76	2.5
Yb	466.5	1.7	486.5	1.6
Lu	73.75	1.9	76.48	1.8
Hf	487.1	0.5	491.1	1.1
Ta	91.13	2.6	92.97	3.5
Pb	6510	5.1	7167	6.4
Th	809.8	3.1	819.5	0.2
U	484.9	11.0	518.9	14.3

Table A6.5. *(continued)*

	IOC-1 n = 5 100 mg	*m = 17*	*IOC-1 n = 3 200 mg*	*m = 11*
(ppb)	***mean***	***1rsd (%)***	***mean***	***1rsd (%)***
Li	651.6	3.0	630.2	1.6
Be	632.7	26.7	693.8	12.7
Sc	758.8	11.3	1096	3.1
Ti	239200	3.5	239100	3.2
V	40920	0.8	40940	1.5
Cr	167500	1.6	170900	0.7
Co	20480	1.3	20700	0.9
Ni	11230	1.6	11660	2.8
Cu	7830	0.3	8041	2.2
Zn	8771	0.4	8192	6.9
Ga	1858	1.2	2040	1.0
Rb	132.1	4.7	129.9	3.0
Sr	4571	4.3	4435	0.6
Y	2631	5.8	2619	0.6
Zr	7098	4.1	7027	3.6
Nb	3148	2.6	3099	1.0
Cd	8.557	21.2	4.833	13.9
Sn	692.5	1.9	715.3	1.1
Sb	366.7	1.3	406.2	2.3
Cs	5.391	13.8	5.181	2.7
Ba	25150	4.8	26840	4.6
La	6971	4.2	7257	8.1
Ce	13110	4.0	13490	7.3
Pr	1455	4.4	1489	7.1
Nd	5108	4.8	5186	7.2
Sm	685.8	4.6	684.9	6.8
Eu	190.7	4.0	192.2	6.4
Gd	513.2	3.5	520.0	5.7
Tb	69.30	2.7	69.38	3.9
Dy	383.7	2.1	386.5	2.8
Ho	81.97	2.5	82.69	1.5
Er	237.1	2.8	237.3	0.8
Tm	35.39	2.2	35.57	0.4
Yb	217.5	2.1	220.3	0.2
Lu	30.81	1.7	31.25	0.8
Hf	85.86	4.3	88.31	4.4
Ta	44.96	2.5	46.10	2.6
Pb	1476	6.1	1480	3.4
Th	799.7	3.8	789.0	4.3
U	64.04	3.5	63.32	3.6

APPENDIX 7: SAMPLED AREAS FOR SEM-MLA MAPS

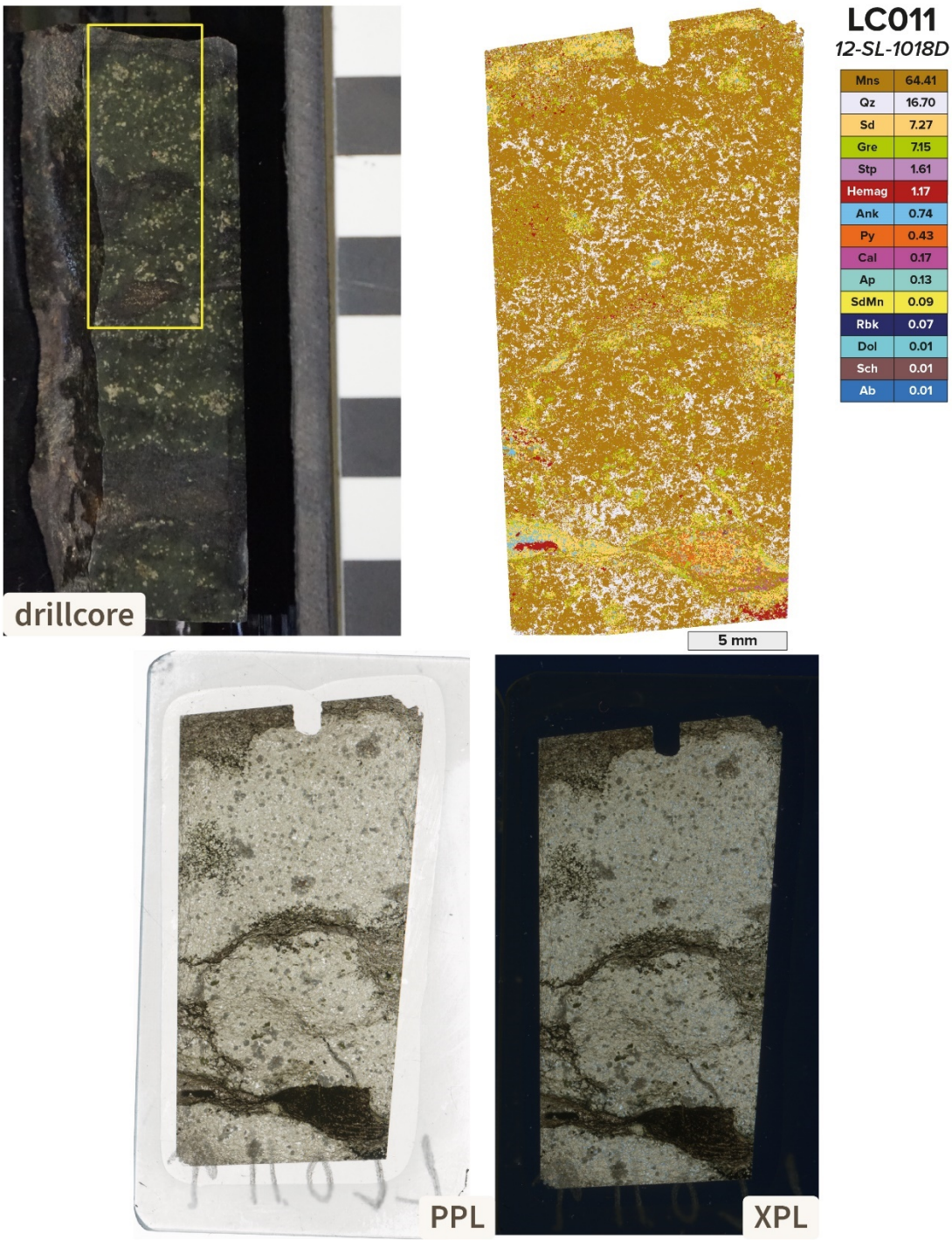

Figure A7.1. False-colour MLA map of sample LC011 and corresponding drillcore photo and thin section scans in plane-polarized (PPL) and cross-polarized light (XPL). The yellow bounding box delineates the area covered by the thin section.

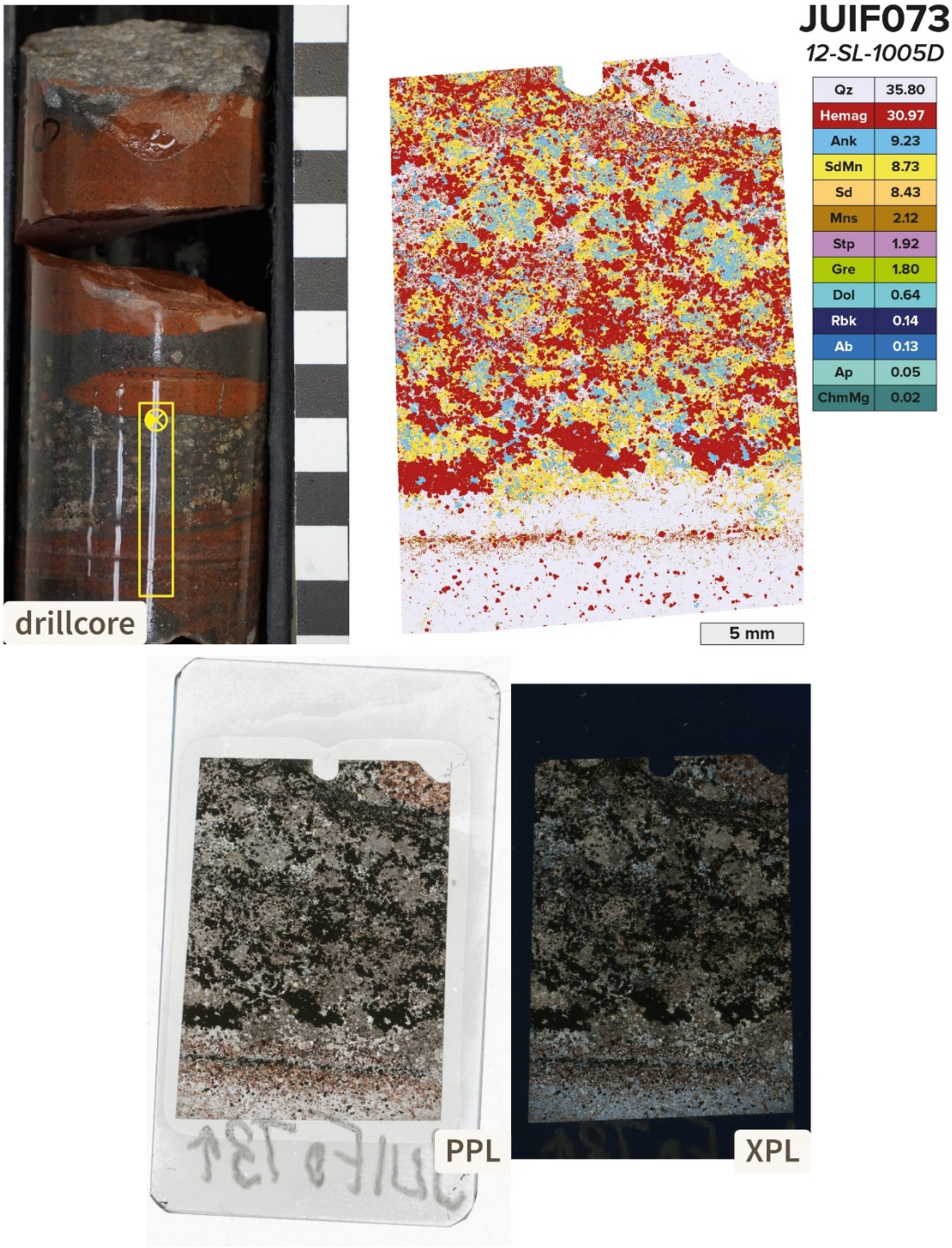

Figure A7.2. False-colour MLA map of sample JUIF073 and corresponding drillcore photo and thin section scans in plane-polarized (PPL) and cross-polarized light (XPL). The yellow bounding box delineates the area covered by the thin section. The cross indicates that the sampled area goes into the page and the corresponding fill indicates the direction.

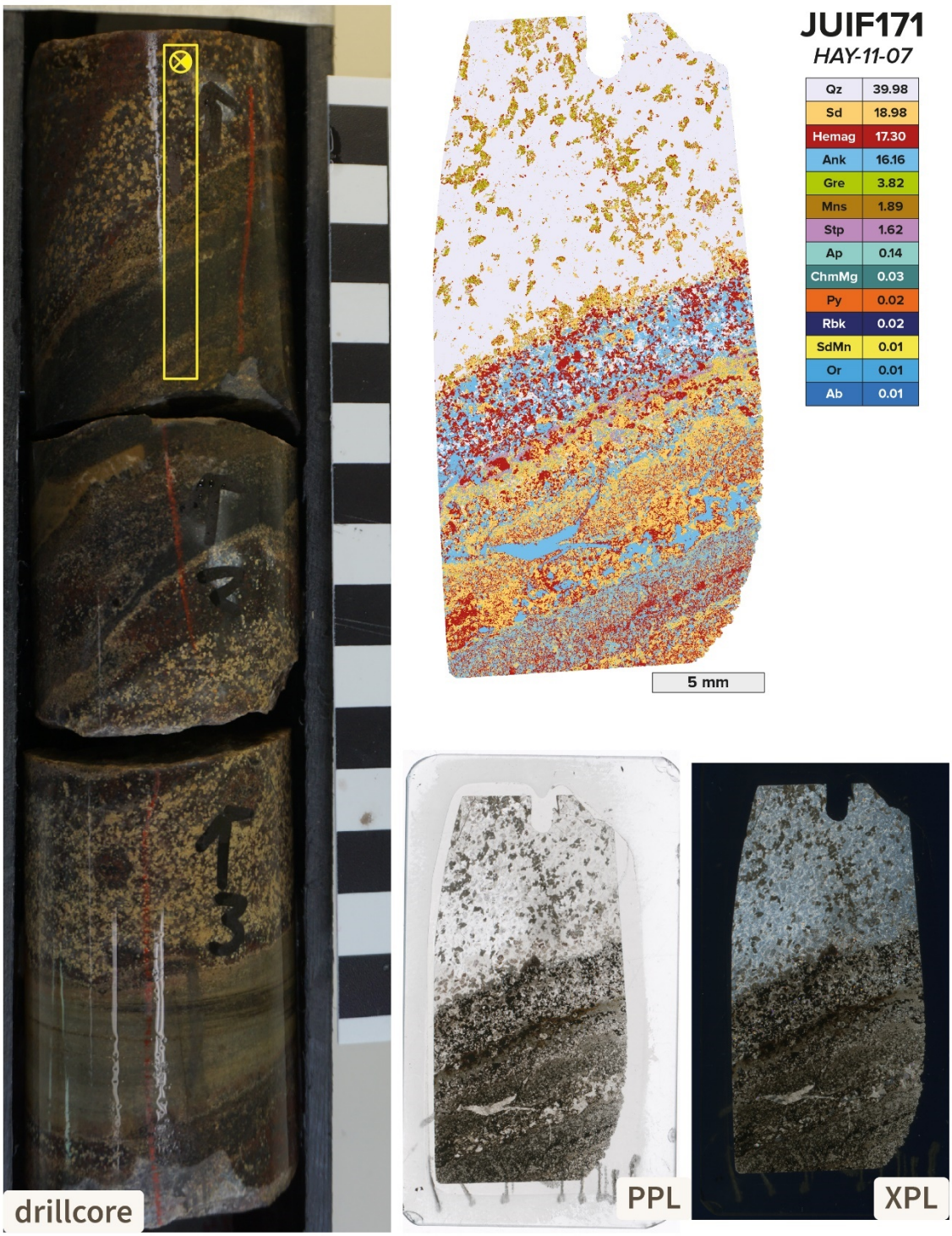

Figure A7.3. False-colour MLA map of sample JUIF171 and corresponding drillcore photo and thin section scans in plane-polarized (PPL) and cross-polarized light (XPL). The yellow bounding box delineates the area covered by the thin section. The cross indicates that the sampled area goes into the page and the corresponding fill indicates the direction.

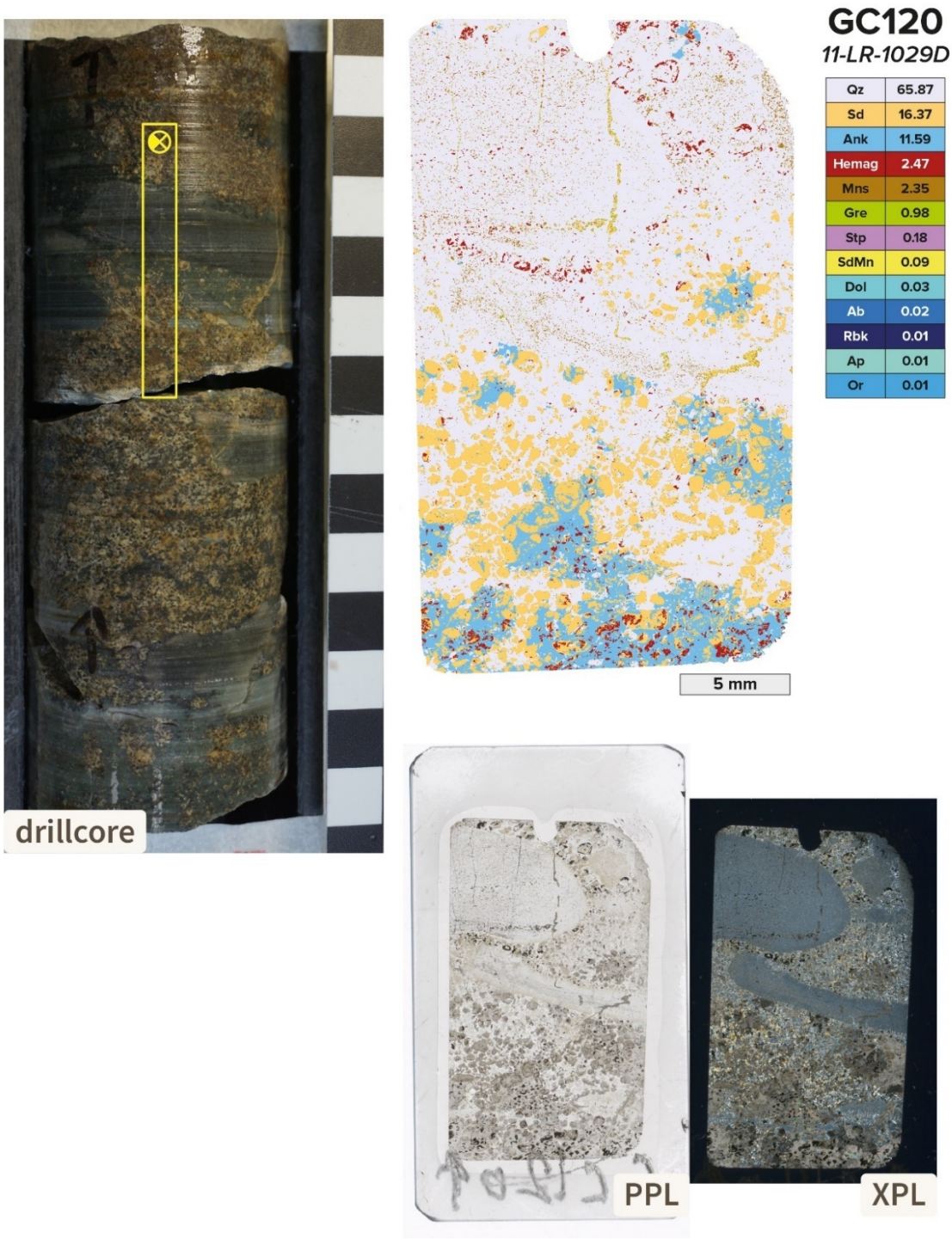

Figure A7.4. False-colour MLA map of sample GC120 and corresponding drillcore photo and thin section scans in plane-polarized (PPL) and cross-polarized light (XPL). The yellow bounding box delineates the area covered by the thin section. The cross indicates that the sampled area goes into the page and the corresponding fill indicates the direction.

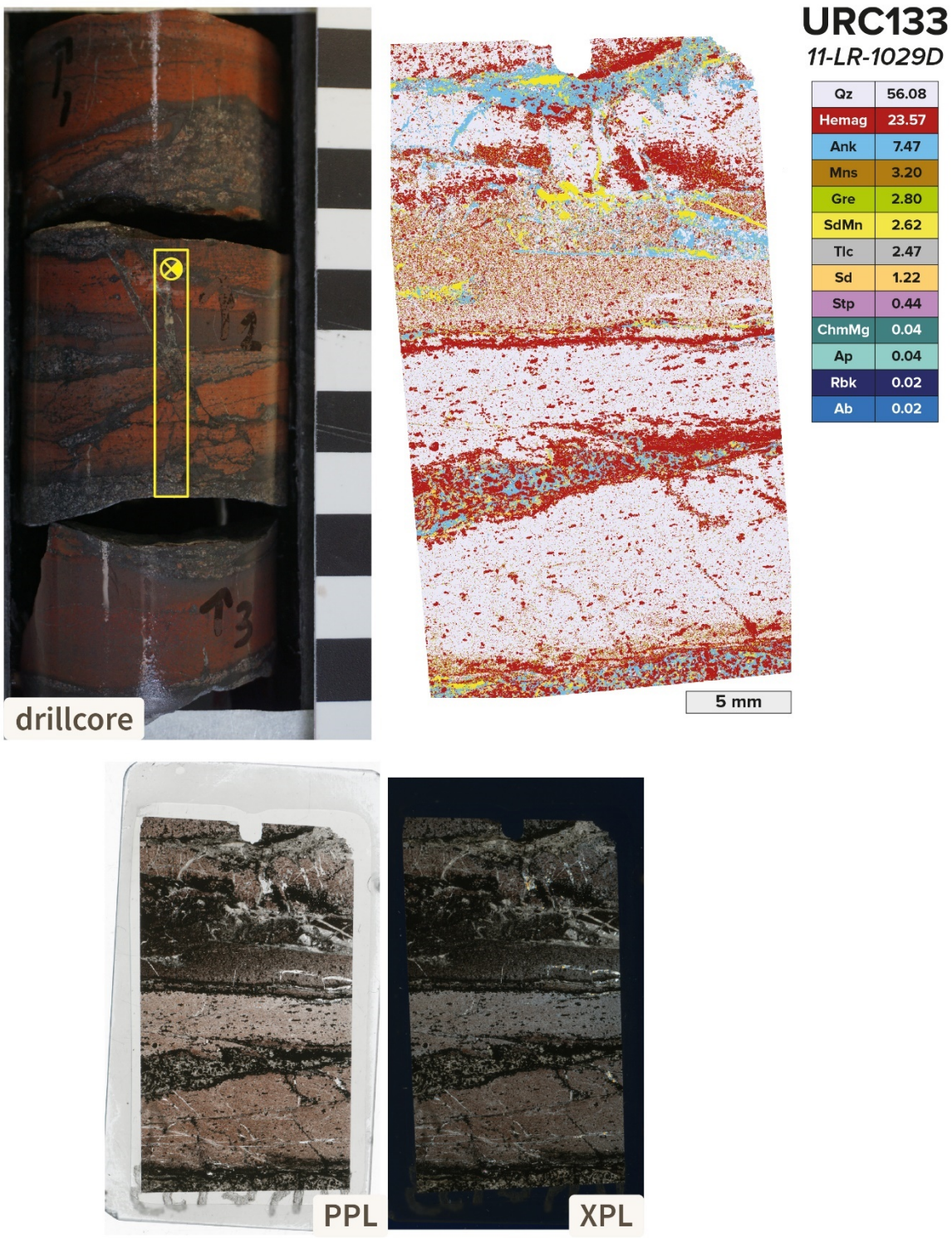

Figure A7.5. False-colour MLA map of sample URC133 and corresponding drillcore photo and thin section scans in plane-polarized (PPL) and cross-polarized light (XPL). The yellow bounding box delineates the area covered by the thin section. The cross indicates that the sampled area goes into the page and the corresponding fill indicates the direction.

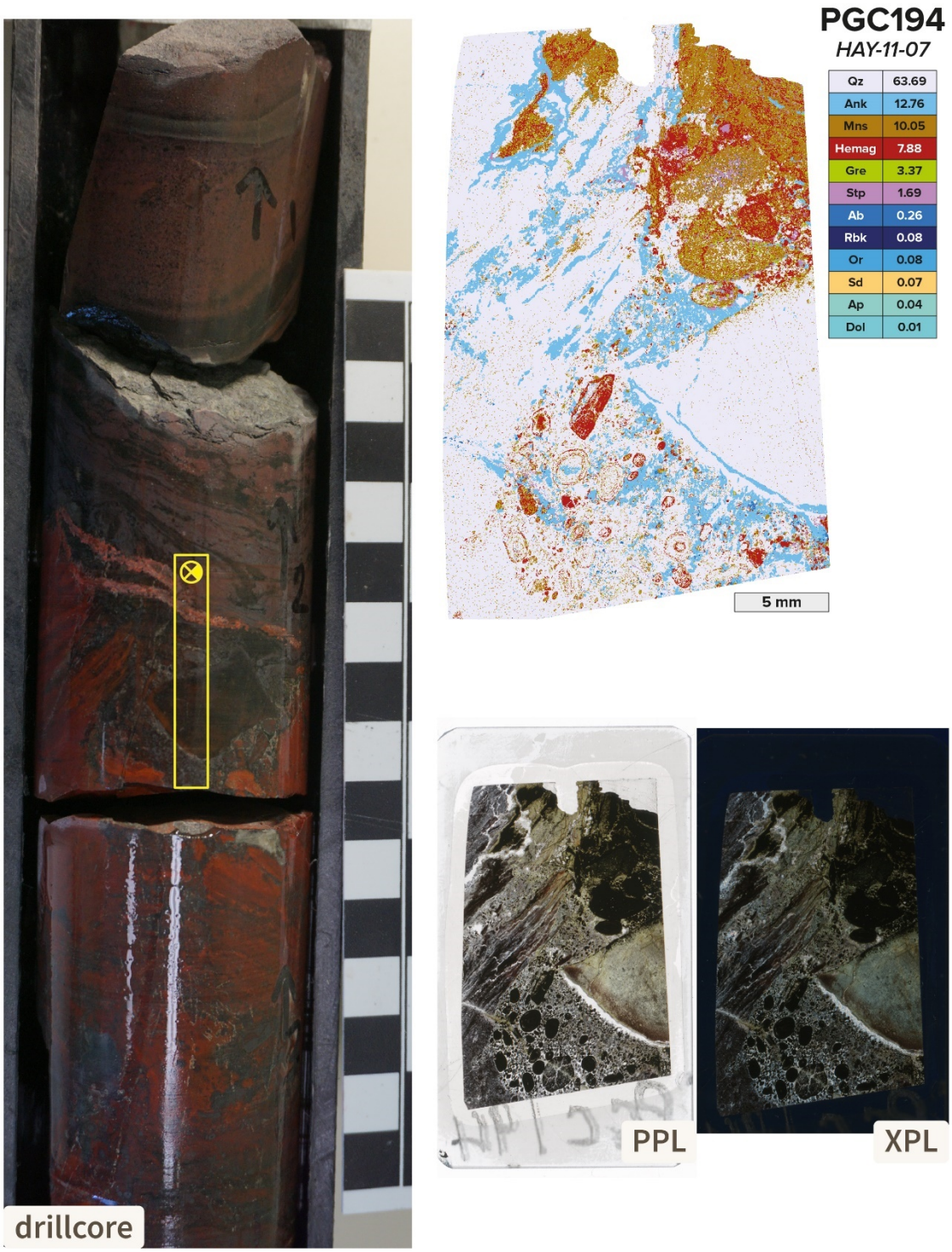

Figure A7.6. False-colour MLA map of sample PGC194 and corresponding drillcore photo and thin section scans in plane-polarized (PPL) and cross-polarized light (XPL). The yellow bounding box delineates the area covered by the thin section. The cross indicates that the sampled area goes into the page and the corresponding fill indicates the direction.

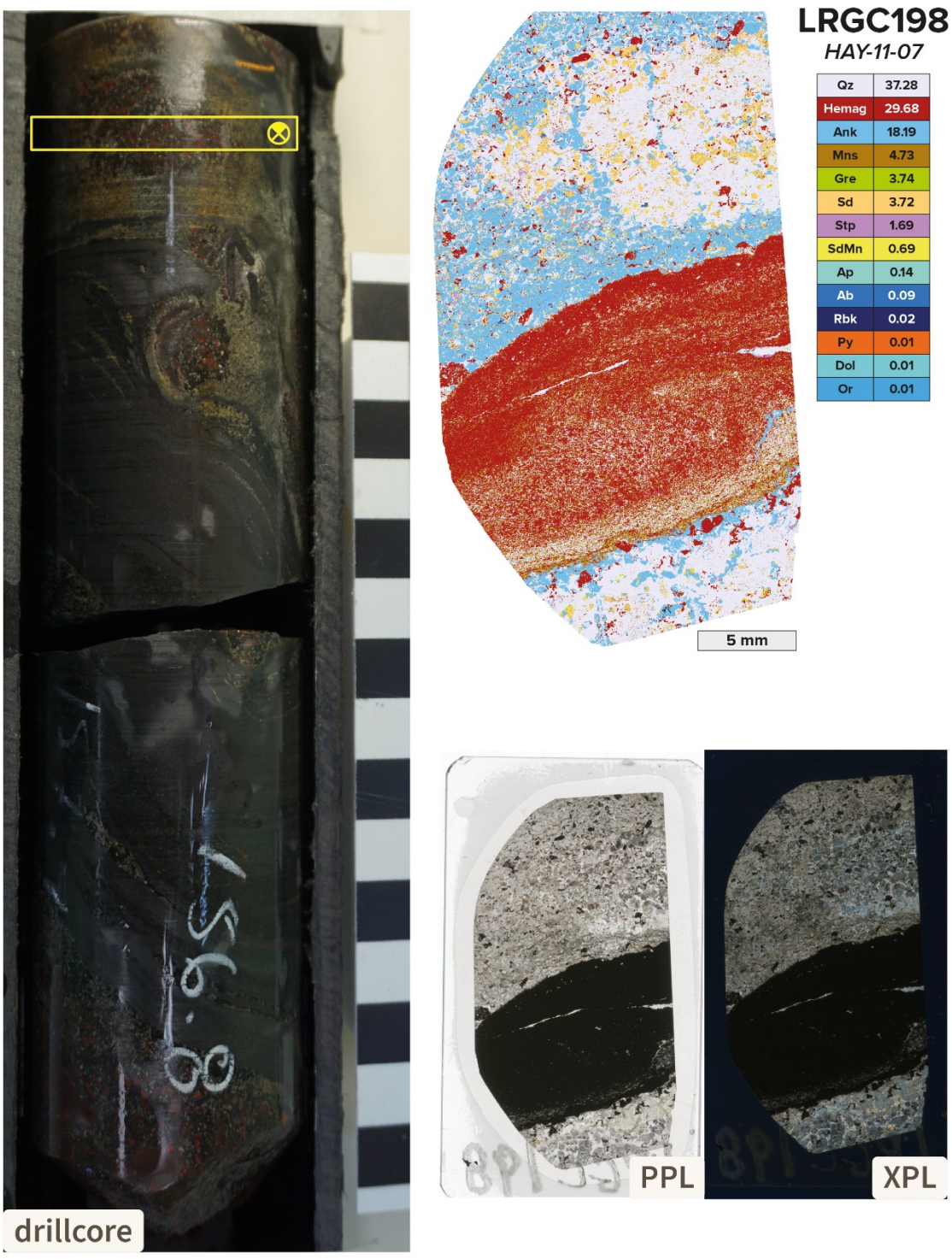

Figure A7.7. False-colour MLA map of sample LRGC198 and corresponding drillcore photo and thin section scans in plane-polarized (PPL) and cross-polarized light (XPL). The yellow bounding box delineates the area covered by the thin section. The cross indicates that the sampled area goes into the page and the corresponding fill indicates the direction.

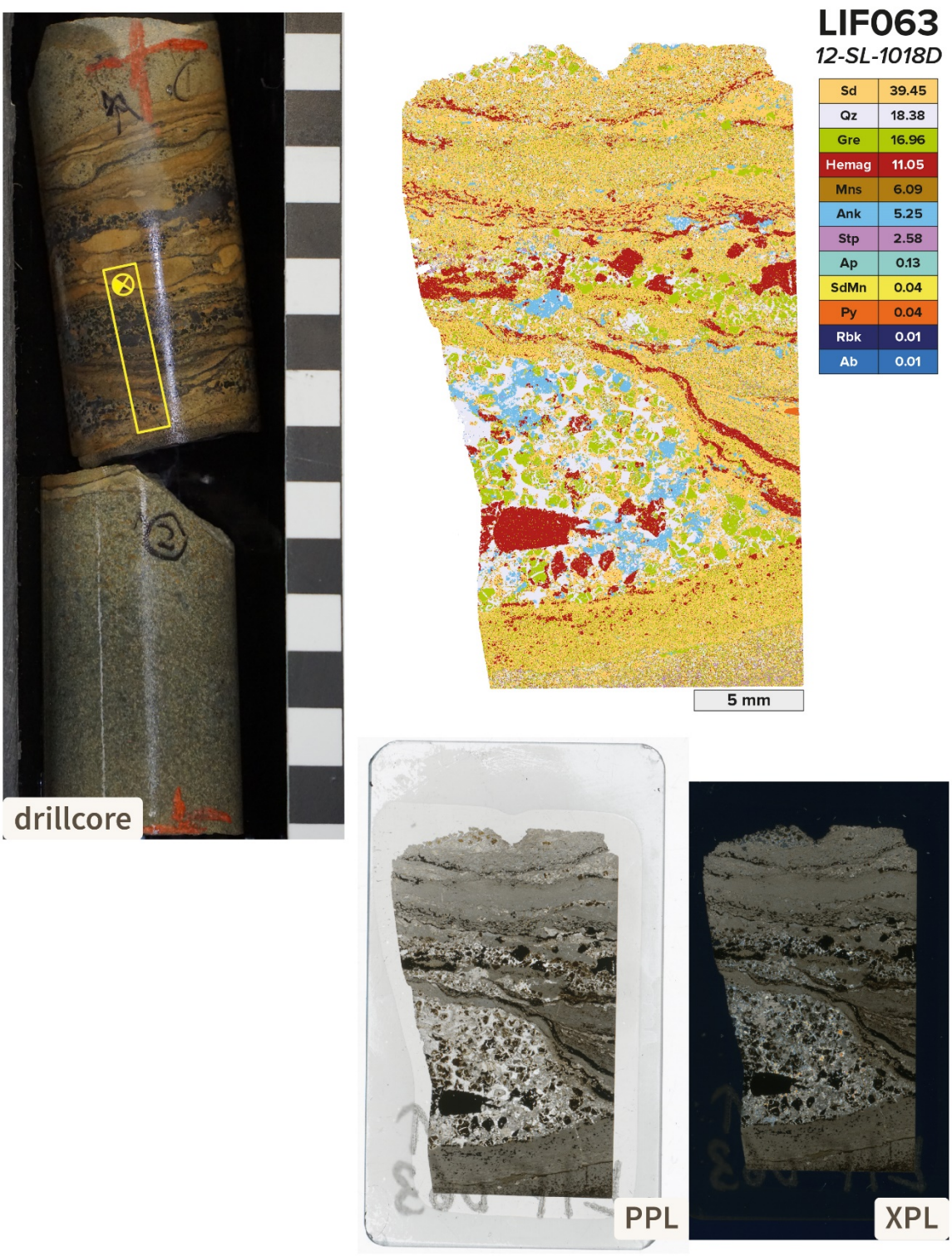

Figure A7.8. False-colour MLA map of sample LIF063 and corresponding drillcore photo and thin section scans in plane-polarized (PPL) and cross-polarized light (XPL). The yellow bounding box delineates the area covered by the thin section. The cross indicates that the sampled area goes into the page and the corresponding fill indicates the direction.

APPENDIX 8: DRILL CORE PHOTOGRAPHS AND THIN SECTION SCANS

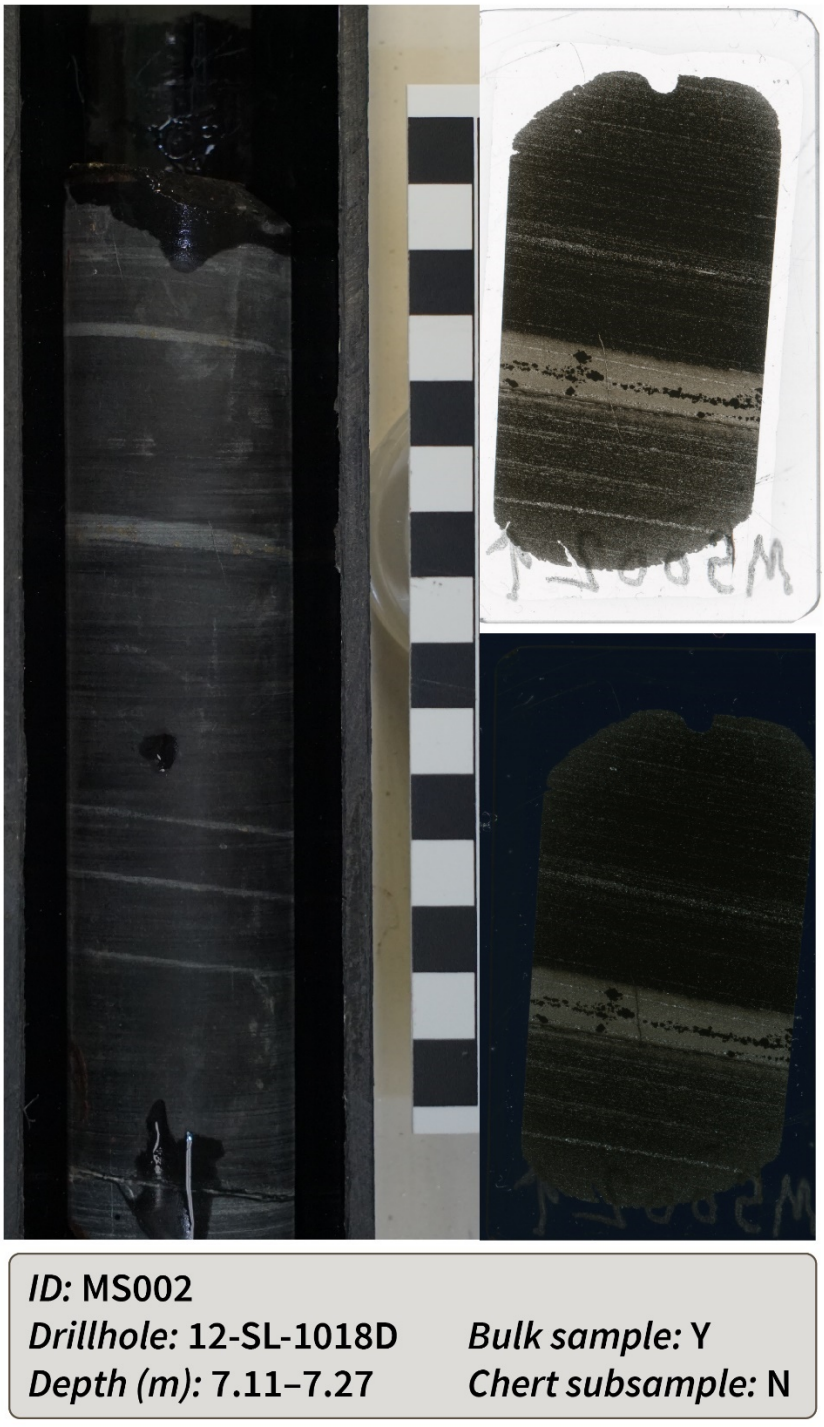

Figure A8.1. Drill core photograph and thin section scans (PPL, XPL) for sample MS002. Thin section dimensions are 25 x 46 mm.

Figure A8.2. Drill core photograph and thin section scans (PPL, XPL) for sample MS005. Thin section dimensions are 25 x 46 mm.

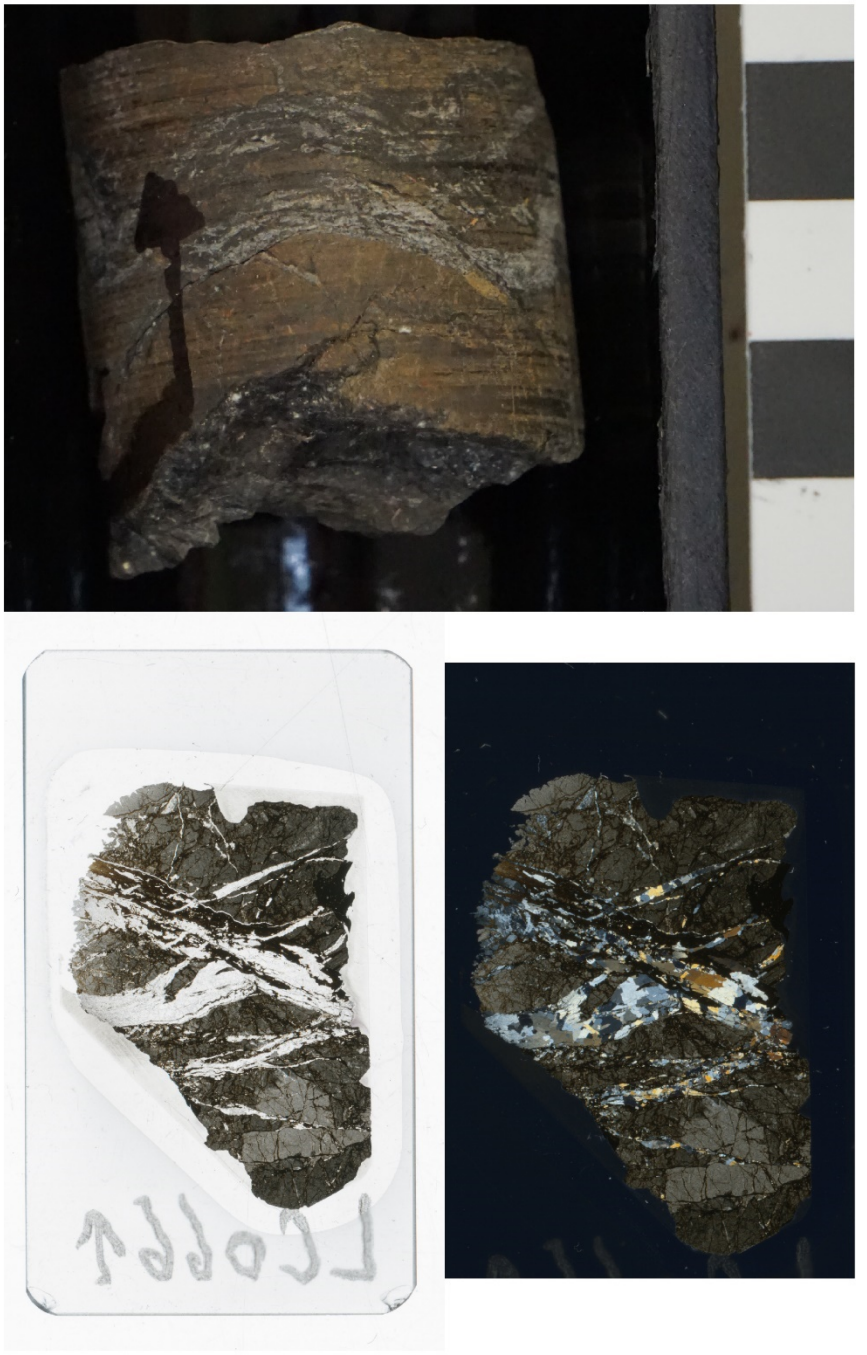

Figure A8.3. Drill core photograph and thin section scans (PPL, XPL) for sample LC066. Thin section dimensions are 25 x 46 mm.

ID: LC011
Drillhole: 12-SL-1018D *Bulk sample:* Y
Depth (m): 39.29–39.35 *Chert subsample:* N

Figure A8.4. Drill core photograph and thin section scans (PPL, XPL) for sample LC011. Thin section dimensions are 25 x 46 mm.

Figure A8.5. Drill core photograph and thin section scans (PPL, XPL) for sample LC016. Thin section dimensions are 25 x 46 mm.

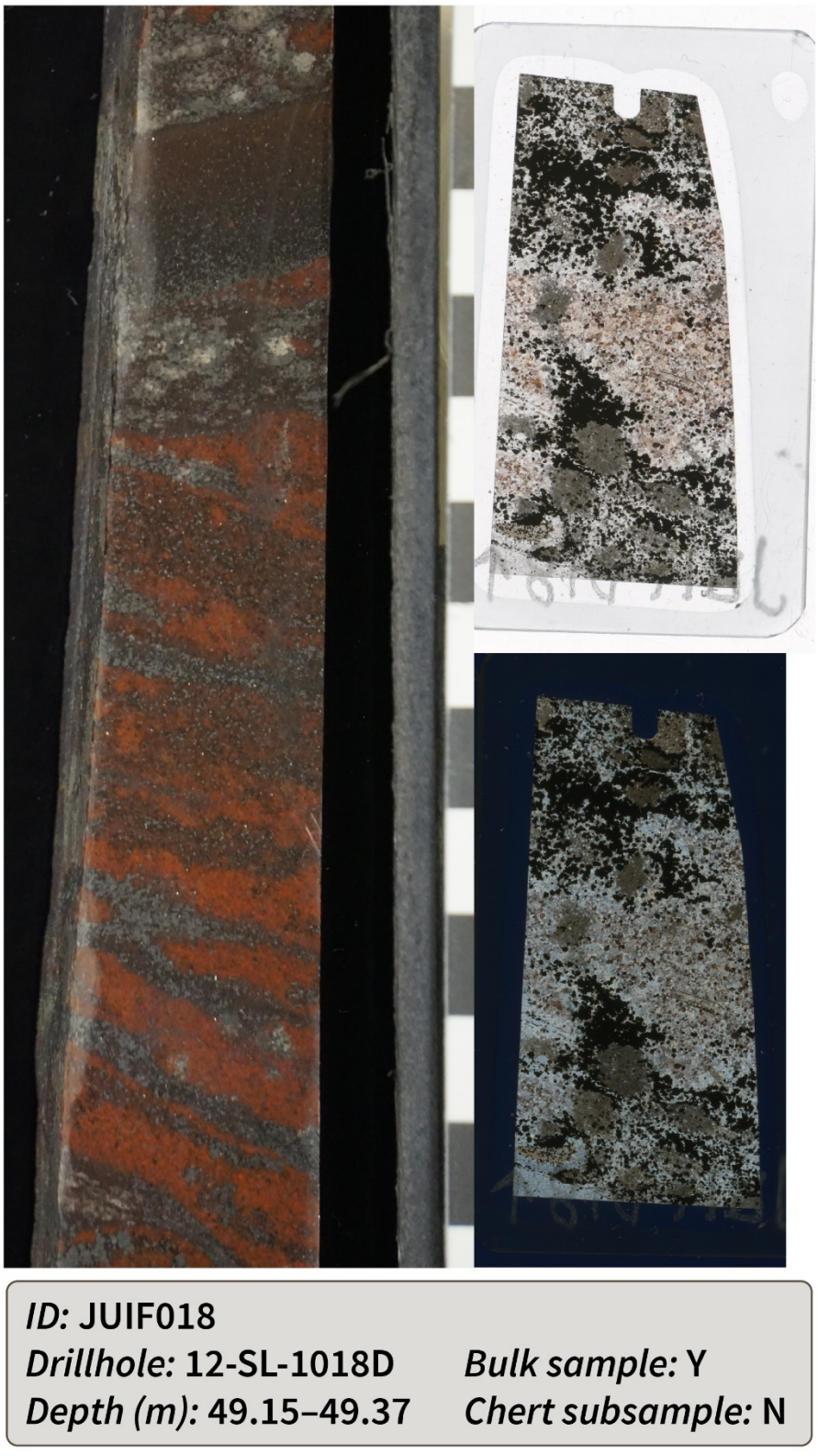

Figure A8.6. Drill core photograph and thin section scans (PPL, XPL) for sample JUIF018. Thin section dimensions are 25 x 46 mm.

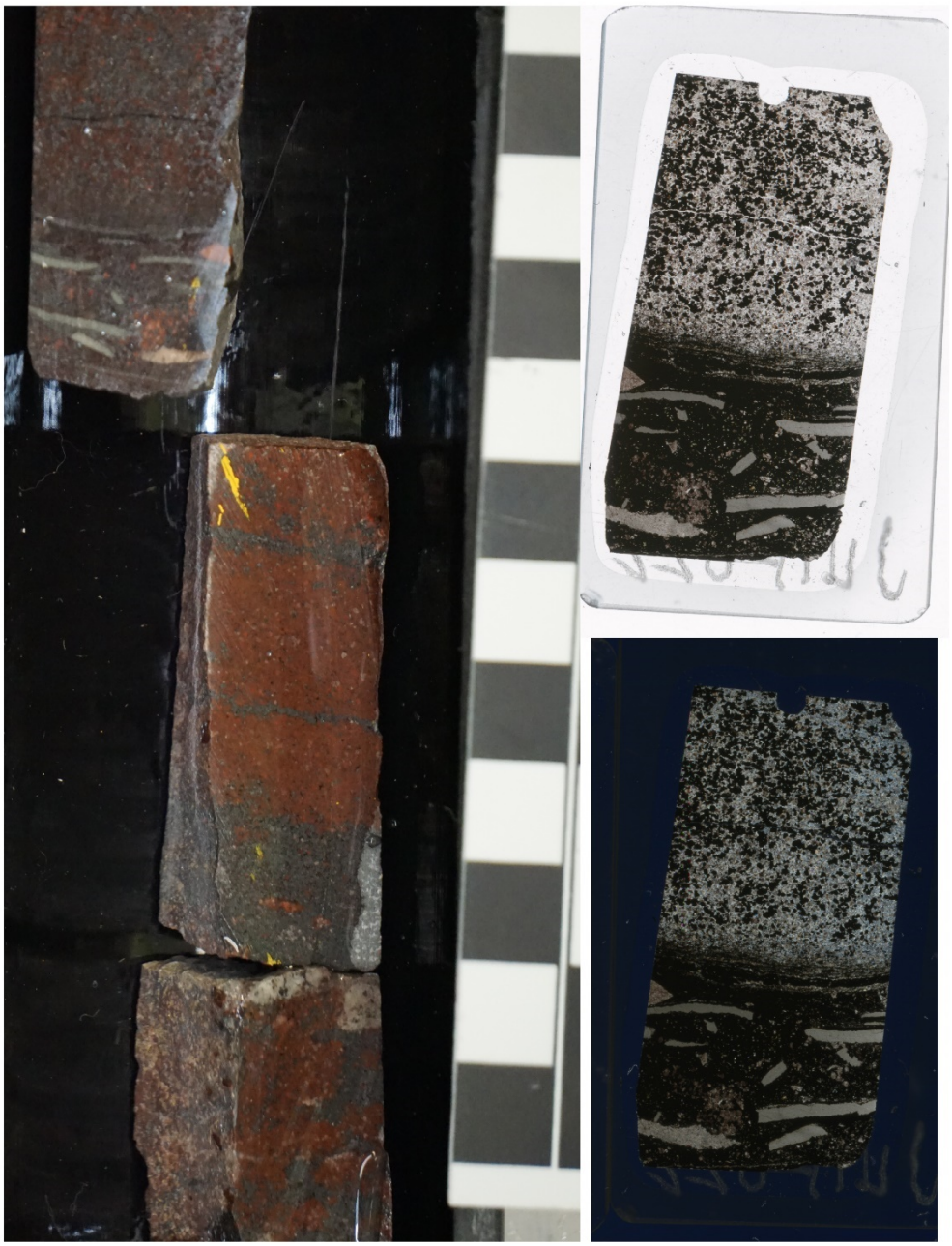

Figure A8.7. Drill core photograph and thin section scans (PPL, XPL) for sample JUIF022. Thin section dimensions are 25 x 46 mm.

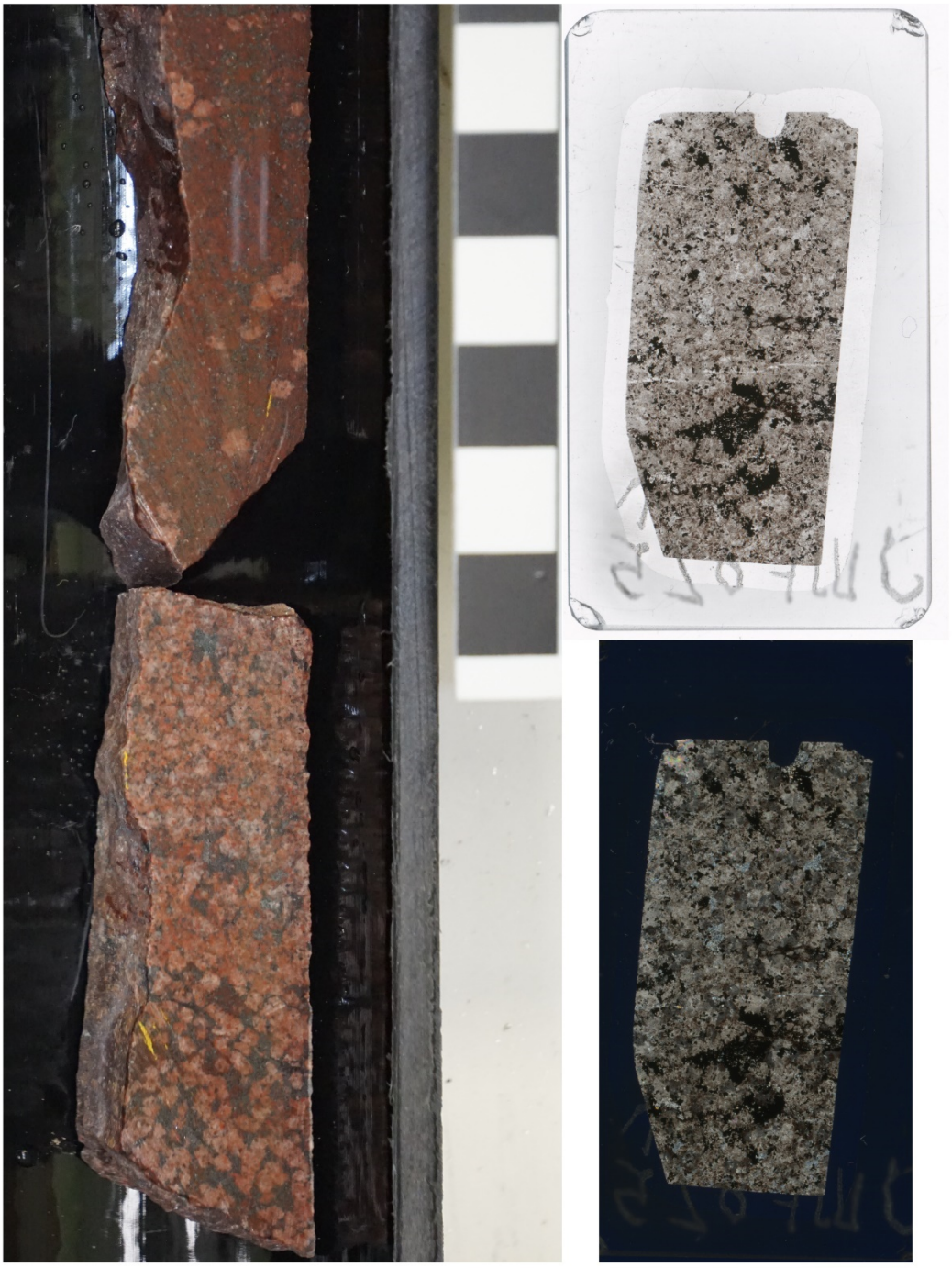

Figure A8.8. Drill core photograph and thin section scans (PPL, XPL) for sample JUIF025. Thin section dimensions are 25 x 46 mm.

Figure A8.9. Drill core photograph and thin section scans (PPL, XPL) for sample JUIF026. Thin section dimensions are 25 x 46 mm.

Figure A8.10. Drill core photograph and thin section scans (PPL, XPL) for sample JUIF032. Thin section dimensions are 25 x 46 mm.

Figure A8.11. Drill core photograph and thin section scans (PPL, XPL) for sample JUIF037. Thin section dimensions are 25 x 46 mm.

Figure A8.12. Drill core photograph and thin section scans (PPL, XPL) for sample GC038. Thin section dimensions are 25 x 46 mm.

Figure A8.13. Drill core photograph and thin section scans (PPL, XPL) for sample GC039. Thin section dimensions are 25 x 46 mm.

Figure A8.14. Drill core photograph and thin section scans (PPL, XPL) for sample URC040. Thin section dimensions are 25 x 46 mm.

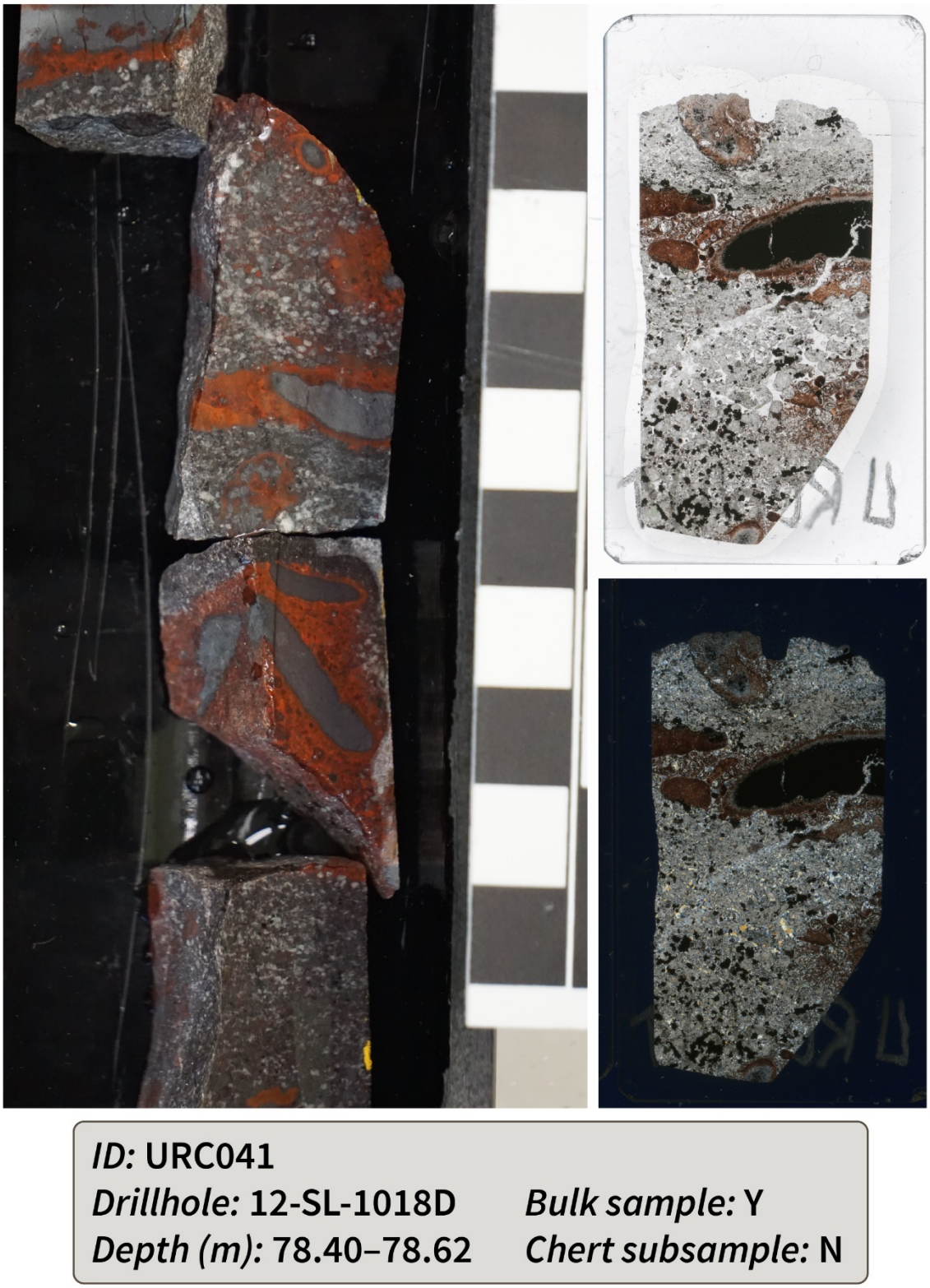

Figure A8.15. Drill core photograph and thin section scans (PPL, XPL) for sample URC041. Thin section dimensions are 25 x 46 mm.

Figure A8.16. Drill core photograph and thin section scans (PPL, XPL) for sample URC042. Thin section dimensions are 25 x 46 mm.

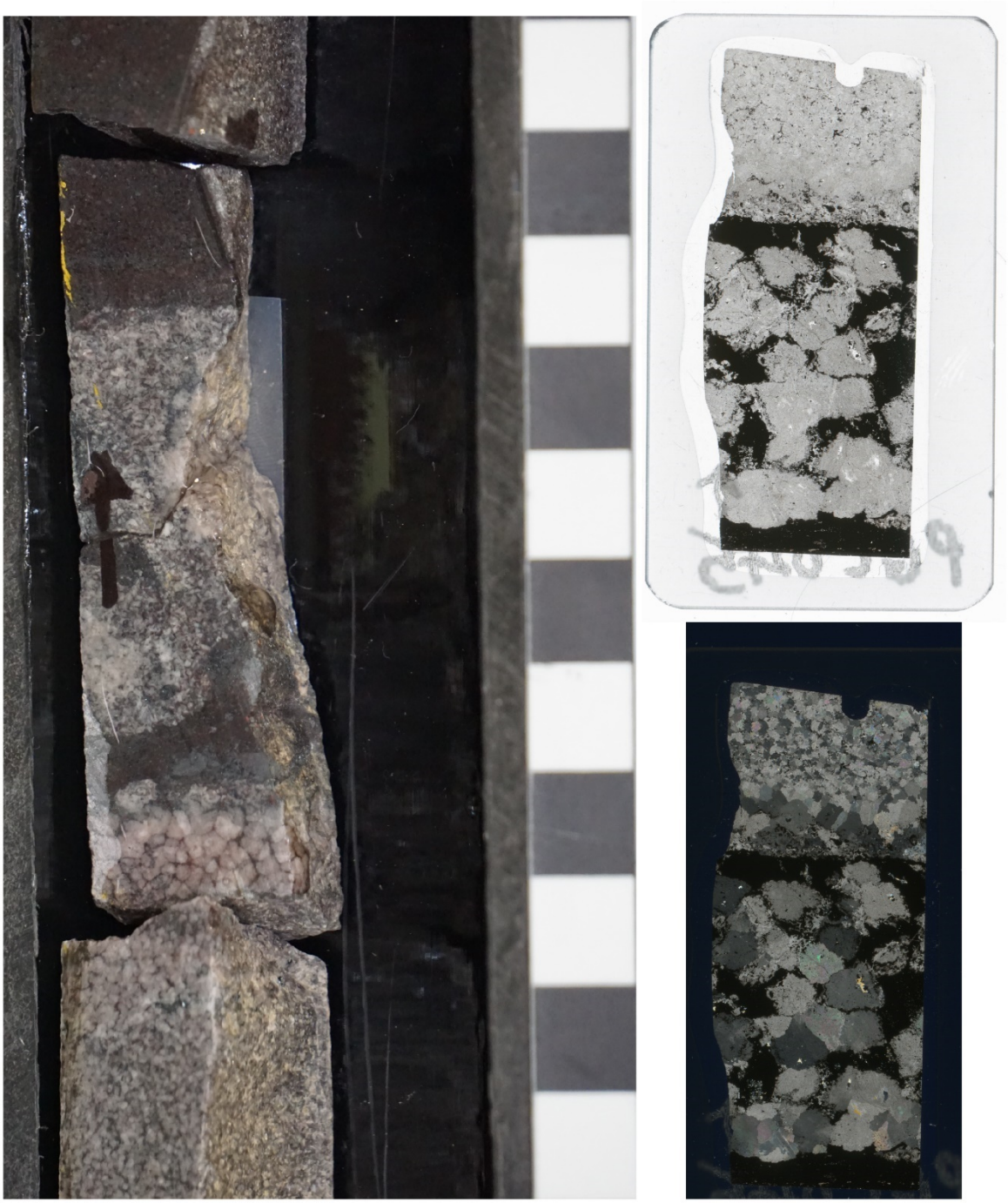

Figure A8.17. Drill core photograph and thin section scans (PPL, XPL) for sample PGC045. Thin section dimensions are 25 x 46 mm.

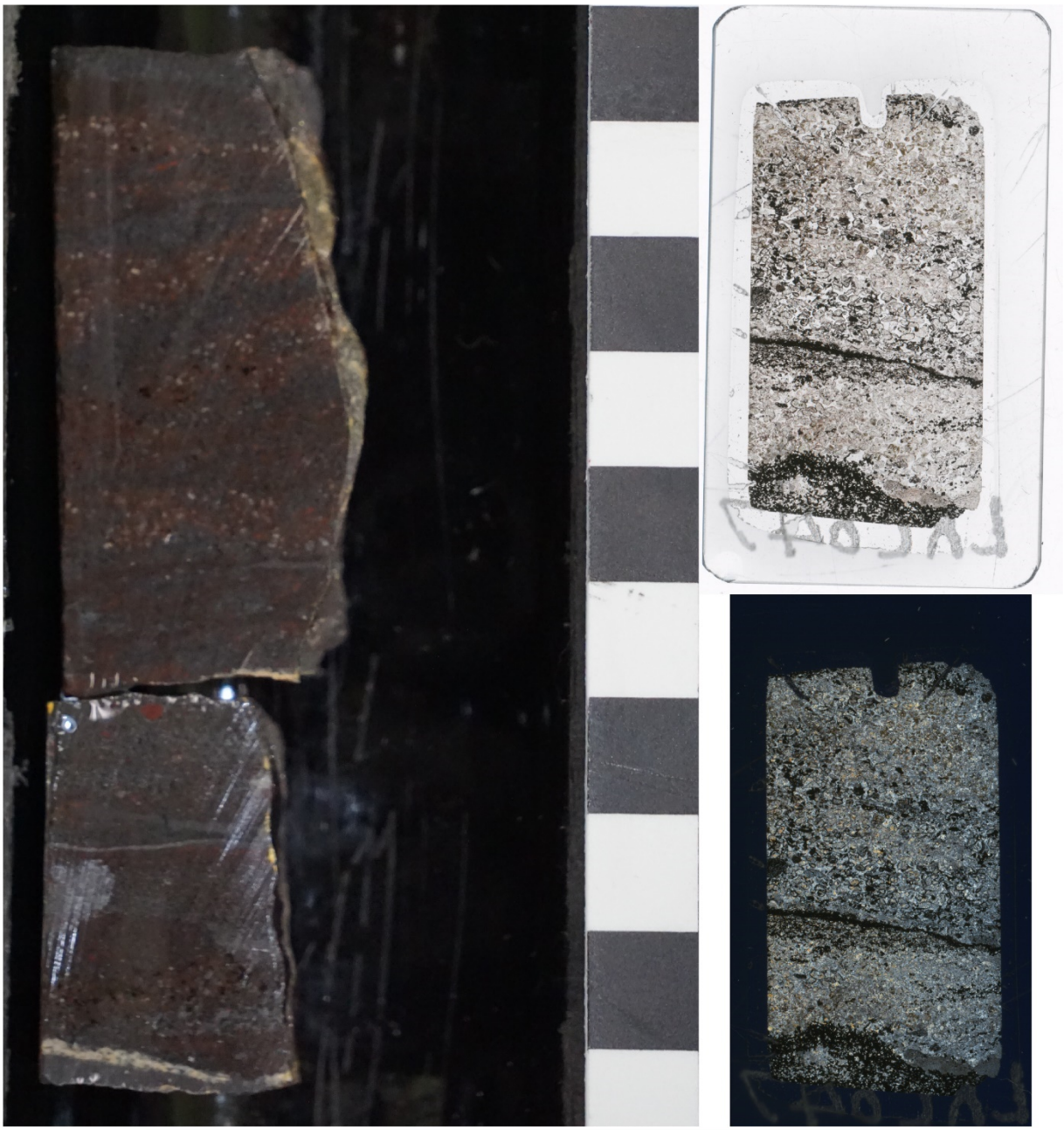

Figure A8.18. Drill core photograph and thin section scans (PPL, XPL) for sample LRC047. Thin section dimensions are 25 x 46 mm.

Figure A8.19. Drill core photograph and thin section scans (PPL, XPL) for sample LRGC051. Thin section dimensions are 25 x 46 mm.

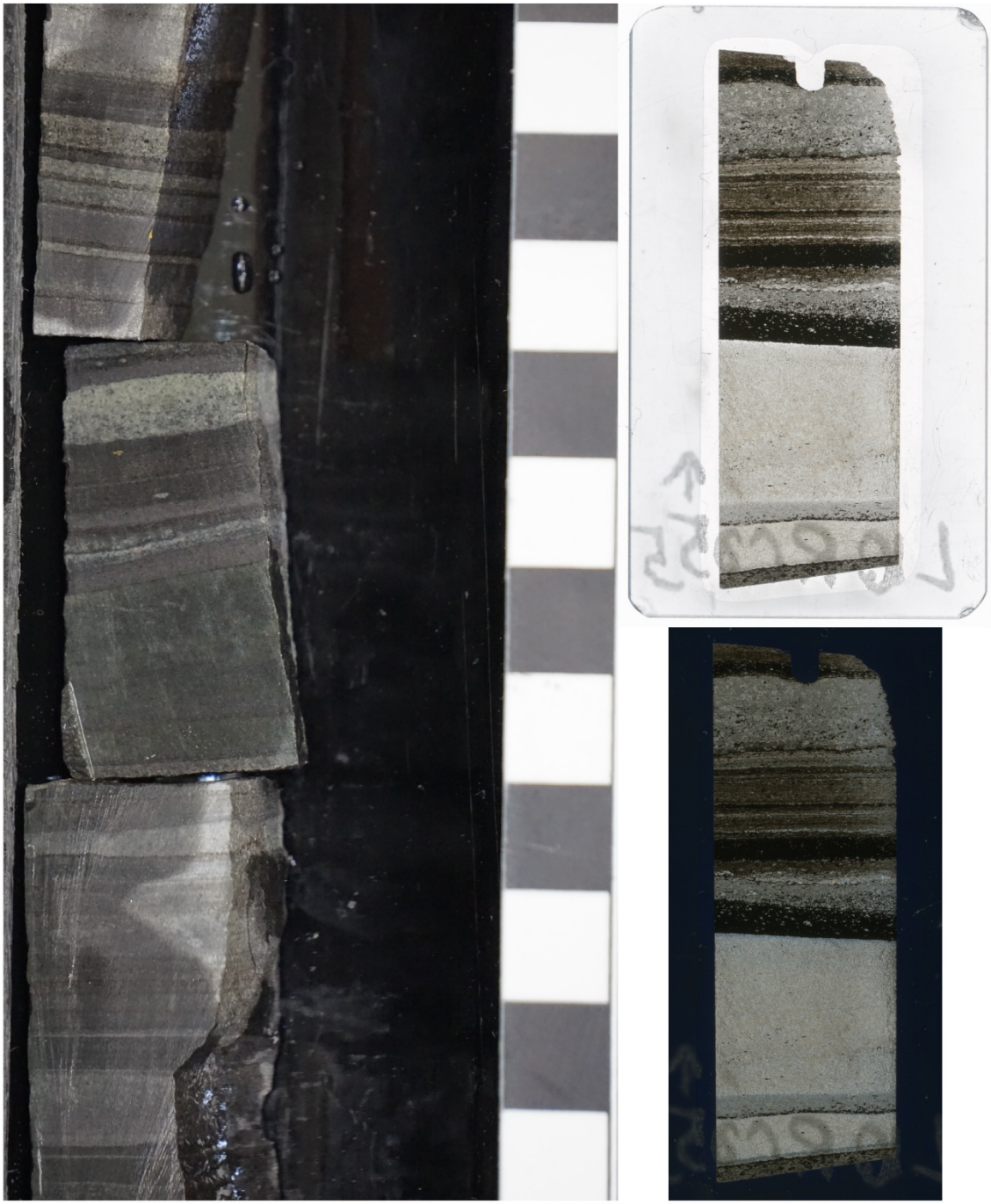

Figure A8.20. Drill core photograph and thin section scans (PPL, XPL) for sample LRGC055. Thin section dimensions are 25 x 46 mm.

Figure A8.21. Drill core photograph and thin section scans (PPL, XPL) for sample LRGC061. Thin section dimensions are 25 x 46 mm.

ID: LIF063
Drillhole: 12-SL-1018D *Bulk sample:* Y
Depth (m): 126.30–126.45 *Chert subsample:* N

Figure A8.22. Drill core photograph and thin section scans (PPL, XPL) for sample LIF063. Thin section dimensions are 25 x 46 mm.

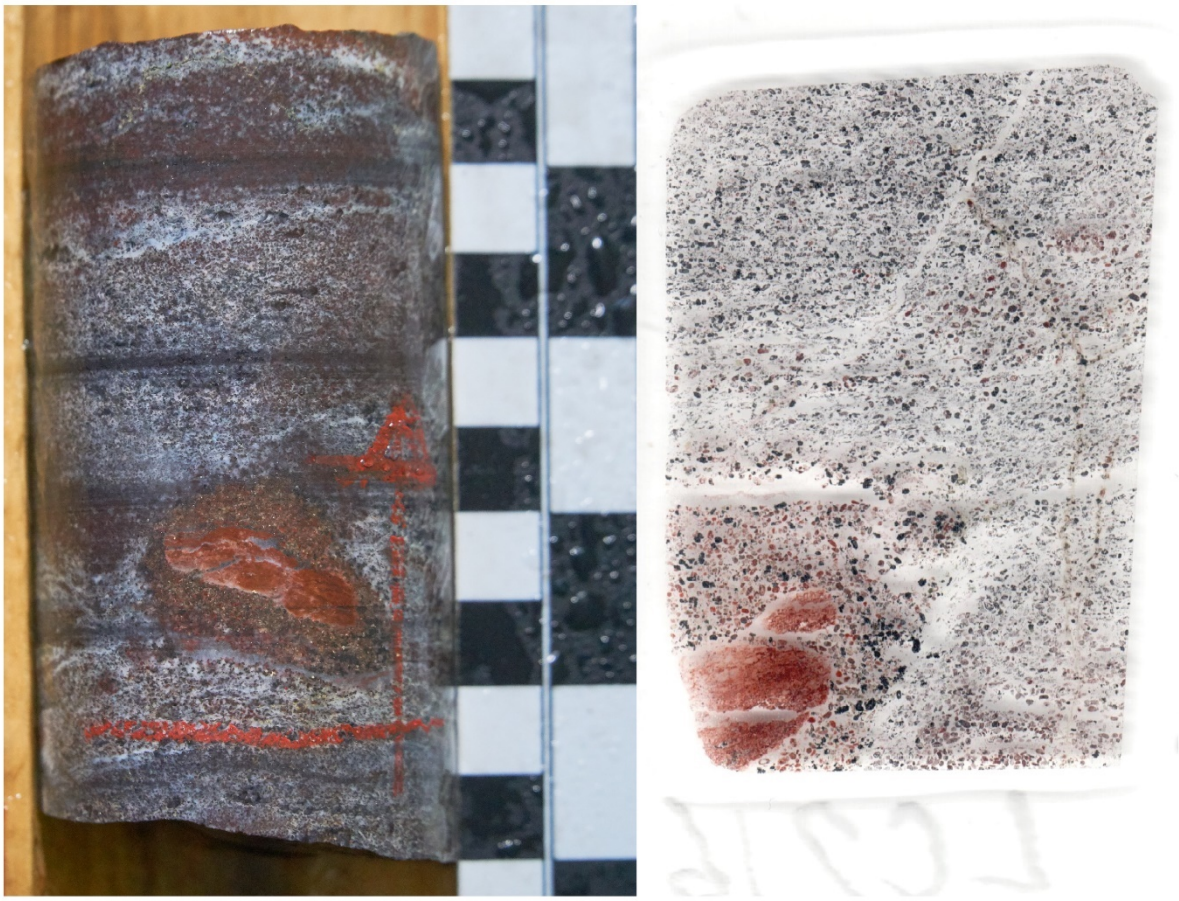

Figure A8.23. Drill core photograph and thin section scans (PPL, XPL) for sample LC216. Thin section dimensions are 25 x 46 mm.

ID: LC217
Drillhole: 12-SL-1018D *Bulk sample:* Y
Depth (m): 37.91–38.00 *Chert subsample:* N

Figure A8.24. Drill core photograph of sample LC217.

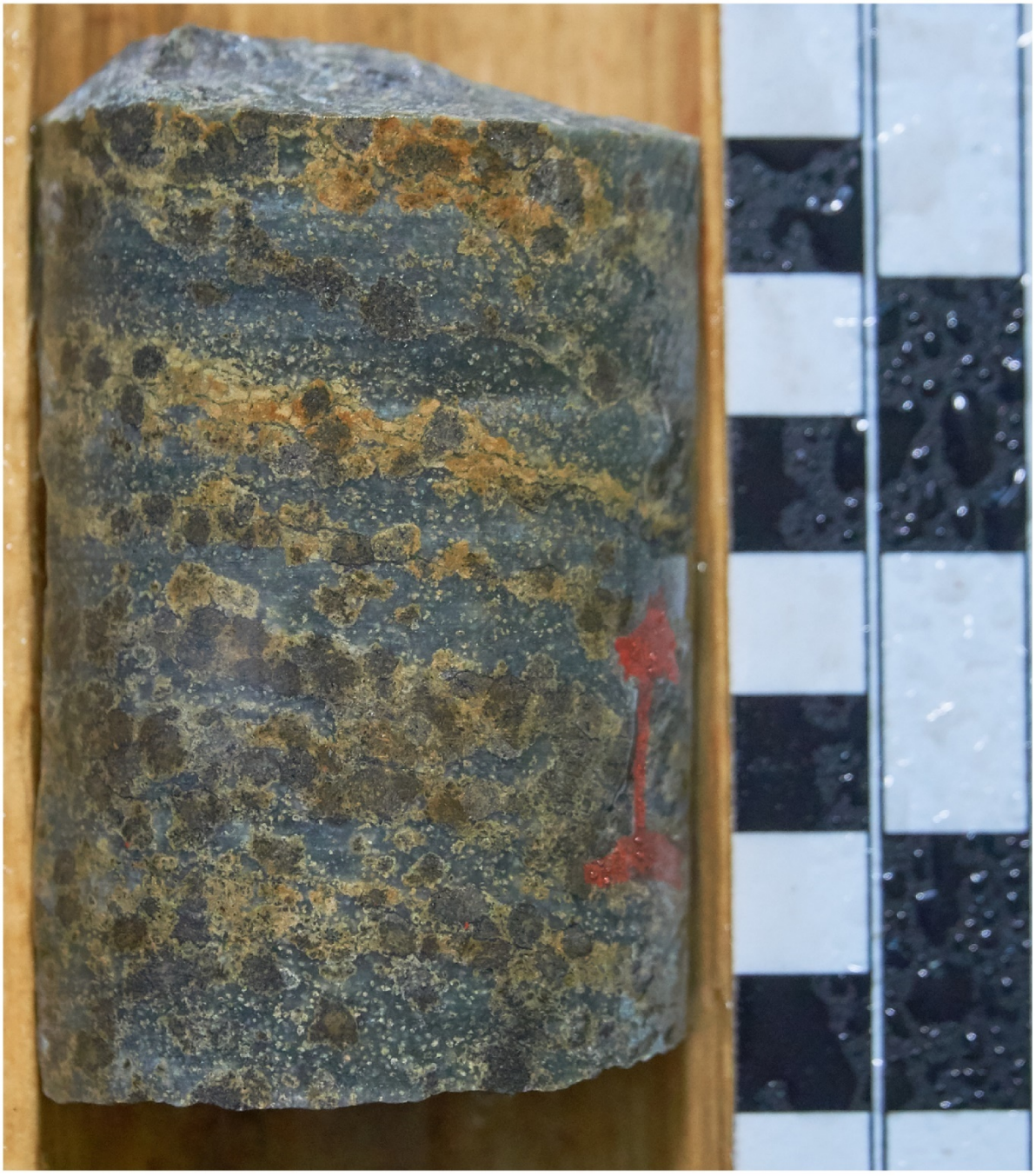

Figure A8.25. Drill core photograph of sample LC221.

Figure A8.26. Drill core photograph of sample LC224.

Figure A8.27. Drill core photograph and thin section scans (PPL, XPL) for sample LC226. Thin section dimensions are 25 x 46 mm.

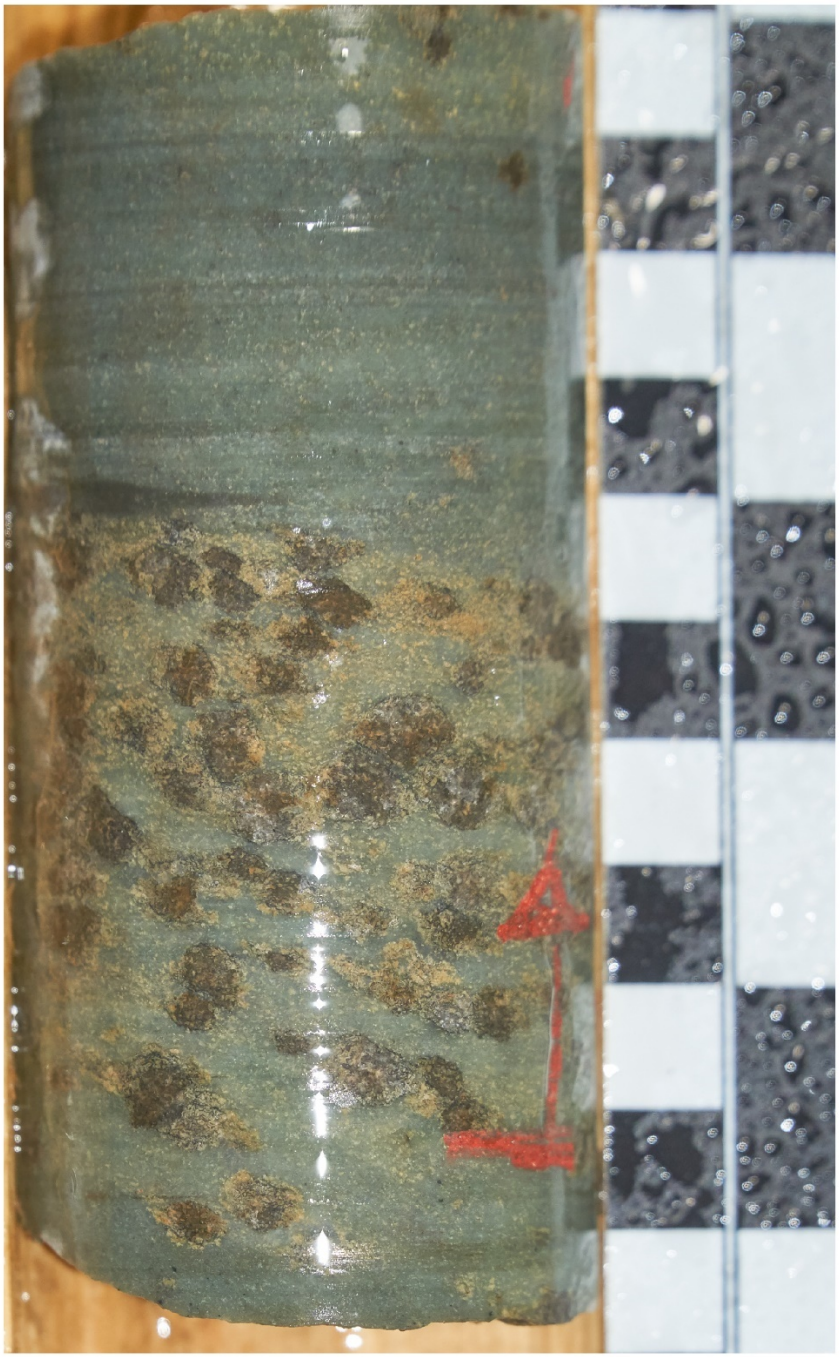

ID: LC227
Drillhole: 12-SL-1017D *Bulk sample:* Y
Depth (m): 65.25–65.35 *Chert subsample:* N

Figure A8.28. Drill core photograph of sample LC227.

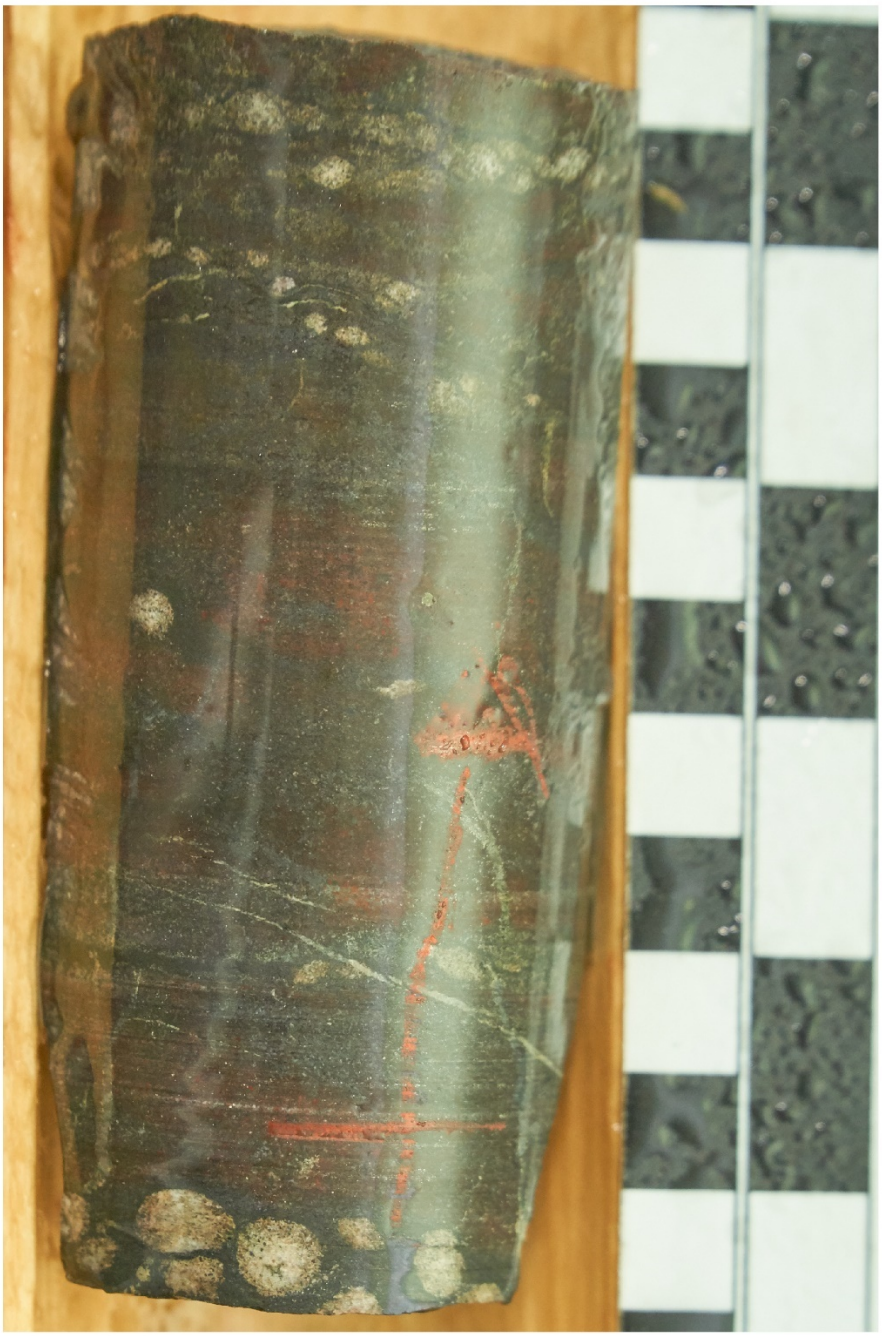

ID: JUIF228
Drillhole: 12-SL-1017D *Bulk sample:* Y
Depth (m): 67.32–67.42 *Chert subsample:* N

Figure A8.29. Drill core photograph of sample JUIF228.

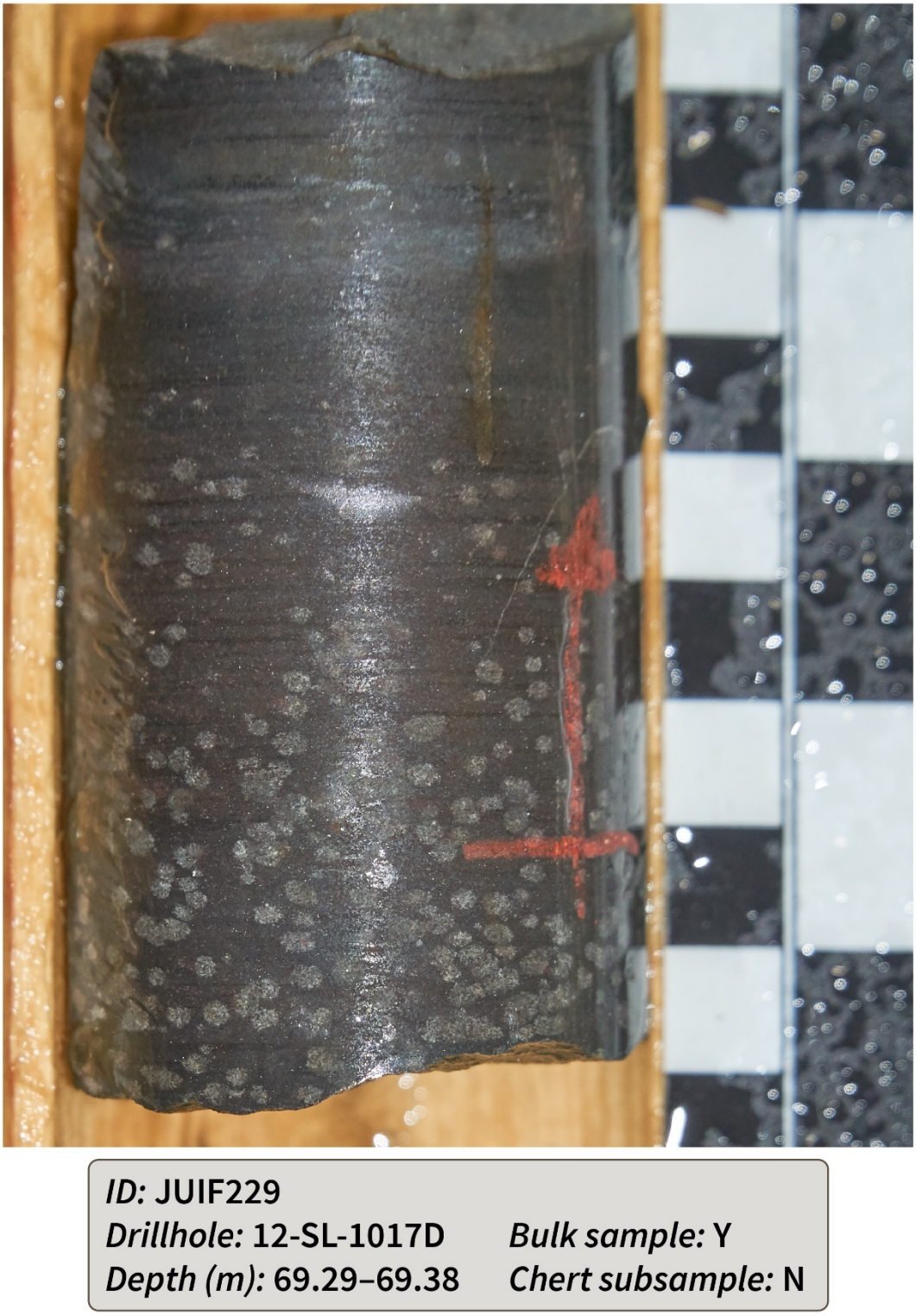

Figure A8.30. Drill core photograph of sample JUIF229.

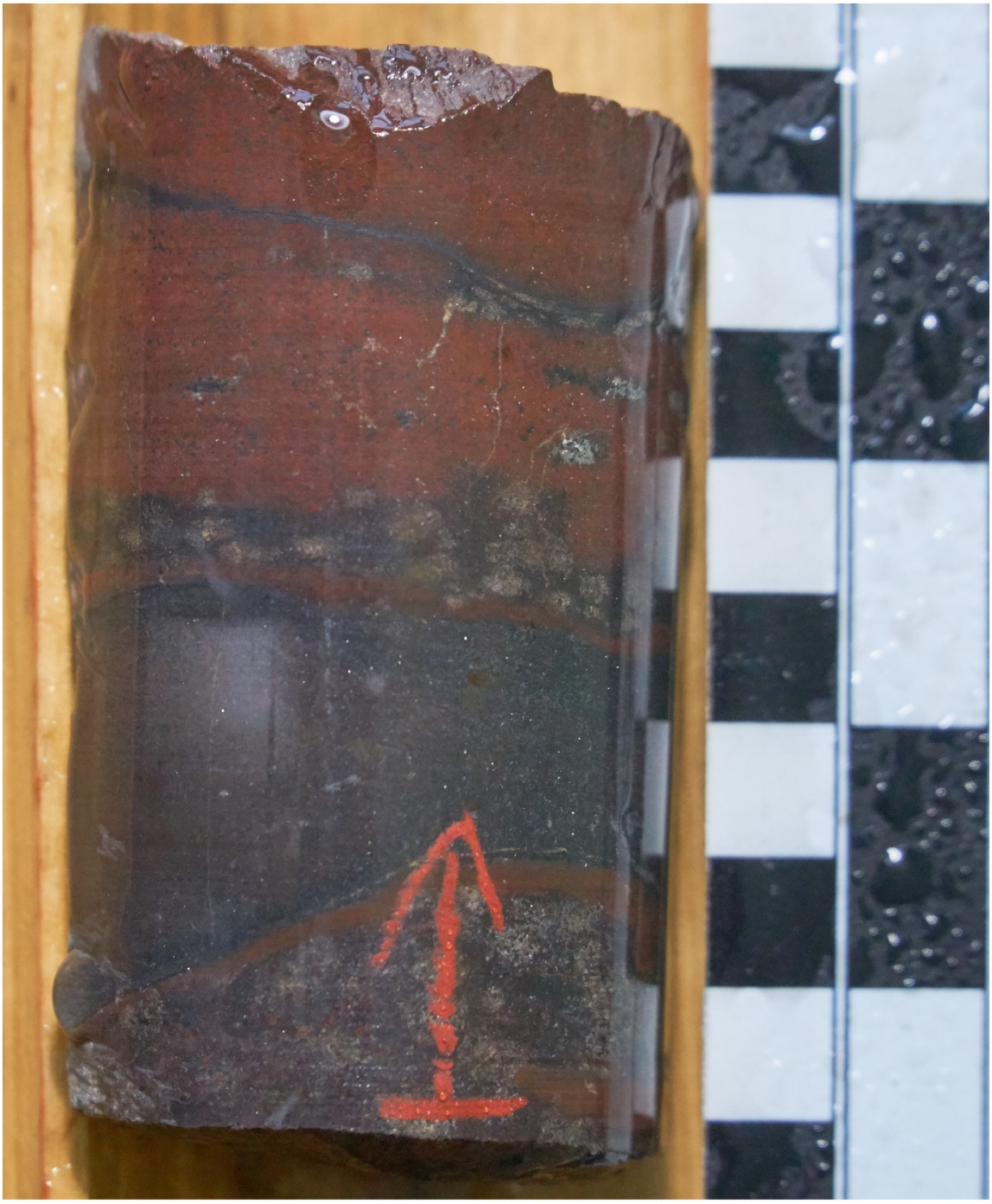

Figure A8.31. Drill core photograph of sample JUIF230.

ID: JUIF231
Drillhole: 12-SL-1017D *Bulk sample:* Y
Depth (m): 74.19–74.29 *Chert subsample:* N

Figure A8.32. Drill core photograph of sample JUIF231.

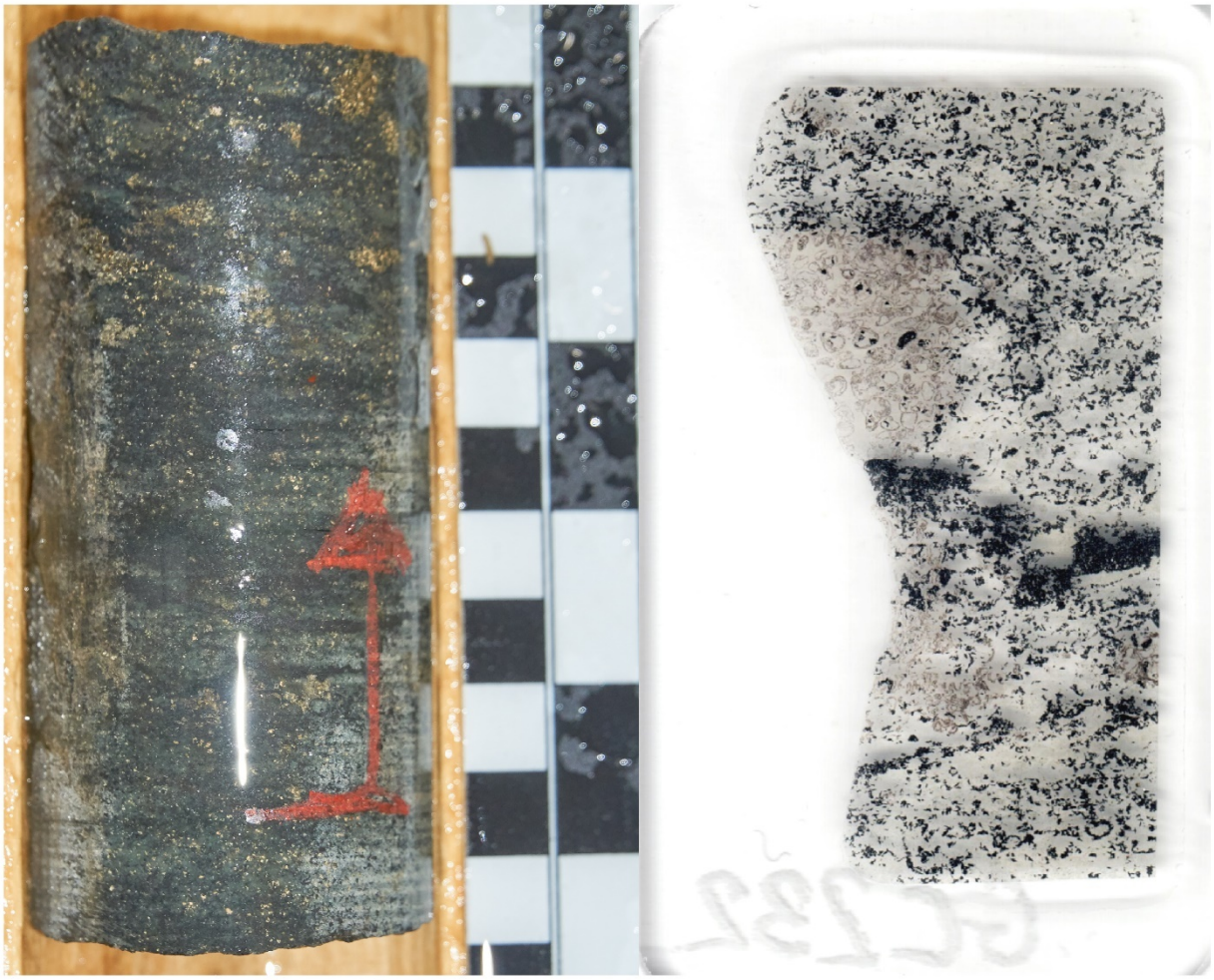

ID: GC232
Drillhole: 12-SL-1017D *Bulk sample:* Y
Depth (m): 79.50–79.60 *Chert subsample:* N

Figure A8.33. Drill core photograph and thin section scans (PPL, XPL) for sample GC232. Thin section dimensions are 25 x 46 mm.

ID: URC233
Drillhole: 12-SL-1017D *Bulk sample:* Y
Depth (m): 81.18–81.28 *Chert subsample:* N

Figure A8.34. Drill core photograph of sample URC233.

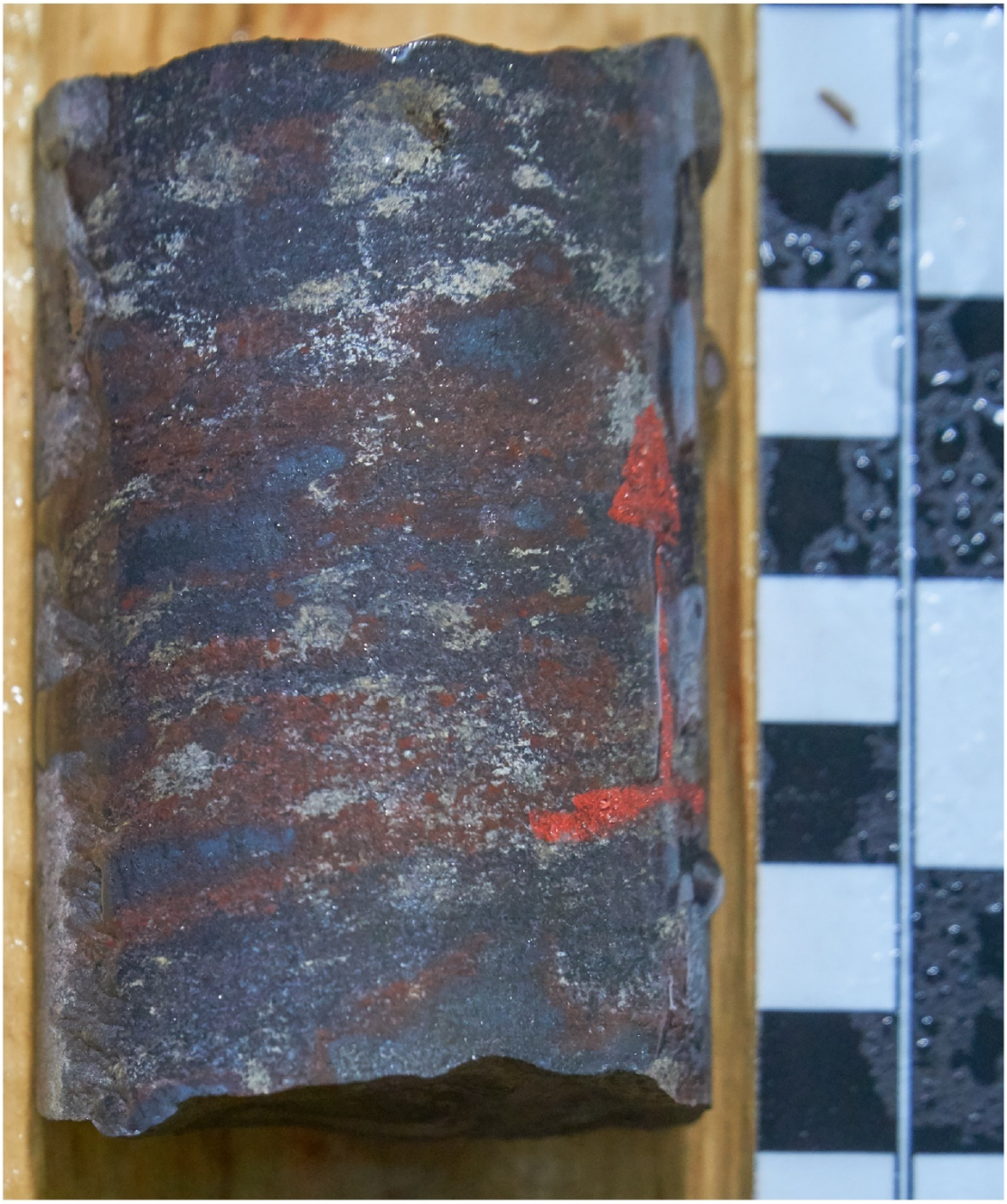

ID: URC235
Drillhole: 12-SL-1017D *Bulk sample:* Y
Depth (m): 83.31–83.38 *Chert subsample:* N

Figure A8.35. Drill core photograph of sample URC235.

ID: PGC236
Drillhole: 12-SL-1017D *Bulk sample:* Y
Depth (m): 85.14–85.24 *Chert subsample:* N

Figure A8.36. Drill core photograph of sample PGC236.

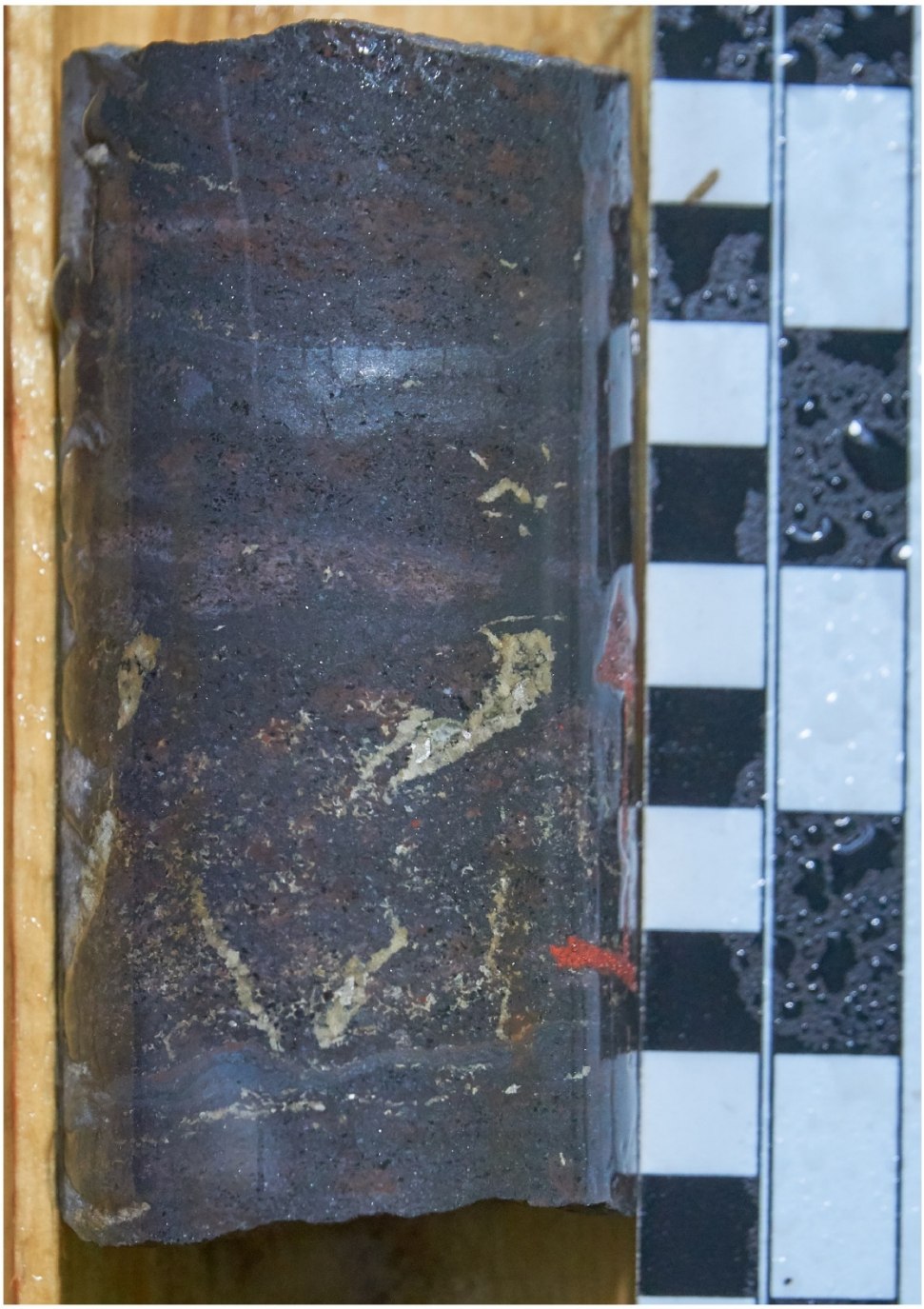

ID: PGC238
Drillhole: 12-SL-1017D *Bulk sample:* Y
Depth (m): 90.66–90.75 *Chert subsample:* N

Figure A8.37. Drill core photograph of sample PGC238.

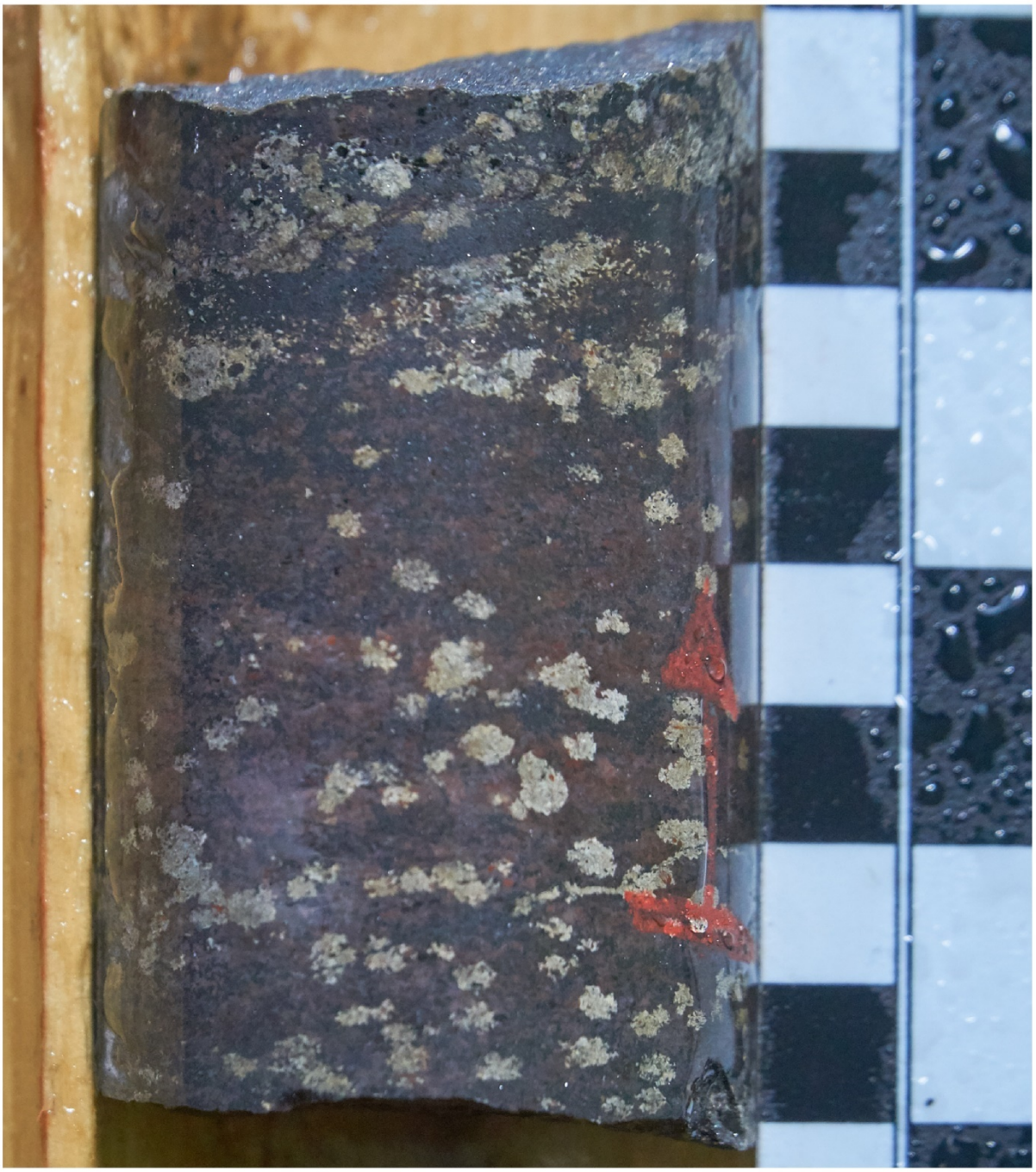

ID: LRC239
Drillhole: 12-SL-1017D *Bulk sample:* Y
Depth (m): 91.96–92.04 *Chert subsample:* N

Figure A8.38. Drill core photograph of sample LRC239.

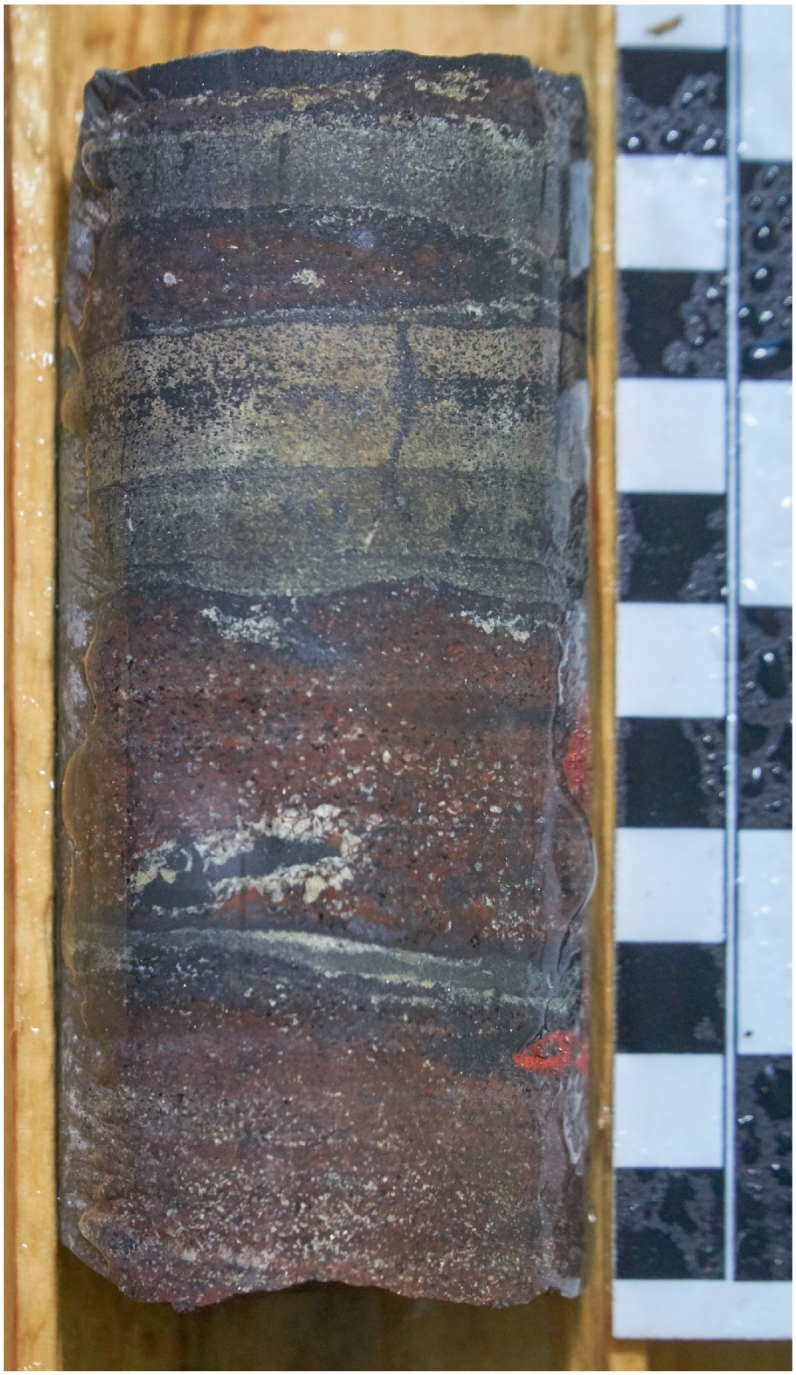

ID: LRGC241
Drillhole: 12-SL-1017D *Bulk sample:* Y
Depth (m): 95.10–95.21 *Chert subsample:* N

Figure A8.39. Drill core photograph of sample LRGC241.

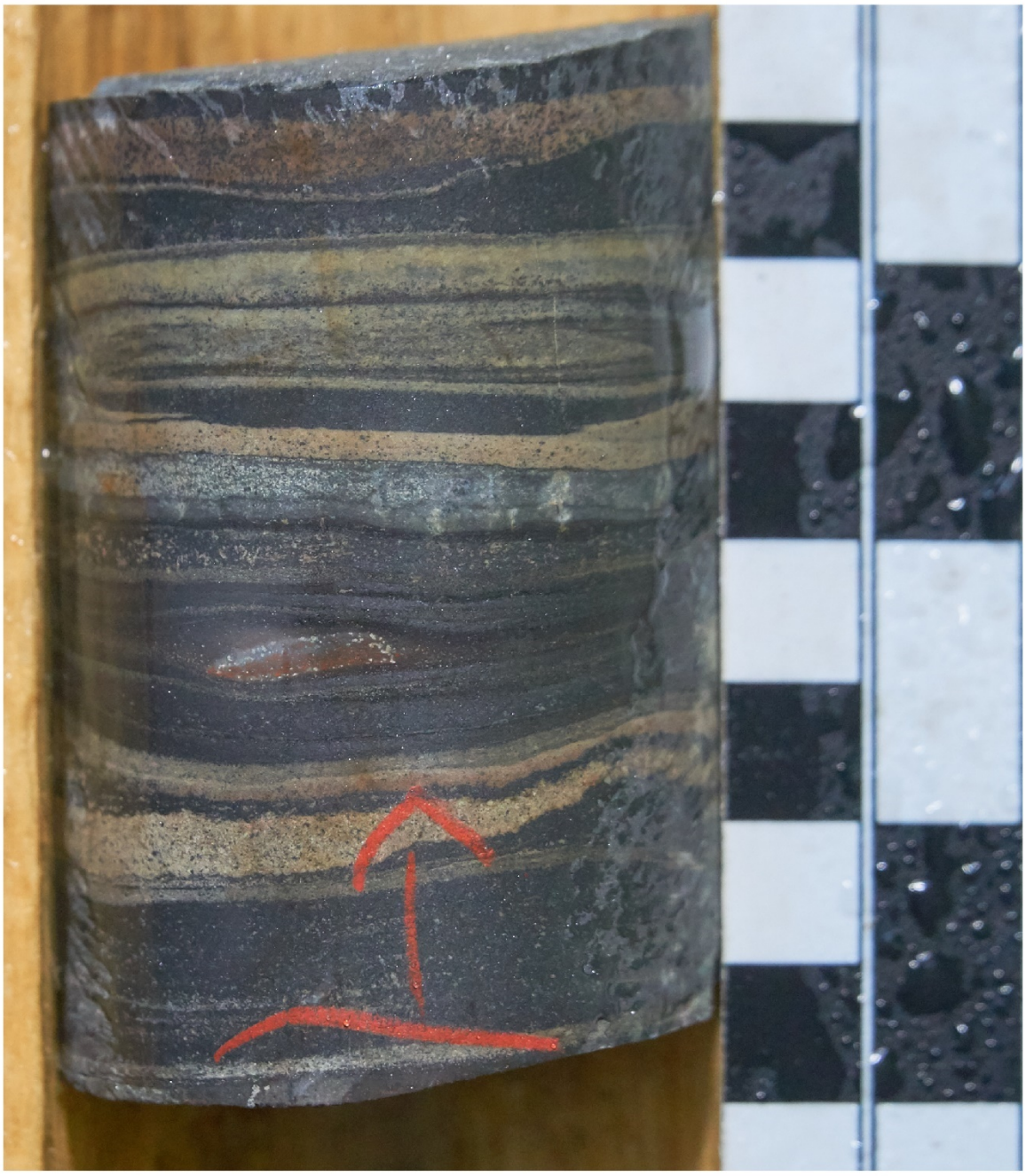

ID: LRGC247
Drillhole: 12-SL-1017D *Bulk sample:* Y
Depth (m): 116.39–116.46 *Chert subsample:* N

Figure A8.40. Drill core photograph of sample LRGC247.

ID: LRGC250
Drillhole: 12-SL-1017D *Bulk sample:* Y
Depth (m): 126.63–126.74 *Chert subsample:* N

Figure A8.41. Drill core photograph of sample LRGC250.

ID: LIF252
Drillhole: 12-SL-1017D *Bulk sample:* Y
Depth (m): 131.14–131.24 *Chert subsample:* N

Figure A8.42. Drill core photograph of sample LIF252.

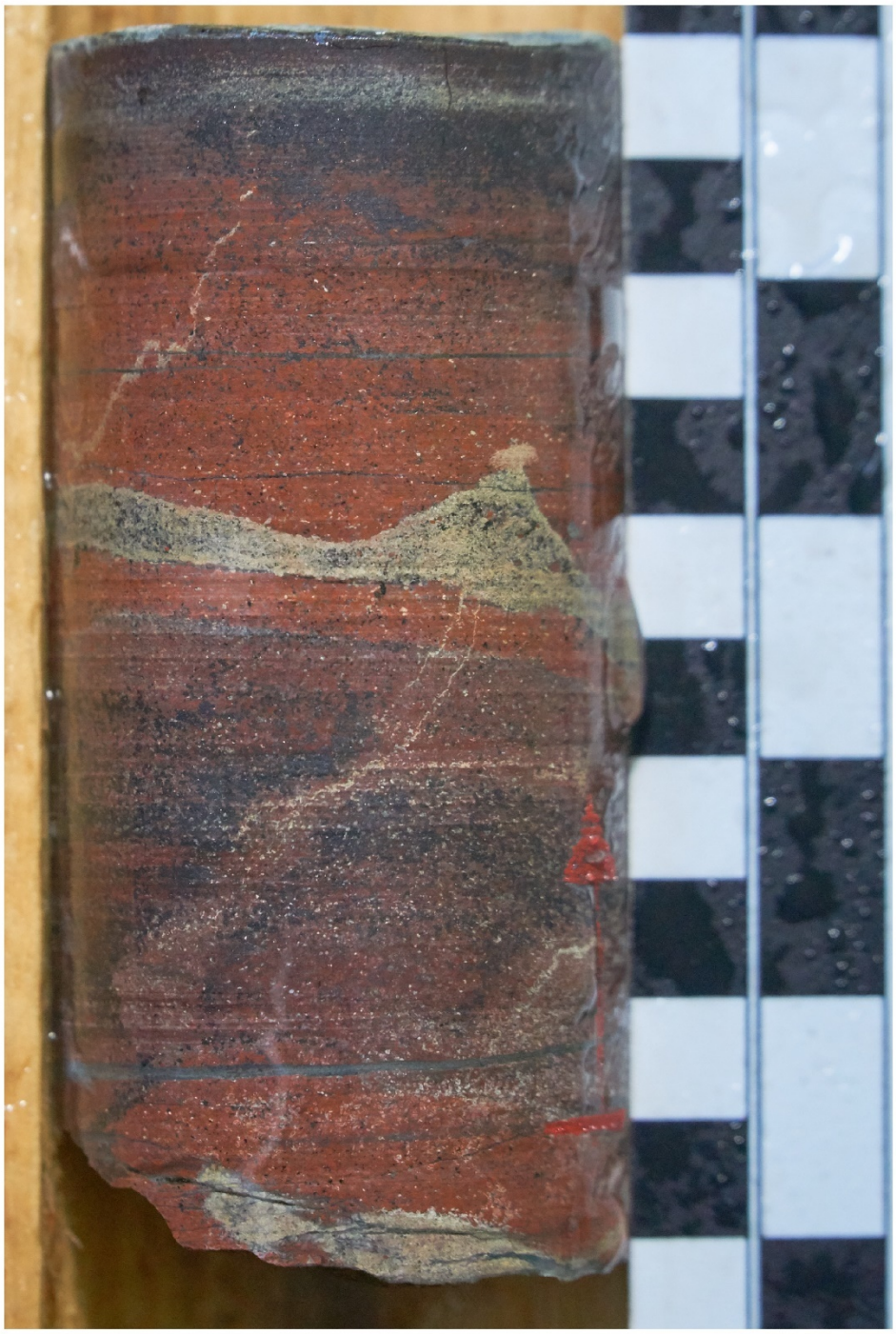

ID: JUIF254
Drillhole: 12-SL-1011D *Bulk sample:* Y
Depth (m): 72.43–72.53 *Chert subsample:* N

Figure A8.43. Drill core photograph of sample JUIF254.

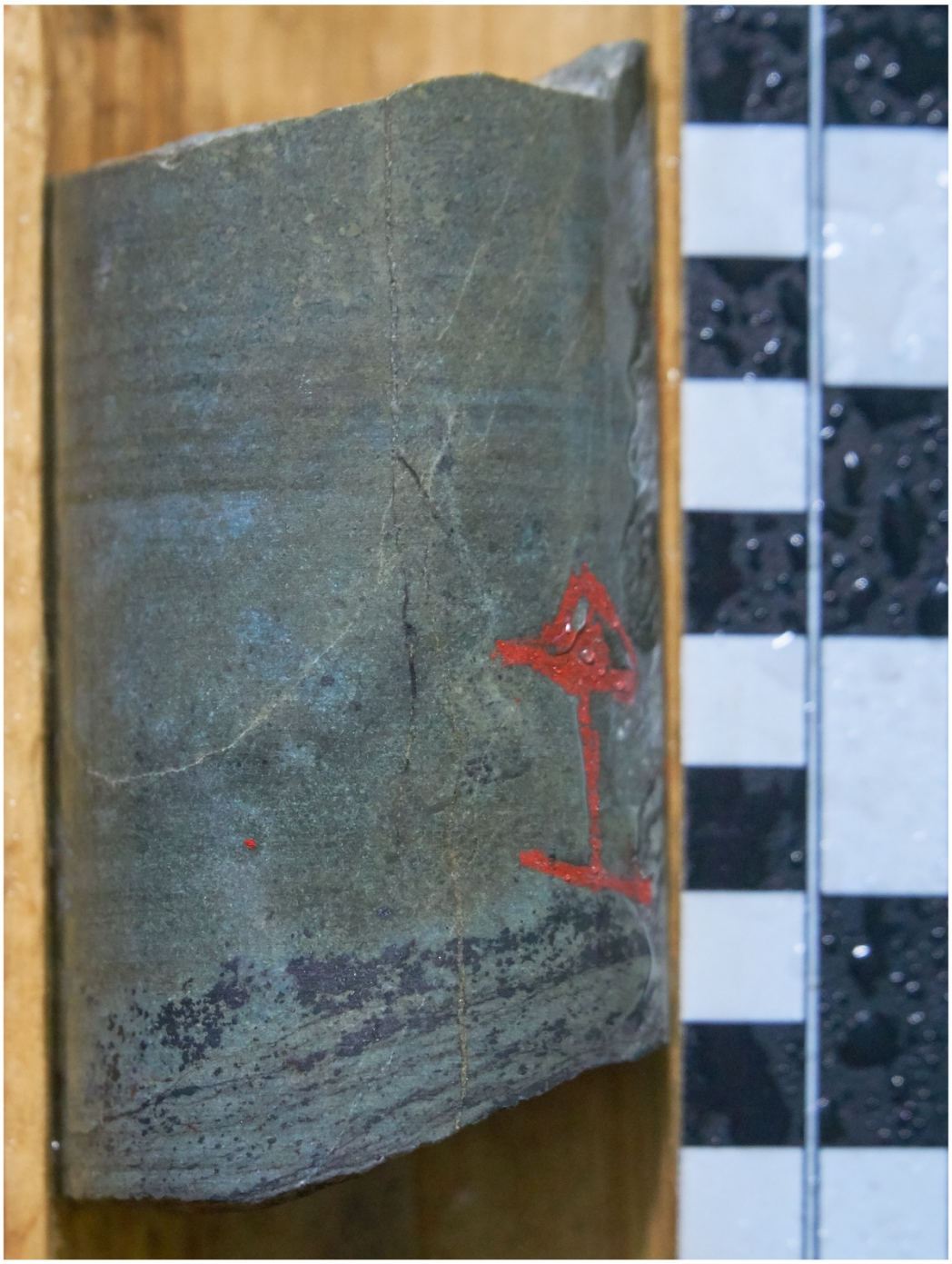

ID: GC256
Drillhole: 12-SL-1011D *Bulk sample:* Y
Depth (m): 75.05–75.13 *Chert subsample:* N

Figure A8.44. Drill core photograph of sample GC256.

Figure A8.45. Drill core photograph and thin section scans (PPL, XPL) for sample LC069. Thin section dimensions are 25 x 46 mm.

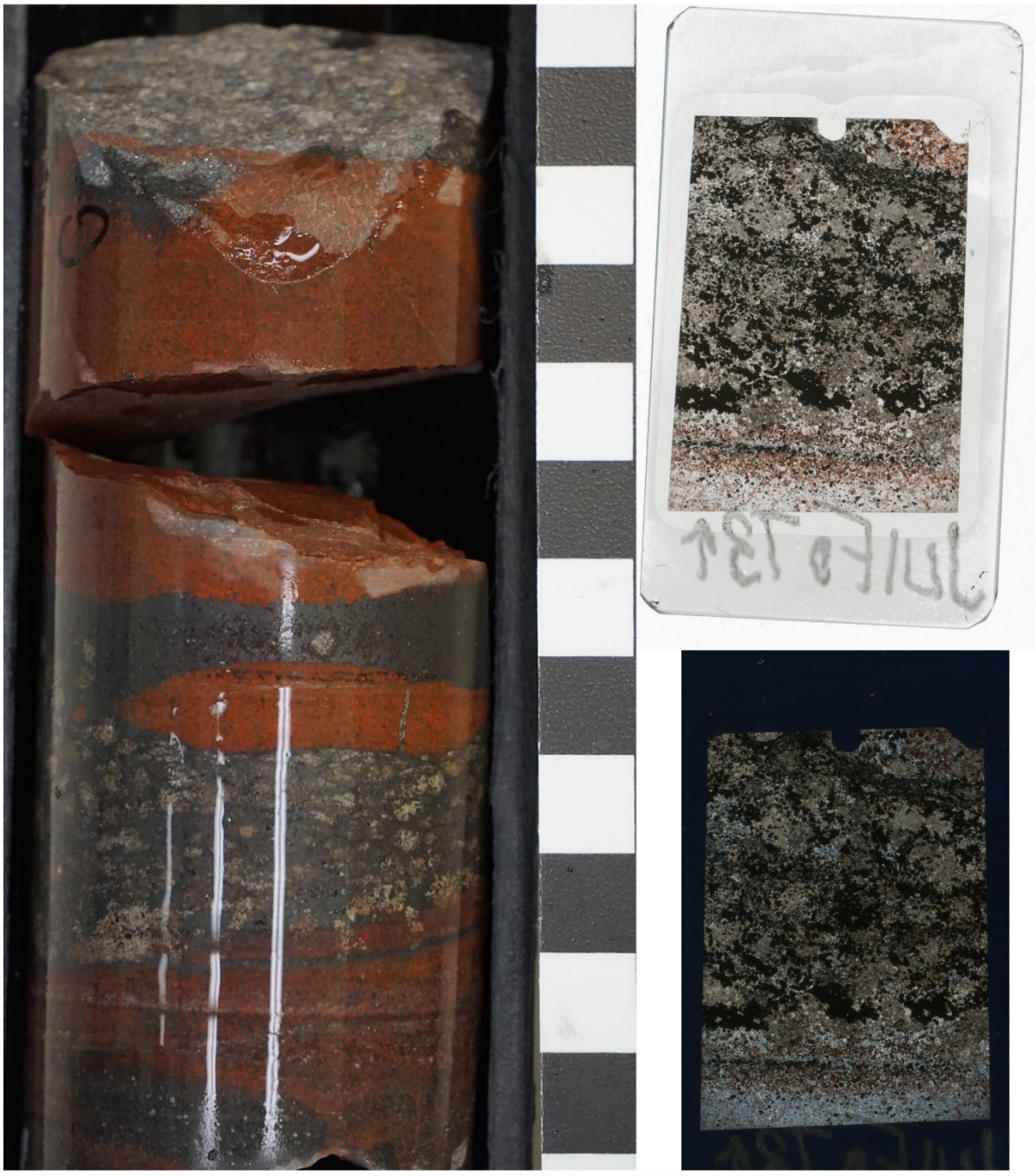

ID: JUIF073
Drillhole: 12-SL-1005D *Bulk sample:* Y
Depth (m): 30.26–30.36 *Chert subsample:* Y

Figure A8.46. Drill core photograph and thin section scans (PPL, XPL) for sample JUIF073. Thin section dimensions are 25 x 46 mm.

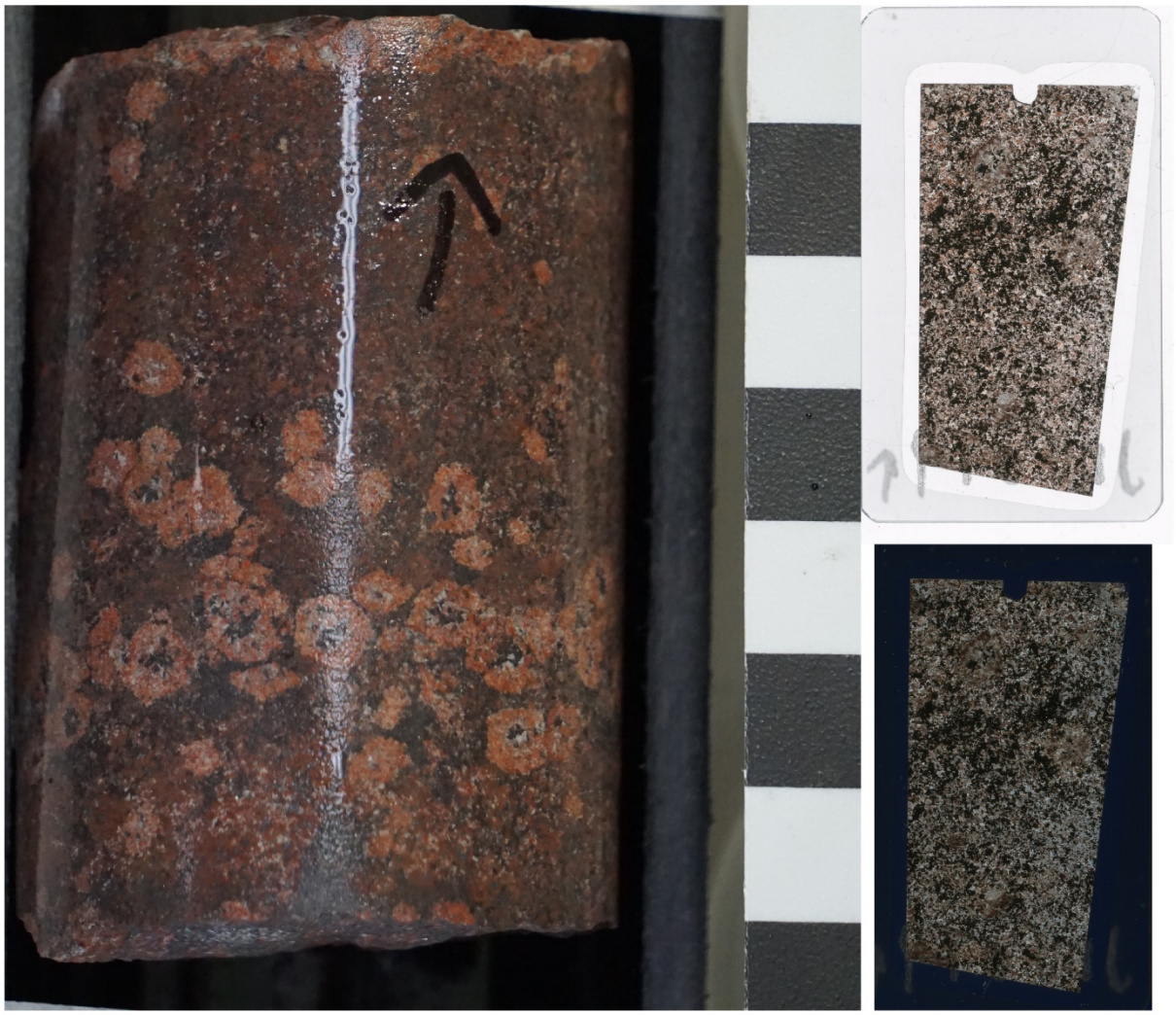

ID: JUIF079
Drillhole: 12-SL-1005D *Bulk sample:* Y
Depth (m): 42.91–42.98 *Chert subsample:* N

Figure A8.47. Drill core photograph and thin section scans (PPL, XPL) for sample JUIF079. Thin section dimensions are 25 x 46 mm.

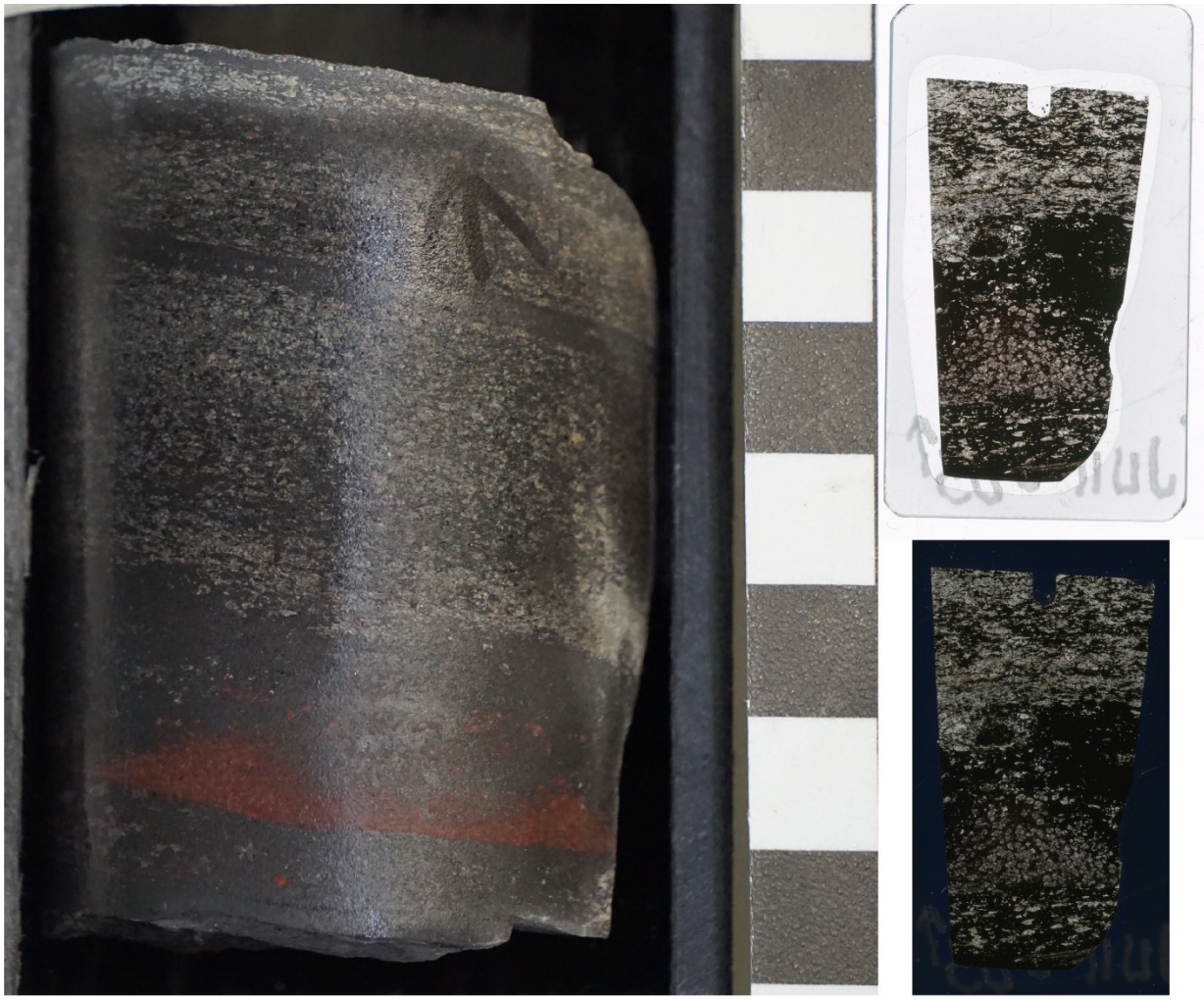

ID: JUIF083
Drillhole: 12-SL-1005D *Bulk sample:* Y
Depth (m): 54.27–54.33 *Chert subsample:* N

Figure A8.48. Drill core photograph and thin section scans (PPL, XPL) for sample JUIF083. Thin section dimensions are 25 x 46 mm.

Figure A8.49. Drill core photograph and thin section scans (PPL, XPL) for sample GC084. Thin section dimensions are 25 x 46 mm.

Figure A8.50. Drill core photograph and thin section scans (PPL, XPL) for sample GC085. Thin section dimensions are 25 x 46 mm.

Figure A8.51. Drill core photograph and thin section scans (PPL, XPL) for sample URC086. Thin section dimensions are 25 x 46 mm.

ID: URC087
Drillhole: 12-SL-1005D *Bulk sample:* N
Depth (m): 59.90–59.97 *Chert subsample:* N

Figure A8.52. Drill core photograph and thin section scans (PPL, XPL) for sample URC087. Thin section dimensions are 25 x 46 mm.

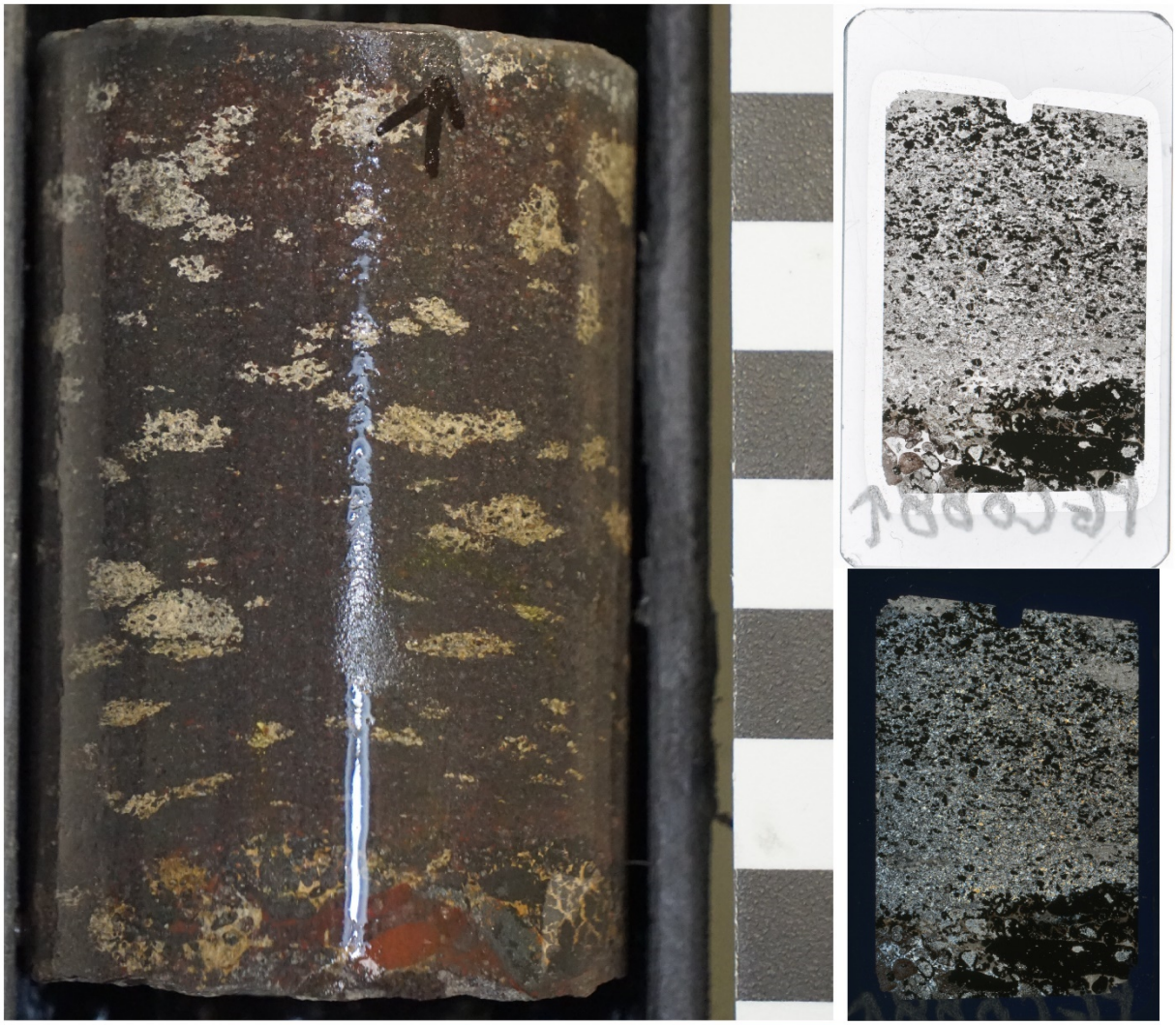

ID: PGC088
Drillhole: 12-SL-1005D *Bulk sample:* Y
Depth (m): 61.12–61.19 *Chert subsample:* N

Figure A8.53. Drill core photograph and thin section scans (PPL, XPL) for sample PGC088. Thin section dimensions are 25 x 46 mm.

Figure A8.54. Drill core photograph and thin section scans (PPL, XPL) for sample LRC092. Thin section dimensions are 25 x 46 mm.

Figure A8.55. Drill core photograph and thin section scans (PPL, XPL) for sample LRGC094. Thin section dimensions are 25 x 46 mm.

ID: LRGC103
Drillhole: 12-SL-1005D *Bulk sample:* Y
Depth (m): 93.00–93.08 *Chert subsample:* N

Figure A8.56. Drill core photograph and thin section scans (PPL, XPL) for sample LRGC103. Thin section dimensions are 25 x 46 mm.

ID: LIF109
Drillhole: 12-SL-1005D *Bulk sample:* Y
Depth (m): 106.83–106.94 *Chert subsample:* N

Figure A8.57. Drill core photograph and thin section scans (PPL, XPL) for sample LIF109. Thin section dimensions are 25 x 46 mm.

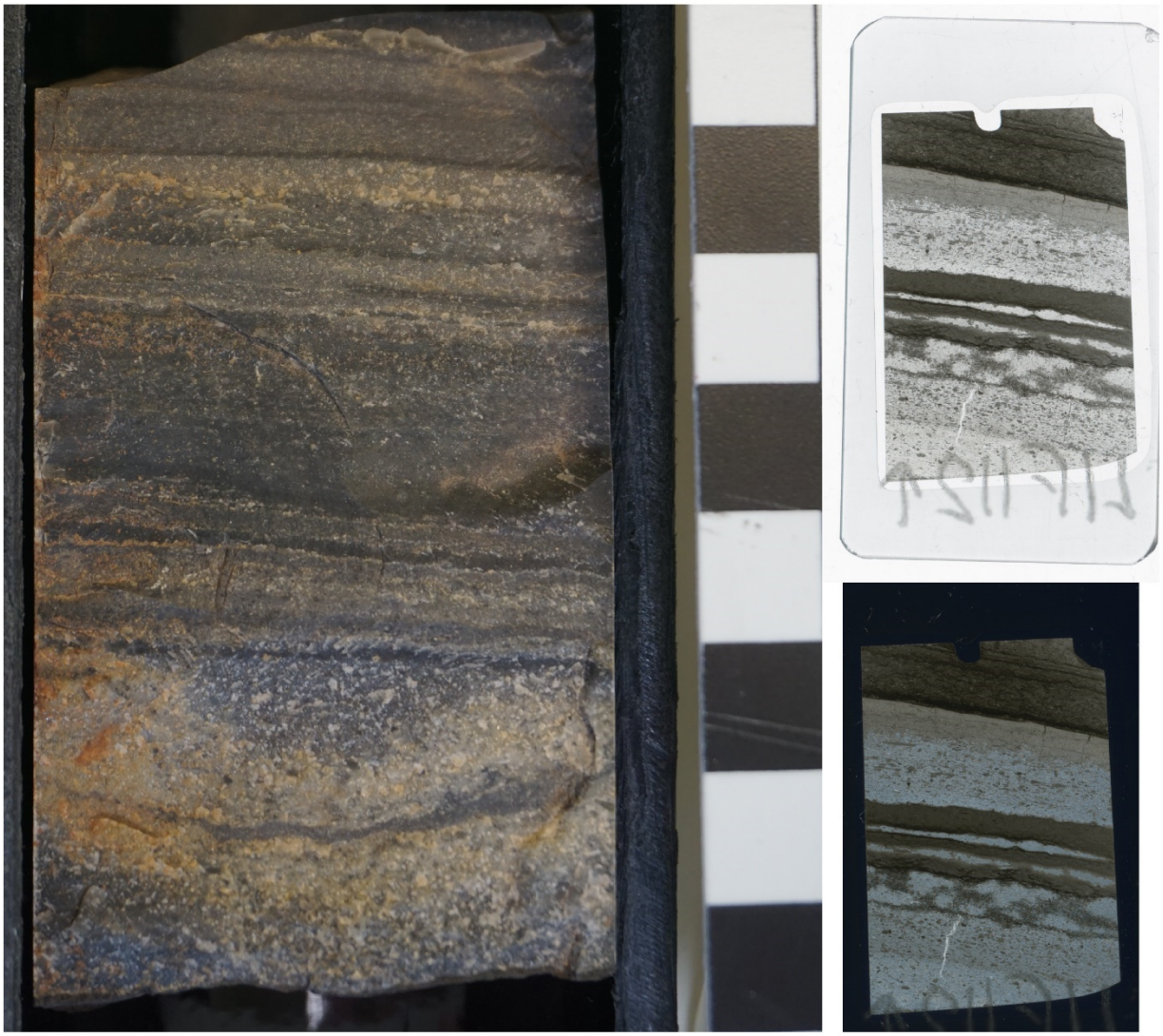

Figure A8.58. Drill core photograph and thin section scans (PPL, XPL) for sample LIF112. Thin section dimensions are 25 x 46 mm.

Figure A8.59. Drill core photograph and thin section scans (PPL, XPL) for sample LC145. Thin section dimensions are 25 x 46 mm.

ID: JUIF146
Drillhole: 11-LR-1010D *Bulk sample:* Y
Depth (m): 13.67–13.78 *Chert subsample:* N

Figure A8.60. Drill core photograph of sample JUIF146.

ID: GC147
Drillhole: 11-LR-1010D *Bulk sample:* Y
Depth (m): 18.21–18.29 *Chert subsample:* N

Figure A8.61. Drill core photograph of sample GC147.

ID: URC148
Drillhole: 11-LR-1010D *Bulk sample:* Y
Depth (m): 19.86–20.00 *Chert subsample:* Y

Figure A8.62. Drill core photograph and thin section scans (PPL, XPL) for sample URC148. Thin section dimensions are 25 x 46 mm.

Figure A8.63. Drill core photograph and thin section scans (PPL, XPL) for sample PGC150. Thin section dimensions are 25 x 46 mm.

Figure A8.64. Drill core photograph and thin section scans (PPL, XPL) for sample PGC152. Thin section dimensions are 25 x 46 mm.

Figure A8.65. Drill core photograph and thin section scans (PPL, XPL) for sample LRGC154. Thin section dimensions are 25 x 46 mm.

ID: JSP158
Drillhole: 11-LR-1010D *Bulk sample:* Y
Depth (m): 58.70–58.80 *Chert subsample:* Y

Figure A8.66. Drill core photograph and thin section scans (PPL, XPL) for sample JSP158. Thin section dimensions are 25 x 46 mm.

ID: JSP163
Drillhole: 11-LR-1010D *Bulk sample:* Y
Depth (m): 72.18–72.24 *Chert subsample:* Y

Figure A8.67. Drill core photograph of sample JSP163.

ID: DOL300
Drillhole: 11-LR-1005D *Bulk sample:* Y
Depth (m): 11.17–11.42 *Chert subsample:* N

Figure A8.68. Drill core photograph of sample DOL300.

ID: LC301
Drillhole: 11-LR-1005D *Bulk sample:* N
Depth (m): 14.00–14.21 *Chert subsample:* N

Figure A8.69. Drill core photograph and thin section scans (PPL, XPL) for sample LC301. Thin section dimensions are 25 x 46 mm.

ID: LC302
Drillhole: 11-LR-1005D *Bulk sample:* Y
Depth (m): 15.90–16.11 *Chert subsample:* N

Figure A8.70. Drill core photograph of sample LC302.

ID: JUIF304
Drillhole: 11-LR-1005D *Bulk sample:* Y
Depth (m): 25.00–25.33 *Chert subsample:* N

Figure A8.71. Drill core photograph of sample JUIF304.

ID: JUIF307
Drillhole: 11-LR-1005D *Bulk sample:* Y
Depth (m): 31.70–31.86 *Chert subsample:* N

Figure A8.72. Drill core photograph of sample JUIF307.

ID: JUIF309
Drillhole: 11-LR-1005D *Bulk sample:* Y
Depth (m): 35.15–35.29 *Chert subsample:* N

Figure A8.73. Drill core photograph of sample JUIF309.

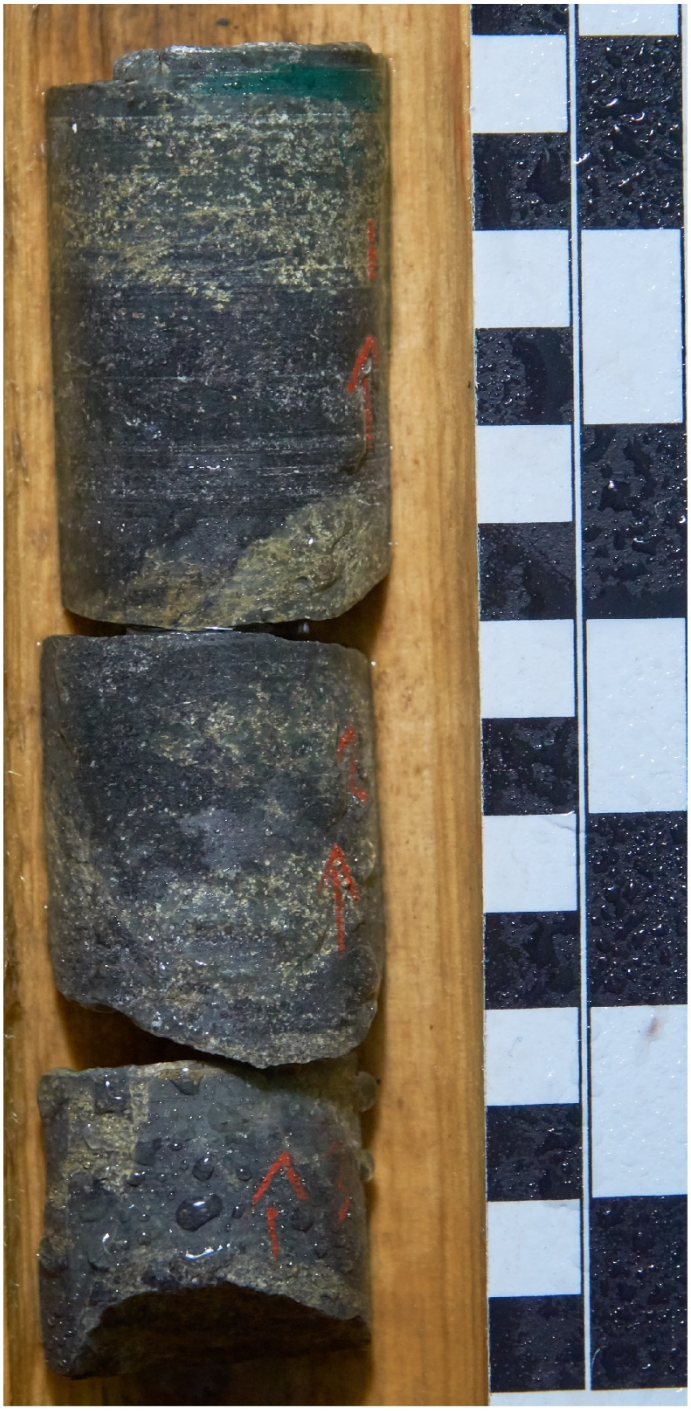

ID: JUIF311
Drillhole: 11-LR-1005D *Bulk sample:* Y
Depth (m): 40.61–40.74 *Chert subsample:* N

Figure A8.74. Drill core photograph of sample JUIF311.

ID: LC260
Drillhole: 11-LR-1012D *Bulk sample:* Y
Depth (m): 16.90–17.05 *Chert subsample:* N

Figure A8.75. Drill core photograph of sample LC260.

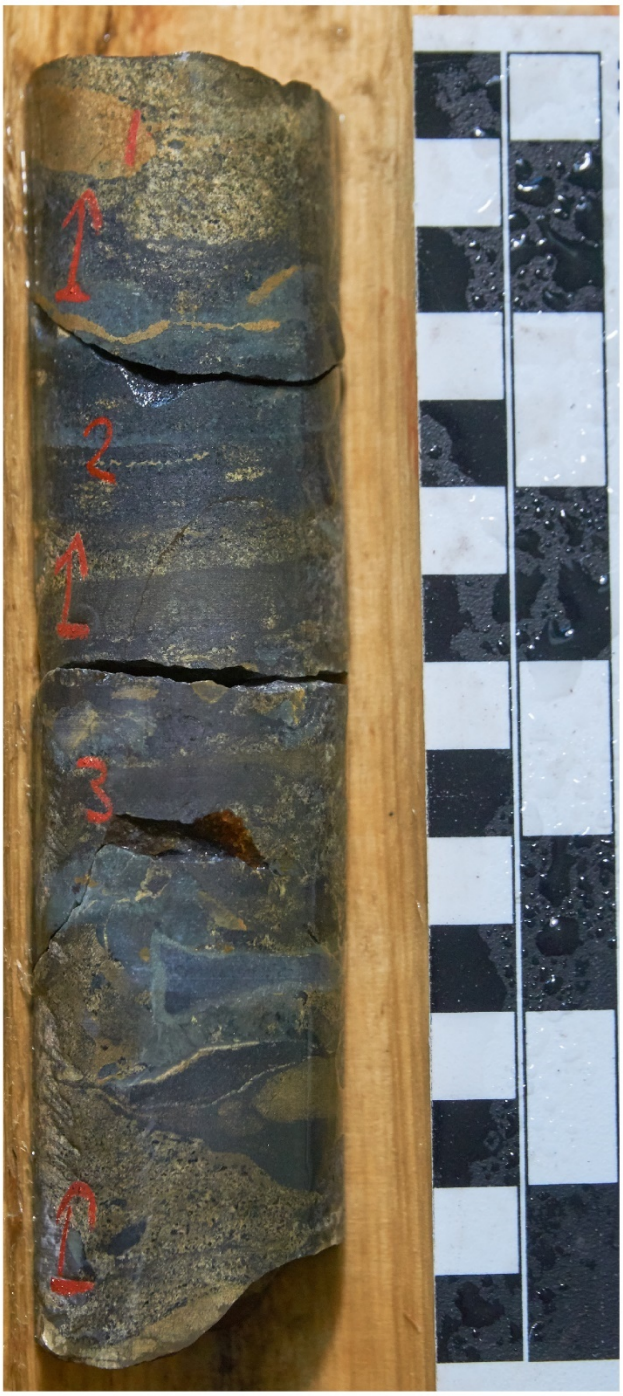

ID: LC263
Drillhole: 11-LR-1012D *Bulk sample:* Y
Depth (m): 24.00–24.15 *Chert subsample:* N

Figure A8.76. Drill core photograph of sample LC263.

ID: LC264
Drillhole: 11-LR-1012D *Bulk sample:* Y
Depth (m): 34.70–34.84 *Chert subsample:* N

Figure A8.77. Drill core photograph of sample LC145.

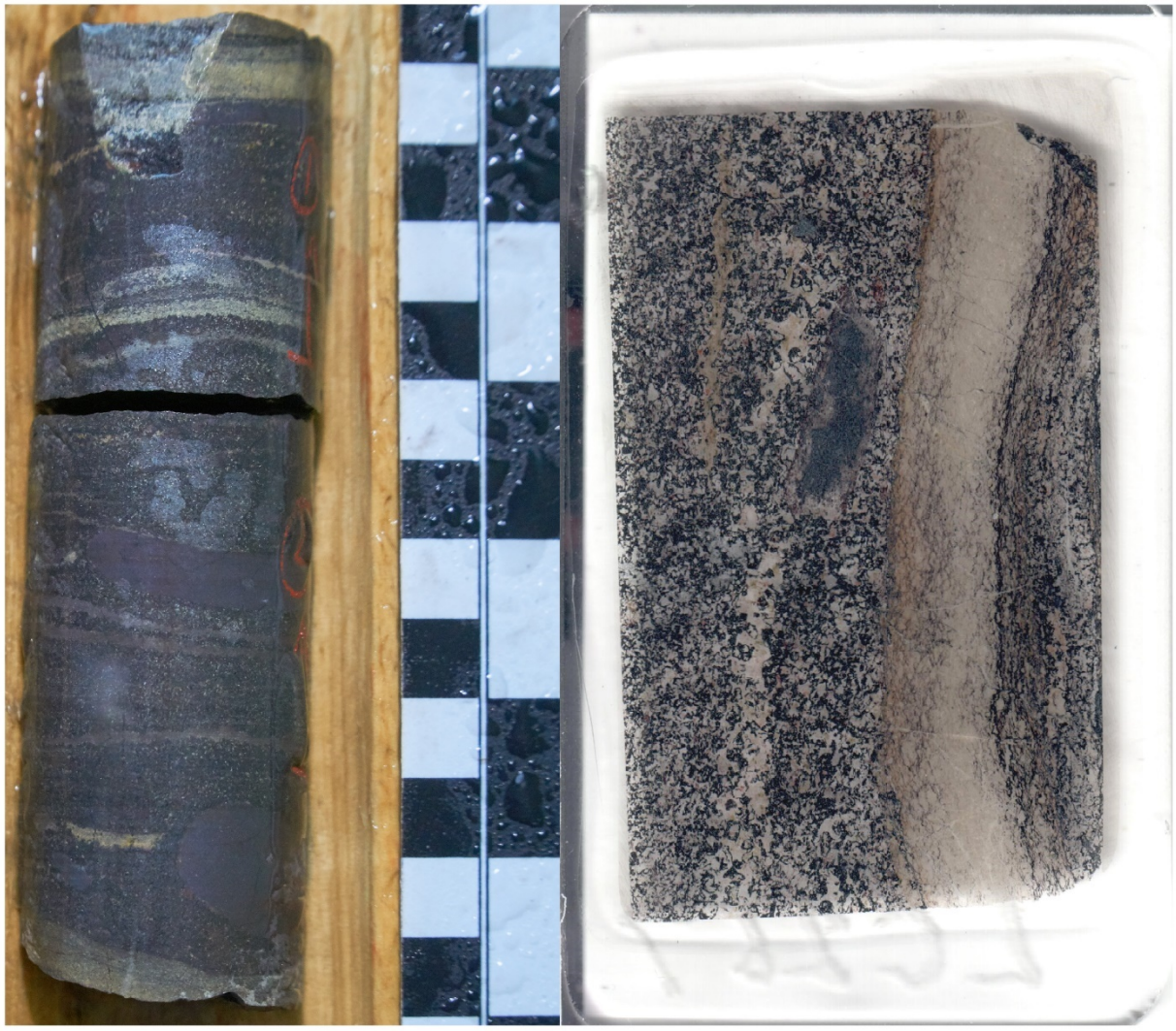

Figure A8.78. Drill core photograph and thin section scans (PPL, XPL) for sample LC267. Thin section dimensions are 25 x 46 mm.

ID: GC269
Drillhole: 11-LR-1012D *Bulk sample:* Y
Depth (m): 51.16–51.30 *Chert subsample:* N

Figure A8.79. Drill core photograph of sample GC269.

ID: URC272
Drillhole: 11-LR-1012D *Bulk sample:* Y
Depth (m): 57.16–57.30 *Chert subsample:* N

Figure A8.80. Drill core photograph of sample URC272.

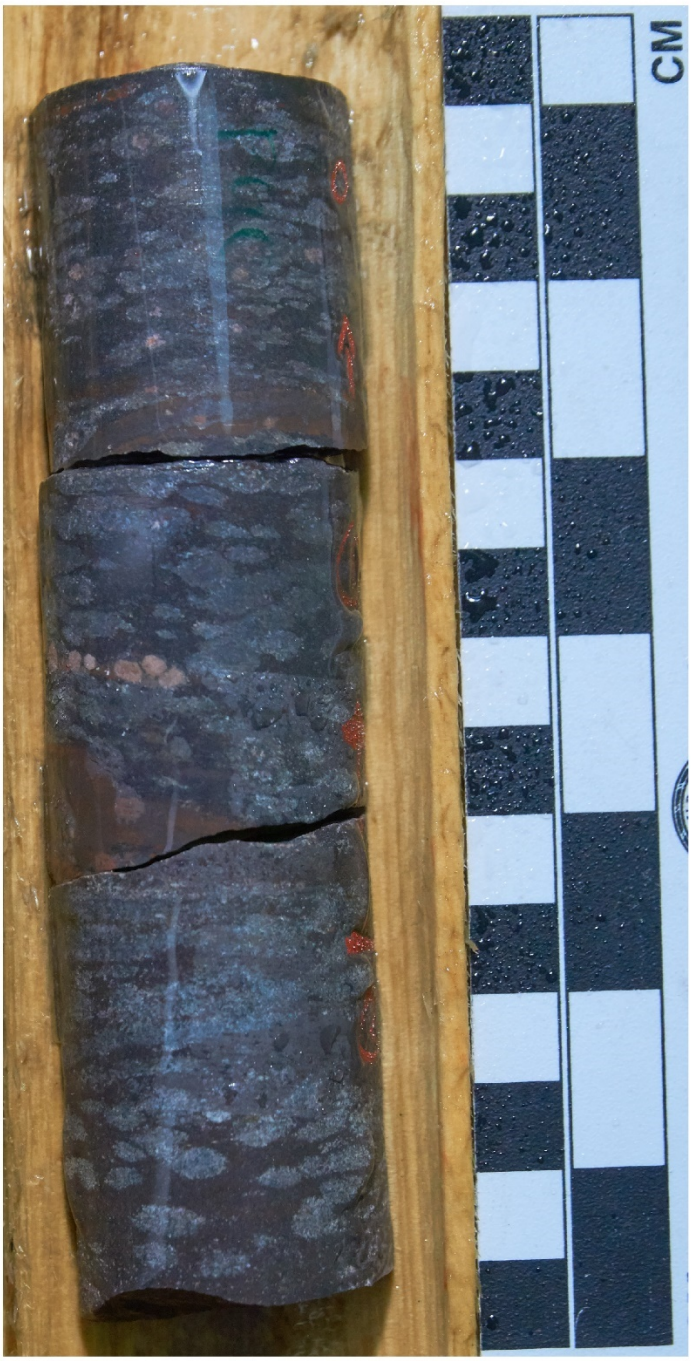

ID: PGC276
Drillhole: 11-LR-1012D *Bulk sample:* Y
Depth (m): 61.88–62.02 *Chert subsample:* N

Figure A8.81. Drill core photograph of sample PGC276.

ID: LRGC280
Drillhole: 11-LR-1012D *Bulk sample:* Y
Depth (m): 70.24–70.42 *Chert subsample:* N

Figure A8.82. Drill core photograph of sample LRGC280.

ID: LRGC284
Drillhole: 12-SL-1018D *Bulk sample:* Y
Depth (m): 84.39–84.63 *Chert subsample:* N

Figure A8.83. Drill core photograph of sample LRGC284.

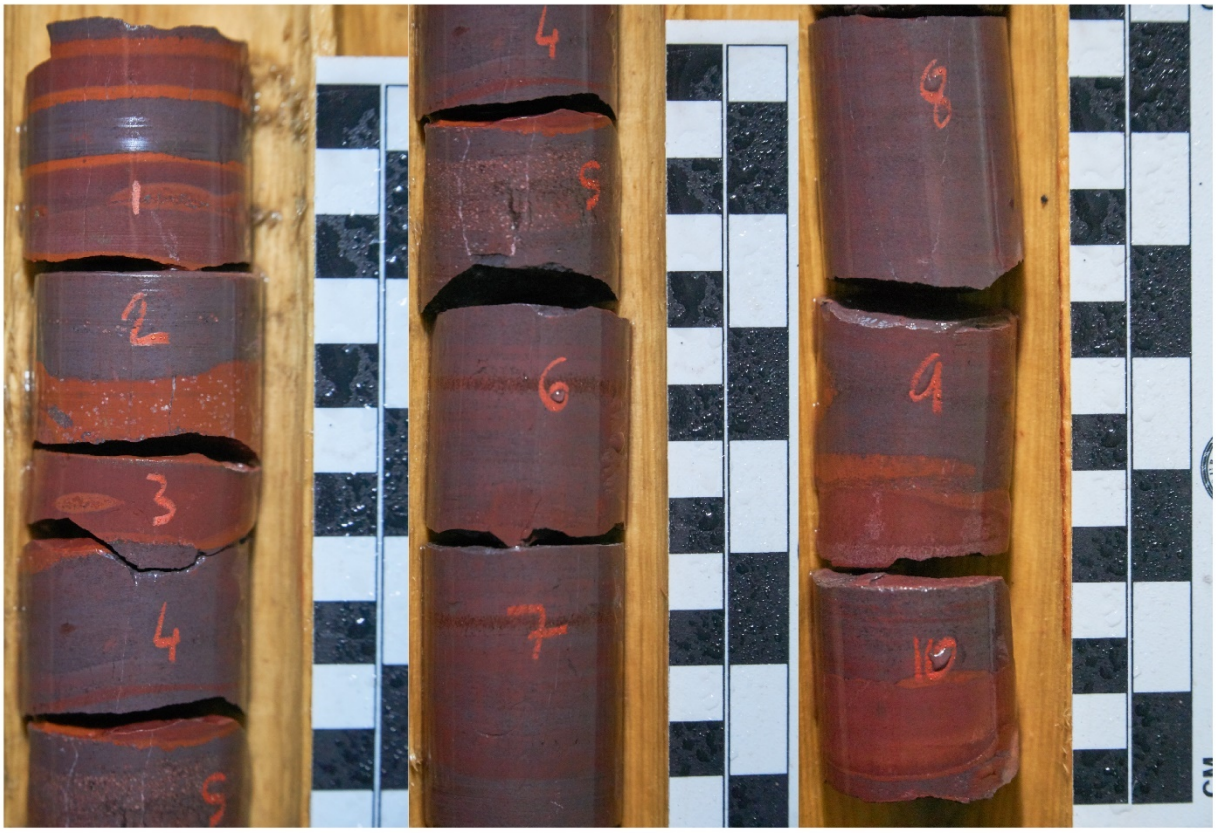

ID: JSP289
Drillhole: 11-LR-1012D *Bulk sample:* Y
Depth (m): 94.86–95.13 *Chert subsample:* N

Figure A8.84. Drill core photograph of sample JSP289.

ID: JSP294
Drillhole: 11-LR-1012D *Bulk sample:* Y
Depth (m): 113.20–113.43 *Chert subsample:* N

Figure A8.85. Drill core photograph and thin section scans (PPL, XPL) for sample JSP294. Thin section dimensions are 25 x 46 mm.

ID: RTH296
Drillhole: 11-LR-1012D *Bulk sample:* Y
Depth (m): 115.12–115.28 *Chert subsample:* N

Figure A8.86. Drill core photograph of sample RTH296.

Figure A8.87. Drill core photograph and thin section scans (PPL, XPL) for sample DOL113. Thin section dimensions are 25 x 46 mm.

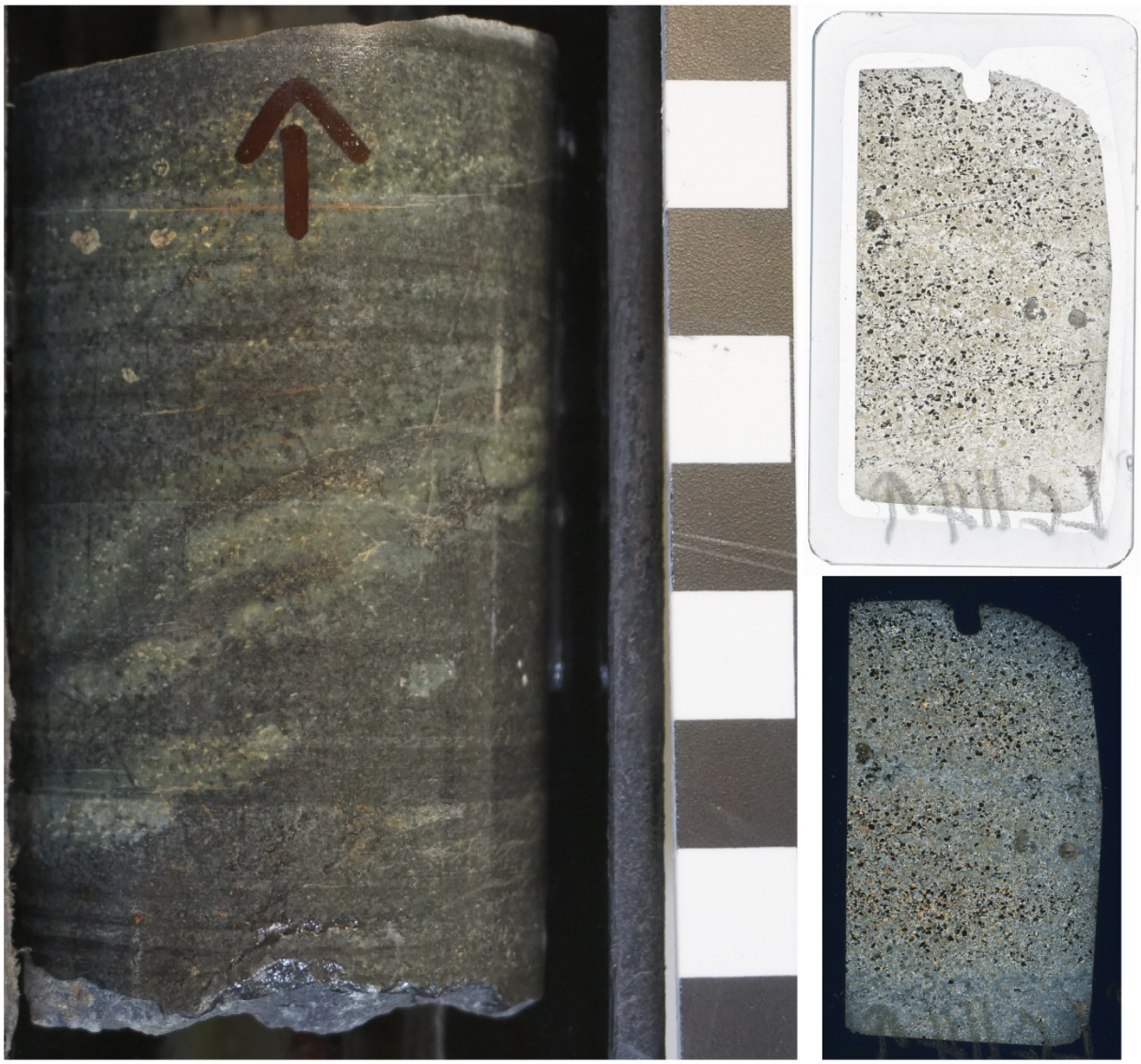

ID: LC114
Drillhole: 11-LR-1029D *Bulk sample:* Y
Depth (m): 36.13–36.21 *Chert subsample:* N

Figure A8.88. Drill core photograph and thin section scans (PPL, XPL) for sample LC114. Thin section dimensions are 25 x 46 mm.

Figure A8.89. Drill core photograph and thin section scans (PPL, XPL) for sample JUIF116. Thin section dimensions are 25 x 46 mm.

Figure A8.90. Drill core photograph and thin section scans (PPL, XPL) for sample JUIF119. Thin section dimensions are 25 x 46 mm.

Figure A8.91. Drill core photograph and thin section scans (PPL, XPL) for sample GC120. Thin section dimensions are 25 x 46 mm.

Figure A8.92. Drill core photograph and thin section scans (PPL, XPL) for sample JUIF121. Thin section dimensions are 25 x 46 mm.

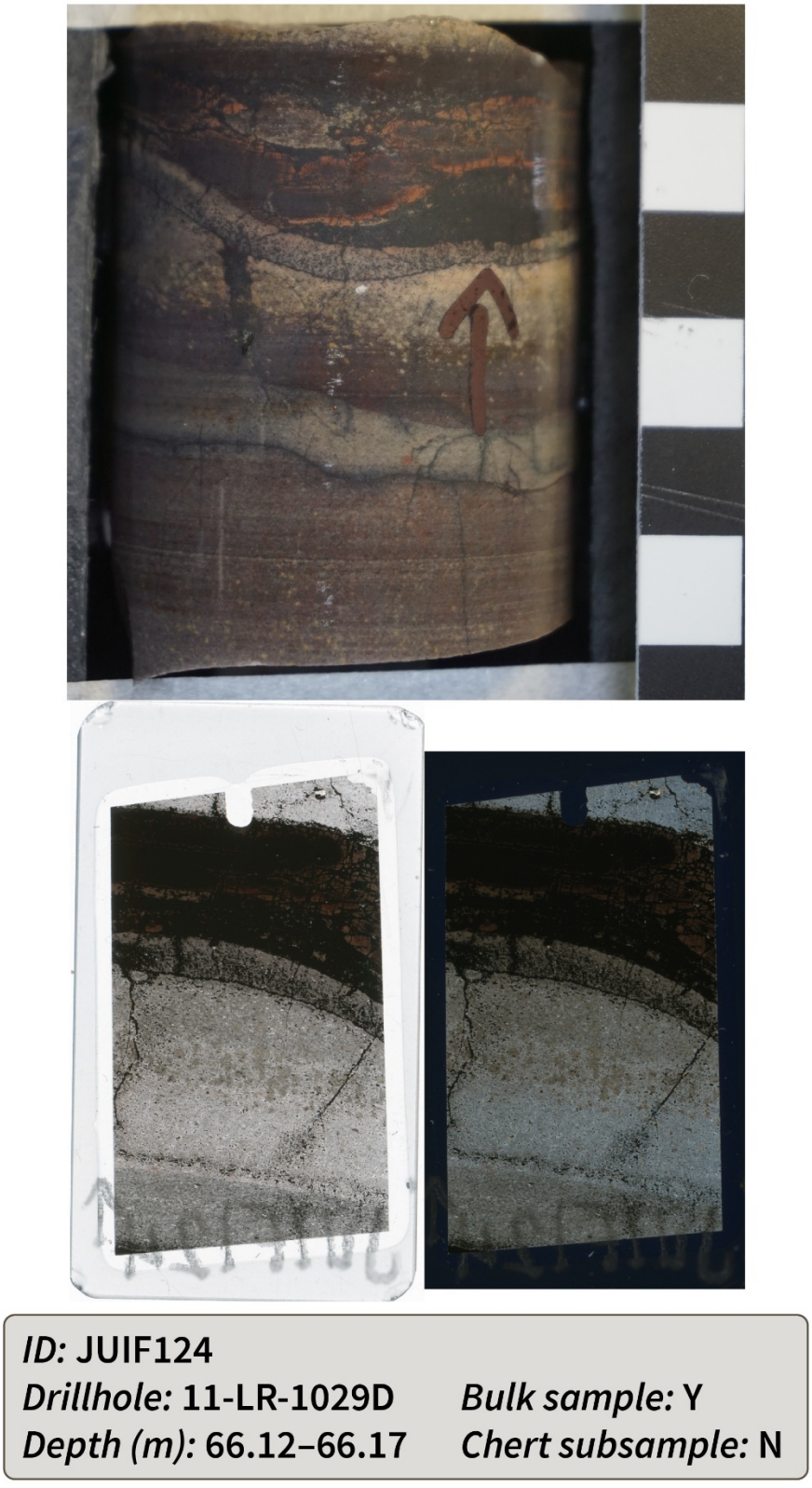

Figure A8.93. Drill core photograph and thin section scans (PPL, XPL) for sample JUIF124. Thin section dimensions are 25 x 46 mm.

ID: JUIF127
Drillhole: 11-LR-1029D *Bulk sample:* Y
Depth (m): 73.10–73.16 *Chert subsample:* N

Figure A8.94. Drill core photograph and thin section scans (PPL, XPL) for sample JUIF127. Thin section dimensions are 25 x 46 mm.

Figure A8.95. Drill core photograph and thin section scans (PPL, XPL) for sample JUIF131. Thin section dimensions are 25 x 46 mm.

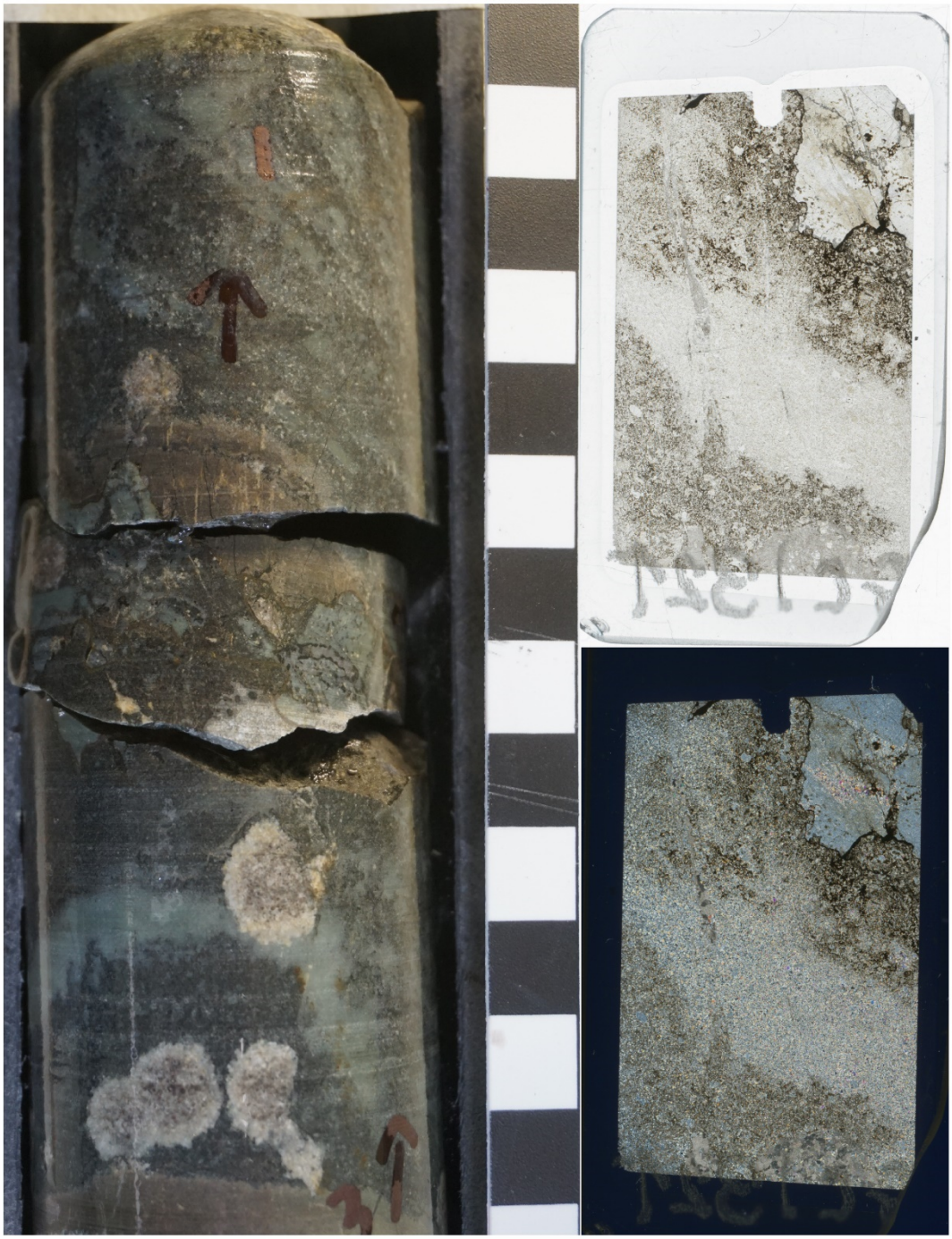

ID: GC132
Drillhole: 11-LR-1029D *Bulk sample:* Y
Depth (m): 95.45–95.58 *Chert subsample:* N

Figure A8.96. Drill core photograph and thin section scans (PPL, XPL) for sample GC132. Thin section dimensions are 25 x 46 mm.

Figure A8.97. Drill core photograph and thin section scans (PPL, XPL) for sample URC133. Thin section dimensions are 25 x 46 mm.

Figure A8.98. Drill core photograph and thin section scans (PPL, XPL) for sample PGC135. Thin section dimensions are 25 x 46 mm.

Figure A8.99. Drill core photograph and thin section scans (PPL, XPL) for sample LRGC138. Thin section dimensions are 25 x 46 mm.

ID: JSP140
Drillhole: 11-LR-1020D *Bulk sample:* Y
Depth (m): 5.25–5.35 *Chert subsample:* Y

Figure A8.100. Drill core photograph and thin section scans (PPL, XPL) for sample JSP140. Thin section dimensions are 25 x 46 mm.

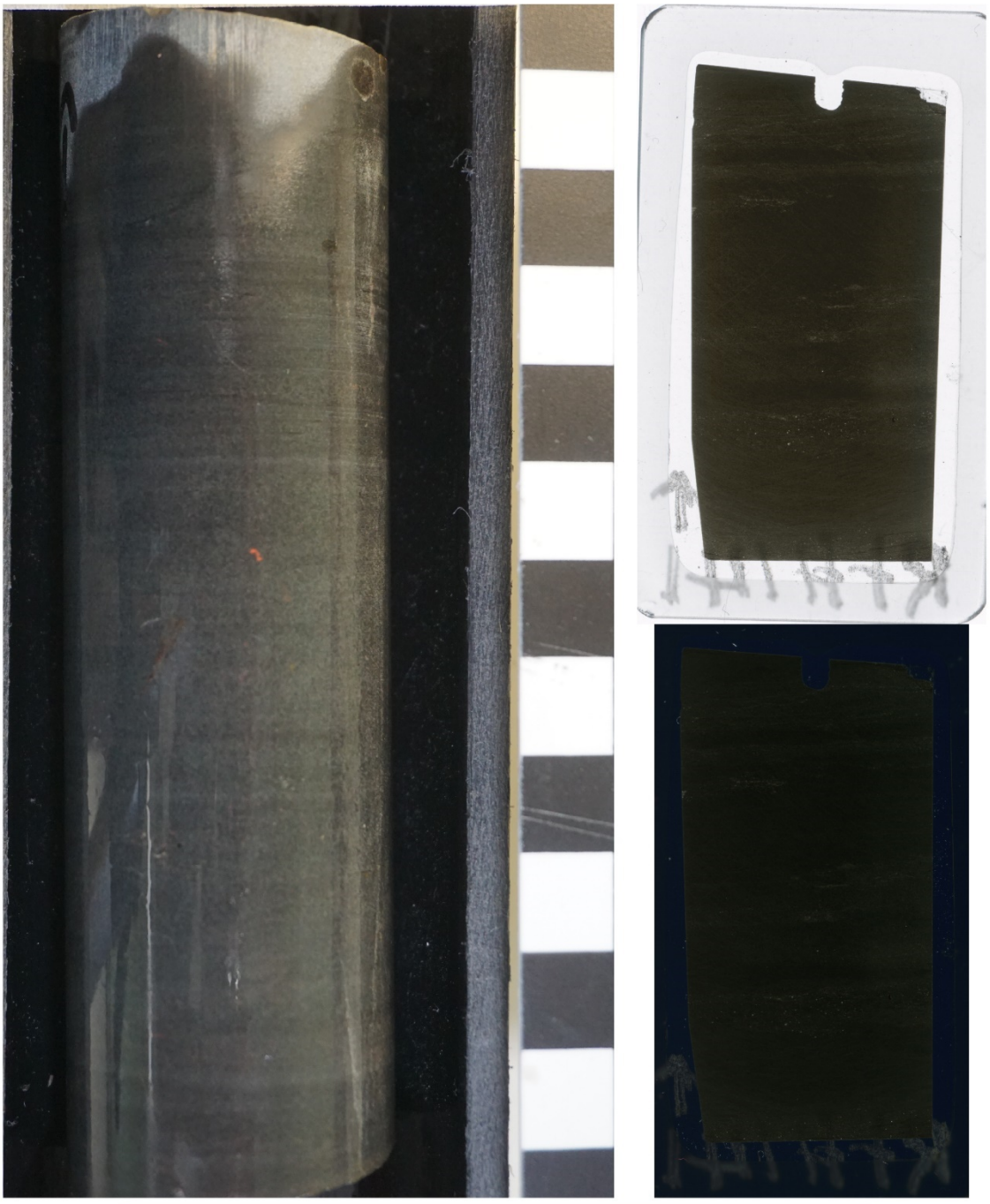

Figure A8.101. Drill core photograph and thin section scans (PPL, XPL) for sample RTH141. Thin section dimensions are 25 x 46 mm.

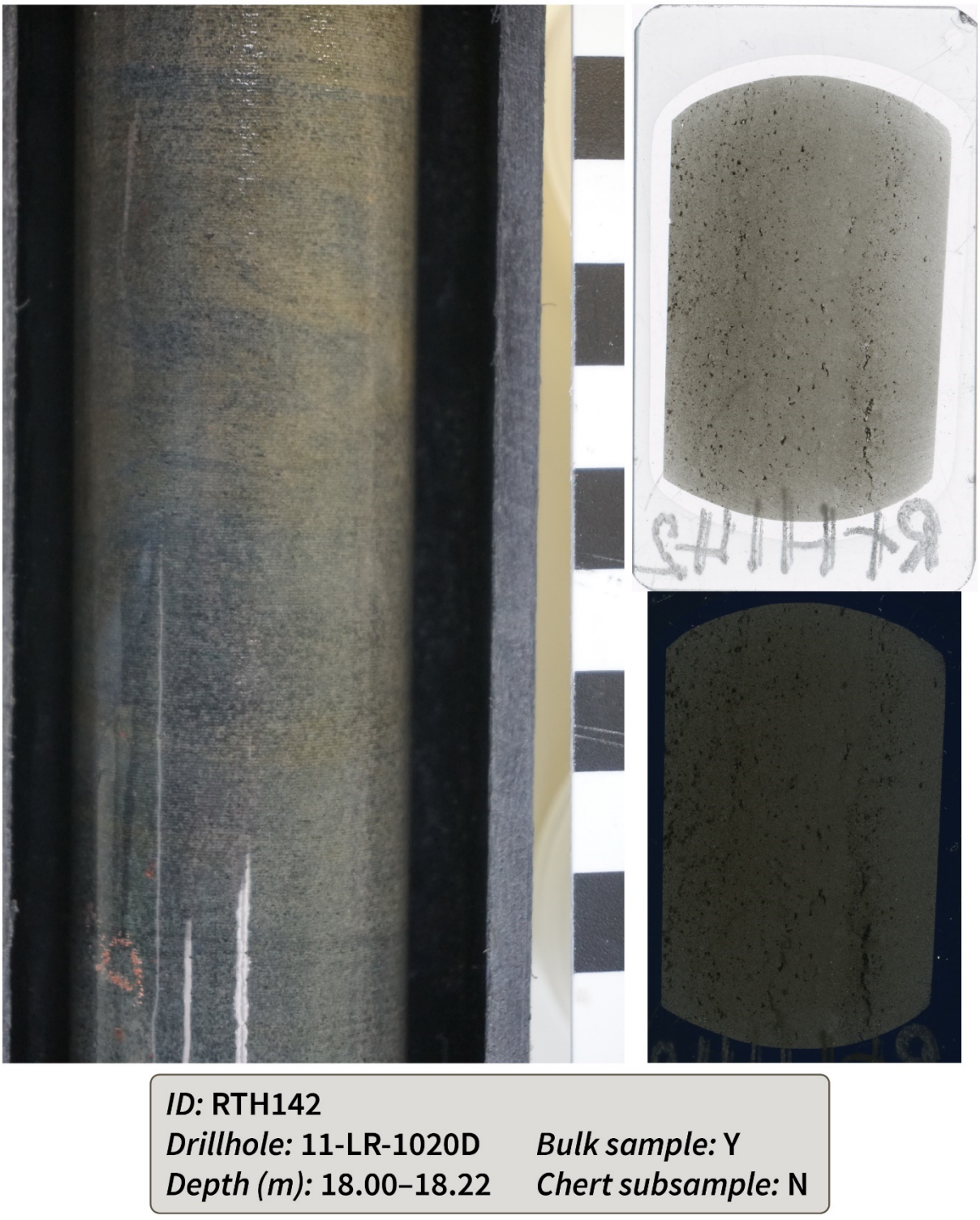

Figure A8.102. Drill core photograph and thin section scans (PPL, XPL) for sample RTH142. Thin section dimensions are 25 x 46 mm.

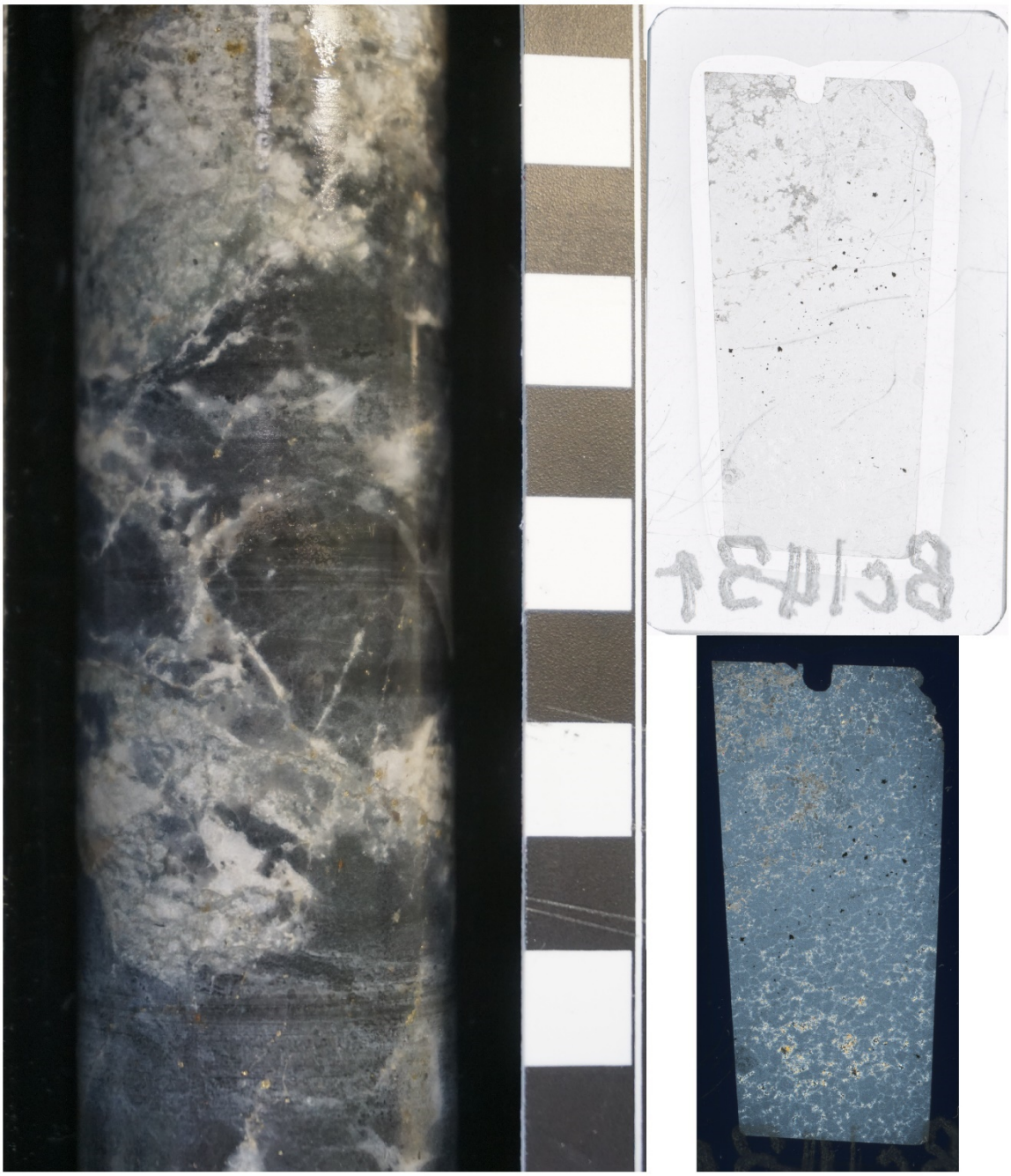

Figure A8.103. Drill core photograph and thin section scans (PPL, XPL) for sample BC143. Thin section dimensions are 25 x 46 mm.

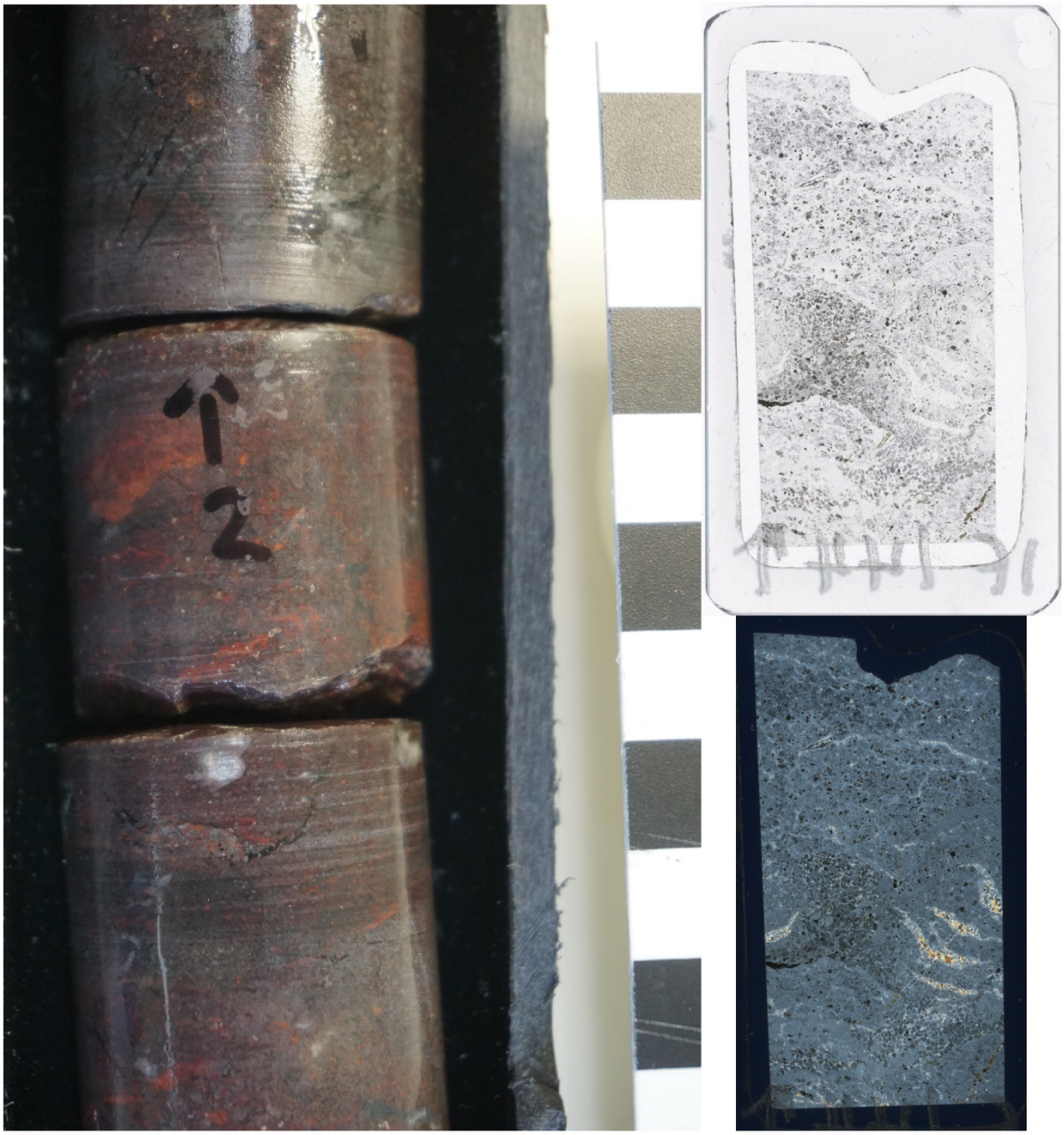

ID: IF144
Drillhole: 11-LR-1020D *Bulk sample:* Y
Depth (m): 22.15–22.30 *Chert subsample:* N

Figure A8.104. Drill core photograph and thin section scans (PPL, XPL) for sample IF144. Thin section dimensions are 25 x 46 mm.

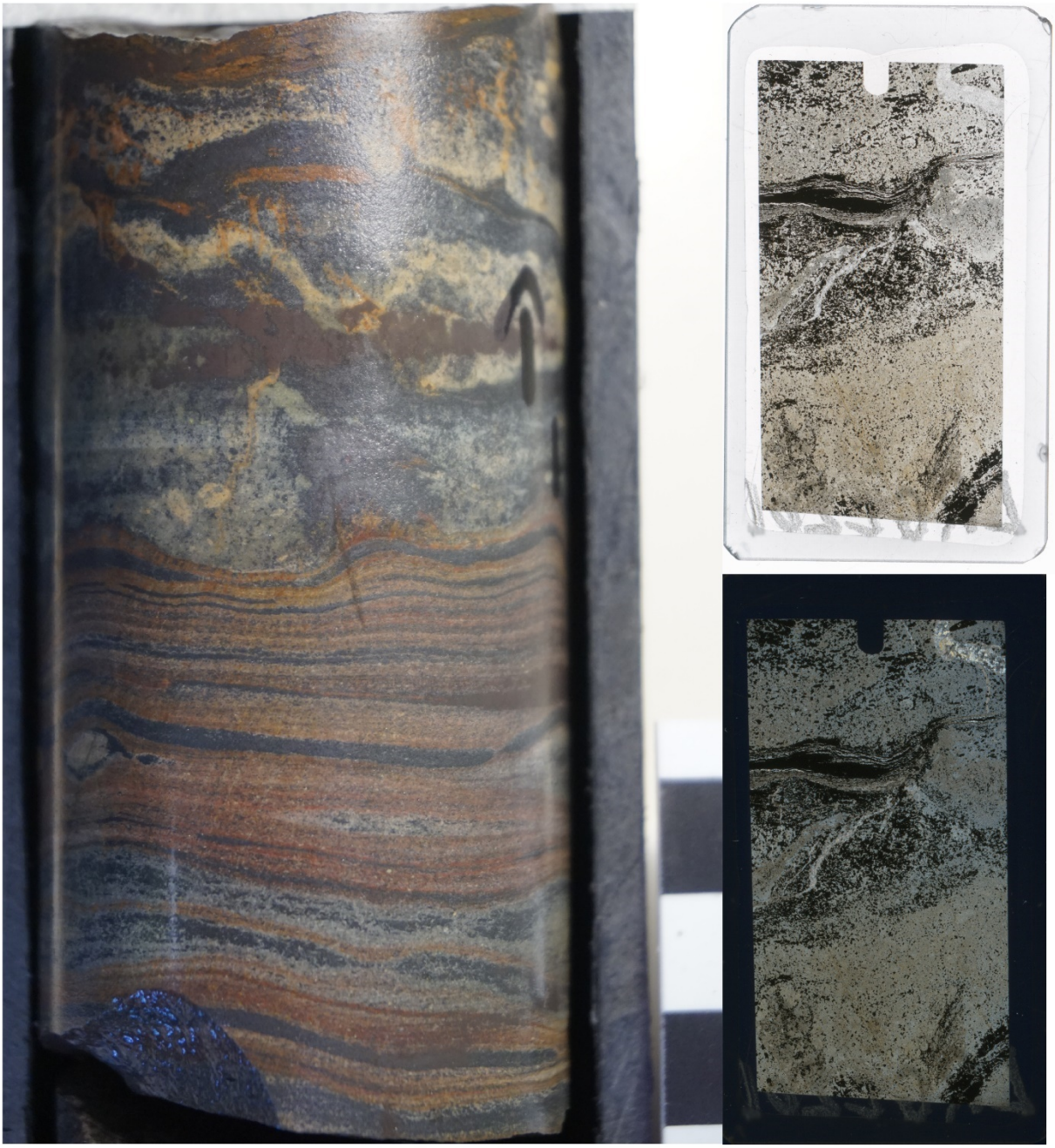

Figure A8.105. Drill core photograph and thin section scans (PPL, XPL) for sample LRGC201. Thin section dimensions are 25 x 46 mm.

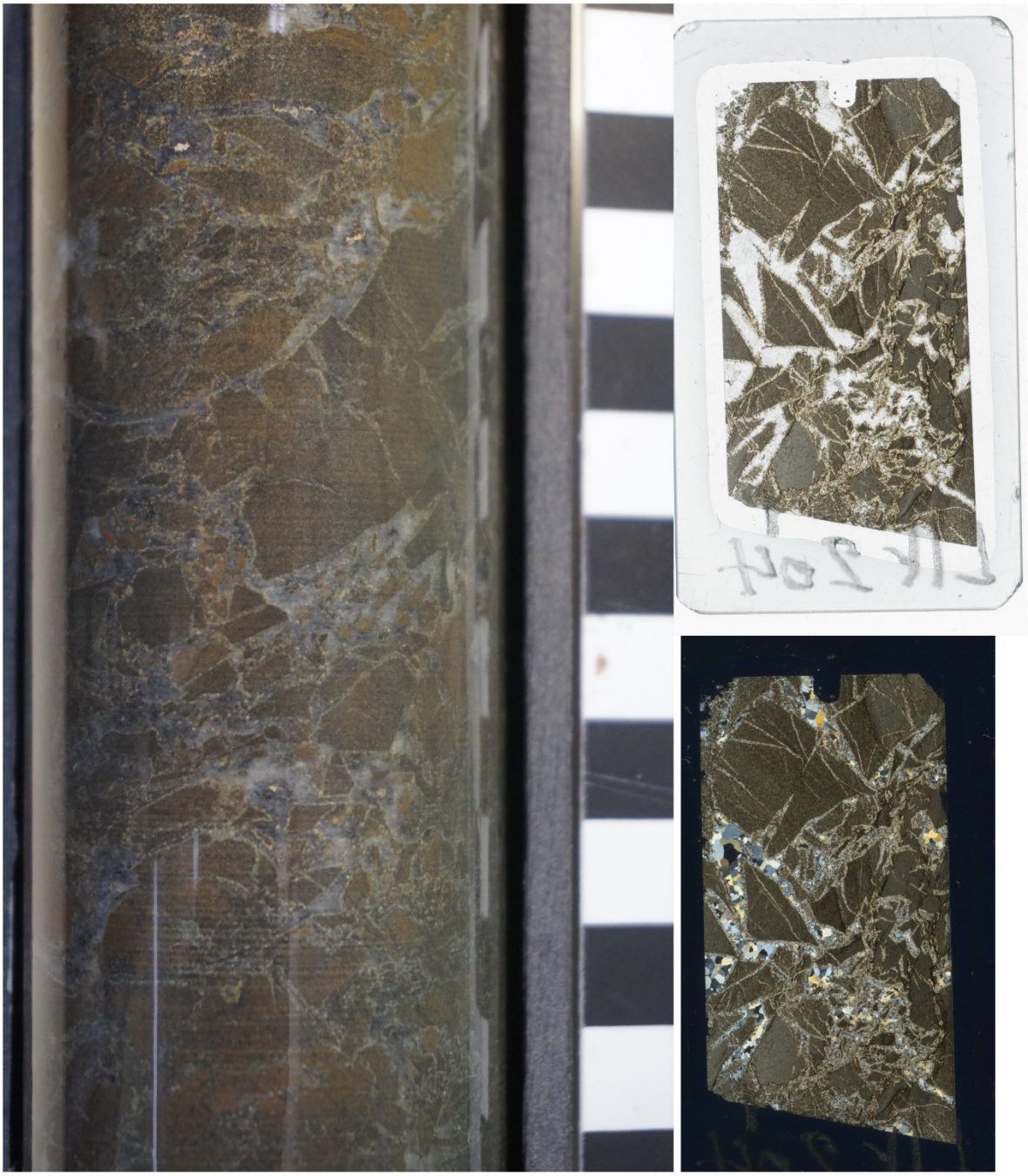

Figure A8.106. Drill core photograph and thin section scans (PPL, XPL) for sample LIF204. Thin section dimensions are 25 x 46 mm.

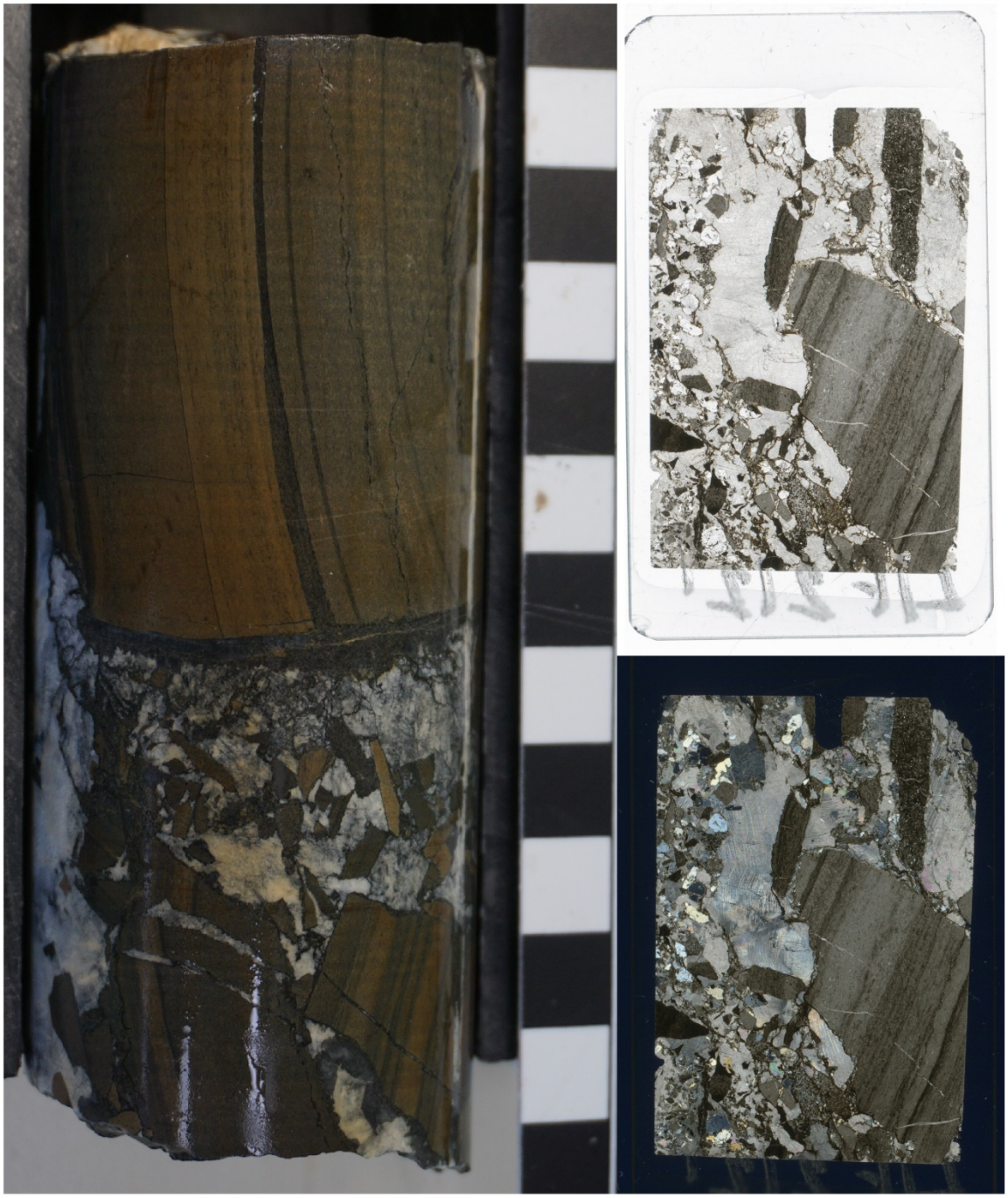

Figure A8.107. Drill core photograph and thin section scans (PPL, XPL) for sample LIF212. Thin section dimensions are 25 x 46 mm.

ID: LC166
Drillhole: HAY-11-07 *Bulk sample:* Y
Depth (m): 59.14–59.29 *Chert subsample:* N

Figure A8.108. Drill core photograph and thin section scans (PPL, XPL) for sample LC166. Thin section dimensions are 25 x 46 mm.

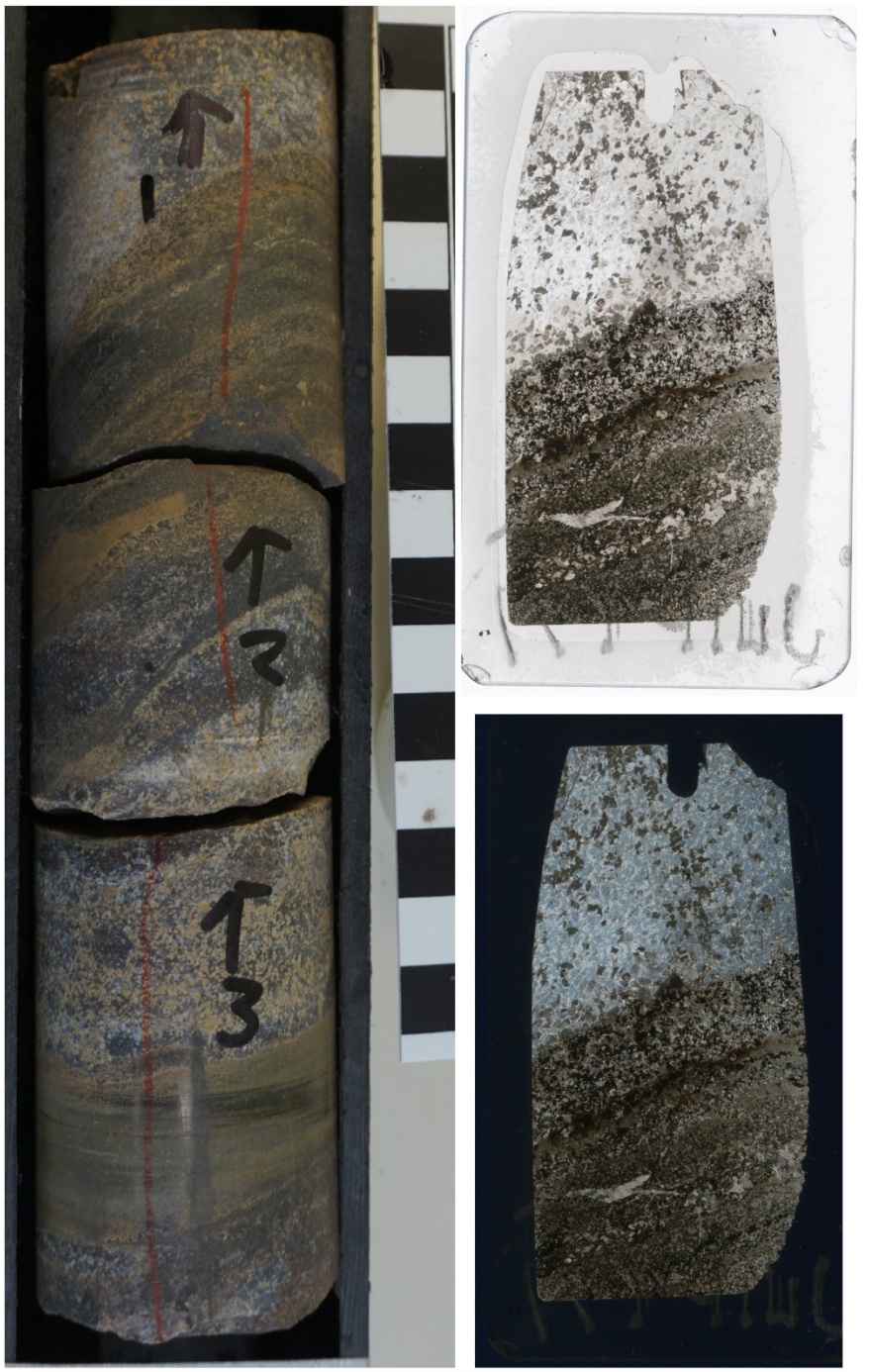

Figure A8.109. Drill core photograph and thin section scans (PPL, XPL) for sample JUIF171. Thin section dimensions are 25 x 46 mm.

ID: JUIF175
Drillhole: HAY-11-07 *Bulk sample:* Y
Depth (m): 85.40–85.50 *Chert subsample:* N

Figure A8.110. Drill core photograph of sample JUIF175.

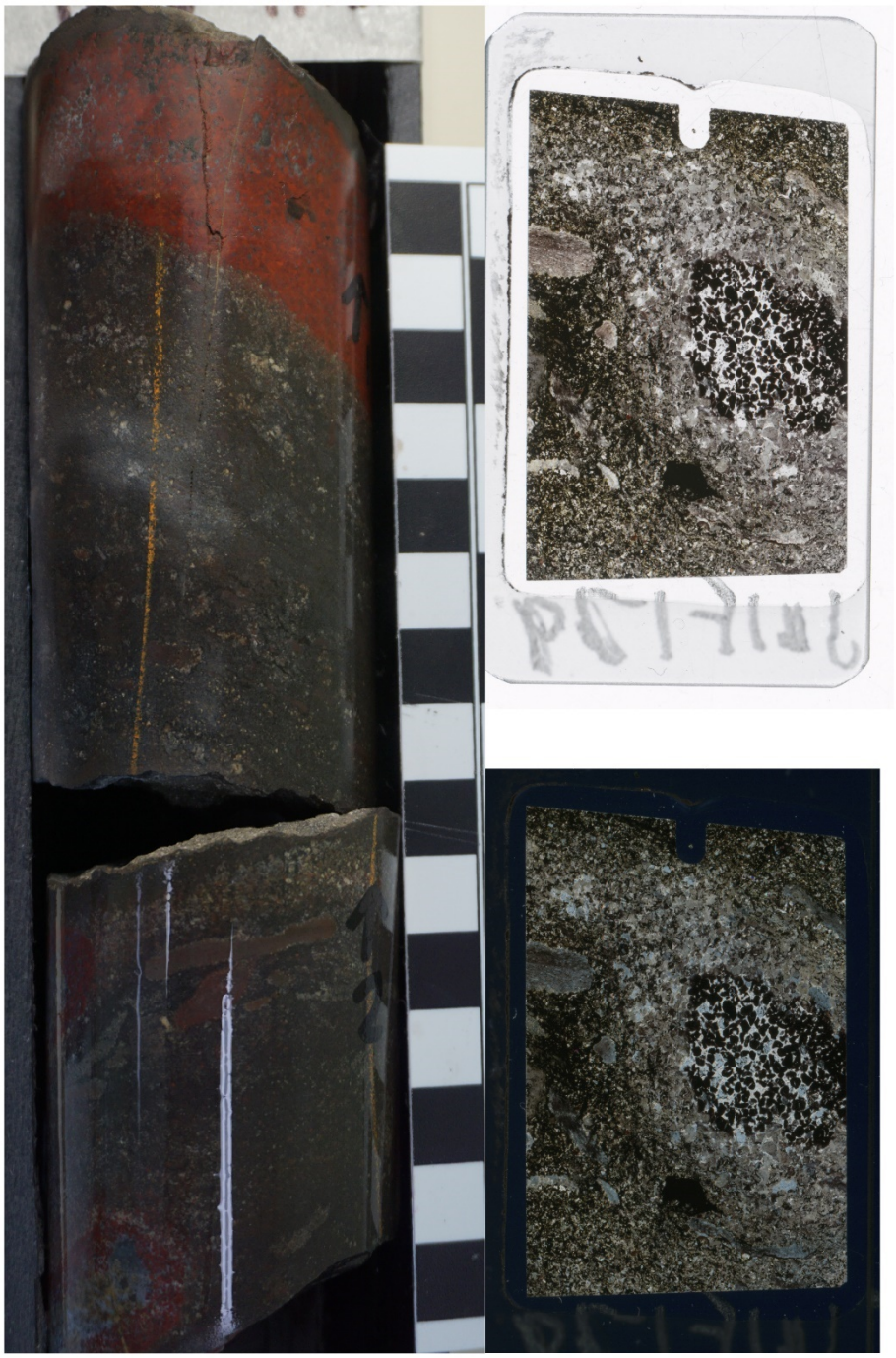

Figure A8.111. Drill core photograph and thin section scans (PPL, XPL) for sample JUIF179. Thin section dimensions are 25 x 46 mm.

ID: GC184
Drillhole: HAY-11-07 *Bulk sample:* Y
Depth (m): 110.89–111.14 *Chert subsample:* N

Figure A8.112. Drill core photograph and thin section scans (PPL, XPL) for sample GC184. Thin section dimensions are 25 x 46 mm.

Figure A8.113. Drill core photograph and thin section scans (PPL, XPL) for sample URC191. Thin section dimensions are 25 x 46 mm.

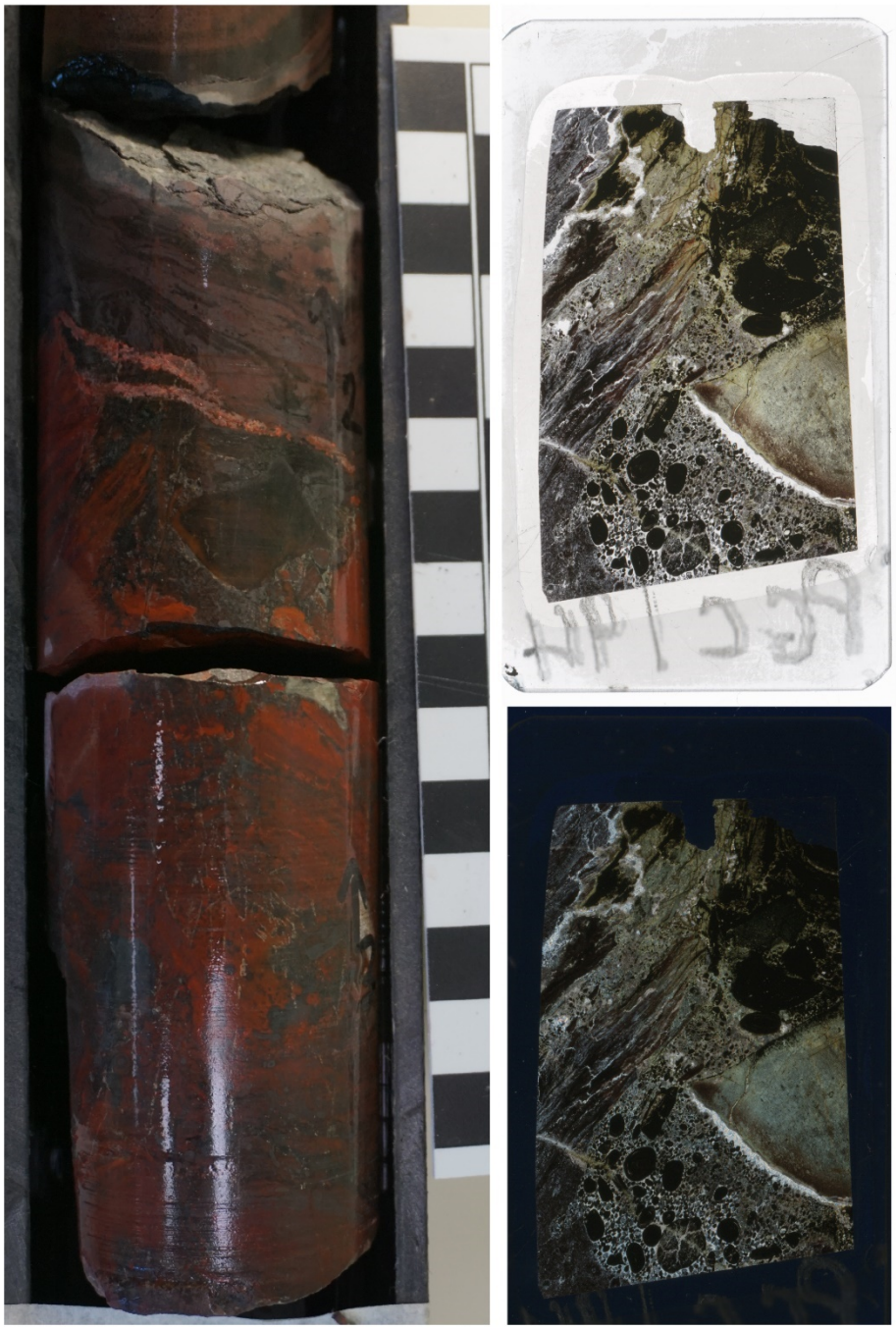

Figure A8.114. Drill core photograph and thin section scans (PPL, XPL) for sample PGC194. Thin section dimensions are 25 x 46 mm.

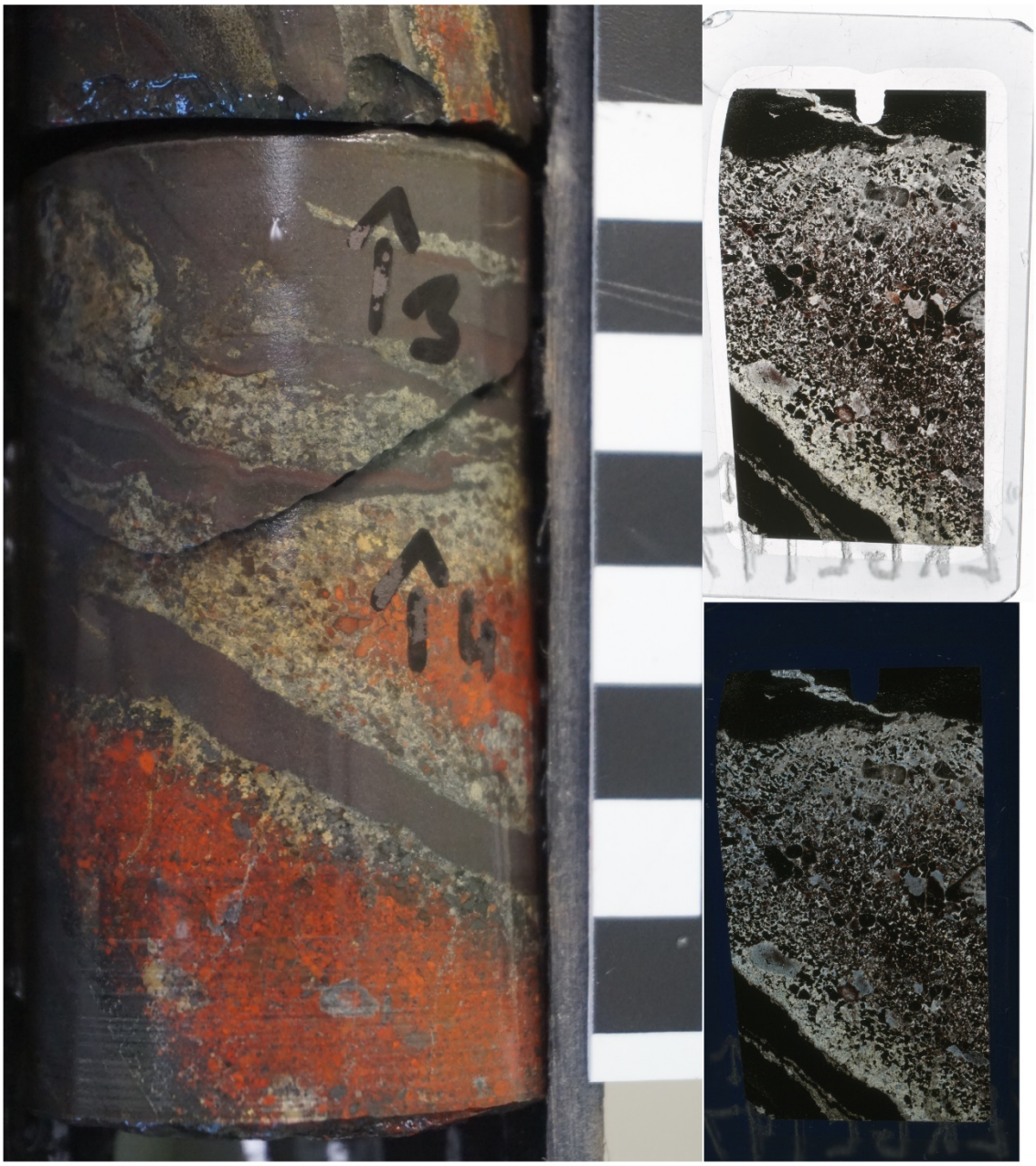

ID: LRGC197
Drillhole: HAY-11-07 *Bulk sample:* Y
Depth (m): 152.82–153.00 *Chert subsample:* Y

Figure A8.115. Drill core photograph and thin section scans (PPL, XPL) for sample LRGC197. Thin section dimensions are 25 x 46 mm.

ID: LRGC198
Drillhole: HAY-11-07 *Bulk sample:* Y
Depth (m): 156.60–156.80 *Chert subsample:* N

Figure A8.116. Drill core photograph and thin section scans (PPL, XPL) for sample LRGC198. Thin section dimensions are 25 x 46 mm.